Stability of welded I-section steel members

Maxime Lebastard

THESE DE DOCTORAT DE

L'INSTITUT NATIONAL DES SCIENCES APPLIQUEES RENNES

ECOLE DOCTORALE N° 602
Sciences pour l'Ingénieur
Spécialité : *Génie civil*

Par

Maxime LEBASTARD

Stability of welded I-section steel members

Thèse présentée et soutenue à l'INSA de Rennes, le 29/11/2022
Unité de recherche : Laboratoire de Génie Civil et Génie Mécanique
Thèse N° : 22ISAR 30 / D22 - 30

Rapporteurs avant soutenance :

Prof. Nicolas BOISSONNADE Université Laval (Canada)
Prof. Jean-Pierre JASPART Université de Liège (Belgique)

Composition du Jury :

Président	Prof. Abdelhamid BOUCHAIR	Université Clermont Auvergne (France)
Examinateurs	Prof. Luis SIMOES DA SILVA	Universidade de Coimbra (Portugal)
	Dr. Laurence DAVAINE	Ingérop (France)
Dir. de thèse	Prof. Mohammed HJIAJ	INSA de Rennes
Co-dir. de thèse	Associate Prof. Maël COUCHAUX	INSA de Rennes

Invité
Alain BUREAU Chef du Service Recherche Construction Métallique – CTICM (France)

Intitulé de la thèse :

Stability of welded I-section steel members.

-

Stabilité des Profilés en acier Reconstitués en I par Soudage

Maxime LEBASTARD

Abstract

Welded I-section members are of common use in steel structures where they are employed as columns and beams. Consequently, such members are subjected to compression force and/or bending moment and may therefore fail owing to out-of-plane buckling.

The present work is organized in two Parts. Elastic buckling is investigated in Part I where lateral-torsional buckling (LTB) with or without web distortion is studied. Analytical expressions are recommended in Chapter II to compute the elastic critical bending moments for both buckling modes based on existing formulations. Chapter III focuses on the elastic LTB of beams with warping restraints at both ends. The derivation of an analytical model yields propositions for the critical bending moment.

Elasto-plastic buckling is studied in Part II. After a review of design rules in Chapter IV, the distribution of residual stresses in welded members is investigated in Chapter V. An influence of the flange fabrication process is noticed and a new model is proposed for members with flame-cut flanges. This model is based on the results of an experimental programme that also included four LTB tests described in Chapter VI. Test results are used to validate the numerical model developed in Chapter VII. Numerical results highlighting a clear influence of the flange fabrication process on the buckling resistance, a parametric study is led. The results are used to propose adaptations of the *Eurocode 3* rules for welded members with flame-cut flanges in Chapter VIII.

Keywords: *Welded members, Elastic buckling, Residual stresses, Buckling resistance.*

Acknowledgments

To every person who has contributed to the outcome of these last three years of doctoral work, I would like to express my deepest gratitude.

First of all, I would like to thank my supervisor, Professor Mohammed Hjiaj without whom working this thesis would not have been possible. I am thankful for having provided me with this opportunity to enter the field of research. All his wise advices and encouragements were of great help to accomplish this work.

I am also very grateful to my co-supervisor Professor Maël Couchaux for all his goodwill, guidance and dedication to my work. His implication in my doctoral work through accurate and constructive criticisms was of great importance. He always pushed me forward and our discussions brought me into the bottom of the matter.

My last co-supervisor, Alain Bureau, is deeply acknowledged as well. As the Head of the Steel Construction Research Division of CTICM, his experience and knowledge were essential to this work. His words helped me to step back from my work and to always keep in mind that research is to be applied.

For the successful execution of the experimental programme described in this thesis, I express my gratitude to the laboratories of Polytech' Clermont and the University of Liège. In particular, I thank Professor Sébastien Durif and Carl Vroomen with their respective teams for their very professional work. This experimental programme owes also a lot to Briand Group that is deeply acknowledged for the generous fabrication of all the test specimens.

Besides, I would like to thank all my coworkers at CTICM for their continuous support and friendship. Special thanks to my collegues of the Steel Construction Research Division for the great working atmosphere. In particular, I would like to express my gratitude to Véronique for her thorough proofreading of this thesis and to André for all his relevant advices regarding my research work.

For the financial support of my doctoral work, I would like to express my deepest gratitude to the CTICM.

I would like to express my sincere gratitude to Professors Nicolas Boissonnade, Jean-Pierre Jaspart, Abdelhamid Bouchair and Luis Simões da Silva, and to Dr. Laurence Davaine who agreed to devote some of their valuable time to evaluate my work.

Eventually, I thank all of my friends and family for their continuous support at all times. In particular, I address all my loving gratitude to my parents, my sister Émilie, and my true love Blandine.

Résumé étendu

Grâce à la liberté de conception qu'ils offrent théoriquement, les Profilés en acier Reconstitués par Soudage (PRS) sont couramment employés pour la construction de portiques de bâtiments. En effet, contrairement aux profilés laminés à chaud, les PRS permettent une optimisation de la matière, le choix des dimensions des sections transversales et de leurs éventuelles variations étant libres.

Utilisés en tant que poteaux ou bien traverses de portique, ces éléments sont généralement soumis à des efforts de compression uniaxiale et/ou de flexion dans leur plan de forte inertie. Les composants structuraux de bâtiments métalliques pouvant être relativement élancés, leur ruine résulte généralement d'instabilités telles que le flambement (cas des poteaux) ou le déversement (poutres et poteaux). Lors de la conception de ces éléments comprimés et/ou fléchis, il convient alors de se prémunir contre tout risque d'instabilité en appliquant les prescriptions de la norme de calcul européenne, l'*Eurocode 3 Partie 1-1*.

Le calcul de la résistance élasto-plastique d'un PRS vis-à-vis du flambement et/ou du déversement $R_{b,Rd}$ selon l'*Eurocode 3 Partie 1-1* est basée sur les aspects suivants :

- La détermination d'un effort critique d'instabilité élastique R_{cr} et
- La prise en compte des imperfections inhérentes à la fabrication d'un PRS à travers un facteur d'imperfection α.

L'objectif du présent travail portant sur la stabilité des PRS de bâtiments est d'améliorer la pratique actuelle concernant ces deux aspects comme décrit au Chapitre I. Par conséquent, la présente thèse est divisée en deux parties : la Partie I concerne les instabilités élastiques et la Partie II traite le cas des instabilités élasto-plastiques.

En s'appuyant sur la méthode énergétique, les expressions des efforts critiques les plus courants sont rappelés au Chapitre II. Celles-ci concernent le flambement par flexion (voir Figure 1a)) suivant les deux directions principales, par torsion ou bien par flexion-torsion des poteaux, et le déversement des poutres (voir Figure 1b)). L'expression exacte de cette dernière charge critique est obtenue dans le cas simple d'une distribution uniforme des moments alors que d'autres distributions sont plus fréquemment rencontrées en pratique.

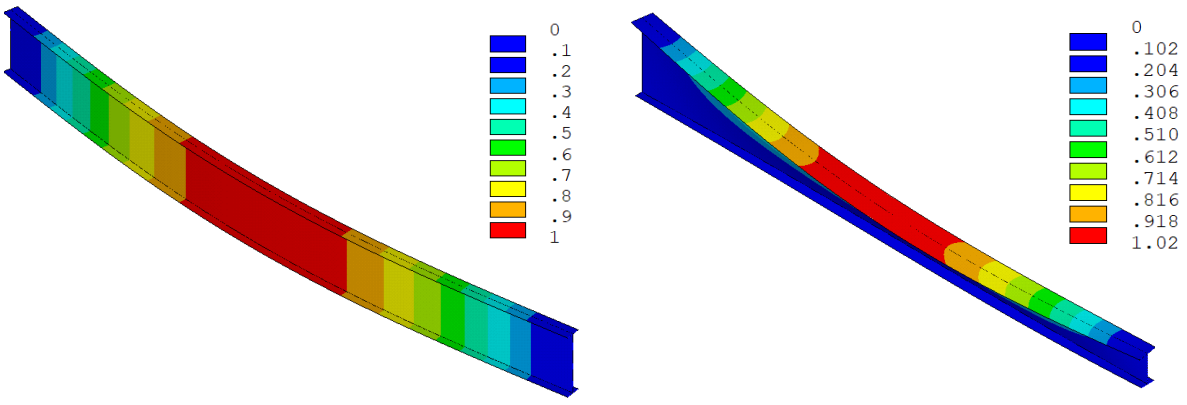

a) *Flambement latéral d'un poteau uniforme* b) *Déversement d'une poutre en fuseau*

Figure 1 : Modes d'instabilité élastique (déplacements totaux)

Des modèles analytiques existants permettant de déterminer le moment critique de déversement élastique d'une poutre à section mono-symétrique (symétrie par rapport au plan de flexion) sont alors présentés. Ils concernent différents cas de chargement : moments d'extrémités, charge(s) transversale(s) ponctuelle(s) ou répartie. Les prévisions de ces modèles sont comparées à des résultats de référence obtenus par l'intermédiaire d'analyses par éléments finis réalisés en utilisant des éléments de type poutre. De ces comparaisons résulte la recommandation d'un modèle analytique, principalement basé sur les propositions de l'*Eurocode 9 Partie 1-1* qui s'appliquent à l'acier en utilisant les caractéristiques matériaux adéquates.

Les instabilités élastiques des éléments uniformes comprimés et fléchis et/ou à inertie variable sont également évoquées. Du fait de la complexité des phénomènes, il est recommandé de procéder à un calcul par éléments finis, de type poutre (via le logiciel *LTBeamN* par exemple) ou coque.

Alors que le déversement est caractérisé par le déplacement latéral et la rotation de torsion des sections transversales (voir Figure 2a)), la ruine de certaines poutres présentant des âmes très élancées et/ou de larges et épaisses semelles est causée par un déversement avec distorsion d'âme. Ce type d'instabilité est investigué dans le cas de poutres à section doublement symétrique et soumises à un moment constant, pour lesquelles l'âme se déforme en double courbure (voir Figure 2b)). Un état de l'art des expressions existantes de ce moment critique d'instabilité élastique est proposé. Parmi ces expressions, différentes approches sont adoptées :

- L'utilisation de l'expression du moment critique (âme non déformée) avec des rigidités équivalentes pour la torsion, le gauchissement et éventuellement la flexion hors du plan de sollicitation ;
- L'utilisation de l'expression du moment critique (âme indéformée) multipliée par un coefficient réducteur, en négligeant éventuellement l'inertie de torsion ;
- L'utilisation d'une expression obtenue par la méthode énergétique basée sur des champs de déplacement et rotation adaptés.

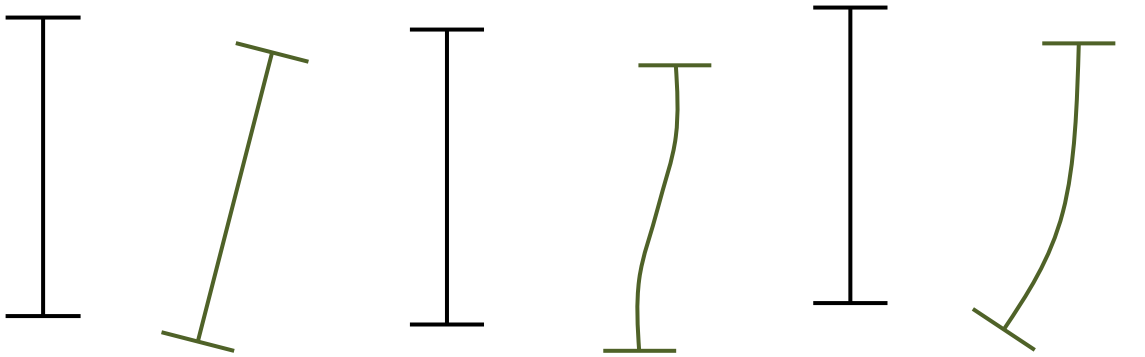

Figure 2 : Section transversale initiale et à la ruine d'une poutre ayant déversé

Par comparaison à des résultats numériques obtenus en utilisant des éléments finis de type coque, les modèles analytiques résultant de la dernière approche offrent les meilleurs résultats. L'utilisation de rigidités équivalentes en torsion et gauchissement (seulement) peut également produire des résultats satisfaisants. L'un des modèles développés à partir de la méthode énergétique est exploité pour déterminer une limite quant à l'influence de la distorsion de l'âme sur le déversement, dans le cas d'un moment constant.

L'influence de la forme du diagramme de moment sur la distorsion d'âme est ensuite analysée. Alors que différents modèles analytiques existent pour déterminer le moment critique de déversement avec distorsion d'âme dans le cas d'un moment constant, un manque de propositions est noté pour d'autres diagrammes de moments. Les prédictions des modèles analytiques satisfaisants pour un moment constant sont étudiées pour un moment linéairement variable en faisant intervenir le coefficient de moment uniforme équivalent C_1. La comparaison au calcul par éléments finis de type coque montre que ces modèles sont acceptables lorsque le ratio ψ entre moments d'extrémités est élevé. L'âme se déforme toujours en double courbure. Pour des valeurs plus faibles de ψ, l'âme se déforme en simple courbure (voir Figure 2c)) et aucun modèle analytique existant n'est satisfaisant. Ce problème très complexe requiert la détermination de champs de déplacement et de rotation adaptés pour appliquer la méthode énergétique et obtenir des expressions analytiques adéquates. Puisque de telles expressions font actuellement défaut, l'utilisation du calcul par éléments finis de type coque reste la meilleure option pour déterminer le moment critique de déversement d'une poutre dont l'âme est susceptible de se déformer.

Le moment critique de déversement d'une poutre est généralement calculé en supposant des appuis à fourches à ses extrémités avec le gauchissement et la rotation hors plan libres. Néanmoins, la présence d'assemblages poteau-poutre ou de continuité de poutres peut induire un maintien significatif vis-à-vis du gauchissement. Cet effet est couramment négligé bien que son incidence sur le moment critique ne soit pas neutre. Ainsi, l'influence de maintiens vis-à-vis du gauchissement aux extrémités d'une poutre à section doublement symétrique sur son moment critique de déversement est étudiée (voir Figure 3) au Chapitre III. Des expressions existantes sont présentées mais se limitent généralement à un cas de chargement. Le modèle plus général de *Piotrowski* (2019) est présenté mais les expressions correspondantes sont lourdes à utiliser. Par conséquent, un modèle analytique est développé en utilisant la méthode énergétique basée sur des expressions du déplacement latéral et de la rotation de torsion adaptées faisant usage de fonctions trigonométriques.

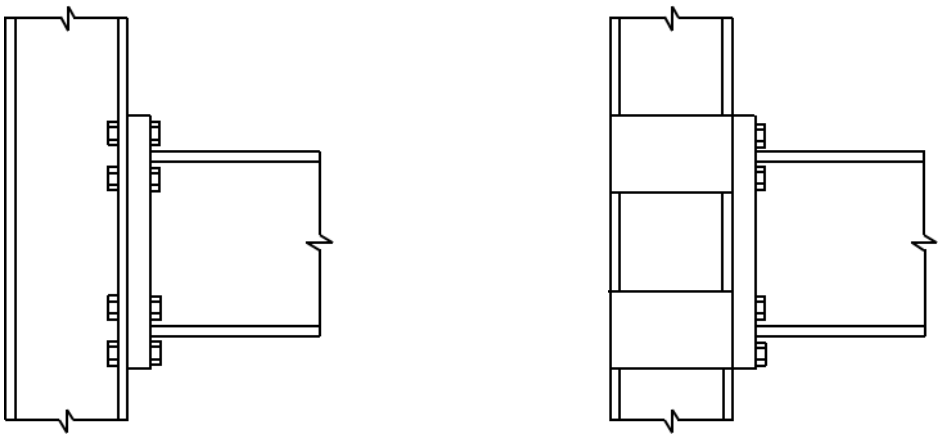

a) *Platine d'extrémité* b) *Platine et raidisseurs*

Figure 3 : Assemblages poteau-poutre permettant un maintien vis-à-vis du gauchissement

L'utilisation d'un unique terme pour les champs de déplacement de rotation est acceptable dans le cas d'un moment constant ou bien d'un chargement transversal ponctuel à mi-portée ou réparti le long de la poutre. Pour un diagramme des moments linéairement variable, les champs de déplacement et de rotation sont enrichis d'un second terme. Quel que soit le diagramme des moments, la raideur c_w des maintiens au gauchissement est explicitement prise en compte dans les expressions de C_1 et du coefficient de

gauchissement k_w. L'expression de k_w est unique quel que soit le chargement alors que C_1 dépend également de la forme du diagramme des moments.

Des expressions simplifiées sont également proposées pour C_1 correspondant à la multiplication de :

- Un facteur dépendant uniquement du diagramme des moments, par
- Un facteur dépendant uniquement de la raideur des maintiens au gauchissement.

Les prédictions du modèle analytique développé sont comparées aux résultats de simulations par éléments finis réalisés en utilisant des éléments finis de type poutre ou coque. La comparaison à ces résultats de référence permet de valider le modèle analytique développé comme le montre la Figure 4 dans le cas d'un moment constant. Celle-ci expose un net gain du moment critique M_{cr} lorsque des maintiens au gauchissement sont pris en compte par rapport à sa valeur $M_{cr,0}$ qui les néglige. Lorsque le gauchissement est totalement bloqué, le moment critique peut être doublé par rapport au cas où il est supposé libre.

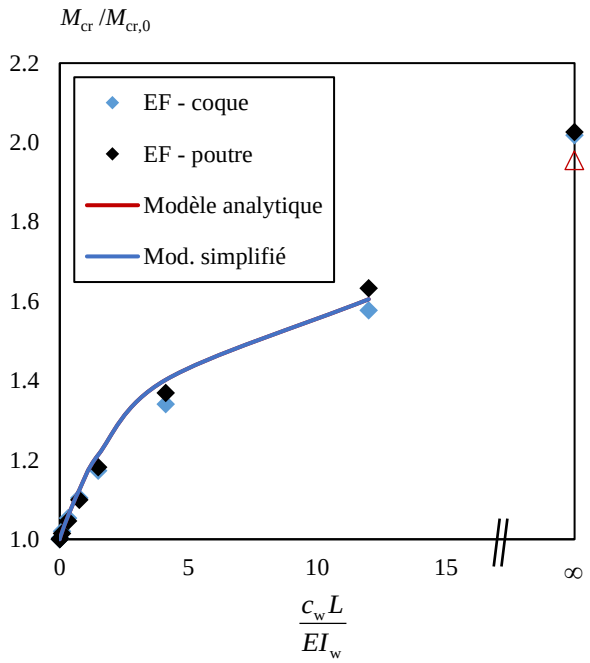

Figure 4 : Augmentation du moment critique en fonction de la raideur des maintiens au gauchissement

Pour compléter cette étude, une valeur limite de la raideur c_w est développée à partir de laquelle le moment critique de déversement peut être déterminé en supposant le gauchissement totalement bloqué aux extrémités. La raideur de différentes configurations de maintiens au gauchissement communément mis en place est rappelée et celle d'un pied de poteau encastré en flexion est développée. La possibilité d'étendre le critère pour supposer le gauchissement totalement bloqué à une seule extrémité est étudié. Des résultats analytiques sont comparés à des résultats de référence obtenus numériquement en faisant intervenir des éléments finis de type poutre, validant une adaptation de ce critère.

Comme suite à l'étude des instabilités élastiques, la seconde partie de ce travail porte sur les instabilités élasto-plastiques, prenant en compte les différentes imperfections des éléments « réels ». Dans un premier temps, le Chapitre IV rappelle l'ensemble des règles de calcul permettant de déterminer la résistance d'un PRS vis-à-vis du flambement et/ou du déversement. Les règles de l'actuel *Eurocode 3 Partie 1-1* et de sa révision sont présentées avec leurs adaptations dans son *Annexe Nationale Française*.

La résistance vis-à-vis du flambement ou du déversement peut s'obtenir en utilisant l'une des courbes de flambement de l'*Eurocode 3 Partie 1-1* représentées à la Figure 5. La résistance $R_{b,Rd}$ à un effet donné se calcule alors en diminuant la résistance caractéristique en section R_{Rk} en fonction de (i) l'élancement de l'élément et (ii) la courbe de flambement utilisée. Chaque courbe de flambement étant associée à un facteur d'imperfection, le choix de la courbe dépend du niveau d'imperfection affilié à l'élément étudié. Ainsi, ce choix dépend du mode de fabrication de l'élément, de sa nuance d'acier, de ses dimensions transversales et du mode d'instabilité étudié, la stabilité hors plan des PRS étant associée aux deux courbes les plus pénalisantes (*c* et *d*). D'autres méthodes de vérification des éléments simplement fléchis peuvent faire intervenir un coefficient d'imperfection dépendant des propriétés géométriques de la section transversale ainsi que la forme du diagramme des moments.

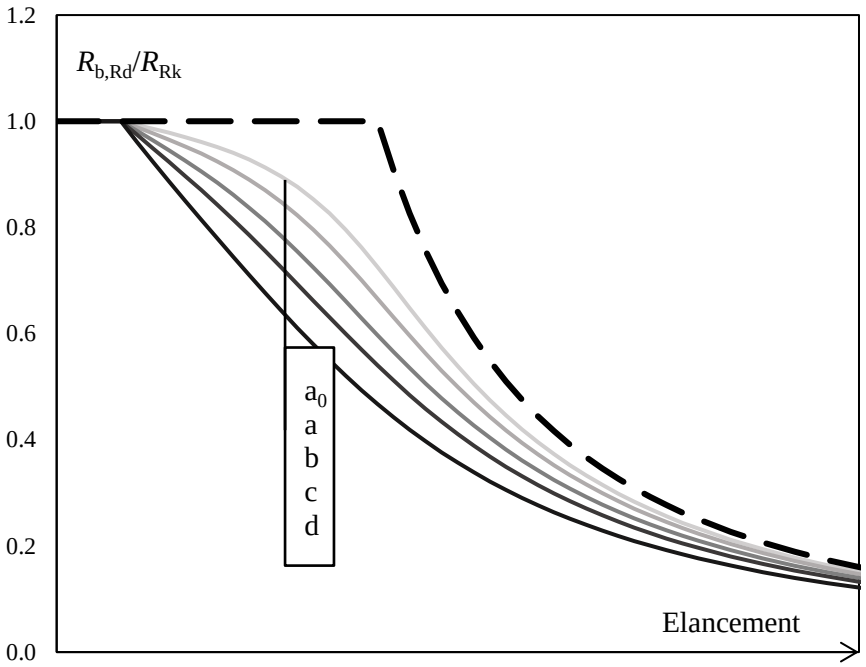

*Figure 5 : Courbes de flambement de l'*Eurocode 3 Partie 1-1

Pour la vérification des éléments simultanément comprimés et fléchis, l'*Eurocode 3 Partie 1-1* propose deux méthodes. Une première méthode n'est utilisable que dans le cas de poteau-poutres à section uniforme et doublement symétrique. Dans ce cas, il convient de vérifier parallèlement deux formules d'interaction correspondant à des directions de ruine différentes et indépendantes (dans le plan et hors du plan de forte inertie). La seconde méthode permet de s'assurer de la stabilité d'un élément comprimé et fléchi n'ayant pas nécessairement une section uniforme et doublement symétrique. La combinaison du flambement et du déversement est interprétée comme une instabilité globale hors plan mais cette méthode implique un couplage des comportements suivant les deux directions principales. Cette seule méthode proposée pour vérifier la stabilité d'un élément non uniforme étant discutée, des méthodes de calcul récentes sont décrites.

L'une des trois approches détaillées propose notamment de déterminer la résistance vis-à-vis du déversement en utilisant le coefficient d'imperfection pour le flambement d'axe faible et les propriétés en torsion de la section transversale (voir *Naumes* (2009)). Cette méthode manque toutefois d'indications concernant le traitement de poutres à inertie variable. Une autre approche propose d'étudier les éléments comprimés et/ou fléchis à inertie variable en suivant les règles de l'*Eurocode 3*

Partie 1-1, initialement adaptées aux éléments uniformes, moyennant quelques modifications (voir *Marques* (2012 a)). Une adaptation des formules d'interaction aux éléments à inertie variable est alors proposée en utilisant des indications résultant d'études paramétriques.

Enfin, une méthode de calcul plus générale est décrite permettant d'attester la stabilité d'un élément comprimé et/ou fléchi, présentant des conditions de maintiens arbitraires et une section uniforme ou non (voir *Tankova* (2018a)). Cette dernière méthode utilise une approche très réaliste mais requiert la détermination de la forme du mode propre d'instabilité élastique de l'ensemble étudié, c'est-à-dire de l'élément et des conditions de chargements et maintiens. Pour ce faire, l'utilisation de logiciels de calcul par éléments finis, tels que *LTBeamN* est possible. Néanmoins, la dérivée seconde de la forme du mode propre doit également être connue, ce qui limite le déploiement de cette méthode pour un usage régulier.

Selon l'ensemble des méthodes de calcul existantes, la résistance d'un PRS est identique quel que soit son mode de fabrication. Cependant, différents modes de fabrication des semelles impliquent différentes contraintes résiduelles, faisant l'objet du Chapitre V. Ces imperfections de matériau sont, avec les imperfections géométriques (défaut de rectitude global, imperfections locales), les deux types d'imperfections influençant la stabilité élasto-plastique d'un élément structural. Les règles de calcul actuelles correspondent aux PRS ayant pour semelles de larges plats laminés à chaud alors que d'autres étapes de fabrication supplémentaires sont couramment utilisés en pratique, comme l'oxycoupage. Les semelles de PRS étant de larges plats laminés sont appelées « *semelles laminées* ». Celles correspondant à des plats laminés séparés sur leur largeur par oxycoupage sont appelées « *semelles oxycoupées* ». La forme des contraintes résiduelles est présentée à la Figure 6a) pour les PRS à semelles laminées et à la Figure 6b) pour ceux à semelles oxycoupées.

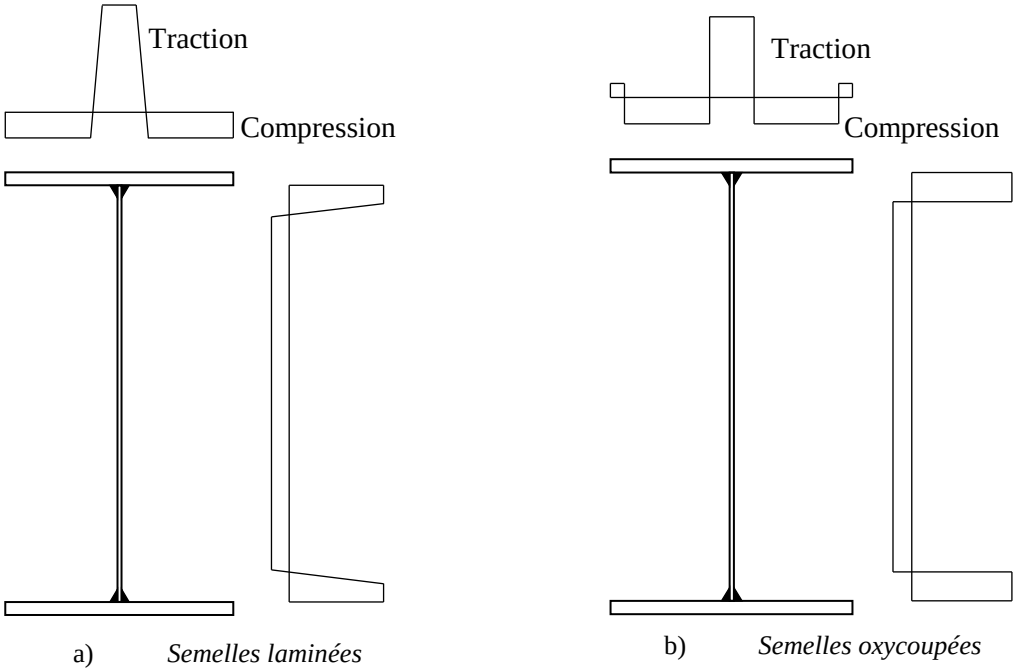

Figure 6 : Distribution des contraintes résiduelles dans un PRS

Un recensement des modèles existants de contraintes résiduelles de PRS à semelles laminées ou oxycoupées sur leurs deux bords est donc entrepris. Bien que les modèles varient suivant les références, l'oxycoupage des semelles a un impact significatif sur les contraintes résiduelles. En effet, alors que les bords libres des semelles laminées sont initialement en compression (voir Figure 6a)), ceux des semelles oxycoupées sont en traction (voir Figure 6b)), les intensités de ces contraintes variant suivant les études.

La présence de traction initiale aux bords libres de semelles permet de retarder le début de leur plastification entraînant la ruine par instabilité hors plan du PRS. L'oxycoupage présente alors un intérêt bénéfique vis-à-vis de la stabilité d'un PRS.

Les différents modèles de contraintes résiduelles pour PRS à semelles oxycoupées présentant de nettes divergences, une campagne expérimentale visant à mesurer les contraintes résiduelles dans huit PRS est menée à l'Université de Liège. Les caractéristiques des éprouvettes sont déterminées de sorte à être représentatives de la pratique courante. Ainsi, les poutrelles étudiées sont fabriquées en acier S355. Alors que les dimensions des âmes sont identiques entre les 8 spécimens, les dimensions des semelles et leur mode de fabrication varient. Des épaisseurs de 12, 15 et 20 mm sont étudiées pour des largeurs de 200 et 250 mm. Deux couples de spécimens présentent des dimensions similaires avec, dans chaque cas, un PRS à semelles oxycoupées et l'autre à semelles laminées. Les quatre autres spécimens présentent tous des semelles oxycoupées dont une section mono-symétrique.

L'analyse des résultats montre une incidence significative du mode de fabrication des semelles sur la distribution des contraintes résiduelles. Par ailleurs, la largeur des semelles influe légèrement sur cette répartition contrairement à leur épaisseur. Les distributions expérimentales mesurées dans les PRS à semelles oxycoupées s'avèrent différentes des modèles existants. En conséquence, les résultats expérimentaux sont étudiés avec une vingtaine d'autres résultats issus de la littérature concernant des PRS à semelles oxycoupées représentatifs de la pratique courante.

L'ensemble de ces résultats montre que l'intensité de la contrainte de compression dans les semelles diminue lorsque leur élancement augmente. De même une diminution de l'intensité de la contrainte de traction aux bords libres des semelles est observée lorsque le rapport hauteur/largeur de la section transversale augmente. La largeur relative en traction de la partie centrale des semelles augmente également avec ce ratio. Cette analyse a permis d'aboutir à un nouveau modèle de contraintes résiduelles adapté aux PRS à semelles oxycoupées représenté schématiquement à la Figure 6b). Ce modèle est constitué de blocs de contraintes dont les largeurs et intensités dépendent :

- Du rapport largeur/épaisseur de semelle,
- Du rapport hauteur totale/largeur de la section transversale, et
- De l'auto-équilibre des contraintes.

Le flambement et le déversement expérimental de PRS sont ensuite investigués au Chapitre VI. Un recensement des campagnes expérimentales concernant des PRS comprimés et/ou fléchis dans leur plan de forte inertie, décrites dans la littérature, est présenté. Certains essais confirment un gain significatif de résistance apporté par l'oxycoupage en comparaison à des PRS à semelles laminées de dimensions équivalentes. Cette revue de la littérature montre néanmoins un manque de résultats expérimentaux concernant des PRS à semelles oxycoupées à section non-uniforme et/ou mono-symétrique représentatifs de la pratique courante.

Un nouveau programme expérimental réalisé à Polytech' Clermont est alors présenté, visant l'étude du déversement de quatre poutres PRS ayant des semelles oxycoupées. Parmi ces spécimens, fabriqués en acier S355, se trouvent :

- Une poutre à section constante et doublement symétrique (représentée à la Figure 7a)),
- Une poutre à section constante et mono-symétrique,
- Une poutre à section variable et doublement symétrie, et
- Une poutre à section variable et mono-symétrique (représentée à la Figure 7b)).

Pour simplifier la mise en place expérimentale, les spécimens à section mono-symétrique présentent des semelles de même largeur, 200 mm, ce qui correspond à une partie de la pratique courante. Dans ce cas, les épaisseurs de semelles varient, la semelle comprimée étant de 20 mm et la semelle tendue de 15 mm, soit la même épaisseur que les deux semelles de chaque spécimen à section doublement symétrique. La variation de hauteur d'âme est similaire dans les deux poutres à inertie variable (voir Figure 7b)).

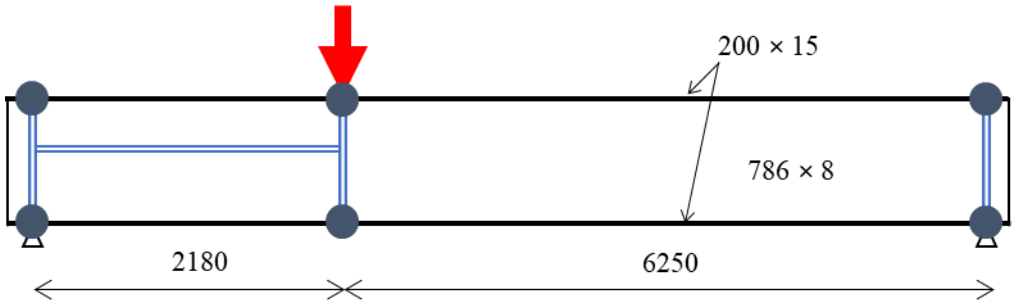

a) *Poutre à section uniforme et doublement symétrique*

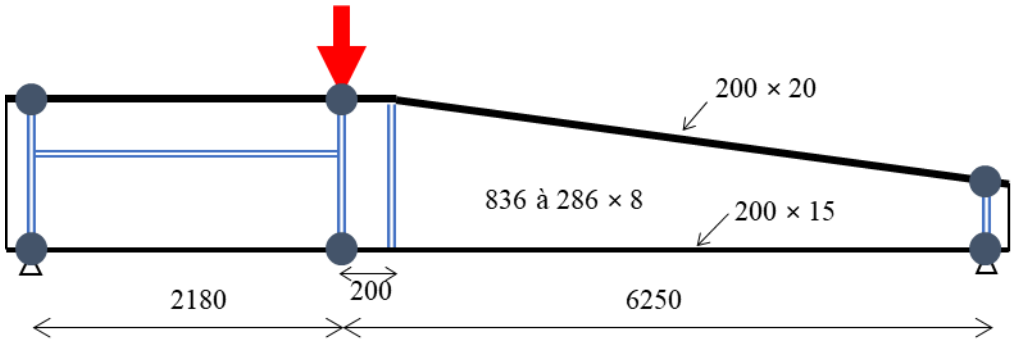

b) *Poutre à section variable et mono-symétrique*

Figure 7 : Spécimens d'essais au déversement

Le schéma statique des quatre essais est similaire (voir Figure 7). Les poutres reposent sur des appuis à fourche à leurs extrémités, le gauchissement et la rotation hors du plan de sollicitation étant libres. Une section intermédiaire est maintenue latéralement sur toute sa hauteur et chargée par un vérin hydraulique appliqué au centre de la semelle comprimée.

Pour les quatre spécimens testés, le mode de ruine correspond au déversement comme le montre la Figure 8 dans le cas de la poutre à section variable et mono-symétrique. Par ailleurs, une distorsion de l'âme dans le domaine post-pic est observée dans le cas de la poutre à section constante et mono-symétrique. Les ruines sont observées à la frontière des domaines élastique et élasto-plastique, sauf pour le spécimen à section constante doublement symétrique dont la ruine a eu lieu dans le domaine élastique. Alors que les charges de ruine des deux spécimens à section doublement symétrique sont proches, l'augmentation de 5 mm de l'épaisseur de la semelle comprimée accroît de plus de 20% la charge de ruine dans le cas de sections constantes. L'augmentation de la charge de ruine est plus mesurée dans le cas des spécimens à inertie variable, la différence étant de 8%.

Pour l'ensemble des spécimens, la comparaison de la charge de ruine expérimentale à celle obtenue analytiquement en suivant les prescriptions de l'*Eurocode 3 Partie 1-1* en utilisant les courbes de flambement montre des écarts de 62 à 81%. La prise en compte explicite du diagramme de moment à l'aide du facteur *f* réduit l'écart qui se situe alors entre 42 et 58%. Les méthodes de calcul actuelles, qui ne prennent pas en compte l'effet bénéfique de l'oxycoupage des semelles, sont excessivement

sécuritaires. Ce constat a motivé la nécessité de prendre en compte explicitement le mode de fabrication des semelles d'un PRS dans le calcul de la résistance aux instabilités hors plan.

Figure 8 : Ruine de la poutre à section variable et mono-symétrique

Le développement de méthodes de calcul adaptées aux PRS à semelles oxycoupées doit s'appuyer sur un grand nombre de résultats de référence. Ceux-ci sont obtenus par des essais réalisés en laboratoire, ou bien par des simulations numériques équivalentes, réalisées à partir d'éléments finis de type coque permettant d'obtenir un plus grand nombre de résultats à moindre coût. Ces analyses intégrant les non-linéarités géométriques et de matériau prennent en compte les imperfections géométriques et contraintes résiduelles de l'élément étudié. Alors que le modèle de contraintes résiduelles pour PRS à semelles oxycoupées précédemment proposé est utilisé pour les imperfections de matériau, les imperfections géométriques sont basées sur les modes propres d'instabilité appropriés. Une description détaillée du modèle numérique est exposée au Chapitre VII.

Le modèle numérique ainsi développé est adapté à la campagne d'essais de déversement. Les contraintes résiduelles, lois de matériau et amplitudes des imperfections géométriques mesurées expérimentalement sont intégrées au modèle numérique avec les conditions aux limites expérimentales. La comparaison des résultats numériques et expérimentaux valide le modèle numérique développé. Les charges de ruine sont en effet similaires à 5.6% près et les mesures de déplacements et rotations montrent des raideurs analogues, aussi bien lors de la phase de chargement que dans le domaine post-pic. L'évolution des déplacements verticaux expérimentaux et numériques, mesurés dans le vérin lors de l'essai sur la poutre uniforme et bissymétrique, présentés à la Figure 9, sont caractéristiques de la bonne concordance entre les deux modèles.

Des analyses par éléments finis correspondant aux essais sont également menées en remplaçant les contraintes résiduelles mesurées (résultats numériques de référence) par le modèle normatif correspondant aux PRS à semelles laminées ou par le nouveau modèle développé au cours du présent travail. Alors que les résultats numériques de référence sont 4 à 6% supérieurs à ceux obtenus avec le nouveau modèle pour PRS à semelles oxycoupées, l'intégration de contraintes résiduelles pour PRS à semelles laminées fait chuter les résultats d'environ 14% par rapport aux valeurs de référence. Le calcul numérique, réalisé en utilisant le nouveau modèle pour PRS à semelles oxycoupées, donne des résultats légèrement inférieurs aux résultats expérimentaux, l'écart ne dépassant pas 7%. L'utilisation de

contraintes pour PRS à semelles laminées produit des résultats 9 à 16% inférieurs aux résultats expérimentaux.

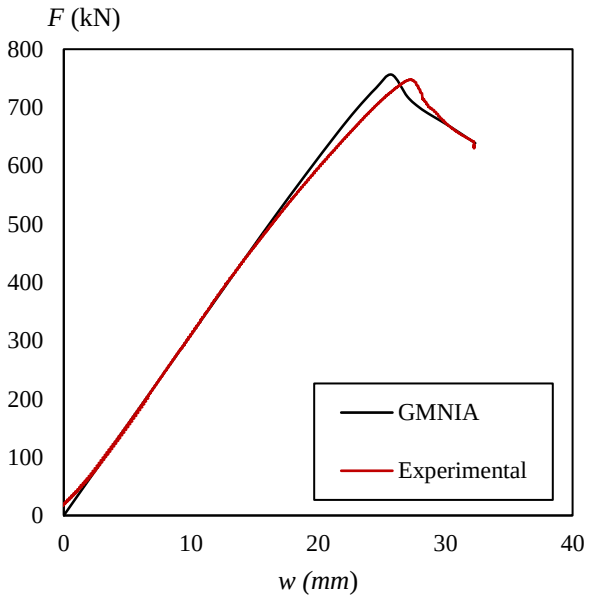

Figure 9 : Courbe force-déplacement du vérin pour l'essai sur PRS à section uniforme bissymétrique

L'effet bénéfique de l'oxycoupage des semelles est également montré à travers une étude de sensibilité concernant le déversement d'un PRS simplement fléchi où différents modèles sont utilisés. L'influence du mode de fabrication des semelles, et plus généralement du modèle de contraintes résiduelles, sur la résistance vis-à-vis du déversement est significative pour un élancement réduit faible ou moyen. Lorsque l'élancement réduit dépasse une valeur comprise entre 1 et 1.2, les résultats obtenus sont très proches quel que soit le modèle utilisé. Par ailleurs, des analyses numériques complémentaires montrent que l'amplitude de l'imperfection géométrique globale a une influence limitée sur la résistance au déversement d'un PRS à semelles oxycoupées. L'incidence des imperfections locales de plaque est à peine notable.

En utilisant le modèle numérique calibré par les résultats expérimentaux, un grand nombre de simulations non-linéaires utilisant des éléments finis de type coque sont menées. Alors que la grande majorité de ces simulations concernent des PRS à semelles oxycoupées, la stabilité des poutres et poteaux PRS à semelles laminées est également explorée. Les éléments étudiés sont maintenus vis-à-vis des déplacements dans le plan et hors plan et de la rotation de torsion au droit de leurs extrémités (appuis à fourche). Le gauchissement et la rotation hors plan sont laissés libres. Les éléments sous charge axiale sont soumis à une compression uniforme alors que les éléments fléchis sont soumis à un diagramme de moment linéairement variable. Les dimensions des sections transversales ainsi que leur type sont jugés représentatifs de la pratique courante. Par conséquent, des composants à section constante ou en fuseau sont étudiés, les sections étant doublement ou mono-symétriques.

Les résultats de cette étude paramétrique sont ensuite exploités au Chapitre VIII. Le cas des éléments uniformément comprimés, flambant hors plan, est traité dans un premier temps. L'influence du mode de fabrication des semelles est significative lorsque l'élancement réduit est faible ou intermédiaire comme le montre la Figure 10 pour les poteaux à section uniforme bissymétrique. Les résultats numériques montrent également que plus l'élancement augmente, moins l'effet des imperfections de l'élément est significatif. Le calcul de coefficients partiels de sécurité γ_{M1} associés à la méthode de calcul

actuelle de l'*Eurocode 3 Partie 1-1* montre que celle-ci est excessivement sécuritaire. Il convient de préciser que la détermination d'un coefficient partiel de sécurité est effectuée selon les prescriptions de l'*Eurocode 0* et les recommandations du projet RFCS *SAFEBRICTILE*. Des adaptations de la méthode de calcul actuelle sont alors proposées pour les PRS à semelles oxycoupées. Deux méthodes alternatives sont exposées :

- L'utilisation d'une courbe de flambement plus favorable ;
- L'utilisation d'un facteur d'imperfection dépendant de l'élancement réduit de l'élément et de ses dimensions.

Les coefficients γ_{M1} associés à ces deux méthodes sont satisfaisants, la deuxième alternative produisant les résultats les plus fidèles aux résultats de référence.

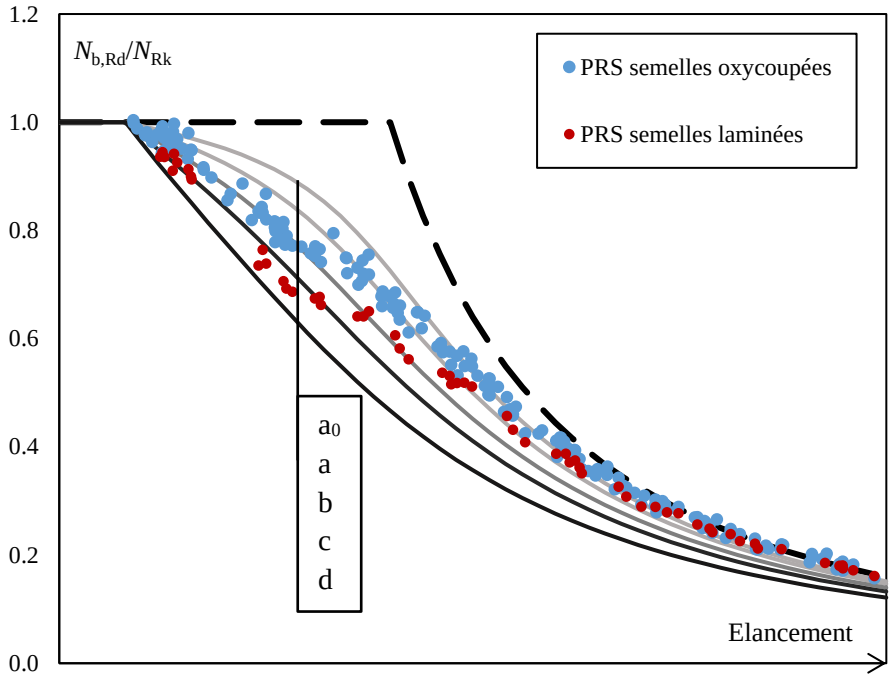

Figure 10 : Résultats de l'étude paramétrique pour poteaux PRS uniformes bissymétriques

Le cas des PRS simplement fléchis est ensuite étudié. A nouveau, les résultats numériques montrent une influence du mode de fabrication des semelles pour des élancements faibles ou intermédiaires (voir Figure 11 pour des poutres uniformes bissymétriques sous moment constant). Puis, l'impact des imperfections sur la résistance diminue lorsque l'élancement augmente. Enfin, une incidence de la forme du diagramme des moments sur la résistance est notée, le cas du moment constant produisant les résultats les plus défavorables.

Les niveaux de sécurité et de précision apportés par la méthode de calcul de l'*Eurocode 3 Partie 1-1* faisant intervenir les courbes de flambement sont analysés. Les coefficients partiels de sécurité obtenus montrent que cette méthode produit des résultats trop conservatifs, particulièrement dans les gammes d'élancements intermédiaires et élevés. La nouvelle méthode de calcul présente dans la révision de l'*Eurocode 3 Partie 1-1* est nettement plus précise et toujours sécuritaire pour les poutres à section constante et doublement symétrique, ce qui correspond à son domaine d'application.

De même que pour les éléments comprimés, des adaptations de la méthode de calcul basée sur les courbes de flambement sont développées pour les poutres PRS à semelles oxycoupées. Les deux approches sont similaires au cas du flambement d'axe faible :

- L'utilisation d'une courbe de flambement plus favorable ;
- L'utilisation d'un facteur d'imperfection dépendant de l'élancement réduit de l'élément et de ses dimensions, couplée à une prise en compte de la forme du diagramme des moments.

Les coefficients partiels de sécurité correspondant à ces deux méthodes sont adéquats. La première alternative est associée à un niveau de sécurité important dans les élancements intermédiaires et élevés alors que la seconde option produit des résultats plus précis.

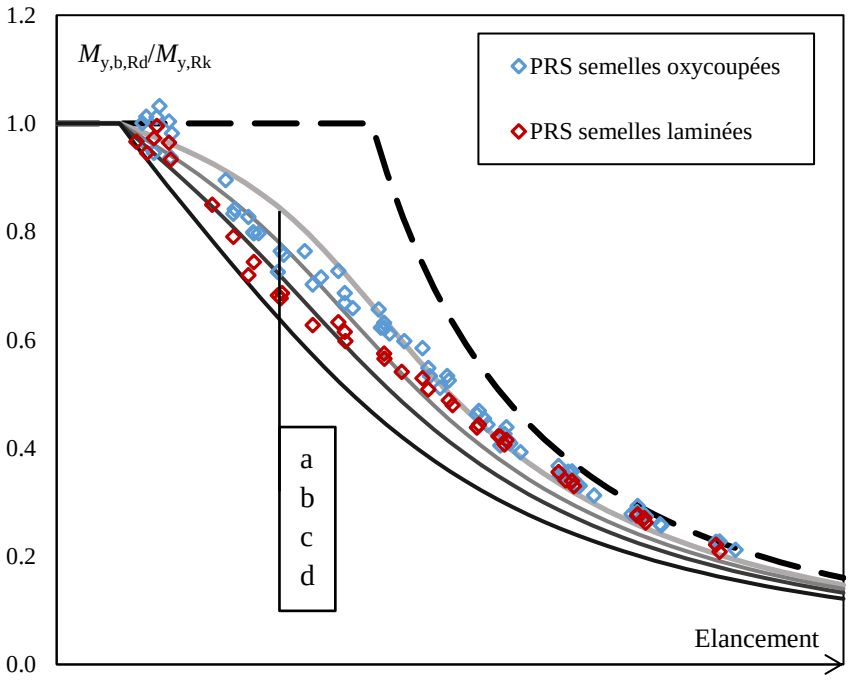

Figure 11 : Résultats de l'étude paramétrique pour poutres PRS uniformes bissymétriques sous moment constant

Le domaine d'application de la nouvelle méthode de calcul de la résistance au déversement du *prEurocode 3 Partie 1-1* étant limité aux poutres à section constante et doublement symétrique, son extension est proposée. En utilisant des hypothèses semblables à celles ayant conduit à cette méthode (voir *Taras* (2010a/b)), des développements analytiques montrent la possibilité de l'utiliser pour des poutres en fuseau à section mono-symétrique, moyennant quelques étapes supplémentaires de calcul. Un coefficient d'imperfection légèrement modifié est proposé pour adapter cette méthode de calcul aux PRS à semelles oxycoupées. A nouveau, les coefficients partiels de sécurité associés à cette méthode de calcul s'avèrent satisfaisants.

Enfin, les résultats de l'étude paramétrique concernant la stabilité des poteau-poutres sont analysés. Les résultats des éléments simultanément comprimés et fléchis montrent également que, pour des élancements réduits intermédiaires ou élevés, l'effet des imperfections sur l'instabilité diminue. L'incidence de la forme du diagramme des moments est en revanche peu significative. Les coefficients partiels de sécurité associés aux deux méthodes de vérification de l'actuel *Eurocode 3 Partie 1-1* et de sa révision sont évalués.

L'utilisation des formules d'interaction négligeant l'oxycoupage des semelles, limitées aux poutres à section constante et doublement symétrique, montre un certain niveau de sécurité. La prise en compte de l'oxycoupage des semelles en utilisant les propositions faites pour les éléments sous chargement seul est alors étudiée. D'après les résultats d'une analyse statistique, la combinaison des propositions faites pour les éléments sous chargement seul produit des résultats acceptables.

La seule méthode permettant d'attester la stabilité d'un élément non uniforme selon l'*Eurocode 3 Partie 1-1* et sa révision montre un excès de sécurité lorsque le mode de fabrication des semelles est négligé. Une amélioration de cette méthode est proposée (i) en découplant les effets dans le plan et hors du plan de sollicitation, aucun maintien intermédiaire n'étant appliqué, et (ii) en prenant en compte le mode de fabrication des semelles. Celui-ci est intégré en utilisant les propositions faites pour les poteaux uniformément comprimés et les poutres simplement fléchies. Une analyse statistique des résultats confirme la validité de cette approche.

Le Chapitre IX conclut ce travail, précisant ses contributions majeures et les aspects à développer s'agissant de la stabilité des PRS. La résistance d'un PRS aux instabilités dépend de son effort critique d'instabilité élastique et de ses imperfections. Au cours de la Partie I consacrée aux instabilités élastiques, des modèles analytiques permettant de prendre en compte certains effets fréquents dans la pratique de poutres PRS sont étudiés, tels que :

- La mono-symétrie de la section transversale ;
- La distorsion de l'âme ;
- La présence de maintiens au gauchissement aux sections d'extrémités.

La Partie II traite des instabilités élasto-plastiques, notamment influencées par les imperfections régnant au sein des PRS. Ainsi, les contraintes résiduelles des PRS à semelles laminées ou oxycoupées sont étudiées. En complément d'essais de déversement, un modèle numérique adapté aux PRS à semelles oxycoupées est développé, les deux modèles donnant des résultats très proches. Ce modèle numérique est alors utilisé pour réaliser de nombreuses simulations non-linéaires concernant des PRS comprimés et/ou fléchis. Les résultats sont finalement utilisés pour proposer des modifications des méthodes de calcul actuelles afin de les adapter aux PRS à semelles oxycoupées.

Table of contents

I. Introduction

I.1 Context and motivation

Steel welded I-section members are commonly used in practice. Contrary to hot-rolled steel members, built-up ones may be defined with any arbitrary dimensions. Besides, the employed steel welded members may present cross-sections defined as doubly or mono-symmetrical (i.e. symmetrical about the bending plane only). Cross-sections may also vary along a welded member length (see Figure I-1) depending on the distribution of the acting loads.

Figure I-1: Tapered column in a steel building (Lisses (91), France)

Steel building members are usually subjected to compression forces and/or bending moments about their major axis. Owing to medium or high distances between restraints against out-of-plane displacements

and/or twist rotations, such members generally fail in global out-of-plane buckling. Flexural or flexural-torsional buckling of columns (see Figure I-2a)) and lateral-torsional buckling of beams (see Figure I-2b)) are accounted for when assessing the stability of a steel member according to current design codes. To that end, second order internal forces and moments are included in the design methods which depend on imperfection factors. These are conditioned by the members dimensions and fabrication process but they also vary between design standards.

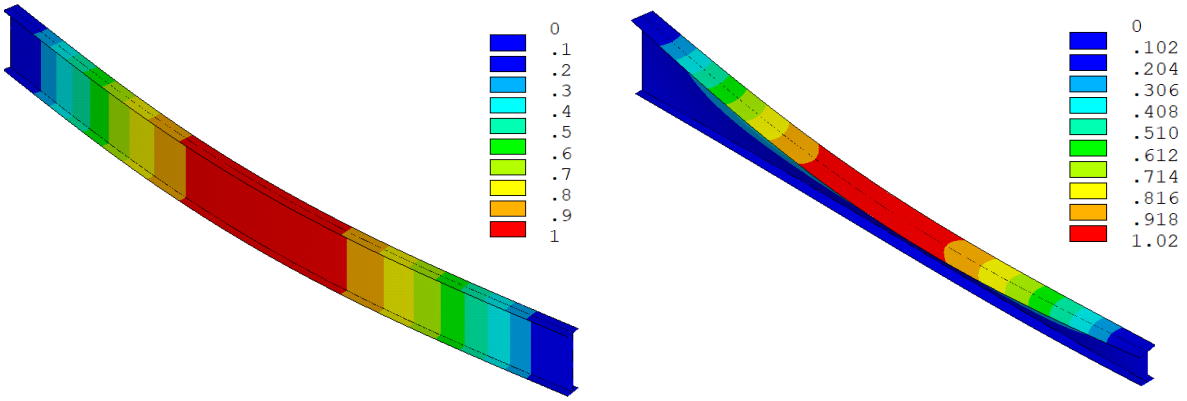

a) *Flexural buckling of a uniform column* b) *Lateral-torsional buckling of a tapered beam*

Figure I-2: Out-of-plane buckling modes (global displacements)

The present work was initiated following the general observation made by French steel manufacturers that the *Eurocode 3* design rules yields less economical steel building members than the previous French standards (*CM66* and *Additif 80*). Indeed, the comparison of these codes shows that the *Eurocode 3* design methods provide more conservative design resistances than the previous French ones.

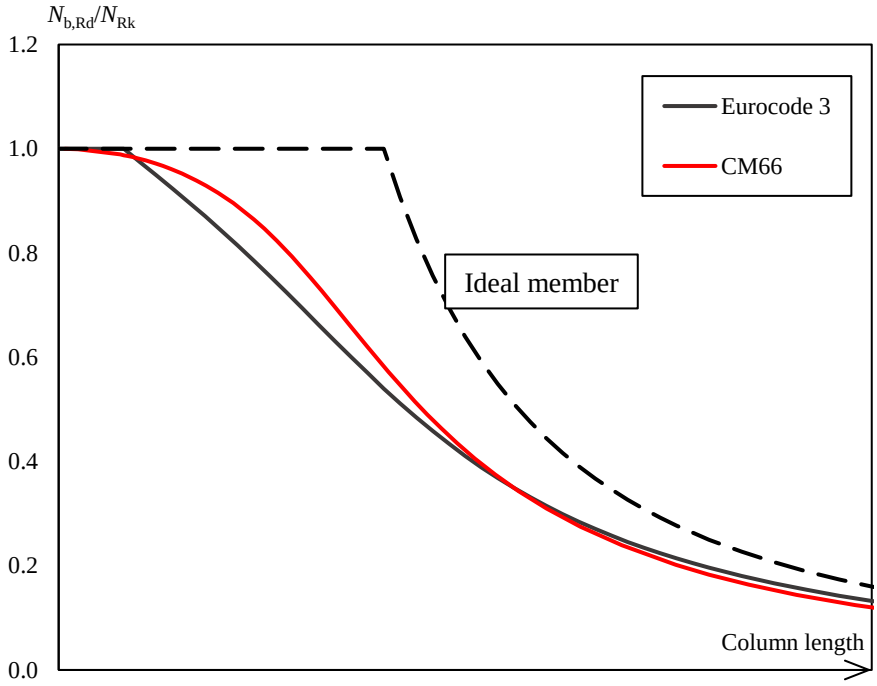

Figure I-3: Reduction of the resistance to compression of a welded building column due to lateral buckling

Such result is exposed in Figure I-3 where the resistance to compression $N_{b,Rd}$ of a uniform doubly-symmetric column, normalized to its cross-sectional characteristic resistance N_{Rk}, is shown to decrease while its length increases. The decrease of the member resistance is more pronounced when using the prescriptions of *Eurocode 3* than when using the *CM 66* code for usual lengths.

The choice of the buckling curve obviously impacts the member resistance. In addition, design methods also depend on its elastic critical load for the investigated buckling mode through (normalized) slenderness. The critical bending moment of a beam and the critical axial load of a column depend on the cross-sectional properties and length of the member and on the position and distribution of the acting loading. All these aspects are accounted for within the different existing analytical models.

However, additional restraints present at the member ends cannot always be explicitly accounted for when analytically computing a critical load. In particular, some beam-to-beam or beam-to-column connection configurations significantly restrain warping by binding the out-of-plane rotations of both flanges. Such restraints affect the critical bending moment and the buckling behaviour but a lack of guidance can be noticed when analysing existing formulations.

Besides, the stability of welded members is assessed according to the *Eurocode 3* design rules using imperfection factors developed for those made hot-rolled flanges. Yet, nowadays the flanges fabrication process of welded members frequently involves longitudinal flame-cuts to separate a wide hot-rolled plate into several flanges or web plates, resulting in different material imperfections. Flanges corresponding to wide hot-rolled plates are then referred to as "*hot-rolled flanges*". Wide plates divided into several member flanges using flame-cuts are referred to as "*flame-cut flanges*".

The influence of the flanges fabrication process on the ultimate load carrying capacities of welded steel members was studied by *Beyer* (2019b) and *Couto* (2019) using shell finite elements. The former found that the *Eurocode 3 Part 1-1* rules provide an accurate lower bound of reference results for welded members made of hot-rolled flanges having a low normalized slenderness while being safe-sided whatever the slenderness. In addition, both investigations concluded on the significant impact of the flanges fabrication process on the members resistance. Indeed, deviations between the ultimate loads for welded members with flame-cut or hot-rolled flanges were noticed in both references, especially for low and medium slenderness that are of common use. *Beyer* (2019b) found even greatest resistances for welded members made of flame-cut flanges than for equivalent hot-rolled profiles.

These preliminary observations have motivated the investigation of the stability of welded I-section steel members to provide guidance helping practitioners making more economical members while maintaining an adequate safety level.

I.2 Scope and objectives

The present work focuses on the stability of I-section welded steel members corresponding to the current common practice of steel buildings. Therefore, the studied steel welded members are:

- Uniform or not along their length with a doubly or mono-symmetric cross-section;
- Subjected to an axial load and/or in-plane bending moment;
- Resting on fork supports at both ends, i.e. in and out-of-plane displacements are prevented along with twist rotation, longitudinal displacement being fully restrained at one of the member end;
- Made of usual steel grade, up to S460;
- Made of hot-rolled or flame-cut flanges.

Analytical methods yielding a reduced utilization of material for such members when compared to the actual design methods are investigated. Consequently, various approaches are investigated that consist in:

- A better inclusion of connection configurations at a beam ends. In particular, the influence of warping restraints on a beam elastic critical lateral-torsional buckling bending moment is studied;
- An enhanced consideration of the members cross-section type. The characteristics of double or mono-symmetry of the cross-section, uniform or tapered along their length are explored, their integration into accurate design methods being sought;
- A distinction between the most usual flanges fabrication process when determining the resistance of a welded member. Indeed, for welded members made of flame-cut flanges, design methods different from those adapted to welded members with hot-rolled flanges are pursued.

These analytical approaches rely on consistent numerical and experimental investigations. An experimental study is performed, the results of which being employed to develop an accurate numerical model. Finite element analyses are led in order to comprehend the actual out-of-plane buckling behaviour of welded steel members. The numerical results are operated to validate the derived analytical approaches.

The analytical developments are led based on a consistent mechanical background using the formalism of *Eurocode 3 Part 1-1* and other existing approaches. Indeed, the developments should yield analytical expressions easily applicable in design offices. In addition to their ease of use, the accuracy and safety level of the proposed analytical methods must reveal satisfactory.

I.3 Structure of the dissertation

Following Chapter I introducing the motivation, scope and objectives of the present work, the dissertation is organised in two general parts:

- Part I: Elastic buckling,
- Part II: Elasto-plastic buckling.

Part I focusing on the computation of elastic critical loads is composed of two chapters. In Chapter II, well-known elastic critical loads are derived in the simple case of uniform members subjected to either a constant axial load or uniform bending moment. An analytical model is recommended for the critical bending moment of mono-symmetric beams based on existing formulations. The complex cases of uniform members subjected to compression and bending, and non-uniform members subjected to compression or bending are discussed. Chapter II continues with the investigation of lateral-torsional buckling featuring web distortion. When compared against the results of finite element analyses performed using shell elements, some of the existing formulations reveal satisfying. Using an accurate existing model, a boundary between the significant and the negligible influence of web distortion on lateral-torsional buckling is proposed.

Part I then proceeds to Chapter III concerning the elastic lateral-torsional buckling of uniform doubly symmetric beams with warping restraints at both ends. Existing expressions for the critical bending

moment of such members and for the stiffness of some common connection configurations are presented. Consistent analytical expressions are then derived for various bending moment distributions. In addition, a limit stiffness between semi-rigid and rigid warping connections is proposed.

Part II regarding the elasto-plastic buckling behaviour of welded I-steel members comprises five chapters. Firstly, Chapter IV presents the existing and future design rules provided by *Eurocode 3*. The single design method adapted to non-uniform members, i.e. the *General Method*, presenting controversial features, recent analytical developments on non-uniform members are presented.

Chapter V investigates residual stresses in welded I-section steel members. Existing models are listed in two sub-sections depending on the flange fabrication process. Owing to visible differences between existing models adapted to welded members made of flame-cut flanges, an experimental programme is described. The sectioning method was used to measure the residual stresses distributions in eight welded specimens, made of hot-rolled or flame-cut flanges. In addition to the flanges fabrication process, the incidence of their widths and thickness is investigated. Differences being noticed between the measured distributions and existing models, a new residual stress pattern for welded members made of flame-cut flanges is proposed.

Next, Chapter VI focuses on the experimental buckling behaviour of welded steel members subjected to bending moment and/or compression force. In particular, a new experimental programme is presented that consists in lateral-torsional buckling tests of four specimens. The welded beams studied, made of flame-cut flanges are uniform or tapered, with a doubly or mono-symmetric cross-section. A single load jack was applied at an intermediate restrained location while the specimens were resting on fork supports at both ends.

The experimental results are then exploited in Chapter VII to validate the numerical model based on shell elements. Using the experimentally measured imperfections and material laws, the numerical results show a good agreement with experimental ones. The numerical model is generalized to welded members made of hot-rolled or flame-cut flanges using idealized material laws and imperfection models. The residual stress model developed in Chapter V is employed for welded members made of flame-cut flanges. The numerical model is further used to perform a large number of non-linear finite element analyses on welded members deemed representative of the current practice.

Chapter VIII concludes Part II where the results obtained using the numerical model described in Chapter VII are exploited. Analytical developments are led relying on similar mechanical background as the current and future *Eurocode 3 Part 1-1*. The predictions of the derived analytical models are compared against the numerical results and adequate partial safety factors γ_{M1} are determined. The analytical models developed for welded members made of flame-cut flanges reveal better suited than the *Eurocode 3* design rules with satisfactory resulting safety levels.

Eventually, Chapter IX summarizes the present work. Major conclusions are presented along with the propositions developed in Parts I and II. Research work broadening the findings of this dissertation are finally discussed.

PART I: ELASTIC BUCKLING

II. Elastic critical loads

II.1 Introduction

Slender members that are of common use in steel structures usually fail owing to global buckling, leading many researchers to investigate the stability resistance of steel members. The current European standard *Eurocode 3 Part 1-1* makes use of elastic critical loads to determine the resistance of a steel member against flexural, torsional, flexural-torsional or lateral-torsional buckling. Since *Euler* (1744) who proposed the first expression of an elastic critical load, in the case of a uniformly compressed member pinned at both ends, analytical models have been developed to estimate the elastic critical loads of a steel member subjected to an axial load N_{Ed} and/or a bending moment $M_{y,Ed}$ about the *y*-axis.

The energy method is commonly used to derive analytical expressions of elastic critical loads, as shown by *Timoshenko* (1963). This resolution method is firstly recalled in the general case of a uniform steel member unrestrained between both ends and subjected to both an axial load and a bending moment distribution. This method is then adapted to the specific case of uniform members subjected to an axial load only (M_y = 0), yielding well-known elastic critical loads. Similarly, the resolution method is adjusted to the case of uniform members with a mono-symmetric cross-section, resting on fork supports subjected to a bending moment distribution only (N = 0). The common expression of the critical bending moment in the case of a constant bending moment is derived. Besides, existing analytical models to determine the critical bending moment of mono-symmetric members are presented. The predictions of these models are compared against the results of finite element analyses, resulting in recommendations.

Then, the case of beam-columns that are simultaneously subjected to an axial load and bending moment is mentioned. The evaluation of the elastic critical loads of a non-uniform steel member is discussed afterwards.

Eventually, the case of bent members failing in a lateral-distortional mode is studied. Such failure mode corresponding to lateral-torsional buckling supplemented with web distortion is of interest in the case of welded beams that generally present a slender web and possibly one or two stocky flange(s). Existing analytical expressions for the critical bending moment are presented for a constant distribution, their predictions being confronted against the results of finite element analyses. The influence of the bending moment distribution is then discussed.

II.2 General case

II.2.1 Total potential energy

The energy method that can be employed to obtain the elastic critical loads of a steel member consists in the minimisation of the total potential energy Π, which is the difference between the elastic strain energy U and the work performed by the external loads W. The member reaches an unstable equilibrium when subjected to the critical values of the applied loads, which corresponds to:

$$\delta\Pi = \delta(U - W) = 0 \tag{II.1}$$

Using the axis and notations from Figure II-1, the elastic internal strain energy U of a member is:

$$U = \int_0^L \left[\frac{EI_y}{2}\left(\frac{d^2w}{dx^2}\right)^2 + \frac{EI_z}{2}\left(\frac{d^2v}{dx^2}\right)^2 + \frac{EI_w}{2}\left(\frac{d^2\theta}{dx^2}\right)^2 + \frac{GI_t}{2}\left(\frac{d\theta}{dx}\right)^2 \right] dx \qquad \text{(II.2)}$$

with:

E: Modulus of elasticity

G: Shear modulus, depending on the modulus of elasticity and Poisson's ratio ν:

$$G = \frac{E}{2(1-\nu)} \qquad \text{(II.3)}$$

I_y: Second moment of area about the y-axis (see Figure II-1)

I_z: Second moment of area about the z-axis (see Figure II-1)

I_w: Warping constant

I_t: Torsional constant

L: Distance between supports

w: vertical displacement (see Figure II-1)

v: lateral displacement (see Figure II-1)

θ: twist rotation (see Figure II-1)

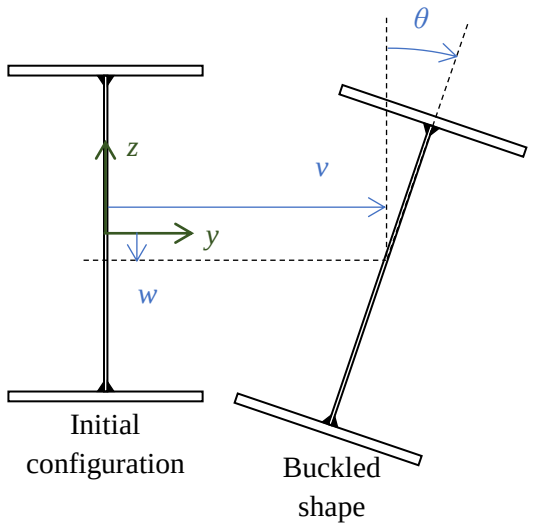

Figure II-1: Coordinate system and notations

In addition, the elastic strain energy of continuous or discrete restraints must be accounted for in the total potential energy of the studied member

As fully derived by *Beyer* (2017), the work performed by the external loads is given in Table II-1 for some usual loading conditions. A linear combination of these loading conditions would result in a linear combination of the corresponding work of the external loads. The works presented in Table II-1

correspond to members unrestrained between both ends. At both ends, lateral and vertical displacements are restrained along with twist rotation.

Load case #1 from Table II-1 corresponds to the usual case of a uniformly compressed member having a doubly symmetric cross-section where i_o is the polar radius of gyration, determined with:

$$i_0^2 = \frac{I_y + I_z}{A} \tag{II.4}$$

where A is the cross-section area.

Load case #2 relates a common set up corresponding to a beam having a mono-symmetric cross-section subjected to end moments. The ratio between both end moments is ψ (comprised between -1 and 1). The Wagner factor z_j explicitly accounts for mono-symmetry of the member. The determination of this parameter is discussed in sub-section II.4.2.

Load case #3 corresponds to a doubly symmetric beam subjected to a uniformly distributed load applied at the compression flange along with a point load applied at the shear centre of the mid-span section. The distance z_g between the shear centre and the location of the uniformly distributed load application, resulting in a stabilizing or destabilizing effect, is considered in the work expression. A shift in the vertical position of the point load application would be accounted for in the expression of W. Details about the sign of z_g are provided in section II.4.

#	Loading condition	W
1	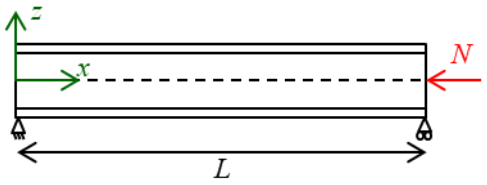	$W = -\int_0^L \frac{N}{2}\left[\left(\frac{dv}{dx}\right)^2 + \left(\frac{dw}{dx}\right)^2 + i_0^2\left(\frac{d\theta}{dx}\right)^2\right]dx$
2	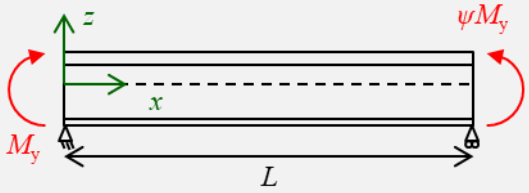	$W = -\int_0^L M_y(x)\left[\theta\frac{d^2v}{dx^2} + z_j\left(\frac{d\theta}{dx}\right)^2\right]dx$
3	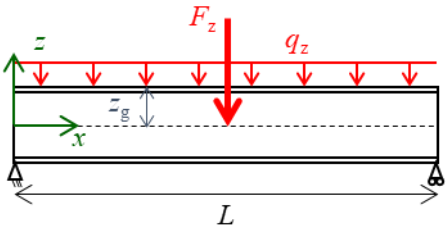	$W = -\int_0^L \left[M_y(x)\theta\frac{d^2v}{dx^2}\right]dx + \frac{1}{2}\int_0^L q_z z_g \theta(x)^2\,dx$

Table II-1: Work performed by various external loading conditions

The total potential energy of a member having been provided for different load cases, one can obtain the elastic critical load(s) of a member using the resolution method described next.

II.2.2 Resolution method

A good approximation of an elastic critical load can be obtained using the Rayleigh-Ritz method (see *Ritz* (1908)) employing linearly independent admissible functions that fulfil both kinematic and static conditions. The case of a member resting on fork supports at both ends without any intermediate restraints and subjected to an arbitrary bending moment and axial load distributions is studied hereafter. In such case, admissible functions for the lateral v and vertical w displacement, and for the twist rotation θ are described by infinite series of sine functions:

$$v(x) = \sum_{k=1}^{n} v_k \sin\left(k\frac{\pi x}{L}\right) \tag{II.5}$$

$$w(x) = \sum_{k=1}^{n} w_k \sin\left(k\frac{\pi x}{L}\right) \tag{II.6}$$

$$\theta(x) = \sum_{k=1}^{n} \theta_k \sin\left(k\frac{\pi x}{L}\right) \tag{II.7}$$

where v_k, w_k and θ_k are the lateral and vertical displacement and twist rotation magnitudes associated with the k^{th} sine-shape function.

The amplitudes v_k, w_k and θ_k are the unknown constants to be determined using the minimum potential energy principle. Substituting v(x), w(x) and θ(x) into the expression of the total potential energy Π given by (II.1) and performing the integration with respect to x yields an algebraic expression of such energy. The values of the magnitudes minimizing the total potential energy Π should therefore satisfy:

$$\frac{\partial \Pi}{\partial v_k} = 0,\ \frac{\partial \Pi}{\partial w_k} = 0,\ \frac{\partial \Pi}{\partial \theta_k} = 0 \tag{II.8}$$

deriving as the following eigenvalue problem:

$$\begin{Bmatrix} \frac{\partial \Pi}{\partial v_1} \\ \vdots \\ \frac{\partial \Pi}{\partial v_n} \\ \frac{\partial \Pi}{\partial w_1} \\ \vdots \\ \frac{\partial \Pi}{\partial w_n} \\ \frac{\partial \Pi}{\partial \theta_1} \\ \vdots \\ \frac{\partial \Pi}{\partial \theta_n} \end{Bmatrix} = \begin{bmatrix} K_{1,1} & \cdots & K_{1,3n} \\ \vdots & \ddots & \vdots \\ K_{3n,1} & \cdots & K_{3n,3n} \end{bmatrix} \begin{Bmatrix} v_1 \\ \vdots \\ v_n \\ w_1 \\ \vdots \\ w_n \\ \theta_1 \\ \vdots \\ \theta_n \end{Bmatrix} = \begin{Bmatrix} 0 \\ \vdots \\ 0 \\ 0 \\ \vdots \\ 0 \\ 0 \\ \vdots \\ 0 \end{Bmatrix} \tag{II.9}$$

The elastic critical buckling load (amplifier) of a steel member is found when the determinant of the matrix from equation (II.9) is equal to zero, matching with non-trivial solutions for the magnitudes v_k, w_k and θ_k. Equating to zero the determinant of the matrix leads to an equation having $3n$ solutions, the lowest corresponding to the first elastic critical buckling mode, which is associated with a corresponding elastic critical load R_{cr} or load amplifier α_{cr}.

In the following section, existing expressions for the elastic critical loads of a compressed member are provided resulting from the energy method. Then, existing expressions of the elastic lateral-torsional buckling load of a bent member having a mono-symmetric cross-section derived from the energy method are given.

II.3 Flexural and/or torsional buckling of columns

The energy method is applied to uniform members with a doubly symmetric cross-section and subjected to a constant axial load. Such members may undergo flexural or torsional buckling which are independent from each other, distinct critical loads characterizing each phenomenon.

When investigating flexural buckling about the *z*-axis of a doubly symmetric member subjected to a constant axial load and pinned at both ends, one may assume that the exact solution for the lateral displacement is half a sine wave:

$$v(x) = v_1 \sin\left(\frac{\pi x}{L}\right) \tag{II.10}$$

Figure II-2 shows the buckled shape of a doubly symmetric column failing in a lateral buckling mode. The out-of-plane displacement *v* is highlighted in both flanges.

The contribution of both the twist rotation and the vertical displacement being zero, the total potential energy reads:

$$\Pi = \frac{EI_z}{2}\left(\frac{\pi}{L}\right)^4 \frac{L}{2} v_1^2 - \frac{N}{2}\left(\frac{\pi}{L}\right)^2 \frac{L}{2} v_1^2 \tag{II.1}$$

Expression (II.1) depends on the magnitude v_1 only. Equating to zero the potential energy leads to the well-known expression for the elastic critical value of the axial load for flexural buckling about the *z*-axis:

$$N_{cr,z} = \frac{\pi^2 EI_z}{L^2} \tag{II.2}$$

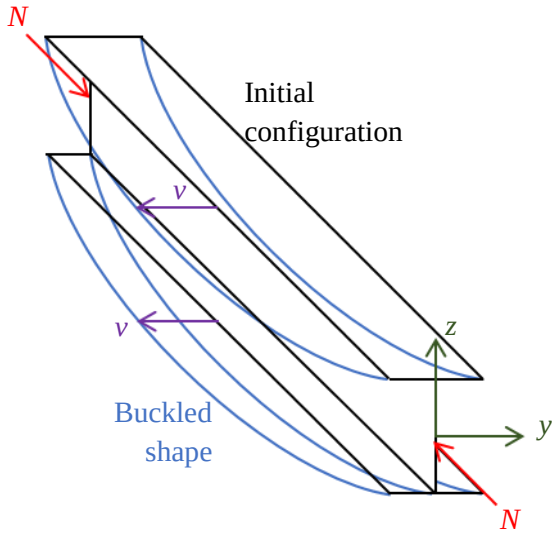

Figure II-2: Lateral buckling of a compressed member

Similarly, the buckled shape of a doubly symmetric compressed member pinned at both ends undergoing flexural buckling about the *y*-axis is half of a sine wave. Applying the energy method leads to the following elastic critical load:

$$N_{cr,y} = \frac{\pi^2 E I_y}{L^2} \qquad \text{(II.3)}$$

Half a sine wave also stands for the exact buckled shape of a doubly symmetric compressed member pinned at both ends that may experience torsional buckling:

$$\theta(x) = \theta_1 \sin\left(\frac{\pi x}{L}\right) \qquad \text{(II.4)}$$

The buckled shape of a column failing in a torsional buckling mode is exposed in Figure II-3.

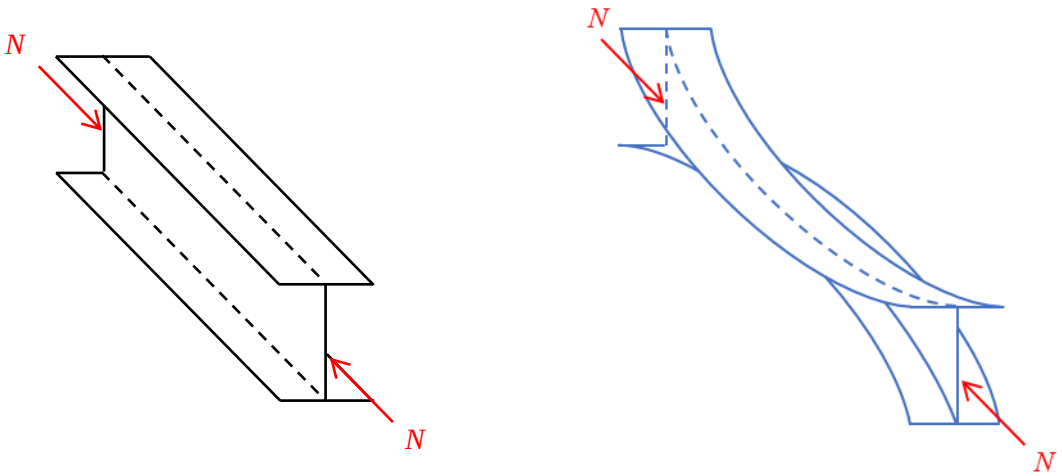

a) *Initial configuration* b) *Buckled shape*

Figure II-3: Torsional buckling of a doubly symmetric column

The contributions of the vertical and lateral displacements being zero, the total potential energy is:

$$\Pi = \frac{EI_{\mathrm{w}}}{2}\left(\frac{\pi}{L}\right)^4 \frac{L}{2}\theta_1^2 + \frac{GI_{\mathrm{t}}}{2}\left(\frac{\pi}{L}\right)^2 \frac{L}{2}\theta_1^2 - \frac{N}{2}\left(\frac{\pi}{L}\right)^2 \frac{L}{2} i_0^2 \theta_1^2 \qquad \text{(II.5)}$$

The only unknown in equation (II.5) is the magnitude of the twist rotation. Equating to zero the total potential energy results in the following common expression for the elastic critical value of the axial load for torsional buckling (see *Timoshenko* (1963)):

$$N_{\mathrm{cr,T}} = \frac{1}{i_0^2}\left[\frac{\pi^2 EI_{\mathrm{w}}}{L^2} + GI_{\mathrm{t}}\right] \qquad \text{(II.6)}$$

Boundary conditions that differ from end restrains against vertical and lateral displacement and against twist rotation must be accounted for. For this purpose, the length L is multiplied with a relevant buckling length factor in the expressions of the elastic critical axial loads.

Mono-symmetric members commonly used in practice present a single axis of symmetry corresponding to the z-axis. Therefore the flexural buckling about the y-axis of such member is characterized by the elastic critical load $N_{\mathrm{cr,y}}$, given by expression (II.3). However, the torsional and lateral flexural buckling modes combine in a flexural-torsional buckling mode owing to the difference between the second moments of area about the z-axis of both flanges.

Owing to the cross-section mono-symmetry, the work performed by the external load given in load case #1 from Table II-1 is modified as:

$$W = -\int_0^L \frac{N}{2}\left[\left(\frac{dv}{dx}\right)^2 + \left(\frac{dw}{dx}\right)^2 + (i_0^2 + z_s^2)\left(\frac{d\theta}{dx}\right)^2 + 2z_s \frac{dv}{dx}\frac{d\theta}{dx}\right] dx \qquad \text{(II.7)}$$

where z_s is the vertical distance between the cross-section shear centre and centroid.

The flexural-torsional buckling mode of a mono-symmetric steel member can be characterized by half of a sine wave for both the lateral displacement and the twist rotation (see expressions (II.10) and (II.4), respectively) while the vertical displacement is zero. The total potential energy therefore reads:

$$\Pi = \left(\frac{\pi}{L}\right)^2 \frac{L}{4}\left\{EI_{\mathrm{z}}\left(\frac{\pi}{L}\right)^2 v_1^2 + EI_{\mathrm{w}}\left(\frac{\pi}{L}\right)^2 \theta_1^2 + GI_{\mathrm{t}}\theta_1^2 - N\left[v_1^2 + \left(z_s^2 + i_0^2\right)\theta_1^2 + z_s v_1 \theta_1\right]\right\} \qquad \text{(II.8)}$$

Equating to zero the derivatives of the total potential energy with respect to both amplitudes v_1 and θ_1 leads to a 2×2 matrix. The critical value of the applied axial load, is obtained by equalling to zero the matrix determinant leading to a second order equation. The lowest of the two roots is $N_{\mathrm{cr,TF}}$:

$$N_{\mathrm{cr,TF}} = \frac{1}{2\left(1 - \dfrac{z_s^2}{z_s^2 + i_0^2}\right)}\left[N_{\mathrm{cr,z}} + N_{\mathrm{cr,T}} - \sqrt{\left(N_{\mathrm{cr,z}} + N_{\mathrm{cr,T}}\right)^2 - 4N_{\mathrm{cr,z}}N_{\mathrm{cr,T}}\left(1 - \frac{z_s^2}{z_s^2 + i_0^2}\right)}\right] \qquad \text{(II.9)}$$

The critical loads for flexural buckling about the z or y-axis, torsional buckling or flexural-torsional buckling of uniform members pinned at both ends subjected to a constant axial load are given by

expressions (II.2), (II.3), (II.6) and (II.9). These formulae are similar to those provided by the background document from TC 250/SC 3. Besides, *Kováč* (2019) and *Annex I from Eurocode 9 Part 1-1* provide similar expressions involving buckling length factors. They account for the members boundary conditions regarding vertical and lateral displacement and twist rotation.

The global buckling of compressed uniform members having been investigated, next section deals with the global buckling of uniform members subject to bending moment.

II.4 Lateral-torsional buckling of beams

II.4.1 General expression

The lateral-torsional buckling of a uniform beam having a mono-symmetric cross-section, subjected to a uniform bending moment distribution $M_{y,o}$ is investigated. When resting on fork supports at both ends, out-of-plane rotation and warping being free, such beam exhibits a mode shape where the exact solutions for the lateral displacement and twist rotation are half a sine wave:

$$v(x) = v_1 \sin\left(\frac{\pi x}{L}\right) \tag{II.10}$$

$$\theta(x) = \theta_1 \sin\left(\frac{\pi x}{L}\right) \tag{II.11}$$

The buckled shape of a doubly symmetric beam subjected to a uniform bending moment distribution is presented in Figure II-4a). The typical twist rotation θ and lateral displacement v of the mid-span cross-section are displayed in Figure II-4b).

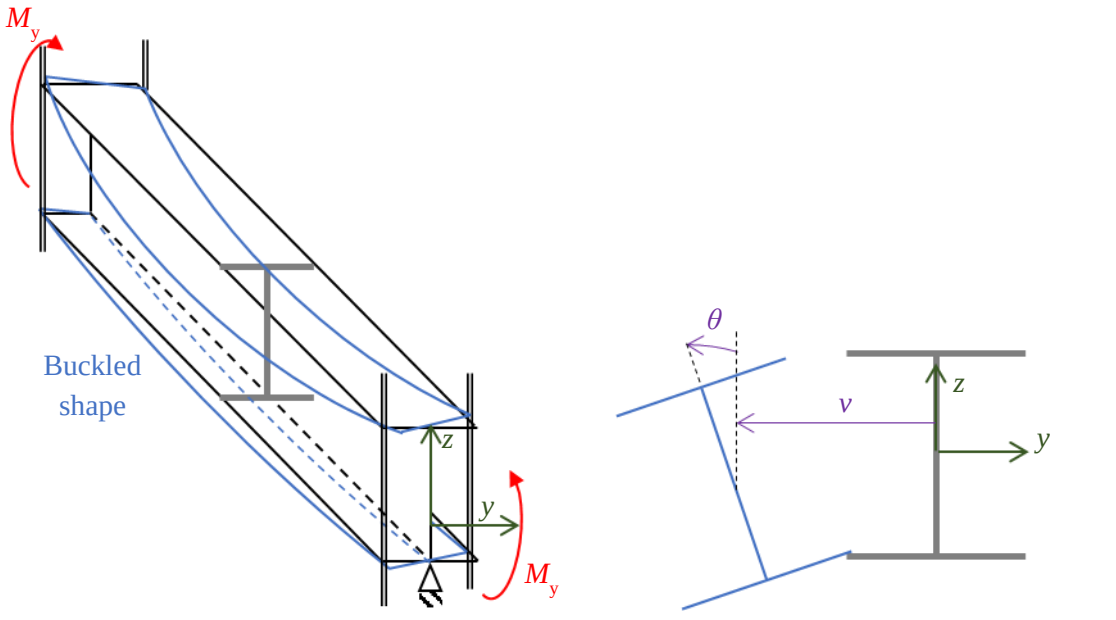

a) *Buckled shape* b) *Cross-sectional displacements*

Figure II-4: Lateral-torsional buckling of a doubly symmetric beam

The contribution of the in-plane displacement *w* is ignored, being generally negligible when compared to the out-of-plane displacement and twist rotation. The total potential energy therefore reads:

$$\Pi = \left(\frac{\pi}{L}\right)^2 \frac{L}{4}\left\{EI_z\left(\frac{\pi}{L}\right)^2 v_1^2 + EI_w\left(\frac{\pi}{L}\right)^2 \theta_1^2 + GI_t\theta_1^2 - 2M_{y,0}\left(v_1\theta_1 - z_j\theta_1^2\right)\right\} \tag{II.12}$$

Taking the derivative of the potential energy defined by expression (II.12) with respect to the magnitudes and employing the minimum potential energy principle yields the following system of linear equations:

$$\frac{\partial\Pi}{\partial v_1} = \left(\frac{\pi}{L}\right)^2 \frac{L}{2}\left\{EI_z\left(\frac{\pi}{L}\right)^2 v_1 - M_{y,0}\theta_1\right\} = 0 \tag{II.13}$$

$$\frac{\partial\Pi}{\partial \theta_1} = \left(\frac{\pi}{L}\right)^2 \frac{L}{2}\left\{EI_w\left(\frac{\pi}{L}\right)^2 \theta_1 + GI_t\theta_1 - M_{y,0}\left(v_1 - 2z_j\theta_1\right)\right\} = 0 \tag{II.14}$$

The usual ratio between both amplitudes in the case of a uniform bending moment distribution arises from expression (II.13):

$$v_1 = \frac{M_{y,cr}}{EI_z\left(\frac{\pi}{L}\right)^2}\theta_1 \tag{II.15}$$

Inserting expression (II.15) into (II.14) results in the common expression for the critical bending moment of a uniform mono-symmetric beam under a constant bending moment distribution and resting on fork supports at both ends:

$$M_{y,cr} = \frac{\pi^2 EI_z}{L^2}\left\{\sqrt{\frac{I_w}{I_z} + \frac{L^2 GI_t}{\pi^2 EI_z} + z_j^{\,2}} + z_j\right\} \tag{II.16}$$

The previous expression is generalized to account for an arbitrary bending moment distribution, transverse load(s) application outside the shear centre, and elastic end restraint(s) against warping and out-of-plane rotation:

$$M_{y,cr} = C_1\frac{\pi^2 EI_z}{\left(k_z L\right)^2}\left\{\sqrt{\left(\frac{k_z}{k_w}\right)^2\frac{I_w}{I_z} + \frac{\left(k_z L\right)^2 GI_t}{\pi^2 EI_z} + \left(C_2 z_g - C_3 z_j\right)^2} - \left(C_2 z_g - C_3 z_j\right)\right\} \tag{II.17}$$

The warping and the out-of-plane rotation coefficients, k_w and k_z, respectively, vary between 0.5 when fully restrained and 1 when unrestrained. Coefficients C_1, C_2 and C_3 account for the bending moment distribution. The distance z_g between the location of the transverse loading application point and the cross-section shear centre is defined as positive when the transverse loading applies towards the shear centre (destabilizing effect) and negative when in the opposite direction. Besides, the Wagner factor z_j accounts for the cross-section mono-symmetry, its computation being treated in the next sub-section II.4.2.

While *Eurocode 3 Part 1-1* does not provide any guidance on how to determine the elastic critical lateral-torsional buckling bending moment, the general expression (II.17) can be found in the *experimental version of Eurocode 3 Part 1-1* (ENV) and in *Part 1-1 of Eurocode 9*. The *French National Annex to Eurocode 3 Part 1-1* also provides some guidance to determine the critical lateral-torsional buckling bending moment but restricted to the case of doubly symmetric beams. Expression (II.17) is therefore proposed without the term $C_3 z_j$ that vanishes (z_j being zero).

Values for the three C_i coefficients from expression (II.17) accounting for the variations in the bending moment distribution are proposed for common bending moment diagrams in *ENV*, *Eurocode 9 Part 1-1* and in the *French National Annex to Eurocode 3 Part 1-1*, the latter providing values for C_1 and C_2 only.

It is worth mentioning that contrary to a usual assumption, the constant bending moment distribution does not always lead to the lowest value of the critical bending moment of an arbitrary beam. Indeed, as exposed by *Camotim* (2012), the critical bending moment of a mono-symmetric I-beam might be lower when subjected to a uniformly distributed loading applied at the shear centre than under a constant bending moment distribution. Therefore, the cross-section mono-symmetry should be properly accounted for through the Wagner factor, which is detailed next sub-section II.4.2.

II.4.2 Wagner factor

The expression of the Wagner factor z_j is:

$$z_j = z_s - \frac{1}{2I_y}\int z\left(z^2 + y^2\right)dA \tag{II.18}$$

where z_s is the location of the shear centre with respect to the cross-section centroid.

The integral in the previous expression can be decomposed as follows:

$$\int z\left(z^2 + y^2\right)dA = S_{M,fs} + S_{M,w} + S_{M,fi} \tag{II.19}$$

with:

$$S_{M,fs} = \frac{b_s t_{fs}}{4}\left[2h_T - 2z_g - t_{fs}\right]\left[\frac{b_s^2}{6} + \left(h_T - z_g\right)^2 + \left(h_T - t_{fs} - z_g\right)^2\right]$$

$$S_{M,w} = \frac{h_w t_w}{4}\left[h_w - 2z_g + 2t_{fi}\right]\left[\frac{t_w^2}{6} + \left(z_g - h_w - t_{fi}\right)^2 + \left(z_g - t_{fi}\right)^2\right]$$

$$S_{M,fi} = \frac{b_i t_{fi}}{4}\left[t_{fi} - 2z_g\right]\left[\frac{b_i^2}{6} + \left(z_g - t_{fi}\right)^2 + z_g^2\right]$$

where the geometric parameters are depicted in Figure II-5.

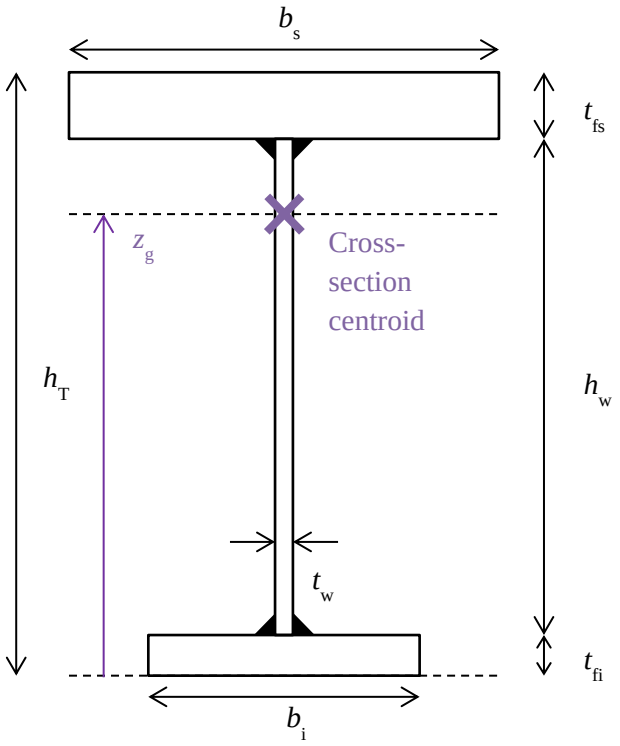

Figure II-5: Cross-section dimensions

Expression (II.18) used along with (II.19) provides the exact value of the Wagner factor for welded members. The flange-to-web fillets in hot-rolled members are neglected, but such profiles are mostly doubly symmetric in practice (leading to z_j=0).

Annex I from *Eurocode 9 Part 1-1* proposes to approximate z_j using:

$$z_j = 0.45 \psi_f h_s \qquad \text{(II.20)}$$

with:

$$\psi_f = \frac{I_{fc} - I_{ft}}{I_{fc} + I_{ft}}$$

$$h_s = h_w + \frac{t_{fs} + t_{fi}}{2}$$

I_{fc} and I_{ft} are the second moment of area about the *z*-axis of the compression and tension flanges, respectively.

Eurocode 9 Part 1-1 assigns a positive sign to z_j when the flange having the greatest second moment of area about the *z*-axis is compressed at the cross-section located:

- At the end subjected to the maximal bending moment intensity when the bending moment distribution is linear, or
- At mid-span when subjected to a transverse load.

Annex F of *ENV 1993-1-1* provides the following approximation for z_j:

$$z_j = \begin{cases} 0.5\psi_f h_s & \text{if } I_{fc} < I_{ft} \\ 0.4\psi_f h_s & \text{if } I_{fc} > I_{ft} \end{cases} \quad \text{(II.21)}$$

The sign convention given in *ENV* and *Eurocode 9* are similar for a linear bending moment distribution. However, both sign conventions are slightly different for beams subjected to a transverse loading. Indeed, *ENV* defines z_j as positive when the flange having the largest second moment of area about the z-axis is compressed at the location of the maximal bending moment intensity.

The results of both approximations provided by *Eurocode 9* and *ENV* are compared against the Wagner coefficients obtained using expression (II.18) and numerical integrations computed with the software *PropSection*, which is used as a reference model, for the mono-symmetric beams presented in Table II-2. The dimensions of one flange are labelled with the exponent "1" while those of the second flange are labelled with the exponent "2".

The beams depicted in Table II-2 concern two hot-rolled members #B – corresponding to an IPE 330 – and #B_M having web-to-flange fillets with a 18 mm-radius. The remaining beams are welded, solely one being doubly symmetric. Within mono-symmetric beams, the flanges thickness always varies with a ratio up to more than 2. In addition, in some cases the flanges width varies, the maximum ratio between the flanges width being 1.56, for specimen #B_M. Only the Wagner factor being investigated for beams #C_M to #H_M, no length is defined for these members.

Designation	h_w (mm)	t_w (mm)	b (mm)	t_f (mm)	L (m)
#A	780	8	200	15	2; 6; 12
#B	307	8	160	11.5	1.5; 4; 9
#A_M	780	8	200	30^1; 15^2	2; 6; 12
#B_M	310	8	250^1; 160^2	25^1; 12^2	2; 4; 9
#C_M	900	6	250	25^1; 18^2	/
#D_M	900	6	350^1; 250^2	35^1; 18^2	/
#E_M	600	6	300^1; 200^2	25^1; 16^2	/
#F_M	600	10	300^1; 200^2	30^1; 20^2	/
#G_M	450	5	230	24^1; 12^2	/
#H_M	450	5	230^1; 150^2	24^1; 12^2	/

Table II-2: Geometry of the beams studied in section II.4

The Wagner factors of the mono-symmetric beams are determined using expressions (II.18), (II.20) and (II.21) and by numerical integration using *PropSection*. Beam #B_M is also studied with and without the flange-to-web fillets – designated as #B_M_Ø. The results are given in Table II-3 where it can be seen that the presence of flange-to-web fillets have a negligible influence on the Wagner coefficient according to the reference values (less than 0.1% deviation). The difference is slightly greater when using expression (II.18), being 3%. This deviation can be attributed to the shift of the shear centre and centroid locations between the calculations performed accounting for the fillet and neglecting the fillets.

Calculation method	**Numerical integration**	**Analytical**	**Approximation (II.20)**	**Approximation (II.21)**
Reference	*PropSection*	*Exp. (II.18)*	*Eurocode 9*	*ENV*
#A_M	117.0 mm	117.0 mm	120.4 mm	107.0 mm
#B_M_Ø	113.3 mm	113.3 mm	124.2 mm	110.4 mm
#B_M	113.1 mm	109.6 mm		
#C_M	67.2 mm	67.2 mm	67.4 mm	59.9 mm
#D_M	294.4 mm	294.4 mm	285.2 mm	253.5 mm
#E_M	196.3 mm	196.3 mm	190.1 mm	168.9 mm
#F_M	192.6 mm	192.6 mm	188.2 mm	167.3 mm
#G_M	71.4 mm	71.4 mm	70.2 mm	62.4 mm
#H_M	162.7 mm	162.7 mm	159.2 mm	141.5 mm

Table II-3: Wagner coefficients according to different calculation methods

For welded members, the predictions of expression (II.18) match perfectly with the numerical results. Using the approximated expression of the Wagner coefficient provided in *Eurocode 9 Part 1-1* causes a deviation up to 3% from the reference values, except for #B_M where the difference is almost 10%. The *Eurocode 9* expression can over or under estimate the value of z_j while the *ENV* expression underestimates its value in every case. The predictions of the *ENV 1993 Part 1-1* expression are 8.6 to 14 % lower than the reference results except for #B_M where the difference is below 3%.

For the studied welded members, that are preferably slender, the approximation proposed in *Eurocode 9* produces more accurate results than that from *ENV*. However, expression (II.18) producing exact values of the Wagner factor for welded members should be employed.

II.4.3 C_i Coefficients

II.4.3.1. Linear bending moment distribution

The values of the coefficient C_1 proposed by the *French National Annex to Eurocode 3 Part 1-1* and *Eurocode 9 Part 1-1* for a beam subjected to a linear bending moment distribution are very close, being less than 1% different. *ENV 1993-1-1* suggests values of C_1 greater than the two other standards (up to +15%), as shown in Table II-4 as a function of the ratio ψ between end moments. The values of C_1 extracted from *Eurocode 9* presented in Table II-4 are those provided in the safe case where:

$$\chi_t = \frac{\pi}{L}\sqrt{\frac{EI_w}{GI_t}} \qquad \text{(II.22)}$$

The *French National Annex to Eurocode 3 Part 1-1* does not provide any value for C_3 since solely doubly symmetric members entre its scope. *Eurocode 9* and *ENV* propose to use different values of C_3, presented in Table II-4. It is worth mentioning that the *ECCS*'s *Technical Committee 8* (TC8) (2006) recommends the same values as *Eurocode 9 Part 1-1* for C_1 and C_3.

ψ	*Eurocode 9 Part 1-1*			*ENV 1993-1-1*	
	C_1	C_3		C_1	C_3
		$-0.9 < \psi_f < 0$	$0 < \psi_f < 0.9$		
1.00	1.000	1.000		1.000	1.000
0.75	1.139	1.000		1.141	0.998
0.50	1.312	1.000		1.323	0.992
0.25	1.522	1.000		1.563	0.977
0.00	1.770	1.000		1.879	0.939
-0.25	2.047	1.000	0.850	2.281	0.855
-0.50	2.331	1.000	$1.3-1.2\psi_f$	2.704	0.676
-0.75	2.547	1.000	$0.55-\psi_f$	2.927	0.366
-1.00	2.555	$-\psi_f$		2.752	0.000

Table II-4: Coefficients C_1 and C_3 for a linear bending moment distribution

Eurocode 9 proposes a constant value of 1 for C_3 when both end moments have the same sign. When $\psi < 0$, the value of C_3 can depend both on the cross-section dimensions, through the parameter ψ_f, and on the ratio between end moments. When $\psi = -1$, the cross-section from which ψ_f must be determined is not specified. However, a consistent calculation implies to determine ψ_f and the sign of z_j at the same location.

ENV proposes values of C_3 ranging from 1 to 0 as ψ varies from 1 to -1. C_3 is very close to 1 when the ratio between end moments is positive. In this case, the differences with the *Eurocode 9* values are 6% at most, which is still admissible. However, when ψ is negative, the deviation between the values of C_3 recommended by both standards increases as ψ tends towards -1, the difference becoming significant when $\psi < -0.5$.

The maximum deviation between the values of C_3 is found when the bending moment distribution varies between M and $-M$. In such case, *ENV* considers no impact of the cross-sectional mono-symmetry upon the lateral-torsional buckling behaviour. Such assumption implies that the elastic critical lateral-torsional buckling mode shapes of a doubly and a mono-symmetric beam are similar, to the amplitudes, and symmetrical about the beam mid-span. The twist rotation θ and lateral displacement v corresponding to the elastic critical buckling mode are determined using the software *LTBeamN* (see *Beyer* 2015a/b), which makes use of two-noded beam finite elements. The results for beams #A and #A_M subjected to end moments with $\psi = -1$ are shown in Figure II-6.

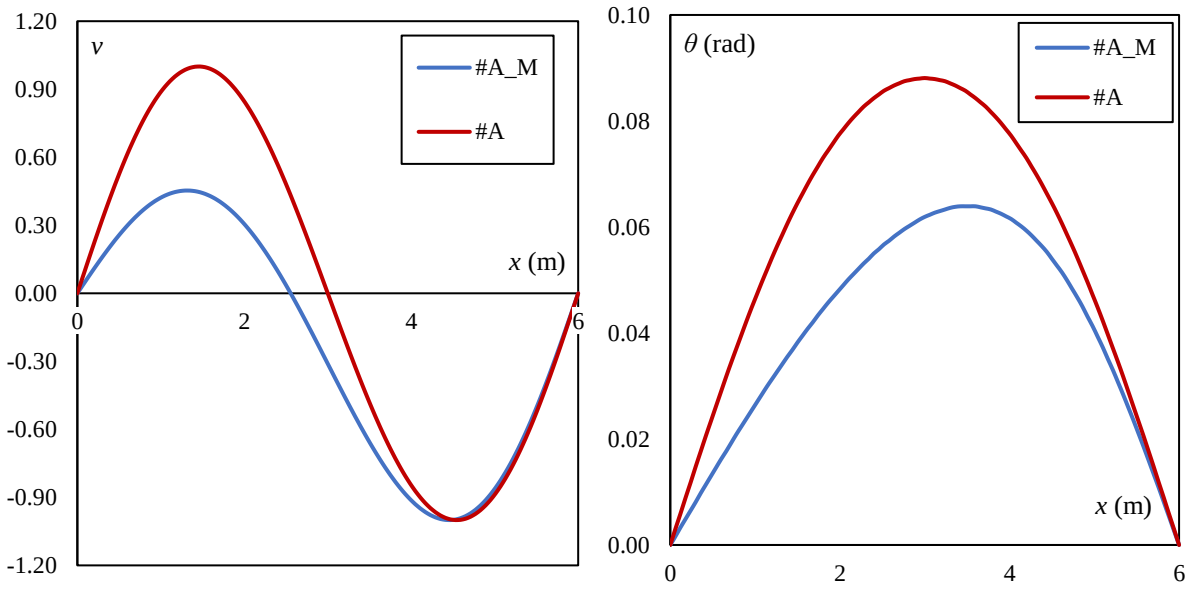

a) *Lateral displacement* b) *Twist rotation*

Figure II-6: Components of the elastic critical mode shape of a doubly and a mono-symmetrical beam

Figure II-6 exhibits significant differences between the mode shapes of both beams. Neither the twist rotation nor the lateral displacement of the mono-symmetric beam are symmetrical about mid-span. Besides, the rotations and displacements maximum intensities are not found at the same position along the doubly and the mono-symmetrical beams. The cross-section being mono-symmetric has a significant impact on the elastic lateral-torsional buckling behaviour of a beam: C_3 being zero when ψ = -1 according to *ENV* is therefore inconsistent.

For a linear bending moment distribution, the differences between C_1 and C_3 proposed by *Eurocode 9* and *ENV*, along with inconsistencies of the latter standard were pointed out in the past, e.g. by *Mohri* (2000) and *Braham* (2001). Both references detailed the derivations of the coefficients C_1 and C_3 given by *ENV*. It is worth mentioning that the values of C_1 proposed by *ENV* are similar to those from the former French standards *CM 66* and *Additif 80* (to 1%). Those values were obtained using the Galerkin method assuming that, whatever ψ, the twist rotation could be approximated using solely half a sine wave (see expression (II.4)), which is inconsistent with the distribution of the torsional twist shown in Figure II-6b) for a mono-symmetric beam. The questionable assumption regarding the torsional twist distribution results in the following expressions for the coefficients C_1 and C_3:

$$C_1 = \sqrt{\frac{6\pi^2}{\left(2\pi^2-3\right)\left(1+\psi^2\right)+\left(2\pi^2+6\right)\psi}} \qquad \text{(II.23)}$$

$$C_3 = C_1\frac{1+\psi}{2} \qquad \text{(II.24)}$$

Expressions (II.23) and (II.24) were used to obtain the tabulated values of C_1 and C_3, respectively, given by *ENV*. A simplified expression (II.23) can be found in the former *CM 66* and *Additif 80*. In addition to tabulated values, *ENV* also contains an analytical expression for C_1 differing from (II.23) while having an upper bound of 2.70, which is lower than some of the tabulated values.

Mohri (2000) and *Braham* (2001) used a few examples to show the *ENV* rules could reveal significantly unsafe. To supplement their studies, the elastic critical lateral-torsional buckling bending moments of beams #A, #A_M, #B and #B_M from Table II-2 subjected to a linear being moment distribution with ψ = -1 are determined numerically, using *LTBeamN*. These reference results are compared in Table II-5 against the analytical critical bending moments obtained using coefficients C_1 and C_3 from *Eurocode 9 Part 1-1* and *ENV 1993-1-1*. The Wagner factors are determined by numerical integrations performed using the software *PropSection*.

Beam	L (m)	M_{EC9}/M_{FE}	M_{ENV}/M_{FE}
#A	2	0.926	0.997
	6	0.935	1.007
	12	0.944	1.017
#B	1.5	0.932	1.003
	4	0.937	1.009
	9	0.953	1.026
#A_M	2	0.989	1.169
	6	0.993	1.154
	12	1.008	1.143
#B_M	2	0.843	1.707
	4	0.958	1.625
	9	1.046	1.431

Table II-5: Critical bending moments for a distribution varying from M *to* -M

For doubly symmetric beams, Table II-5 shows that the critical bending moments obtained using the coefficients from *Eurocode 9* are slightly on the safe side. The results obtained using the *ENV* coefficients are closer to the reference ones, but some are slightly on the unsafe side. For doubly symmetric members, the difference between the results using the coefficients from both standards is 8%, corresponding to the difference on the C_1 coefficient.

In the case of mono-symmetric beams, the difference between the critical bending moments obtained using both standards coefficients can be more than 100%. The use of the *ENV* coefficients provides significantly unsafe results since the deviation from the reference numerical results are up to 70%. As stated by *Mohri* (2000) and *Braham* (2001), the analytical computation of the elastic critical bending moment of a beam having a mono-symmetric cross-section subjected to a linear bending moment distribution should not be performed using the coefficients C_1 and especially C_3 proposed by *ENV*, those from *Eurocode 9 Part 1-1* being valid.

II.4.3.2. Transverse loading

Presentation

The C_i coefficients for a beam subjected to a linear bending moment distribution having been analyzed, the case of mono-symmetric beams subjected to a transverse loading, applied or not at the shear centre, is investigated hereafter. The coefficients C_1, C_2 and C_3 given in Table F.1.2 from *ENV 1993-1-1*, Table I.2 from *Eurocode 9 Part 1-1* and Table M.2 from the *French National Annex to EN 1993-1-1* (except

for C_3) are presented in Table II-6 for the corresponding load cases. It is worth mentioning that the *TC8 from ECCS* (2006) recommends the same values as *Eurocode 9 Part 1-1* for members pinned at both ends, no values being provided for beams fixed at both ends.

#	Boundary conditions	*FNA to EN 1993-1-1*		*Eurocode 9 Part 1-1*			*ENV 1993-1-1*		
		C_1	C_2	C_1	C_2	C_3	C_1	C_2	C_3
F_a		1.35	0.45	1.348	0.553	0.411	1.365	0.553	1.730
F_e		1.69	1.50	1.683	1.388	-0.716	1.565	1.267	2.640
q_a		1.13	0.45	1.127	0.459	0.525	1.132	0.459	0.525
q_e		2.57	1.55	2.576	1.562	-0.859	1.258	1.562	0.753
FF_a	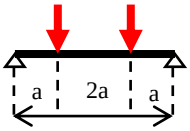	Not provided		1.038	0.431	0.562	1.046	0.430	1.120

Table II-6: C_1, C_2 and C_3 coefficients for a beam under transverse load(s)

Table II-6 shows that the values of C_1 proposed by the *French National Annex* are very close to those given in *Eurocode 9*. Some deviations are noticed for C_2 in the case of a point load applied at mid span. The C_i coefficients given in *ENV* and *Eurocode 9* are similar in load case #q_a, while only C_3 varies distinctly in load cases F_a and FF_a. In both cases of beams fixed at both ends, the values of C_2 proposed by *ENV* and *Eurocode 9* are very close whereas C_1 and C_3 vary significantly. Opposite signs between the values of C_3 fixed at both ends are linked with the different sign conventions used for z_j.

For a beam fixed at both ends subjected to a distributed loading, the ratio between the values of C_1 proposed by *Eurocode 9* and *ENV* is close to 2. The former associates the critical bending moment with the bending moment at supports while the latter associates it with the bending moment at mid-span – having an intensity twice as low as that at supports. However, the critical bending moment is related to the maximum intensity of the bending moment distribution, corresponding to the *Eurocode 9* approach.

Load application at the shear centre

Finite element analyses are employed to estimate the safety level provided by *ENV* and *Eurocode 9* when at least C_1 or C_3 are different in the two references. The elastic critical bending moments of beams #A to #B_M from Table II-2 are determined numerically, using *LTBeamN*, and analytically using the coefficients C_1 and C_3 from *Eurocode 9 Part 1-1* and the *ENV 1993-1-1*. The Wagner factors are determined by numerical integrations performed using the software *PropSection*. In beams having a mono-symmetric cross-section, the flange having the greatest second moment of area about the *z*-axis is compressed at mid span, corresponding to the common practice. The results are presented in Table II-7.

It is worth mentioning that the sign of z_j for load case #F_e according to *ENV* is determined from the end cross-section. Determining this sign using the cross-section at mid span – where the bending

moment intensity is similar – would lead to extremely unsafe values of the critical bending moment (up to 8 times greater than the results of finite element analyses).

Table II-7 shows that the critical bending moments determined using the C_i coefficients from *Eurocode 9* are close to the numerical ones, the maximum deviation being 5.6%. On the contrary, the critical bending moments determined with the *ENV* coefficients can result in values significantly deviating from the numerical results.

Beam	L (m)	F_a		FF_a		F_e		q_e	
		M_{EC9}/M_{FE}	M_{ENV}/M_{FE}	M_{EC9}/M_{FE}	M_{ENV}/M_{FE}	M_{EC9}/M_{FE}	M_{ENV}/M_{FE}	M_{EC9}/M_{FE}	M_{ENV}/M_{FE}
#A	2					0.970	0.902	0.948	0.473
	6					0.977	0.908	0.988	0.493
	12					0.982	0.914	0.994	0.496
#B	1.5					0.978	0.909	0.993	0.495
	4					0.968	0.900	0.988	0.493
	9					0.981	0.912	0.990	0.494
#A_M	2	1.053	1.883	1.048	1.230	1.046	0.599	0.967	0.497
	6	1.041	1.696	1.048	1.196	1.039	0.643	1.052	0.537
	12	1.035	1.466	1.043	1.145	1.026	0.715	1.039	0.527
#B_M	2	1.000	3.421	1.014	1.510	1.003	0.350	1.008	0.542
	4	0.994	2.739	1.011	1.375	1.008	0.410	1.056	0.558
	9	0.989	1.866	1.002	1.194	0.990	0.543	1.042	0.537

Table II-7: Critical bending moments for a transverse load at the shear centre

Determining the critical bending moment of doubly symmetrical beams fixed at both ends using the values of C_1 proposed by *ENV* leads to slightly safe-sided results when under point load and very safe-sided results when the load is uniformly distributed. In this load case, the ratios of analytical to numerical results are close to 0.5, the actual value of C_1 is therefore approximately twice the value proposed by *ENV*.

The analytical evaluation of the critical bending moments of beams having a mono-symmetric cross-section carried out using C_1 and C_3 given in *ENV* leads to very unsafe results for beams pinned at both ends. Their values are up to more than three times greater than those determined numerically. On the contrary, the results are very safe for beams fixed at both ends.

In load case #F_e, the value of C_3 increases the safety level of the critical bending moment determined using the coefficients from *ENV*. In the other load cases, the coefficient C_3 decreases the safety level of the critical bending moment.

The safety level resulting from the analytical determination of the critical bending moment involving the C_i coefficients provided by *Eurocode 9 Part 1-1* is acceptable. The same cannot be said regarding the results obtained using the *ENV* coefficients.

Load application outside the shear centre

The *French National Annex to EN 1993-1-1, ENV 1993-1-1* and *Eurocode 9 Part 1-1* propose different values of C_2 for a point load applied at mid-span, whether the beam is fixed or pinned at both ends. In both load cases, the critical bending moments of beams #A to #B_M from Table II-2 are computed using finite element analyses (*LTBeamN*) and analytically using the C_i coefficients from the three standards. The Wagner factors are determined via numerical integrations performed with *PropSection*. The calculations are run considering that the load is applied at the top flange – having the greatest I_{fz} – and directed towards the shear centre ($z_g > 0$) or away from it ($z_g < 0$).

Beam	L (m)	$z_g > 0$			$z_g < 0$		
		M_{FNA}/M_{FE}	M_{EC9}/M_{FE}	M_{ENV}/M_{FE}	M_{FNA}/M_{FE}	M_{EC9}/M_{FE}	M_{ENV}/M_{FE}
#A	2	0.936	0.993	0.994	1.028	0.960	0.830
	6	0.943	0.999	0.996	1.041	0.974	0.845
	12	0.960	1.011	1.001	1.034	0.974	0.851
#B	1.5	0.938	0.995	0.994	1.056	0.987	0.854
	4	0947	0.999	0.991	1.036	0.974	0.849
	9	0.972	1.010	0.984	1.016	0.970	0.861
#A_M	2	Outside the scope	1.097	0.778	Outside the scope	1.004	1.223
	6		1.081	0.784		0.995	1.187
	12		1.060	0.806		1.005	1.143
#B_M	2		0.982	0.425		1.214	2.411
	4		0.977	0.464		1.183	2.168
	9		0.980	0.567		1.118	1.672

Table II-8: Critical bending moments for a transverse load applied outside the shear centre – load case #F_e

Table II-8 shows the results obtained in load case #F_e while Table II-9 presents those in load case #F_a

For doubly symmetric members, Table II-8 shows that the critical bending moments determined using the coefficients from *Eurocode 9* are very close to the reference values, regardless of the direction of the point load. The results obtained using the *ENV* coefficients are also very close to the numerical ones for a load applied towards the shear centre. They reveal safe when the load is applied outside the shear centre, the mean deviation being 15%. The results obtained using C_1 and C_2 from the *French National Annex* are slightly conservative when the transverse load is destabilizing while being slightly unsafe in the case of a stabilizing effect.

The critical bending moments of mono-symmetric members subjected to load case #F_e determined using the C_i coefficients from *ENV* are very safe when z_g is positive and very unsafe otherwise. The ratio with the reference value is in some cases lower than 0.5 and greater than 2, respectively. The results obtained with the coefficients from *Eurocode 9* are closer to the reference values but some deviations on the unsafe side can be noticed. The maximum difference reaches more than 20% when the load is applied away from the shear centre.

Table II-8 shows that for doubly symmetric members in load case #F_e, using the C_i coefficients from *Eurocode 9* results in the best level of safety. However, for mono-symmetric members the safety level provided by *Eurocode 9* is not satisfactory when z_g and z_j are simultaneously non-zero. In such case, the determination of the critical bending moment for lateral-torsional buckling should be performed by means of finite element analyses.

Table II-9 shows that for doubly symmetric beams pinned at both ends subjected to a point load at mid-span outside the shear centre, the critical bending moments obtained using the *Eurocode 9* and *ENV* C_i coefficients are close to the numerical results. Using the coefficients from the *French National Annex to Eurocode 3 Part 1-1* produces slightly unsafe results when the load acts with a destabilizing effect. The results are slightly conservative when the load is applied away from the shear centre. The maximum deviation from the numerical values is 10% in both cases. The results obtained using the *Eurocode* 9 C_i coefficients present the best safety level.

Beam	L (m)	$z_g > 0$			$z_g < 0$		
		M_{FNA}/M_{FE}	M_{EC9}/M_{FE}	M_{ENV}/M_{FE}	M_{FNA}/M_{FE}	M_{EC9}/M_{FE}	M_{ENV}/M_{FE}
#A	2	1.090	0.992	1.005	0.903	0.989	1.001
	6	1.088	0.998	1.011	0.909	0.988	1.001
	12	1.080	1.006	1.019	0.926	0.991	1.004
#B	1.5	1.090	0.994	1.007	0.905	0.989	1.002
	4	1.074	0.997	1.009	0.920	0.988	1.001
	9	1.049	1.001	1.014	0.946	0.988	1.000

Table II-9: Critical bending moments for a transverse load applied outside the shear centre – load case #F_a

II.4.4 Summary

The general expression of the elastic lateral-torsional buckling bending moment (II.17) can be employed for mono-symmetric members resting on fork supports at both ends employing expression (II.18) along with (II.19) for z_j – using the sign convention from *Eurocode 9 Part 1-1* – and the coefficients C_1, C_2 and C_3 given in Table II-10.

When studying a beam subjected to a bending moment distribution different from that of Table II-10, one should determine its elastic critical bending moment performing finite elements analyses, e.g. via *LTBeamN, ANSYS, ABAQUS, FINELG...*

Linear bending moment distribution				*Transverse loading*			
ψ	C_1	C_3		Boundary conditions	C_1	C_2	C_3
		$-0.9 < \psi_f < 0$	$0 < \psi_f < 0.9$				
1.00	1.00	1.00			1.35	0.55	0.41
0.75	1.14	1.00					
0.50	1.31	1.00			1.68	1.39*	-0.72*
0.25	1.52	1.00					
0.00	1.77	1.00			1.13	0.45	0.53
-0.25	2.05	1.00	0.85				
-0.50	2.33	1.00	$1.3 - 1.2\psi_f$		2.57	1.55	-0.86
-0.75	2.55	1.00	$0.55 - \psi_f$				
-1.00	2.55	$-\psi_f$		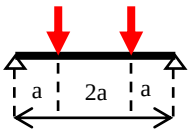	1.04	0.43	0.56

Table II-10: C_i coefficients

*: Load case where the analytical computation of the critical bending moment is not recommended for beams with a mono-symmetric cross-section under a transverse load applied outside the shear centre.

The elastic critical loads of steel members subjected to either compression or bending having been investigated, members simultaneously bent and compressed are studied in the next section.

II.5 Buckling of beam-columns

A uniform doubly symmetric member subjected to a constant bending moment distribution $M_{y,0}$ and a constant axial load N_0, unrestrained between both ends where resting on fork supports, generally buckles in a lateral-torsional way owing to the fact that $I_z << I_y$. The mode shape is composed of half a sine wave for both the lateral displacement and twist rotation:

$$v(x) = v_1 \sin\left(\frac{\pi x}{L}\right) \tag{II.25}$$

$$\theta(x) = \theta_1 \sin\left(\frac{\pi x}{L}\right) \tag{II.26}$$

The elastic critical buckling happens when both the acting bending moment and axial load are multiplied by the amplifier α_{cr}. The total potential energy is then:

$$\Pi = \left(\frac{\pi}{L}\right)^2 \frac{L}{4}\left\{EI_z\left(\frac{\pi}{L}\right)^2 v_1^2 + EI_w\left(\frac{\pi}{L}\right)^2 \theta_1^2 + GI_t\theta_1^2 - \alpha_{cr}\left[2M_{y,0}v_1\theta_1 + N_0\left(i_0^2\theta_1^2 + v_1^2\right)\right]\right\} \tag{II.27}$$

Employing the minimum potential energy principle results in the following coupled equations:

$$\frac{\partial \prod}{\partial v_1} = 0 \rightarrow EI_z \left(\frac{\pi}{L}\right)^2 v_1 = \alpha_{cr}\left[M_{y,0}\theta_1 + N_0 v_1\right] \tag{II.28}$$

$$\frac{\partial \prod}{\partial \theta_1} = 0 \rightarrow EI_w \left(\frac{\pi}{L}\right)^2 \theta_1 + GI_t\theta_1 = \alpha_{cr}\left[M_{y,0}v_1 + N_0 i_0^2 \theta_1^2\right] \tag{II.29}$$

Reorganizing expression (II.28) leads to the relationship between both amplitudes of the lateral displacement v_1 and twist rotation θ_1:

$$\theta_1 = \frac{N_{cr,z} - \alpha_{cr} N_0}{\alpha_{cr} M_{y,0}} v_1 \tag{II.30}$$

where $N_{cr,z}$ is given by expression (II.2).

Inserting expression (II.30) into equation (II.29), one obtains the critical load amplifier α_{cr}:

$$\alpha_{cr} = \frac{\left(\frac{N_0}{N_{cr,z}} + \frac{N_0}{N_{cr,T}}\right) - \sqrt{\left(\frac{N_0}{N_{cr,z}} - \frac{N_0}{N_{cr,T}}\right)^2 + 4\frac{{M_{y,0}}^2}{{M_{y,cr}}^2}}}{2\left(\frac{{N_0}^2}{N_{cr,z}N_{cr,T}} - \frac{{M_{y,0}}^2}{{M_{y,cr}}^2}\right)} \tag{II.31}$$

where $N_{cr,T}$ and $M_{y,cr}$ are given by expressions (II.6) and (II.16) (with $z_j = 0$), respectively.

Even in the simplest case of a uniform doubly symmetric member, resting on fork supports and subjected to constant axial and bending loadings, determining the critical load amplifier analytically is a tedious process. When confronted to steel beam-columns with more complex boundary conditions, one should perform Linear Bifurcation Analyses (LBA) using shell or beam finite elements to determine the critical load amplifier.

The specific case of uniform members has been studied, the determination of elastic critical loads of non-uniform members will be discussed next section.

II.6 Non-uniform members

II.6.1 Flexural buckling

Non-uniform steel members are of common use in practice but determining their elastic critical loads can be a challenging step when computing their buckling resistance. Nowadays, finite elements analyses can be performed to obtain the minimum amplifier of the in-plane loads to reach the elastic critical resistance of a non-uniform member subjected to compression and/or bending. However, several analytical methods were developed in the past to estimate the elastic critical loads of a non-uniform member.

The elastic critical load for flexural buckling about the *y*-axis of a tapered column has been investigated e.g. by *Ermopoulos* (1986, 1997). In the case of a quadratic variation of the in-plane second moment of area along the member, solutions were proposed making use of a buckling length coefficient to be determined involving abacus. For such members pinned at both ends, *Serna* (2011) proposed to compute the elastic critical load for flexural buckling about the *y*-axis of a tapered column subjected to a variable distribution of the axial load using:

$$N_{\mathrm{cr,y}} = C\frac{\pi^2 E I_{\mathrm{y,m}}}{L^2} \tag{II.32}$$

where $I_{\mathrm{y,m}}$ is the minimum second moment of area about the *y*-axis along the column and C is a factor accounting for the variable axial load distribution and cross-section dimensions, which can be approximated by (see *Serna* (2011)):

$$C = \frac{21 c_{\max} N_{\max}}{c_{\max} N_{\max} + 4\left(c_1 N_1 + c_4 N_4\right) + 6\left(c_2 N_2 + c_3 N_3\right)} \tag{II.33}$$

where N_1 to N_4 are the values of the axial load acting at every $L/3$ of the column and:

$$c(x) = \frac{I_{y,\mathrm{m}}^{0.30}}{I_y(x)^{0.30}} \frac{I_{y,1}^{0.30} I_{y,2}^{0.15} I_{y,3}^{0.30}}{I_{y,\max}^{0.75}} \tag{II.34}$$

The powers applied to the second moments of area were fitted using the results of finite element analyses.

II.6.2 Lateral-torsional buckling

Elastic critical loads for lateral-torsional buckling of non-uniform beams have also be studied in the past. Using the minimum potential energy principle on a tapered doubly symmetric beam resting on fork supports at both ends subjected to an arbitrary bending moment diagram, *Galéa* (1986) derived an expression for an equivalent height. The equivalent uniform member is supposed to have the same elastic critical bending moment as the actual tapered member. Considering half a sine wave for the twist rotation, the equivalent height h_{eq} is:

$$h_{\mathrm{eq}} = h_{\max}\sqrt{0.283\left(1+\left(\frac{h_{\min}}{h_{\max}}\right)^2\right)+0.434\frac{h_{\min}}{h_{\max}}} \tag{II.35}$$

where $h_{\max}$ is the maximum web height and $h_{\min}$ is the minimum web height.

Braham (1993) noticed that expression (II.35) led to an equivalent height close to the mean of the heights at both end sections. Ignoring the contribution of the Saint-Venant torsional constant, *Braham* (1993) proposed to determine the elastic critical bending moment of a mono-symmetric tapered beam subjected to a linear bending moment distribution using:

$$M_{cr} = C_1 \frac{\pi^2 E I_{z,fc}}{L^2}\left(h_{eq} + \frac{t_{fi} + t_{fs}}{2}\right) \tag{II.36}$$

where h_{eq} is the mean of the web heights at both ends, $I_{z,fc}$ is the second moment of area about the z-axis of the compressed flange of the beam and C_1 is a coefficient accounting for the bending moment distribution and the cross-section variation. No expression is provided for C_1 but values are given as a function of the ratio ψ between end moments when the ratio between heights at both ends is 1, 3 and 5.

For a beam subjected to a linear bending moment distribution that is tapered on a portion ηL between restraints – the remaining part being uniform –, *Galéa* (2010) proposed a different expression of the equivalent web height. This expression was suggested using numerical critical bending moments obtained by means of the *LTBeam* software:

$$h_{eq} = h_m \delta\left(1 - \eta + \frac{\eta^{\gamma}}{2}\left(1 + \frac{h_{max}}{h_{min}}\right)\right) \geq h_{min} \tag{II.37}$$

with:

$$\gamma_{eq} = 1 + 0.25\left(\frac{h_{max}}{h_{min}} - 1\right)$$

$$\delta = \begin{cases} 1 + 0.12\eta\left(\dfrac{h_{max}}{h_{min}} - 1\right)(1 + \psi) & \text{if } \psi \leq -0.5 \\ 1 + 0.04\eta\left(\dfrac{h_{max}}{h_{min}} - 1\right)(1 - \psi) & \text{if } \psi \geq -0.5 \end{cases}$$

As exposed by *Andrade* (2010), these approaches considering that the critical bending moment of a tapered beam can be determined using an equivalent prismatic member fail to capture the impact of the web tapering on the bimoment behaviour as expressed by *Kitipornchai* (1972, 1975).

Later, *Boissonnade* (2002a) demonstrated the impact of the tapering of the member on its total potential energy *II*. This taper effect, affecting the torsional behaviour of the beams, was accounted for when defining the new beam finite element resulting from this work. Besides, this effect was quantified on few examples by comparing the elastic critical loads of two similar tapered members. One was treated as an addition of uniform elements having different heights (see Figure II-7a)) while the other was divided in tapered elements (see Figure II-7 b)). In the case of a tapered member subjected to a bending moment acting at its highest end, neglecting the taper effect yielded a critical load up to 16% lower than that accounting for that effect.

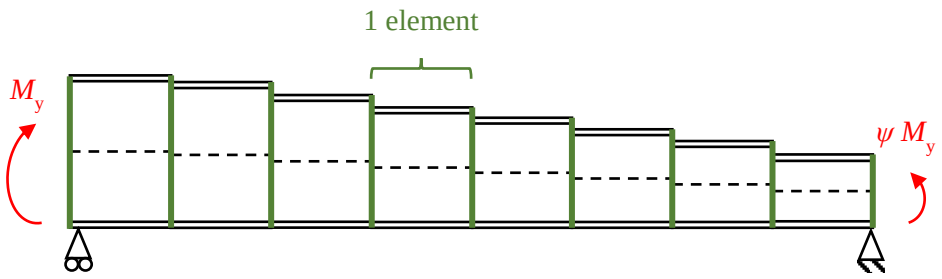

a) *Neglecting the flanges inclination*

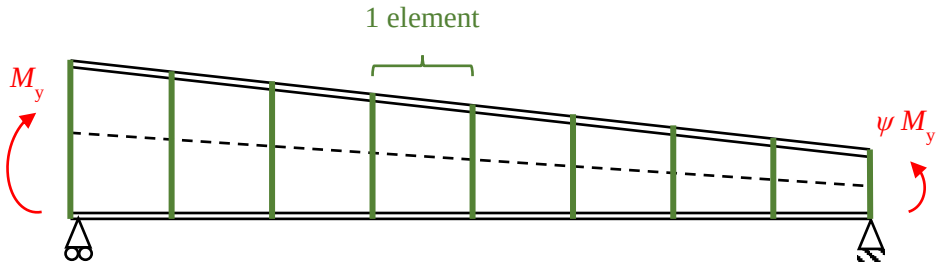

b) *Accounting for the flanges inclination*

Figure II-7: Discretization of a tapered beam

Accounting for the flanges gradient, *Benyamina* (2013) developed an expression for the critical bending moment of a doubly tapered beam resting on fork supports and subjected to a uniformly distributed transverse load (see Figure II-8) applied, or not, at the cross-sections shear centres. Using the energy method and considering that half a sine wave is an accurate solution for the lateral displacement and twist rotation of the buckling mode, *Benyamina* (2013) obtained:

$$M_{cr} = C_1 \frac{\pi^2 E I_z}{L^2} \left\{ \sqrt{2 \frac{A_{32}}{C_1} \frac{I_w}{I_z} + 2 A_{31} \frac{L^2 G I_t}{\pi^2 E I_z} + \left(C_2 z_g \right)^2} - C_2 z_g \right\} \qquad \text{(II.38)}$$

with:

$$C_1 = \frac{1}{2 A_b} \left(\frac{16}{\pi^3 A_{21}} \right)^2$$

$$C_2 = A_{33}$$

$$A_b = -\left[\left(\frac{3\pi^2}{8} - \frac{32}{9} \right) \left(\frac{I_z}{I_y} \right)^2 + \left(A_{34} - \frac{16}{3\pi} A_{11} \right) \frac{I_z}{I_y} - \frac{2}{\pi^2} A_{11}^2 \right]$$

where I_y and I_z are the values corresponding to the mid-span cross-section while coefficients A_{ij}, presented in Table II-11, depend only on the taper ratio α.

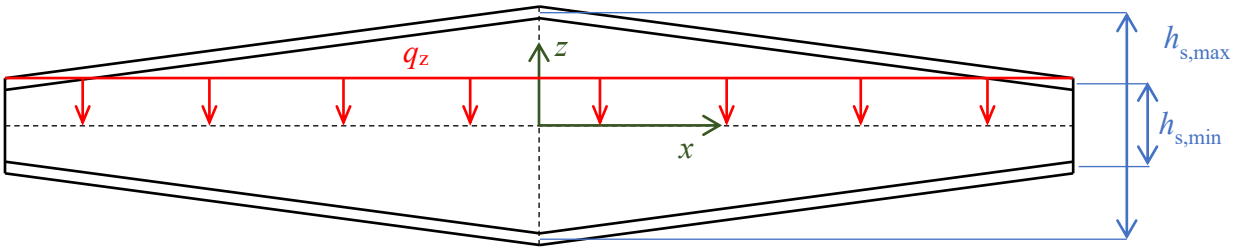

Figure II-8: Doubly tapered beam (Benyamina, 2013)

Coefficient	Expression
A_{32}	$\left(11+\frac{\pi^2}{6}\right)\alpha^2-\left(6+\frac{\pi^2}{2}\right)\alpha+\frac{\pi^2}{2}$
A_{31}	$\frac{1}{2}-\left(\frac{1}{4}+\frac{1}{\pi^2}\right)\alpha$
A_{21}	$\frac{\pi^2}{2}\left(\frac{\alpha^2}{3}-\alpha+1\right)$
A_{33}	$\frac{2}{\pi^2}\left[\left(\frac{4}{\pi^2}-1\right)\alpha+2\right]$
A_{34}	$\left(\frac{9}{16}-\frac{\pi^2}{8}\right)\alpha^2+\left(\frac{3\pi^2}{8}-1\right)\alpha-\frac{3\pi^2}{8}$
A_{11}	$\left(\frac{272}{27\pi}-\frac{4\pi}{3}\right)\alpha^2+\left(\frac{8\pi}{3}-\frac{44}{9}\right)\alpha-\frac{4\pi}{3}$

Table II-11: Coefficients A_{ij} from Benyamina *(2013)*

with:

$$\alpha = 1-\frac{h_{s,\min}}{h_{s,\max}}$$

The elastic critical loads of a non-uniform member can be approximated using hand calculation in some simple cases but performing finite element analyses is better suited whatever the boundary conditions. LBA type calculations of non-uniform members must account for the taper effect using shell elements or appropriate beam elements.

The elastic critical loads for members with non-deformable sections have been presented when subjected to compression force and/or bending moment. In the following section, the failure mode of beams including web distortion is studied. Existing analytical models, developed for a constant bending moment distribution are depicted.

II.7 Lateral-distortional buckling

II.7.1 Presentation

While welded I-section beams usually fail in a Lateral-Torsional Buckling (*LTB*) mode, they generally present slender webs and possibly one or two very stocky flange(s), which may induce a Lateral-Distortional Buckling (*LDB*) mode. The lateral-torsional buckling failure mode represented in Figure II-9a) corresponds to the cross-sectional lateral displacement and twist rotation. They are supplemented by web distortion in the lateral-distortional buckling failure mode. Web distortion can correspond to a single (see Figure II-9b)) or a double curvature (see Figure II-9c)).

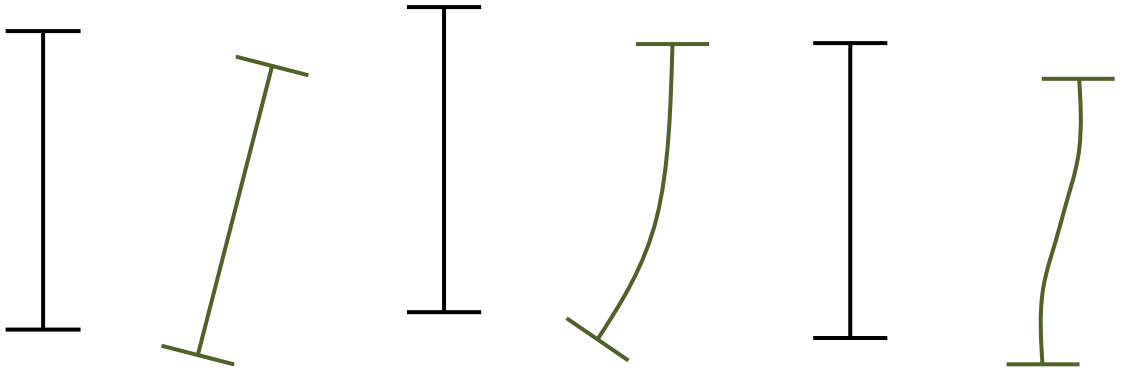

Figure II-9: Lateral-torsional and distortional buckling modes

Under a constant bending moment diagram, doubly symmetric members resting on fork supports at both ends undergoing lateral-distortional buckling would preferably buckle in double curvature. For such members, existing analytical models to determine the elastic critical bending moment for LDB are given. Using an adequate existing formulation, a boundary between LTB and LDB is then derived. The predictions of the analytical formulations are compared against the results of finite element analyses using shell elements performed with *ANSYS* software. The influence of the bending moment distribution on the LDB behaviour and critical bending moment is then discussed. The possibility to extend the existing analytical formulations to linear bending moment distributions is confronted to Finite Element results.

II.7.2 Analytical models for a uniform bending moment distribution

II.7.2.1. Critical bending moment for LTB with equivalent stiffness

When subjected to a uniform bending moment distribution, the elastic critical load for LTB of a doubly symmetric I-section steel member resting on fork supports at both ends obtained using expression (II.17) reduces to:

$$M_{\mathrm{cr,LTB}} = \frac{\pi^2 EI_{\mathrm{z}}}{L^2}\sqrt{\frac{I_{\mathrm{w}}}{I_{\mathrm{z}}} + \frac{L^2 GI_{\mathrm{t}}}{\pi^2 EI_{\mathrm{z}}}} \qquad \text{(II.39)}$$

For such members and boundary conditions, *Dekker* (1998) proposed to evaluate the elastic critical bending moment for LDB, $M_{\mathrm{cr,LDB}}$, using the previous expression with equivalent stiffness. The modified values of the warping constant I_{w}, torsional constant I_{t} and z-axis second moment of area I_{z} were determined employing equivalent spring systems (see Figure II-10).

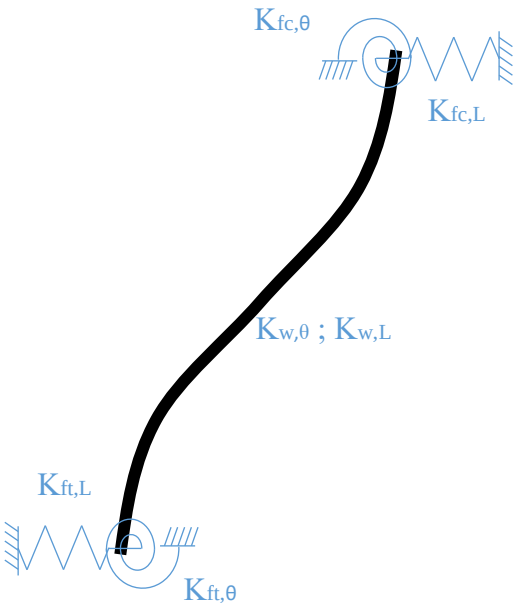

Figure II-10: Spring model employed by Dekker *(1998)*

The equivalent spring systems for the warping and torsional constants and for out-of-plane stiffness proposed by *Dekker* (1998) are depicted in Figure II-11a), Figure II-11b) and Figure II-11c), respectively.

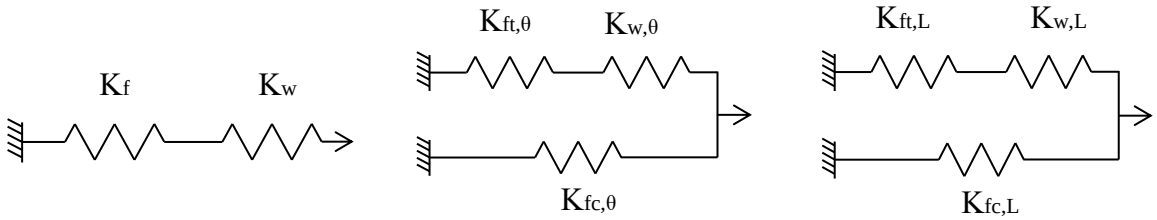

a) *Warping constant* b) *Torsional constant* c) *Lateral stiffness*

Figure II-11: Simplified spring systems for equivalent stiffness

with:

$$\frac{K_{\mathrm{w}}}{K_{\mathrm{f}}} = \frac{K_{\mathrm{w,L}}}{K_{\mathrm{f,L}}} + \frac{K_{\mathrm{w,\theta}}}{K_{\mathrm{f,\theta}}} = R_1 + R_2$$

The equivalent stiffness to the three above systems are obtained, and their ratios with the spring stiffness of one flange are shown by *Dekker* (1998) to be equal to the equivalent I_w, I_z and I_t divided by that of one flange or the global cross-section:

$$\frac{K_{\mathrm{warping,eq}}}{K_{\mathrm{f}}} = \frac{I_{\mathrm{w,eq}}}{I_{\mathrm{w}}} = \frac{R_1 + R_2}{R_1 + R_2 + 1} \qquad \text{(II.40)}$$

$$\frac{K_{\mathrm{L,eq}}}{K_{\mathrm{f,L}}} = \frac{I_{\mathrm{z,eq}}}{I_{\mathrm{z,f}}} = 1 + \frac{R_1}{R_1 + 4} \qquad \text{(II.41)}$$

$$\frac{K_{\theta,eq}}{K_{\theta,L}} = \frac{I_{t,eq}}{I_{t,f}} = 1 + \frac{R_2}{R_2 + 6} \tag{II.42}$$

where $I_{z,f}$ is the second moment of area about the z-axis of a single flange and $I_{t,f}$ is the torsional constant of a single flange.

Besides, *Dekker* (1998) derived the coefficients R_1 and R_2:

$$R_1 = \frac{12 t_w^{\,3} L^4}{\pi^4 t_f b^3 h_w^{\,3}} \tag{II.43}$$

$$R_2 = \frac{3E}{2\pi^2 G} \frac{L^2}{b h_w} \left(\frac{t_w}{t_f} \right)^3 \tag{II.44}$$

Using the relationship between the modulus of elasticity E and the shear modulus G that depends on Poisson's ratio v (see expression (II.2)), one can rewrite expression (II.44) as:

$$R_2 = \frac{3(1-\nu)}{\pi^2} \frac{L^2}{b h_w} \left(\frac{t_w}{t_f} \right)^3 \tag{II.45}$$

The equivalent stiffness approach was also adopted by *Pi* (2000) to determine the elastic critical bending moment for LDB. Indeed, it was suggested to estimate the critical bending moment for LDB in the case of a constant bending moment using:

$$M_{cr,LTB} = \frac{\pi^2 E I_z}{L^2} \sqrt{\frac{1}{k_{wd}^{\,2}} \frac{I_w}{I_z} + \frac{L^2 (G I_t)_{eq}}{\pi^2 E I_z}} \tag{II.46}$$

where the effective torsional rigidity $(GI_t)_{eq}$ is:

$$(G I_t)_{eq} = \frac{2 G I_t \times \frac{12 D_w L^2}{\pi^2 h_w}}{2 G I_t + \frac{12 D_w L^2}{\pi^2 h_w}} \tag{II.47}$$

with:

$$D_w = \frac{E t_w^{\,3}}{12(1-\nu^2)}$$

and the warping distortion effective length factor k_{wd} is:

$$k_{wd} = \sqrt{1 + \left[\min\left(\frac{t_f}{t_w}; 2 \right) \right]^3 \left(\frac{h_w}{12L} \right) \left(1 + \frac{b}{h_w} \right)} \tag{II.48}$$

Pi (2000) also proposed to use expression (II.46) but with the distortion effective length factor k_{wd} equal to 1. The predictions of such expression showed a good agreement with finite element and finite stripe results for flanges having a substantial torsional rigidity. The predictions of expression (II.46) showed a good agreement with the reference numerical results for a wider range of flanges dimensions.

Both analytical models proposed by *Dekker* (1998) and *Pi* (2000) consist in the use of equivalent rigidities to determine the elastic critical bending moment for LDB. This approach leads to expressions adapted to hand calculation but the consistency between LTB and LDB critical loads is questionable. Indeed, a lack of transition between both critical bending moments is noticed and one may wonder which buckling mode is the most relevant when confronted to an arbitrary case.

Other existing approaches are depicted within the next sub-sections.

II.7.2.2. Modified critical bending moment for LTB

Besides the equivalent stiffness method, one may determine the critical LDB bending moment by multiplying the critical bending moment for LTB (exp. (II.39)) by a reducing coefficient. Using the results of finite element analyses, *Bradford* (1985) proposed expression (II.49) for monosymmetric members under a bending moment gradient. This expression concerns beams having flanges of equal thickness but different widths.

$$M_{cr,LDB} = \left[1 - \frac{490 \frac{t_f^{\,2}}{b_t t_w}\left(1 - 0.56 \frac{b_c}{b_t}\right)}{\frac{E W_y}{M_{cr,LTB}}}\right] M_{cr,LTB} \qquad \text{(II.49)}$$

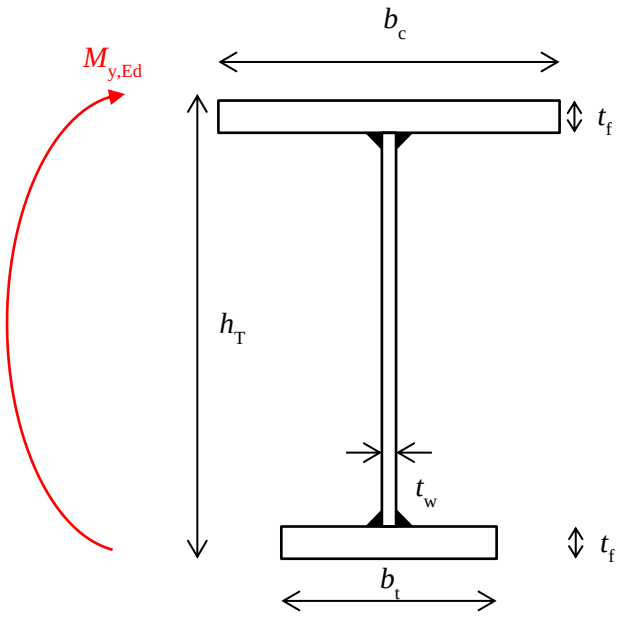

Figure II-12:Cross-section studied by Bradford *(1985)*

where b_c and b_t are the compression and tensile flanges widths, respectively (see Figure II-12). Expression (II.49) is applicable when:

$$1 \le \frac{b_t}{b_c} \le 4 \tag{II.50}$$

$$1 \le \frac{t_f}{t_w} \le 4 \tag{II.51}$$

$$10 \le \frac{b_t}{t_f} \le 20 \tag{II.52}$$

Bradford (1985) recommended to use expression (II.49) when the largest flange is in tension. In the opposite case, conservative results should be obtained by setting $b_c / b_t = 1$ in expression (II.49).

No current design standard explicitly accounts for LDB but the *AISC* rules consider the impact of the web distortion on the elastic critical bending moment for LTB. Indeed, for doubly and mono-symmetric I-section beams having a slender web, the American code proposes to determine the elastic critical LDB bending moment using:

$$M_{cr,LDB} = R_{pg} M_{cr,LTB}\left(I_t = 0\right) \tag{II.53}$$

where the bending strength reduction factor R_{pg} is:

$$R_{pg} = 1 - \frac{a_w}{1200 + 300 a_w}\left(\frac{h_w}{t_w} - 170\varepsilon\right) \le 1.0 \tag{II.54}$$

The parameter a_w corresponds to the ratio of the web area to the compression flange area with a maximum value of 10. The factor R_{pg} is generally comprised between 0.9 and 1.0. Indeed, when a_w is equal to 10, R_{pg} is lower than 0.9 if:

$$\frac{h_w}{t_w} > 170\varepsilon + 42 \tag{II.55}$$

For S355 beams, the previous web slenderness limit value is 180, corresponding for instance to a web 5 mm thick and 900 mm high not commonly used in practice.

It is worth mentioning that the *AISC* standard defines webs as slender when:

$$\frac{h_w}{t_w} > 170\varepsilon \tag{II.56}$$

with:

$$\varepsilon = \sqrt{\frac{235}{f_y}}$$

The previous criterion is adapted to the *Eurocode 3 Part 1-1* cross-section classification formalism assuming that the elasticity modulus E is equal to 210 000 MPa. Slender webs according to the American code correspond to Class 4 webs in pure bending according to *Eurocode 3 Part 1-1*, which are defined by:

$$\frac{h_w}{t_w} > 124\varepsilon \tag{II.57}$$

The *AISC* code implicitly proposes a lower limit value of the web slenderness (170ε) above which the web distortion may influence the global buckling of the beam. However, a lack of consistency between the critical bending moments for beams having a web slenderness slightly under and right above 170ε is noted. Besides, the *AISC* limit value does not account for the flanges dimensions which can have a significant impact on the distortional buckling mode, as shown by *Bradford* (1985). The predictions of the *AISC* expressions were compared against results of finite strip analyses conducted by *Zirakian* (2008). Very conservative results were obtained neglecting the member torsional constant when compared to the reference results.

Similarly, *Naderian* (2014) used results obtained employing the finite strip method to conclude that expression (II.53) from *AISC* was overly conservative. The following expression was proposed as an alternative:

$$M_{cr,LDB} = 1.02 R_{pg} M_{cr,LTB}\left(I_t = 0\right) \tag{II.58}$$

The previous expression corresponds to that proposed by the American code increased by 2%; the difference between both expressions for the critical bending moment is negligible.

For mono-symmetric members subjected to a constant axial load and bending moment distribution, *Wang* (1991) expressed the total potential energy using an appropriate expression for the web lateral displacement v_w:

$$v_w(x,z) = \left(\alpha_1 + \frac{2\alpha_2 z}{h_w} + \frac{4\alpha_2 z^2}{h_w^2} + \frac{8\alpha_3 z^3}{h_w^3}\right)\sin\left(\frac{\pi x}{L}\right) \tag{II.59}$$

where the α_i coefficients depend on the displacements and twist rotation of both flanges.

The energy method was then employed to perform a numerical parametric study. The results of this parametric study were then used to provide a fitted expression for the LDB critical bending moment, which is for doubly symmetric members:

$$M_{cr,LDB} = C_{LDB}\frac{\pi^2 E I_z}{L^2}\sqrt{\frac{I_w}{I_z} + \frac{L^2 G I_t}{\pi^2 E I_z}} \tag{II.60}$$

where the distortion factor C_{LDB} is:

$$C_{LDB} = 1 - 0.06\frac{t_f}{t_w}\frac{h_w}{L}\left(1 + \frac{20 t_f^2}{h_w t_w}\right) \leq 1.0 \tag{II.61}$$

For mono-symmetric beam-columns, a more general expression is provided by *Wang* (1991).

In addition to the equivalent rigidities approach, one can determine the critical bending moment for LDB multiplying that for LTB with a coefficient lower than 1, and possibly assuming that the torsion constant is zero. However, no expression depicted in this sub-section relies on a solid mechanical background, the results of numerical studies being employed.

The following sub-section II.7.2.3 concerns the analytical model derived by *Hancock* (1980). The approach was similar to that of *Wang* (1991), based on the energy method computed using appropriate displacement and rotation fields. The energy method is fully derived leading to a consistent analytical expression for the elastic critical bending moment for lateral distortional buckling.

II.7.2.3. Energy method with appropriate displacement and rotation fields

In the case of doubly symmetric members subjected to both a constant axial load and bending moment, *Hancock* (1980) employed the energy method using appropriate functions for the displacement and rotation fields (see Figure II-13). Indeed, the web lateral displacement was approximated using expression (II.59) while the flanges vertical and lateral displacements were approximated by half sine waves with appropriate magnitudes.

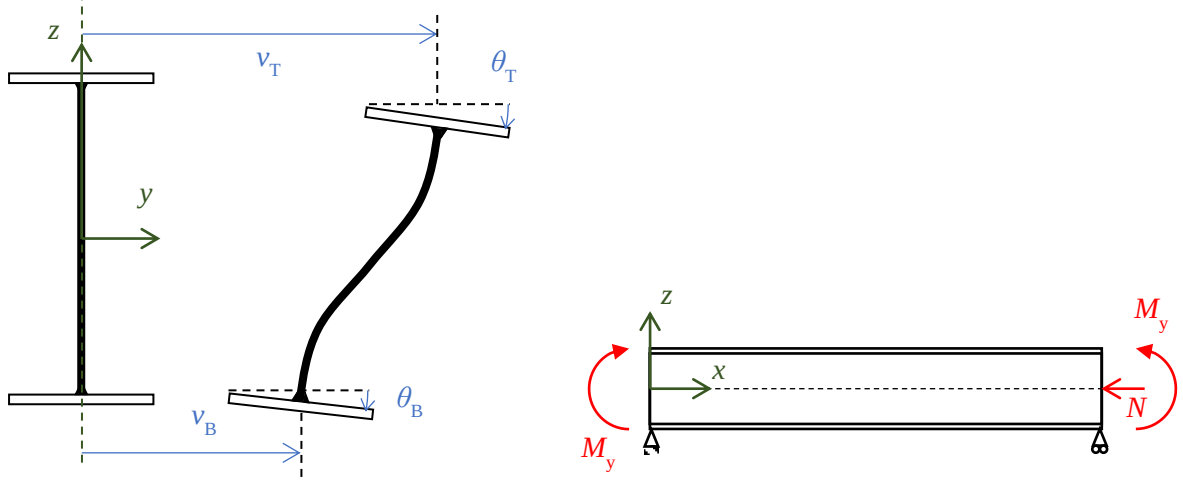

a) *LDB displacements* b) *Studied loading condition*

Figure II-13: Hancock*'s (1980) assumptions*

In the case of a constant bending moment acting without axial load, and assuming that I_z is negligible when compared to I_y, the minimum potential energy principle results in the following expression for the critical bending moment for LDB:

$$M_{cr,LDB} = \frac{\pi^2 EI_z}{L^2}\sqrt{\frac{I_w}{I_z} + \frac{L^2 GI_t}{\pi^2 EI_z}\left(\frac{K + I_{t,w}/I_t}{K+1}\right)} \qquad \text{(II.62)}$$

where $I_{t,w}$ is the torsional constant of the web and:

$$K = \frac{3}{\pi^2(1+\nu)}\frac{L^2}{bh_w}\left(\frac{t_w}{t_f}\right)^3 \qquad \text{(II.63)}$$

One can notice the following relationship between K and R_2 from *Dekker* (1998):

$$K = R_2\frac{1-\nu}{1+\nu} \qquad \text{(II.64)}$$

The expression for the critical bending moment for LDB derived using *Hancock*'s (1980) approach proposes a continuity between LTB and LDB. Indeed, when K tends towards the infinite, the critical bending moment obtained is similar to that for LTB while if $K = 0$, the flanges torsional constants are neglected. A limit lower value of K above which the elastic critical bending moment of a beam under a constant moment distribution can be determined assuming that web distortion is negligible is therefore discussed in the next sub-section II.7.2.4.

II.7.2.4. Boundary between LTB and LDB

For a constant bending moment distribution, expression (II.62) that relies on a strong theoretical basis can be employed to determine the critical bending moment of a beam that may undergo lateral torsional buckling with possible web distortion. This expression depends on a coefficient K given by expression (II.63). For the extreme cases where K tends towards the infinite or zero, the critical bending moment obtained corresponds to a LTB or LDB mode, respectively. A lower limit value of K can therefore be derived above which one may neglect the web distortion when computing the critical bending moment.

When K is greater than a limit value $K_{\lim}$, the deviation of the critical bending moment determined using expression (II.62) from that determined using (II.39), neglecting web distortion, is lower than a value ε:

$$\frac{M_{\text{cr,LDB}}}{M_{\text{cr,LTB}}} = \sqrt{\frac{1}{\frac{1}{\chi_{\text{t}}^2}+1} + \frac{1}{\chi_{\text{t}}^2+1}\frac{K+{I_{\text{t,w}}}/{I_{\text{t}}}}{K+1}} \geq 1-\varepsilon \tag{II.65}$$

with:

$$\chi_{\text{t}} = \frac{\pi}{L}\sqrt{\frac{EI_{\text{w}}}{GI_{\text{t}}}}$$

When χ_{t} goes to infinity, the ratio between $M_{\text{cr,LDB}}$ and $M_{\text{cr,LTB}}$ tends to 1. No deviation between both critical loads is obtained, therefore web distortion is negligible and one may employ expression (II.39).

The minimum value of the square root in the previous expression is obtained when χ_{t} goes to zero, yielding:

$$K \geq K_{\lim} = \frac{\left(1-\varepsilon\right)^2 - {I_{\text{t,w}}}/{I_{\text{t}}}}{1-\left(1-\varepsilon\right)^2} \tag{II.66}$$

Assuming that a 10% deviation on the critical bending moment is still admissible, the previous expression rewrites:

$$K \geq 4.26 - 5.26\,{I_{\text{t,w}}}/{I_{\text{t}}} \tag{II.67}$$

One may conservatively simplify the previous criterion as:

$$K \geq 1 \tag{II.68}$$

which corresponds to the case where:

$$I_{t,w} / I_t \leq 0.62 \qquad \text{(II.69)}$$

For the vast majority of welded steel members, the preceding inequality is valid. In particular, beams that are susceptible to web distortion when undergoing global buckling generally present flanges having a greater torsional constant than their web.

Introducing the value of K given by expression (II.63) and assuming that the Poisson's ratio is 0.3, the criterion given by (II.68) rewrites as a function of the member dimensions:

$$\frac{L^2}{bh_w}\left(\frac{t_w}{t_f}\right)^3 \geq 4.28 \qquad \text{(II.70)}$$

Eventually, the critical bending moment of beams under a uniform moment distribution that verify the previous criterion may be computed neglecting web distortion, i.e. using expression (II.39).

For a beam subjected to a constant bending moment distribution, the predictions of the presented existing expressions are compared against the results of finite element analyses using shell element in the following section.

II.7.3 Finite element analyses

Linear Bifurcation Analyses (*LBA*) are performed using a shell element model developed with *ANSYS* software. The shell elements possess 8 nodes, each of them presenting 6 degrees of freedom. The numerical analyses are led for a constant bending moment distribution, end moments being enforced by nodal forces varying linearly between both flanges, as depicted in Figure II-14. This figure also shows the boundary conditions corresponding to fork supports: the lateral and vertical displacements are fully prevented along with the twist rotation at both ends. To prevent any rigid body motion, the longitudinal displacement is fully prevented at one end.

For obvious reasons web distortion is unrestrained along the beam length.

A large number of LBA calculations were led on beams having cross-section dimensions entering the scope defined in Table II-12. The numerical simulations are performed considering a Young's modulus E = 210 000 MPa and a Poisson's ratio ν = 0.3.

h_w (mm)	t_w (mm)	h_w/t_w	b (mm)	t_f (mm)	b/t_f	L (m)
400 to 1000	4 to 8	48 to 165	160 to 280	10 to 46	4.3 to 28	4 to 8

Table II-12: Scope of the parametric study for LDB

The numerical results are used as reference values and compared against the predictions of the analytical models proposed by *Dekker* (1998), *Pi* (2000), *Bradford* (1985), the *AISC* code, *Wang* (1991) and *Hancock* (1980). The results obtained using expression (II.39) neglecting web distortion are also compared to the reference values.

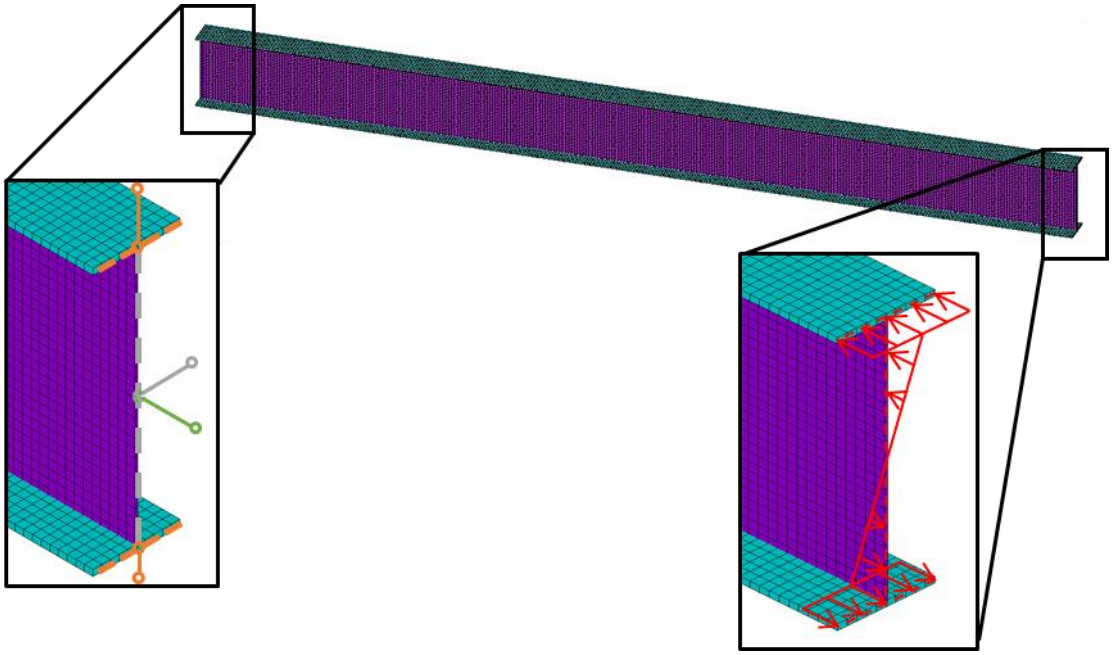

Figure II-14: Numerical boundary conditions

The comparison between analytical predictions and finite element results is shown in Figure II-15 where the dimensionless critical bending moment m_{cr} is given as a function of the distortion coefficient K calculated with expression (II.63). The dimensionless ratio m_{cr} corresponds to the ratio of the analytical prediction $M_{cr,analytical}$ to the numerical reference value $M_{cr,FEA}$:

$$m_{cr} = \frac{M_{cr,analytical}}{M_{cr,FEA}} \tag{II.71}$$

Figure II-15a) shows that for values of K greater than unity, neglecting web distortion yields critical bending moments very close to the numerical results. Web distortion is therefore insignificant when K is greater than 1, which corresponds to the limit value of this parameter set in sub-section II.7.2.4. Besides, for lower values of K, the prediction of expression (II.39) are unsafe when compared to FEA results. Most of the results obtained using the expression from *AISC* are equal to the predictions neglecting web distortion, except for slender webs for which the analytical predictions are up to 20% on the safe side. However, the K coefficient for members having slender webs scarcely falls under 1: the criterion proposed by the American standard is therefore inconsistent.

The results obtained using *Wang*'s (1991) model are similar to the reference values when K is greater than 1. For lower values of this parameter, the predictions of such model are on the safe side. The deviation from the numerical values slightly increases as K diminishes, the maximum deviation being 16%. The predictions of *Dekker*'s (1998) expression are overly conservative for low values of K, while as this coefficient increases, analytical predictions get closer to the numerical results but with an average deviation close to 20% on the safe side.

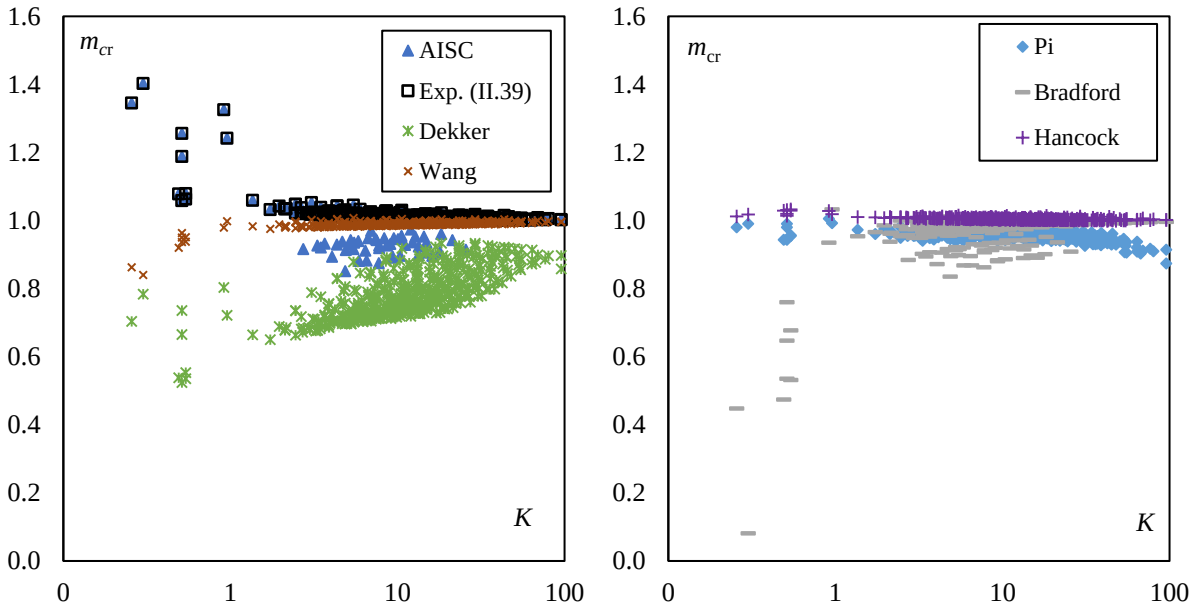

a) Exp. (II.39), AISC, Dekker *and* Wang *proposals*

b) Pi, Bradford *and* Hancock *proposals*

Figure II-15: $M_{cr,LDB}$ *analytical predictions compared to FEA results for a constant bending moment distribution*

Figure II-15b) shows that the predictions of *Bradford*'s (1985) proposal are overly conservative when K is lower than 1 For higher values of K, the analytical predictions are closer to the reference results, laying on the safe side with a maximum deviation from the reference results greater than 15%. On the contrary, the results obtained using *Pi*'s (2000) and *Hancock*'s (1980) proposals are very close to the reference results, particularly for low values of K. When $K > 10$, the predictions of *Pi*'s (2000) proposal become safe while the results obtained using *Hancock*'s (1980) proposal are very close to the numerical results whatever K. The maximum deviation on the unsafe side is then 3% which is still admissible.

		Exp. (II.39)	***AISC***	***Dekker* (1998)**	***Wang* (1991)**	***Pi* (2000)**	***Bradford* (1985)**	***Hancock* (1980)**
$K < 5$	*M*	*1.049*	*1.036*	*0.707*	*0.979*	*0.965*	*0.913*	*1.010*
	SD	0.0789	0.0915	0.0581	0.0260	0.0144	0.1590	0.0062
$K < 2$	*M*	*1.167*	*1.167*	*0.659*	*0.945*	*0.973*	*0.695*	*1.020*
	SD	0.1323	0.1323	0.0951	0.0477	0.0197	0.2803	0.0090

Table II-13: Comparison between analytical and numerical results for a uniform bending moment distribution

The mean (M) and standard deviation (SD) of the ratios m_{cr} obtained using the predictions of the analytical models proposed by *Hancock* (1980), *Bradford* (1985), *Wang* (1991), *Dekker* (1998), *Pi* (2000), the *AISC* code and expression (II.39) are given in Table II-13. The results are presented for beams where $K < 5$ and 2.

Table II-13 shows that neglecting web distortion (using expression (II.39)) results in significantly unsafe and scattered critical bending moments for low values of K, as for the predictions of the American code. On the contrary, the predictions of *Dekker*'s (1998) proposal are very safe, the mean deviation from the numerical results being approximately 30%. The results obtained using *Dekker*'s (1998) model present a low standard deviation when $K < 5$ while it increases for lower values of K. Using *Bradford*'s (1985)

expression yields safe results, especially when $K < 2$ where the mean deviation from the numerical results is 30%. Besides, for the lowest values of K, the standard deviation is overly high.

The predictions of *Wang*'s (1991), *Pi*'s (2000) and *Hancock*'s (1980) expressions are very close to the numerical results, the mean deviation being 5% at most. The analytical model derived by *Hancock* (1980) is slightly better suited than those of *Wang* (1991) and *Pi* (2000), the results presenting a lower standard deviation that is less than 1%.

A second set of finite element analyses was performed considering the numerical model previously introduced but where the web distortion is prevented along the beam enforcing kinematic constraints. The critical bending moment thus obtained corresponding to a LTB mode is $M_{cr,LTB}$. The critical bending moments for LTB and LDB having been computed for a large number of beams, their ratio is expressed as a function of K in Figure II-16.

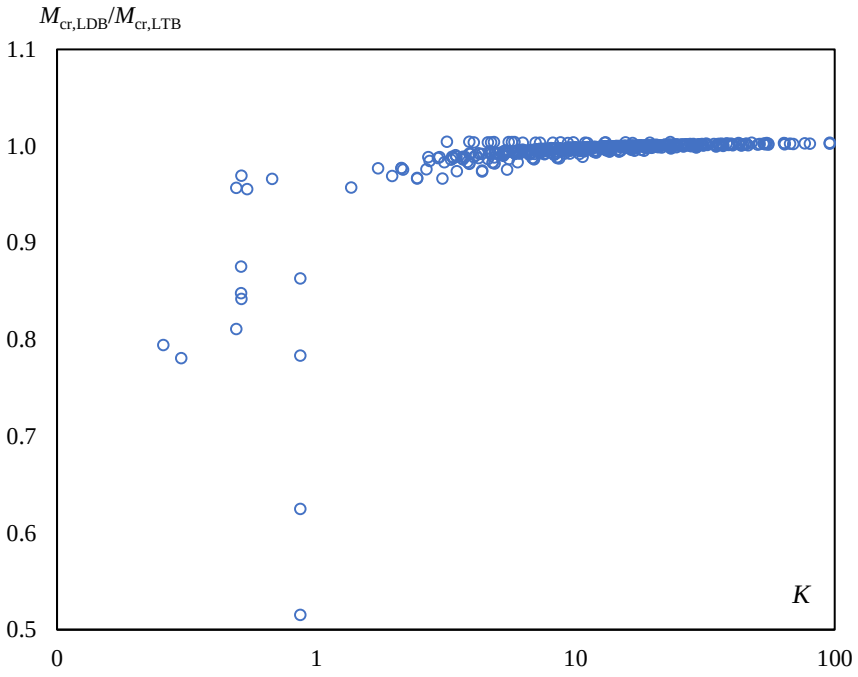

Figure II-16: Ratio of the numerical critical bending moments for LDB and LTB

One can notice that web distortion influences the critical bending moment when $K < 1$ while for greater values, the deviation of the critical bending moments for LDB from that for LTB is at most 5%. The FEA results depicted in Figure II-16 are in line with the lower limit value of K (see expression (II.63)) above which the critical bending moment of a beam can be computed neglecting web distortion.

In the simple case of a constant bending moment distribution, one may determine the critical bending moment for lateral distortional buckling of a uniform doubly symmetric beam resting on fork supports at both ends using expression (II.62). Expression (II.60) may also be used although providing safe results for low values of K with a deviation up to 16% from the numerical results. The analytical model from *Pi* (2000) can also be employed though a lack of consistency between LDB and LTB is noticed. Furthermore, if criterion (II.68) is satisfied for the studied member, its critical bending moment can be computed assuming no web distortion.

The uniform bending moment distribution having been investigated, the influence of the bending moment distribution on the buckling behaviour is discussed in the following section. The possibility to

extend the existing models adapted to a constant moment diagram to a linearly varying bending moment distribution is then studied.

II.7.4 Linear bending moment distribution

II.7.4.1. Buckling mode

In addition to the constant bending moment distribution case, FEA were performed for beams from Table II-14 subjected to a linear bending moment distribution. The ratios ψ between end moments studied are 0.5, 0, -0.5 and -1. Two types of FEA were run:

(i) Unrestraining web distortion (thus obtaining $M_{cr,LDB}$), and
(ii) Fully preventing web distortion by implementing kinematic conditions ($M_{cr,LTB}$).

#	h_w (mm)	t_w (mm)	b (mm)	t_f (mm)	L (m)	K (II.63)
B1	400	6	200	27	4	0.513
B2	400	8	200	36	4	0.513
B3	400	6	200	34	4	0.257
B4	400	8	200	43	4	0.301
B5	800	8	200	46	8	0.492
B6	800	6	200	34	8	0.514
B7	800	8	200	20	4.5	1.894
B8	800	6	200	18	6	1.948
B9	800	8	200	20	5	2.338
B10	800	6	200	18	8	3.464
B11	800	8	250	18	6	3.695
B12	800	8	200	20	7	4.583

Table II-14: Geometry of the studied beams under a linear bending moment distribution

Figure II-17 shows the cross-section displacement of beam *#B7* for different values of ψ. The cross-section displacements are shown at a specific location along the beam which varies between $L/2$ and $L/4$ as ψ fluctuates from 1 to -1. For beam *#B7*, K is 1.894, therefore greater than the lower limit value of 1 defined by expression (II.68) above which web distortion is negligible.

The criterion is in good agreement with the cross-section displacement shown in Figure II-17a) ($\psi = 1$) where web distortion is barely visible. The same can be said in the case where $\psi = 0.5$ (see Figure II-17b)) while for $\psi = 0$ (Figure II-17c)), web distortion slightly appears in single curvature. For negative values of the ratio between end moments, web distortion gets more pronounced as ψ diminishes to -1.

For a beam with $K > 1$, Figure II-17 shows that when the ratio between end moments ψ is lower than a limit value ψ_{lim}, web distortion can be observed in single curvature. Similarly, for beams with $K < 1$, when ψ is lower than a certain limit value ψ_{lim}, web distortion corresponds to single curvature. Therefore, for such members, when $\psi > \psi_{lim}$, web distortion matches with double curvature while when $\psi < \psi_{lim}$, web distortion in single curvature appears.

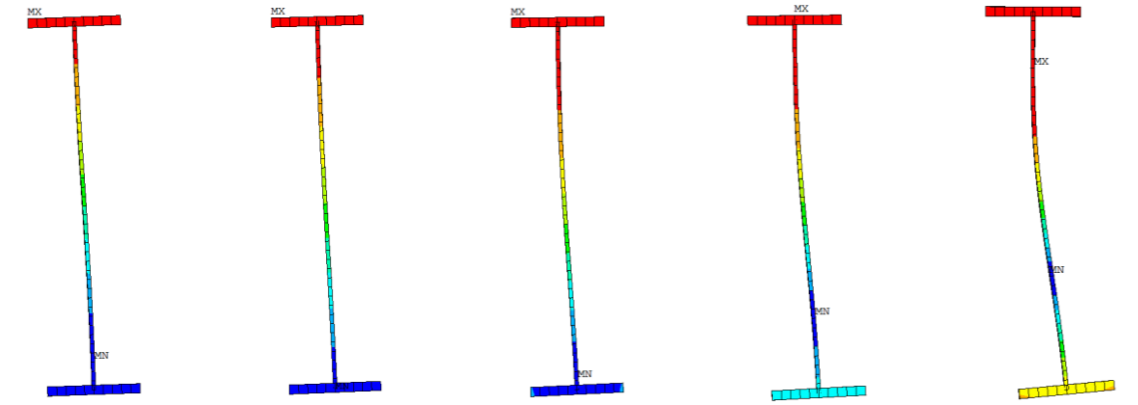

*Figure II-17: Cross-section displacements for beam #*B7 *(K>1)*

Accordingly, in the following sub-section II.7.4.2 the predictions of *Hancock*'s (1980), *Wang*'s (1991) and *Pi*'s (2000) proposals multiplied by the equivalent uniform moment factor C_1 (see equation (II.17)) are compared against the results of FEA performed for various ψ. In addition, the ratio between both FEA results for each beam, $M_{cr,LDB}$ and $M_{cr,LTB}$, are also provided.

II.7.4.2. Critical bending moment

In the present sub-section, the predictions of the analytical models provided by *Hancock* (1980), *Wang* (1991), *Dekker* (1998) and *Pi* (2000) to determine the critical LDB bending moment are compared to the results of FEA calculations. The analytical critical bending moments being derived in the case of a linear bending moment distribution, their values are multiplied by the coefficient C_1 having the values suggested in sub-section II.4.4. The ratios m_{cr} between the analytical critical bending moment and the reference value (FEA with unrestrained web distortion) are depicted in Figure II-18 as a function of K.

It is worth mentioning that some FEA with unrestrained web distortion have resulted in a local buckling mode, particularly for low values of ψ in the case of beams with $K < 1$. Those results are not reported in Figure II-18.

Figure II-18 shows very close results in the cases of $\psi = 1$ or 0.5, the analytical models of *Hancock* (1980), *Wang* (1991), and *Pi* (2000) providing accurate results. When $\psi \geq 0$, the analytical expressions of *Hancock* (1980) and *Pi* (2000) yield similar values of the critical bending moment as the reference ones, the maximum deviation being 11% when $\psi = 0$. The predictions of *Wang*'s (1991) model are similar to those from the previously cited ones except for very low values of K (< 0.35). In such case, this model provides results on the safe side with a deviation comprised between 10 and 16% from the FEA values. The results obtained using *Dekker*'s (1998) proposal are safe-sided with an average deviation of 28%. The comparisons between analytical and numerical results when ψ is 0.5 or 0 show results similar to the constant bending moment distribution case.

When $\psi = -0.5$, similar results are noticed for beams with $K < 1$ though the predictions of all proposals except *Dekker*'s (1998) become slightly unsafe. For beams having $K > 1$, the results obtained using these models can be very unsafe (deviation up to 40%) while for some beams, the analytical and numerical critical bending moments are similar. Using *Dekker*'s (1998) expression produces safe-sided results whatever K with a mean deviation of 18%.

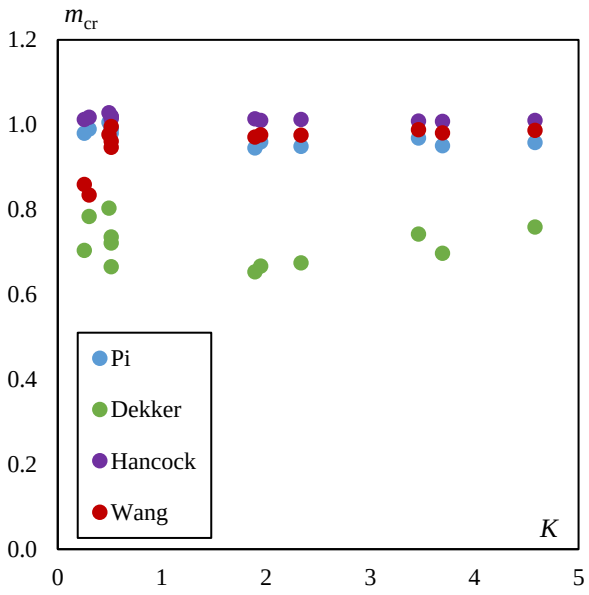

a) $\psi = 1$

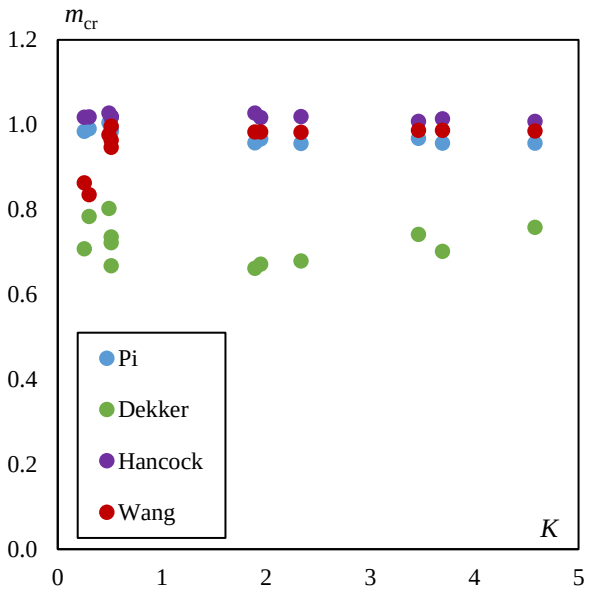

b) $\psi = 0.5$

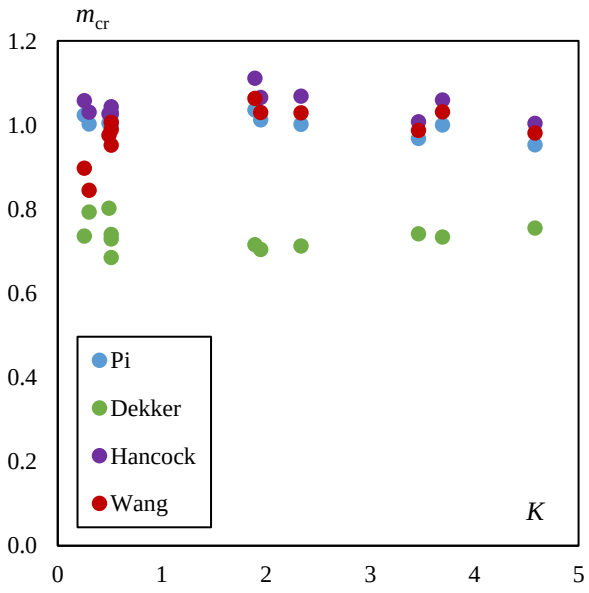

c) $\psi = 0$

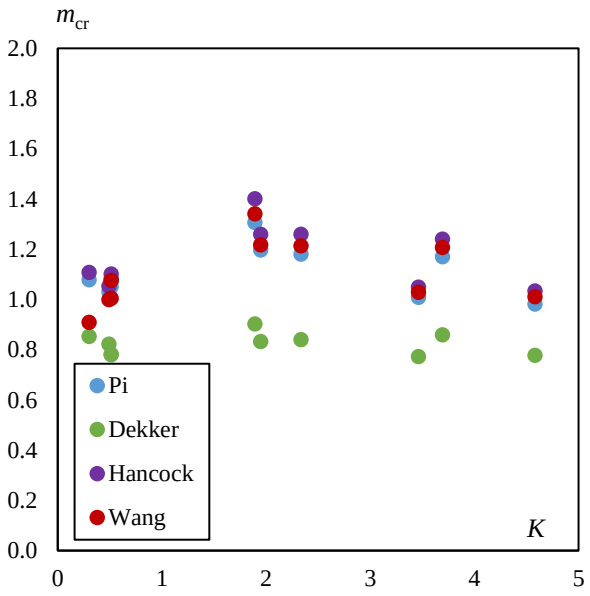

d) $\psi = -0.5$

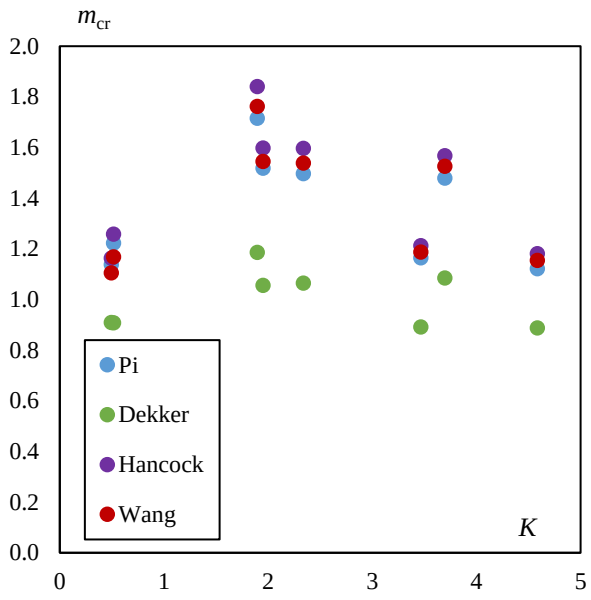

e) ψ = -1

Figure II-18: $M_{cr,LDB}$ *analytical predictions compared to FEA results for a linear bending moment distribution*

In the case where ψ = -1, the results are more scattered than for the other values of ψ. For beams presenting K < 1, the analytical predictions of *Hancock*'s (1980) and *Pi*'s (2000) proposals are on the unsafe side with a 20% deviation from the reference results However, when K > 1 these analytical predictions can reveal significantly unsafe, the deviation being up to 90%. Similar results are obtained using *Wang*'s (1991) model when K > 1. For lower values of K, this analytical model yields slightly unsafe results with a 14% mean deviation from the numerical results. The predictions of *Dekker*'s (1998) model can be unsafe with a maximum deviation from the numerical results of 19% though the mean deviation is zero.

In addition, the ratios of the numerical critical bending moments $M_{cr,LDB}$ to $M_{cr,LTB}$ are given in Table II-15 for each beam as a function of ψ. The empty cells correspond to beams failing in an elastic web local buckling mode.

Table II-15 shows that as ψ diminishes, the ratio $M_{cr,LDB}$ / $M_{cr,LTB}$ gets lower, and therefore web distortion gets more important though almost similar values are obtained when ψ = 1 or 0.5. When $\psi \geq 0.5$, the ratios are greater than 0.95 for beams with K > 1 but their values range between 0.85 and 0.95 when ψ = 0. For negative values of ψ, the results are found between 0.50 and 0.87 for these members.

The results given in Table II-15 are in agreement with those depicted in Figure II-18. Indeed, when ψ = 0.5, the failure mode is associated with a web in double curvature for beams with K < 1 while no web distortion appears when K > 1 When ψ = 0, web distortion slightly appears in some of the beams with K > 1 while the LDB mode remains unchanged for the other members. Besides, for negative values of ψ, all beams with K > 1 fail in LDB with single curvature, though web distortion is smaller in beams *#B10* and *#B12*. Beams with K < 1 fail in LDB with a web in between single and double curvature.

#	K (II.63)	$M_{cr,LDB}$ / $M_{cr,LTB}$				
		ψ = 1	ψ = 0.5	ψ = 0	ψ = -0.5	ψ = -1
B1	0.513	0.874	0.865	0.820		
B2	0.513	0.846	0.841	0.818	0.741	0.653
B3	0.257	0.793	0.784	0.736		
B4	0.301	0.779	0.775	0.751	0.672	
B5	0.492	0.808	0.805	0.790	0.739	0.667
B6	0.514	0.839	0.834	0.805	0.716	
B7	1.894	0.974	0.955	0.854	0.636	0.504
B8	1.948	0.971	0.958	0.884	0.703	0.574
B9	2.338	0.976	0.963	0.888	0.708	0.581
B10	3.464	0.976	0.971	0.940	0.849	0.759
B11	3.695	0.986	0.973	0.900	0.722	0.595
B12	4.583	0.982	0.978	0.951	0.868	0.786

Table II-15: Comparison between LDB and LTB numerical critical bending moments

Eventually, when $K < 1$, ψ_{lim} is lower than 0.5 and expressions (II.46), (II.60) and (II.62) multiplied by the appropriate value of C_1 can be employed to determine the critical LDB bending moment. For beams with $K > 1$, web distortion is negligible when ψ is 0.5 and the value of ψ_{lim} is not unique but lower than 0.5. When $\psi < \psi_{lim}$, the analytical models of *Hancock* (1980), *Wang* (1991) and *Pi* (2000) are very unsafe and should therefore not be used. The predictions of *Dekker*'s (1998) model, which are overly conservative for double curvature, are the closest to the numerical results but a maximum deviation of 19% is noticed on the unsafe side when ψ = -1.

II.7.5 Summary

Existing formulations for the critical bending moment for lateral-distortional buckling have been presented for doubly symmetric members under a constant bending moment distribution. In such case, steel beams may undergo web distortion in double curvature. The use of equivalent rigidities is suggested by *Dekker* (1998) and *Pi* (2000). On the contrary, *Bradford* (1985), *Wang* (1991), the *AISC* standard and *Naderian* (2014) propose to use the critical bending moment for LTB with a reducing coefficient. For slender webs, the American code and *Naderian* (2014) suggest to equate the torsional constant to zero. The energy method was employed by *Hancock* (1980) using adapted expressions for the displacement and rotation fields yielding an expression depending on a distortion coefficient *K*. A limit lower value of *K* has been established above which web distortion is negligible under a constant bending moment. When compared against the results of finite element analyses, the predictions of *Hancock*'s (1980), *Wang*'s (1991) and *Pi*'s (2000) models are the most accurate. The formulations from the *AISC* and *Naderian* (2014) can be unsafe while those from *Bradford* (1985) and *Dekker* (1998) are overly conservative.

For a linear bending moment distribution, the analytical models of *Hancock* (1980), *Wang* (1991) and *Pi* (2000) and the limit value of *K* are accurate above a certain value of the ratio between end moments.

Indeed, for lower values of the ratio between end moments, steel members may fail in a LDB mode with web distortion in single curvature. In such case, none of the depicted analytical models provides accurate results when compared to numerical values.

Besides critical bending moments for LDB, design resistances should be investigated accounting for web distortion. A lack of analytical models predicting the ultimate strength of beams undergoing LDB can be noticed though *Rossi* (2022) lately developed formulae for a few load cases. However the proposed expressions, based on artificial neural network, reveal very tedious for a daily use.

II.8 Conclusion

Existing analytical expressions for the elastic critical loads of uniform members subjected to bending and/or compression have been derived using the energy method that involves the strain energy and the work performed by the external loads. Compressed members having a doubly symmetric cross-section may undergo in-plane or out-of-plane flexural or torsional buckling. Mono-symmetric members subjected to an axial load may fail either in a flexural-torsional or in-plane flexural buckling mode. The elastic critical loads corresponding to such buckling modes were provided for columns pinned at both ends subjected to a constant axial load.

A general expression of the elastic critical bending moment for lateral-torsional buckling adapted to mono-symmetric members is given. In the case of fork supports at both ends, existing values of the coefficients C_1, C_2 and C_3 on which the critical bending moment depends are presented. Analytical critical bending moments were computed using the C_i coefficients, which account for the bending moment distribution, provided by different standards. The analytical results were compared against reference values obtained using beam finite element analyses. Within the existing values from different design codes, C_i coefficients that provided the best safety level when compared to finite element analyses were suggested for beams resting on fork supports at both ends and subjected to various bending moment distributions.

The analytical determination of the elastic critical load of a uniform member subjected to either compression force or bending moment can be direct. However, obtaining that of a uniform member subjected simultaneously to compression and bending is not a straightforward process. Indeed, though hand calculation can be employed when both the axial load and bending moment intensities are uniform and the steel beam-column rests on fork supports at both ends, finite element analyses are required when the boundary conditions are not that trivial.

The treatment of non-uniform members has been discussed, existing propositions to determine the critical axial load for in-plane buckling or lateral-torsional buckling being given. As already shown in the past, one can notice that accurately accounting for the taper of the member leads to cumbersome expressions even for simple boundary conditions. Similarly to the case of uniform beam-columns, the elastic critical loads of a tapered member subjected to bending and/or compression should be obtained employing finite element analyses, e.g. using the software *LTBeamN*.

Eventually, the lateral-distortional buckling of doubly symmetric beams have been investigated. Existing formulations proposed in the case of a uniform bending moment distribution were depicted, their predictions being compared against numerical results. Expressions relying on a consistent derivation of appropriate displacement and rotation fields provide critical bending moment in good agreement with the numerical ones. The use of equivalent stiffness may produce a good approximation

of the numerical results (*Pi* (2000)) or provide overly conservative results (*Dekker* (1998)). A boundary between LDB and LTB failure modes have been derived using an existing analytical model of *Hancock* (1980) for a constant bending moment and validated against numerical results.

Besides, the bending moment distribution has a significant impact on the distortion mode, the web being either in single or double curvature. However, the comparison against numerical results highlighted that none of the depicted formulation can be employed in the case of an arbitrary bending moment distribution. Indeed, the accurate analytical models for a constant distribution provide unsafe results for end moments having opposite signs.

Expressions for the elastic critical bending moment for lateral-torsional buckling were presented assuming fork supports at both ends, warping and out-of-plane rotations being unrestrained. However, the presence of end restraints may affect the critical bending moment. Consequently, next chapter focuses on the elastic critical bending moment of doubly symmetric beams with warping restraints at supports.

III. *Elastic lateral-torsional buckling of I-beams with warping restraints*

III.1 Introduction

While the elastic lateral torsional buckling of a doubly symmetric uniform I-section beam is commonly investigated considering free warping and out-of-plane rotation at supports, the presence of welded transverse stiffeners or connection may maintain the opposite flange out-of-plane rotations, significantly reducing warping at supports. However, except for a beam with unrestrained or fully restrained warping, a lack of close-form solutions for lateral-torsional buckling of simply supported beams that account for warping restraints is noticed in the literature.

The current *Eurocode 9 Part 1-1* and *French National Annex to Eurocode 3 Part 1-1* provide analytical models, as depicted in Chapter II, of the elastic critical lateral-torsional buckling bending moment for different loading conditions but are restricted to fork supports. Despite a substantial impact on the buckling behaviour, the influence of connection typologies, such as bolted end plates or column base plates on warping is usually neglected.

As explained in Chapter II, the warping coefficient k_w is present in the expression of the critical bending moment to account for warping restraints, however no standard provides any guidance on how to evaluate this coefficient. Expressions for k_w can be found in the literature as depicted in section III.2. *Eurocode 9 Part 1-1* points out the increase of the equivalent uniform moment factor C_1 with warping restraints. Existing formulations for such coefficient are therefore provided in section III.2 mainly in the case of warping fully restrained at both ends, few researches having investigated the case of elastic restraints.

The lack of existing analytical models concerning the elastic lateral-torsional buckling of doubly symmetric beams with warping restraints at both ends led to the analytical model derived in section III.4 for members subjected to a linear bending moment distribution or a pointwise or uniformly distributed transverse load. The energy method is applied using appropriate trigonometric series for the twist rotation and lateral displacement, along with infinite power series based solutions for the shape functions. The buckling shapes obtained using the two methods are compared against those resulting from finite element analyses. Besides, the warping stiffness of some end connections are derived.

Since significant warping stiffness can be encountered in practice, a criterion for a limit stiffness is proposed to consider fully restrained warping at both ends when determining the elastic critical bending moment. In the case of column bases, the criterion is enriched to assume warping as fully restrained at one of the two ends. Finite element analyses permit to validate this simplification.

It is found that the critical bending moment depends on the stiffness of the warping restraints through both k_w and C_1, the latter depending also on the bending moment distribution. The comparison of the analytical results against the numerical ones obtained using 8-noded shell elements in *ANSYS* and 2-noded beam elements in *LTBeamN* software shows a good agreement.

III.2 Existing formulations

III.2.1 Critical bending moment

As depicted in Chapter II, the *French National Annex to Eurocode 3 Part 1-1*, *Eurocode 9 Part 1-1* and *TC8 from ECCS* (2006) the elastic critical bending moment expression accounts for warping restraints through the warping coefficient k_w for which no expression is provided in the codes. The elastic critical bending moment of a uniform beam having a doubly symmetrical cross-section subjected to a linear bending moment distribution or to a transverse load applied at the shear centre and resting on fork supports, the out-of-plane rotations being unrestrained at both ends, is:

$$M_{cr} = C_1 \frac{\pi^2 E I_z}{L^2} \sqrt{\frac{I_w}{I_z k_w^2} + \frac{L^2 G I_t}{\pi^2 E I_z}} \tag{III.1}$$

The warping coefficient k_w varies between 0.5 and 1 for fully restrained to unrestrained warping at both ends. Due to the lack of knowledge regarding the evaluation of k_w, a safe value of 1 is usually adopted in practice.

Kováč (2019) suggested adopting a value of k_w based on the twist rotation boundary conditions similarly to the evaluation of the k_z coefficient from the kinematic constraints on the out-of-plane rotations at supports.

The C_1 coefficient is generally assumed to be related to the bending moment diagram only and the *French National Annex to EN 1993-1-1* does not consider any influence of the elastic warping restraints. However, *Eurocode 9 Part 1-1* provides values of C_1 for fully restrained warping in the case of a transverse loading that increase comparatively to unrestrained warping. Besides, *Gosowski* (2007) showed a significant influence of different types of end restraints against warping on the experimental distribution of the twist rotation. *Wierzbicki* (2019) noticed, by means of finite element analyses, that the critical bending moment can be multiplied by up to 6 when end transverse stiffeners are present parallel to the web to restrain warping. Existing warping restraints can hardly be explicitly accounted for when evaluating the critical bending moment despite their recognized significant influence.

Živner (2012) employed finite element analyses to develop expression of the warping stiffness c_w and connect them to the warping coefficient k_w for hot-rolled IPE 200 and HEB 400 cross-sections. Based on the work of *Lindner* (1984), *ECCS' TC8* (2006) proposed an expression for the warping coefficient:

$$k_w = 1 - \frac{0.5}{1 + \frac{2}{\bar{c}_w}} \tag{III.2}$$

with:

$$\bar{c}_w = \frac{c_w L}{E I_w}$$

c_w: Stiffness of the warping restraints.

In presence of end transverse stiffeners at supports (see Figure III-1), the warping stiffness is:

$$c_w = \frac{G b t_p^{\,3} h_s}{3} \tag{III.3}$$

where t_p is the end plate thickness and h_s the distance between the flanges centres.

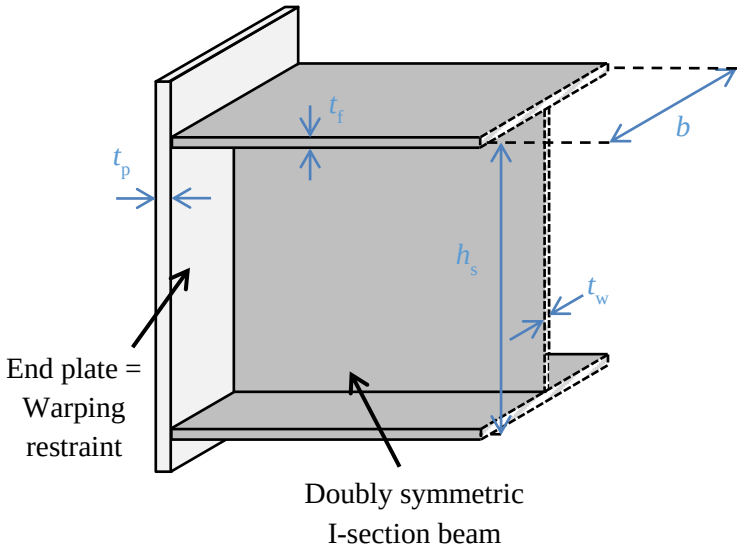

Figure III-1: Beam and end plate geometries

Expression (III.2) of the warping coefficient depends on the beam warping stiffness EI_w and length L, and on the spring warping stiffness c_w. The bending moment distribution for which expression (III.2) is valid is not specified and neither is the coefficient C_1. For a uniform bending moment distribution, *Pi* (2000) proposed to estimate the warping coefficient using:

$$k_w = \frac{6.5 + \overline{c}_w}{6.5 + 2.25\overline{c}_w} \tag{III.4}$$

Under the same bending moment distribution, *Trahair* (1993) suggested to use:

$$k_w = \frac{4 + \overline{c}_w}{4 + 2\overline{c}_w} \tag{III.5}$$

In the case of different warping restraints at both ends, *Wierzbicki* (2020) provided an expression of the warping coefficient, no bending moment distribution being specified:

$$k_w = 0.5 + 0.14\left(\mathrm{K}_{w,1} + \mathrm{K}_{w,2}\right) + 0.055\left(\mathrm{K}_{w,1} + \mathrm{K}_{w,2}\right)^2 \tag{III.6}$$

where the coefficients $K_{w,I}$ of the fixations stiffness at each end restrain against warping vary between 0 and 1 for fully restrained and unrestrained warping, respectively:

$$\mathrm{K}_{w,i} = \frac{1}{1 + \frac{\overline{c}_{w,i}}{2}} \tag{III.7}$$

Details on the derivation of expressions (III.2) and (III.4) to (III.6) are missing in the corresponding references.

In the case of cantilever beams, *Khanh* (2021) proposed an expression of the warping coefficient determined using the results of finite element analyses performed for a uniform bending moment distribution. The numerical expression, which does not account for the influence of the warping restrains on C_1, is:

$$k_w = 0.7\frac{2.8 + 0.7\overline{c}_w}{2.8 + 0.98\overline{c}_w} \tag{III.8}$$

The equivalent uniform moment factor has also been studied for fully restrained warping at both ends. Using the finite differences method, expression for C_1 were proposed by *Djalaly* (1974) for beams with fully restrained warping at supports subjected to end moments, their ratio ψ being comprised between -1 and +1, or a uniformly distributed load (UDL):

End moments $$C_1 = \frac{2}{\sqrt{1 + \psi + \psi^2}} \tag{III.9}$$

UDL $$C_1 = 1.581 \tag{III.10}$$

The finite differences method has also been employed by *Serna* (2006) to derive an expression for C_1 considering a general bending moment distribution and warping restraints. The expression is however restricted to the specific case of equal warping and out-of-plane coefficients ($k_w = k_z = k$):

$$C_1 = \frac{\sqrt{\sqrt{k}A_1 + \left[A_2\frac{1-\sqrt{k}}{2}\right]^2} + A_2\frac{1-\sqrt{k}}{2}}{A_1} \tag{III.11}$$

with:

$$A_1 = \frac{M_{max}^2 + 9kM_2^2 + 16M_3^2 + 9kM_4^2}{(17 + 18k)M_{max}^2}$$

$$A_2 = \frac{M_{max} + 4M_1 + 8M_2 + 12M_3 + 8M_4 + 4M_5}{37M_{max}}$$

where M_1 to M_5 are the values of the bending moment acting at every $L/4$ and M_{max} the design bending moment.

Sherbourne (1989) employed the Galerkin method to derive an expression of C_1 for beams subjected to end moments and with fully restrained warping and unrestrained out-of-plane rotation at both supports:

$$C_1 = \sqrt{\frac{13.37}{3(1+\psi^2)+5\psi}} \tag{III.12}$$

Assuming similar boundary conditions, *Lim* (2003) employed a beam finite element model to develop an expression of the equivalent uniform bending moment factor:

$$C_1 = \frac{2}{\sqrt{0.8}\sqrt{(1+\psi)^2 + 0.1(1-\psi)^2}} \tag{III.13}$$

Bresser (2020) used the energy method to develop an expression of C_1 in the case of beams with full warping restraints at both ends and simultaneously subjected to a point load F located along the beam length L and to end moments αFL and βFL:

$$C_1 = \frac{M_{\max}}{FL\sqrt{0.27(\alpha^2+\beta^2) + 0.46\alpha\beta + D_3\alpha + D_4\beta + D_5}} \tag{III.14}$$

where factors D_3 to D_5 depend on the location of the point load along the beam, a transverse load applied at mid-span resulting in -0.1925 for D_3 and D_4 and 0.0388 for D_5.

In addition, *Piotrowski* (2019) employed the energy method to derive a general expression for the elastic critical bending moment explicitly accounting for warping restraints. The lateral displacement v and twist rotation θ were approximated using power polynomial shape functions. For a beam subjected to a linear bending moment distribution with unrestrained out-of-plane rotation, *Piotrowski* (2019) proposed to use:

$$M_{cr} = D_1\sqrt{\frac{EI_z\left(C_1GI_tL^2 + C_2EI_w\right)}{C_3L^2}} \tag{III.15}$$

where the coefficients C_1, C_2, C_3 and D_1 are given in Table III-1.

	$-1 < \psi \le -0.5$	$-0.5 < \psi \le 1$
C_1	$347.75\left(1.457 - 2.4\kappa_w + \kappa_w^2\right)$	$57.6\left(1.457 - 2.4\kappa_w + \kappa_w^2\right)$
C_2	$4149\left(1.2 - \kappa_w\right)$	$691.2\left(1.2 - \kappa_w\right)$
C_3	$\left(1-\psi\right)\sqrt{1.681 - 2.88\kappa_w + 1.235\kappa_w^2}$	$\left(1+\psi\right)\sqrt{2.124 - 3.497\kappa_w + 1.44\kappa_w^2}$
D_1	$d_1 - e^{3\psi}d_2$	$d_1 - e^{-2.5\psi}d_2$
d_1	$1.068 + 0.014\kappa_w^2$	$1.018 + 0.000297\kappa_w - 0.009\kappa_w^6$
d_2	$1.704 + 0.099\kappa_w + 0.215\kappa_w^6$	$0.108 - 0.001\kappa_w - 0.014\kappa_w^6$

*Table III-1: Coefficients C_1 to C_3 and D_1 (*Piotrowski *2019)*

The index of fixity against warping κ_w varying from 0 to 1 for unrestrained and fully restrained warping, respectively, is given by:

$$\kappa_w = \frac{1}{1 + \frac{2}{\bar{c}_w}} \tag{III.16}$$

The warping coefficient can be identified from equation (III.15):

$$k_w = \pi\sqrt{\frac{C_1}{C_2}} = \frac{\pi}{2\sqrt{3}}\sqrt{\frac{1,457 - 2,4\kappa_w + \kappa_w^2}{1,2 - \kappa_w}} \qquad \text{(III.17)}$$

In addition, the C_1 coefficient is extracted form expression (III.15) and depends on the bending moment distribution and the warping stiffness. For a linear bending moment distribution, C_1 is determined using expression (III.15) for unrestrained and fully restrained warping at both ends. The values are given in Table III-2 along with those provided by Table M.1 from the *French National Annex to EN 1993-1-1 (FNA)* for unrestrained warping. For fully restrained warping, the increase of C_1, when compared to the unrestrained case, varies between 10% and 30% when ψ varies between 1 and -1. For unrestrained warping, the *FNA* provides values of C_1 that are lower than those of *Piotrowski* (2019), particularly for negative values of ψ.

Reference	**Warping**	**ψ**				
		1	**0.5**	**0**	**-0.5**	**-1**
French NA	Unrestrained	1.00	1.31	1.77	2.33	2.55
Piotrowski (2019)	Unrestrained	1.01	1.32	1.82	2.53	2.71
	Fully restrained	1.11	1.46	2.04	3.01	3.57

Table III-2: C_1 for unrestrained and fully restrained warping

The C_1 coefficient provided for fully restrained warping in case of a linear bending moment distributions provided by several authors (*Djalaly* (1974), *Sherbourne* (1989), *Lim* (2003), *Serna* (2006) and *Piotrowski* (2019)) are compared in Figure III-2 as function of the ratio between end moments that ranges between -1 and +1. The values provided by the *FNA* are also given in the case of unrestrained warping.

The values provided by *Sherbourne* (1989), *Lim* (2003) and *Piotrowski* (2019) are very close, the discrepancy being less than 10%. The predictions of *Djalaly* (1974) are close to the previously cited ones for positive values of ψ while they fall significantly below for negative values of the ratio. The proposal of *Serna* (2006) was developed for fully restrained warping and out-of-plane rotation at supports. The obtained values are significantly different from those provided by the former approaches. However, these values are very close to the values provided by the *FNA* in the case of unrestrained warping (and out-of-plane rotation) at supports. Finite element analyses must therefore be employed to assess the accuracy of the different methods.

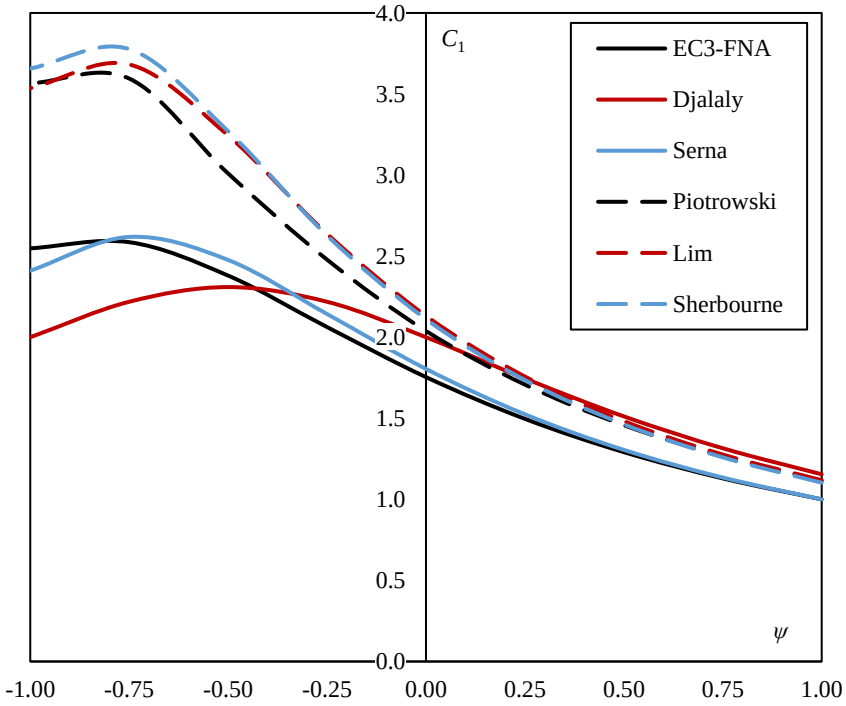

Figure III-2: C_1 for fully restrained warping

Expressions were proposed for the warping coefficient k_w in the case of a uniform bending moment distribution and for the coefficient C_1 in the fully restrained warping case, mainly for a linear bending moment distribution. *Piotrowski* (2019) developed an analytical mode explicitly accounting for warping restraints but which involves equations too cumbersome for a daily use. Simple expressions based on the consistent derivation of an analytical model are therefore developed in section III.4.

III.2.2 Stiffness of warping restraints

III.2.2.1. Beam ends connection configurations

Gil (2019) derived the warping stiffness of non-reinforced bolted end plate beam-to-column joints (see Figure III-3a)) employing the component method improved by specifically-derived new components. The model was extended by *Gil* (2020) to cover bolted end-plate beam-to-column joints reinforced with additional web plates (see Figure III-3b)). The reinforcement multiply by 3 the warping stiffness of the connection. Besides, the warping stiffness of the non-reinforced joints is 2.4 to 9.7 times greater than those of typologies using stiffeners at beam ends.

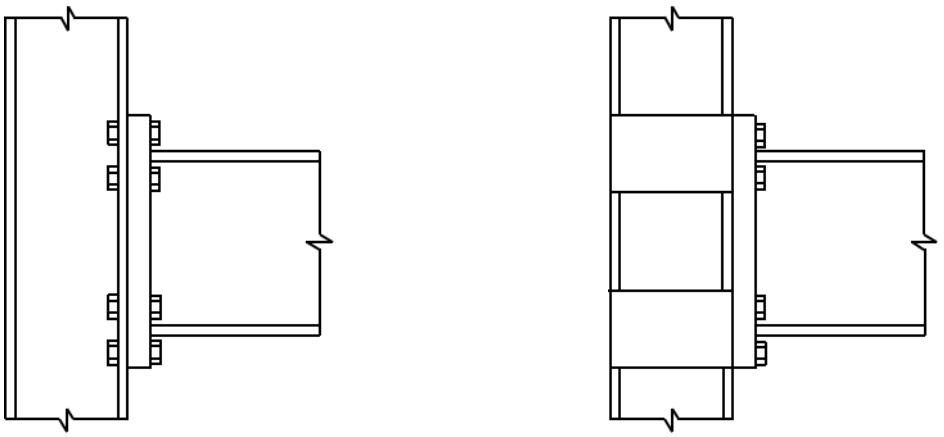

a) *Non-reinforced solution* b) *Reinforced solution*

Figure III-3: Bolted end-plate beam to column joint

Živner (2012) proposed estimates for the warping stiffness of some beam-to-column joints involving specifically hot-rolled HEB and IPE members that depend on the torsional constant of the column and the beam depth. In the case of portal frames built with IPE 500 and HEA 500 members having specific lengths, *Masarira* (2002) gave numerical values of the warping stiffness of the beam-to-column joints. Besides, *Pi* (2000) derived analytical expressions for the stiffness of the warping restraints induced by some connection configurations that are developed hereafter. These expressions rely on the displacements and rotations presented in Figure III-4.

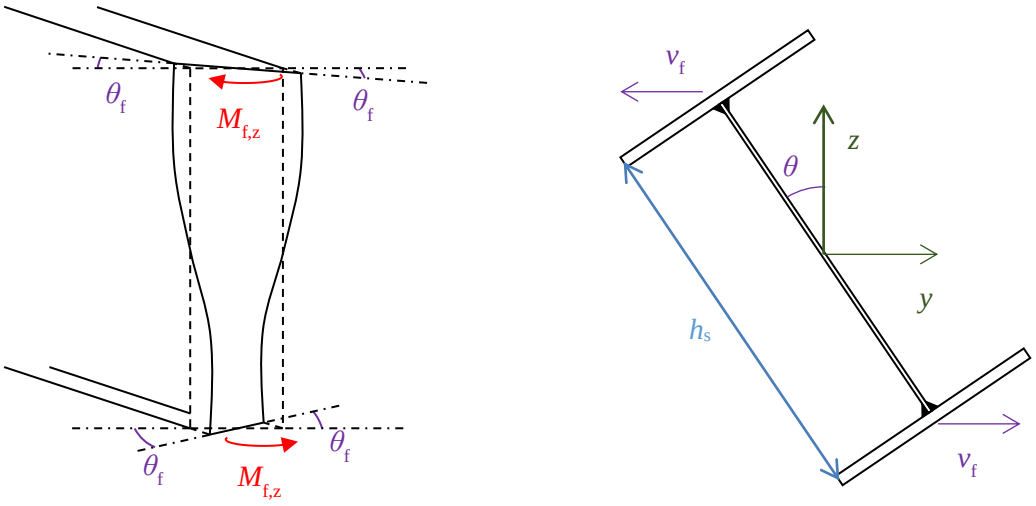

a) *Warping of an end plate* b) *Torsional rotation of an I-member*

Figure III-4: Displacements due to torsion

One can analyze warping as out-of-plane bending moments $M_{f,z}$ acting in both flanges, the bending moments intensities being similar in both flanges while the sign differs. The out-of-plane bending moments produce in each flange a rotation θ_f having different signs (see Figure III-4a) in the case of an end plate). The work performed by the bending moment $M_{f,z}$ acting in each both flanges is:

$$W = -\frac{1}{2} 2 M_{f,z} \theta_f \qquad \text{(III.18)}$$

Besides, the torsional moment producing the twist rotation of an I-section member can be interpreted as the lateral displacement v_f of each flange having the same intensity but directed towards opposite directions (see Figure III-4b)), therefore the following expression arises:

$$v_f = \theta \frac{h_s}{2} \tag{III.19}$$

In addition, owing to kinematic compatibility:

$$\frac{dv_f}{dx} = \theta_f \tag{III.20}$$

The derivative of the twist rotation can thus be expressed as a function of the rotation θ_f in the flanges:

$$\frac{d\theta}{dx} = \theta_f \frac{2}{h_s} \tag{III.21}$$

When warping is elastically restrained at the member ends, the spring stiffness c_w can be expressed as a function of the bimoment B and the derivative of the twist rotation θ is:

$$c_w = \left| \pm \frac{B\big|_{x=0,L}}{d\theta/dx\big|_{x=0,L}} \right| \tag{III.22}$$

along with the conservation of energy stating that the sum of the work W and the strain energy U stored in the warping restraints is zero.

In the case of end plates, the strain energy U_p is:

$$U_p = \int_0^{h_s} \left[\frac{GI_{t,p}}{2} \left(\frac{d\theta}{dx} \right)^2 \right] dx = \frac{2GI_{t,p}\theta_f^{\ 2}}{h_s} \tag{III.23}$$

with:

$$I_{t,p} = \frac{bt_p^{\ 3}}{3}$$

The end plate warping stiffness is therefore:

$$c_w = \frac{B\big|_{x=0}}{\left.\frac{d\theta}{dx}\right|_{x=0}} = \frac{M_{f,z}h_s}{\frac{2\theta_f}{h_s}} = \frac{Gbt_p^{\ 3}h_s}{3} \tag{III.24}$$

The stiffness of warping restraints were given by *Pi* (2000) for other connection configurations that are depicted in Figure III-5. The strain energy corresponding to each connection configuration is derived in Table III-3 along with the corresponding warping stiffness.

#	***Strain energy* U**	***Warping stiffness* c_w**
a)	$\frac{2GI_{t,p}\theta_f^{\ 2}}{h_s} + \frac{2EI_{z,i}\theta_f^{\ 2}\cos(\alpha)^3}{L_i}$	$\frac{Gb\left(t_{p,1}^{\ 3} + t_{p,2}^{\ 3}\right)h_s}{3} + \frac{Eb^3 t_i h_s^{\ 2}\cos(\alpha)^3}{12L_i}$
b)	$\frac{2GI_{t,bs}\theta_f^{\ 2}}{h_s}$	$\frac{2Gt_{bs}L_{bs}^{\ 2}b^2h_s}{L_{bs}+b}$
c)	$\frac{2GI_{t,wp}\theta_f^{\ 2}}{h_s}$	$\frac{2GL_{wp}t_{wp}^{\ 3}h_s}{3}$

Table III-3: Strain energy and warping stiffness of connection configuration from Figure III-5

with:

$$I_{t,p} = \frac{b\left(t_{p,1}^{\ 3} + t_{p,2}^{\ 3}\right)}{3}$$

$$I_{z,i} = \frac{b^3 t_i}{12}$$

$$I_{t,bs} = \frac{2t_{bs}L_{bs}^{\ 2}b^2}{L_{bs}+b}$$

$$I_{t,wp} = \frac{L_{wp}2t_{wp}^{\ 3}}{3}$$

For web open stiffeners, *Pi* (2000) provides an expression of the warping stiffness in the specific case of $t_{p,1} = t_{p,2}$ while a contribution of the strain energy of torsion stored in the flanges is accounted for in the case of additional web plates. This contribution is neglected here because when t_{wp} tends towards 0, the warping stiffness must as well tend towards 0.

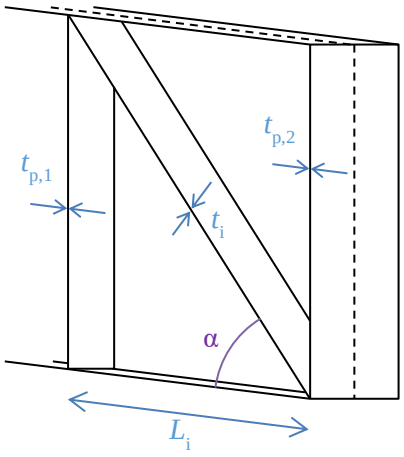

a) *Web open stiffeners*

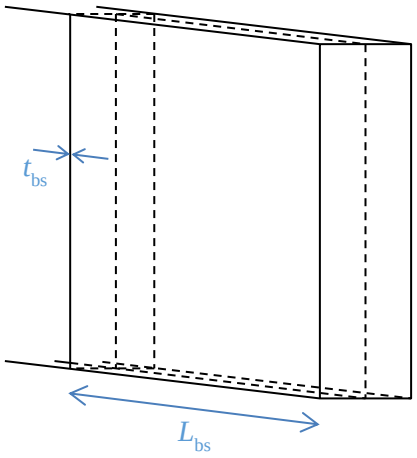

b) *Web box stiffeners*

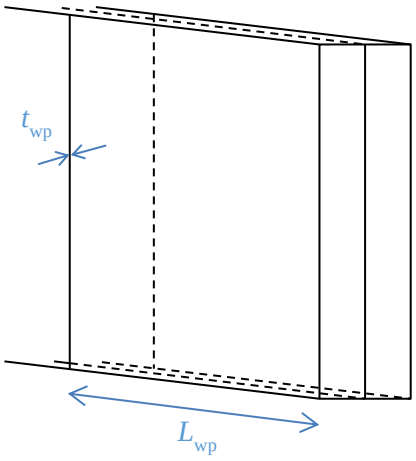

c) *Additional web plates*

Figure III-5: Connection configurations investigated by Pi *(2000)*

III.2.2.2. Fixed column base

A column base considered as fixed regarding out-of-plane rotation induces also a significant restrain against warping, the stiffness of which being derived hereafter. The warping restraints present at one of the column ends can be symbolised as rotational springs about the *z*-axis, having different stiffness, present at both flange-to-web junctions, as depicted in Figure III-6. The acting bending moment about the *y*-axis induces compressive stresses in a flange and tensile stresses in the other flange. Hence, the stiffness of the rotational springs at the top and bottom flanges, $S_{j,t}$ and $S_{j,b}$, are different. Their values can be calculated as exposed by *Amaral* (2014).

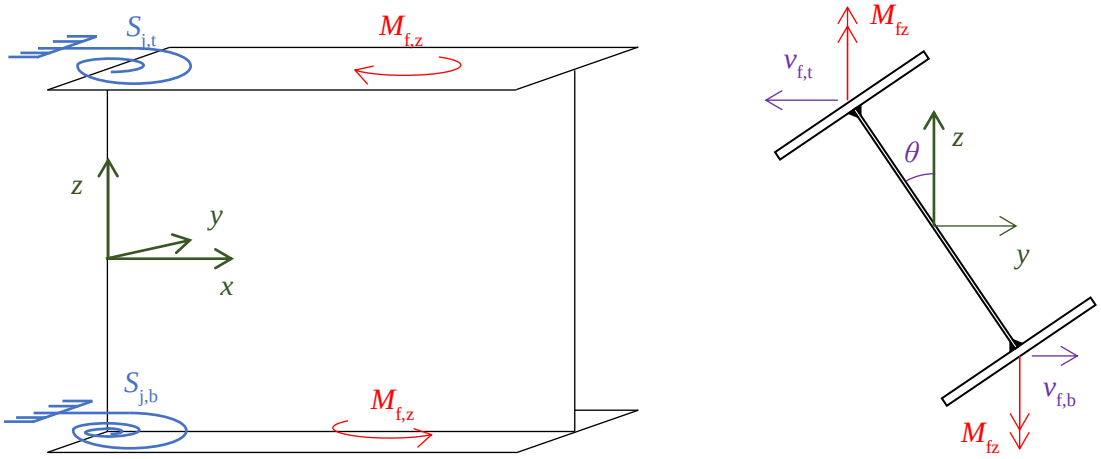

a) *Torsional springs* *b)* *Torsional rotation*

Figure III-6: Fixed column base

Owing to the difference between both stiffness $S_{j,t}$ and $S_{j,b}$, the flanges lateral displacements $v_{f,t}$ and $v_{f,b}$ are unlike, their boundary conditions being:

$$\left.\frac{dv_{f,t}}{dx}\right|_{x=0} = \frac{M_{f,z}|_{x=0}}{S_{j,t}} \qquad \text{(III.25)}$$

$$\left.\frac{dv_{\mathrm{f,b}}}{dx}\right|_{x=0} = \frac{M_{\mathrm{f,z}}|_{x=0}}{S_{\mathrm{j,b}}} \tag{III.26}$$

Besides, the flanges displacements are related to the cross-section twist rotation by:

$$\theta(x) = \frac{v_{\mathrm{f,t}}(x) + v_{\mathrm{f,b}}(x)}{h_{\mathrm{s}}} \tag{III.27}$$

Combining expression (III.27) with (III.25) and (III.26), one obtains:

$$\left.\frac{d\theta}{dx}\right|_{x=0} h_{\mathrm{s}} = \frac{B|_{x=0}}{h_{\mathrm{s}}}\left(\frac{1}{S_{\mathrm{j,t}}} + \frac{1}{S_{\mathrm{j,b}}}\right) \tag{III.28}$$

Eventually, the warping stiffness of a fixed column base is:

$$c_{\mathrm{w}} = \frac{B|_{x=0}}{\left.\frac{d\theta}{dx}\right|_{x=0}} = \frac{{h_{\mathrm{s}}}^2}{\left(\frac{1}{S_{\mathrm{j,t}}} + \frac{1}{S_{\mathrm{j,b}}}\right)} \tag{III.29}$$

The warping stiffness induced by a fixed column base may be significant enough to assume warping as fixed at the member end(s). A lower limit on the stiffness of the warping restraints is therefore investigated in sub-section III.5.3 to assume warping as fixed at both ends when computing the elastic critical bending moment.

III.3 Resolution method

The energy method described in Chapter II is employed in the case of a doubly symmetric beam subjected to either a linear bending moment or a transverse load applied at mid span or uniformly distributed at the shear centre and having warping restraints at supports. The strain energy is composed of a part stored in the beam and a part stored in the warping springs:

$$U = U_{\mathrm{beam}} + U_{\mathrm{springs}} \tag{III.30}$$

With:

$$U_{\mathrm{beam}} = \int_0^L \left[\frac{EI_{\mathrm{z}}}{2}\left(\frac{d^2v}{dx^2}\right)^2 + \frac{EI_{\mathrm{w}}}{2}\left(\frac{d^2\theta}{dx^2}\right)^2 + \frac{GI_{\mathrm{t}}}{2}\left(\frac{d\theta}{dx}\right)^2\right] dx$$

$$U_{\mathrm{springs}} = \frac{c_{\mathrm{w}}}{2}\left[\left(\left.\frac{d\theta}{dx}\right|_{x=0}\right)^2 + \left(\left.\frac{d\theta}{dx}\right|_{x=L}\right)^2\right]$$

Besides, the work performed by a uniform bending moment distribution $M_{\mathrm{y,0}}$ is:

$$W = -\int_0^L M_{y,0}\,\theta\,\frac{d^2v}{dx^2}\,dx \tag{III.31}$$

For a beam resting on fork supports at both ends, the lateral and vertical displacements and twist rotation being fully restrained, and with free out-of-plane rotation, the boundary conditions concerning the lateral displacement v and twist rotation θ are:

$$v(0) = v(L) = 0 \tag{III.32}$$

$$\left.\frac{d^2v}{dx^2}\right|_{x=0} = \left.\frac{d^2v}{dx^2}\right|_{x=L} = 0 \tag{III.33}$$

$$\theta(0) = \theta(L) = 0 \tag{III.34}$$

Besides, when the beam ends are elastically restrained against warping, the spring stiffness being c_w, the bimoment B at the beam ends is:

$$B(0) = -c_w \left.\frac{d\theta}{dx}\right|_{x=0} \tag{III.35}$$

$$B(L) = c_w \left.\frac{d\theta}{dx}\right|_{x=L} \tag{III.36}$$

In addition, the distribution of the bimoment along the beam is related to the second derivative of the twist rotation and to the beam warping stiffness with:

$$B = -EI_w \frac{d^2\theta}{dx^2} \tag{III.37}$$

Combining expressions (III.35) and (III.36) with (III.37) leads to the following boundary conditions regarding the twist rotation:

$$\left.\frac{d\theta}{dx}\right|_{x=0} = \frac{EI_w}{c_w}\left.\frac{d^2\theta}{dx^2}\right|_{x=0} \tag{III.38}$$

$$\left.\frac{d\theta}{dx}\right|_{x=L} = \frac{EI_w}{c_w}\left.\frac{d^2\theta}{dx^2}\right|_{x=L} \tag{III.39}$$

In the specific case of unrestrained warping ($c_w = 0$), the bimoment vanishes at the beams ends resulting in:

$$\left.\frac{d^2\theta}{dx^2}\right|_{x=0} = 0 \tag{III.40}$$

$$\left.\frac{d^2\theta}{dx^2}\right|_{x=L} = 0 \tag{III.41}$$

In the other specific case of fully restrained warping where c_w tends towards infinity, the right hand side of expressions (III.38) and (III.39) tends towards zero leading to:

$$\left.\frac{d\theta}{dx}\right|_{x=0} = 0 \tag{III.42}$$

$$\left.\frac{d\theta}{dx}\right|_{x=L} = 0 \tag{III.43}$$

The principle of minimum total potential energy (see expression (II.1)) employed with the boundary conditions regarding out-of-plane displacements, twist rotations and warping restraints (see equations (III.32) to (III.34), (III.38) and (III.39)) results in the following coupled equilibrium equations:

$$EI_w \frac{d^4\theta}{dx^4} - GI_t \frac{d^2\theta}{dx^2} + M_y \frac{d^2v}{dx^2} = 0 \tag{III.44}$$

$$EI_z \frac{d^4v}{dx^4} + \theta \frac{d^2M_y}{dx^2} + 2\frac{dM_y}{dx}\frac{d\theta}{dx} + M_y \frac{d^2\theta}{dx^2} = 0 \tag{III.45}$$

Integrating twice the previous equation (III.45) and combining with (III.44) yields the uncoupled differential equilibrium equations:

$$\frac{d^2v}{dx^2} = -\frac{M_y\theta}{EI_z} \tag{III.46}$$

$$EI_w \frac{d^4\theta}{dx^4} - GI_t \frac{d^2\theta}{dx^2} - \frac{M_y^{\,2}}{EI_z}\theta = 0 \tag{III.47}$$

The differential equations are linear with a non-constant term as the bending moment which is assumed to be a polynomial function of order *p*. An exact closed-form solution for the twist angle lie in the form of an infinite power series (see *Timoshenko* (1963)), as developed in the upcoming section III.4.

III.4 Infinite power-series based solution

III.4.1 Solution method

The resolution of the differential equation (III.47) is investigated hereafter for beams subjected to a polynomial shaped bending moment distribution. The dimensionless form of equilibrium differential equation (III.47) reads:

$$\frac{d^4\theta}{ds^4} - \lambda^2 \frac{d^2\theta}{ds^2} - m^2\theta = 0 \tag{III.48}$$

with:

$$s = \frac{x}{L},\ \ \lambda = L\sqrt{\frac{GI_{\mathrm{t}}}{EI_{\mathrm{w}}}},\ m = \frac{M_{\mathrm{y}}(s)L^2}{E}\sqrt{\frac{1}{I_{\mathrm{z}}I_{\mathrm{w}}}}.$$

The primary unknown in the previous equation is the twist rotation that can be expressed as an infinite power series. The twist rotation dimensionless boundary conditions are in the case of elastically restrained warping:

$$\theta(0) = \theta(1) = 0 \tag{III.49}$$

$$\left.\frac{d^2\theta}{ds^2}\right|_{s=0} = \bar{c}_{\mathrm{w}}\left.\frac{d\theta}{ds}\right|_{s=0} \tag{III.50}$$

$$\left.\frac{d^2\theta}{ds^2}\right|_{s=1} = -\bar{c}_{\mathrm{w}}\left.\frac{d\theta}{ds}\right|_{s=1} \tag{III.51}$$

The bending moment distribution assumed to be a polynomial function of order p is given by:

$$M_{\mathrm{y}}(s) = \sum_{k=0}^{p} M_{\mathrm{k}} s^{\mathrm{k}} \tag{III.52}$$

Therefore, the dimensionless term m^2 from equation (III.48) can be expressed as:

$$m^2(s) = \sum_{a=0}^{p}\sum_{b=0}^{p}\frac{M_{\mathrm{a}}M_{\mathrm{b}}L^4 s^{\mathrm{a+b}}}{E^2 I_{\mathrm{w}}I_{\mathrm{z}}} = \sum_{b=0}^{2p}\frac{m_{\mathrm{k}}\, s^{\mathrm{k}}}{E^2 I_{\mathrm{w}}I_{\mathrm{z}}} \tag{III.53}$$

with:

$$m_{\mathrm{k}} = \sum_{\mathrm{j=max(0,k-p)}}^{\mathrm{min(k,p)}}\frac{M_{\mathrm{j}}M_{\mathrm{k\text{-}j}}L^4}{E^2 I_{\mathrm{w}}I_{\mathrm{z}}}$$

The twist rotation is expressed as an infinite power series:

$$\theta(s) = \sum_{k=0}^{\infty}\theta_{\mathrm{k}} s^{\mathrm{k}} \tag{III.54}$$

The n^{th} derivative of the twist angle is then:

$$\frac{d^{\mathrm{n}}\theta}{ds^{\mathrm{n}}} = \sum_{k=0}^{\infty}\frac{(k+n)!}{k!}\theta_{\mathrm{k+n}} s^{\mathrm{k}} \tag{III.55}$$

Combining expressions (III.53) and (III.54) yields:

$$m^2\theta = \sum_{\mathrm{k=0}}^{\infty}\sum_{\mathrm{q=0}}^{\mathrm{min(k,2p)}} m_{\mathrm{q}}\theta_{\mathrm{k\text{-}q}} s^{\mathrm{k}} \tag{III.56}$$

A general expression for the power series terms θ_{k} can eventually be obtained combining equations (III.48), (III.55) and (III.56):

$$\theta_{k+4} = \lambda^2 \frac{(k+2)!}{(k+4)!}\theta_{k+2} + \frac{(k)!}{(k+4)!}\sum_{q=0}^{\min(k,2p)} m_q \theta_{k-q} \tag{III.57}$$

III.4.2 Fully restrained warping

In the specific case of fully restrained warping at supports, enforcing the boundary conditions at $s = 0$ in expression (III.54) yields:

$$\theta_0 = 0 \tag{III.58}$$

$$\theta_1 = 0 \tag{III.59}$$

The power series terms θ_k can then be determined as a function of θ_2 and θ_3 using the recursive expression (III.57) yielding:

$$\theta_k = a_k \theta_2 + b_k \theta_3 \tag{III.60}$$

with:

$$a_{k+4} = \lambda^2 \frac{(k+2)!}{(k+4)!}a_{k+2} + \frac{(k)!}{(k+4)!}\sum_{q=0}^{\min(k,2p)} m_q a_{k-q} \tag{III.61}$$

$$b_{k+4} = \lambda^2 \frac{(k+2)!}{(k+4)!}b_{k+2} + \frac{(k)!}{(k+4)!}\sum_{q=0}^{\min(k,2p)} m_q b_{k-q} \tag{III.62}$$

Applying the boundary conditions of the twist rotation at $s = 1$ leads to:

$$\sum_{k=0}^{\infty} \theta_k = 0 \tag{III.63}$$

$$\sum_{k=0}^{\infty} (k+1)\theta_{k+1} = 0 \tag{III.64}$$

The following homogenous system of linear equations can therefore be obtained by expressing θ_k using θ_2 and θ_3:

$$\begin{bmatrix} \sum_{k=0}^{\infty} a_k & \sum_{k=0}^{\infty} b_k \\ \sum_{k=0}^{\infty} (k+1)a_{k+1} & \sum_{k=0}^{\infty} (k+1)b_{k+1} \end{bmatrix} \begin{Bmatrix} \theta_2 \\ \theta_3 \end{Bmatrix} = \begin{Bmatrix} 0 \\ 0 \end{Bmatrix} \tag{III.65}$$

The matrix coefficients are non-linearly dependent on the polynomial coefficients corresponding to the applied bending moment. The elastic buckling load factor, associated with the critical bending moment is found when the determinant of the 2×2 matrix is zero. The corresponding eigenvector of the linear system can be then employed to determine the direction of the eigenvector containing the terms θ_2 and θ_3 and therefore the remaining θ_k. The exact solution for the beam buckled shape can then be known. In

practice, the solution can be obtained only to an arbitrary level of precision by truncating the infinite series at a given order *n* and computing the resulting linear system.

III.4.3 Elastically restrained warping

Considering the general case of partially restrained warping at supports, implementing the boundary conditions at $s = 0$ in expression (III.54) leads to:

$$\theta_0 = 0 \tag{III.66}$$

$$\theta_2 = \frac{\overline{c}_w}{2}\theta_1 \tag{III.67}$$

The remaining terms of the power series are now related to terms θ_1 and θ_3 using:

$$\theta_k = a_k\theta_1 + b_k\theta_3 \tag{III.68}$$

where the a_k and b_k coefficients are obtained using expressions (III.61) and (III.62), respectively.

Applying the boundary conditions of the twist rotation at $s = 1$ leads to the homogenous system of linear equations relating the terms θ_k to θ_1 and θ_3:

$$\begin{bmatrix} \sum_{k=0}^{\infty} a_k & \sum_{k=0}^{\infty} b_k \\ \sum_{k=0}^{\infty} \frac{(k+2)!}{(k)!} a_{k+2} + \overline{c}_w \frac{(k+1)!}{(k)!} a_{k+1} & \sum_{k=0}^{\infty} \frac{(k+2)!}{(k)!} b_{k+2} + \overline{c}_w \frac{(k+1)!}{(k)!} b_{k+1} \end{bmatrix} \begin{Bmatrix} \theta_1 \\ \theta_3 \end{Bmatrix} = \begin{Bmatrix} 0 \\ 0 \end{Bmatrix} \tag{III.69}$$

The resolution method is similar to that presented in sub-section III.4.2. Again, given a polynomial shape for the bending moment, the elastic critical load (amplifier) is obtained by setting the determinant of the 2×2 matrix to zero. The buckling shape of the beam can be obtained by determining the eigenvector containing θ_1 and θ_3 and therefore the remaining θ_k using the eigenvector of the linear system associated with the null eigenvalue. Again, the solution in practice can only be obtained to an arbitrary level of precision by truncating the infinite series at a given order *n* and computing the resulting linear system.

III.5 Analytical model

III.5.1 Shape functions

Computing the exact solution for the elastic critical bending moment using the pseudo infinite power-series-based solution for the twist rotation is very challenging: simplest analytical solutions are required for a daily use. The derivation of the minimum potential energy principle is therefore performed in sub-section III.5.2 using approximate trigonometric series for the lateral displacement and twist rotation.

Whatever the bending moment distribution, for unrestrained warping and out-of-plane displacement at both ends, kinematically admissible for the lateral displacement *v* and twist rotation θ are infinite series of sine waves:

$$v(x) = \sum_{k=1}^{n} v_k \sin\left(k\frac{\pi x}{L}\right) \tag{III.70}$$

$$\theta(x) = \sum_{k=1}^{n} \theta_k \sin\left(k\frac{\pi x}{L}\right) \tag{III.71}$$

where v_k and θ_k are the magnitudes of the out-of-plane displacement and twist rotation, respectively, associated with the k^{th} sine shape function.

In the specific case of a uniform bending moment distribution, the exact solutions for the lateral displacement and twist rotation are half a sine wave when warping and out-of-plane rotation are unrestrained at supports:

$$v(x) = v_1 \sin\left(\frac{\pi x}{L}\right) \tag{III.72}$$

$$\theta(x) = \theta_1 \sin\left(\frac{\pi x}{L}\right) \tag{III.73}$$

where v_1 and θ_1 are the magnitudes of the out-of-plane displacement and twist rotation, respectively.

In the case of fully restrained warping at both supports, obtaining an admissible shape function is not trivial. *Vlasov* (1961) and *Djalaly* (1974) for a uniform bending moment distribution, and *Bresser* (2020) for a beam subjected to end moments and a transverse load, proposed to use a single admissible trigonometric function to approximate the twist rotation:

$$\theta(x) = \theta_1\left[1 - \cos\left(2\frac{\pi x}{L}\right)\right] \tag{III.74}$$

Therefore, a combination of expressions (III.73) and (III.74) is used for a beam with elastic warping restraints at both ends when subjected to a constant bending moment diagram. The following expression is employed for the twist rotation, fulfilling the boundary conditions given in equations (III.34), (III.38) and (III.39):

$$\theta(x) = \theta_1\left\{4\pi \sin\left(\frac{\pi x}{L}\right) + \bar{c}_w\left[1 - \cos\left(\frac{\pi x}{L}\right)\right]\right\} \tag{III.75}$$

Expression (III.75) is generalized by considering a linear combination of infinite number of base functions:

$$\theta(x) = \sum_{k=0}^{n} \theta_k\left\{\frac{4k^2}{2k-1}\pi \sin\left[(2k-1)\frac{\pi x}{L}\right] + \bar{c}_w\left[1 - \cos\left(2k\frac{\pi x}{L}\right)\right]\right\} \tag{III.76}$$

The magnitudes v_k and θ_k from expressions (III.70) and (III.76) are the unknown to be determined from the minimum potential energy principle depicted in Chapter II.

III.5.2 Critical bending moment

III.5.2.1. Uniform bending moment distribution

The buckled shape of a beam subjected to a uniform bending moment can be described using a single shape function for the twist rotation θ and the lateral displacement v, which are the first term of infinite series (III.76) and (III.70), respectively:

$$v(x) = v_1 \sin\left(\frac{\pi x}{L}\right) \tag{III.77}$$

$$\theta(x) = \theta_1 \left\{ 4\pi \sin\left(\frac{\pi x}{L}\right) + \bar{c}_w \left[1 - \cos\left(\frac{\pi x}{L}\right) \right] \right\} \tag{III.78}$$

The distribution of the twist rotation predicted by expression (III.78) is compared against that given by the beam finite element code *LTBeamN* and the Power-Series-Based (PSB) solution, using 50 terms, in Figure III-7. The example consists in 8 m-span doubly symmetric beam subjected to a constant bending moment. The steel cross-section is an I-profile with a web of 800×8 mm and flanges of 200×14 mm. At its both ends, the beam is connected to steel plates of 30 mm thickness. The warping stiffness is determined using equation (III.3).

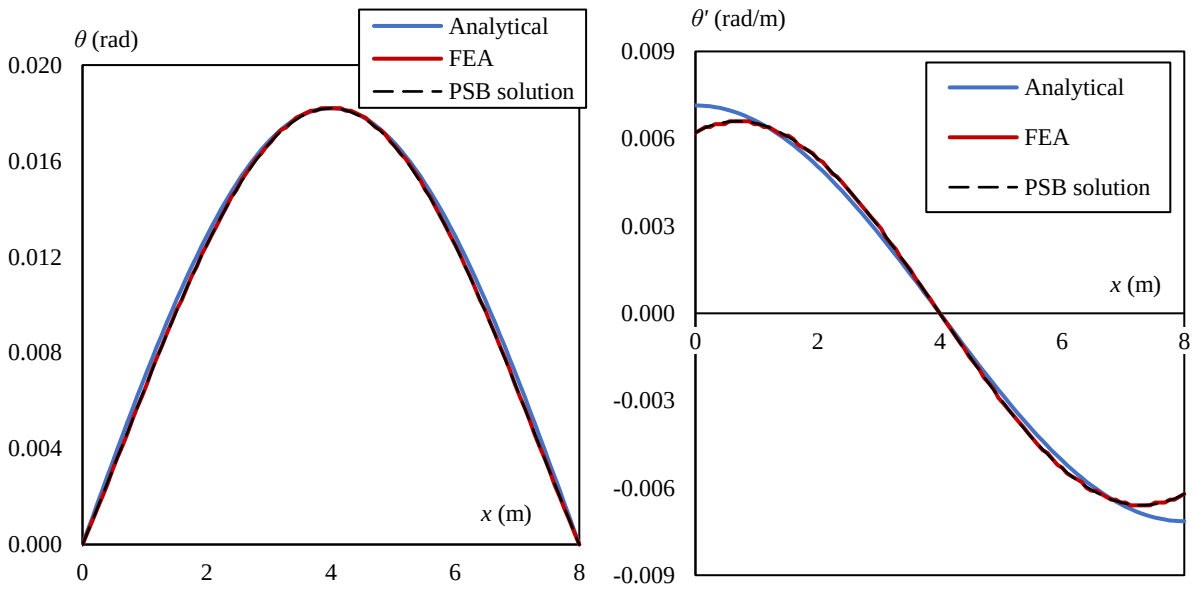

a) *Twist rotation* b) *Warping*

Figure III-7: Twist rotation and warping fields for a uniform bending moment

Figure III-7 shows that the analytical and numerical results match very well except for the warping near supports where some differences are noticed. The results using the PSB solution and FEA match perfectly for both the twist rotation and warping.

Inserting expressions (III.77) and (III.78) into the expression of the total potential energy described by (III.30) and (III.31) results in the following expression:

$$\Pi = \frac{L}{4}\left\{ EI_{\mathrm{z}}\left(\frac{\pi}{L}\right)^4 v_1^2 + EI_{\mathrm{w}}\left(\frac{\pi}{L}\right)^4 \xi_{\mathrm{w}}\theta_1^2 + GI_{\mathrm{t}}\left(\frac{\pi}{L}\right)^2 \theta_1^2\xi_{\mathrm{t}} - M_{\mathrm{y},0}\left(\frac{\pi}{L}\right)^2 \xi_{\mathrm{M}} v_1\theta_1 + \left(\frac{\pi}{L}\right)^2 \theta_1^2\xi_{\mathrm{s}} \right\} \qquad \text{(III.79)}$$

with:

$$\xi_{\mathrm{M}} = 8\pi + \frac{32}{3\pi}\bar{c}_{\mathrm{w}},$$

$$\xi_{\mathrm{t}} = 16\pi^2 + \frac{128}{3}\bar{c}_{\mathrm{w}} + 4\bar{c}_{\mathrm{w}}^2,$$

$$\xi_{\mathrm{w}} = \xi_{\mathrm{t}} + 12\bar{c}_{\mathrm{w}}^2,$$

$$\xi_{\mathrm{s}} = 64\frac{c_{\mathrm{w}}}{L}\pi^2.$$

Differentiating the potential energy with respect to amplitudes θ_1 and v_1, one obtains:

$$\frac{\partial\Pi}{\partial v_1} = \frac{L}{2}\left\{ EI_{\mathrm{z}}\left(\frac{\pi}{L}\right)^4 v_1 - M_{\mathrm{y},0}\left(\frac{\pi}{L}\right)^2 \frac{\xi_{\mathrm{M}}}{2}\theta_1 \right\} = 0 \qquad \text{(III.80)}$$

$$\frac{\partial\Pi}{\partial \theta_1} = \frac{L}{2}\left\{ EI_{\mathrm{w}}\left(\frac{\pi}{L}\right)^4 \xi_{\mathrm{w}}\theta_1 + GI_{\mathrm{t}}\left(\frac{\pi}{L}\right)^2 \xi_{\mathrm{t}}\theta_1 - M_{\mathrm{y},0}\left(\frac{\pi}{L}\right)^2 \frac{\xi_{\mathrm{M}}}{2} v_1 + \left(\frac{\pi}{L}\right)^2 \xi_{\mathrm{s}}\theta_1 \right\} = 0 \qquad \text{(III.81)}$$

Equation (III.80) provides the following relationship between both amplitudes:

$$v_1 = \frac{M_{\mathrm{y},0}}{EI_{\mathrm{z}}\left(\frac{\pi}{L}\right)^2}\frac{\xi_{\mathrm{M}}}{2}\theta_1 \qquad \text{(III.82)}$$

Equations (III.81) and (III.82) are combined together to derive the expression of the elastic critical bending moment:

$$M_{\mathrm{cr}} = \sqrt{\frac{4\xi_{\mathrm{t}}}{\xi_{\mathrm{M}}^2}}\frac{\pi^2 EI_{\mathrm{z}}}{L^2}\sqrt{\frac{I_{\mathrm{w}}}{I_{\mathrm{z}}}\left[\frac{\xi_{\mathrm{w}}}{\xi_{\mathrm{t}}} + \frac{\xi_{\mathrm{s}}}{\xi_{\mathrm{t}}}\frac{L^2}{\pi^2 EI_{\mathrm{w}}}\right] + \frac{L^2 GI_{\mathrm{t}}}{\pi^2 EI_{\mathrm{z}}}} \qquad \text{(III.83)}$$

Expressions for the equivalent uniform moment factor C_1 and the warping coefficient k_{w} are identified from the previous equation:

$$C_1 = \frac{\sqrt{\pi^2 + \frac{8}{3}\bar{c}_{\mathrm{w}} + \frac{\bar{c}_{\mathrm{w}}^2}{4}}}{\pi + \frac{4}{3\pi}\bar{c}_{\mathrm{w}}} \qquad \text{(III.84)}$$

$$k_w = \sqrt{\frac{\pi^2 + \frac{8}{3}\bar{c}_w + \frac{\bar{c}_w^2}{4}}{\pi^2 + \frac{20}{3}\bar{c}_w + \bar{c}_w^2}} \tag{III.85}$$

The coefficient C_1 ranges from 1 to $3\pi/8$ (≈ 1.18) for unrestrained and fully restrained warping, respectively while k_w varies between 1 and 0.5 in the same conditions. The elastic critical bending moment of a doubly symmetric beam subjected to a uniform bending moment with warping restraints at both ends using expression (III.1) where C_1 and k_w are given by expressions (III.84) and (III.85), respectively.

III.5.2.2. Linear bending moment distribution

Using the distribution of the lateral displacement and twist rotation expressed by (III.77) and (III.78), respectively, the critical bending moment of a beam subjected to end moments – their ratio being ψ – is derived, resulting in the following expressions for the coefficients C_1 and k_w:

$$C_1 = \frac{2}{1+\psi} \frac{\sqrt{\pi^2 + \frac{8}{3}\bar{c}_w + \frac{\bar{c}_w^2}{4}}}{\pi + \frac{4}{3\pi}\bar{c}_w} \tag{III.86}$$

$$k_w = \sqrt{\frac{\pi^2 + \frac{8}{3}\bar{c}_w + \frac{\bar{c}_w^2}{4}}{\pi^2 + \frac{20}{3}\bar{c}_w + \bar{c}_w^2}} \tag{III.87}$$

The warping coefficient remains unchanged while the equivalent uniform moment factor is the product of a factor $C_{1,\psi}$ depending only on ψ and a factor $C_{1,w}$ depending only on the stiffness of the warping restraints that is similar to expression (III.84).

For free warping at supports, expression (III.86) leads to inconsistent values of C_1 for negative values of ψ since C_1 goes to infinity when ψ = -1. This inconsistency is a consequence of the choice of displacement and rotation fields assuming half a sine wave which is not appropriate when ψ is lower than 0.5.

Both the displacement and rotation fields are therefore enhanced with the second term of the series (III.70) and (III.76), respectively:

$$v(x) = v_1 \sin\left(\frac{\pi x}{L}\right) + v_2 \sin\left(\frac{2\pi x}{L}\right) \tag{III.88}$$

$$\theta(x) = \theta_1(x) + \theta_2(x) \tag{III.89}$$

with:

$$\theta_1(x) = \theta_1 \left\{ 4\pi \sin\left(\frac{\pi x}{L}\right) + \bar{c}_w \left[1 - \cos\left(\frac{2\pi x}{L}\right) \right] \right\}$$

$$\theta_2(x) = \theta_2 \left\{ \frac{16}{3} \pi \sin\left(\frac{3\pi x}{L}\right) + \bar{c}_w \left[1 - \cos\left(\frac{4\pi x}{L}\right) \right] \right\}$$

The distributions of the twist rotation predicted by expression (III.89) are compared to those given by FEA, using the *LTBeamN* programme, and the PSB solution, using 50 terms, in Figure III-8. The example consists in the same beam as employed to obtain the results shown in Figure III-7 but subjected to a linear bending moment distribution with the ratio between end moments ψ being 0, -0.75 and -1.

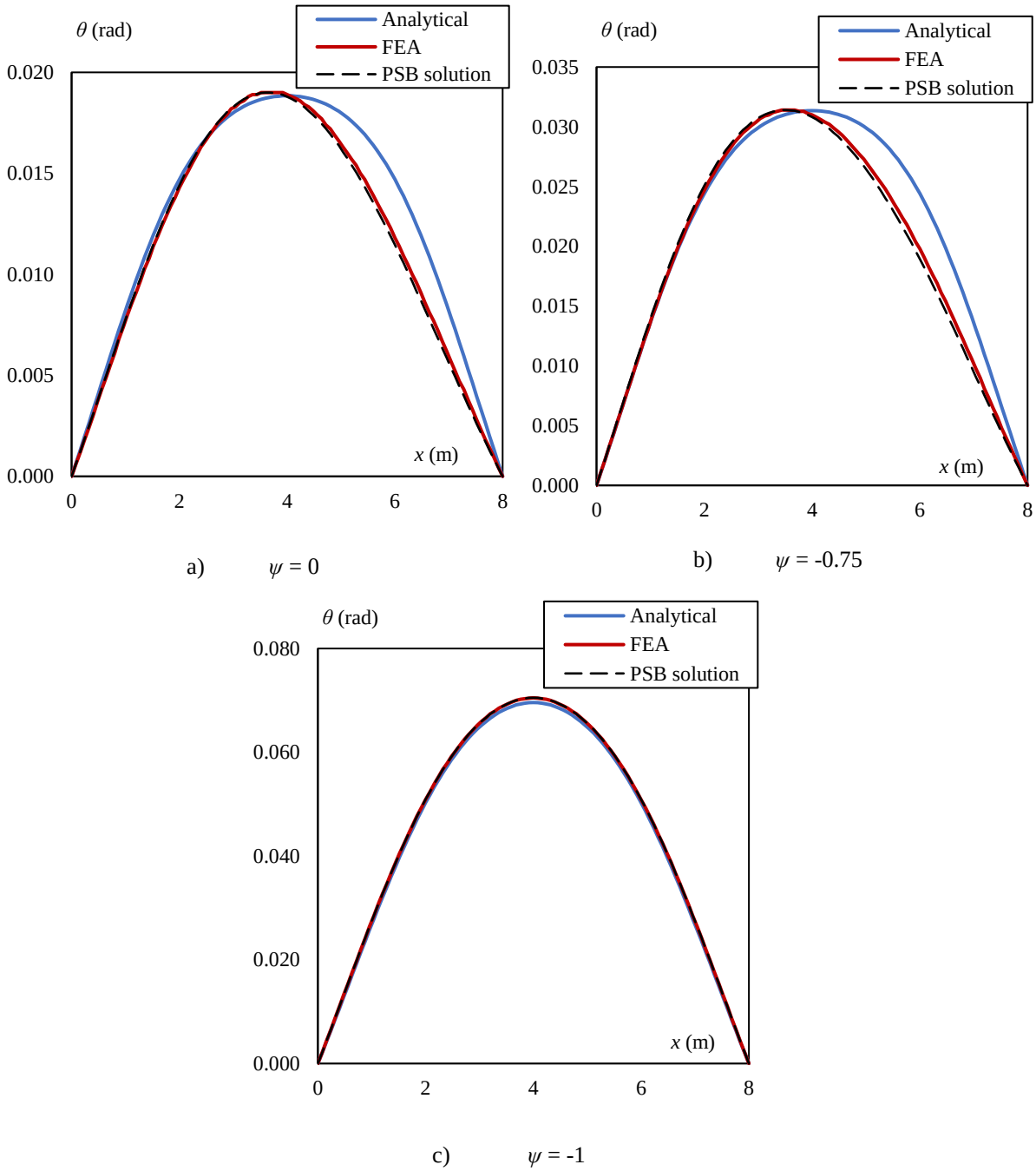

Figure III-8: Twist rotation for a linear bending moment distribution

For every value of ψ, Figure III-8 shows an almost perfect match between the results obtained using FEA and the PSB solution. Besides, the numerical and analytical results coincide when ψ is -1. For ψ = 0 or -0.75, the numerical and analytical results estimate a similar peak value but which is not obtained

at the same position *x* along the beam. Indeed, according to FEA the position of the peak value varies with the ratio between end moments while the proposed analytical expression is symmetric about mid-span. This difference may induce small deviations between the value of the critical bending moment computed numerically and analytically.

Expressions (III.88) and (III.89) are inserted into the total potential energy *Π*. Performing the integration along the beam length, an algebraic expression for the potential energy arises, allowing for the calculation of its derivatives about the magnitudes. The minimum potential energy principle yields the following homogenous system:

$$\begin{Bmatrix} \frac{\partial \Pi}{\partial v_1} \\ \frac{\partial \Pi}{\partial v_2} \\ \frac{\partial \Pi}{\partial \theta_1} \\ \frac{\partial \Pi}{\partial \theta_2} \end{Bmatrix} = \begin{bmatrix} K_{11} & 0 & M_{cr}K_{13} & M_{cr}K_{14} \\ 0 & K_{22} & M_{cr}K_{23} & M_{cr}K_{24} \\ M_{cr}K_{13} & M_{cr}K_{23} & K_{33} & K_{34} \\ M_{cr}K_{14} & M_{cr}K_{24} & K_{34} & K_{44} \end{bmatrix} \begin{Bmatrix} v_1 \\ v_2 \\ \theta_1 \\ \theta_2 \end{Bmatrix} = \begin{Bmatrix} 0 \\ 0 \\ 0 \\ 0 \end{Bmatrix} \tag{III.90}$$

Where the K_{ij} coefficients are:

$$K_{11} = EI_z \left(\frac{\pi}{L}\right)^4 \frac{L}{2}$$

$$K_{22} = 8EI_z \left(\frac{\pi}{L}\right)^4 L$$

$$K_{33} = EI_w \left(\frac{\pi}{L}\right)^4 \xi_w + GI_t \left(\frac{\pi}{L}\right)^2 \xi_t + \left(\frac{\pi}{L}\right)^2 \xi_s$$

$$K_{44} = EI_w \left(\frac{\pi}{L}\right)^4 \xi_{w,2} + GI_t \left(\frac{\pi}{L}\right)^2 \xi_{t,2} + 16\left(\frac{\pi}{L}\right)^2 \xi_s$$

$$K_{13} = -\left(\frac{\pi}{L}\right)^2 \sqrt{\frac{L}{2}} \xi_M (1+\psi)$$

$$K_{14} = -\left(\frac{\pi}{L}\right)^2 \frac{16L}{15\pi} \bar{c}_w (1+\psi)$$

$$K_{23} = \left(\frac{\pi}{L}\right)^2 \frac{L}{\pi} \xi_{M,2} (\psi - 1)$$

$$K_{24} = \left(\frac{\pi}{L}\right)^2 \frac{L}{\pi} \xi_{M,3} (\psi - 1)$$

$$K_{34} = -EI_w \left(\frac{\pi}{L}\right)^4 \frac{3328 L\bar{c}_w}{15} - GI_t \left(\frac{\pi}{L}\right)^2 \frac{256 L\bar{c}_w}{15} + 4\left(\frac{\pi}{L}\right)^2 \xi_s$$

with:

$$\xi_{t,2} = 128\pi^2 L + \frac{1024}{7} L\bar{c}_w + 8L\bar{c}_w^2$$

$$\xi_{w,2} = 9\xi_{t,2} + 56L\bar{c}_w^2$$

$$\xi_{M,2} = \frac{128}{9} + \frac{3}{2}\bar{c}_w$$

$$\xi_{M,3} = \frac{512}{25} + \frac{8}{3}\bar{c}_w$$

Equating to zero the determinant of the 4×4 previous matrix results in a 4th order equation on M_{cr} where the terms associated with the 1st and 3rd order are zero. Expression (III.1) is inserted in the 4th order equation from, identifying the same expression as (III.85) for k_w and the following equation on C_1:

$$A_1 C_1^4 - A_2 C_1^2 + A_3 = 0 \tag{III.91}$$

One obtains the lowest value of C_1, providing conservative results, assuming that:

$$\chi_t = \frac{\pi}{L}\sqrt{\frac{EI_w}{GI_t}} = 0 \tag{III.92}$$

This assumption leads to the following values for the A_i coefficients:

$$A_1 = \left(\psi^2 - 1\right)^2 \left[40856 + 18612\bar{c}_w + 3406\bar{c}_w^2 + 290.1\bar{c}_w^3 + 9.51\bar{c}_w^4\right] \tag{III.93}$$

$$A_2 = \pi^2 \left[\left(\psi + 1\right)^2 A_{21} + \left(\psi - 1\right)^2 A_{22}\right] \tag{III.94}$$

$$A_3 = 4\pi^4 \left[\frac{\xi_{t,2}\xi_t}{L^2} - \left(\frac{256}{15}\bar{c}_w\right)^2\right] \tag{III.95}$$

with:

$$A_{21} = \frac{4\pi^2}{L^2}\xi_M^2\xi_{t,2} + 2\left(\frac{32}{15}\bar{c}_w\right)^2\left[\frac{\xi_t}{L} + 16\pi\sqrt{\frac{2}{L}}\xi_M\right]$$

$$A_{22} = \frac{\xi_{M,2}^2\xi_{t,2} + \xi_{M,3}^2\xi_t}{2L} + \frac{256}{15}\bar{c}_w\xi_{M,2}\xi_{M,3}$$

The positive solution to the previous equation is provided in Table III-4 as a function of the ratio between end moments.

$\psi = -1$	$1 < \psi < 1$	$\psi = 1$
$C_1 = \frac{1}{\sqrt{8\xi_2\xi_3}}$	$C_1 = \sqrt{\frac{4\pi^2\xi_1}{\left(\psi^2-1\right)^2}\left[\Delta - \sqrt{\Delta^2 - \frac{\left(\psi^2-1\right)^2}{4\pi^2\xi_1\xi_3}}\right]}$	$C_1 = \frac{1}{\sqrt{8\xi_3}}$

Table III-4: Expression of C_1 for various ψ

with:

$$\Delta = \left(\psi + 1\right)^2 + \xi_2\left(\psi - 1\right)^2$$

$$\xi_1 = \frac{123058 + 47499\bar{c}_w + 7324\bar{c}_w^2 + 543.4\bar{c}_w^3 + 16.5\bar{c}_w^4}{40856 + 18612\bar{c}_w + 3406\bar{c}_w^2 + 290.1\bar{c}_w^3 + 9.51\bar{c}_w^4}$$

$$\xi_2 = \frac{18041 + 6938\bar{c}_w + 1049\bar{c}_w^2 + 73.57\bar{c}_w^3 + 2.01\bar{c}_w^4}{123058 + 47499\bar{c}_w + 7324\bar{c}_w^2 + 543.4\bar{c}_w^3 + 16.5\bar{c}_w^4}$$

$$\xi_3 = \frac{123058 + 47499\bar{c}_w + 7324\bar{c}_w^2 + 543.4\bar{c}_w^3 + 16.5\bar{c}_w^4}{984463 + 379988\bar{c}_w + 59097\bar{c}_w^2 + 4572\bar{c}_w^3 + 157.9\bar{c}_w^4}$$

The C_1 coefficient depends both on the bending moment distribution, through ψ, and on the warping stiffness, through the ξ_i parameters. The values of C_1 for fully restrained and unrestrained warping at both ends are given in Table III-5 along with the values provided by the *FNA* in the unrestrained case. The *FNA* values are lower than those calculated using the analytical model in the case of free warping. Besides, the increase of the C_1 coefficients provided by full warping restraints ranges between 9.4 and 20%. The highest values are found as ψ approaches -1.

ψ	$C_{1,0}$ (free warping)	$C_{1,\infty}$ (fully restrained warping)	$C_{1,\infty}$ / $C_{1,0}$	C_1 (Table M.1, FNA)
1.00	1.000	1.094	1.094	1.00
0.75	1.141	1.249	1.094	1.14
0.50	1.324	1.451	1.097	1.31
0.25	1.563	1.723	1.102	1.52
0.00	1.880	2.095	1.115	1.77
-0.25	2.275	2.597	1.141	2.05
-0.50	2.665	3.146	1.181	2.33
-0.75	2.813	3.377	1.200	2.57
-1.00	2.612	3.134	1.200	2.55

Table III-5: C_1 for free and fully restrained warping

The expressions for C_1 given in Table III-4 are too cumbersome to be used in a day-to-day design, simplifications being very much required. The coefficient C_1 is approximated as the product of a factor $C_{1,\psi}$ depending only on the bending moment distribution and a factor $C_{1,w}$ depending only on the stiffness of the warping restraints:

$$C_1 = C_{1,w} C_{1,\psi} \tag{III.96}$$

The $C_{1,w}$ factor corresponds to that given in Table III-4 in the case of a uniform bending moment, providing the lowest value of the ratio $C_{1,\infty}$ / $C_{1,0}$:

$$C_{1,w} = \sqrt{\frac{7458 + 2879\bar{c}_w + 447.7\bar{c}_w^2 + 34.64\bar{c}_w^3 + 1.196\bar{c}_w^4}{7458 + 2879\bar{c}_w + 443.9\bar{c}_w^2 + 32.93\bar{c}_w^3 + \bar{c}_w^4}} \tag{III.97}$$

Besides, the factor $C_{1,\psi}$ is expressed in a similar format to that adopted by existing expressions (see *French National Annex to EN 1993-1-1*, *Djalaly* (1974), *Sherbourne* (1989), *Lim* (2003)):

$$C_{1,\psi} = \frac{1}{\sqrt{\alpha_1 \psi^2 + \alpha_2 \psi + \alpha_3}} \tag{III.98}$$

where the α_i coefficients are determined using the value of C_1 for free warping when ψ = 1, 0 and -1, which results in:

$$C_{1,\psi} = \frac{1}{\sqrt{0.209\psi^2 + 0.427\psi + 0.283}} \tag{III.99}$$

The predictions of the proposed expression (III.85) for the warping coefficient k_w are compared against those from *Lindner* (1984) and *ECCS* (2006), *Trahair* (1993), *Pi* (2000), *Piotrowski* (2019) and *Wierzbicki* (2020) in Figure III-9.

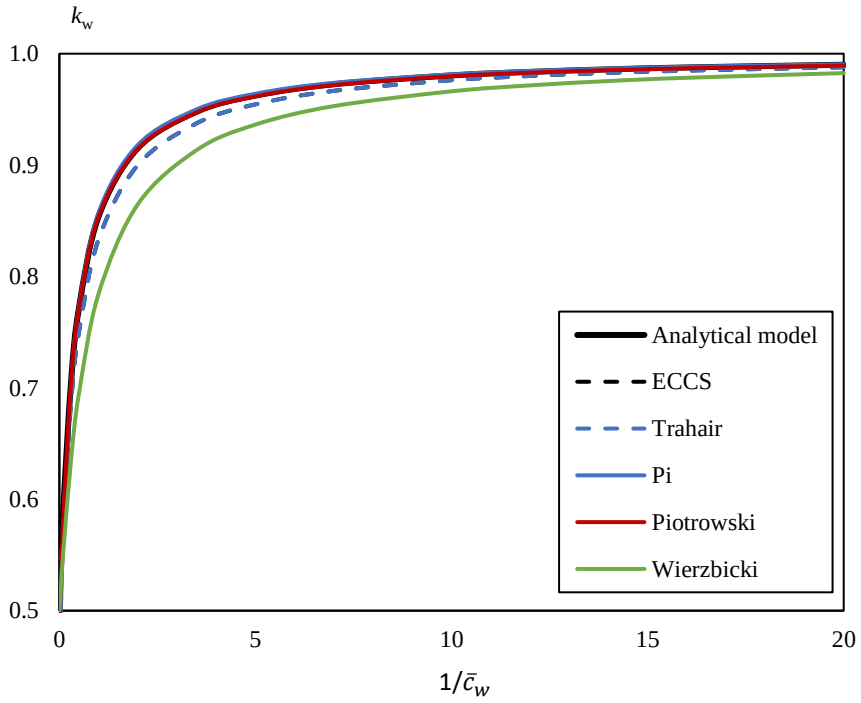

Figure III-9: Warping coefficient

Similar results are found using these approaches except for that of *Trahair* (1993) standing slightly below the results obtained according to the analytical model and the expressions suggested by *ECCS* (2006), *Pi* (2000) and *Piotrowski* (2019). The predictions of *Wierzbicki* (2020) are even lower. Besides, deviations are noted in the case of warping fully restrained where the predictions of *Pi*'s (2000) and *Piotrowski*'s (2019) expression tend toward 0.44 and 0.48, respectively, which are slightly below 0.50 obtained with other methods.

III.5.2.3. Beam under transverse loading

The present sub-section deals with the elastic critical bending moment of beams with warping restraints at both ends subjected to either a uniformly distributed load or a mid-span pointwise force, applied without eccentricity with respect to the shear centre. For such bending moment distributions the critical bending moment is derived assuming a single shape function for both the lateral displacement and twist rotation, given by expressions (III.77) and (III.78), respectively.

The twist rotation and warping distributions determined using the analytical model are compared in Figure III-10 against those resulting from FEA, preformed with *LTBeamN*, using the example studied in sub-sections III.5.2.1 and III.5.2.2 but subjected to a mid-span point load. It can be seen that the twist angle and warping distributions obtained numerically and analytically match very well, justifying the choice of the twist rotation fields. The same conclusion can be drawn when analysing a beam subjected to a uniformly distributed load applied at the shear centre.

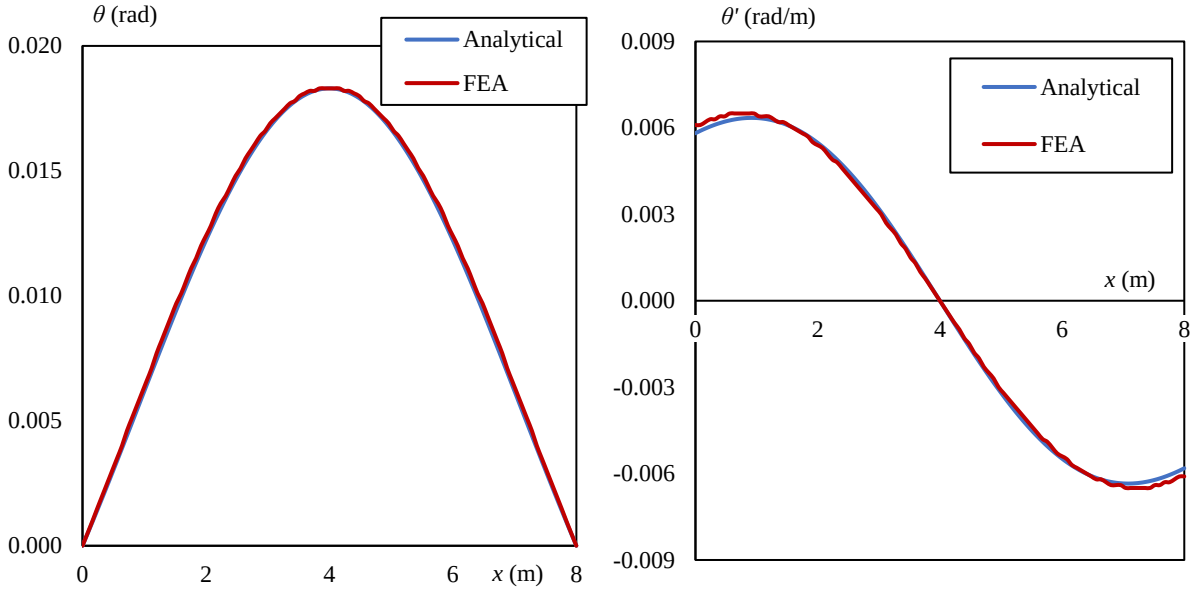

a) *Twist rotation* b) *Warping*

Figure III-10: Twist rotation and warping fields for a pointwise force at mid-span

Using expressions (III.77) and (III.78) for the lateral displacement and twist rotation fields, the minimization of the total potential energy yields the following expression for the warping coefficient, which is similar to that derived in the case of linear bending moment distribution:

$$k_w = \sqrt{\frac{\pi^2 + \frac{8}{3}\bar{c}_w + \frac{\bar{c}_w^2}{4}}{\pi^2 + \frac{20}{3}\bar{c}_w + \bar{c}_w^2}} \qquad \text{(III.100)}$$

In addition, in the case of a pointwise force at mid span, the C_1 coefficient is:

$$C_1 = \sqrt{\frac{4\pi^2 + \frac{32}{3}\bar{c}_w + \bar{c}_w^2}{\frac{24+4\pi^2}{3} + \frac{64}{27\pi^2}(21\pi - 40)\bar{c}_w + \frac{17+2\pi^2}{8\pi^2}\bar{c}_w^2}} \qquad \text{(III.101)}$$

while in the case of a uniformly distributed load, C_1 is:

$$C_1 = \sqrt{\frac{4\pi^2 + \frac{32}{3}\overline{c}_w + \overline{c}_w^2}{32\left(\frac{45+\pi^4}{15\pi^2}\right) + \frac{2048}{81\pi^4}\left(182-15\pi^2\right)\overline{c}_w + \frac{945+16\pi^4}{40\pi^4}\overline{c}_w^2}} \quad \text{(III.102)}$$

The previous expressions for C_1 are simplified in the case of pointwise force and uniformly distributed load, respectively, in expressions (III.103) and (III.104):

$$C_1 = \sqrt{\frac{39.48 + 10.67\overline{c}_w + \overline{c}_w^2}{21.16 + 6.24\overline{c}_w + 0.465\overline{c}_w^2}} \quad \text{(III.103)}$$

$$C_1 = \sqrt{\frac{39.48 + 10.67\overline{c}_w + \overline{c}_w^2}{30.78 + 8.81\overline{c}_w + 0.643\overline{c}_w^2}} \quad \text{(III.104)}$$

Closed form expressions for the elastic critical bending moment have been derived in the case of a linear bending moment distribution, a transverse pointwise force at mid span or a uniformly distributed along the beam. It has been demonstrated that both the warping coefficient k_w and the equivalent uniform moment factor C_1 depend on the stiffness of the warping restraints, the latter depending also on the bending moment diagram.

The warping stiffness induced by common connection configurations (see sub-section III.2.2) being significant, warping might be assumed as fixed at the member end(s). A lower limit on the stiffness of the warping restraints is therefore derived next to assume warping as fixed at both ends when computing the elastic critical bending moment.

III.5.3 Limit stiffness for fully restrained warping

For many connections used in practice, warping may be assumed as fully restrained at both end. A lower limit of the warping stiffness $c_{w,lim}$ to consider warping as fully prevented at both supports is thus proposed. When the stiffness of the warping restraints is greater than $c_{w,lim}$, one may compute the warping coefficient k_w and the equivalent uniform moment factor assuming warping as fully restrained at both ends. The limit stiffness is determined using the same approach as that adopted for the rotational stiffness of connection in *Eurocode 3 Part 1-8* for column base plate by *Jaspart* (2008) and for beam-to-column joints by *Bijlaard* (1991).

For a stiffness c_w of the warping restraints greater than the limit value $c_{w,lim}$, the deviation of the critical bending moment assuming elastic restraints $M_{cr,cw}$ from that assuming full warping restraints $M_{cr,\infty}$ is lower than a certain value ε:

$$\frac{M_{cr,cw}}{M_{cr,\infty}} = \frac{C_{1,cw}}{C_{1,\infty}}\sqrt{\frac{1}{k_{w,cw}^2}\frac{1}{\frac{1}{k_{w,\infty}^2}+\frac{1}{\chi_t^2}} + \frac{1}{\frac{\chi_t^2}{k_{w,\infty}^2}+1}} \geq 1-\varepsilon \quad \text{(III.105)}$$

Assuming that $C_{1,cw} = C_{1,\infty}$, the previous expression can be rewritten as:

$$k_{\mathrm{w,cw}}^2 \le \left(k_{\mathrm{w,cw}}^2\right)_{\lim} = \frac{1}{\left((1-\varepsilon)^2 - \dfrac{k_{\mathrm{w},\infty}^2}{\chi_{\mathrm{t}}^2 + k_{\mathrm{w},\infty}^2}\right)\left(\dfrac{1}{k_{\mathrm{w},\infty}^2} + \dfrac{1}{\pi^2 \chi_{\mathrm{t}}^2}\right)} \tag{III.106}$$

The minimum value of the limit warping coefficient $(k_{\mathrm{w,cw}})_{\lim}$ is obtained when the parameter χ_{t} goes to infinity, resulting in:

$$\left(k_{\mathrm{w,cw}}\right)_{\lim} = \frac{k_{\mathrm{w},\infty}}{1-\varepsilon} \tag{III.107}$$

Besides, using expression (III.2) of the warping coefficient given by *Lindner* (1984) and *ECCS TC 8* (2006) yields:

$$\frac{EI_{\mathrm{w}}}{c_{\mathrm{w}} L} \le \left(\frac{EI_{\mathrm{w}}}{c_{\mathrm{w}} L}\right)_{\lim} = \frac{1}{4\left(1-\left(k_{\mathrm{w,cw}}\right)_{\lim}\right)} - \frac{1}{2} \tag{III.108}$$

which combined together with expression (III.107) produces the following criterion on the warping stiffness:

$$c_{\mathrm{w}} \ge \frac{EI_{\mathrm{w}} / L}{\left(EI_{\mathrm{w}} / L\right)_{\lim}} = \frac{EI_{\mathrm{w}}}{L} \frac{4\left((1-\varepsilon) - k_{\mathrm{w},\infty}\right)}{2k_{\mathrm{w},\infty} - (1-\varepsilon)} \tag{III.109}$$

The value of the warping coefficient for fully restrained warping, i.e. 0.5 is employed for $k_{\mathrm{w},\infty}$ while assuming that a 10%-deviation on the warping coefficient is admissible, resulting in as deviation up to 10% on the critical bending moment, one may assume warping as fully restrained at both ends provided that:

$$c_{\mathrm{w}} \ge 16 \frac{EI_{\mathrm{w}}}{L} \tag{III.110}$$

Eventually, if the stiffness c_{w} of the warping restraint present at both ends fulfils the previous condition, the critical bending moment of the beam can be computed assuming warping as fully prevented at both ends.

Applying the criterion (III.110) for a warping stiffness determined using expression (III.29), one obtains:

$$\frac{h_{\mathrm{s}}^{\ 2}}{\left(\dfrac{1}{S_{\mathrm{j,t}}} + \dfrac{1}{S_{\mathrm{j,b}}}\right)} \ge 16 \frac{EI_{\mathrm{z}}}{L} \frac{h_{\mathrm{s}}^{\ 2}}{4} \rightarrow \frac{1}{\left(\dfrac{1}{S_{\mathrm{j,t}}} + \dfrac{1}{S_{\mathrm{j,b}}}\right)} \ge 4 \frac{EI_{\mathrm{z}}}{L} \tag{III.111}$$

In the particular case where $S_{\mathrm{j,b}} = S_{\mathrm{j,t}} = S_{\mathrm{j}}$, the previous expression rewrites:

$$S_{\mathrm{j}} \ge 8 \frac{EI_{\mathrm{z}}}{L} \tag{III.112}$$

Besides, in the other particular case where $S_{j,t}$ is negligible when compared to $S_{j,b}$, expression (III.111) becomes:

$$S_{j,t} \geq 4\frac{EI_z}{L} \tag{III.113}$$

The possibility to extend the criterion for fully restrained warping at both ends (III.110) to fully restrained at one end, e.g. using expression (III.111) for fixed column bases, will be confronted to *FEA* in section III.6.

III.5.4 Summary of the propositions

Deriving the analytical model has resulted to a single expression for the warping coefficient k_w that depends only on the stiffness of the warping restraints while expressions for the coefficient C_1 depend both on the stiffness of the warping restraints and the bending moment distribution. Besides, the warping stiffness of some connection configurations has been developed along with a lower limit value for such stiffness to assume warping as fully prevented at both ends.

The warping coefficient can be obtained whatever the bending moment diagram using:

$$k_w = \sqrt{\frac{\pi^2 + \frac{8}{3}\bar{c}_w + \frac{\bar{c}_w^2}{4}}{\pi^2 + \frac{20}{3}\bar{c}_w + \bar{c}_w^2}} \tag{III.114}$$

In the case of a linear bending moment distribution, the value of C_1 can be obtained using the expressions provided in Table III-4 or the simplified expression:

$$C_1 = C_{1,w} C_{1,\psi} \tag{III.115}$$

where $C_{1,\psi}$ depends only on the bending moment distribution and $C_{1,w}$ depends only on the stiffness of the warping restraints:

$$C_{1,w} = \sqrt{\frac{7458 + 2879\bar{c}_w + 447.7\bar{c}_w^2 + 34.64\bar{c}_w^3 + 1.196\bar{c}_w^4}{7458 + 2879\bar{c}_w + 443.9\bar{c}_w^2 + 32.93\bar{c}_w^3 + \bar{c}_w^4}} \tag{III.116}$$

$$C_{1,\psi} = \frac{1}{\sqrt{0.209\psi^2 + 0.427\psi + 0.283}} \tag{III.117}$$

In addition, for a pointwise force and a uniformly distributed load, equations (III.101) and (III.102), respectively, are given to compute the C_1 coefficient, which are simplified as, respectively:

$$C_1 = \sqrt{\frac{39.48 + 10.67\bar{c}_w + \bar{c}_w^2}{21.16 + 6.24\bar{c}_w + 0.465\bar{c}_w^2}} \tag{III.118}$$

$$C_1 = \sqrt{\frac{39.48 + 10.67\overline{c}_w + \overline{c}_w^2}{30.78 + 8.81\overline{c}_w + 0.643\overline{c}_w^2}} \qquad \text{(III.119)}$$

The k_w and C_1 coefficients both depend on the stiffness of the warping restraints, their determination assuming warping as fully prevented at both ends being admissible provided that the restraints stiffness c_w complies with:

$$c_w \geq 16\frac{EI_w}{L} \qquad \text{(III.120)}$$

The critical bending moments determined using the expressions derived from the analytical model will be compared against the predictions of finite element analyses using either beam or shell elements, making use of the programmes *LTBeamN* and *ANSYS*, respectively. Besides, the accuracy of the limit stiffness value proposed in the case of a fixed column base to consider warping as fixed at one of the member end will be investigated using *Finite Element Analyses*.

III.6 Numerical analyses

III.6.1 Models

Finite elements analyses have been computed using either a beam-element model with *LTBeamN* or a shell-element model with *ANSYS*. While the beam elements contain 2 nodes, each having 7 degrees of freedom that includes warping, the shell elements possess 8 nodes, each having 6 degrees of freedom. In both cases, the Linear Bifurcation Analyses (*LBA*) were carried out considering a Young's modulus E = 210 000 MPa and a Poisson's ratio v = 0.3.

In both the beam and the shell models, the fork supports are implemented by fully preventing the lateral and vertical displacements along with the twist rotation at both ends while the longitudinal displacement is blocked at one end to avoid any rigid body motion (see Figure III-11 for the shell model).

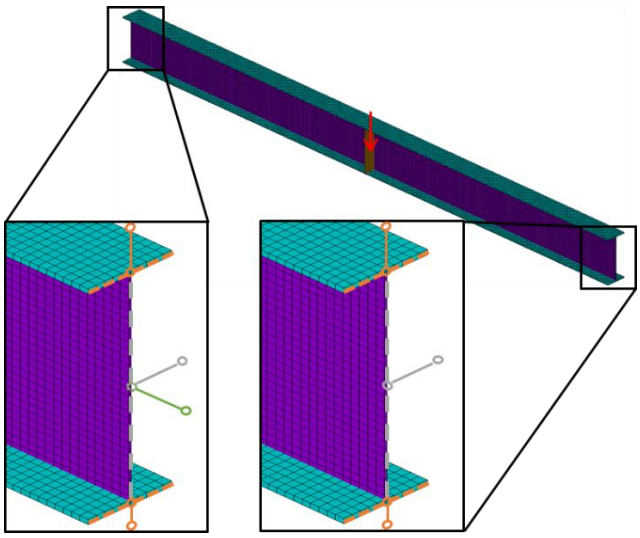

Figure III-11: Fork support conditions and pointwise load

In the beam model, the degree of freedom corresponding to warping can be free, fully fixed at supports, or connected to a warping spring having a stiffness c_w defined using expression (III.3) corresponding to end plates. In the shell model, end plates restraining warping having the width and height of the flange and web, respectively, are modelled at supports using shell elements. To fully restrained warping, rigid beam elements are implemented at both end sections, imposing the same out-of-plane rotation within these cross-sections. Besides, distortion modes along the beam are prevented by enforcing appropriate kinematic conditions in the shell model.

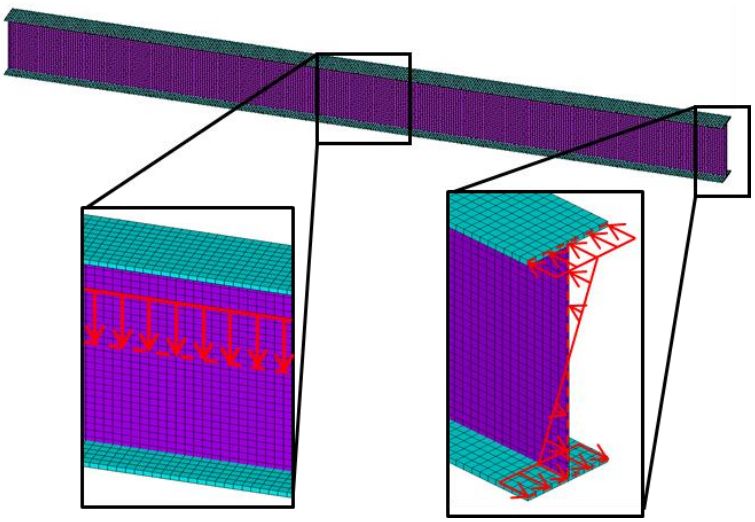

Figure III-12: Uniformly distributed loading and end moment

In the shell model, a mid-span transverse pointwise force is applied at the shear centre where a transverse stiffener is added to avoid unwanted local effects (see Figure III-11). The uniformly distributed loading are also enforced at the cross-sections shear centre while nodal forces varying linearly with the section depth are applied at the beam ends to produce end moments (see Figure III-12).

Designation	h_s (mm)	t_w (mm)	b (mm)	t_f (mm)	L (m)
P1	600	6	200	14	6
P2	800	10	280	14	10
P3	800	6	280	12	10
P4	650	6	180	14	5
P5	650	6	180	10	5
P6	650	5	200	12	4
P7	650	5	200	16	4, 6 & 8
P8	800	8	200	15	6
P9	500	8	200	15	6
P10	300	4	100	6	6 & 9
P11	300	6	100	10	6 & 9
P12	347.3	8	170	12.7	6
P13	337.5	12.5	300	22.5	3 & 6

Table III-6: Geometry of the studied beams

Table III-6 provides the dimensions of the beams studied in the present chapter. The lengths are ranging between 3 and 10 m while the web and flange slenderness vary between 27 and 131, and between 6.1 and 11.4, respectively. At both ends, warping is either free, fully restrained, or partially restrained by end plates having 7 to 70 mm-thick to extend the study beyond common practice.

III.6.2 Elastic critical buckling

III.6.2.1. Linear bending moment

Coefficient C_1

The values of C_1 determined using the analytical model (see Table III-4), the simplified model (see expression (III.96)), the *FNA* and *FEA* – using LTBeamN –are depicted in Figure III-13 as functions of the ratio ψ for beams *P1* to *P7*, *P12* and *P13*. The results are given in the two extreme cases of free warping and fully restrained warping (labelled "fixed").

The predictions of the analytical model in the unrestrained warping are in good agreement with the numerical results though the analytical model slightly overestimates C_1 (by less than 3%) when the ratio between end moments is comprised between -0.5 and 0. The deviations between the twist rotation distributions depicted in Figure III-8 may explain the differences between the values of C_1. The predictions of the simplified expression are similar to those of the analytical model. Besides, the predictions of the *FNA* are conservative, C_1 being underestimated by up to 10%.

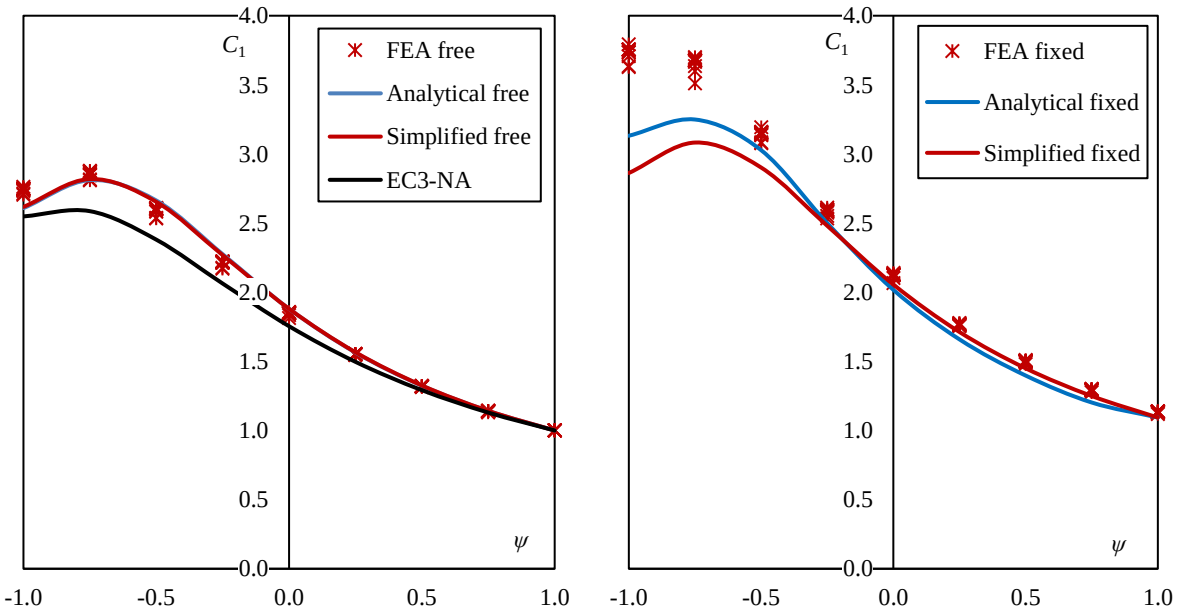

Figure III-13: C_1 for free and fully restrained warping

In the fully restrained warping case, the predictions of the analytical model match very well the *FEA* results when ψ is greater than -0.75. For lower values of the ratio, the analytical model lays on the safe side with a deviation up to 15% from the numerical predictions. The simplified expression provides values similar to the analytical and numerical ones for ψ >-0.5 while for lower values, the simplified expression provides values lower than those of the analytical model, therefore laying on the safe side. The difference between the simplified and analytical expressions can be attributed to the $C_{1,w}$ factor that

produces a 9.4% increase of C_1 from the unrestrained to the fully restrained case whatever ψ while Table III-5 exhibits an incidence of the value of ψ on the C_1 increase.

Critical bending moment

The elastic critical bending moments obtained using *FEA* are compared against the predictions of the analytical model using Table III-4 for C_1 or using the simplified expression (III.96) for beam *P2* in Figure III-14 where the dimensionless ordinate axis is $M_{cr}/M_{cr,0}$ with $M_{cr,0}$ being the critical bending moment for the unrestrained warping case. The predictions of the analytical and simplified models are shown in solid lines for warping restraints corresponding to end plates (up to 70 mm) and by empty triangular markers for the fully restrained warping case.

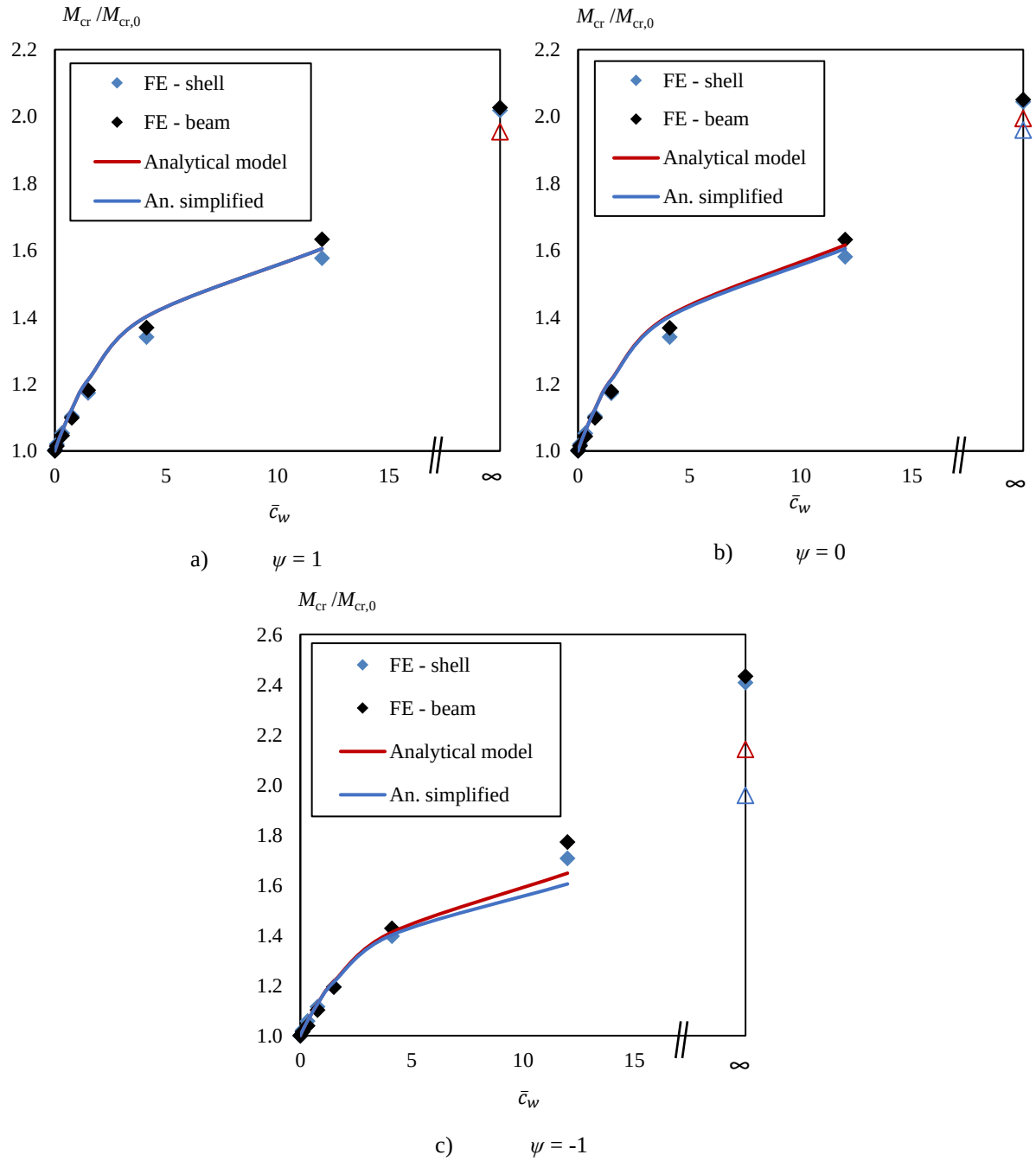

Figure III-14: Ratio $M_{cr}/M_{cr,0}$ for beam P2 *under a linear bending moment distribution*

Figure III-14 shows that the critical bending moment increases significantly when warping is fully restrained, its value being almost twice that obtained in the free warping case for all values of ψ. For ψ comprised between 0 and 1, the predictions of the different methods are very close for values of the dimensionless stiffness up to 1.50. For greater stiffness, the analytical model slightly overestimates (by less than 5%) the critical bending moment when compared to numerical results. When warping is fully prevented, the predictions of the analytical model are on the safe side while being close to the numerical ones, the difference being 3% at most. Besides, using the simplified and the analytical expressions yields similar results in the uniform bending moment case. When $\psi = 0$ small differences are observed for fully restrained warping, the predictions of the simplified model being in every case lower than those of the analytical model.

For $\psi = -1$, the results obtained using the different methods coincide for small-to-medium values of the warping stiffness. As the stiffness increases, the analytical model slightly deviates from the numerical model but lays on the safe side, the predictions of the simplified model being safer. In the fully restrained case, the analytical and numerical predictions exhibit differences close to 12%, placing the analytical model on the safe side.

Table III-7 provides the mean and standard deviation of the ratio between the predictions of the analytical or simplified model and the numerical values of the critical bending moments (M_{cr}) as well as the relative critical ones ($M_{cr}/M_{cr,0}$) for beams P1 to P11 subjected to end moments.

The relative critical bending moments determined using the analytical and the simplified models are very close to the numerical ones. The mean deviation is less than 1.5% and 3% whatever ψ, respectively. The standard deviation of predictions of the dimensionless critical bending moment using the simplified model increases as ψ decreases as a consequence of the factor $C_{1,w}$ that does not account for the bending moment distribution while numerical analyses have shown an impact of the bending moment diagram on this factor.

ψ		1	0.5	0	-0.5	-1
$\frac{\left(M_{cr}/M_{cr,0}\right)_{analytical}}{\left(M_{cr}/M_{cr,0}\right)_{FEA\text{-}shell}}$	*M*	*1.012*	*1.013*	*1.014*	*1.009*	*0.987*
	SD	0.0253	0.0252	0.0256	0.0413	0.0385
$\frac{M_{cr,analytical}}{M_{cr,FEA\text{-}shell}}$	*M*	*1.024*	*1.027*	*1.047*	*1.064*	*0.961*
	SD	0.0277	0.0275	0.0281	0.0298	0.0366
$\frac{\left(M_{cr}/M_{cr,0}\right)_{simplified}}{\left(M_{cr}/M_{cr,0}\right)_{FEA\text{-}shell}}$	*M*	*1.012*	*1.012*	*1.010*	*0.993*	*0.970*
	SD	0.0249	0.0253	0.0283	0.508	0.0626
$\frac{M_{cr,simplified}}{M_{cr,FEA\text{-}shell}}$	*M*	*1.024*	*1.028*	*1.042*	*1.043*	*0.947*
	SD	0.0273	0.0276	0.0299	0.0405	0.0593

M: Mean

SD: Standard Deviation

Table III-7: Comparison between analytical, simplified and numerical predictions for linear bending moment distribution

Small differences are noticed when comparing the analytical and numerical critical bending moments, particularly for values of ψ comprised between -0.5 and 0, the mean deviation being 6.4% at most. This acceptable difference results from the use of symmetrical shape functions as approximate solutions for the mode shapes which cannot reproduce the shift of the peak value of the twist rotation as the bending moment distribution varies. The predictions of the simplified model are slightly lower than those of the analytical model for negative values of ψ with 4.3% deviation on the unsafe side and a 5.3% deviation on the safe side. Besides, the standard deviation between the simplified and numerical models increases as ψ decreases, similarly to the comparison between the analytical and numerical models.

Enhancing the shape functions with a third term would increase the complexity of the expressions for k_w and C_1 without a significant difference in the critical bending moment values. In addition, a maximum 6% deviation on the critical bending moment is reduced when computing the lateral-torsional buckling resistance according to *Eurocode 3 Part 1-1* design rules.

III.6.2.2. Beam under transverse loading

The critical bending moments resulting from finite element analyses using both the shell and beam models are confronted to those calculated using the analytical model. The results are presented in Figure III-15 for beam *P2* subjected to a transverse load, either uniformly distributed (UDL) or applied at mid-span, without eccentricity with respect to the shear centre. Similarly to the linear bending moment distribution case, the critical bending moment increase between free and fully restrain warping is substantial, being almost doubled.

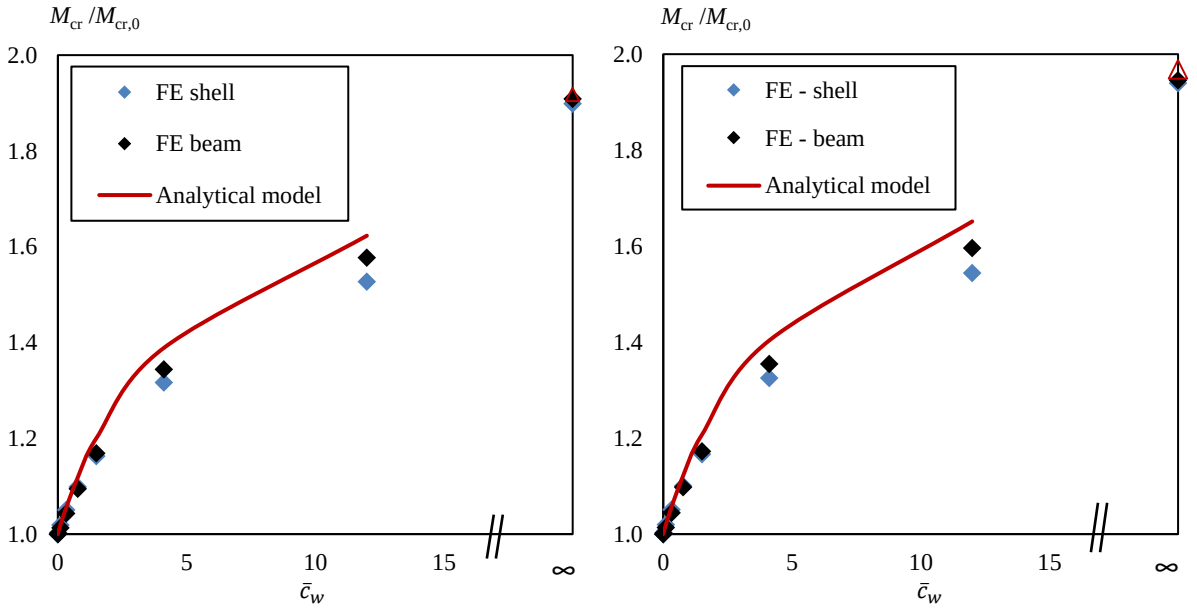

a) *Point load at mid-span* b) *Uniformly distributed loading*

Figure III-15: Ratio $M_{cr}/M_{cr,0}$ for beam P2 *under transverse loading*

In both load cases studied in Figure III-15, the different methods give similar results for very low values of the dimensionless warping stiffness while for increased thickness, the analytical model slightly overestimates the critical bending moment by up to 8%. When warping is fully restrained, the analytical and numerical models give similar results.

Transverse loading		Point load	UDL
$\frac{\left(M_{cr}/M_{cr,0}\right)_{analytical}}{\left(M_{cr}/M_{cr,0}\right)_{FEA\text{-}shell}}$	*M*	*1.028*	*1.030*
	SD	0.0293	0.0314
$\frac{M_{cr,analytical}}{M_{cr,FEA\text{-}shell}}$	*M*	*1.036*	*1.037*
	SD	0.0297	0.0318

Table III-8: Comparison between analytical and numerical predictions for a beam subjected to transverse loading

Table III-8 gives the mean and standard deviation of the ratio between the predictions of the analytical model and the numerical values of the critical bending moments (M_{cr}) as well as the relative critical ones ($M_{cr}/M_{cr,0}$) for beams P1 to P5 under transverse loading. The results obtained with both methods are very close, the mean difference between them being approximately 3% in both cases.

III.6.3 Limit stiffness for fully fixed warping at one end

Expression (III.111) that provides a lower value for the limit warping stiffness to consider warping as fully prevented at a fixed column base is derived from the limit value proposed to consider warping as fixed at both ends. *FEA* are therefore employed to assess the accuracy of the criterion for fully fixed warping at a single end by comparing the critical bending moments:

- $M_{cr,w}$ computed assuming that warping is free at one end while a warping spring is connected to the other end. Two values are used in turn for the stiffness of the warping spring. A value corresponding to the lower bound of expression (III.110) is firstly used, i.e. assuming a 10% deviation from the warping coefficient for fully restrained warping at both ends:

$$c_w = 16\frac{EI_w}{L} \qquad \text{(III.121)}$$

  An alternate value is also used assuming a 5% deviation from the warping coefficient for fully restrained warping at both ends (see equation (III.109)):

$$c_w = 36\frac{EI_w}{L} \qquad \text{(III.122)}$$

- $M_{cr,\infty}$ calculated assuming that warping is free at one end and fully prevented at the other end.

The comparisons are performed for a IPE 400 cross-section member having a length ranging from 3 to 6 m and for P2 (see Table III-6) having a length ranging from 3 to 9 m. In both cases, the studied members are subjected to a linear bending moment distribution with ψ = 1, 0 and -1. In the case of a triangular bending moment (ψ = 0), the bending moment is zero at the end where warping is free, in line with the common practice. The ratios $M_{cr,w}$ / $M_{cr,\infty}$ are given in Table III-9 where $M_{cr,90}$ is associated with the warping stiffness computed using expression (III.121), $M_{cr,95}$ being related to (III.122).

Whatever the stiffness of the warping restraints, results are very close when ψ = 1 or -1, lower values of $M_{cr,w}$ / $M_{cr,\infty}$ being found in the case of a triangular bending moment distribution. Using expression

(III.121) for the warping stiffness provides values of $M_{cr,w}$ / $M_{cr,\infty}$ greater than 0.9 except when $\psi = 0$ where slightly lower values are obtained, the maximum deviation being 3%. When a greater value of the warping stiffness is introduced, using expression (III.122), all the ratios are greater than 0.9, the results being comprised between 0.93 and 0.97.

Cross-section	*L (m)*	$M_{cr,90}$ / $M_{cr,\infty}$			$M_{cr,95}$ / $M_{cr,\infty}$		
		$\psi = 1$	$\psi = 0$	$\psi = -1$	$\psi = 1$	$\psi = 0$	$\psi = -1$
IPE 400	3	0.915	0.876	0.920	0.955	0.933	0.959
	3.5	0.917	0.879	0.925	0.957	0.934	0.963
	4	0.920	0.880	0.926	0.958	0.935	0.963
	4.5	0.923	0.884	0.928	0.959	0.937	0.964
	5	0.925	0.886	0.931	0.960	0.938	0.965
	5.5	0.927	0.888	0.933	0.961	0.939	0.966
	6	0.930	0.891	0.935	0.962	0.940	0.966
P2	3	0.908	0.868	0.916	0.952	0.930	0.958
	4	0.908	0.869	0.917	0.952	0.930	0.958
	5	0.910	0.873	0.913	0.952	0.932	0.953
	6	0.910	0.873	0.916	0.953	0.931	0.957
	7	0.911	0.872	0.917	0.954	0.932	0.960
	8	0.912	0.874	0.919	0.954	0.932	0.960
	9	0.914	0.875	0.921	0.955	0.933	0.961

Table III-9: Ratio $M_{cr,w}/M_{cr,\infty}$ for a linear bending moment

The criterion (III.110) was proposed assuming a maximum deviation on the critical bending moment of 10%. Because the use of expression (III.121) provides deviations greater than 10%, the same criterion cannot be applicable for members with warping prevented at a single end. A more restrictive criterion is therefore to be used, based on expression (III.122):

$$c_w \geq 36\frac{EI_w}{L} \qquad \text{(III.123)}$$

One may compute the critical bending moment of a doubly symmetrical I-profile with a warping restraint at a single end assuming fully restrained warping at that end provided that the previous expression (III.123) is satisfied.

III.7 Summary

The elastic lateral-torsional buckling of doubly symmetric beams have been investigated in this chapter where an analytical model has been developed, resulting in a general expression for the critical bending moment. The stiffness of the warping restraints is explicitly accounted for when computing the critical bending moment within the warping coefficient k_w and the equivalent uniform moment factor C_1. Beams

resting on fork supports with free out-of-plane rotation and warping springs at both ends were studied when subjected to a linear bending moment distribution, a pointwise transverse load at mid-span, or a uniformly distributed load along the member. Transverse loading is applied without eccentricity with respect to the shear centre.

The use of two trigonometric base functions for both the lateral displacement and twist rotation was shown to be consistent with the distributions obtained numerically though small differences were noticed, particularly when looking at the position of the peak value of the twist rotation along the member.

Employing the principle of minimum potential energy, a single expression for k_w has been obtained whatever the shape of the bending moment diagram and depending on the warping stiffness of the beam and the restraints and on the member length. Besides, expressions for C_1 have been derived that depend both on the bending moment diagram and on the stiffness of the warping restraints. For a linear bending moment distribution, C_1 is simply expressed as the product of two terms, one related to the bending moment distribution and the other to the stiffness of the warping restraints. When confronted to numerical results, computed using either a shell or a beam model, the predictions of the analytical and simplified models showed a good accuracy.

The stiffness of some connection configuration restraining warping at a beam ends has been given based on the work of *Pi* (2000) while the warping stiffness of a fixed column base has been derived. Some connection configurations inducing significant warping restraints, the possibility to compute the critical bending moment assuming warping as fully prevented at both ends was investigated. For members with warping restraints at both ends, a proposition has been made for a lower limit of the warping stiffness. Above this limit, the critical bending moment may be computed assuming fully restrained warping at both ends. This simplification results in a maximum 10% deviation on the critical bending moment. Based on the results of finite element analyses, this limit value is adapted to warping restraints present at one end only.

PART II: ELASTO-PLASTIC BUCKLING

IV. *Stability design rules for welded steel members*

IV.1 Introduction

The resistance of an ideal member subjected to compression and/or bending can be determined as the minimum value between its cross-section resistance and its elastic critical buckling load. However, in a "real" member, the structural and geometrical imperfections resulting from its fabrication reduce this resistance. Determining the reduction from the ideal resistance depending on the shapes and magnitudes of the structural and geometrical imperfections is the most critical point to assess the stability of a steel member.

In 1966, the former French *CM66* design rules made use of a single buckling curve whatever the cross-sectional dimensions and the fabrication process, but the distribution of the bending moment was accounted for when determining the lateral-torsional buckling resistance. In the years 1960-70, an extensive European experimental campaign on compressed steel columns was led, as described by *Sfintesco* (1970), and has resulted in several buckling curves. *Maquoi* (1978) and *Rondal* (1979) have developed an analytical model based on the work of *Ayrton and Perry* (1886) and *Robertson* (1925) to determine the flexural buckling resistance of a compressed member based on three, then five buckling curves.

The use of three buckling curves was adopted in 1981 in the French standard *Additif 80* to determine the buckling resistance of a member subjected to compression or bending. The current *Eurocode 3 Part 1-1* guidelines for members subjected to compression and/or bending are described in section IV.2 were one can notice that the number of buckling curves has then been extended in the European standard to five curves for compressed members and four curves for members in bending. The complementary prescriptions of the *French National Annex to EN 1993-1-1* are also provided.

Using the formalism of *Eurocode 3* based on an Ayrton-Perry type derivation, a new verification format developed by *Taras* (2010a/b) is proposed in *prEN 1993-1-1* to determine the lateral-torsional buckling of a beam. Based on a strong mechanical basis, this new method does not make use of the current buckling curves but requires the determination a buckling curve per cross-section and bending moment diagram. This novel method along with the modified *Simplified method* of the equivalent compression flange are exposed within subsection IV.2.2.6. Besides, the design rules of the former French standards *Additif* 80 and *CM66* are mentioned in section IV.3.

Determining the buckling resistance of a uniform steel member according to *EN 1993-1-1* can be direct using the buckling curves. However, the buckling resistance of a tapered member according to the European standard is more difficult to determine because tapered members fall beyond the scope of the verification formats employing the buckling curves in *EN 1993-1-1*. The stability of tapered steel members has captivated of many researchers in the last few years, leading to new analytical methods as in the work of *Naumes* (2009), *Marques* (2012a) and *Tankova* (2018a) that will eventually be depicted in section IV.4.

IV.2 Eurocode 3 design rules

IV.2.1 Members in compression

The resistance of a compressed steel member (see Figure IV-1a)) is given in §6.3.1 of *Eurocode 3 Part 1-1* where clause (6.46) applies, stating that the stability of the member is verified if:

$$\frac{N_{Ed}}{N_{b,Rd}} \leq 1.0 \qquad \text{(IV.1)}$$

$$N_{b,Rd} = \chi_i \frac{N_{Rk}}{\gamma_{M1}} \qquad \text{(IV.2)}$$

with:

N_{Ed}: maximal applied axial force;

N_{Rk}: characteristic value of the member resistance to compression;

χ_i: reduction factor considering the appropriate buckling mode.

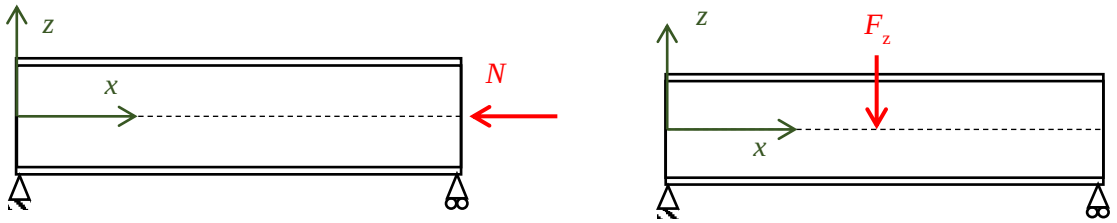

a) *In compression* b) *In bending*

Figure IV-1: Uniform members

The reduction factor is determined using expression (6.49):

$$\chi_i = \frac{1}{\phi_i + \sqrt{\phi_i^2 - \bar{\lambda}_i^2}} \leq 1.0 \qquad \text{(IV.3)}$$

$$\phi_i = 0.5\left[1 + \alpha_i\left(\bar{\lambda}_i - 0.2\right) + \bar{\lambda}_i^2\right] \qquad \text{(IV.4)}$$

where $\bar{\lambda}_i = \sqrt{N_{Rk}/N_{cr,i}}$ is the normalized slenderness for flexural buckling and α_i the imperfection factor for flexural buckling given in Table IV-1, corresponding to Table 6.1 of *Eurocode 3 Part 1-1*.

Buckling curve	**d**	**c**	**b**	**a**	**a_0**
Imperfection factor α_i	0.76	0.49	0.34	0.21	0.13

Table IV-1: Buckling curves imperfection factors

The buckling curve must be chosen according to the member fabrication process, cross-section shape and dimensions, steel grade and the buckling mode analyzed. The relevant buckling curve to use for a welded I-section member is given in Table IV-2, extracted from Table 6.2 of *EN 1993-1-1*.

Limits	Buckling axis	Buckling curve
$t_f \leq 40$ mm	y-y	b
	z-z	c
$t_f > 40$ mm	y-y	c
	z-z	d

Table IV-2: Buckling curve selection for flexural buckling of welded I-columns

Using the appropriate elastic critical load, the buckling curve related to the *z*-axis should also be used for torsional or torsional-flexural buckling according to *Eurocode 3 Part 1-1*.

IV.2.2 Members in bending

IV.2.2.1. Introduction

The lateral-torsional buckling resistance of a member in bending (see Figure IV-1b)) must be assessed according to §6.3.2 of *Eurocode 3 Part 1-1*. Either (i) the *General case* based on the buckling curves for flexural buckling; (ii) the *Special case* based on modified buckling curves; or (iii) the *Simplified method* that consists in the verification against lateral buckling of the equivalent compressed flange can be employed. The three approaches are presented next, along with the modifications suggested in the *French National Annex to Eurocode 3 Part 1-1*.

Eventually, the new verification format developed by *Taras* (2010a/b) that replaces the *Special case* in *prEN 1993-1-1* will be presented along with the modified *Simplified method* of the equivalent compressed flange in *prEN 1993-1-1* based on the work of *Schaper* (2019).

IV.2.2.2. General case

According to *Eurocode 3 Part 1-1*, the stability of a uniform member in bending according to the *General case* or the *Special case* requires clause (6.54) to be satisfied:

$$\frac{M_{y,Ed}}{M_{b,Rd}} \leq 1.0 \tag{IV.5}$$

$$M_{b,Rd} = \chi_{LT} \frac{M_{y,Rk}}{\gamma_{M1}} \tag{IV.6}$$

with:

$M_{y,Ed}$: maximal applied bending moment about *y-y*;

$M_{y,Rk}$: characteristic value of the member resistance to bending about *y-y*;

χ_{LT}: reduction factor for lateral-torsional buckling.

The *General case* defines the reduction factor in expression (6.56):

$$\chi_{LT} = \frac{1}{\phi_{LT} + \sqrt{\phi_{LT}^2 - \bar{\lambda}_{LT}^2}} \leq 1.0 \qquad \text{(IV.7)}$$

$$\phi_{LT} = 0.5\left[1 + \alpha_{LT}\left(\bar{\lambda}_{LT} - 0.2\right) + \bar{\lambda}_{LT}^2\right] \qquad \text{(IV.8)}$$

where $\bar{\lambda}_{LT} = \sqrt{M_{y,Rk}/M_{y,cr}}$ is the normalized slenderness for lateral-torsional buckling and α_{LT} the imperfection factor for lateral-torsional buckling given in Table 6.3 of *Eurocode 3 Part 1-1* which is similar to Table IV-1 without curve a_0.

The buckling curve selection of a welded member depends on the *h*/*b* ratio of its cross-section according to Table IV-3 extracted from Table 6.4 of *Eurocode 3 Part 1-1*.

Limits	Buckling curve
$h/b \leq 2$	c
$h/b > 2$	d

Table IV-3: Buckling curve for lateral-torsional buckling of welded I-beams

IV.2.2.3. Special case

The *Special case* for "equivalent welded sections" proposes to use the reduction factor given by expression (6.57):

$$\chi_{LT} = \frac{1}{\phi_{LT} + \sqrt{\phi_{LT}^2 - \beta\bar{\lambda}_{LT}^2}} \leq \begin{cases} 1.0 \\ 1/\bar{\lambda}_{LT}^2 \end{cases} \qquad \text{(IV.9)}$$

$$\phi_{LT} = 0.5\left[1 + \alpha_{LT}\left(\bar{\lambda}_{LT} - \bar{\lambda}_{LT,0}\right) + \beta\bar{\lambda}_{LT}^2\right] \qquad \text{(IV.10)}$$

Values of 0.4 and 0.75 are recommended for $\bar{\lambda}_{LT,0}$ and β, respectively, along with the use the imperfection factor α_{LT} from the *General case*. Those parameters are modified in the *French National Annex*.

A modification of the reduction factor given by expression (6.58) is allowed to account for the bending moment distribution using a coefficient *f*:

$$\chi_{LT,mod} = \frac{\chi_{LT}}{f} \leq 1.0 \qquad \text{(IV.11)}$$

$$f = 1 - 0.5(1 - k_c)\left[1 - 2.0\left(\bar{\lambda}_{LT} - 0.8\right)^2\right] \leq 1.0 \qquad \text{(IV.12)}$$

The coefficient *f* depends on the normalized slenderness and on the bending moment distribution through the correction factor k_c given in Table IV-4 extracted from *EN 1993-1-1* (*Table 6.6*).

Bending moment distribution	k_c
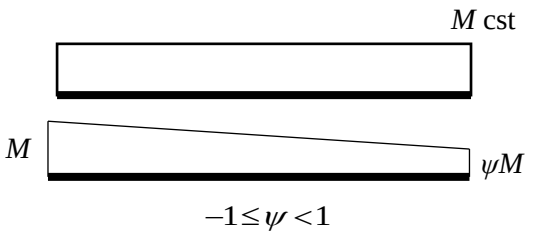	1.0 $\frac{1}{1.33-0.33\psi}$
	0.94
	0.90
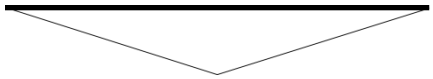	0.86
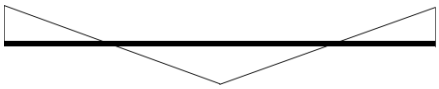	0.77

Table IV-4: Correction factors according to EN 1993-1-1

IV.2.2.4. Simplified method

The approach of the *Simplified method* differs from the *General* and *Special cases* because lateral-torsional buckling of a beam is analyzed as the lateral buckling of an equivalent compressed part of the beam composed of the compression flange and a third of the compressed part of the web (see Figure IV-2). The buckling resistance determined according to the *Simplified method* is given by:

$$M_{b,Rd} = k_{fl}\chi\frac{M_{y,Rk}}{\gamma_{M1}} \le \frac{M_{y,Rk}}{\gamma_{M1}} \qquad \text{(IV.13)}$$

with:

k_{fl}: modification factor;

χ: reduction factor of the equivalent compression flange.

The reduction factor χ is determined using the normalized slenderness of the equivalent compression flange $\bar{\lambda}_f$ given by:

$$\bar{\lambda}_f = \frac{k_c L_c}{i_{f,z}\lambda_1} \qquad \text{(IV.14)}$$

with:

L_c: distance between lateral-torsional restraints;

i_{fz}: radius of gyration of the equivalent compression flange about the minor axis of the section;

$$\lambda_1 = \pi\sqrt{\frac{E}{f_y}}$$

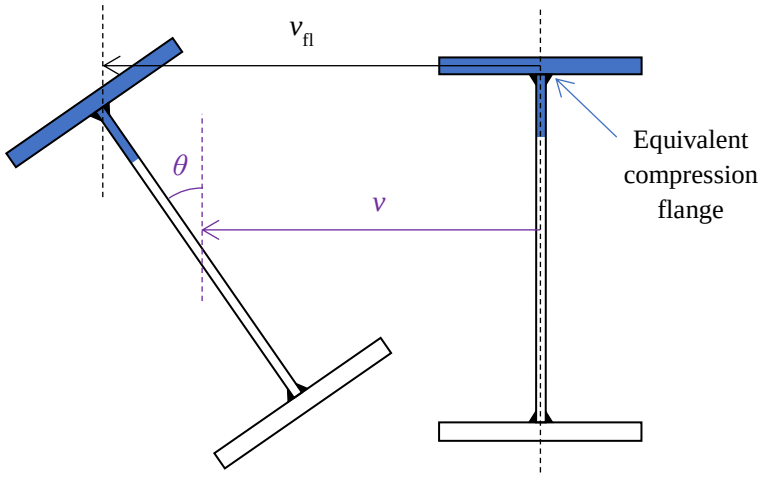

Figure IV-2: Lateral buckling of the equivalent compression flange

The reduction factor χ is determined using buckling curve *d* for welded sections for which the method applies provided that:

$$\frac{h}{t_f} \leq 44\varepsilon \qquad \text{(IV.15)}$$

The previous criterion is quite restrictive for welded building beams. Indeed, for a S355 member with flanges thickness of 15 mm, the simplified method can be applied only if the height does not exceed a medium value of 537 mm, regardless of the cross-sectional classification.

The modification factor k_{fl}, increases the resistance of the beam against lateral-torsional buckling because of the supposed conservatism of the *Simplified method*. *Eurocode 3 Part 1-1*-proposes a value of 1.10 for this factor, which is modified in the *French National Annex*.

IV.2.2.5. Adaptations in the French National Annex

The *French National Annex to Eurocode 3 Part 1-1* does not propose changes regarding the design of the buckling resistance of compressed member but suggests some modifications in the verification methods against lateral-torsional buckling. The *General case* remains unchanged but the *French National Annex* allows its reduction factor to be modified with the coefficient *f* using expression (IV.11).

Parameter	*Eurocode 3 Part 1-1*	*French NA to Eurocode 3 Part 1-1*
α_{LT}	Similar to *General case*	$0.5 - 0.25\frac{b}{h}\bar{\lambda}_{LT}^{2} \geq 0$
$\bar{\lambda}_{LT,0}$	0.4	$0.3\frac{b}{h}$
β	0.75	1.0
k_{fl}	1.10	$1 + \frac{\bar{\lambda}_f}{10} \leq 1.20$

Table IV-5: Parameters of the Special case and the Simplified method according to EC3 *and its* French NA *for welded beams*

The modifications proposed in the *French National Annex* regarding the *Special case* and the *Simplified method* are given in Table IV-5 for welded I-section beams. The scope of the modified *Special case* is extended from doubly symmetric to mono-symmetric I-section beams for which the ratio between the second moments of area about the minor axis of the two flanges is between 0.80 and 1.25. The modifications are however valid only if the thickness ratio between the thickest flange and the web is lower than or equal to three.

The *French National Annex* does not provide a significant change in the *Simplified method*, but the modifications are significant regarding the *Special case*. Buckling curves *c* and *d* according to the *Special case* from *Eurocode* 3 (referred to as *Sc*) are plotted in Figure IV-3 along with buckling curves determined according to the prescriptions of the *French National Annex* for welded sections having a ratio *h*/*b* equal to one and five (referred to as *FNA*). The buckling curves to be used according to the *General case* from *Eurocode 3* for welded sections (referred to as *Gc*) are also represented.

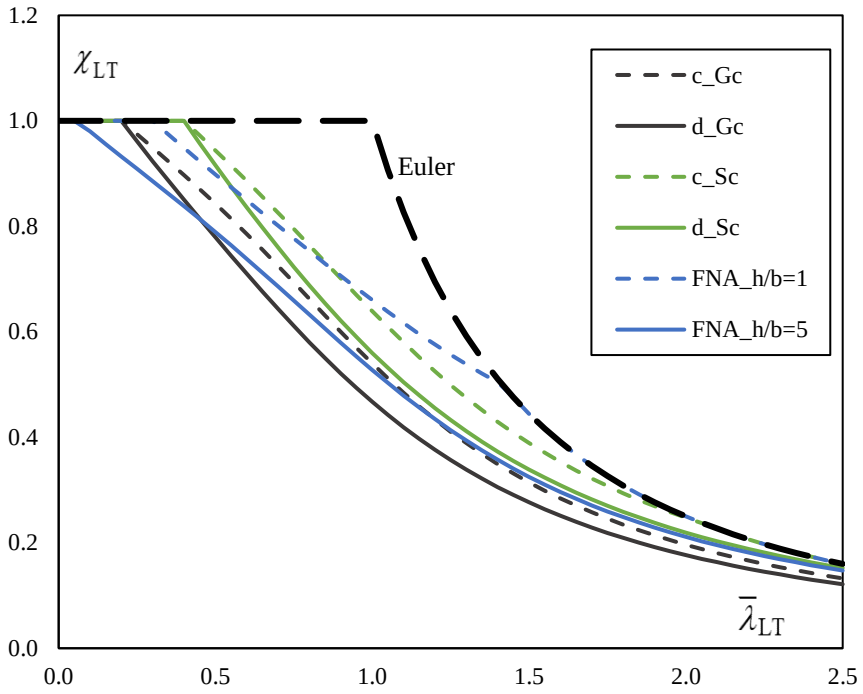

Figure IV-3: Buckling curves for welded members in Eurocode 3 *and its* French National Annex

Major differences can be seen on Figure IV-3 between the buckling curves to use for a welded section according to the three methods. When $h/b=5$, the *Special case* provides the most favourable buckling curve, especially for a low slenderness range. Despite a very short plateau length, the *FNA* provides a higher resistance than the *General case* except for very low slenderness. When $h/b=1$, the *General case* prescripts the lowest buckling curve while the *FNA* provides the highest curve except for low slenderness for which the *Special case* give the most favourable buckling resistance due to its important plateau length.

IV.2.2.6. Verification methods in prEN 1993-1-1

New verification format

The new *Eurocode 3* contains a verification format based on the work of *Taras* (2010a/b) where the reduction factor of doubly symmetric I-section beams resting on fork supports at both ends is:

$$\chi_{LT} = \frac{f_M}{\phi_{LT} + \sqrt{\phi_{LT}^2 - f_M \bar{\lambda}_{LT}^2}} \le 1.0 \qquad \text{(IV.16)}$$

$$\phi_{LT} = 0.5\left[1 + f_M\left(\left(\frac{\bar{\lambda}_{LT}}{\bar{\lambda}_z}\right)^2 \alpha_{LT}\left(\bar{\lambda}_z - 0.2\right) + \bar{\lambda}_{LT}^2\right)\right] \qquad \text{(IV.17)}$$

The factor f_M, always greater than unity, accounts for the bending moment distribution and its value is given for some bending moment diagrams in Table IV-6 extracted from Table 8.6 of *prEN 1993-1-1* while the imperfection factors α_{LT} are given in Table IV-7 for welded beams.

Bending moment distribution	k_c		f_M	
	$\frac{M_0}{M_h} < 1$	$\frac{M_0}{M_h} \ge 1$	$0 < \frac{M_0}{M_h} < 2$	$\frac{M_0}{M_h} \ge 2$
M cst	1.0		1.0	
M, ψM, $-1 \le \psi < 1$	$\frac{1}{1.33 - 0.33\psi}$		$1.25 - 0.1\psi - 0.15\psi^2$	
M_h, M_0	0.94		1.05	
M_h, M_0	1.0	0.9	$1 + 1.35\frac{M_0}{M_h} - 0.33\left(\frac{M_0}{M_h}\right)^3$	1.05
M_h, M_0	0.86		1.10	
M_h, M_0	1.0	0.77	$1 + 1.25\frac{M_0}{M_h} - 0.3\left(\frac{M_0}{M_h}\right)^3$	1.1

Table IV-6: Factors f_M and k_c in prEN 1993-1-1

where M_0 is the free bending moment at mid-span which can be determined on an equivalent member with simply supported end conditions.

Limits	α_{LT}
$t_f \leq 40$ mm	$0.21\sqrt{\frac{W_{el,y}}{W_{el,z}}} \leq 0.64$
$t_f > 40$ mm	$0.25\sqrt{\frac{W_{el,y}}{W_{el,z}}} \leq 0.76$

Table IV-7: Imperfection factor for welded members according to the new verification format

Modified Simplified method

Beyer (2019a) highlighted that the *Simplified method* could be unsafe for mono-symmetric beams or beams subjected to a transverse load applied out of the shear centre and causing destabilizing effects ($z_g \geq 0$). Modifications of the *Simplified method* have then been proposed by (i) omitting the modification factor k_{fl} and (ii) choosing the imperfection factor α_{LT} according to the *General case*. *Schaper* (2019) have proposed supplementary modifications based on an extensive finite element parametric study that led to the modified *Simplified method* of *prEN 1993-1-1*.

The design resistance according to the revised *Simplified method* of a doubly or mono-symmetric I-cross-section beam is given by:

$$M_{b,Rd} = \chi_{c,z} \frac{M_{y,Rk}}{\gamma_{M1}} \tag{IV.18}$$

The buckling resistance depends on a reduction factor $\chi_{c,z}$ determined from the normalized slenderness $\bar{\lambda}_{c,z,mod}$ using the buckling curve *d* for welded members.

$$\bar{\lambda}_{c,z,mod} = k_c \beta_c \bar{\lambda}_{c,z} = k_c \beta_c \frac{L_c}{i_{f,z} \lambda_1} \tag{IV.19}$$

with:

$$\beta_c = \sqrt{\frac{0.06 \frac{h}{t_{f,max}}}{\bar{\lambda}_{c,z} + \frac{t_{f,min}}{t_{f,max}}}} \leq 1.0$$

The factor β_c accounts for the possible mono-symmetry and the torsional properties of the cross-section while the correction factor k_c accounts for the bending moment distribution. Values of k_c given in Table IV-4 extracted from *EN 1993-1-1* still apply in *prEN1993-1-1*, but more complex bending moment distributions are treated in Table 8.6 of *prEN 1993-1-1*, some of them being depicted in Table IV-6.

IV.2.3 Members in bending and compression

IV.2.3.1. Interaction formulae for uniform members

The stability of uniform members having a doubly symmetrical cross-section subjected to bi-axial bending and compression can be assessed provided that clauses (6.61) and (6.62) from §6.3.3 of *Eurocode 3 Part 1-1* are satisfied:

$$\frac{N_{\mathrm{Ed}}}{\frac{\chi_{\mathrm{y}} N_{\mathrm{Rk}}}{\gamma_{\mathrm{M1}}}} + k_{\mathrm{yy}} \frac{M_{\mathrm{y,Ed}} + \Delta M_{\mathrm{y,Ed}}}{\frac{\chi_{\mathrm{LT}} M_{\mathrm{y,Rk}}}{\gamma_{\mathrm{M1}}}} + k_{\mathrm{yz}} \frac{M_{\mathrm{z,Ed}} + \Delta M_{\mathrm{z,Ed}}}{\frac{M_{\mathrm{z,Rk}}}{\gamma_{\mathrm{M1}}}} \leq 1 \qquad \text{(IV.20)}$$

$$\frac{N_{\mathrm{Ed}}}{\frac{\chi_{\mathrm{z}} N_{\mathrm{Rk}}}{\gamma_{\mathrm{M1}}}} + k_{\mathrm{zy}} \frac{M_{\mathrm{y,Ed}} + \Delta M_{\mathrm{y,Ed}}}{\frac{\chi_{\mathrm{LT}} M_{\mathrm{y,Rk}}}{\gamma_{\mathrm{M1}}}} + k_{\mathrm{zz}} \frac{M_{\mathrm{z,Ed}} + \Delta M_{\mathrm{z,Ed}}}{\frac{M_{\mathrm{z,Rk}}}{\gamma_{\mathrm{M1}}}} \leq 1 \qquad \text{(IV.21)}$$

with:

$M_{\mathrm{z,Ed}}$: maximal applied bending moment about *z-z*;

$M_{\mathrm{z,Rk}}$: characteristic value of the member resistance to bending about *z-z* ;

$\Delta M_{\mathrm{i,Ed}}$: bending moments due to the shift of the centroidal axis for Class 4 sections.

Interaction factor	*Class 3, Class 4*	*Class 1, Class 2*
k_{yy}	$C_{my}\left(1+0.6\bar{\lambda}_y\frac{N_{Ed}}{\chi_y N_{Rk}/\gamma_{M1}}\right)$ $\le C_{my}\left(1+0.6\frac{N_{Ed}}{\chi_y N_{Rk}/\gamma_{M1}}\right)$	$C_{my}\left(1+0.6\left(\bar{\lambda}_y-0.2\right)\frac{N_{Ed}}{\chi_y N_{Rk}/\gamma_{M1}}\right)$ $\le C_{my}\left(1+0.8\frac{N_{Ed}}{\chi_y N_{Rk}/\gamma_{M1}}\right)$
k_{yz}	k_{zz}	$0.6k_{zz}$
k_{zy}	$\left(1-\frac{0.05\bar{\lambda}_z}{(C_{mLT}-0.25)}\frac{N_{Ed}}{\chi_z N_{Rk}/\gamma_{M1}}\right)$ $\ge\left(1-\frac{0.05}{(C_{mLT}-0.25)}\frac{N_{Ed}}{\chi_z N_{Rk}/\gamma_{M1}}\right)$	$\left(1-\frac{0.1\bar{\lambda}_z}{(C_{mLT}-0.25)}\frac{N_{Ed}}{\chi_z N_{Rk}/\gamma_{M1}}\right)$ $\ge\left(1-\frac{0.1}{(C_{mLT}-0.25)}\frac{N_{Ed}}{\chi_z N_{Rk}/\gamma_{M1}}\right)$ For $\bar{\lambda}_z<0.4$: $k_{zy}=0.6+\bar{\lambda}_z\le 1-\frac{0.1\bar{\lambda}_z}{(C_{mLT}-0.25)}\frac{N_{Ed}}{\chi_z N_{Rk}/\gamma_{M1}}$
k_{zz}	$C_{mz}\left(1+0.6\bar{\lambda}_z\frac{N_{Ed}}{\chi_z N_{Rk}/\gamma_{M1}}\right)$ $\le C_{mz}\left(1+0.6\frac{N_{Ed}}{\chi_z N_{Rk}/\gamma_{M1}}\right)$	$C_{mz}\left(1+\left(2\bar{\lambda}_z-0.6\right)\frac{N_{Ed}}{\chi_z N_{Rk}/\gamma_{M1}}\right)$ $\le C_{mz}\left(1+1.4\frac{N_{Ed}}{\chi_z N_{Rk}/\gamma_{M1}}\right)$

Table IV-8: Interaction factors for welded I-section members

The interaction factors k_{ij} can be conveniently determined according to Annex A or Annex B of the current *Eurocode 3 Part 1-1* but its new version requires the use of the current Annex B. Analytical derivations leading to Annex A can be found in *Greiner* (2006) while *Boissonnade* (2002b, 2004) presents the derivation of Annex B. The interaction factors for welded I-section steel members that are susceptible to torsional deformations proposed in Annex B are given in Table IV-8. They make use of equivalent uniform moment factors $C_{m,i}$, that account for the bending moment distribution. Factors $C_{m,i}$ should be determined according to the appropriate bending axis (*z-z* for C_{mz} and *y-y* for C_{my} and C_{mLT}) and the relevant direction of the bracing points (*z-z* for C_{my} and *y-y* for C_{mz} and C_{mLT}).using expressions given in Table IV-9 corresponding to Table B.3 of *Eurocode 3 Part 1-1*.

Moment diagram	Range		C_{my}, C_{mz} and C_{mLT}	
			Uniform loading	Concentrated load
	$-1 \le \psi \le 1$		$0.6 + 0.4\psi \ge 0.4$	
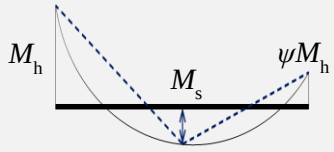 $\alpha_s = M_s/M_h$	$0 \le \alpha_s \le 1$	$-1 \le \psi \le 1$	$0.2 + 0.8\alpha_s \ge 0.4$	
	$-1 \le \alpha_s < 0$	$0 \le \psi \le 1$	$0.1 - 0.8\alpha_s \ge 0.4$	$-0.8\alpha_s \ge 0.4$
		$-1 \le \psi < 0$	$0.1(1-\psi) - 0.8\alpha_s \ge 0.4$	$0.2(-\psi) - 0.8\alpha_s \ge 0.4$
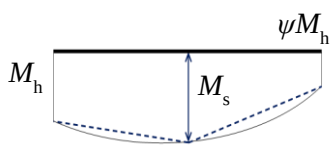 $\alpha_s = M_h/M_s$	$0 \le \alpha_h \le 1$	$-1 \le \psi \le 1$	$0.95 + 0.05\alpha_h$	$0.9 + 0.1\alpha_h$
		$0 \le \psi \le 1$		
	$-1 \le \alpha_h < 0$	$-1 \le \psi < 0$	$0.95 + 0.05\alpha_h(1+2\psi)$	$0.9 + 0.1\alpha_h(1+2\psi)$

Table IV-9: Equivalent uniform moment factors according to Annex B of Eurocode 3 Part 1-1

IV.2.3.2. General Method

Design method

The design resistance of a uniform steel member subjected to compression force and/or bending moment about the *y*-axis can be determined using §6.3.1 to §6.3.3 of *Eurocode 3 Part 1-1*. To minimize the amount of steel in a building, tapered members, mainly built-up, are commonly used and can be designed using the *General Method* from §6.3.4 of *EN 1993-1-1*. Bases of this design method can be found within the work of *Müller* (2003).

The *General Method* can be applied on isolated structural components with doubly or mono-symmetrical cross-sections, built-up or not, uniform or not, with complex support conditions or not, or plane frames or subframes composed of such members. The overall out-of-plane stability of such components is satisfied provided that clause (6.63) is verified:

$$\frac{\chi_{op}\alpha_{ult,k}}{\gamma_{M1}} \ge 1.0 \qquad \text{(IV.22)}$$

where $\alpha_{ult,k}$ is the minimum amplifier of the design loads to reach the characteristic resistance of the most critical cross-section of the component. Flexural and lateral-torsional buckling are not taken into account but the in-plane behaviour of the component (global and local in-plane geometrical deformation and imperfections) is considered. Besides, χ_{op} is the reduction factor for the normalized slenderness $\bar{\lambda}_{op}$ that accounts for lateral and lateral-torsional buckling:

$$\bar{\lambda}_{op} = \sqrt{\frac{\alpha_{ult,k}}{\alpha_{cr,op}}} \qquad \text{(IV.23)}$$

where $\alpha_{cr,op}$ is the minimum amplifier for the in-plane design load to reach the elastic critical resistance of the component accounting for lateral and lateral-torsional buckling without considering in-plane flexural buckling.

According to *Eurocode3 Part 1-1*, the reduction factor can be conveniently determined considering either the minimum value between χ_z and χ_{LT}, each calculated for the normalized slenderness $\bar{\lambda}_{op}$, or an interpolated value between both reduction factors. Using the interpolation option, which will no longer be permitted in *prEN 1993*, rewrites expression (IV.22) as:

$$\frac{N_{Ed}}{\frac{\chi_z N_{Rk}}{\gamma_{M1}}} + \frac{M_{y,Ed}}{\frac{\chi_{LT} M_{y,Rk}}{\gamma_{M1}}} \leq 1.0 \qquad \text{(IV.24)}$$

where the reduction factors are determined for the slenderness $\bar{\lambda}_{op}$, and the design loads account for in-plane global and local geometrical deformation and imperfections.

Discussion

Using the *General Method* on tapered members raises some difficulties. For such structural components, determining the ultimate load amplifier $\alpha_{ult,k}$ is not direct, but a simplified method has been presented by *Bureau* (2007). The analytical determination of the critical load amplifier $\alpha_{cr,op}$ is also a challenging step, but the software *LTBeamN* that uses beam finite elements may provide some help.

The reliability of the *General Method* has been extensively discussed in the past. *Taras* (2010a) has shown for uniform hot-rolled members that using the minimum value between the two reduction factors could lead to over-conservative results while using the interpolation alternative could result in unsafe estimates of the buckling resistance for low slenderness. However, studying the accuracy of the *General Method* on uniform hot-rolled IPE or HE-section beam-columns, *Hadjú* (2018, 2022) concluded that the use of the interpolation alternative is suitable, the maximum deviation on the unsafe side being 5%. Again, it was demonstrated that the minimum reduction factor could reveal overly-conservative.

The treatment of hot-rolled or welded uniform members has also been investigated by *Simões da Silva* (2010). It was concluded that determining the reduction factor using the interpolation option leads to more accurate results than using the minimum value of the reduction factors, which can turn out to be overly conservative. The *General Method* applied to tapered members has been studied by *Marques* (2012a), particularly for hot-rolled sections. The design method could be unsafe even when the reduction factor was the minimum reduction factor. This result is obtained considering different positions of the critical cross-section for compression and bending, one related to N_{Ed} and the other related to $M_{y,Ed}$.

As pointed out in the previously cited references, the lack of mechanical background of the *General Method* results in some inconsistencies. While using the *General Method* for a uniform member subjected to bending leads to the same clause as expression (IV.5), when designing the same member but compressed according to the *General Method* yields:

$$\frac{N_{Ed}}{N_{b,Rd}} \leq 1.0 \qquad \text{(IV.25)}$$

$$N_{b,Rd} = \chi_y \chi_z \frac{N_{Rk}}{\gamma_{M1}} \quad \text{(IV.26)}$$

In expression (IV.25), the reduction factor χ_z is determined from the normalized slenderness $\bar{\lambda}_{op}$ that accounts for in-plane effects:

$$\bar{\lambda}_{op} = \sqrt{\chi_y \frac{N_{Rk}}{N_{cr,z}}} \quad \text{(IV.27)}$$

The reduction factor χ_y being lower than or equal to unity, $\bar{\lambda}_{op}$ is lower than or equal to $\bar{\lambda}_z$. Due to a lack of consistency, *prEN 1993-1-1* will impose to determine the reduction factor as the minimum value between χ_z and χ_{LT}, which can result in very safe results as shown in the past (*Taras* (2010a)); (*Simões da Silva* (2010)). The stability of a structural component according to the *General Method* imposes a coupling between in-plane effects and out-of-plane buckling while the interaction formulae detailed in §IV.2.3.1 propose separate verifications for out-of-plane and in-plane stabilities. The latter approach could be sought to improve the consistency of the *General Method*.

The current and future design verification formats for the global buckling of compressed and/or bent steel members having been detailed, the previous French rules are depicted next section before investigating the recent developments on non-uniform members.

IV.3 Former French standards

IV.3.1 Members in compression

In the previous French *CM66*, the verification formats involved stresses because the cross-section resistance of a member was based on its elastic capacity. According to §3,41 of the former code, the stability of a compressed member subjected to the design stress $\sigma_{N,Ed}$ had to satisfy:

$$k\sigma_{N,Ed} \leq f_y \quad \text{(IV.28)}$$

$$k = \left[0.5 + 0.65\bar{\lambda}^2_{i,CM}\right] + \sqrt{\left[0.5 + 0.65\bar{\lambda}^2_{i,CM}\right]^2 - \bar{\lambda}^2_{i,CM}} \quad \text{(IV.29)}$$

with:

$\bar{\lambda}_{i,CM} = \sqrt{f_y / \sigma_{cr,i}}$, the critical stress $\sigma_{cr,i}$ corresponding to the axial critical load $N_{cr,i}$.

The buckling coefficient k can be seen as the inverse of the reduction factor χ_z, leading to major differences between both standards regarding the imperfection term η_i:

$$\eta_{i,EC3} = \alpha_i\left(\bar{\lambda}_i - 0.2\right) \quad \text{(IV.30)}$$

$$\eta_{\text{i,CM66}} = 0.15\bar{\lambda}_{\text{i, CM}}^{2} \tag{IV.31}$$

The former *CM66* standard proposed a single buckling curve that is compared to the five buckling curves form *Eurocode 3 Part 1-1* in Figure IV-4. It is worth mentioning that the *Additif 80* proposed a design method for compressed members using buckling curves *a*, *b* and *c* from *Eurocode 3*. Figure IV-4 shows that the buckling curve from *CM66* provides, for usual slenderness, an equal or higher resistance than buckling curves *c* and *d* that must be used for the lateral buckling of welded members in *Eurocode 3 Part 1-1*.

However, as the normalized slenderness increases, the buckling curves from both standards do not tend towards the same asymptote, (see *Villette* (2014)). Indeed, as the normalized slenderness goes to infinity, the *Eurocode 3* design rules yield:

$$\chi_{\text{i, EC3}} \to \frac{1}{\bar{\lambda}_{\text{i}}^{2}} \tag{IV.32}$$

while the *CM66* standard yielded:

$$\chi_{\text{i, CM}} = \frac{1}{k} \to \frac{1}{1.3\bar{\lambda}_{\text{i}}^{2}} \tag{IV.33}$$

Because members with a very high slenderness (i.e. > 2.5) are barely found in practice, the former *CM66* standard resulted in higher buckling resistances than the *Eurocode 3* rules for welded columns.

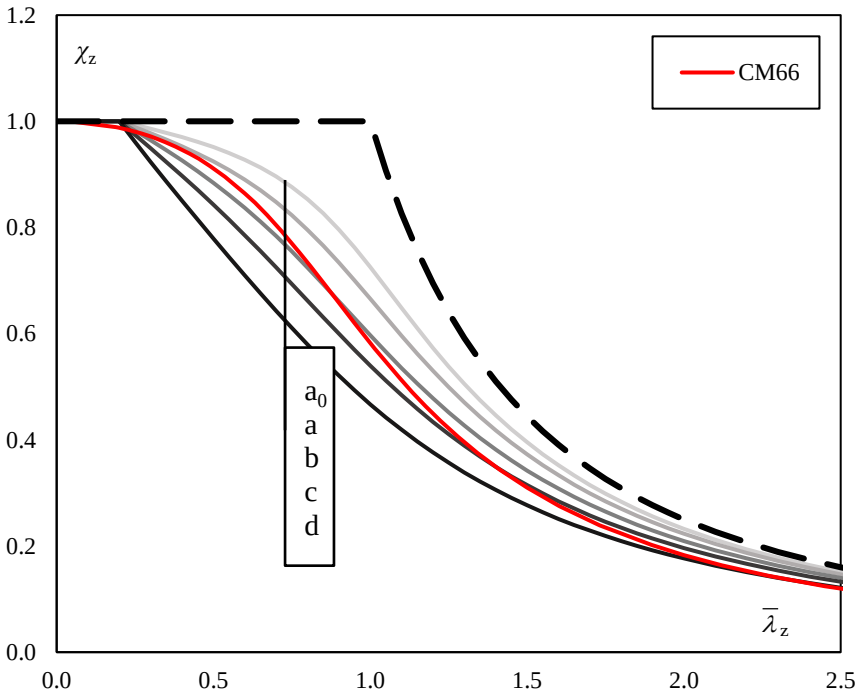

Figure IV-4: Buckling curves form CM66 *and* Eurocode 3 Part 1-1

IV.3.2 Members in bending

The stability of a member in bending was analyzed in *CM66* using §3,61 as the lateral buckling of the compressed flange. A beam subjected to the design stress $\sigma_{M,y,Ed}$ resulting from symmetrical loading and boundary conditions had to satisfy:

$$k_d \sigma_{M,y,Ed} \leq f_y \tag{IV.34}$$

$$k_d = \frac{k_0}{1 + \frac{\sigma_d}{f_y}(k_0 - 1)} \tag{IV.35}$$

where k_0 is the lateral buckling coefficient determined applying expression (IV.29) using the slenderness:

$$\lambda_0 = \sqrt{\frac{L^2}{CB}\frac{I_y}{I_w}\left(1 - \frac{\sigma_d}{f_y}\right)} \tag{IV.36}$$

and the "no lateral-torsional buckling" stress σ_d is given by:

$$\sigma_d = CB\frac{2.6h}{I_y}\frac{\pi^2 E I_z}{L^2}\left[\sqrt{\frac{I_w}{I_z} + \frac{G I_t L^2}{E I_z \pi^2}} - \frac{h}{2}\right] \tag{IV.37}$$

where C depends on the bending moment distribution and B on the bending moment distribution and the vertical position of a transverse load, similarly to C_1 and $C_2 z_g$ in the expression of M_{cr}.

For a beam subjected to end moments, the lateral-torsional buckling coefficient k_d is given by:

$$k_d = \frac{k_{d0}}{C} + \frac{C - 1}{5 k_{d0}} \geq 1 \tag{IV.38}$$

where k_{d0} is the buckling coefficient k_d for the same member subjected to a uniform bending moment distribution.

The buckling curves are different for every cross-section dimensions and bending moment distribution according to the *CM66* rules. They are compared against the *Eurocode 3* buckling curves for a beam having a specific cross-section that consists in a 800×10 web and 200×20 flanges and subjected to a linear bending moment distribution (with ψ = 1, 0, -1). The curves are presented in Figure IV-5 with those obtained using the new verification format from *prEN 1993-1-1* for the same member subjected to the same load cases. The design method proposed in *Additif 80* for bent member makes use of buckling curves *a*, *b* and *c* from *Eurocode 3*.

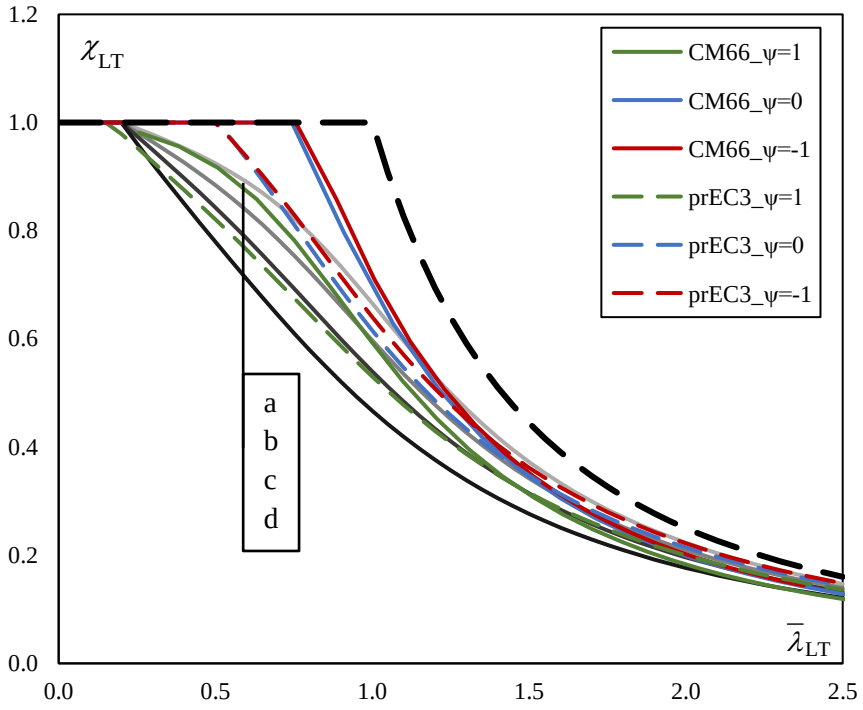

Figure IV-5: Lateral-torsional buckling curves from CM66 *and* Eurocode 3 Part 1-1

In the common case of a beam having a Class 3 cross-section in bending, Figure IV-5 shows that the *CM66* buckling curve for the constant bending moment distribution is very close to that for flexural buckling prescribed by the same code (see Figure IV-4). Such buckling curve lies significantly above *Eurocode 3* buckling curves *c* and *d*, particularly for low and medium slenderness.

The curves from *CM66* when ψ = 0, -1, which are similar, exhibit a large plateau length that ends for a slenderness close to 0.75, and decreases down to curve *b* in the worst case for a slenderness up to 2. Obviously, the buckling resistance obtained using the *CM66* rules is considerably greater than that determined using the *General case* from *Eurocode 3* in the most common slenderness range (0.5 to 1.2).

Similarly to the case of columns, it is worth mentioning that the *CM66* buckling curves remain distant from the *Euler* curve for very high slenderness, the buckling curves asymptote depending on the bending moment distribution.

According to the new verification method, the buckling curve obtained for a constant bending moment distribution lays between buckling curves *c* and *d*. For ψ = 0 or -1, both curves are very close and present a plastic plateau up to a normalized slenderness close to 0.5 then decrease down to curve *b* for medium-to-high slenderness.

IV.3.3 Members in bending and compression

In the former French code, the stability of a member subjected the design stresses $\sigma_{N,Ed}$, $\sigma_{M,y,Ed}$ and $\sigma_{M,z,Ed}$ due to compression and bending about *y* and *z*-axis respectively, had to be verified both in-plane and out-of-plane, similarly to *Eurocode 3* interaction formulae:

$$k_{1y}\sigma_{N,Ed} + k_{fy}k_{d}\sigma_{M,y,Ed} + k_{fz}\sigma_{M,z,Ed} \leq f_{y} \qquad \text{(IV.39)}$$

$$k_{1z}\sigma_{N,Ed} + k_{fy}k_d\sigma_{M,y,Ed} + k_{fz}\sigma_{M,z,Ed} \leq f_y \quad \text{(IV.40)}$$

Where k_{fy} and k_{fz}, both greater than unity, depend on the bending moment diagram about *y* and *z*-axis respectively and the flexural buckling coefficient k_{li}, lower than *k* is given by:

$$k_{1z} = \frac{\sigma_{cr,i} - \sigma_{N,Ed}}{\sigma_{cr,i} - 1.3\sigma_{N,Ed}} \quad \text{(IV.41)}$$

The design rules for members subjected to compression or/and bending according to the current and future *Eurocode 3 Part 1-1* and according to the former French *CM66* and *Additif 80* have been depicted. The buckling curves from *CM66* were significantly more favourable than those from the current *Eurocode 3*, especially for beams subjected to a linear bending moment distribution. The new verification format in *prEurocode 3* will increase the lateral-torsional buckling resistance of welded beams when compared to the *General case*.

For non-uniform members, the single *General Method* applies according to *EN 1993-1-1* but presents some inconsistencies, leading many researchers to develop new analytical methods that are described next section.

IV.4 Recent developments on non-uniform members

IV.4.1 Introduction

While the design rules for the stability verification of prismatic members given in *Eurocode 3 Part 1-1* are easy to use, the same cannot be said for tapered members for which only the *General Method* applies. The lack of mechanical background and accuracy of the *General Method* has encouraged many researchers in the recent years to pursue an accurate and safe method to evaluate the resistance to out-of-plane buckling of a non-prismatic column, beam, or beam-column.

An extensive work conducted at RWTH Aachen and TU Delft led *Naumes* (2008 and 2009), *Feldmann* (2009) and *Bijlaard* (2010) to develop new methods for prismatic members or not, adapted from *Eurocode 3*. Their propositions include a different value of the imperfection factor for lateral-torsional buckling α_{LT} based on the torsional properties of the design cross-section. Based on these studies, *Wieschollek* (2012) proposed alternative expressions of the second order analyses proposed *in Eurocode 3 Part 1-1*, applicable to non-prismatic members provided that the elastic buckling mode shape is known.

Kim (2010) proposed to evaluate the lateral-torsional buckling of a non-uniform beam according to *AISC* rules considering an equivalent prismatic beam with the same elastic critical bending moment and a different length. Similarly, *Badari* (2015) exposed a new method to estimate the resistance against lateral-torsional buckling of a non-prismatic member by dividing the beam into a sufficient number of segments. Each segment is separately considered as an equivalent uniform beam with the same slenderness as the tapered segment. The imperfection factor determined for each segment is modified to account for the relative importance of its displacements in the elastic buckling mode.

In Coimbra, modifications of the current *Eurocode 3* were proposed by *Marques* (2012a/b, 2013 and 2014) to assess the stability of tapered members subjected to compression force and/or bending moment.

The interaction formulae along with Annex B have been modified to apply to non-uniform members. Later, *Tankova* (2018a and 2018b) developed a general formulation standing out from the *Eurocode 3 Part 1-1* design rules. Previous developments yielded a design method to assess the overall out-of-plane stability of uniform members (*Tankova* (2017)). Non-prismatic members come within the scope of the proposed method, derived from second order analyses using the work of *Szalai* (2010) considering equivalent uniform members.

More recently, numerical solutions have been used to evaluate the buckling resistance of a non-uniform member. *Kucukler* (2019) and *White* (2020) have developed a stiffness reduction method that consists in performing Linear Bifurcation Analyses (*LBA*) on a Finite Element Model (*FEM*) with beam elements. Steel material law has to be implemented to each element with a reduction factor – depending on the boundary conditions and the bending moment distribution – to minimize the Young's and shear moduli E and G. It can be noted that analytical expressions were developed by *Chiorean* (2020) based on a stiffness matrix adaptation to be used with MatLab to evaluate the elastic critical amplifier of a beam-column, tapered or not. The software *LTBeamN* performs the same numerical calculations (*Beyer* (2015a/b)).

In the following sections, the most refined methods, proposed by *Naumes* (2008 and 2009), *Feldmann* (2009) and *Bijlaard* (2010); by *Marques* (2012a, 2012b, 2013 and 2014); and by *Tankova* (2018a and 2018b) are detailed.

IV.4.2 Members in compression

The verification format of a non-uniform compressed column (see Figure IV-6) against flexural buckling is:

$$\varepsilon(x) = \frac{N_{\mathrm{Ed}}}{N_{\mathrm{Rk}}}(x) + \frac{M_{\mathrm{i,Ed}}^{\mathrm{II}}}{M_{\mathrm{i,Rk}}}(x) \leq 1.0 \tag{IV.42}$$

The utilization ratio ε depends on the applied axial force N_{Ed} provoking a second order bending moment $M_{\mathrm{i,Ed}}^{\mathrm{II}}$. The second order bending moment depends on the second derivative of the deflection δ:

$$M_{\mathrm{i,Ed}}^{\mathrm{II}}(x) = -EI_{\mathrm{i}}\frac{d^2\delta}{dx^2}(x) \tag{IV.43}$$

The deflection δ due to buckling can be determined from the initial imperfection δ_0 which can be assumed to have the same shape as the buckling mode δ_{cr}. The amplification relationship expressed by *Marques* (2012a) and *Tankova* (2018a) is:

$$\frac{d^2\delta}{dx^2}(x) = \frac{1}{\alpha_{\mathrm{cr}} - 1}\frac{d^2\delta_0}{dx^2}(x) = \frac{1}{\alpha_{\mathrm{cr}} - 1}e_0\frac{d^2\delta_{\mathrm{cr}}}{dx^2}(x) \tag{IV.44}$$

Using the previous equation and the common assumption that:

$$e_0\frac{N_{\mathrm{Rk}}(x_{\mathrm{c}}^{\mathrm{II}})}{M_{\mathrm{y,Rk}}(x_{\mathrm{c}}^{\mathrm{II}})} = \alpha(x_{\mathrm{c}}^{\mathrm{II}})\left(\bar{\lambda}(x_{\mathrm{c}}^{\mathrm{II}}) - 0.2\right) \tag{IV.45}$$

Marques (2012a) rewrites expression (IV.42) at the second order failure location x_c^{II} where the utilization ratio equals to unity, proposing the verification format:

$$\chi(x_c^{II}) + \frac{\chi(x_c^{II})}{1-\chi(x_c^{II})\bar{\lambda}^2(x_c^{II})}\alpha(x_c^{II})\left(\bar{\lambda}(x_c^{II})-0.2\right)\beta(x_c^{II}) = 1.0 \qquad \text{(IV.46)}$$

with:

$$\beta(x_c^{II}) = \frac{EI_i(x_c^{II})\left|\frac{d^2\delta_{cr}}{dx^2}(x_c^{II})\right|}{\alpha_{cr}N_{Ed}(x_c^{II})}$$

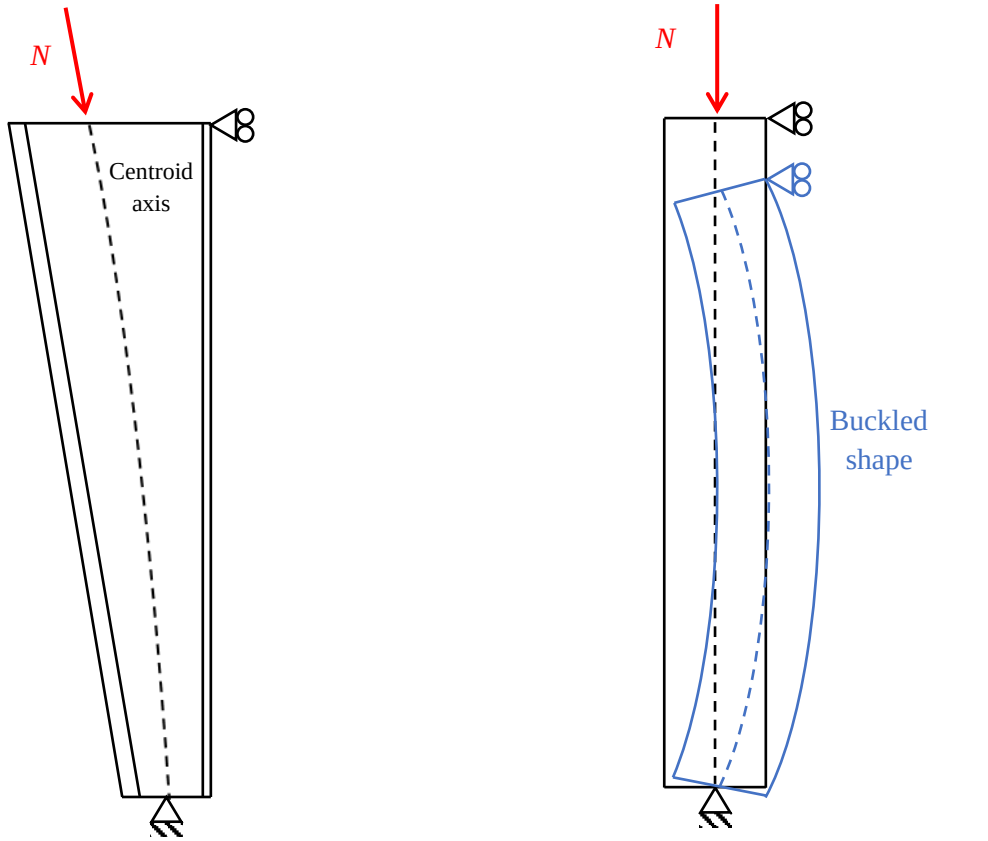

a) *Centrally loaded column* b) *Column undergoing flexural buckling*

Figure IV-6: Non-uniform member in compression

A parametric study was performed by *Marques* (2012a) resulting in guiding expressions for of x_c^{II} and $\beta(x_c^{II})$. They depend on the first order x_c^{I} the failure location and geometrical properties of the column. A further simplification is proposed replacing $\beta(x_c^{II})$ by its maximum value of 1.0 with some guidance to determine the corresponding limit failure location $x_{c,lim}^{II}$.

An alternative form of equation (IV.46) is then proposed to get the design method closer to *Eurocode 3 Part 1-1*. This alternative consists in the evaluation of the reduction factor at the location x_c^{I} using an « over-strength » factor φ that depends on the dimensions of the smallest and largest cross-sections:

$$\chi_{\mathrm{i}} = \frac{\varphi}{\phi_{\mathrm{i}} + \sqrt{\phi_{\mathrm{i}}^2 - \varphi \bar{\lambda}_{\mathrm{i}}^2\left(x_{\mathrm{c}}^{\mathrm{I}}\right)}} \leq 1.0 \tag{IV.47}$$

$$\phi_{\mathrm{i}} = 0.5\left[1 + \alpha_{\mathrm{i}}\left(\bar{\lambda}_{\mathrm{i}}\left(x_{\mathrm{c}}^{\mathrm{I}}\right) - 0.2\right) + \varphi \bar{\lambda}_{\mathrm{i}}^2\left(x_{\mathrm{c}}^{\mathrm{I}}\right)\right] \tag{IV.48}$$

The ease of use of the design method proposed by *Marques* (2012a) relies on a strong mechanical background and an extensive parametric study.

Some of those derivations were performed by *Naumes* (2009) who proposed to check the stability of a compressed member using §6.3.1 of *Eurocode 3 Part 1-1* (see equations (IV.1) and (IV.3)) at the failure location $x_{\mathrm{c}}^{\mathrm{II}}$. No direct expression is given to evaluate $x_{\mathrm{c}}^{\mathrm{II}}$ which must be evaluated performing a series of iteration using:

$$\chi(x) + \frac{\chi(x)}{1 - \chi(x)\bar{\lambda}^2(x)} \alpha\left(\bar{\lambda}(x) - 0.2\right)\left[\frac{EI_{\mathrm{i}}(x)}{EI_{\mathrm{i}}(x_{\mathrm{c}}^{\mathrm{II}})} \frac{N_{\mathrm{Rk}}(x) M_{\mathrm{i,Rk}}(x_{\mathrm{c}}^{\mathrm{II}})}{N_{\mathrm{Rk}}(x_{\mathrm{c}}^{\mathrm{II}}) M_{\mathrm{i,Rk}}(x)} \frac{\delta_{\mathrm{cr}}^{\mathrm{II}}(x)}{\delta_{\mathrm{cr}}^{\mathrm{II}}(x_{\mathrm{c}}^{\mathrm{II}})}\right] = 1.0 \tag{IV.49}$$

An alternative verification format, similar to expression (IV.47), is also proposed but *Naumes* (2009) provides no guidance to evaluate the buckling shape and the over-strength ratio making this design method tricky to apply.

Along with expressions (IV.43) and (IV.44), the second order bending moment is analyzed by *Tankova* (2018a) as a result of the applied axial load on an equivalent uniform member:

$$M_{\mathrm{i,Ed}}^{\mathrm{II}}(x_{\mathrm{c}}^{\mathrm{II}}) = N_{\mathrm{Ed,max}}\left(\delta + \delta_0\right) = \frac{N_{\mathrm{Ed,max}}}{1 - 1/\alpha_{\mathrm{cr}}} e_0 \tag{IV.50}$$

Equating expressions (IV.43) with (IV.44) related to the real member to (IV.50) associated with the equivalent uniform member leads to the amplitude of the imperfection:

$$\delta_0 = \frac{\alpha_{\mathrm{cr}} N_{\mathrm{Ed,max}}}{EI_{\mathrm{i}}(x_{\mathrm{c}}^{\mathrm{II}})\left|\frac{d^2\delta_{\mathrm{cr}}}{dx^2}(x_{\mathrm{c}}^{\mathrm{II}})\right|} e_0 \tag{IV.51}$$

The utilization ratio can then be rewritten considering the second order bending moment given by equation (IV.43) where the deflection is considered similar to the elastic buckling shape with an amplitude given by expression (IV.51), leading to the equivalent imperfection factor:

$$e_0 \frac{N_{\mathrm{Rk}}(x)}{M_{\mathrm{y,Rk}}(x)} = \alpha(x)\left(\bar{\lambda}(x) - 0.2\right)\delta_{\mathrm{cr}} \tag{IV.52}$$

The maximum value of the displacement shape being equal to unity, expressions (IV.45) and (IV.52) are identical when calculating at the position $x_{\mathrm{c}}^{\mathrm{II}}$ where the deflection reaches its maximum. The buckling resistance of a compressed member is obtained when:

$$\chi(x)+\frac{\chi(x)}{1-\chi(x)\bar{\lambda}^{2}(x)}\alpha\left(\bar{\lambda}(x)-0.2\right)\left[\frac{EI_{\mathrm{i}}(x)}{EI_{\mathrm{i}}(x_{\mathrm{c}}^{\mathrm{II}})}\frac{N_{\mathrm{Ed,max}}}{N_{\mathrm{Ed}}(x_{\mathrm{c}}^{\mathrm{II}})}\left|\frac{\frac{d^{2}\delta_{\mathrm{cr}}}{dx^{2}}(x)\delta_{\mathrm{cr}}(x)}{\frac{d^{2}\delta_{\mathrm{cr}}}{dx^{2}}(x_{\mathrm{c}}^{\mathrm{II}})}\right|\right]=1.0 \qquad \text{(IV.53)}$$

The method developed by *Tankova* (2018a) relies on a consistent theoretical background that requires the determination of the second derivative of the elastic buckling shape, which can be an obstacle for a daily use. Some help may be found using software packages like *LTBeamN* to compute the elastic critical mode shape and its first derivative.

IV.4.3 Members in bending

The verification format of a beam bent about the major axis (see Figure IV-7) is:

$$\varepsilon(x)=\frac{M_{\mathrm{y,Ed}}}{M_{\mathrm{y,Rk}}}(x)+\frac{M_{\mathrm{z,Ed}}^{\mathrm{II}}}{M_{\mathrm{z,Rk}}}(x)+\frac{B_{\mathrm{Ed}}^{\mathrm{II}}}{B_{\mathrm{Rk}}}(x)\le 1.0 \qquad \text{(IV.54)}$$

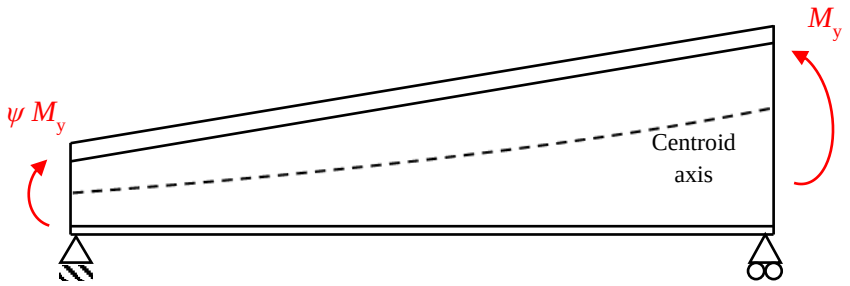

a) *Initial configuration*

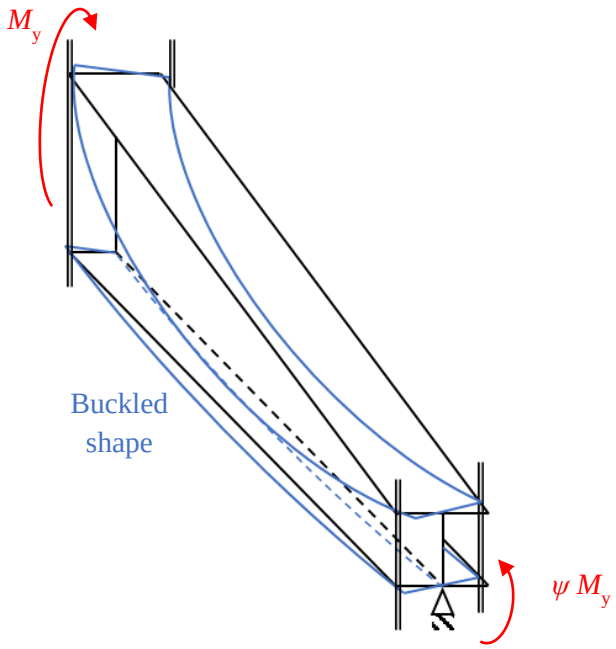

b) *Beam undergoing lateral-torsional buckling*

Figure IV-7: Non-uniform member in bending about the major axis

Marques (2012a) proposed to assume that the relationship between the magnitudes of the torsional rotation θ and the out-of-plane displacement v is similar for prismatic and non-prismatic beams, which is for a tapered beam under uniform bending moment:

$$\frac{\bar{v}}{\bar{\theta}} = \frac{M_{\text{y,cr,tap}}}{N_{\text{cr,z,tap}}} \tag{IV.55}$$

Similarly to expression (IV.44), amplification relationships are given considering the coupling between the magnitudes by:

$$\theta^{\text{II}}(x) = \frac{M_{\text{y,Ed}}}{M_{\text{y,cr,tap}} - M_{\text{y,Ed}}} \theta_0^{\text{II}}(x) \tag{IV.56}$$

$$v^{\text{II}}(x) = \frac{M_{\text{y,Ed}}}{M_{\text{y,cr,tap}} - M_{\text{y,Ed}}} \frac{M_{\text{y,cr,tap}}}{N_{\text{cr,z,tap}}} \theta_0^{\text{II}}(x) \tag{IV.57}$$

The second order contributions are given by:

$$M_{\text{z,Ed}}^{\text{II}}(x) = -EI_{\text{z}} \frac{d^2 v}{dx^2}(x) \tag{IV.58}$$

$$B_{\text{Ed}}^{\text{II}}(x) = -EI_{\text{w}} \frac{d^2 \theta}{dx^2}(x) \tag{IV.59}$$

The initial imperfection proposed by *Marques* (2012a) is weighted to account for the variation of the cross-section:

$$\frac{d^2 \theta_0}{dx^2}(x) = \frac{e_0 \delta_{\text{cr,h,min}}}{\frac{M_{\text{y,cr,tap}}}{N_{\text{cr,z,tap}}} + \frac{h_{\text{min}}}{2}} \frac{d^2 \delta_{\text{cr,h,min}}}{dx^2}(x) \tag{IV.60}$$

Where $\delta_{\text{cr,h,min}}$ is the magnitude of the lateral displacement measured at the height of the compressed flange from the smallest cross-section in the critical mode.

After some algebraic manipulations, *Marques* (2012a) proposed to determine the buckling resistance of a tapered beam equating to unity the utilization ratio at the failure location x_{c}^{II}:

$$\chi_{\text{LT}}(x_{\text{c}}^{\text{II}}) + \frac{\chi_{\text{LT}}(x_{\text{c}}^{\text{II}}) \alpha_{\text{LT}} \left(\bar{\lambda}_{\text{z}}(x_{\text{c}}^{\text{II}}) - 0.2 \right)}{1 - \chi_{\text{LT}}(x_{\text{c}}^{\text{II}}) \bar{\lambda}_{\text{LT}}^2(x_{\text{c}}^{\text{II}})} \left(\frac{\bar{\lambda}_{\text{LT}}(x_{\text{c}}^{\text{II}})}{\bar{\lambda}_{\text{z}}(x_{\text{c}}^{\text{II}})} \right)^2 \beta(x_{\text{c}}^{\text{II}}) = 1.0 \tag{IV.61}$$

with:

$$\beta(x_c^{II}) = \frac{EI_z(x_c^{II})\left|\frac{d^2\delta_{cr,h,min}}{dx^2}(x_c^{II})\right|\delta_{cr,h,min}\,1+\frac{N_{cr,z,tap}}{M_{y,cr,tap}}\frac{h(x_c^{II})}{2}}{N_{cr,z,tap}\;\;1+\frac{N_{cr,z,tap}}{M_{y,cr,tap}}\frac{h_{min}}{2}}$$

Again, an alternative method was developed to simplify its use and consists in the verification of the utilization ratio at the first order failure position x_c^I using an over-strength ratio φ and the limit failure position $x_{c,lim}^{II}$:

$$\frac{\chi_{LT}(x_c^I)}{\varphi}+\frac{\chi_{LT}(x_c^I)/\varphi}{1-\varphi\bar{\lambda}_{LT}^{-2}(x_c^{II})\chi_{LT}(x_c^I)/\varphi}\alpha_{LT}\varphi\left(\frac{\bar{\lambda}_{LT}(x_c^I)}{\bar{\lambda}_z(x_{c,lim}^{II})}\right)^2\left(\bar{\lambda}_z(x_{c,lim}^{II})-0.2\right)=1.0 \qquad \text{(IV.62)}$$

An extensive parametric study led by *Marques* (2012a) has resulted in expressions to determine the limit failure location and the over-strength ratio that depend on the geometrical properties of the smallest and largest cross-sections and on the bending moment distribution. This simplified alternative is easy to use provided that the beam is subjected to a bending moment distribution treated during the parametric study: a linear distribution of the bending moment or a uniformly distributed load.

Tankova (2018a) proposed a general formulation for the stability of a tapered beam using expression (IV.58) for the second order bending moment about the *z*-axis and an expression of the second order bimoment accounting for the inclination of the flanges, as developed by *Kitipornchai* (1975):

$$B_{Ed}^{II}(x) = -EI_w(x)\left(\frac{d^2\theta}{dx^2}(x)+\frac{2}{h}\frac{d\theta}{dx}(x)\frac{d\theta}{dx}(x)\right) \qquad \text{(IV.63)}$$

The second order out-of-plane bending moment and bimoment were also studied considering the applied bending moment on an equivalent prismatic member having the cross-section of the real member at the location x_c^{II}. Amplification relationships are used to express the torsional rotation and out-of-plane displacement of the equivalent uniform member:

$$M_{z,Ed}^{II}(x_c^{II}) = M_{y,Ed}(\theta+\theta_0) = \frac{e_0 M_{y,Ed}}{1-1/\alpha_{cr}}\theta_{cr}(x_c^{II}) \qquad \text{(IV.64)}$$

$$B_{Ed}^{II}(x_c^{II}) = M_{y,Ed}(v+v_0) - GI_t = \frac{e_0 M_{y,Ed}}{1-1/\alpha_{cr}}\theta_{cr}(x_c^{II})\left[\frac{v_0}{\theta_0}-\frac{GI_t}{M_{y,cr}}\right] \qquad \text{(IV.65)}$$

Equating the second order forces for the equivalent uniform member and the real beam at the failure location x_c^{II}, the amplitude of the imperfection arises:

$$\delta_0 = \frac{1}{EI_z(x_c^{II})}\frac{e_0 N_{cr,z}}{\frac{d^2 v_{cr}}{dx^2}(x_c^{II})+\frac{h}{2}\frac{d^2\theta_{cr}}{dx^2}(x_c^{II})+\frac{d\theta_{cr}}{dx}(x_c^{II})\frac{dh}{dx}(x_c^{II})} \qquad \text{(IV.66)}$$

The imperfections associated with the lateral displacement and the torsional rotation are assumed to have the same amplitude δ_0 and shapes similar to that of the critical buckling mode.

The utilization ratio is rewritten considering the second order forces given by expressions (IV.58) and (IV.63) assuming that the equivalent geometrical imperfection factor is:

$$e_0 \frac{N_{\mathrm{Rk}}(x)}{M_{\mathrm{y,Rk}}(x)} = \alpha_{\mathrm{LT}}(x)\left(\bar{\lambda}_{\mathrm{z}}(x) - 0.2\right)\left|\delta_{\mathrm{cr}}^{\mathrm{fl}}(x)\right| \tag{IV.67}$$

The verification format proposed by *Tankova* (2018a) is then:

$$\chi_{\mathrm{LT}}(x) + \frac{\chi_{\mathrm{LT}}(x)}{1 - \chi_{\mathrm{LT}}(x)\bar{\lambda}_{\mathrm{LT}}^2(x)} \alpha_{\mathrm{LT}} \left(\frac{\bar{\lambda}_{\mathrm{LT}}(x)}{\bar{\lambda}_{\mathrm{z,eq}}(x)} \right)^2 \left(\bar{\lambda}_{\mathrm{z,eq}}(x) - 0.2\right) f = 1.0 \tag{IV.68}$$

with:

$$f = \frac{EI_{\mathrm{z}}(x)}{EI_{\mathrm{z}}(x_{\mathrm{c}}^{\mathrm{II}})} \frac{\dfrac{d^2 v_{\mathrm{cr}}}{dx^2} + \dfrac{h}{2}\dfrac{d^2\theta_{\mathrm{cr}}}{dx^2}(x) + \dfrac{d\theta_{\mathrm{cr}}}{dx}(x)\dfrac{dh}{dx}(x)}{\dfrac{d^2 v_{\mathrm{cr}}}{dx^2} + \dfrac{h}{2}\dfrac{d^2\theta_{\mathrm{cr}}}{dx^2}(x_{\mathrm{c}}^{\mathrm{II}}) + \dfrac{d\theta_{\mathrm{cr}}}{dx}(x_{\mathrm{c}}^{\mathrm{II}})\dfrac{dh}{dx}(x_{\mathrm{c}}^{\mathrm{II}})} \left| v_{\mathrm{cr}}(x) + \frac{h}{2}\theta_{\mathrm{cr}}(x) \right|$$

where the equivalent normalized slenderness $\bar{\lambda}_{\mathrm{z,eq}}(x)$ is given by:

$$\bar{\lambda}_{\mathrm{z,eq}}(x) = \sqrt{\frac{N_{\mathrm{Rk}}(x)}{EI_{\mathrm{z}}(x_{\mathrm{c}}^{\mathrm{II}}) \dfrac{\left|\dfrac{d^2 v_{\mathrm{cr}}}{dx^2}(x_{\mathrm{c}}^{\mathrm{II}})\right|}{\left|v_{\mathrm{cr}}(x_{\mathrm{c}}^{\mathrm{II}})\right|}}} \tag{IV.69}$$

Similarly to the flexural buckling case, the general formulation proposed by *Tankova* (2018a) to assess the stability of a tapered beam relies on an important mechanical background and can be applied whatever the boundary conditions and bending moment distribution. However, this method is hardly applicable in design offices since it requires to know the second derivative of the buckling mode shape though existing programs like *LTBeamN* already provide the mode shape and its first derivative.

The method developed by *Naumes* (2009) is based on the modification of the imperfection factor α_{LT} in the *General* and *Special cases* (see §IV.2.2.2 and §IV.2.2.3). The verification format was studied as the lateral buckling of the compressed flange, leading to the following utilization ratio:

$$\varepsilon(x) = \frac{N_{\mathrm{Ed,Fl}}}{N_{\mathrm{Rk,Fl}}}(x) + \frac{M_{\mathrm{z,Ed,Fl}}^{\mathrm{II}}}{M_{\mathrm{z,Rk,Fl}}}(x) = 1.0 \tag{IV.70}$$

Equation (IV.70) is equivalent to equation (IV.54) since the second order bending moment about the *z*-axis in the flanges accounts for the bimoment and:

$$\frac{N_{\mathrm{Ed,Fl}}}{N_{\mathrm{Rk,Fl}}}(x)=\frac{M_{\mathrm{y,Ed}}}{M_{\mathrm{y,Rk}}}(x) \tag{IV.71}$$

Considering fork supports at both ends of the uniform beam, the critical mode is assumed to be composed of a torsional rotation and out-of-plane displacement that are both a half sine wave:

$$\theta_{\mathrm{cr}}=\sin\left(\frac{\pi x}{L}\right) \tag{IV.72}$$

$$v_{\mathrm{cr}}=\sqrt{\frac{I_{\mathrm{w}}}{I_{\mathrm{z}}}}\varepsilon_{\mathrm{It}}\sin\left(\frac{\pi x}{L}\right) \tag{IV.73}$$

where $\varepsilon_{\mathrm{It}}=\sqrt{1+\frac{GI_{\mathrm{t}}L^2}{EI_{\mathrm{w}}\pi^2}}\geq 1$ is a parameter accounting for the torsional properties of the cross-section.

Expressing the relationship between both amplitudes of the critical buckling mode given by expressions (IV.72) and (IV.73) leads to the common value of this ratio for uniform beams with a doubly symmetrical cross-section subjected to a uniform bending moment distribution and resting on fork supports at both ends:

$$\frac{\bar{v}_{\mathrm{cr}}}{\bar{\theta}_{\mathrm{cr}}}=\sqrt{\frac{I_{\mathrm{w}}}{I_{\mathrm{z}}}}\varepsilon_{\mathrm{It}}=\frac{M_{\mathrm{y,cr}}}{N_{\mathrm{cr,z}}} \tag{IV.74}$$

The second order bending moment about the weak axis acting in the compressed flange is determined using expressions (IV.43) and (IV.44), leading to the design value:

$$M^{\mathrm{II}}_{\mathrm{z,Ed,Fl}}=EI_{\mathrm{z,Fl}}\frac{d^2v_{\mathrm{Fl}}}{dx^2}=EI_{\mathrm{z,Fl}}\frac{L^2}{\pi^2}e_0\frac{M_{\mathrm{y,Ed}}}{M_{\mathrm{cr}}}\frac{1}{1-\frac{M_{\mathrm{y,Ed}}}{M_{\mathrm{cr}}}} \tag{IV.75}$$

The utilization ratio then becomes:

$$\frac{M_{\mathrm{y,Ed}}}{M_{\mathrm{y,Rk}}}+\frac{N_{\mathrm{cr,z,Fl}}}{M_{\mathrm{z,Rk,Fl}}}e_0\frac{M_{\mathrm{y,Ed}}}{M_{\mathrm{cr}}}\frac{1}{1-\frac{M_{\mathrm{y,Ed}}}{M_{\mathrm{cr}}}}=1.0 \tag{IV.76}$$

$$\rightarrow \chi_{\mathrm{LT}}+\frac{\chi_{\mathrm{LT}}}{1-\chi_{\mathrm{LT}}\bar{\lambda}^2_{\mathrm{LT}}}\alpha_{\mathrm{z}}\left(\frac{\bar{\lambda}_{\mathrm{LT}}}{\bar{\lambda}_{\mathrm{z,Fl}}}\right)^2\left(\bar{\lambda}_{\mathrm{LT}}-0.2\right)=1.0 \tag{IV.77}$$

The previous equation is similar to expression (IV.7) from the *General case* with a modified imperfection factor:

$$\alpha_{LT} = \left(\frac{\bar{\lambda}_{LT}}{\bar{\lambda}_{z,Fl}} \right)^2 \alpha_z = \frac{1}{\varepsilon_{I_t}^2} \alpha_z \tag{IV.78}$$

The modification of the imperfection factor relies on a solid mechanical background in the simple case of a uniform beam with a doubly symmetric cross-section subjected to a uniform distribution of the bending moment and resting on fork supports at both ends. This method is adapted to non-prismatic beams according to *Naumes* (2009) by performing the verification at the failure location. However, no guidance is provided to determine the failure location.

IV.4.4 Members in bending and compression

The verification format of a member subjected to compression and bending about the *y*-axis against overall out-of-plane buckling is:

$$\varepsilon(x) = \frac{N_{Ed}}{N_{Rk}}(x) + \frac{M_{y,Ed}}{M_{y,Rk}}(x) + \frac{M^{II}_{z,Ed}}{M_{z,Rk}}(x) + \frac{B^{II}_{Ed}}{B_{Rk}}(x) \leq 1.0 \tag{IV.79}$$

Marques (2012a) proposed a design method adapted form *Eurocode 3* interaction formulae that can be used for tapered members, which is for a member subjected to axial force and in-plane bending:

$$\frac{\frac{N_{Ed}(x^I_{c,N})}{\chi_y(x^I_{c,N}) N_{Rk}(x^I_{c,N})}}{\gamma_{M1}} + k_{yy} \frac{\frac{M_{y,Ed}(x^I_{c,M})}{\chi_{LT}(x^I_{c,M}) M_{y,Rk}(x^I_{c,M})}}{\gamma_{M1}} \leq 1 \tag{IV.80}$$

$$\frac{\frac{N_{Ed}(\chi^I_{c,N})}{\chi_z(x^I_{c,N}) N_{Rk}(x^I_{c,N})}}{\gamma_{M1}} + k_{zy} \frac{\frac{M_{y,Ed}(x^I_{c,M})}{\chi_{LT}(x^I_{c,M}) M_{y,Rk}(x^I_{c,M})}}{\gamma_{M1}} \leq 1 \tag{IV.81}$$

with:

$x_{c,N}^I$: first order failure position due to the design axial force acting alone;

$x_{c,M}^I$: first order failure position due to the design bending moment about *y-y* acting alone.

The reduction factors χ_i are determined according to the methods proposed by *Marques* (2012a) described in the previous sections. The proposed design method makes use of interaction factors determined using Annex B from *Eurocode 3* adapted to tapered members, modifying expressions from Table IV-8 with the following assumptions:

- The equivalent uniform moment factors $C_{m,I}$ depend on the first order bending moment utilization;
- The terms related to the compressed member are determined at the location $x_{c,N}^I$.

The approximations employed to develop the adaptation of Annex B and the parametric studies performed to derive this simplified method soften its mechanical background but simplifies its use, provided that the member falls into the scope of the parametric studies.

The verification format developed by *Tankova* (2018a) for a beam-column against lateral-torsional buckling relies on the same assumptions as the verification of a beam, with some adjustments due to the presence of the axial load. The utilization ratio is:

$$\varepsilon_{MN}^{I}(x)+\varepsilon_{MN}^{II}(x)\,f=1.0 \tag{IV.82}$$

where the value of coefficient f is given by expression (IV.68) and the first $\varepsilon_{MN}{}^{I}$ and second order $\varepsilon_{MN}{}^{II}$ utilization ratios are:

$$\varepsilon_{MN}^{I}(x)=\frac{N_{Ed}}{N_{Rk}}(x)+\frac{M_{y,Ed}}{M_{y,Rk}}(x) \tag{IV.83}$$

$$\varepsilon_{MN}^{II}(x)=\frac{\chi_{op}(x)}{1-\chi_{op}(x)\bar{\lambda}_{op}^{2}(x)}\alpha_{op}(x)\left(\frac{\bar{\lambda}_{op}(x)}{\bar{\lambda}_{z,eq}(x)}\right)^{2}\left(\bar{\lambda}_{z,eq}(x)-0.2\right) \tag{IV.84}$$

When the member is mainly compressed, expression (IV.82) tends towards expression (IV.53) proposed to assess the stability of a tapered member subjected to axial force, while for a member mainly bent, it tends towards expression (IV.68) developed to evaluate the stability of a tapered member subjected to bending. To simplify the determination of the second order utilization ratio, one may use:

$$\chi_{op}\bar{\lambda}_{op}^{2}=\frac{1}{\alpha_{cr,op}} \tag{IV.85}$$

where the critical load amplifier $\alpha_{cr,op}$ can be easily obtained by numerical analyses, using *LTBeamN*.

The imperfection factor $\alpha_{op}(x)$ is determined as an interpolated value of the imperfection factors for flexural and lateral-torsional buckling $\alpha_z(x)$ and $\alpha_{LT}(x)$ considering the first order utilization:

$$\alpha_{op}(x)=\begin{cases}\alpha_{LT}(x)\left[1-\dfrac{\phi(x)}{2}\right]+\alpha_z(x)\dfrac{\phi(x)}{2} & \text{if } \phi(x)\le 1\\ \alpha_{LT}(x)\dfrac{1}{2\phi(x)}+\alpha_z(x)\left[1-\dfrac{1}{2\phi(x)}\right] & \text{if } \phi(x)\ge 1\end{cases} \tag{IV.86}$$

with:

$$\phi(x)=\frac{M_{y,Rk}/M_{y,Ed}}{N_{Rk}/N_{Ed}}(x)$$

The comments expressed about the verification format proposed by *Tankova* (2018a) regarding members subjected to compression or bending are valid for member subjected to both loadings.

Naumes (2009) proposed a modification of the *General Method* where the reduction factor χ_{op} only depends on the imperfection factor for lateral-torsional buckling α_{LT} that accounts for flexural buckling and the torsional properties of the cross-section. A new verification format is also proposed for members subjected to axial force, bi-axial bending moments and bimoment:

$$\frac{1}{\frac{\chi_{LT}(x)\alpha_{ult,k}(x)}{\gamma_{M1}}} + \frac{M_{z,Ed}}{M_{z,Rk}}(x) + \frac{B_{Ed}}{B_{Rk}}(x) \leq \Delta n_r \qquad \text{(IV.87)}$$

with:

$$\Delta n_r = 1 - \frac{\chi_{LT}(x)\alpha_{ult,k}(x)}{\gamma_{M1}}\left[1 - \frac{\chi_{LT}(x)\alpha_{ult,k}(x)}{\gamma_{M1}}\right]\chi_{LT}^2(x)\bar{\lambda}_{LT}^2(x) \geq 0.9$$

Similarly to the lateral-torsional buckling case, a non-prismatic member can be verified using expression (IV.87) either (i) at the failure location, when known, or (ii) considering the maximum values of the first order utilization ratios ($M_{z,Ed}$ and B_{Ed}) and the minimum value of $\alpha_{ult,k}$ along the member.

IV.5 Summary

Calculating the resistance of a welded uniform member against flexural or lateral-torsional buckling is a straightforward process using the buckling curves from *Eurocode 3 Part 1-1*. Accounting for the bending moment distribution to increase the lateral-torsional buckling resistance of a beam is an option in *Eurocode 3* and remains possible in the new verification format from *prEN 1993-1-1*. The latter, only applicable to doubly symmetric beams, come with an imperfection factor that depends on the cross-section dimensions. Besides, buckling coefficients provided in the former French standard *CM66* half a century ago were more favourable than those from *Eurocode 3 Part 1-1* to assess the stability of a welded member against flexural or lateral-torsional buckling.

Designing a non-uniform member using the European code involves the *General Method* which combines both in-plane and out-of-plane behaviours. It has been shown in the past, including by *Taras* (2010a), *Simões da Silva* (2010) and *Marques* (2012a), that the *General Method* could reveal unsafe or significantly conservative because of the light mechanical background on which the design method rely. This observation motivated researchers to develop more accurate design methods to assess the overall stability of tapered members.

Naumes (2009), *Marques* (2012a) and *Tankova* (2018a) have developed analytical methods to assess the stability of a tapered member subjected to compression force and/or bending moment using different approaches. *Naumes* (2009) and *Marques* (2012a) have proposed modifications to *Eurocode 3* design rules in order to include tapered members, *Marques* (2012a) adapting interaction formulae and *Naumes* (2009) the *General case*. Both methods rely on a consistent theoretical background with calibrated expressions given by *Marques* (2012a) for common bending moment distributions while a lack of guidance in the method proposed by *Naumes* (2009) makes its use challenging for tapered members. *Tankova* (2018a) have developed a general formulation based on strong mechanical bases that can be applied whatever the loading and boundary conditions. This design method requires the elastic buckling shape to be known that can be obtained numerically, e.g. using *LTBeamN* also providing the first derivative of the mode shape. However, the method developed by *Tankova* (2018a) also involves the second derivative of the mode shape, which can question its use in design offices. Numerical programmes performing finite element analyses may be developed to obtain such information concerning the buckling of non-uniform steel members.

Newly developed analytical methods to assess the stability of a non-uniform member can be employed in simple cases but the *General Method* should also be enhanced to cope with the shortcomings discussed above. Besides, no existing method account for the welded member fabrication process however it will be shown next chapter that it affects the residual stresses distribution, and consequently the overall buckling behaviour. Accurate design method should therefore be developed considering the fabrication process.

V. *Residual stresses in welded steel members*

V.1 Introduction

The fabrication process of a steel member induces both geometrical and material imperfections that influence its buckling behaviour and resistance. Geometrical imperfections in steel members are visible and easily measurable to ensure that the requirements of *EN 1090-2* are fulfilled. However, evaluating residual stresses requires specific measurements. The residual stresses distribution depends on the fabrication process of the steel member (*ECCS*, 1976).

Residual stresses are in self-equilibrium and do not result from external loads but from the differential cooling rates of a cross-section during the fabrication process. The longest cooling generates tension and the fastest cooling compression. In a steel member built-up from hot-rolled plates, the longitudinal welds create a tension zone at the flange-to-web junctions, equilibrated by compression zones in the remaining parts as shown in Figure V-1a). Similarly, flame cuts at a plate tips create tension zones where cooling is slower than at the plate centre. This phenomenon is explained by *ECCS* (1976) and presented in Figure V-1b). A distinction should be done between the residual stresses distribution in welded members made of hot-rolled flanges and flame-cut flanges.

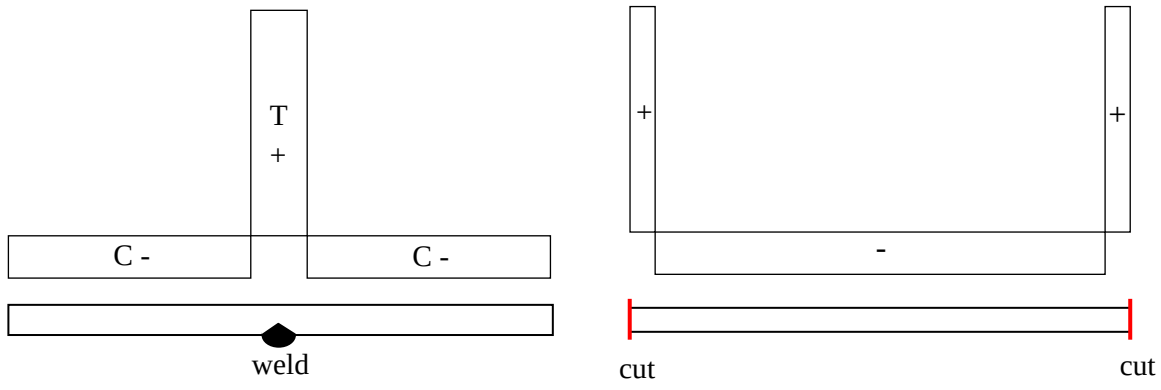

a) *Welded at its centre* b) *Flame-cut*

Figure V-1: Residual stresses in a plate

Residual stresses have a major impact on the overall buckling of a steel member by inducing an early or late first yielding of the member. Indeed, yielding of a member that may undergo out-of-plane buckling initiates at a tip of a single or both flanges. An initial compressive stress at the flanges tips is therefore less favourable than a tensile one. In addition to their distribution, the stresses intensity have an impact on out-of-plane buckling, leading many researchers to provide residual stresses models.

After a description of existing models for welded members made of hot-rolled or flame-cut flanges, a new experimental programme is described that aimed to measure residual stresses in eight welded members. Two beams are composed of hot-rolled flanges and the remaining six of flame-cut flanges. Experimental distributions have been evaluated using the sectioning method. The results of this

experimental campaign are then analyzed along with existing experimental data and a new model adapted to welded members made with flame-cut flanges is eventually proposed.

V.2 Existing models

V.2.1 Hot-rolled flanges

In *prEurocode 3 Part 1-14*, a single model for welded members is proposed based on that from *ECCS* (1984) but corresponds to members made of hot-rolled flanges. The yield strength f_y is reached at the web-to-flange junctions (see Figure V-2). A compressive stress having a magnitude of a quarter of the yield strength develops in the remaining parts.

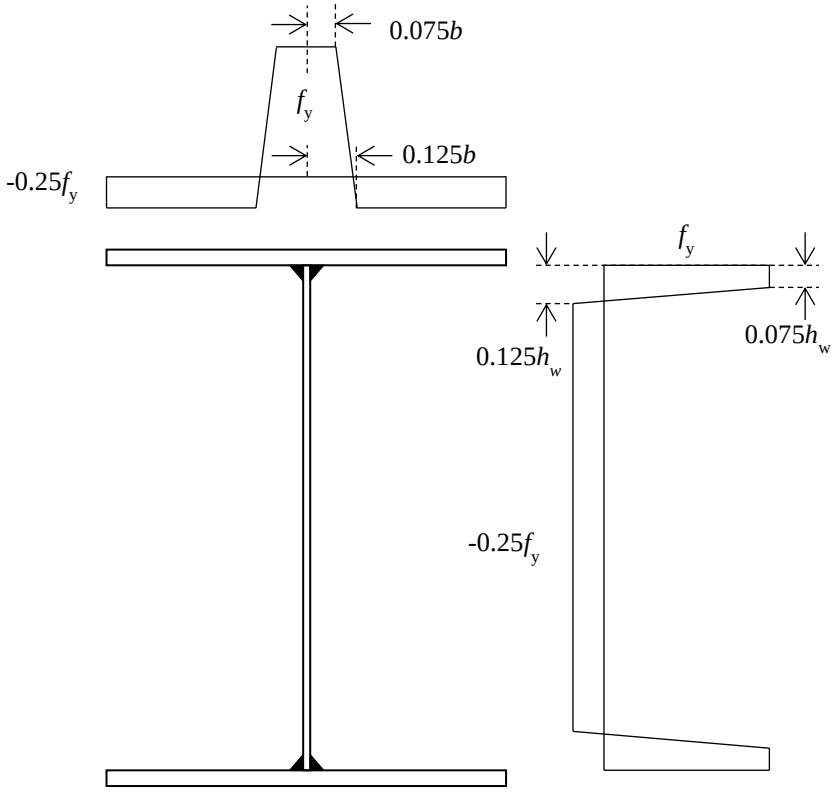

Figure V-2: Residual stresses given in prEurocode 3 Part 1-14

The Swedish code *BSK 99* (2003) proposes a similar distribution presented in Figure V-3a). The tension zone widths depend on the thicknesses t_f and t_w and the compressive stresses in the flanges and web is determined using self-equilibrium. An adaptation of this model was proposed by *Gozzi* (2007) where the stresses are stepped and the width of the tension zones are equal to 2.25 t_f in the flanges and 2.25 t_w in the web (see Figure V-3b)).

Kwon (2012) proposed a stepped model where the magnitudes of the tensile and compressive stresses are equal to f_y and 0.3f_y, respectively. The widths are determined from self-equilibrium. *Trahair* (2012) proposed stress distributions for mono-symmetric members by reducing the compressive stress magnitude in the smaller flange using the ratio between both flanges widths (see in Figure V-4a)). The absence of residual stress in the web is a noticeable feature of this model, justified by the negligible influence of web yielding on out-of-plane buckling.

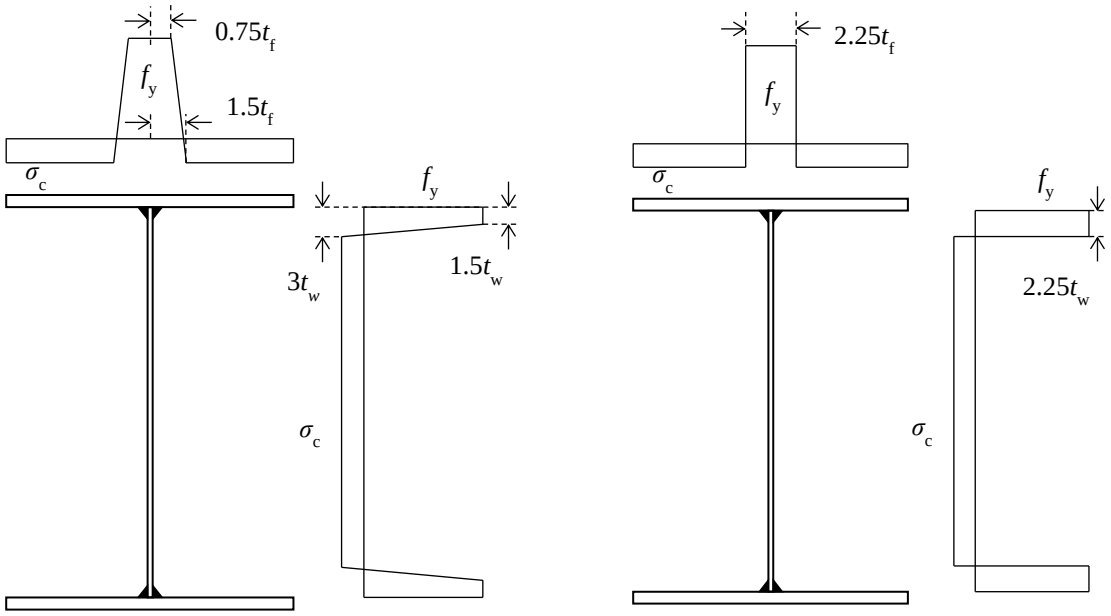

a) *Original model* b) *Model adapted by Gozzi* (2007)

Figure V-3: Residual stresses given in the Swedish code BSK 99

Chernenko (1991) proposed a shape for the residual stresses distribution based on measurements performed at Lehigh University in the 1960s on stocky sections e.g. by *Estuar* (1962) and *Cranston* (1967). The web heights were lower than 250 mm and plates thicknesses greater than 10 mm. This model using linear distribution of the residual stresses is enhanced by *Kabir* (2018) providing values for the peak tensile and compressive stresses of f_y and -0.25f_y, respectively (see Figure V-4b)).

Residual stresses measurements performed on welded tapered members by *Prawel* (1974) lead to the model presented in Figure V-4c). The specimens, which had a yield strength of approximately 290 MPa, were built-up using longitudinal welds placed on one side of the web and involved web and flanges of 2.7 mm and 6.4 mm thickness, respectively. This model stands out from the previously cited models for welded members because the magnitude of the compressive stress in the flanges reaches half the yield strength. This important compression is due to a wide $b/3$ tension zone at the flange centre where the yield strength is reached.

Because the model proposed by *Prawel* (1974) contains a high magnitude of the compressive stress in the flanges, *Kim* (2010) used a modified version referred to as "*best-fit Prawel*" residual stress model. In this alternate model, the stresses magnitudes in the flanges are divided by two, except for the compressive stress near the flanges centres that becomes a tenth of the yield strength. The distribution in the web remains unchanged with a value of -0.176 specified for parameter *k*.

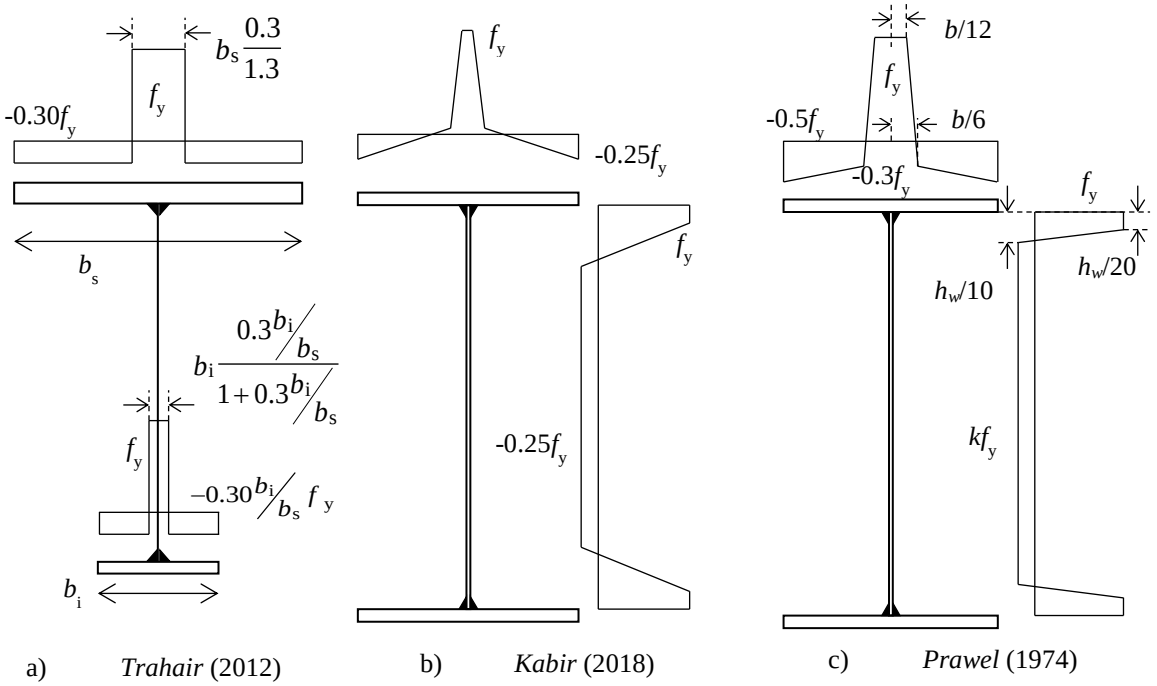

a) *Trahair* (2012) b) *Kabir* (2018) c) *Prawel* (1974)

Figure V-4: Residual stress models for welded members with hot-rolled flanges

The choice of the residual stress pattern for welded sections made of hot-rolled flanges has an impact on the out-of-plane buckling behaviour. This topic was investigated by *Couto* (2019) who depicted a series of Geometrically and Materially Non-linear Analyses with Imperfections (*GMNIA*) using models from *ECCS* (1984), *Gozzi* (2007), and the *best-fit Prawel* pattern. Employing the *ECCS* (1984) model resulted in the most conservative results, up to 10% lower than that using *Gozzi*'s (2007) model. Using the latter or the *best-fit Prawel* model yielded close results.

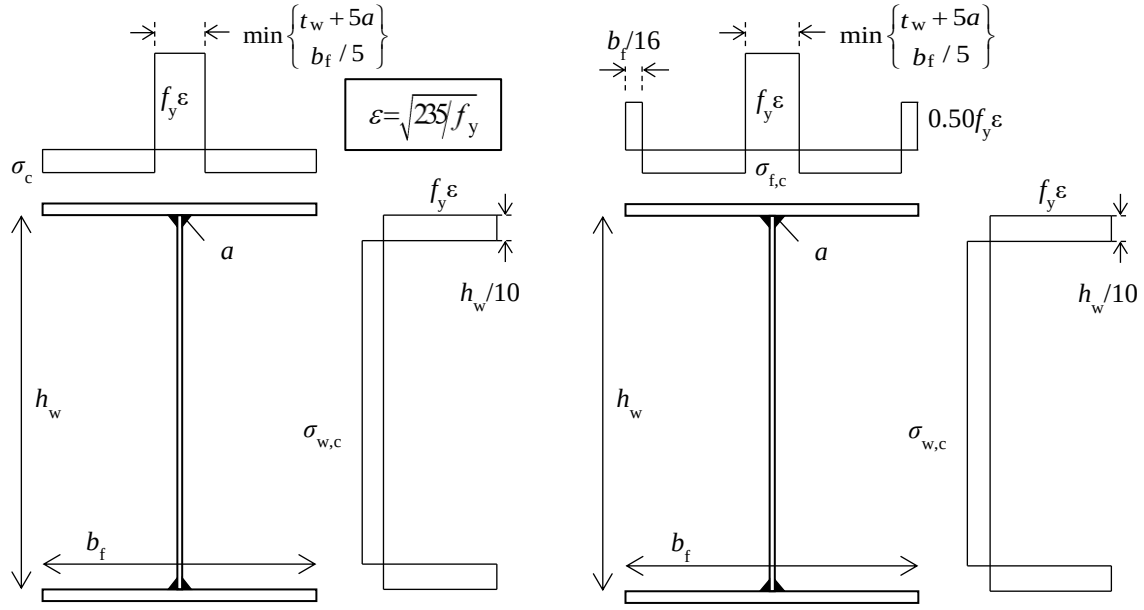

a) *Hot-rolled flanges* b) *Flame-cut flanges*

Figure V-5: Residual stress models proposed by Schaper and Tankova *(2022)*

Among previously mentioned patterns, only those used by *Prawel* (1974) and *Kabir* (2018) rely on experimental measurements performed on limited geometries. The lack of experimental background in most of existing patterns has conducted *Schaper and Tankova* (2022) to develop a novel residual stress model. The proposed model is based on experimentally measured distributions using the sectioning method in twenty-five welded members having a steel grade between S355 and S690 among which one had hot-rolled flanges while the rest had flame-cut flanges.

The model is developed analysing also the distributions measured in almost forty specimen found in the literature, made of flame-cut or hot-rolled flanges and steel grades from S235 to S890. Data from the literature included the mean experimental distribution measured by *Fukumoto* (1981) with the sectioning method on thirty-four 250×100 mm welded members. Using the same experimental method, the residual stress measurements performed by *Kubo* (1988) on small welded members made of hot-rolled flanges should also be mentioned. The specimens had cross-section dimensions comprised between 250×125 mm and 300×150 mm but no residual stress model resulted from this study. Similarly, the residual stresses measured by *Avent* (1982) on seven welded members with hot-rolled flanges should be highlighted. The members were 229 to 610 mm height and 127 to 254 mm wide and fabricated from steel plates having a nominal yield strength of 345 MPa. The plates thicknesses ranged between 3.2 and 6.4 mm in the webs, and from 5.6 to 15.9 mm in the flanges. The welding procedure, particularly amperage and volts, varied between specimens but did not impact the residual stresses distribution.

Liu (2017) investigated numerically the impact of various parameters on the residual stresses distributions in S355 and S690 welded members. Tests results obtained for S690 welded members using the hole drilling method validate the use of a numerical model. The parametric study highlighted an impact of the web and flanges thickness on the residual stress distribution. In particular, numerical results showed a decrease of the magnitude of the flanges compressive stresses as the b/t_f ratio increases. The study analyzed the effect of the welds on the stress distribution and disregarded the impact of thermal cuts made at the flange tips.

Schaper and Tankova (2022) proposed residual stress models for welded members made of hot-rolled flanges and flame-cut flanges, presented in Figure V-5a) and V-5b), respectively. Contrary to the other models depicted in the present sub-section, the one presented in Figure V-5a) exhibits tensile stresses at the web-to-flange junctions that do not reach the yield strength when greater than 235 MPa. Involving ε, no stress is linearly dependent on the yield strength, contrary to existing models.

The models developed by *Schaper and Tankova* (2022) show differences at the flanges tips where flame-cuts provoke a tensile stress having a magnitude of $0.5f_y\varepsilon$, which is half the magnitude of the tensile stress at the flange centres. The compressive stress in the flanges being determined from self-equilibrium, the resulting stress of the model for welded section with hot-rolled flanges is lower than in the model for flame-cut flanges.

- **Conclusions**

The existing residual stress patterns adapted to welded members made of hot-rolled flanges present similar features. Indeed, except in the model of *Schaper and Tankova* (2022), the tensile stress reaches f_y at the flange-to-web junctions while the magnitude of the compressive stresses generally range between 25 and 30% of f_y. The models of *Prawel* (1974) and *Kabir* (2018) rely on experimental measurements but the latter lack parameters and using the former yields overly conservative results. Besides, these models were developed employing a limited number of experimental data, unlike that of *Schaper and Tankova* (2022) that rely on the most important experimental background.

In the following sub-section V.2.2, residual stress models for welded members with flame-cut flanges are described.

V.2.2 Flame-cut flanges

The residual stresses distribution proposed by *ECCS* (1976) for welded members with flame-cut flanges is presented in Figure V-6a). Expressions were given to determine the widths c_i of the stress blocks, but the resulting tension units at the flanges ends are very narrow while the stress magnitude reaches the yield strength, making challenging its use in finite element analyses. For this reason, *Barth* (1998) and *Chacón* (2009) proposed modified versions of the *ECCS* model presented in Figure V-6b) and Figure V-6c), respectively.

The patterns presented in Figure V-6b) and V-6c), which do not rely on experimental data, exhibit a tensile stress reaching a third of the yield strength at the flanges centre significantly lower than the yield strength proposed by *ECCS* (1976, 1984) and commonly assumed for welded members having hot-rolled flanges. Tensile stresses at the flange corners are similar in both models proposed by *Barth* (1998) and *Chacón* (2009), reaching 18% of the yield strength which is lower than the value proposed by *Schaper and Tankova* (2022).

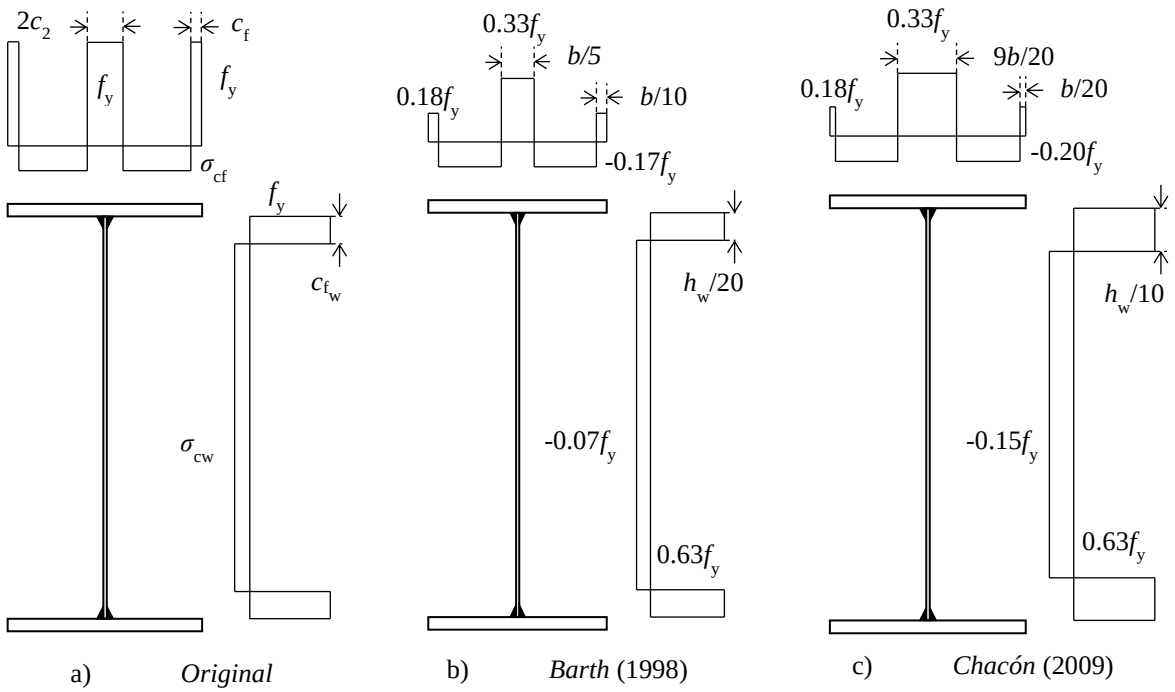

Figure V-6: Residual stress models from ECCS (1976)

It can be noticed that the residual stress pattern proposed by *Chacón* (2009) is not self-equilibrated, an axial tensile load resulting from the stress distribution in the flanges. This is due to a large central tension zone, while the tension blocks at the flanges ends are narrower than in *Barth*'s model. Performing numerical non-linear analyses on bent members, *Couto* (2019) obtained lower results using *Chacón*'s pattern than using *Barth*'s model, highlighting that the tension zone at the tips and the compressed zone have a greater impact on the buckling behaviour than the central tension zone.

Chernenko (1991) suggested a shape for a residual stress pattern presented in Figure V-7a). This proposition is based on experimental results from Lehigh University performed in the 1960s, e.g. by

Cranston (1967), *Kishima* (1969) or *Tebedge* (1973). The specimens tested were composed of stocky welded H-members with flame-cut flanges having cross-section dimensions up to 400×400 mm with thicknesses of 10 mm at least. More recently, residual stresses distributions were measured by *Wang* (2012) in three S460 H-members. The cross-section dimensions were between 168×156 and 320×314 mm with thicknesses of 11 mm for the webs and 21 mm for the flanges. Along with the sectioning method, the distributions were measured using the hole-drilling technique. The semi-destructive hole drilling method consists in measuring the stress field released by the drilling of a small hole that has a diameter and depth of 1.5 and 2 mm, respectively. The hole-drilling method, measuring membrane stresses, has provided more scattered results than the sectioning method but the mean compressive stresses are similar. Based on these test results, *Wang* (2012) proposed the stepped residual stress shape presented in Figure V-7b). The magnitude of the tensile stress at the web-to-flange junctions is between $0.73f_y$ and $1.04f_y$ while the magnitudes at the tips vary between $0.08f_y$ and $0.49f_y$. Compressive stresses have magnitudes comprised between -0.20 f_y and -0.41 f_y in the flanges and -0.13 f_y and -0.24 f_y in the web.

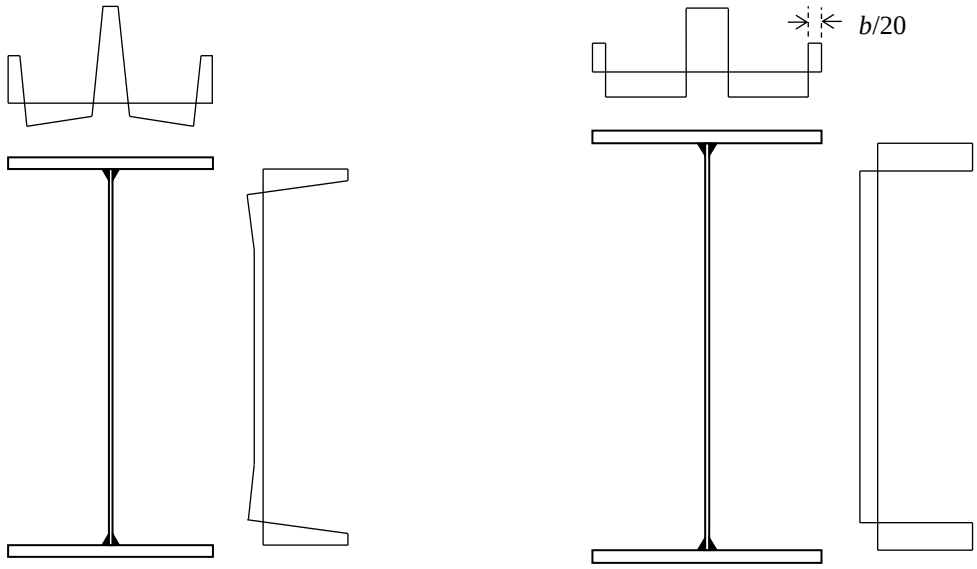

a) *Chernenko* (1991) b) *Wang* (2012)

Figure V-7: Residual stresses shapes for welded members with flame-cut flanges

Thiébaud (2014) measured residual stresses using the sectioning method in isolated flame-cut plates, welded or not at their centre. The flame-cut plates corresponding to bridges beam flanges were 615 or 730 mm-wide with a 60 mm-thickness while the perpendicular welded plates, representing the beams webs were 20 mm-thick. Results showed that the central welds have an influence on the compressive stress but the tensile stresses at the plate tips due to flame-cut remain unchanged. Using its experimental results for S355 welded bridges beams having flame-cut flanges, *Thiébaud* (2014) proposed the residual stress model given in Figure V-8a).

The sectioning method was again used by *Yang* (2017) on four welded specimens with flame-cut flanges having cross-section heights between 300 and 400 mm, involving 8 and 10 mm-thick webs and flanges, respectively. Three 200 mm-wide doubly-symmetric specimens were analyzed along with a mono-symmetric member having 180 and 220 mm-wide flanges, all specimens having a nominal yield strength of 345 MPa. The resulting residual stress model, presented in Figure V-8b), suggests linear transitions between tensile and compressive stresses but no widths or slopes are provided. The pattern proposed by

Yang (2017) is less favourable than those proposed by *Barth* (1998) and *Chacón* (2009) due to a higher compression magnitude in the flanges and a lower tension magnitude at the flanges ends.

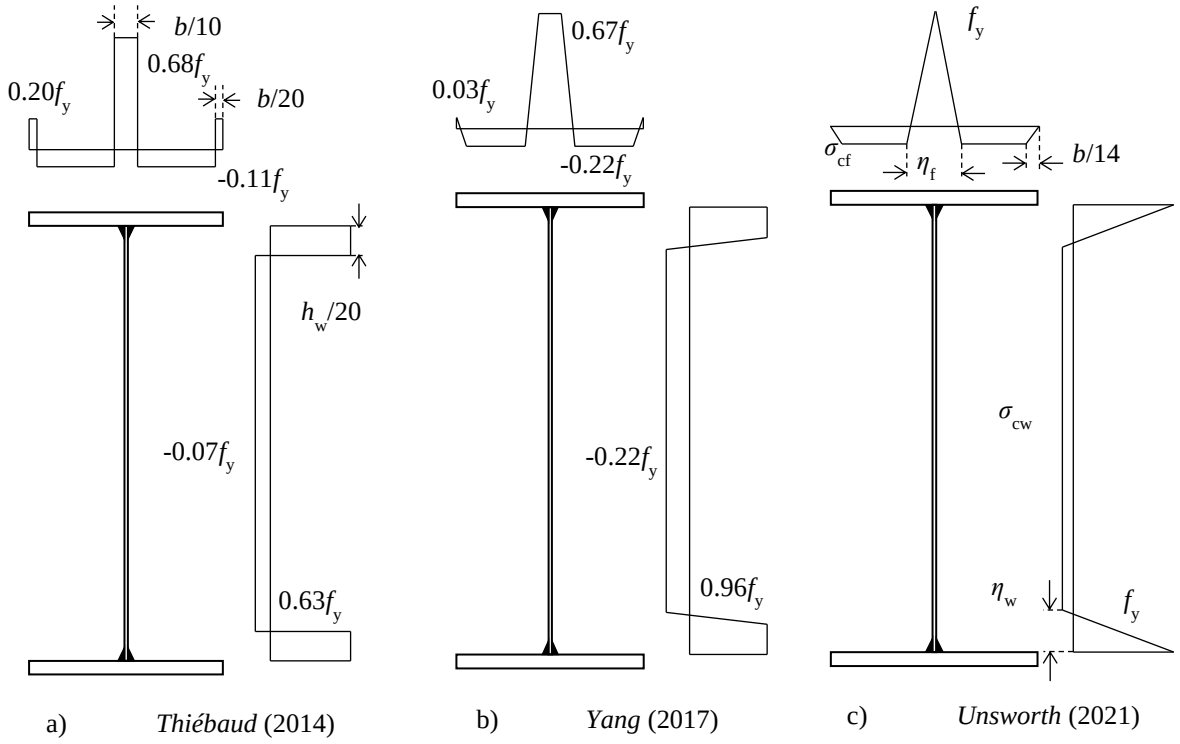

Figure V-8: Existing models for welded members with flame-cut flanges

Unsworth (2020) performed residual stress measurements using the sectioning method in four welded members having cross-section dimensions comprised between 536×300 mm and 749×430 mm, with web and flanges thicknesses of 12.7 and 25.4 to 31.8 mm, respectively. Three of the specimens had plasma-cut flanges while the last had flame-cut flanges. Using these results along with experimental data on twenty-five specimens from the literature that mostly concerned stocky cross-sections (with a maximum total height of 430 mm and a minimum web thickness of 6 mm) made of high strength steel, a residual stress model have been proposed by *Unsworth* (2021). This model is presented in Figure V-8c) where the compressive stresses are found from self-equilibrium while widths are given by:

$$\eta_{\mathrm{f}} = \left(2\frac{C A_{\mathrm{w}}}{f_{\mathrm{y}} \sum t} + t_{\mathrm{w}} \right) \left(1 - \frac{B}{b} \right) \tag{V.1}$$

$$\eta_{\mathrm{w}} = \frac{C A_{\mathrm{w}}}{f_{\mathrm{y}} \sum t} \tag{V.2}$$

where B is a coefficient empirically set to 53, A_{w} is the cross-sectional area of a single weld, and C is given by:

$$C = \frac{96 E \alpha}{16 \times 10^{-3}} \tag{V.3}$$

where α is the coefficient of linear thermal expansion that can be taken as equal to 15×10^{-6} C^{-1}.

It is worth mentioning that the model proposed by *Unsworth* (2021) was developed based on the stepped residual stress model proposed by *Dwight* (1969) for welded members with hot-rolled flanges. The width of the tension zone in the web η_w remains unchanged while the width of the central tension zone proposed by *Dwight* (1969) corresponds to that proposed by *Unsworth* (2021) with $B = 0$.

However, the model of *Unsworth* (2021) provides high values of the magnitudes of the compressive stress for small cross-sections. As an example, the case of a S355 welded member having the cross-sectional dimensions of an IPE 300 member is studied, its total height and width being 300 and 150 mm, respectively. The flanges and web thickness are 10.7 and 7.1 mm, respectively, with an area A_w = 25 mm². The resulting residual stresses distribution in the flanges according to *Unsworth*'s (2021) model is presented in Figure V-9.

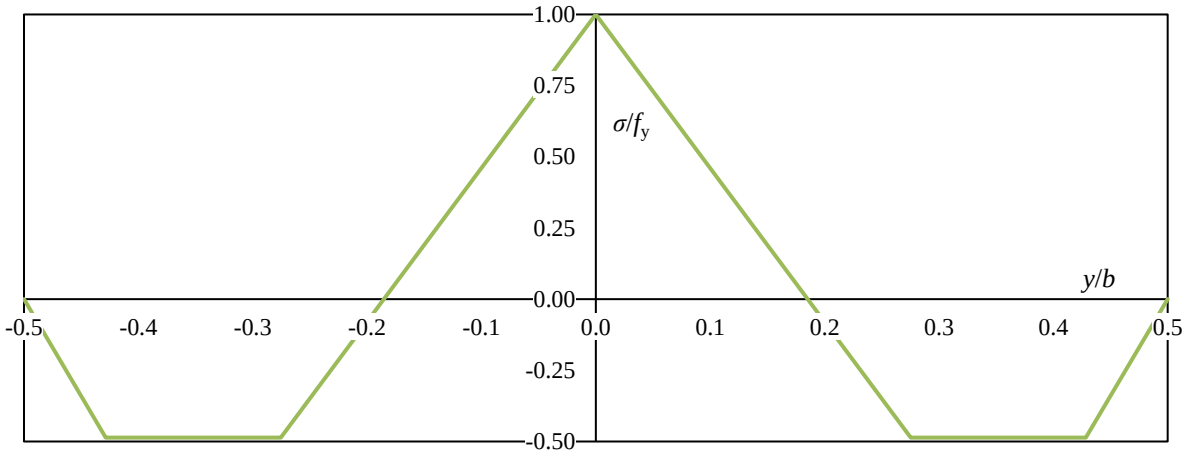

Figure V-9: Residual stresses in the flanges of an IPE 300 type welded member using Unsworth*'s (2021) model*

The compressive stresses reach almost half of the yield strength. This value is significantly greater than those from the other models for welded members made of flame-cut flanges.

- **Conclusions**

Within the many existing residual stress models, *Thiébaud* (2014) has developed a pattern adapted to bridges members that presents the most favourable magnitude of the compressive stress in the flanges while *Chacón* (2009) has suggested a model that is not self-equilibrated. Both patterns should not be employed to perform finite element analyses on building members. The same conclusion can be drawn regarding the residual stress shapes given by *Chernenko* (1991) and *Wang* (2012) that lack general values for stress magnitudes and widths. Appropriately using the model from *Yang* (2017) in finite element analyses seems challenging due to small width of the stress gradient at the flanges ends. The same can be said regarding the small width of the tension blocks at the flanges tips in the model proposed by *ECCS* (1976) for which a modified model proposed by *Barth* (1998) can be used despite a lack of experimental background. The model developed by *Unsworth* (2021) relies on a consistent experimental background but seems unfavourable in small section, the compressive residual stress being very important when compared to other models. Similarly, *Schaper and Tankova* (2022) proposed a model based on strong experimental bases that include high strength steel but a scarcity of specimens having a height greater than 500 mm can be noticed. However, in practice the height of welded members is greater and generally comprised between 500 and 1200 mm in buildings. Experimental results are clearly needed for steel members having usual dimensions and steel grades.

An experimental programme is described next consisting in residual stress measurements in eight S355 welded members chosen to match the current common practice, two having hot-rolled flanges and six flame-cut flanges. The novel experimental results are then analyzed along with existing experimental data, resulting in a new residual stress model adapted to welded members in buildings that have flame-cut flanges and a usual steel grade.

V.3 Experimental programme

V.3.1 Full-scale specimens

The experimental programme consists in residual stress measurements performed on eight S355-welded members at the University of Liège. The web of 780×8 mm is identical for the 8 specimens. The parameters studied are the flanges dimensions (width and thickness) and their fabrication process. The nominal dimensions and steel grade of the specimens are depicted in Table V-1. Three flange thicknesses have been studied 12, 15 and 20 mm as well as two widths 200 and 250 mm. The objective was to study the impact of the flanges slenderness on the residual stresses distribution. In addition, two specimens using hot-rolled flanges have been tested to analyze the influence of the flanges fabrication. The specimens were fabricated by welding first one side of the web with both flanges, then turned over before adding fillet welds connecting the other side of the web to both flanges.

The test specimens having a 3 m-length are assumed long enough to prevent the residual stresses measurements from any boundary effects in agreement with the requirements of *Aschendorff* (1983):

$$L_{\text{specimen}} \geq 3.5 h_{\text{t}} \tag{V.4}$$

where the maximum total height h_{t} is 820 mm within specimens from Table V-1.

Designation	h_{w} (mm)	t_{w} (mm)	b (mm)	t_{f} (mm)	L (m)	Steel grade	Flanges fabrication process
Wfc_200-15	780	8	200	15	3	S355	Flame-cut (FC)
Wfc_200-15/20	780	8	200	15, 20	3	S355	FC
Wfc_250-15	780	8	250	15	3	S355	FC
Wfc_250-12	780	8	250	12	3	S355	FC
Wfc_200-20	780	8	200	20	3	S355	FC
Wfc_200-12	780	8	200	12	3	S355	FC
Whr_200-15	780	8	200	15	3	S355	Hot-rolled (HR)
Whr_200-20	780	8	200	20	3	S355	HR

Table V-1: Nominal properties of the specimens for residual stresses measurements

In addition to the residual stresses, the real cross-section dimensions and material properties have been measured. The material properties have been measured according to standard *ISO 6892-1* on three coupons from each thickness. These coupons were cut from specimens *Wfc_250-12* for 8 and 12 mm-thick plates and *Wfc_200-15/20* for 15 and 20 mm-thick plates. The mean (M) and standard deviation

(*SD*) of the measured elasticity modulus E, the yield strength f_y and the ultimate tensile strength f_u are presented in Table V-2. The yield strength, corresponding to the proof strength for 0.2% plastic extension $R_{p0.2}$, increases as the thickness decreases. It can be noted that the measured yield strength is 11 to 20% - depending on the thickness – higher than its nominal value of 355 N/mm² while the variations of the modulus of elasticity do not exceed 5%.

The cross-section dimensions have been measured on three transverse sections of each specimen having a constant spacing. In Table V-3 the measured dimensions are divided by their nominal values and expressed as means and standard deviations. A negligible deviation on the flanges width and web height are noticed due to the precision of cutting methods currently used by steel manufacturers. Slight differences, which are still acceptable, are noted concerning the plates.

Thickness (mm)	E (N/mm²)		f_y (N/mm²)		f_u (N/mm²)	
	M	***SD***	***M***	***SD***	***M***	***SD***
8	201501	2483	427	0.7	552	3.8
12	203732	2202	410	9.8	545	6.0
15	211527	6559	417	1.9	549	0.7
20	205627	806	395	3.1	541	1.1

Table V-2: Material properties of the steel plates from the residual stress specimens

An extensive description of the most common existing residual stress measurement techniques is presented by *Rossini* (2012) where mechanical – destructive or semi-destructive – methods are separated from non-destructive techniques that can involve diffraction. Despite preserving the specimens, the non-destructive methods such as X-ray or neutron diffraction, or ultrasonic method require advanced calibration, expensive equipment and are hardly applicable to large welded members. Destructive or semi-destructive methods, that include the deep hole, the contour, the hole-drilling and the sectioning methods, consist in measuring the released strains associated with a drilled hole or a cut that must be performed without influencing the existing stress field.

Among existing destructive methods, the sectioning one has been widely used, as noticed in section V.2. Indeed, this method combines a certain ease of use with accuracy despite measuring longitudinal strains only. Because strains in other directions hardly affect a member buckling behaviour when compared to the longitudinal ones, the sectioning method is very well suited for welded beams. Therefore, the sectioning method has been used to measure residual stresses.

Dimension	***M***	SD
Web height	1.000	0.0019
Web thickness	1.022	0.0113
Flanges width	1.001	0.0041
Flanges thicknesses	1.009	0.0092

Table V-3: Statistical parameters of the actual dimensions of the residual stress specimens

Residual stresses are measured at mid-span where longitudinal strips that are approximately 100 mm-long are firstly depicted to measure their initial lengths L_i using the numerical extensometer shown in Figure V-10. The second step has consisted in sawing transversally in each piece a 200 mm-long central

zone, that includes the smaller strips, using a band saw cooled by a liquid containing water and oil. The central zone is then longitudinally cut according to the initially depicted strips of which the final length L_f is eventually measured, as shown in Figure V-10. From the initial and final lengths, the residual uniaxial strain in each strip ε_x is obtained then used along with Hooke's law to calculate the residual uniaxial stress σ_x:

$$\varepsilon_x = \frac{L_i - L_f}{L_i} \tag{V.5}$$

$$\sigma_x = E\varepsilon_x \tag{V.6}$$

The strips initial and final lengths are measured on both sides of the plates, except at the flanges centres were the length cannot be measured on the inner face of the flanges due to the presence of the web and welds. The resulting residual stress of each strip is defined as the mean between the values measured on both faces of the plate. At the flanges centre, the residual stress is defined as the mean between the outer face value and the mean value in the strip located at its immediate vicinity in the web.

Figure V-10: Measurement of the strips final lengths

V.3.2 Measured distributions

V.3.2.1. General results

The residual stresses distributions are presented in the following sections V.3.2.2 and V.3.2.3 where the effects of the flanges fabrication process and slenderness are studied. The theoretical self-equilibrium resulting from the residual stresses in each specimen is analyzed calculating the sums of both the net internal and total internal forces F_{net} and F_{total} in every strips as defined by *Unsworth* (2020) and using the cross-section plastic resistance to an axial load N_{pl}:

$$F_{net} = \sum_{i=1}^{n} \sigma_{res,i} A_i \tag{V.7}$$

$$F_{\text{total}} = \sum_{\text{i=1}}^{\text{n}} \left|\sigma_{\text{res,i}}\right| A_{\text{i}} \tag{V.8}$$

$$N_{\text{pl}} = \sum_{\text{i=1}}^{\text{n}} f_{\text{y,i}} A_{\text{i}} \tag{V.9}$$

where n is the number of strips, A_i, $\sigma_{res,i}$ and f_y are the transverse area, the measured residual stress and the material yield strength in strip i.

Results of expressions (V.7) and (V.8) are obtained using the simplifying assumption that the residual stress is uniform in a strip and given in Table V-4, tensile stresses being negative.

Specimen	F_{net}/F_{total}				F_{net}/N_{pl}
	Top flange	Bottom flange	Web	Cross-section	Cross-section
Wfc_200-15	13.8%	14.5%	-15.5%	1.53%	0.19%
Wfc_200-15/20*	-13.9%	-49.3%	-43.5%	-37.12%	-5.73%
Wfc_250-15	-34.2%	-9.1%	-8.0%	-16.05%	-1.73%
Wfc_250-12	55.5%	62.3%	-25.1%	19.95%	2.28%
Wfc_200-20	-39.3%	13.4%	-42.6%	-26.87%	-4.01%
Wfc_200-12	18.3%	-12.4%	2.2%	1.06%	0.16%
Whr_200-15	28.0%	12.8%	38.8%	26.49%	3.95%
Whr_200-20	-36.8%	-37.7%	-31.4%	-34.82%	-5.71%

Table V-4: Net and total internal forces compared with plastic resistance

*: The top flange of specimen Wfc_200-15/20 is 15 mm-thick.

Owing to the precision of the experimental measures and the limited number of strips in each specimen – eleven in each flange plus twelve in the web – the maximum value of the F_{net}-to-N_{pl} ratio is 5.7%.

Further parameters are determined to characterize the residual stresses distribution in the six specimens having flame-cut flanges that are defined by *Unsworth* (2020) as the parametric compressive stress σ_{pc} and the width of the high stress gradient (HSG) region η at the flange-to-web junctions. The parametric compressive stress can be seen as the average stress in the "uniformly" compressed part of the web or flange:

$$\sigma_{\text{pc}} = \frac{1}{n}\sum_{i=1}^{n}\sigma_{\text{rc,i}} = \overline{\sigma_{\text{rc}}} \tag{V.10}$$

where σ_{rc} are the residual stresses in the plate that are lower than the mean residual stress minus a quarter of their standard deviation:

$$\sigma_{\text{rc}} = \sigma_{\text{res}} \forall \sigma_{\text{res}} \le \overline{\sigma_{\text{res}}} - 0,25\sqrt{\frac{1}{n}\sum_{i=1}^{n}\left(\sigma_{\text{res,i}} - \overline{\sigma_{\text{res}}}\right)^2} \tag{V.11}$$

The HSG region width is defined by *Unsworth* (2020) as the central width in the flanges between the locations of the two closer compressive stresses $\sigma_{p\eta}$ given by equation (V.12). In the web, the widths are defined from the location of such compressive stress to the flange junction. Linear interpolations are employed to determine the HSG widths.

$$\sigma_{p\eta} = \overline{\sigma_{res}} + 1{,}5\sqrt{\frac{1}{n}\sum_{i=1}^{n}\left(\sigma_{res,i} - \overline{\sigma_{res}}\right)^2} \qquad \text{(V.12)}$$

The mean parametric compressive stresses and HSG width due to welding in the flanges and webs are presented in Table V-5 for all specimens with flame-cut flanges along with the mean stresses σ_{tip} measured at the flanges tips.

Specimen	σ_{pc}/f_y		η/plate width		$\sigma_{tip}/f_{y,f}$
	Flanges	Web	Flanges	Web	
Wfc_200-15	-0.17	-0.08	0.37	0.08	0.02
Wfc_200-15/20	-0.19	-0.14	0.41	0.07	0.00
Wfc_250-15	-0.12	-0.06	0.34	0.08	0.03
Wfc_250-12	-0.06	-0.08	0.41	0.08	0.06
Wfc_200-20	-0.17	-0.14	0.46	0.10	0.05
Wfc_200-12	-0.16	-0.09	0.42	0.08	-0.04

Table V-5: Parameters of the residual stresses distributions

Table V-5 shows that the parametric compressive stress are lower in 250 mm-wide flanges than in 200 mm-wide flanges where values are found between 16 and 19% of the yield strength. In the webs, the parametric compressive stresses, ranging between 6 and 14% of the yield strength, seem to slightly decrease with the flange width. Keeping in mind the results from Table V-4, no correlation seems to link the compressive stresses and the flanges thicknesses. The HSG region widths are constant in the webs, ranging between 7 and 10% of the web height. However, in the flanges the variation is more pronounced, fluctuating between a third and almost half of the flange width. The wider flanges provides among the lowest HSG region widths. Stresses measured at the flanges tips are found between 0 and 6% of the yield strength with a specimen that presents compressive residual stresses having a magnitude of $0.04f_y$.

Experimental results show that the predictive tensile stresses at the flanges tips are over estimated by most residual stress models presented in section V.2.2, except for *Yang* (2017) and *Unsworth* (2021) with values of $0.03f_y$ in tension and 0, respectively. Compressive stresses in the flanges are closer to the predictions of the models of *Barth* (1998), *Chacón* (2009) and *Yang* (2017) that range between 17 and 22% of the yield strength. The model proposed by *Thiébaud* (2014) presents a lower magnitude of the compressive stress, $0.11f_y$. The resulting parametric compressive stress in the webs experimentally measured are found between the predictions of the models of *Barth* (1998), *Chacón* (2009) and *Thiébaud* (2014) proposing $0.07f_y$ or $0.15f_y$ while *Yang* (2017) proposes to use 22% of the yield strength, which is almost four time the lowest measured value.

Comparing the width of the HSG region at the flanges centres given in Table V-5 to the width of the central tension zones proposed in residual stress models would not be relevant if the model proposes a

uniform tension block, e.g. in models by *ECCS* (1976), *Barth* (1998), *Chacón* (2009), *Wang* (2012), *Thiébaud* (2014) and *Schaper and Tankova* (2022). The HSG region widths determined with expressions (V.1) and (V.2) from *Unsworth* (2021) yields widths of 0.38*b* in the flanges of *Wfc_200-15* and 0.07h_w in the web of the same specimen. Both predictions correspond to the experimental data given in Table V-5.

The influence of the flange fabrication process and slenderness on the stress distribution is analyzed in §V.3.2.2 and §V.3.2.3, respectively.

V.3.2.2. Effect of the flanges fabrication process

The influence of the flange fabrication process on the residual stresses can be analyzed comparing the experimental distributions measured in specimens *Wfc_200-15* and *Whr_200-15* that have similar dimensions but either flame-cut or hot-rolled flanges. Likewise, the distributions in *Wfc_200-20* and *Whr_200-20* that present similar dimensions are compared. The distributions in the 15 and 20 mm-thick flanges are presented in Figure V-11 and Figure V-12, respectively while in the webs of the corresponding specimens the stresses are presented in Figure V-13.

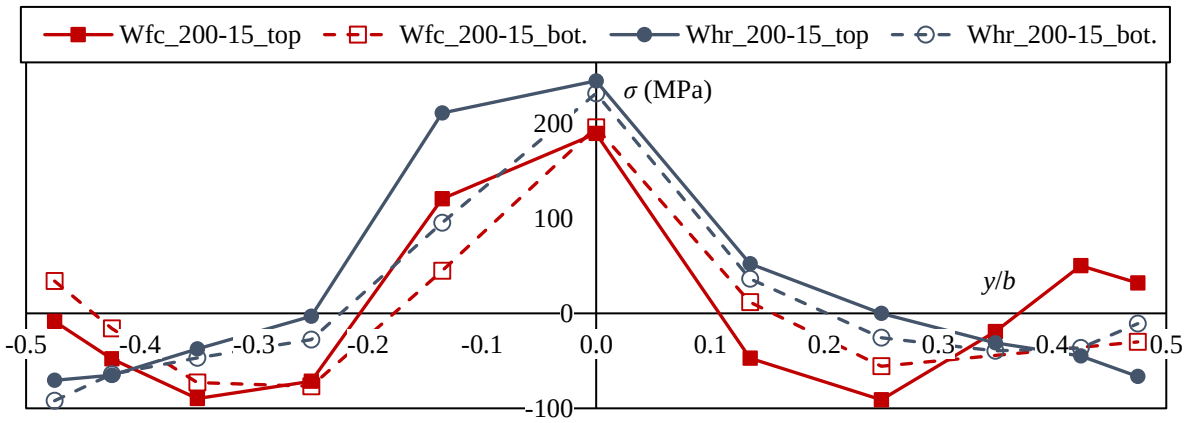

Figure V-11: Residual stresses in 200×15 mm for hot-rolled and flame-cut flanges

Both Figure V-11 and Figure V-12 exhibit significant differences in the residual stresses distributions between welded members having hot-rolled or flame-cut flanges. The differences are particularly visible at the flanges ends where flame-cut flanges present low tensile stresses while hot-rolled flanges present compressive stresses that reach their maximum values. The 15 mm-thick flanges present similar magnitudes of the compressive stresses but the peak values are attained at different locations. In the hot-rolled flanges, the maximum compressive stresses are measured at the flanges tips while they are attained closer to the centre for flame-cut flanges. The same observations can be made concerning the location of the maximum compressive stresses in the 20 mm-thick flanges. However, the compressive stresses magnitude is greater in the hot-rolled than in the flame-cut flanges. The width of the central tension zone is larger in hot-rolled than in flame-cut flanges where the maximum tensile stress near the welds is slightly lower.

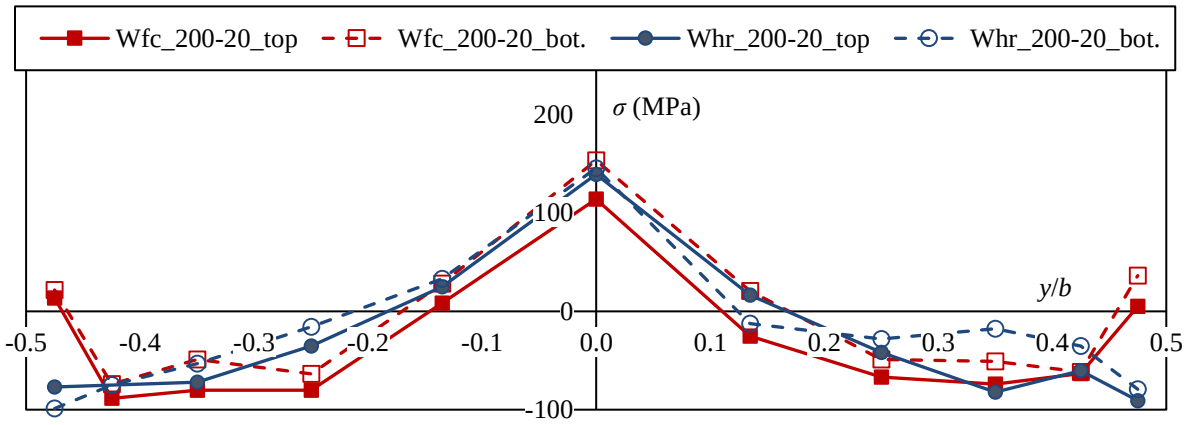

Figure V-12: Residual stresses in 200×20 mm hot-rolled and flame-cut flanges

Residual stresses distributions in the webs illustrated in Figure V-13 show lower compressive and a greater magnitude of the tensile stresses in pieces having hot-rolled flanges. The influence of the flange fabrication process in the web is more pronounced within the 15 mm-thick flanges specimens than in those having 20 mm-thick flanges.

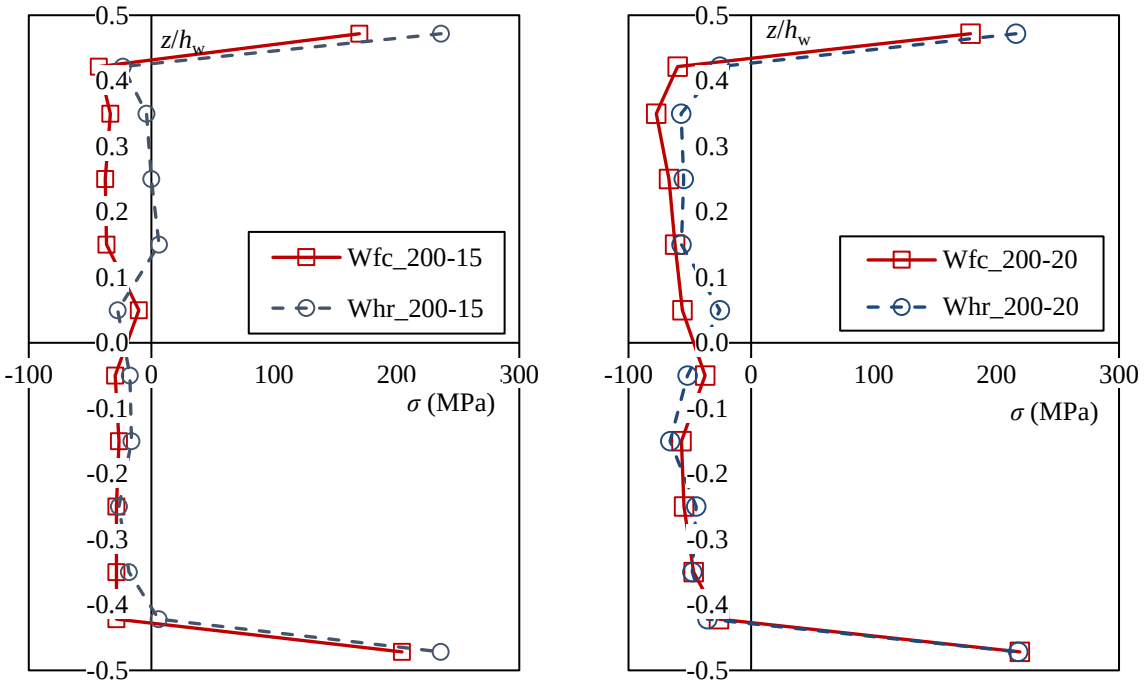

a) *Specimens with 15 mm-thick flanges* b) *Specimens with 20 mm-thick flanges*

Figure V-13: Residual stresses in the webs of specimens with hot-rolled or flame-cut flanges

Figure V-11 to Figure V-13 highlight the impact of the flange fabrication process on the residual stresses distribution in a welded member, proving relevant the development of distinct design methods.

Within members made of hot-rolled flanges, one can note that the measured distributions are quite different from the existing models. Indeed, in each model except that of *Schaper and Tankova* (2022), the yield strength is reached at the flanges centre. However, in Figure V-11 and Figure V-12 the maximum tensile stress is 59% of f_y, in 15 mm flanges. For this test specimen, the tensile stress predicted by the model of *Schaper and Tankova* (2022) is $0.75f_y$, which is closer to the experimental data than the

propositions of the other models. Besides, the maximum compressive stress, measured at a tip of a 20 mm flange, is 25% of the yield strength. This value corresponds to that proposed by the models of *prEC3-1-14* and *Kabir* (2018) while the other models overestimates it.

V.3.2.3. Effect of the flanges slenderness

Among welded members with flame-cut flanges, the effect of the flanges dimensions on the residual stresses configuration is studied. The experimental distributions measured in specimens having 200 and 250 mm-wide flanges with the same thickness are therefore compared. The results are then depicted for both couples of specimens *Wfc_200-15* and *Wfc_250-15*; and *Wfc_200-12* and *Wfc_250-12*.

Besides, the influence of the flanges slenderness being investigated, the effect of mono-symmetry is analyzed comparing results of specimens *Wfc_200-15*, *Wfc_200-20* as well as *Wfc_200-15/20*.

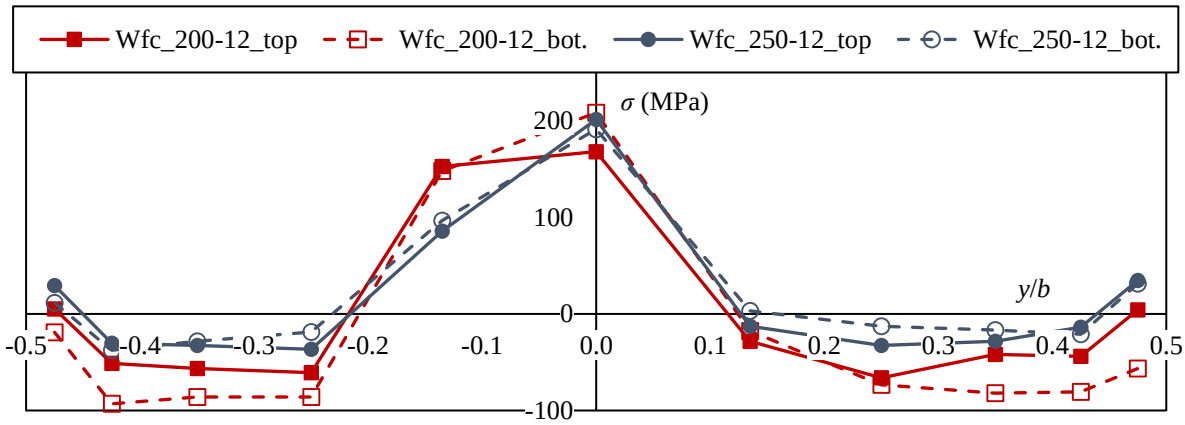

Figure V-14: Residual stresses in 12 mm-thick flame-cut flanges

Figure V-14 and Figure V-15 show the experimental residual stresses distribution in the flame-cut flanges that have a thickness of 12 and 15 mm, respectively. In agreement with results presented in Table V-5, both figures show that the magnitude of the compressive stresses decreases as the flange width increases. Within 15 mm-thick flanges, a larger central HSG zone is noted in the shortest flanges while being similar in all flanges having a thickness of 12 mm. In Figure V-14, stresses at the flanges tips are more favourable in the widest flanges where they attain approximately 30 MPa in tension. At the tips of the 200 mm-wide flanges, residual stresses are either compressive or in tension with a magnitude lower than 10 MPa. No effect of the flange widths on the tips stresses arises from distributions presented in Figure V-15.

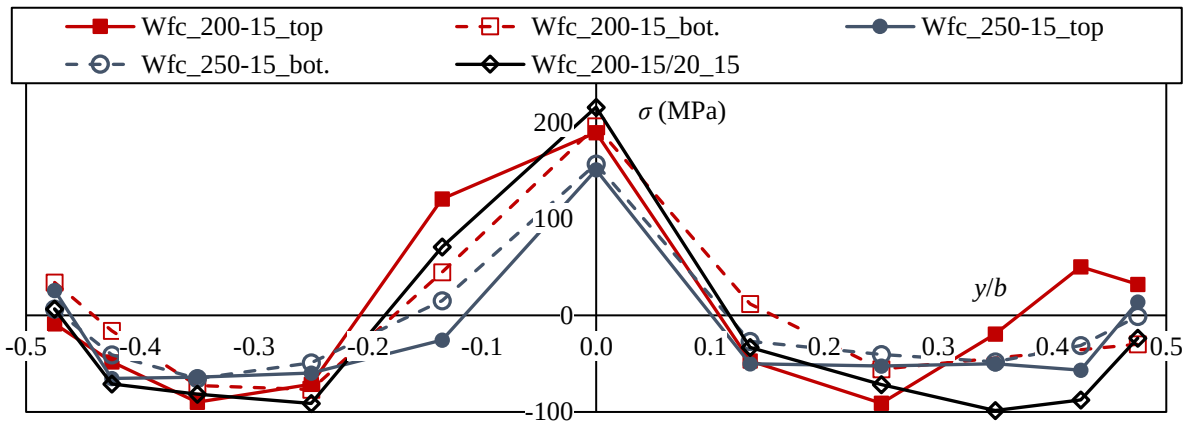

Figure V-15: Residual stresses in 15 mm-thick flame-cut flanges

Residual stresses in the web of specimens having two 12 or 15 mm-thick flanges are depicted in Figure V-16a). The thinner flanges result in lower magnitude of the tensile stress and in a slightly higher magnitude of the compressive stress. The link between the flanges width and the residual stresses distribution in the webs is not highlighted.

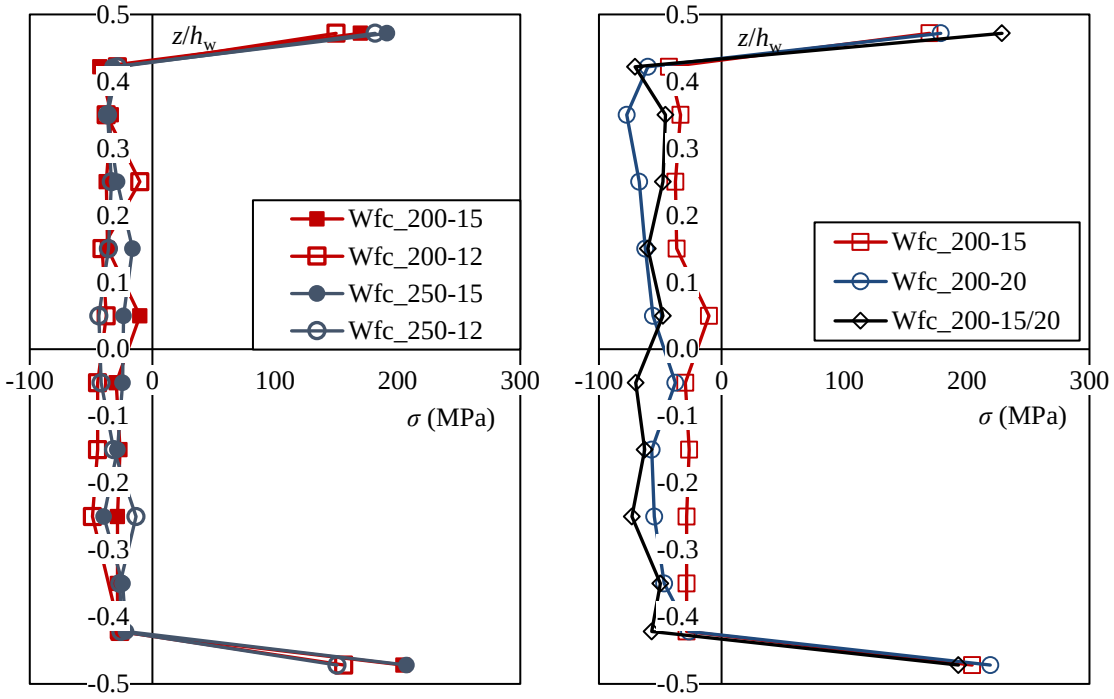

a) *Specimens with 12 or 15 mm-thick flanges*

b) *Specimens with 15/20 mm-thick flanges*

Figure V-16: Residual stresses in the webs of specimens having flame-cut flanges

Figure V-16b) shows the residual stresses distribution in the web of specimens having (i) two 200×15 mm flanges, (ii) two 200×20 mm flanges and (iii) a 200×15 and a 200×20 mm flange for which the top flange is 15 mm-thick. Tensile stresses being alike in both doubly symmetric specimens, no effect of the mono-symmetry can be observed on the web tensile stresses.

In doubly symmetric members, the compressive stresses are lower in the specimen made of 15 mm-thick flanges. The compressive stresses in *Wfc_200-15/20* being slightly more important near the thicker bottom flange, an impact of the mono-symmetry is noted.

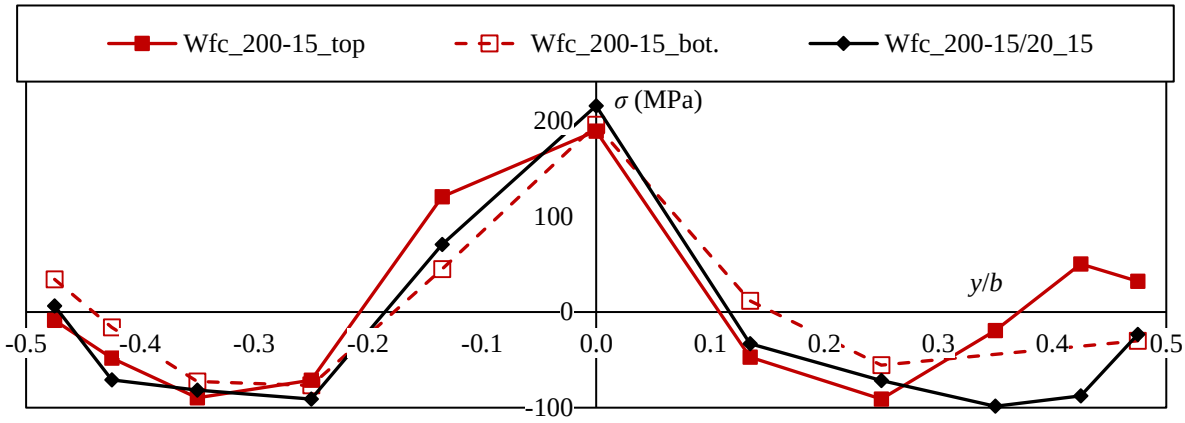

Figure V-17: Residual stresses in 200×15 flame-cut flanges

Residual stresses measured in both flanges of specimen *Wfc_200-15* and in the thinnest flange of specimen *Wfc_200-15/20* are presented in Figure V-17. No major differences are noticed between the three flanges that present similar magnitudes of the compressive and tensile stresses at every location, except near the flanges right end (y>0) where differences can be noted.

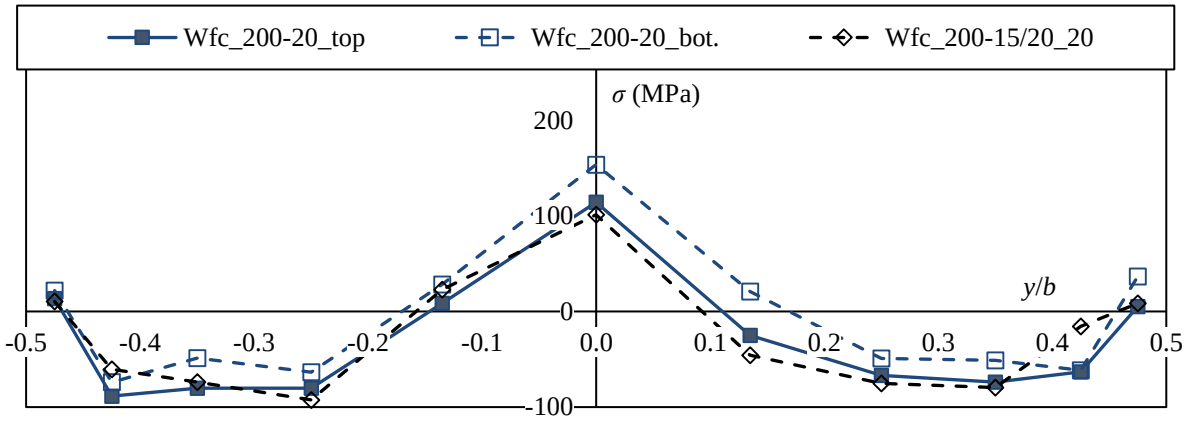

Figure V-18: Residual stresses in 200×20 flame-cut flanges

Figure V-18 exhibits the residual stresses distributions measured in both flanges of specimen *Wfc_200-20* and in the thickest flange of specimen *Wfc_200-15/20*. Similarly to the distributions shown in Figure V-17, no major differences can be noticed between the three 20 mm-thick flanges that present similar stresses at every position.

Both Figure V-17 and Figure V-18 show that the residual stresses in each flange of a mono-symmetric cross-section are not influenced by the distribution in the other flange while a small influence on the compressive stresses in the web can be seen in Figure V-16b). The same conclusions were drawn by *Schaper* (2019) where the residual stresses measurements showed no effect of the mono-symmetry in the flanges while in the web an impact was observed.

As explained in sub-section V.2.2, the model from *Chacón* (2009) is not self-equilibrated, while that of *Thiébaud* (2014) is adapted to bridge beams. In addition, the model of *Unsworth* (2021) revealed inappropriate to certain cross-sectional geometries. Neither of these models should therefore be considered to perform large parametric studies of GMNIA computations. Besides, the experimental distributions show that the models of *Barth* (1998) and *Schaper and Tankova* (2022) visibly overestimate the magnitude of the tensile stresses at the flanges ends. On the opposite, the model of

Yang (2017) clearly overestimates the magnitude of the flanges compressive stress. Using either of these models may produce inaccurate numerical results when performing GMNIA computations. Consequently, a new residual stress model for welded members with flame-cut flanges is proposed in the following section V.4.

V.4 Development of a model for welded I steel members with flame-cut flanges

The shortcomings of existing models led to the development of a new residual stress model. To that end, experimental results are accompanied by experimental data from the literature presented in Table V-6.

Source	Specimen designation	h_w (mm)	t_w (mm)	b (mm)	t_f (mm)	Steel grade	$f_{y,w}$ (N/mm²)	$f_{y,f}$ (N/mm²)
Yang (2017)	H1	280	8	200	10	Q345	398	458
	H2	380	8	200	10	Q345	398	458
	H3	380	8	200	10	Q345	398	458
	H4	332	8	220* 180**	10* 8**	Q345	398	458* 398**
Tankova (2019)	RS_1	317	12	100	12	S355	377	377
	RS_2	230	6	110	12	S355	362	371
	RS_5	311	10	100	16	S355	451	386
	RS_6	143	10	100	16	S355	443	392
Schaper (2019)	Pos. 1	370	8	350	20	S355	365	357
	Pos. 3-1	370	8	200	20	S355	351	340
	Pos. 4-1	370	8	350	12	S355	402	444
	Pos. 5	370	8	200* 350**	20* 40**	S355	462	334
	Pos. 1*	370	8	350	20	S355	363	357
	Pos. 3-1f_y	370	8	200	20	S460	554	452
	Pos. 4-2	370	8	350	40	S355	356	353
	Pos. 3-2	370	8	350	20	S355	365	450
	Pos. 1f_y	370	8	350	20	S460	552	444
	Pos. 2-2	800	8	350	20	S355	338	347
Unsworth (2020)	SP2_2	600	12.7	430	31.8	350W	364	347
Schaper & Tankova (2022)	B1	468	8	200	16	S460	/	/
	B4	278	8	300	16	S460	/	/

Table V-6: Specimens analyzed from the literature

These results have been published during the ten last years and comprise welded members made with flame-cut flanges and steel grade up to S460. The web thickness ranges between 5 and 15 mm, and the flange thickness between 8 and 40 mm.

The twenty-one specimens from Table V-6 present a nominal steel grade comprised between 345 and 460 MPa and concern mostly H-shapes sections with only three pieces having a web height greater than 400 mm while the smallest web is less than 150 mm-high. A wider spectrum is noticed concerning the other cross-section dimensions, thicknesses of the web plates varying between 6 and 12.7 mm while the flanges plates are 8 to 40 mm-thick. Most of the flanges widths are comprised between 100 and 350 mm while specimen SP2_2 from *Unsworth* (2020) present 430 mm-wide flanges.

Source	Specimen	$\sigma_{pc,f}/f_{y,f}$	$\sigma_{pc,w}/f_{y,w}$	η_f/b	η_w/h_w	$\sigma_{tip}/f_{y,f}$
Yang (2017)	H1	-0.14	-0.25	0.33	0.15	0.06
	H2	-0.09	-0.20	0.36	0.10	-0.02
	H3	-0.12	-0.13	0.36	0.11	0.02
	H4	-0.11* -0.20**	-0.18	0.37* 0.40**	0.13	0.07* 0.00**
Tankova (2019	RS_1	-0.25	-0.43	0.55	0.15	0.08
	RS_2	-0.12	-0.12	0.29	0.22	-0.03
	RS_5	-0.15	-0.31	0.48	0.14	0.22
	RS_6	-0.31	-0.39	0.36	0.31	0.11
Schaper (2019)	Pos. 1	-0.21	-0.04	0.13	0.11	0.33
	Pos. 3-1	-0.26	-0.18	0.32	0.11	0.17
	Pos. 4-1	-0.14	-0.10	0.33	0.11	-0.09
	Pos. 5	-0.25* -0.14**	-0.03	0.27* 0.28**	0.19	0.08* 0.12**
	Pos. 1*	-0.15	-0.09	0.18	0.11	0.36
	Pos. 3-1f_y	-0.22	-0.09	0.21	0.11	0.33
	Pos. 4-2	-0.14	Tensile stresses	0.24	0.32	0.35
	Pos. 3-2	-0.13	-0.06	0.14	0.11	0.41
	Pos. 1f_y	-0.13	-0.08	0.16	0.11	0.46
	Pos. 2-2	-0.11	-0.10	0.08	0.06	0.48
Unsworth (2020)	SP2_2	-0.14	-0.17	0.20	0.26	0.03
Schaper & Tankova (2022)	B1	-0.20	-0.20	0.39	0.12	0.15
	B4	-0.15	-0.21	0.36	0.17	0.07

Table V-7: Parameters of the residual stresses distributions from literature

The parametric compressive stress in the flanges $\sigma_{pc,f}$ and web $\sigma_{pc,w}$ along with the HSG zone widths in the flanges η_f and web η_w and the mean tensile stress at the flanges tips σ_{tip} calculated for specimens of Table V-6 are presented in Table V-7.

The parametric compressive stresses in the flanges are mostly comprised between 12 and 15% of the yield strength while some specimens exhibit a significantly higher value, up to 31% of the yield strength. Specimens *RS_1* and *RS_6* that present a flange parametric compressive stress of 25 and 31% of the yield strength correspond to members having unusual cross-section dimensions. *RS_1* have 12 mm-thick web and flanges and *RS_6* very stocky 100×16 mm flanges. Specimens *Pos. 3-1* and *Pos. 5* exhibit compressive stresses of 26 and 25% of the yield strength that are compensated by a low magnitude of the compressive stress in the web or important tensile stresses at the HSG region. Most of the web compressive parametric stresses are found between 8 and 14% of the yield strength. However, higher magnitudes are encountered in uncommon stocky webs at least 10 mm-thick or having a slenderness of 35 in the case of specimen *H1*.

Table V-7 shows that the width of the HSG region in the flanges varies a lot, most of them being comprised between 16 and 36% of the flange width. The width of the HSG is greater in the 100 mm flanges of specimens *RS_1* and *RS_5* as well as in the shortest flange of specimen *H4*. In the webs, most HSG widths are comprised between 10 and 15% of the plate height. This proportion increases up to 31% in specimens *RS_2* and *RS_6* due to small heights of 230 and 143 mm. Specimen *SP2_2* having 12.7 and 31.8 mm-thick web and flanges present a HSG width greater than a quarter of the web height. In specimen *Pos.4-2* having 40 mm-thick flanges, only tensile stresses are measured in the web, leading to a wide HSG zone.

Most residual stresses at the flanges tips are in tension, with extremely varying magnitudes which are null in a flange of specimen *H4* while reaching almost half of the yield strength in specimens *Pos. 1f$_y$* and *Pos. 2-2*. Some tips stresses are found slightly in compression, e.g. in specimens *H2* and *RS_2* where either low compressive stresses magnitude is measured in the flange (*H2*) or low tensile stresses magnitude is measured at the flanges centre (*RS_2*). Compressive stresses are measured at the tips of the slender flanges of specimen *Pos. 4-1*. However, these flanges are uncommon in practice because they are defined as Class 4 flanges according to *Eurocode 3 Part 1-1*.

A new residual stress model is developed for welded members with flame-cut flanges and compared to experimental results presented in Table V-5 and Table V-7. The new model is presented in Figure V-19 where stepped stress blocks are suggested to simplify its implementation in finite element analyses. The width of the tensile stresses at the flanges tips are set to a twentieth of the flange width, matching the width of the strips at the flanges tips from the experimental programme where tensile stresses has been measured and corresponding to the smallest width proposed in existing models.

The three parameters characterizing the model distribution from Figure V-19, $\boldsymbol{\sigma_c}$, $\boldsymbol{\sigma_{t,tip}}$ and $\boldsymbol{b_{HSG}}$ should be firstly calculated according to equations (V.13), (V.14) and (V.15):

$$\sigma_c = -f_y\left(0.25 - 0.005\frac{b}{t_f}\right) \leq -0.14 f_y \qquad \text{(V.13)}$$

$$\sigma_{t,tip} = f_y\left(0.70 - 0.35\frac{h_t}{b}\right) \geq 0.03 f_y \qquad \text{(V.14)}$$

$$b_{\mathrm{HSG}} = b\left(0.1 + 0.036\frac{h_{\mathrm{t}}}{b}\right) \tag{V.15}$$

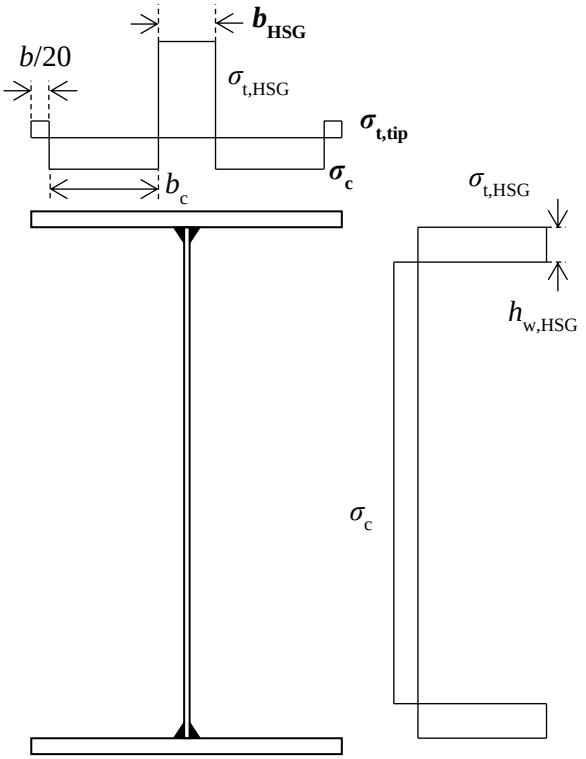

Figure V-19: Proposed residual stress model for welded members with flame-cut flanges

The compression block width b_{c} and the central tensile stress in the flange $\sigma_{\mathrm{t,HSG}}$ are determined from the plate equilibrium:

$$b_{\mathrm{c}} = \frac{9b - 10b_{\mathrm{HSG}}}{20} \tag{V.16}$$

$$\sigma_{\mathrm{t,HSG}} = -\frac{2b_{\mathrm{c}}\sigma_{\mathrm{c}} + \frac{b}{10}\sigma_{\mathrm{t,tip}}}{b_{\mathrm{HSG}}} \tag{V.17}$$

The tensile stress in the HSG region $\sigma_{\mathrm{t,HSG}}$ is identical in the flanges and web, and so are the compressive stresses in the web and the flanges σ_{c}. The widths of the tension and compression zones in the web are determined from the plate equilibrium.

The proposed pattern is applicable to mono-symmetric cross-sections equating the tensile stresses magnitude in the web $\sigma_{\mathrm{t,w}}$ to the mean value of the tensile stresses in the HSG region of both flanges (see equation (V.18)). Similarly, the compressive stress in the web of a mono-symmetric member $\sigma_{\mathrm{c,w}}$ is set as the mean value of that in both flanges (see equation (V.19)).

$$\sigma_{\mathrm{t,w}} = \frac{\sigma_{\mathrm{t,HSG,f1}} + \sigma_{\mathrm{t,HSG,f2}}}{2} \tag{V.18}$$

$$\sigma_{c,w} = \frac{\sigma_{c,f1} + \sigma_{c,f2}}{2} \qquad \text{(V.19)}$$

The stresses calculated with equations (V.13) and (V.14) are proportional to the yield strength and dependent on the cross-section dimensions through the web slenderness b/t_f and the total height-to-width ratio h_t/b. The same can be said concerning the width of the central tension block that also depends on the ratio h_t/b according to equation (V.15).

The parametric compressive and tip stresses, calculated according to the proposed equations, are presented in Figure V-20 and Figure V-21 and compared against experimental results given in Table V-5 and Table V-7. The magnitude of the compressive stresses increases as the flange slenderness decreases, equation (V.13) representing a relevant higher bound. However, some experimental results present more compression than obtained using equation (V.13). As explained before, these results correspond to specimens having flanges stockier than the common practice or where the important compressive stresses are compensated on the rest of the cross-section.

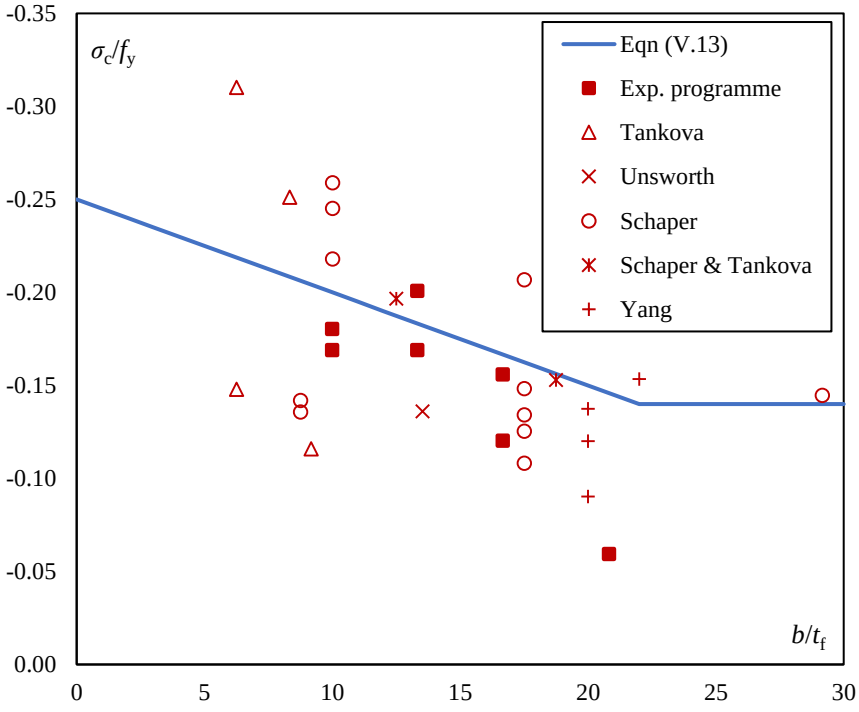

Figure V-20: Compressive stress in flanges

Stresses at the flanges tips displayed in Figure V-21 show a global trend, decreasing while the height-to-width ratio increases. The predictions of equation (V.14) are in good agreement with most experimental results while being a lower bound to the greatest number of results. However, some experimental values are below, especially when in compression.

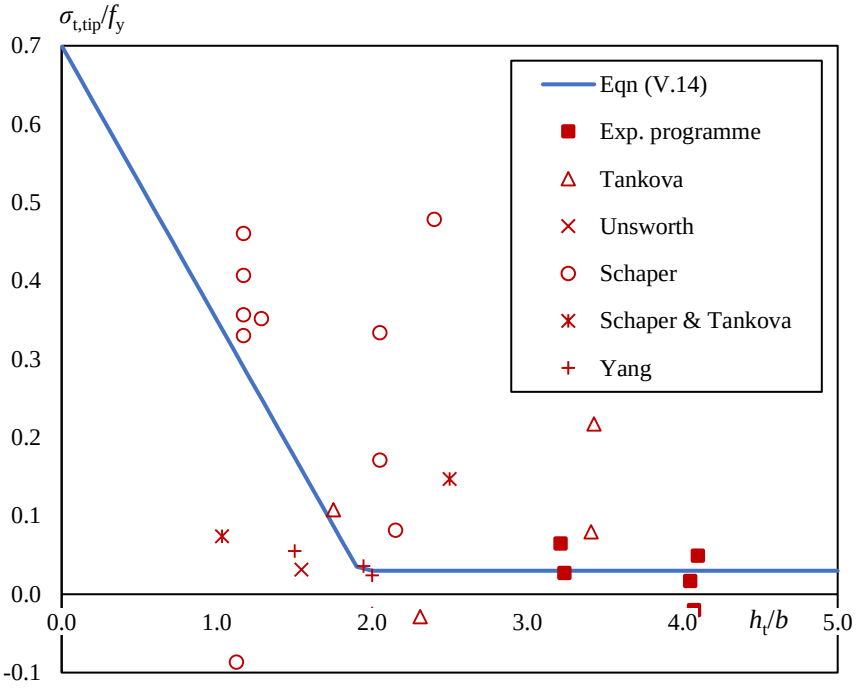

Figure V-21: Stress at the flange tips

The width of the central tension block in the flanges calculated with equation (V.15) is compared to experimental results in Figure V-22. A linear increase of the stress block width with h_t/b is visible, equation (V.15) corresponding to a mean increase. It is worth mentioning that b_{HSG} is different from η_f, the former width corresponding to the width of an "ideal" uniform tension block while the latter corresponds to the width of the "real" tension block, which is between a rectangular and a bi-triangular region.

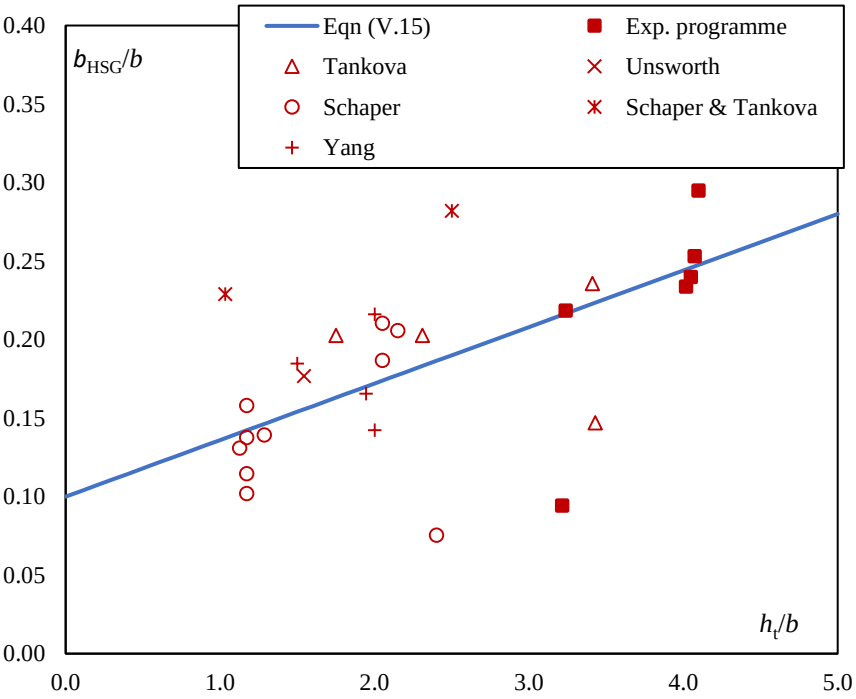

Figure V-22: Width of the central tension zone in flanges

Statistical parameters of the differences between the experimental parametric compressive stresses and those obtained using expression (V.13) are presented in Table V-8. The results concerning stresses at the flange tips are also given (see expression (V.14)). The mean and standard deviation of the difference between the experimental and analytical stresses normalized to the yield strength are given in Table V-8.

The mean deviation for the compressive stresses is very small and corresponds to 1.5% of f_y. In the case of the stresses at the flange tips, the mean value is also very small, being lower than 3% of f_y. Keeping in mind that compressive stresses are negative, positive values of the differences place the analytical stresses on the safe side for both studied parameters.

In addition, the standard deviation for the compressive stress is very low, being lower than 5% of the yield strength. However, as shown in Figure V-21, the results are more scattered for stresses at the flanges tips. Thus, the standard deviation for this parameter is more important, standing just under 16% of f_y.

Parameter of the model		
$\frac{\sigma_{c,exp} - \sigma_{c,(V.13)}}{f_y}$	*M*	*1.5%*
	SD	4.52%
$\frac{\sigma_{t,tip,exp} - \sigma_{t,tip,(V.14)}}{f_y}$	*M*	*2.7%*
	SD	15.62%

Table V-8: Comparison between experimental results and the model values

In spite of the scarcity of experimental data, particularly concerning members having a height greater than 400 mm, the proposed model is based on measurements performed in members having a total height-to-width ratio ranging between 1.03 and 4.10 and flanges slenderness comprised between 6.25 and 29.17, which covers most of the steel building members in practice.

V.5 Conclusion

Experimental tests have been performed at the University of Liège to determine the residual stresses of eight welded members made from S355 steel with 780×8 mm webs while the flanges widths are 200 or 250 mm. The flange thicknesses range between 12 and 20 mm to analyze the impact of the flange slenderness on residual stresses. Both flame-cut and hot-rolled flanges are investigated to confirm the influence of the fabrication process on the stress distribution. Besides, a mono-symmetric cross-section was studied.

The tests results have shown significant differences between hot-rolled and flame-cut flanges, particularly at the flanges tips. Indeed, members with flame-cut flanges present more favourable residual stresses distributions because flanges tips are in tension. Besides, within members made of flame-cut flanges, those with the widest flanges present a (slightly) lower magnitude of the compressive stress. The flange slenderness has a negligible impact on the stress distribution in the web. However, unlike in the flanges, the mono-symmetry has a slight effect on the stress distribution in the web.

Experimental distributions in members having flame-cut flanges are not in line with the predictions of existing models (*Barth* (1998), *Chacón* (2009), *Thiébaud* (2014), *Yang* (2017), *Unsworth* (2021),

Schaper and Tankova (2022)). Therefore a residual stress model is developed, adapted to welded members having flame cut-flanges made using common steel grade. This new model is based on experimental results and on data concerning nineteen specimens from the literature. The flange compressive stress decreases as the flange slenderness increases while the tensile stress at the flanges tips decreases as the height-to-width ratio increases. Besides, the HSG region width increases with the latter ratio. Linear expressions are therefore proposed to determine the compressive stress in the flange depending on the flange slenderness and to obtain the tensile stress at the flanges tips and the width of the central tension block based on the height-to-width ratio of the cross-section. The width of the compressed part as well as the magnitude of the tensile stresses at the flanges centre are determined by self-equilibrium. The stresses in the web having a negligible influence of the buckling behaviour, their values are similar to those in the flanges. The widths of the compressive and tensile zones are determined from the plate equilibrium. In addition, the model is applicable to mono-symmetric members by implementing in the web the average values of the compressive and of the tensile stresses in both flanges.

The new model is then employed in the following chapters to perform GMNIA type calculations of welded members made of flame-cut flanges subjected to a compressive force and/or bending moment.

VI. *Lateral-torsional buckling of welded steel members: Experimental tests*

VI.1 Introduction

The resistance of a steel member against overall out-of-plane buckling is defined in *Eurocode 3 Part 1-1* based on numerous experimental and numerical results. However, as explained in Chapter IV, the existing European design rules, which rely on a consistent mechanical background can exclusively be applied to members having a constant cross-section. However, the General Method, that lacks a coherent background, can be used with non-uniform members. Unlike the elastic buckling behaviour of a steel member, its elasto-plastic behaviour cannot be apprehended without experimental tests that are further used to calibrate a numerical model. Many researchers performed therefore experimental tests on bent and/or compressed steel welded members.

Some of the experimental programmes on welded steel members found in the literature are described first. The original experimental programme is then detailed consisting in four welded members with flame-cut flanges bent by a single hydraulic jack and resting on fork supports at both ends. The main results of the experimental programme are eventually depicted.

VI.2 Experiments from the literature

In Europe, an extensive experimental programme was performed in the 1960s on compressed members, as described by *Sfintesco* (1970) that led to the current *Eurocode 3 Part 1-1* buckling curves. Experiments were also performed at Lehigh University, by *Estuar* (1962) and *Cranston* (1967). Respectively two and twelve welded I-members having compact cross-sections as described in Chapter V and nominal yield strengths ranging between 207 and 345 N/mm² were uniformly compressed. The geometrical out-of-plane slenderness λ_z of the welded specimens were comprised between 32 and 103. Specimens with hot-rolled flanges were studied by *Estuar* (1962) while both hot-rolled and flame-cut flanges tested by *Cranston* (1967). The latter study concluded that the specimens with flame-cut flanges had better resistances than the identical ones with hot-rolled flanges. As described in Chapter V, this difference comes from the residual stresses distribution in the member mainly influenced by the flange fabrication process.

Later, *Prawel* (1974) exposed an experimental programme that consisted in three tapered beams under a linear bending moment and resting on fork supports and twelve tapered or uniform inclined cantilevers subjected to a vertical load at their free end. The ratio between the cross-sections heights at both ends of the beams were 2.67. The values for this ratio were 1, 2 and 3 for the beam-column specimens where half of the specimens were made of flame-cut and half of hot-rolled flanges. The flanges width were 102 and 152 mm while the smallest cross-section had an overall height of 152 mm. Similarly to the

conclusions drawn by *Cranston* (1967), *Prawel* (1974) concluded that the specimens with flame-cut flanges had a higher stability resistance than analogous specimens with hot-rolled flanges.

Fukumoto (1981) led an extensive experimental programme on sixty-eight S235 welded uniform beams having the same cross-section dimensions consisting of 100×8 mm hot-rolled flanges and 234×6 mm webs. The specimens were split in two equal groups of 1.8 and 2.6 m-long members, falling in the inelastic range with normalized slenderness of 0.84 and 1.10, respectively. Initial in-plane, out-of-plane and twist rotational geometrical imperfections were measured at mid span, resulting in mean values of $L/8000$, $L/3378$ and 0.03°, respectively. Using the two series of thirty-four results yields that the standard deviation, when compared to the mean experimental resistance, is slightly greater in the group of 2.6 m-long specimens than within the shortest specimens, being 11 and 10%, respectively. Besides, owing to a greater magnitude of the compression residual stresses and geometrical imperfections, it was concluded that the ultimate resistances of welded members was lower than those of similar hot-rolled members.

Avent (1982) described an experimental programme that consisted in testing eight welded columns with hot-rolled flanges. Two sets of four specimens having similar cross-section dimensions were tested. One set involved stud tests for which the length was thrice the column height. The other set concerned inelastic buckling, normalized slenderness ranged between 0.74 and 1.11. The uniform members had a nominal yield strength of 345 MPa. The web heights were 229 or 305 mm and the flanges widths 127 or 152 mm. The thickness were 3.2 and approximately 6 mm, respectively. It is found that the resistance of these thin-walled welded columns is more important than those suggested by the European buckling curves.

Kubo (1988) investigated the interaction of local and lateral-torsional buckling by testing twenty-two welded uniform specimens made with hot-rolled flanges. The measured yield strengths ranged between 262 and 316 MPa. The overall height of the specimens varied between 200 and 300 mm while their widths were comprised between 125 and 151 mm. The length was chosen to obtain out-of-plane geometrical slenderness λ_z approximately equal to 50, 70 and 100 and thus inelastic buckling. The load jack was applied 25 mm above the top flange at mid span were a thin 3.2 mm stiffener was placed. Failure modes governed by lateral-torsional buckling were found for the longest beams while combined local and global buckling was observed for the other specimens. Initial in-plane and out-of-plane geometric imperfections were measured with mean values of the amplitudes of $L/7300$ and $L/5320$, respectively. The results were used by the authors to propose an interaction formula based on the effective width method.

The interaction between local and lateral-torsional buckling was also investigated in the Master thesis presented by *Richter* (1998) depicting an experimental programme of twenty-eight welded members subjected to a uniform bending moment distribution. All members had either 127×7.8 or 152×6.5 mm flanges. The web height was comprised between 305 and 762 mm with a thickness of 4.1 mm. The length of the test specimens varied between 0.92 and 7.35 m. No information is given about the flange fabrication process but one may assume that the test specimens were made of hot-rolled flanges. Indeed, *Kim* (2010) performed finite element analyses using the *best-fit Prawel* residual stress model (see Chapter V) and obtained an average 10% deviation from the experimental results of *Richter* (1998). The tests results were used to propose adaptation of the American design rules *AISC* regarding the local-global buckling interaction.

As part of the *ESCS Steel RTD Programme* (2001) that concerned the lateral-torsional buckling of steel beams, four S355 tapered beams were tested at the University of Liège (see Figure VI-1a)). The specimens had 180×10 hot-rolled flanges while web height was varying from 300 to 600 or 900 mm

with thickness of 8 or 10 mm. The beams were almost 6 m-long and subjected to a linear bending moment distribution. Three of the specimens were reversed upside down after testing to perform again a lateral-torsional buckling test. The initial out-of-plane imperfections were measured using a virtual reference line, the distance to which being measured at seven cross-sections along the specimen. The maximum lateral imperfection in a compressed flange was equal to $L/1087$ prior to any loading while within the three reversed specimens, the lateral imperfection were ranging between $L/1365$ and $L/748$. The results of this research project were employed to develop the software *LTBeam* that provides the elastic critical bending moment of a bent I-member having, or not, a uniform and doubly symmetric cross-section.

a) *Beam test from* ESCS Steel RTD Programme *(2001)*

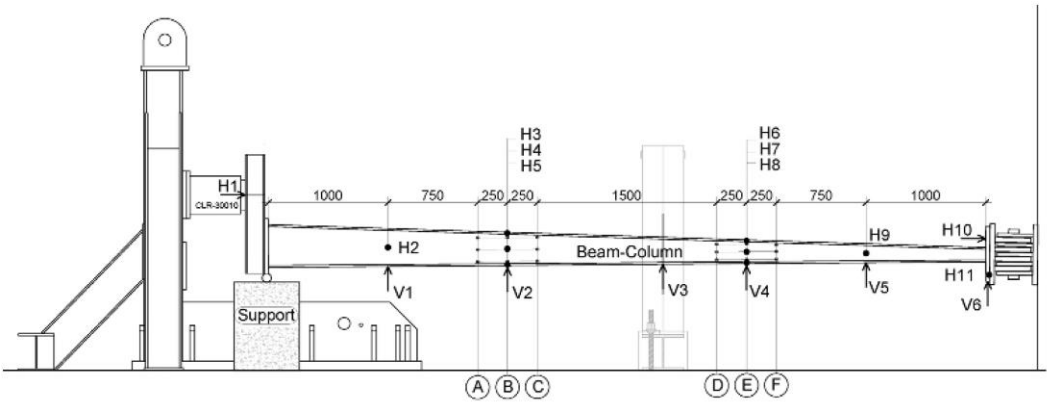

b) *Beam-column test from* Tankova *(2018a/b)*

Figure VI-1: Test set-ups for non-uniform members from the literature

Later, *Kwon* (2007) investigated the interaction of local and global inelastic buckling testing in compression five welded I-section members. The specimens had hot-rolled flanges and were fabricated from 6 mm-thick plates having a nominal yield strength of 240 MPa. The web slenderness varied between 67 and 92 while the flanges slenderness were comprised between 8 and 13. The members length ranged between 1.4 and 2.4 m. The test results were used to develop for welded members the *Direct Strength Method* (DSM) derived initially for cold-formed members. *Kwon* (2012) again studied the

local-global buckling interaction on fifteen beams loaded in bending fabricated from 6 mm-thick hot-rolled plates having a nominal yield strength of 315 N/mm². The webs slenderness were similar to those of the compressed members but the flanges slenderness were more important, ranging between 13 and 33. The members length were 3, 5 or 10 m. The test results were employed to adapt the *DSM* to welded steel members subjected to bending. A summary of *DSM* adaptations proposed by *Kwon* (2007, 2012) on welded members is exposed in 2014 by the same author.

More recently, *Tankova* (2018a) described an experimental programme that concerned six specimens, three being compressed and two bent. The last one was compressed with eccentricity, resulting in both bending and compression in the member. The beam-column test set-up is presented in Figure VI-1b), extracted from *Tankova* (2018b). The six S355 tapered welded specimens were fabricated from flame-cut flanges. The flange widths of the columns and the beam-column were 100 and 110 mm with thicknesses of 12 or 16 mm while both beams had 200×16 mm flanges. The beams had a web height varying from 250 to 1000 m over their length, with a thickness of 6 or 15 mm. In the four other specimens, the webs at their smallest ends were 120 or 185 mm-high and the ratio between the web height at both ends was 2, 3 or 4. Two of the tapered columns, where in-plane buckling was investigated, had both flanges inclined while the four other specimens had a single flange inclined. The global in-plane and out-of-plane out-of-straightness of the columns and the beam-column were measured using a nylon string tied to the members ends and maximum values of the imperfection amplitudes of $L/2727$ and $L/1333$, respectively, were found. A 3D Laser system was used to map the geometric imperfections in the two beams and a maximum imperfection of $L/1039$ was measured, corresponding to combined local and global geometrical imperfections. This study resulted in a new design method to assess the stability of a steel member having, or not, a uniform and doubly symmetric cross-section, which is depicted in Chapter IV.

Schaper (2019) described an experimental programme that consisted in eight uniform welded members made of flame-cut flanges. One specimen had a mono-symmetric cross-section while the other seven had doubly symmetrical cross-sections. The specimens all had a 370×8 mm web with 200 or 350 mm-wide flanges that were 12, 20 or 40 mm-thick. The distance between supports was 6 or 10 m. Using a Laser scanner, the initial in-plane, out-of-plane and twist rotation were measured and maximum values of $L/828$, $L/2125$ and 0.46° were found. The transverse load applied at mid-span was introduced using a hydraulic jack located under the bottom – compressed – flange, as depicted in Figure VI-2a) extracted from *Schaper* (2019). A roller rail system was being employed to allow for a lateral displacement of the hydraulic jack. The test results were used as an experimental background for the modified method of the equivalent compression flange included in *prEN 1993-1-1*.

Ji (2019, 2022) depicted a series of eleven uniform welded members subjected to bending moment having either flame-cut or plasma-cut flanges. The specimens had a nominal yield strength of 350 MPa. The webs height were comprised between 600 and 900 mm with thicknesses of 9.5 or 12.7 mm. The flanges were 300 to 470 mm-wide with thicknesses of 25.4 to 31.8 mm. The beams were resting on fork supports at both ends, the buckling length being 9.75 m. Eight hydraulic load jacks were placed on the beams compression flange with a constant spacing of 1.22 mm except near both ends where the distance was 0.61 m to the fork supports, as depicted in Figure VI-2b) extracted from *Ji* (2019, 2022). Initial global geometrical imperfections were measured in five regularly spaced cross-sections using a string for out-of-plane imperfection, a Laser line for in-plane imperfection and a digital protractor for the twist rotation. The maximum twist rotation was 1.3° while the maximum initial out-of-plane imperfection measured in the compressed flange was $L/1389$ and a maximum in-plane imperfection of $L/1000$ was found. The experimental results showed a negligible difference between the resistances of the specimens

made of flame-cut and plasma-cut flanges. Besides, most experimental results are close to those obtained using the Canadian standard *CSA S16-14*. However, the analytical resistance of one specimen is significantly overestimated while that of a different specimen is underestimated.

a) *Beam test from* Schaper *(2019)*

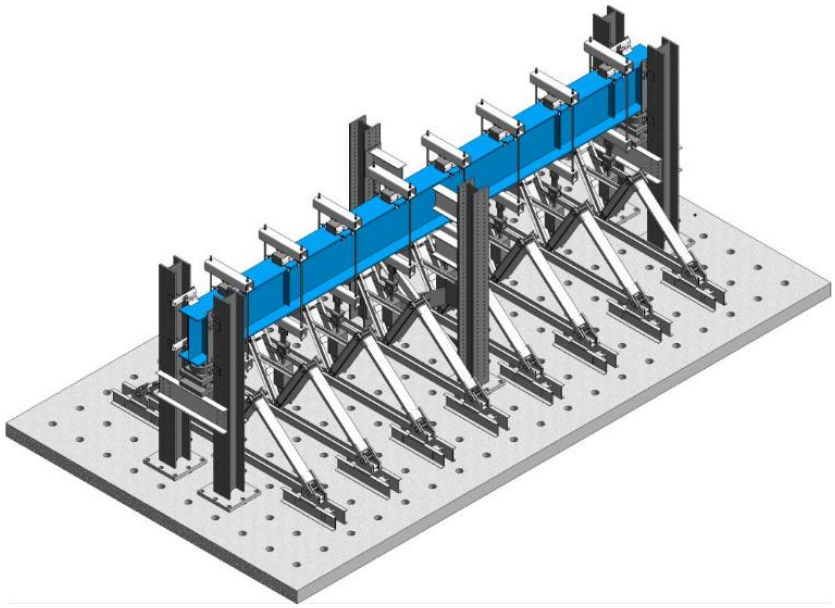

b) *Beam test from* Ji *(2019,* 2022*)*

Figure VI-2: Test set-ups for uniform members from the literature

Previous experimental programmes focusing on the stability of welded steel members have been depicted in the present section. From the results of the experimental studies arose the greater resistance of welded members made of flame-cut flanges when compared to those having hot-rolled flanges, proving relevant the use of distinct design methods. However, a scarcity of experimental data concerning welded members with flame-cut flanges having usual dimensions is noticed.

Indeed, since the experimental programme from *Prawel* (1974), only *Tankova* (2018a), *Schaper* (2019) and *Ji* (2019, 2022) have tested members made of flame-cut flanges. The latter programme contained only uniform doubly symmetric beams though mono-symmetric and/or non-uniform members are of common use for steel buildings. *Schaper* (2019) also presented an experimental programme concerning exclusively uniform members, only one of the tested beams having a mono-symmetric cross-section. Besides, the specimens presented an overall height of approximately 400 mm, which is smaller than the common practice. The stability of non-uniform welded members made of flame-cut flanges was

investigated recently only by *Tankova* (2019a), but all test specimen had a doubly symmetric cross-section.

A new experimental programme is therefore performed and described next, investigating the effects of mono-symmetry and tapering of a welded member made of flame-cut flanges.

VI.3 Experimental tests description

VI.3.1 Full-scale specimens

The experimental programme, conducted at Polytech' Clermont, aims to a better understanding of the global out-of-plane buckling behaviour of welded members with flame-cut flanges. It included lateral-torsional buckling tests on two uniform and two tapered members, one having a mono-symmetric cross-section while the other is doubly symmetrical within both groups. The length of the four S355 beams as well as the test set up was similar. One load jack applied a downward force on the top flange of a laterally restrained cross-section located at 2.18 m from a fork support – defined as left support. The load jack is applied at L_d = 6.25 m from the other support. The nominal dimensions of the tested members are given in Table VI-1. They are also presented in Figure VI-3 with the set up.

Both uniform members *U-DS* and *U-MS* present Class 3 webs according to *Eurocode 3 Part 1-1*, being 786×8 mm. In both non-uniform members, the web height varies linearly from 286 to 836 mm. All flanges are 200 mm-wide while their thickness in both doubly symmetrical members are 15 mm. The tension flanges of both mono-symmetric members are also 15 mm-thick, their compression flanges being 5 mm thicker. In addition, on both sides of the web 30 mm-thick transverse stiffeners are placed at the 3 laterally restrained cross-sections. Besides, a longitudinal 20 mm-thick stiffener is positioned on both sides of the web along the 2.18 m-long segment.

In addition, in both non-uniform beams, 20 mm-thick transverse stiffeners are placed 200 mm away from the loaded section. They are located at the cross-section between the uniform and the tapered parts of the members. The distance of 200 mm was chosen to ensure the jack application on a horizontal surface.

Designation	h_w (mm)	t_w (mm)	b (mm)	t_f (mm)	Steel grade	L_d (m)	Total length (m)
U-DS	786	8	200	15	S355	6.25	8.83
U-MS	786	8	200* 200**	20* 15**	S355	6.25	8.83
T-DS	286 to 836	8	200	15	S355	6.25	8.83
T-MS	286 to 836	8	200* 200**	20* 15**	S355	6.25	8.83

Table VI-1: Nominal properties of the specimens for lateral-torsional buckling tests

*: Compression flange

**: Tension flange

The specimens dimensions as well as their steel grade are chosen to cope with current practice of steel building. The mono-symmetry is implemented by modifying the compressed flange thickness only, its width being unchanged when compared to the tension flange. This choice matches with common practice and leads to simpler lateral restraints set up when compared to different flanges widths. The global out-of-plane buckling being investigated, local and shear buckling have been avoided using 8 mm-thick webs that places only a small portion of specimen *T-DS* in Class 4 according to *Eurocode 3*.

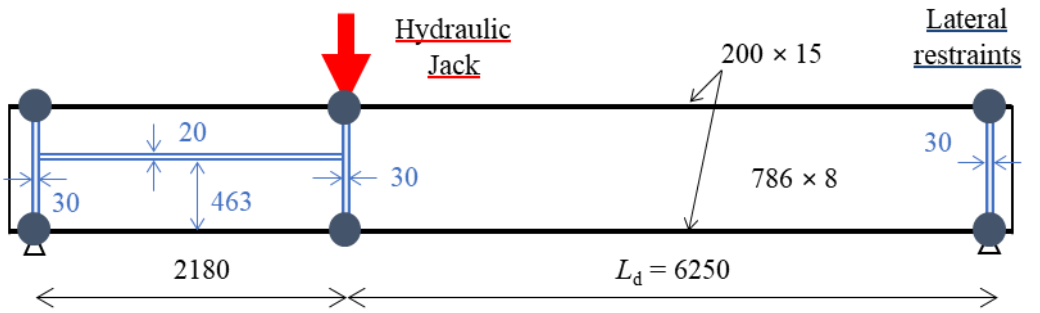

a) *Specimen U-DS*

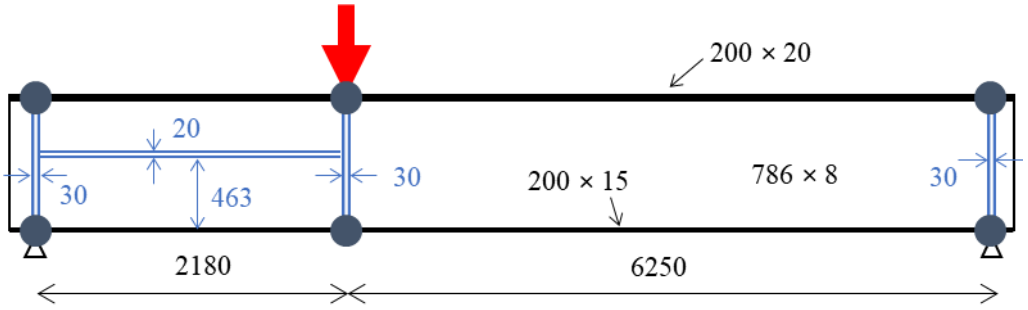

b) *Specimen U-MS*

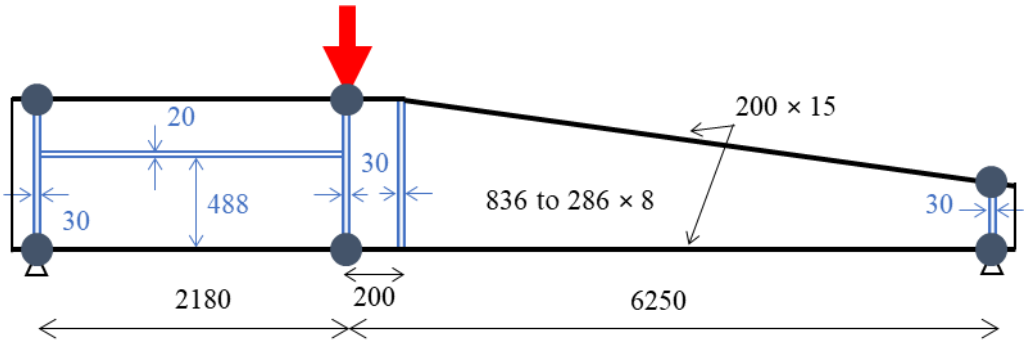

c) *Specimen T-DS*

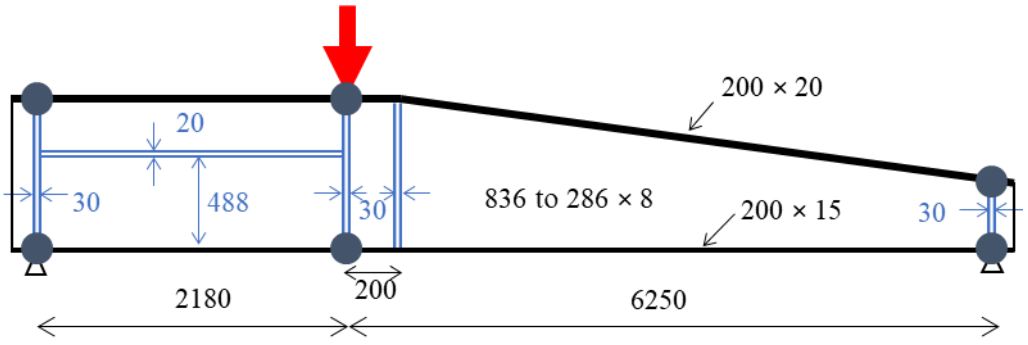

d) *Specimen T-MS*

Figure VI-3: Specimens tested (dimensions in mm)

A fork support and the load introduction set-ups are presented in Figure VI-4.

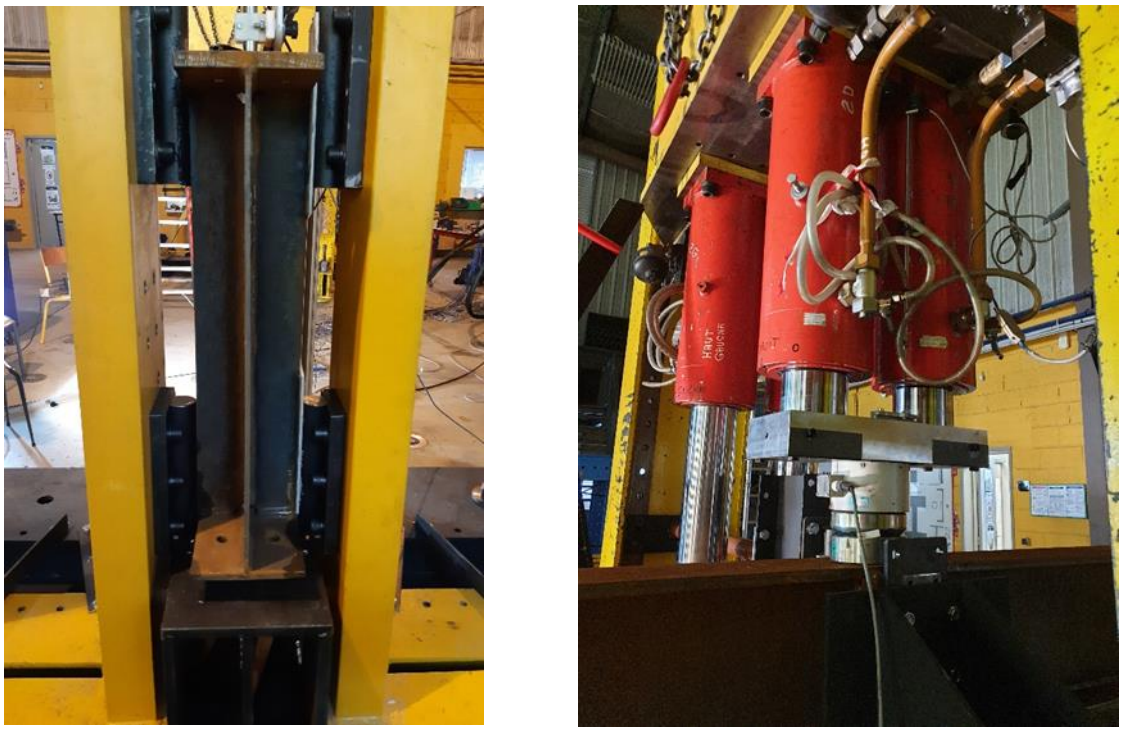

a) *Fork support* b) *Load introduction*

Figure VI-4: Test set-up

VI.3.2 Measurements prior to loading

The cross-section dimension of the test specimens have been measured along with the global and local geometrical imperfections. The material properties have been measured according to standard *ISO 6892-1* on three coupons from 8 and 15 mm-thick plates and on four coupons from 20 mm-thick plates. The 8 and 15 mm-thick- plates and two of the 20 mm-thick coupons are collected from extra 300×400 mm plates delivered with the beams. Two 20 mm-thick coupons were extracted from the compressed flange of specimen *T-MS* after the test.

Thickness (mm)	***E* (N/mm²)**		***f_y* (N/mm²)**		***f_u* (N/mm²)**	
	M	***SD***	***M***	***SD***	***M***	***SD***
8	203283	2937	421	1.6	550	3.4
15	209049	1426	411	6.2	542	3.5
20	197821	4678	390	6.1	539	6.3

Table VI-2: Material properties of the steel plates

The mean (*M*) and standard deviation (*SD*) of the measured elasticity modulus *E*, the yield strength f_y and the ultimate stress f_u are given in Table VI-2. The yield strength increases as the thickness decreases. The actual yield strength is 10 to 19 % greater than its nominal value, the standard deviation being close to 6 N/mm² in 15 and 20 mm-thick plates.

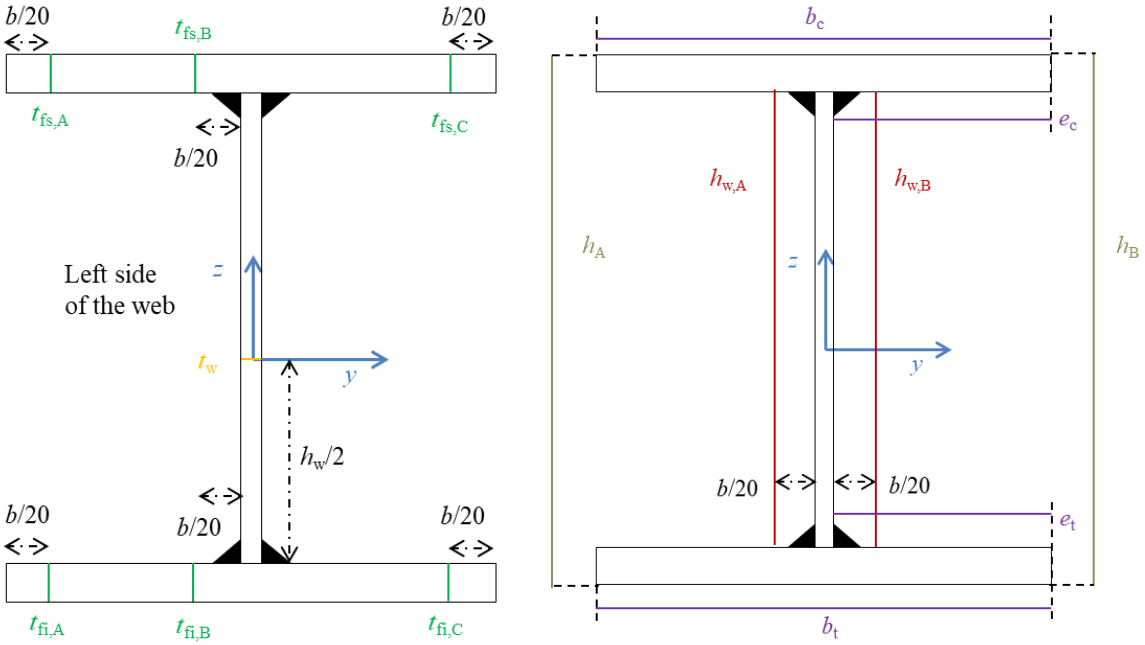

a) *Thickness measures* b) *Width measures*

Figure VI-5: Location of the dimensions measurement

The cross-section dimensions have been measured on four transverse cross-sections located at 1.75, 3.5, 5.25 and 7 m from the left fork support. The dimensions have been measured as exposed in Figure VI-5.

The actual dimensions are divided by their nominal values, the results being used to calculate the mean (*M*) and standard deviation (*SD*) for each measured dimension which are given in Table VI-3. The mean deviation is at most 1%. Standard deviations are lower than 1% except for the web thickness where a larger deviation of 2.3%, which is still admissible, can be assigned to its small dimension.

Dimension	*M*	*SD*
Overall height	1.000	0.0062
Web height	0.999	0.0063
Web thickness	1.005	0.0227
Flange width	1.003	0.0075
Flange thickness	1.011	0.0080

Table VI-3: Statistical parameters of the actual dimensions of the test specimens

Angles at the junction between the web and the compression flange have also been measured within the four cross-sections of interest, the results being given in Table VI-4. The sum of both angles is comprised between 178.4 and 178.9°, characterizing a local imperfection in the flanges shown in Figure VI-6. Although a slight tile shaping of the flanges is noticed, other flange local imperfections exist. Indeed, the sum of all flanges local imperfections yields a greater distance between the flanges tips than their centres, as exposed in Table VI-3 when relating the average overall and web heights and the flanges thickness.

Specimen	U-DS	U-MS	T-DS	T-MS
Angle on the left side of the web (°)	88.1	87.8	88.5	88.7
Angle on the right side of the web (°)	90.3	91.3	90.4	90.2

Table VI-4: Mean angles at the web-to-compression flange junction

In addition to cross-sectional dimensions, web local geometrical imperfections have been measured in the same cross-sections using a steel ruler associated with five callipers. Two callipers were located close to the web-to flange junctions, one at mid-height and the last two at a sixth of the web height from the web centre towards each flange. The magnitudes of the web plate local imperfections in all specimens are given in Table VI-5 along with their values compared to the web height measured at the corresponding cross-section.

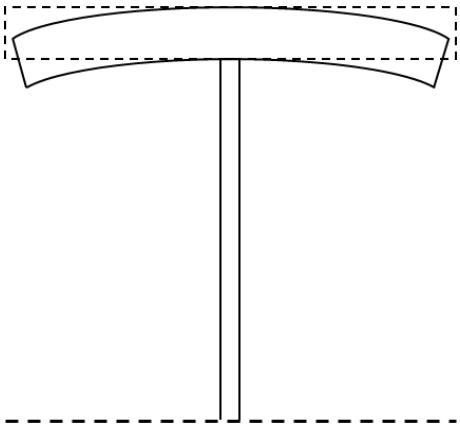

Figure VI-6: Local imperfection of a tile shaped flange

Table VI-5 shows that the amplitude δ of the local imperfections is lower than or equal to 4.83 mm (approximately $h_w/164$) in all specimens, corresponding to the fabrication tolerance according to *EN 1090-2* given by:

$$\delta = \pm \frac{h_w^2}{16000 t_w} \tag{VI.1}$$

which is applicable when:

$$80 \leq \frac{h_w}{t_w} < 200 \tag{VI.2}$$

The imperfection amplitude is significantly lower in specimens *U-DS* and *T-MS* than in the two other specimens where values between $h_w/200$ and $h_w/300$ are found.

Specimen	U-DS	U-MS	T-DS	T-MS
Amplitude of the web local imperfection (mm)	1.3	3.7	2.1	1.6
Amplitude of the web local imperfection in function of h_w	$h_w/584$	$h_w/214$	$h_w/293$	$h_w/485$

Table VI-5: Amplitude of the plate local imperfection measured in the webs

Eventually, global geometrical imperfections have been measured on the four test specimens using a Laser line joining the centre of the top flange at two consecutively laterally restrained cross-sections, the Laser being drawn from a cross-section close to the loaded section and directed to a first fork support, then reversed and pointed at the second fork support. The global imperfection measurement in specimen *U-DS* was slightly different, the Laser line being placed next to the left fork support and pointing at the right fork support. The position of the Laser line was marked on the beams flange every fifty centimetres, providing the resulting amplitudes given in Table VI-6 where their values are also compared to the buckling length L_d.

Specimen	U-DS	U-MS	T-DS	T-MS
Amplitude of global imperfection (mm)	3.4	4.0	3.3	5.0
Amplitude of the global imperfection in function of L_d	L_d/1860	L_d /1547	L_d /1911	L_d /1263

Table VI-6: Amplitude of the global out-of-plane imperfection measured in the compression flange

Table VI-6 shows that the magnitude of the global out-of-plane imperfection of all specimens is lower than L_d/1000 that corresponds to the fabrication tolerance defined in *EN 1090-2*. The maximum measured imperfection amplitude is L_d/1263. It is worth mentioning that the web local and global imperfection amplitudes are very close in specimens *U-MS* and *T-DS*, the difference being 0.3 and 1.2 mm, respectively.

VI.3.3 Tests implementation

During the tests, global displacements were continuously measured using steel wires connected to the web centre of four cross-sections regularly spaced of L_d/6. This distance corresponds to that between the loaded section and the closest cross-section where the global displacement is measured, as shown in Figure VI-7. The twist rotation was measured in the middle of the top flange at the cross-section located at L_d/3 from the loaded section where significant values are expected, as shown in Figure VI-7.

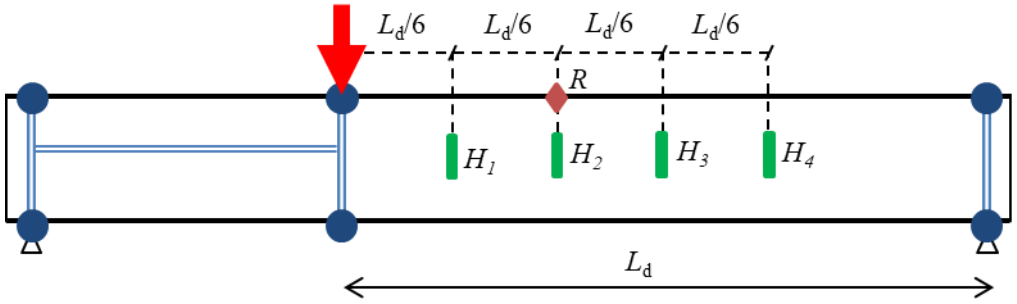

Figure VI-7: Location of the global displacement and rotation measurements

Figure VI-8a) and Figure VI-8b) show the measurements, prior to buckling test of a uniform specimen, of the global displacement and the twist rotation along with vertical displacement, respectively.

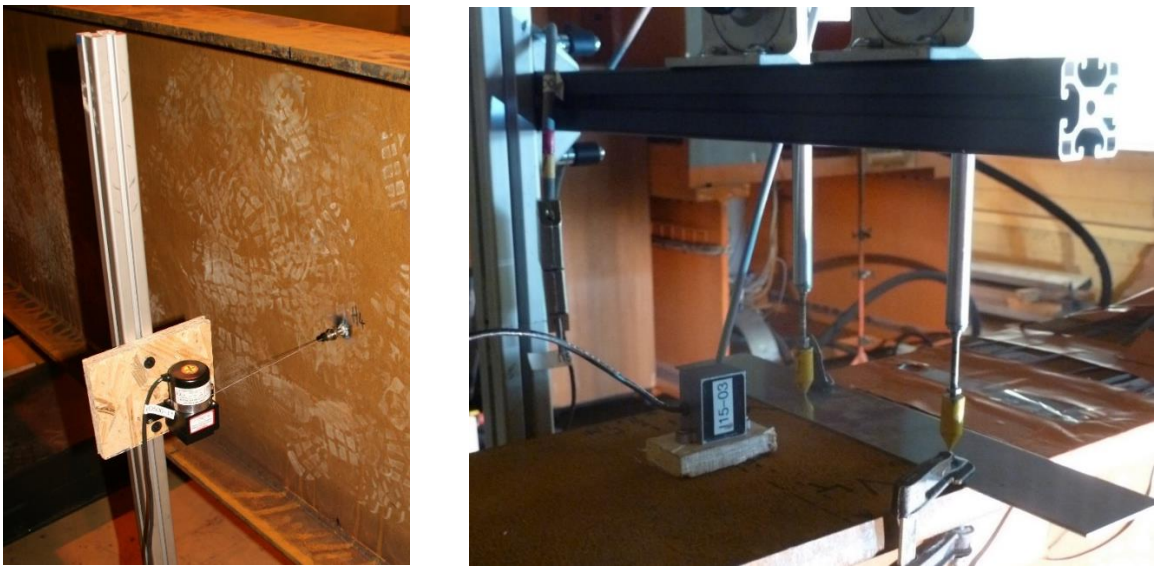

a) *Global displacement* b) *Twist rotation and vertical displacement*

Figure VI-8: Means of continuous measurements during the tests

In-plane displacements have also been measured as shown in Figure VI-9. Displacements were recorded at the centre of the top flange at both fork supports and at the centre of the compression flange at $L_d/6$ from the loaded section towards the right support. The vertical displacement of the hydraulic jack was measured along with the vertical displacement at the centre of the bottom flange of the loaded section for comparison. At the cross-section located at $L_d/3$ from the loaded section, where the twist rotation and a global displacement is being measured, the vertical displacement is measured at the four flange tips to put in perspective the measured twist rotation.

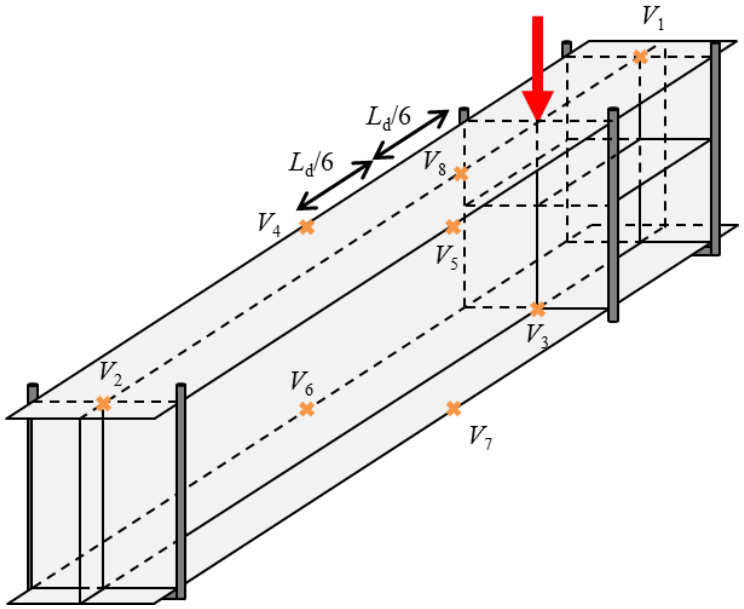

Figure VI-9: Location of the vertical displacement measurements

In addition to displacements and rotations, uniaxial strains were measured continuously in three cross-sections. One was defined *a priori* as the critical cross-section that is 2.3 and 2.8 m away from the load jack for uniform members and non-uniform members, respectively. Strain gauges at the critical cross-

section were placed at the location of each orange triangle presented in Figure VI-10. Nine strain gauges were located on the compression flange, two being placed on the inner. Three gauges were placed on the web, two being close to the junctions with the flanges and the third in the web centre. Eventually, three gauges were placed on the tension flange, two at the tips and the last at the flange centre. The numerous strain gauges in the compression flange were placed so as to study its progressive yielding. Those located in the web and tension flange permitted to determine experimentally the internal forces and bending moments.

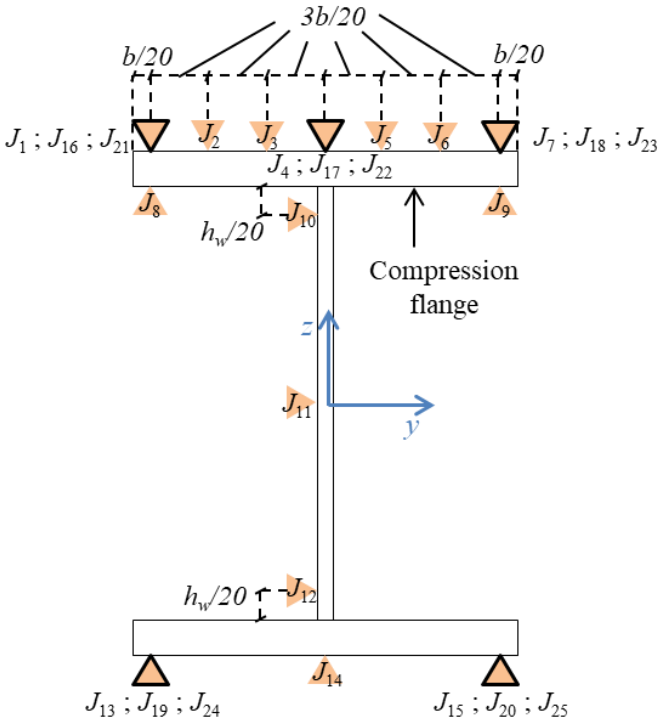

Figure VI-10: Location of the strain gauges

Strains were recorded in two other cross-sections located at $L_d/5$ of the critical one (see Figure VI-11). As there were less cross-sections with strains recording than with global displacement recording, the distance between the cross-sections with strain gauges was increased when compared to that between displacements measurements. Five strain gauges were placed in both cross-sections located as shown by the orange triangles having an exterior black contour in Figure VI-10, namely at the flanges tips and the centre of the compressed flange.

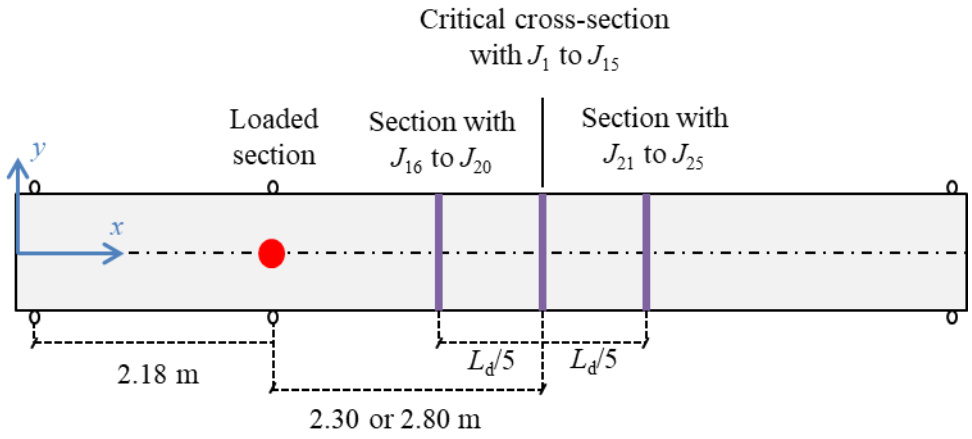

Figure VI-11: Cross-sections with strain gauges

The four beam tests were carried out using the same loading protocol divided in three steps:

- Step A consisted in three cycles of loading and unloading up to 40% of the Ultimate Limit State (*ULS*) design load $F_{0.40}$;
- Step B contained two cycles of loading and unloading. The targeted load in the first cycle corresponds to 70% of the *ULS* design load $F_{0.70}$ while in the second cycle the *ULS* design load $F_{1.00}$ was applied;
- Step C, beams were loaded until failure.

The value of the targeted peak load in steps A and B, corresponding to 40, 70 and 100% of the *ULS* design loads are given in Table VI-7 for the four tested beams.

Specimen	U-DS	U-MS	T-DS	T-MS
$F_{0.40}$ (kN)	154	173	163	197
$F_{0.70}$ (kN)	269	303	285	345
$F_{1.00}$ (kN)	384	433	407	493

Table VI-7: Peak loads during steps A and B of the loading protocol

VI.4 Experimental results

VI.4.1 Overview

The failure mode of the four tests corresponds to lateral-torsional buckling. This buckling mode was observed at the peak load, as shown in Figure VI-12 for all specimen while some web distortion was noticed at post peak in specimen *U-MS*, as shown in Figure VI-13 where a rigid steel ruler is used as a comparison.

The ultimate loads, F_{ult}, of the four tests are presented in Table VI-8, along with the elastic and plastic cross-section resistances, F_{el} and F_{pl}, determined at the loaded section using the nominal dimensions and the measured yield strength for each thickness involved. The table also contains analytical results obtained using *Eurocode 3 Part 1-1* buckling curve *d*, $F_{EC3,d}$, based on the elastic critical loads resulting from Linear Bifurcation Analyses (*LBA*) performed with shell finite elements. The LBA type

calculations were employed to determine the normalized slenderness, presented in Table VI-8. The design load calculated using buckling curve *d* is determined using the measured dimensions and material properties. The simplifying assumption that the yield strength of a member is that of its compression flange is employed. This design load is divided by *f* computed using expression (IV.12) and the corresponding results are added to Table VI-8. Owing to normalized slenderness comprised between 0.74 and 0.93, the coefficient *f* is approximately 0.88 for all specimens.

a) *U-DS*

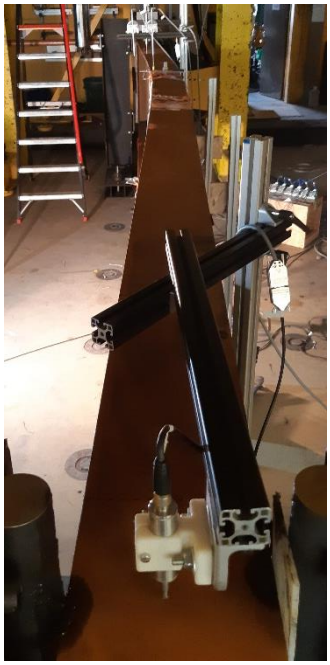

b) *U-MS*

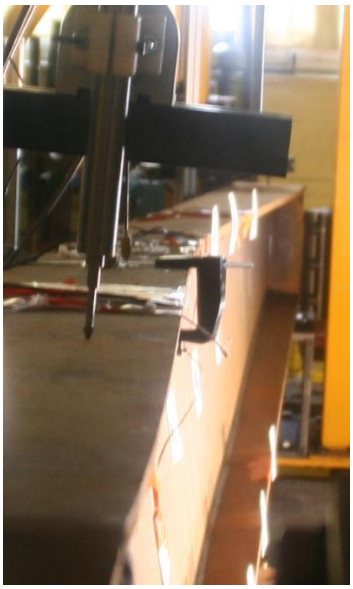

c) *T-DS*

d) *T-MS*

Figure VI-12: Observed failure of the test specimens

Table VI-8 shows significant differences between experimental ultimate loads and analytical design loads according to buckling curve *d* from *Eurocode 3 Part 1-1*. The ultimate loads are 62 to 81% higher than the design loads despite intermediate normalized slenderness (0.74 to 0.93). Accounting for the

bending moment distribution using the coefficient *f* increases the analytical results. The deviation from the experimental ultimate loads then range from 42 to 58% on the safe side.

Figure VI-13: Post-peak web distortion in U-MS

The ultimate load of specimen *U-MS* is greater than its design cross-section resistance that is its elastic resistance, *U-MS* being a Class 3 beam in bending. The failure loads of the three other specimens are 8 to 18% lower than the elastic resistance of the loaded cross-section. This deviation can be attributed to the fact that the elastic resistance of the loaded cross-section differs from the actual design resistance of the failure cross-section. This is obvious for specimens *T-DS* and *T-MS* owing to the cross-sectional variation while *U-DS* is a Class 4 beam in bending, its cross-sectional design resistance is therefore reduced when compared to its elastic resistance. In addition, in the small to intermediate range of slenderness, the impact of the member imperfections increases with the slenderness. Specimen *U-MS* having the lowest normalized slenderness, its buckling resistance is closer to the characteristic resistance of the failure cross-section than for the other specimens.

Specimen	U-DS	U-MS	T-DS	T-MS
$\overline{\lambda}_{LT}$	0.830	0.736	0.927	0.809
F_{ult} (kN)	747.6	903.6	720.6	775.8
$F_{EC3,d}$ (kN)	450.8	499.9	428.7	479.5
$F_{EC3,d}$/f (kN)	514.6	570.0	487.2	547.4
F_{el} (kN)	808.6	796.8	874.3	859.1
F_{pl} (kN)	940.2	1021.2	1021.2	1091.8

Table VI-8: Design and experimental ultimate loads

Besides, the experimental results depicted in Table VI-8 show a significant influence of the cross-section mono-symmetry, particularly in the case of uniform members. Indeed, the ultimate load of specimen *U-MS* is 20% greater than that of *U-DS*. Within the non-uniform members, increasing the compression

flange thickness yields a smaller difference in the ultimate load, being 8%. Besides, the ultimate loads of *U-DS* and *TDS* present a small 4% deviation. A more important difference is noticed between the ultimate loads of both mono-symmetric specimens. The deviation of the *T-MS* failure load from that of *U-MS* is 14%. This result can be attributed to the somewhat lower yield strength measured in the compression flange of specimen *T-MS* that is more than 20 N/mm² lower than in other 20 mm thick coupon tensile tests. Besides, the distribution of the internal forces being different in the four types of beam, one may assume that the failure location is closer to the smaller end in *T-MS* than in *T-DS*.

In addition to results given in Table VI-8, it should be mentioned that the failure load determined according to the new method of *prEN 1993-1-1* and derived by *Taras* (2010a/b) is equal to 658.8 kN for specimen *U-DS*. This value is 12% lower than the experimental failure load and 46% higher than buckling curve *d* ultimate load. The analytical determination of the *prEC3* failure load cannot be performed for the three other specimens which do not enter the scope of this method, limited to uniform members having a doubly symmetrical cross-section.

The substantial differences between experimental and design loads partly result from the flange flame cuts. The design load determination using the *General case* from *Eurocode 3 Part 1-1*, i.e. buckling curve *d*, which does not account for the favourable bending moment linear distribution except when determining the critical load amplifier, can also be pointed out.

VI.4.2 Displacements and rotations

The applied force is presented in Figure VI-14 as a function of the load jack vertical displacement for the four tests. Initial stiffness are alike, though members with a mono-symmetric cross-section are slightly stiffer than the doubly symmetric ones. Some differences can be noted post peak where unloading is more sudden in tapered members (dashed lines) than in uniform members (solid lines). In particular, a drop of 100kN is observed right after the peak for specimen *T-DS* that can correspond to a quasi-elastic lateral-torsional buckling behaviour.

Figure VI-15a) exhibits the global displacements measured by H_2 (see Figure VI-7) considering a similar buckling direction. The buckling directions of the four tests were in line with the initial global imperfection. Specimen *U-DS* buckled towards the left side of the web, i.e. towards $y < 0$ (see Figure VI-11) while the three other beams buckled towards the opposite direction.

Prior to lateral-torsional buckling, global displacements are mainly associated with in-plane bending while as buckling initiates, global displacements are mainly composed by out-of-plane displacements. Figure VI-15b) presents the measured twist rotation, again considering a similar buckling direction.

The displacements and rotations are characteristic of the lateral-torsional buckling behaviour observed for the test beams. Indeed, during loading the displacements and rotations are very small to negligible with an almost constant stiffness. However, in the last 50 to 100 kN before the ultimate load, both the global displacement and twist rotation initiate a clear increase in all tests. As of the ultimate load, they both increase significantly with barely variable slopes, except regarding the twist rotation measured in *U-MS* where the post-peak stiffness varies visibly. This result may owe to the web distortion observed at this stage, the twist rotation being measured in the middle of the compression flange.

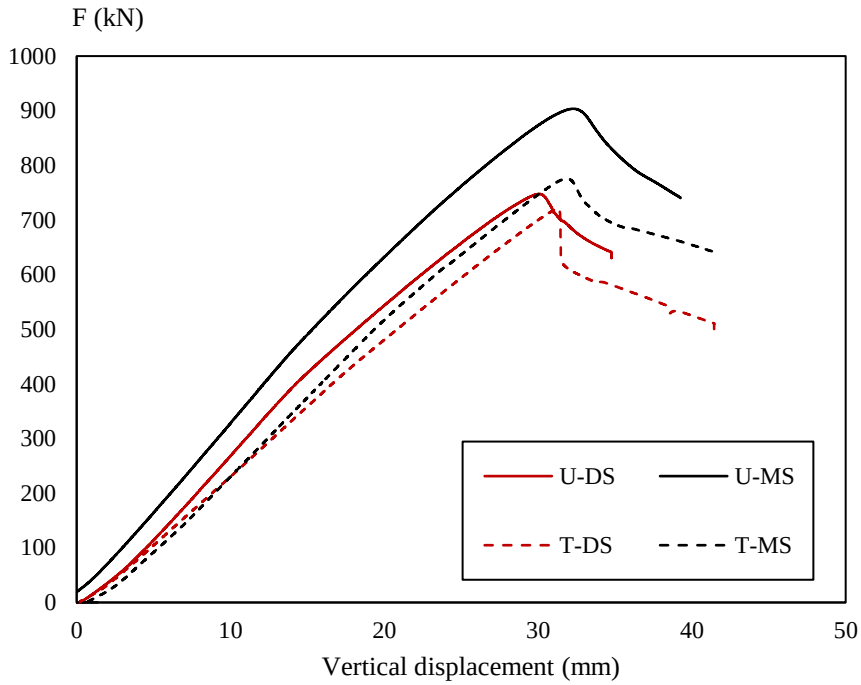

Figure VI-14: Force-vertical displacement curves

Figure VI-15a) shows that specimen *T-DS* presents a quasi-infinite initial stiffness up to approximately 700 kN which is very close to the failure load of 721 kN. Then, the displacement suddenly increases fast and significantly. In addition, the greatest initial stiffness for twist rotation is obtained for specimen *T-DS* (see Figure VI-15b)). Both observations are in line with a failure close to elastic critical buckling with equilibrium bifurcation, as the drop in the force-displacement curve of Figure VI-14 suggests.

The evolutions of the global displacements exposed in Figure VI-15a) are characteristic of the measurements in H_1 to H_4.

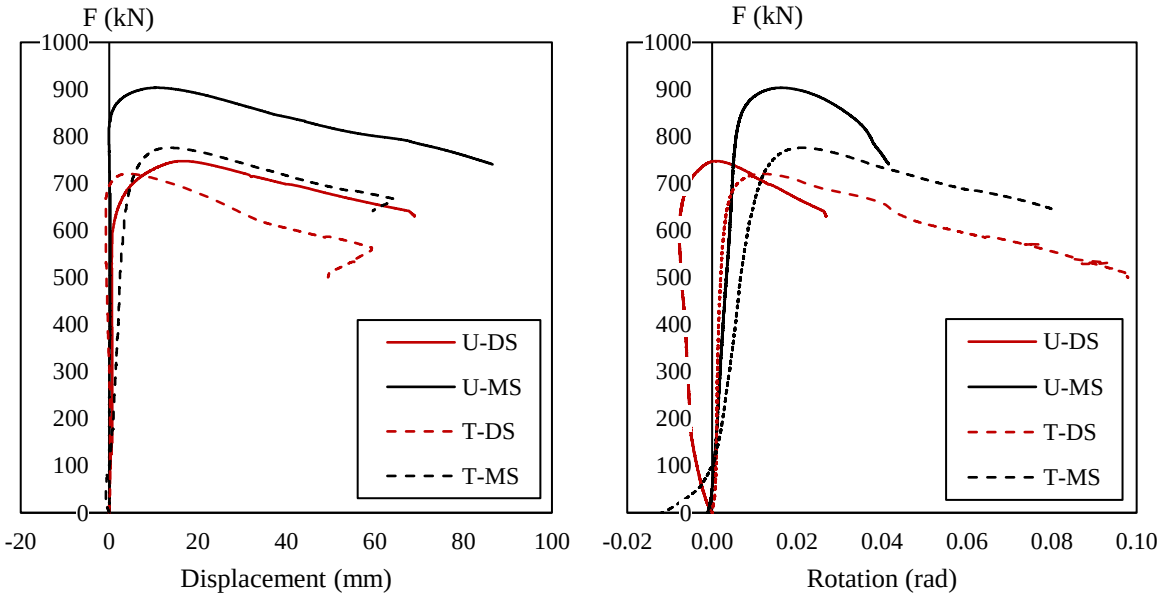

a) *Global displacement measurements in H_2*

b) *Twist rotation measurements in R*

Figure VI-15: Overall displacements and twist rotations

The global displacement u measured at locations H_1 to H_4 are presented in Figure VI-16a) to Figure VI-16d) when under three levels of loading:

- 85% of the ultimate load during loading,
- the ultimate load,
- 90% of the ultimate load during unloading.

In Figure VI-16, the loaded cross-section is positioned at $x = 0$ while the right end fork support is located at $x = 6.25$ m. H_1, H_2, H_3 and H_4 are located at x = 1.04, 2.08, 3.13 and 4.17 m, respectively (see Figure VI-16a)).

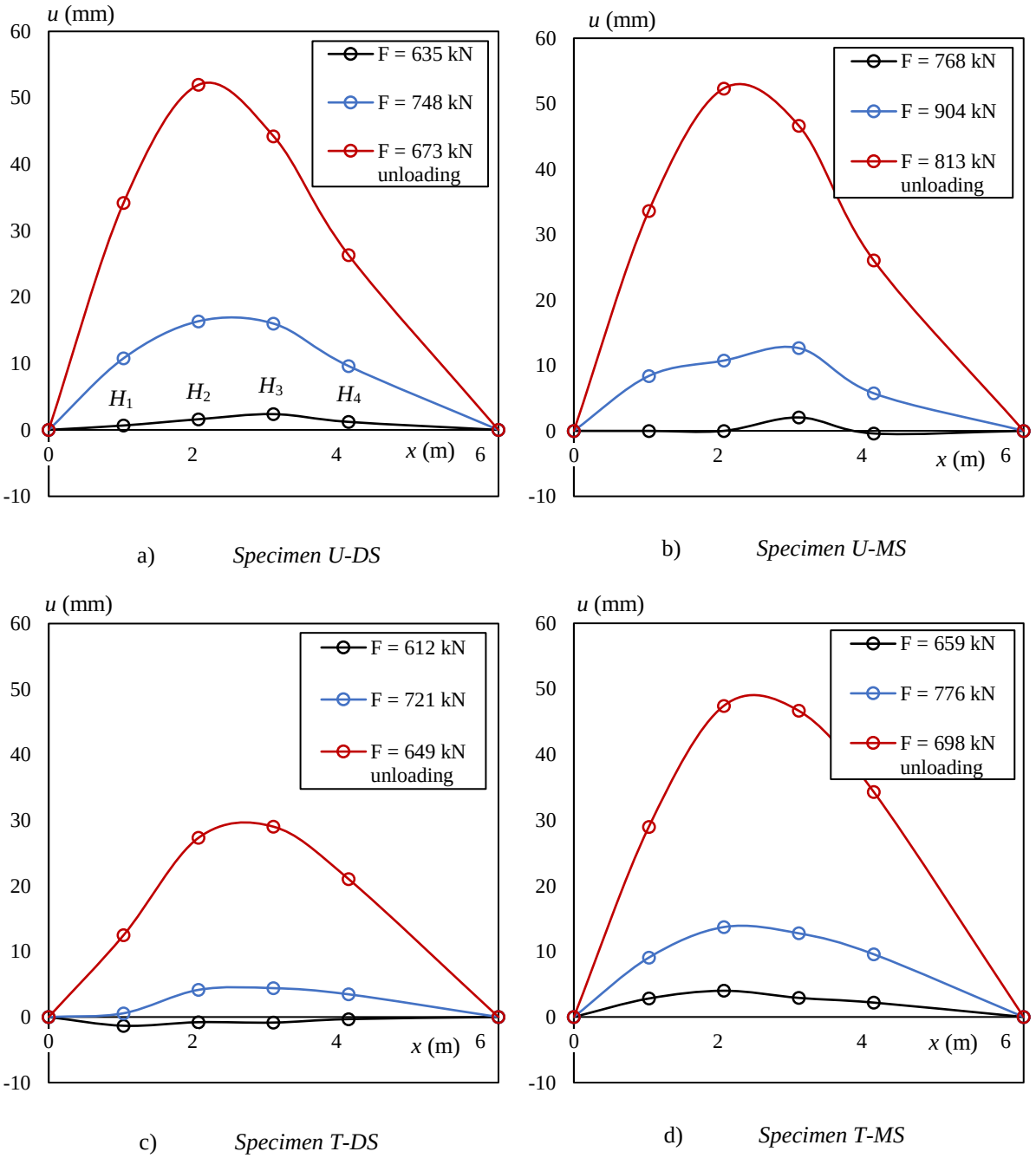

Figure VI-16: Distribution of the global displacement

Figure VI-16 shows distributions of the global displacements along the beams, led by the lateral displacements, corresponding approximately to half sine waves at the ultimate load. The maximum values are obtained close to H_2 in the case of uniform members. In tapered beams, the failure cross-section is located closer to the smaller end owing to the height variation that results in different distributions of the bending moments and bimoment utilizations than in uniform beams. Consequently, the maximum displacements in both tapered specimens are close to H_3, placed at mid-span.

The buckling shapes when under the ultimate load and during unloading are very close in every specimen. Differences are noticed for the displacements measured at H_3 in beam *U-MS* and H_1 in *T-DS*. In the former case, the mid-span (H_3) displacement is the more important under the peak load owing to pre-buckling displacements. However, during the unloading phase, the displacement at H_2 becomes the greatest. In specimen *T-DS*, the differences noticed at H_1 result from the changing of the sign of the global displacements.

The magnitudes of the global displacements are of similar order for all test specimens except *T-DS*. Values close to 15 mm are obtained when under the ultimate load and 50 mm in the unloading stage. In beam *T-DS*, the magnitudes are approximately twice as low as in the three other test specimens. This phenomenon may result from the variation of the global displacements sign as buckling starts.

VI.4.3 Strains

The strain measurements recorded at the two tips of the compressed flange of the "critical" cross-section, i.e. by strain gauges J_1 and J_7 (see Figure VI-10) are shown in Figure VI-17a) and Figure VI-17b), respectively. To provide a consistent comparison of the experimental results, J_1 is for every specimen the gauge located at the flange end corresponding to the buckling direction (see Figure VI-18). Negative values stand for compressive strains. The initial stiffness are close when looking at J_7 strains. However, at the flange other tip, initial stiffness are similar in mono-symmetric members only while those observed in specimens *T-DS* and *U-DS* stand slightly apart.

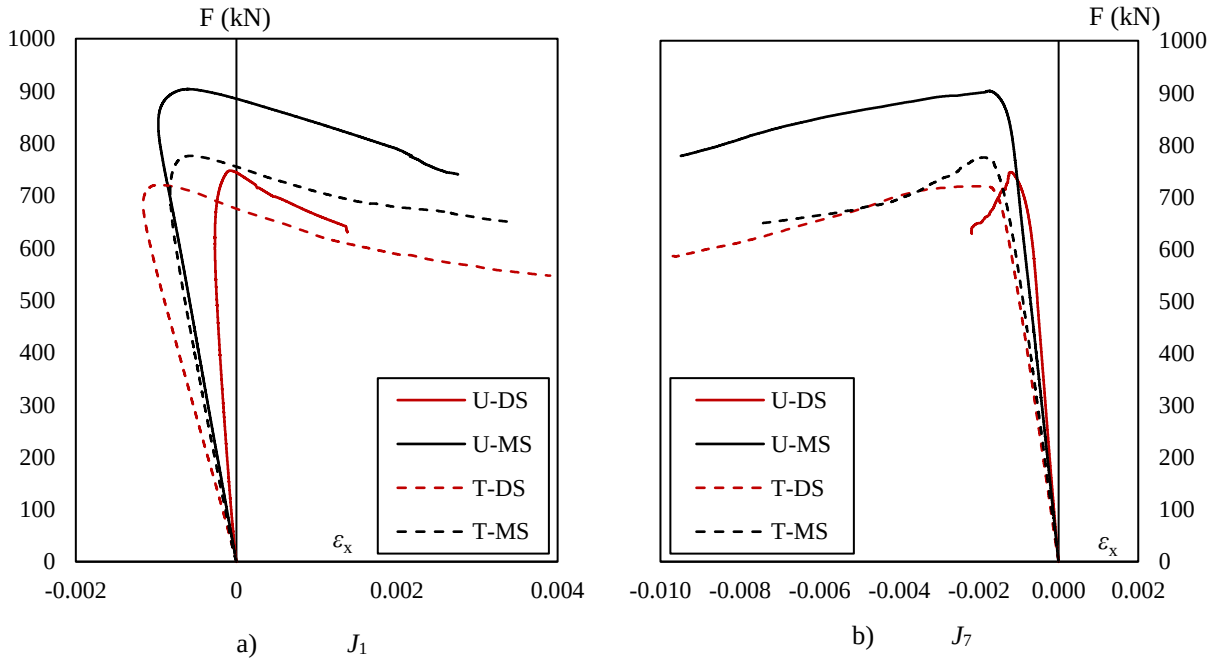

Figure VI-17: Force strain curves

These differences must be seen for the couple of strain gauges (J_1;J_7). They can then be attributed to different values of the second order internal out-of-plane bending moment M_z^{II} and bimoment B^{II}. These second order bending moment and bimoment are more important in the doubly symmetric members than in both mono-symmetric beams.

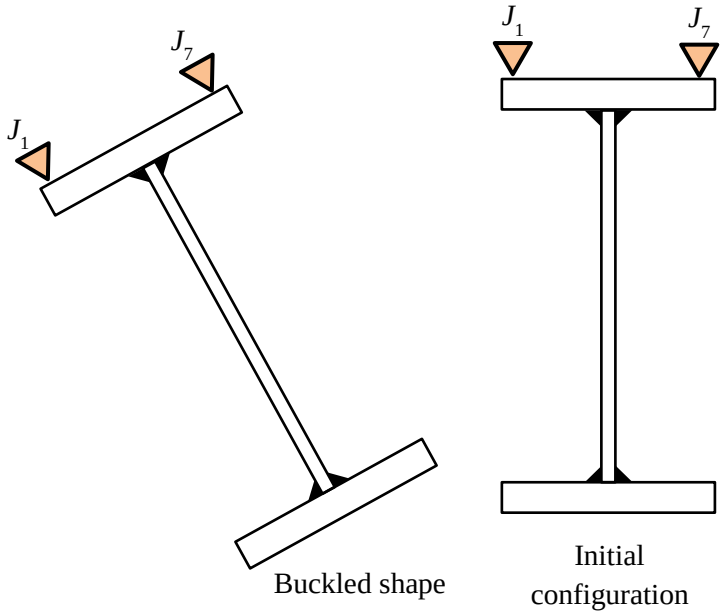

Figure VI-18: Strain gauges locations for Figure VI-17

Figure VI-19 shows the distributions of the strains measured along the width of the compression flange of the critical cross-section for each test specimen. The strains are presented for the loading levels used for the global displacements presented in Figure VI-16. In addition, the strains corresponding to the boundary between the elastic and plastic zones ε_y are depicted using purple solid lines.

$$\varepsilon_y = \frac{f_y}{E} \qquad \text{(VI.3)}$$

The out-of-plane buckling behaviour is featured in the distributions measured in the four specimens. As clearly shown in specimen *U-MS*, during loading the compressive strains are uniform along the flange width up to the peak load. Then, the compressive strain at one of the flange tips increases while decreasing at the other tip. This phenomenon intensifies post peak yielding tensile strains and important compression flange at the two tips.

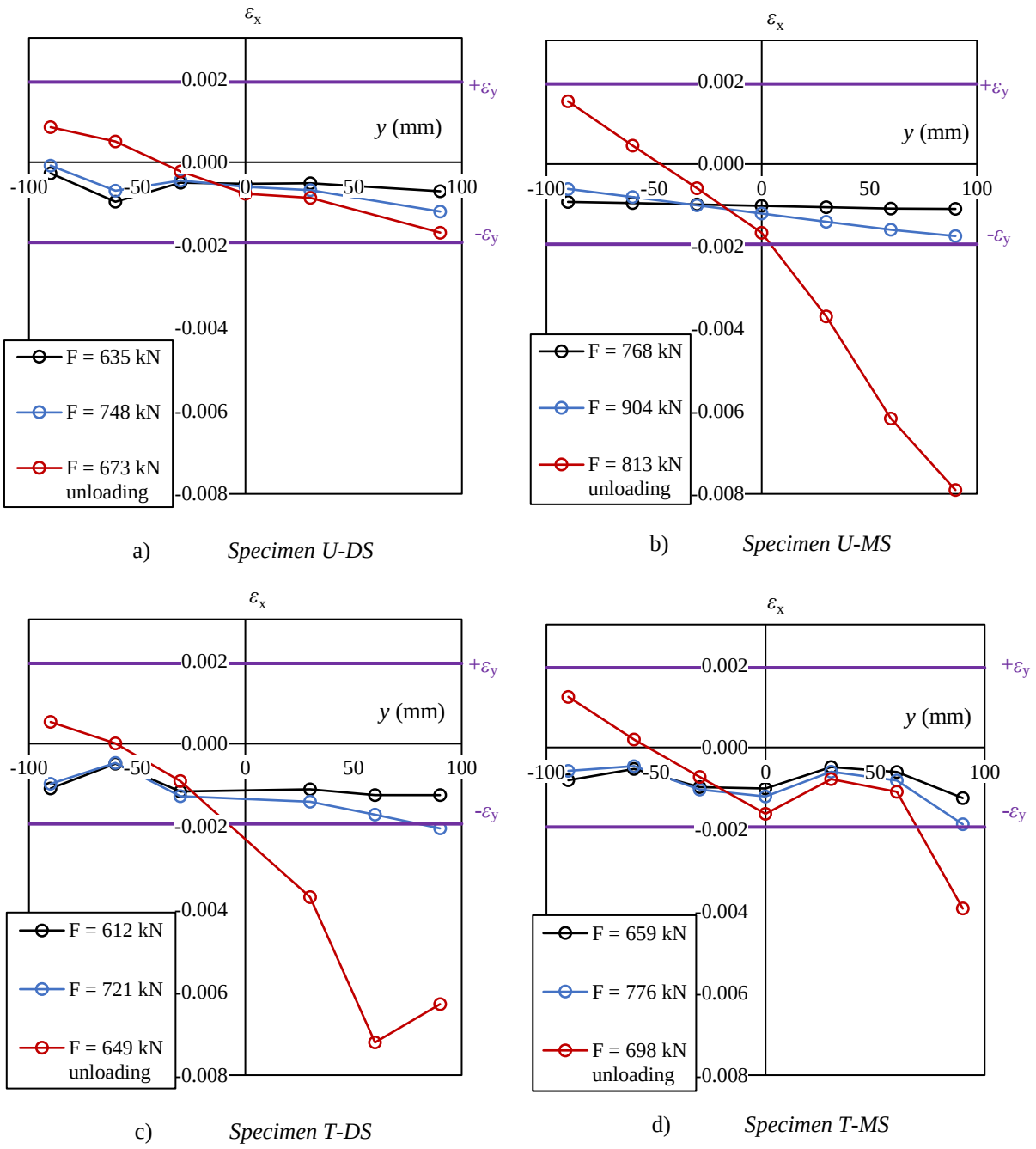

Figure VI-19: Strains distribution in the compression flange of the critical section

When the peak load is reached, the strains at the most compressed fibre of the compression flange are similar in all specimens except in *U-DS* where a lower value is measured. The maximum strain is close to 0.002 in the compression flanges of specimens *U-MS*, *T-DS* and *T-MS* which corresponds approximately to $\varepsilon_y = f_y/E$. Therefore, the experimental failure was found at the boundary between the elastic and inelastic ranges for all specimen except *U-DS* that failed in the elastic range.

VI.5 Summary

The experimental overall buckling behaviour of welded members has been investigated in the past as described in the first section of this chapter. Existing experimental data mostly concern uniform members having hot-rolled flanges. Already in the 1960s, experimental tests showed greater ultimate capacities for welded members made of flame-cut flanges when compared to similar members made of hot-rolled flanges, owing to a more favourable residual stresses distribution. In the recent years, a scarcity of experimental programmes concerning welded members having common dimensions and made of flame-cut flanges is noticed. In particular, very few experimental data concerned mono-symmetric and/or non-uniform members. A new experimental programme is therefore presented investigating the stability of uniform or tapered members having a doubly or mono-symmetric cross-section.

The novel experimental programme led at Polytech' Clermont included lateral-torsional buckling tests performed on four S355 welded beams having flame-cut flanges. Two specimens presented a doubly symmetric cross-section and two had mono-symmetric cross-sections. Each couple of test specimens contained a uniform and a tapered member. The experimental failures, that featured lateral-torsional buckling, were found in the elastic range for the uniform specimen with a doubly symmetrical cross-section and at the boundary of the inelastic range for the three other test specimens.

The experimental results highlighted the benefits of thickening the compression flange of a uniform doubly-symmetric member. Indeed, a 5 mm thickness difference yielded a 20% increase of the ultimate load. The difference is less pronounced within non-uniform members, the exact failure locations corresponding to different cross-sectional dimensions. The ultimate load of the mono-symmetric tapered member is 8% greater than the doubly symmetric one. Besides, the ultimate loads of both doubly symmetric members were very close.

The ultimate design loads determined according to the *General case* from *Eurocode 3 Part 1-1*, which makes use of buckling curve *d*, are found significantly below the experimental failure loads. The difference is slightly reduced when accounting for the bending moment distribution through the factor f. The deviation from the experimental ultimate load is even lower when using the new method in *prEurocode 3 Part 1-1*. However, this design method can only be employed for the uniform and doubly symmetric specimen. The *General case* verification format can then be questioned. In addition to a safety margin, some deviation between experimental and analytical results may be attributed to the beneficial effect of the flame-cuts, which is not accounted for in existing verification formats.

VII. *Numerical model*

VII.1 Introduction

To determine the actual resistance of a steel member subjected to bending moment and/or compression force, the most accurate method consists in performing a large-scale experiment which is a tedious time-consuming process. To obtain a large amount of reference results, experimental results are generally supplemented with numerical *GMNIA* type calculations that comprehend the behaviour of actual members. Indeed, Geometrically and Materially Non-linear Analyses account for the member geometrical and material Imperfections. The current and future design methods of Eurocode 3 rely on a large number of GMNIA calculations. Comprehensive parametric studies are employed to validate analytical design methods and complete experimental results.

Firstly, the numerical model used in the present work is described. The major assumptions on which the numerical model is based are described, i.e. the steel mechanical properties, the residual stress model and the distribution of the geometrical imperfections. The enforced boundary conditions are also depicted.

The lateral-torsional buckling tests described in Chapter VI are then reproduced with this Finite Element Model. Numerical and experimental results are in good agreement. The finite element model is therefore used to perform a parametric study described in section VII.4.

VII.2 Finite Element Model

VII.2.1 Ideal member

The numerical model, developed with ANSYS software v.2020, makes use of 4-noded shell elements with 6 degrees of freedom per node and 5 integration points through the thickness. The steel member is meshed using 20 elements over its width and 30 elements over its height. The longitudinal mesh density depends on the length of the member, one meter of the member being divided by 30 to 40 elements.

The used steel mechanical properties are characterized by the constitutive law depicted in Figure VII-1 which was suggested by *ECCS* (1984) The material law is multilinear isotropic with a plastic plateau when strains are comprised between ε_y and $10\varepsilon_y$. For greater values, the strain hardening response is lower with a slope of $E/50$.

Similarly to the LBA calculations depicted in Chapters II and III, the elastic mechanical properties are characterized by a modulus of elasticity $E = 210\,000$ MPa and a Poisson's ratio $\nu = 0.3$.

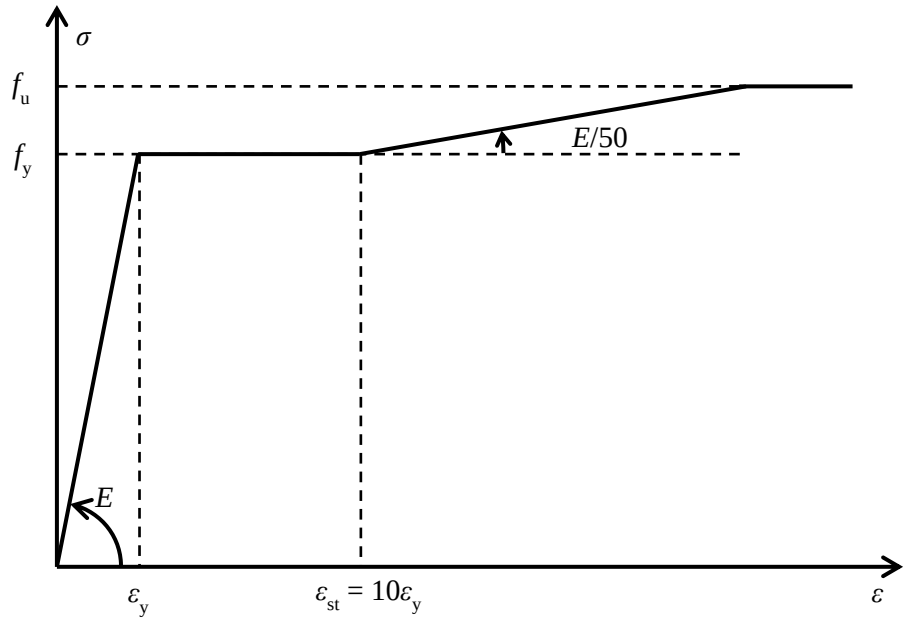

Figure VII-1: Steel stress-strain curve

VII.2.2 Geometrical and material imperfections

Material and geometrical imperfections in actual steel members are accounted for in numerical analyses using simplified models.

The residual stresses distributions introduced in the numerical model are presented in Figure VII-2. The residual stress pattern adapted to welded members with hot-rolled flanges is that recommended by *prEN 1993-1-14* (see Figure VII-2a)). As shown in Chapter V, the measured distributions in welded members made of hot-rolled flanges exhibit similar magnitude of the compressive stresses in the flanges (0.25 f_y) as the *prEurocode 3* model. This maximum value is reached at the flanges tips while the stresses magnitude diminishes near the flanges centre. The measured magnitude of the tensile stress at the flanges centre being 0.59 f_y is lower than that suggested by the employed model, corresponding to the yield strength. The use of the residual stress pattern presented in see Figure VII-2a) is assumed to accurately stand for the measured distributions (see Chapter V), stresses being close especially in the compression areas.

The new initial stress model derived in Chapter V is used for welded members made of flame-cut flanges (see Figure VII-2b)).

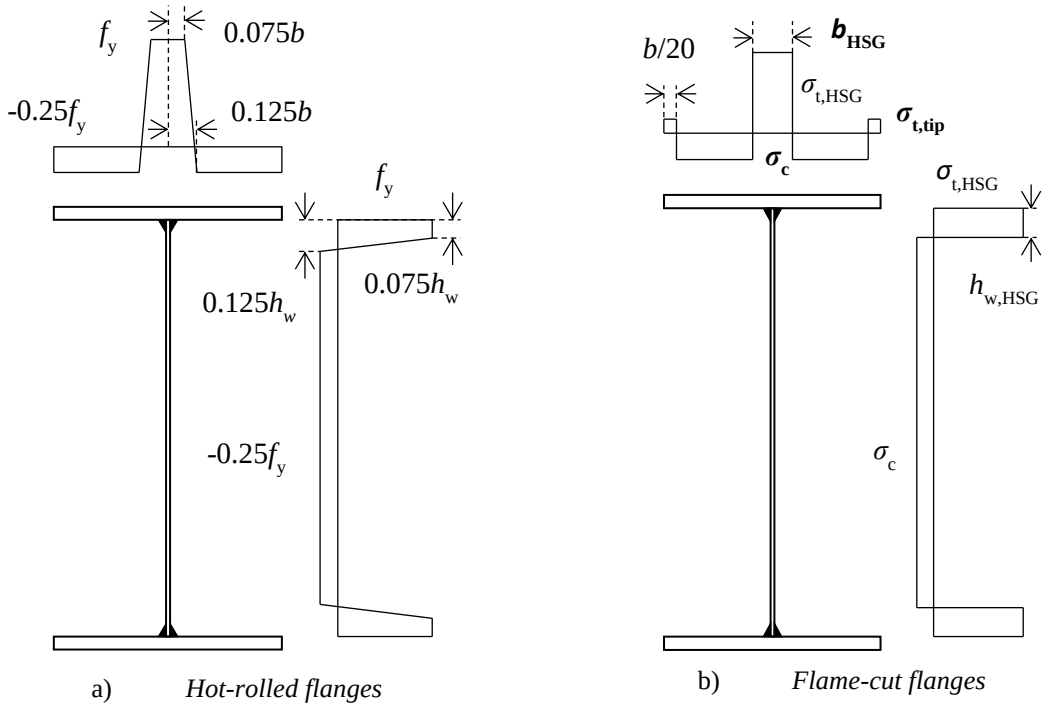

Figure VII-2: Residual stress models for welded members

The following key parameters of the model depicted in Figure VII-2b) are reminded (see Chapter V):

$$\sigma_c = -f_y\left(0.25 - 0.005\frac{b}{t_f}\right) \leq -0.14 f_y \qquad \text{(VII.1)}$$

$$\sigma_{t,tip} = f_y\left(0.70 - 0.35\frac{h_t}{b}\right) \geq 0.03 f_y \qquad \text{(VII.2)}$$

$$b_{HSG} = b\left(0.1 + 0.036\frac{h_t}{b}\right) \qquad \text{(VII.3)}$$

The residual stresses introduced are constant in each element, the assigned stress corresponding to that of the element centroid according to the employed model. Linear interpolations are employed when the centroid is located between a uniform tension and the uniform compression zones.

In addition to residual stresses, geometrical imperfections are applied to the numerical members. The geometrical imperfections comprise both a global and a local component. As recommended by *Couto* (2019), the shape of the global imperfection is proportional to the Linear Bifurcation Analysis (*LBA*) mode shape (see Figure VII-3), scaled to unity. It therefore depends on the actual loading conditions. A lateral imperfection for all loading cases, affine to the elastic out-of-plane flexural buckling mode shape, could also be used. However, *Couto* (2019) obtained slightly lower lateral-torsional buckling ultimate capacities using the actual elastic critical buckling mode shape than using a lateral imperfection.

Despite a recommended value of $L/1250$ according to both *Annex C of Eurocode 3 Part 1-5* and *prEN 1993-1-14*, the global imperfection is scaled to the amplitude of $L/1000$, L being the distance between supports. Indeed, the value recommended by the European standard is 80% of the fabrication tolerance defined in *EN 1090*, which was modified from $L/750$ to $L/1000$ in the 2018 revision of the standard. However, a magnitude of the global imperfection of $L/1000$ provides more conservative results than

L/1250 and was recommended by *Boissonnade* (2012) and *Couto* (2019), both relying on the former version of *EN 1090*.

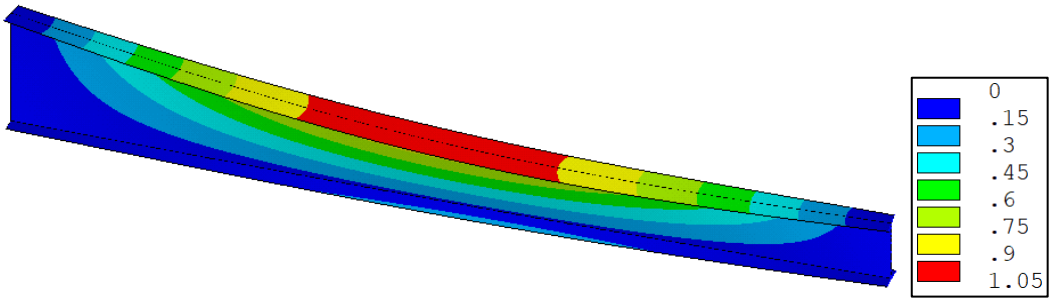

Figure VII-3: Shape of the global imperfection (member subjected to bending)

Plate local imperfections are enforced using sine waves applied by plate, as depicted in Figure VII-4. As recommended by both *Annex C of Eurocode 3 Part 1-5* and *prEN 1993-1-14*, the local imperfections are scaled to an amplitude of $h_w/200$ in the webs and $b/200$ in the flanges. Besides, to maintain the plates perpendicular, the sine-wave period is similar in both flanges and the web as suggested by *Gérard* (2019). Indeed, the half-period is set as the average between the flanges widths and web height, as proposed by *Gérard* (2019). The number of half waves along the member length is however approximated to the closest integer.

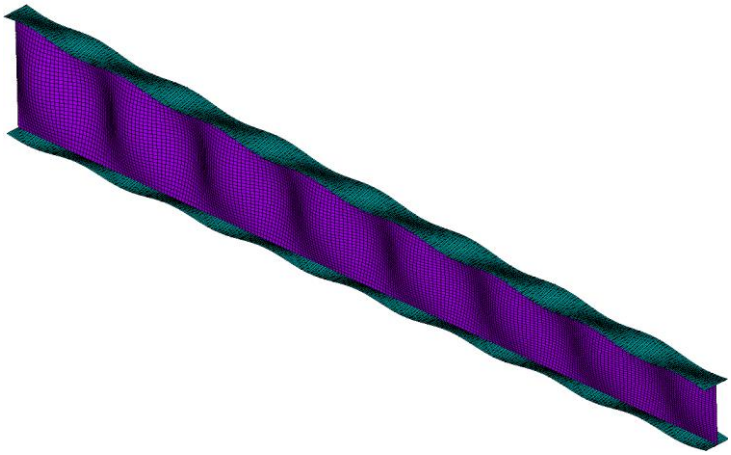

Figure VII-4: Shape of the local imperfections (amplified)

Since both global and local imperfections are used, the amplitude of the plate local imperfection is reduced to 70% of its original value. This reduction is in line with the recommendations from *Annex C of Eurocode 3 Part 1-5* and *prEN 1993-1-14*. Both references recommend to perform two numerical analyses where each imperfection type is reduced in turn, the lowest result being defined as the ultimate capacity. However, it has been chosen to reduce only the amplitude of the local imperfections to spare a significant amount of computation time and because global buckling is of major interest.

VII.2.3 Boundary conditions

The kinematic boundary conditions are applied at the centroid of the end sections (see Figure VII-5). The end fork supports are imposed by fully restraining vertical and lateral displacement (w and v) as well as twist rotation (θ) at both ends. In addition, the longitudinal displacement (u) is fully prevented at a single end. These restraints are applied simultaneously at the end cross-section centroids.

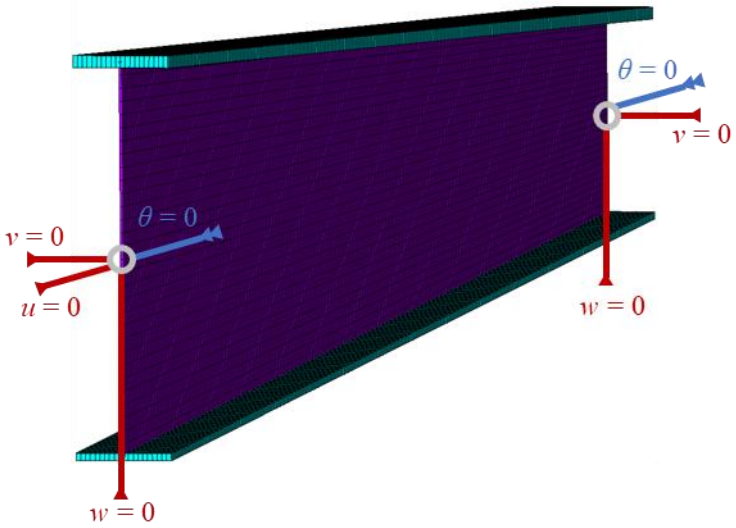

Figure VII-5: Kinematic boundary conditions

In order to prevent any local instability at both ends while warping and out-of-plane rotations remain free, beam elements are added to stiffen the cross-sections at supports, as presented in Figure VII-6. The 2-noded beam elements, adapted to non-linear analyses, are enforced by defining cross-sectional properties where the torsional constant $I_t = 0$ and in-plane and out-of-plane second moments of area I_y and I_z have significant values.

In addition, for LBA computations, distortion modes along the members are prevented by imposing suitable kinematic conditions to the model.

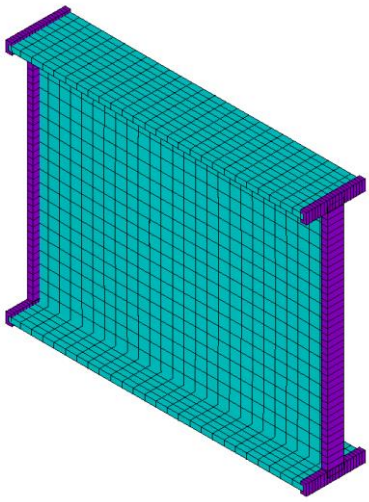

Figure VII-6: Beam elements (in purple) preventing local failure of the shell elements (blue)

External axial loading is applied at the centroid of the end section free to displace longitudinally (see Figure VII-7). Besides, end moments are also applied at the centroid of the members end sections. To enforce a ratio ψ between both end moments, the applied end moments present a ratio $-\psi$ (see Figure VII-7). The non-linear analyses are performed using the Newton-Raphson resolution method proposed in the *ANSYS* software.

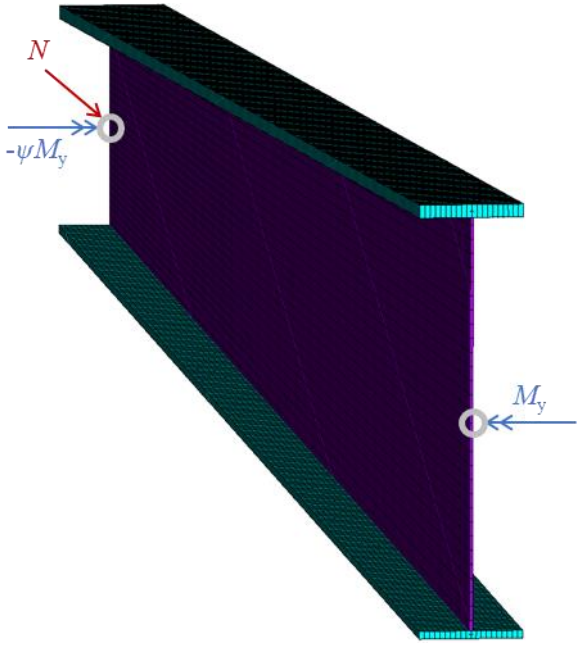

Figure VII-7: Load introduction

The numerical model is employed to perform GMNIA calculations of the lateral-torsional buckling tests depicted in Chapter VI using specific features that are described in the following section VII.3. The numerical results are then compared against the experimental ones.

VII.3 Comparison with experimental tests

VII.3.1 Specific features of the numerical model

One of the main objectives of the experimental programme described in Chapter VI was to assess the accuracy of the numerical model. Major experimental results need therefore to be compared against their numerical equivalents. Consequently, the numerical model described in the two previous sections is adjusted in order to account for the specific features of the specimens and test set-up.

The actual material properties of the test specimens having been determined, the material laws implemented in the numerical model are presented at Figure VII-8 for each thickness involved. The numerical values are reproduced in Table VII-1. Each material law corresponds to the average result of the tensile tests performed for each thickness. The shell elements employed accounting for the change in thickness in non-linear analyses, experimental data have been modified to comprehend the true stress – true strain behaviour. The following expressions provided in *Annex C of Eurocode 3 Part 1-5* and *prEN 1993-1-14* are consequently used:

$$\sigma_{true} = \sigma(1+\varepsilon) \tag{VII.4}$$

$$\varepsilon_{true} = \ln(1+\varepsilon) \tag{VII.5}$$

It is worth mentioning that different material laws are used for the 20 mm flange in specimens *U-MS* and *T-MS*. Indeed, the material law employed for *T-MS* is determined from the results of the tensile tests

performed on the coupons extracted from this beam. The yield strength is more than 20 N/mm² lower than the mean of that obtained with the other 20 mm-thick coupons, which are used for *U-MS*.

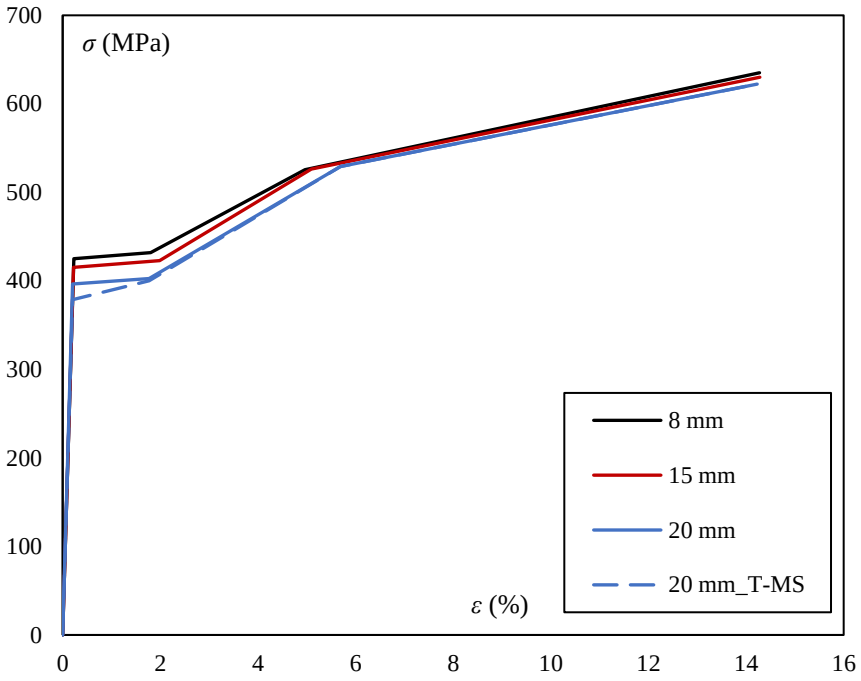

Figure VII-8: Material laws used for the test beams

Besides, the actual residual stresses measured in specimens *Wfc_200-15* and *Wfc_200-15/20* are included in the numerical model of the test beams. Both doubly symmetric specimens (*U-DS* and *T-DS*) make use of the distribution measured in *Wfc_200-15*. The mono-symmetric beams (*U-MS* and *T-MS*) are computed using the experimental distributions measured in *Wfc_200-15/20*. The residual stresses distributions used, presented in Figure VII-9, are averaged in order to be symmetric about the members and flanges web centres.

t = 8 mm		**t = 15 mm**		**t = 20 mm**		
ε (%)	**σ (MPa)**	**ε (%)**	**σ (MPa)**	**ε (%)**	**$\sigma_{U\text{-}MS}$ (MPa)**	**$\sigma_{T\text{-}MS}$ (MPa)**
0.23	424	0.22	414	0.20	396	378
1.82	424	2.00	414	1.79	396	393
5.09	500	5.23	500	5.86	500	500
15.34	551	15.35	546	15.3	540	540

Table VII-1: Strains and stresses used for the test beams

Geometrical imperfections are introduced using the shapes described in sub-section VII.2.2. However, the amplitudes of the imperfections are set to those measured in the specimens (see Chapter VI). The relative amplitudes of the flanges local imperfections are supposed to be similar to those measured in the webs. The imperfections amplitudes are presented in Table VII-2.

The amplitude of the global imperfection is in every cases lower than $L_d/1000$ assumed in sub-section VII.2.2. The amplitudes of the local imperfections are also lower than h_w or $b/200$, as defined in sub-section VII.2.2.

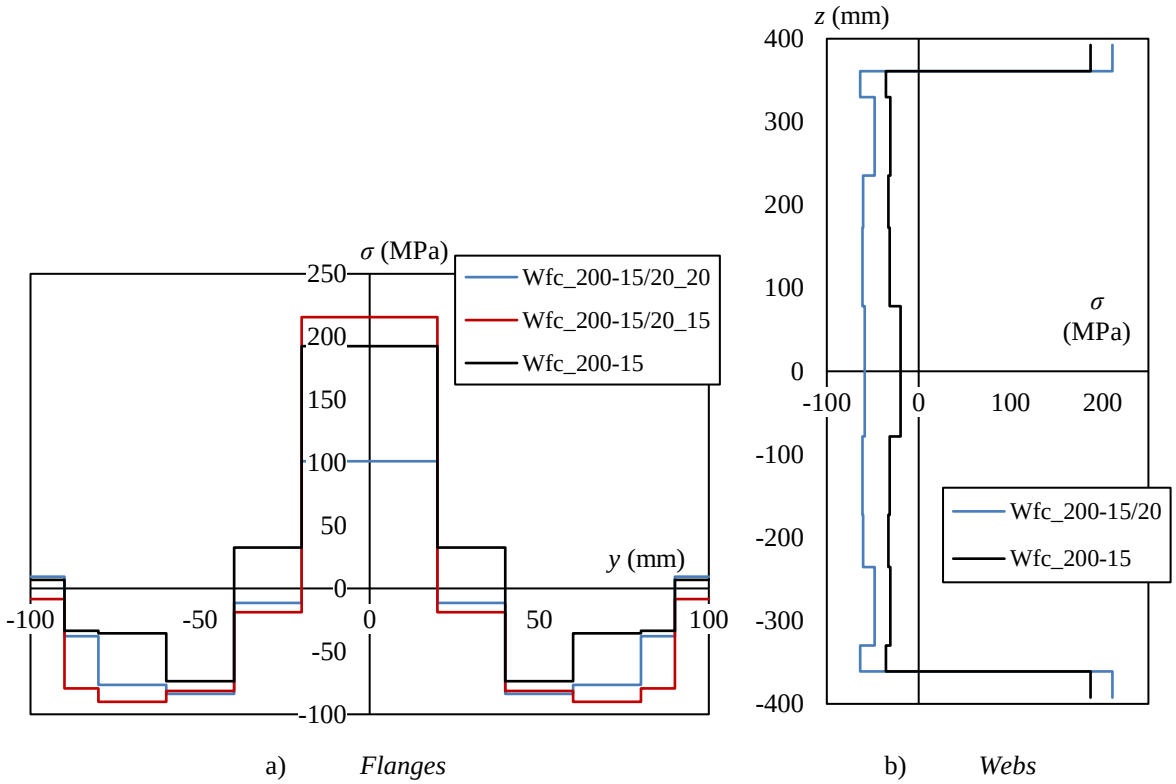

Figure VII-9: Residual stresses used for the test beams

At both supports, the vertical displacements (w) of the bottom flange nodes are prevented. The lateral displacements (v) of the transverse stiffeners free ends are fully restrained on both sides of the web. Similarly, the latter displacements are prevented at the loaded cross-section. The longitudinal displacement (u) is fully restrained at the centre of the bottom flange of the cross-section located at the left support to prevent any rigid body motion.

Imperfection	*U-DS*	*U-MS*	*T-DS*	*T-MS*
Global	L_d/1860	L_d/1547	L_d/1911	L_d/1263
Local: web	h_w/584	h_w/214	h_w/293	h_w/485
Local: flanges	b/584	b/214	b/293	b/485

Table VII-2: Amplitude of the geometrical imperfections

The load jack is represented by a linear loading (for LBA computations) applied along the width of the top flange at the loaded section. A single row of nodes is loaded. For GMNIA calculations, the linear set of point loads is replaced with uniform displacements in order to investigate the numerical post-peak behaviour obtained with the Newton-Raphson resolution type.

VII.3.2 Results

VII.3.2.1. General

Using the numerical model described in the previous VII.3.1, the GMNIA load-carrying capacities of the four test beams are presented in Table VII-3 along with the experimental ones. The numerical values are also normalized to the experimental ultimate loads. The normalized slenderness are also reminded.

	U-DS	*U-MS*	*T-DS*	*T-MS*
$\overline{\lambda}_{LT}$	0.830	0.736	0.927	0.809
F_{GMNIA} (kN)	753.6	898.4	708.1	819.6
$F_{experimental}$ (kN)	747.6	903.6	720.6	775.8
$F_{GMNIA}/F_{experimental}$	1.008	0.994	0.983	1.056

Table VII-3: Numerical and experimental load capacities

The results show a good agreement, especially for both uniform beams and for specimen *T-DS*. Indeed, the deviation of the numerical ultimate load from the experimental one is negligible, being less than 1% for both uniform specimens. A very small deviation of 1.7% is found for the tapered beam having a doubly symmetric cross-section. The comparison between both load bearing capacities of specimen *T-MS* shows a 5.6% difference, which is still acceptable.

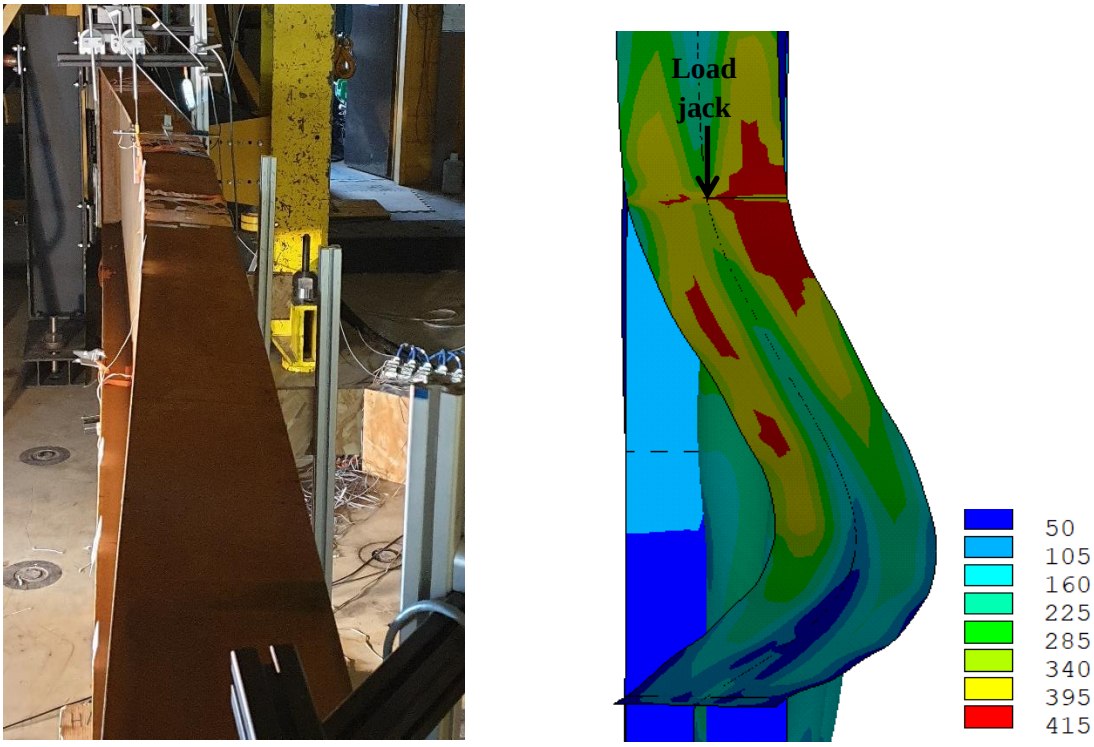

a) *Experimental* b) *Numerical von Mises stresses (MPa)*

Figure VII-10: Buckled shape of specimen U-MS *under peak load*

The experimental and numerical buckled shapes of specimen *U-MS* under peak load are presented in Figure VII-10. A significant lateral displacement of the compression flange can be seen in both the numerical and experimental buckled shape. Figure VII-10b) shows that the maximum von Mises stresses are found very close to the loaded section while the maximum compression flange displacement can be found close to mid-span. Such result can be attributed to the beneficial effect of the bending moment distribution. Indeed, the first order in-plane bending moment M_y is maximum at the loaded section while the second order out-of-plane bending moment M_z and bimoment B are maximum close to mid-span. Assuming that these three effects reach their maximal value at the same cross-section is therefore inconsistent when the bending moment distribution is not uniform. The bending moment distribution

should be accounted for when computing the bending moment resistance of a beam against lateral-torsional buckling.

The GMNIA calculations of the lateral-torsional buckling tests are also performed using alternative models of residual stresses. The numerical analyses are performed considering:

- No residual stresses (labelled *ØRS*);
- Residual stresses according to *prEN 1993-1-14* (see Figure VII-2a)) for welded members with hot-rolled flanges (*W-hr*);
- Residual stresses according to the new model (see Figure VII-2b)) for welded members with flame-cut flanges (*W-fc*).

The corresponding GMNIA ultimate loads are compared against those obtained using the measured stress distributions presented in Figure VII-9 and the experimental results. The normalized results are presented in Table VII-4. The results obtained without residual stresses are 3 to 6% greater than the numerical reference values. Implementing residual stresses for welded members with flame-cut flanges provides 4 to 6% lower results than the numerical reference ones.

When compared against experimental results, neglecting residual stresses provide results in good agreement, except for *T-MS* for which a deviation of 12% is noticed. Besides, using the residual stress model for welded members made of flame-cut flanges yields ultimate loads slightly lower than the experimental ones, the deviation being 7% at most.

Reference value		*U-DS*	*U-MS*	*T-DS*	*T-MS*
Numerical model calibrated	$F_{FEA,ØRS}$ /$F_{FEA,Measured}$	1.031	1.029	1.037	1.063
	$F_{FEA,W\text{-}hr}$ /$F_{FEA,Measured}$	0.860	0.860	0.855	0.860
	$F_{FEA,W\text{-}fc}$ /$F_{FEA,Measured}$	0.965	0.961	0.950	0.943
Experimental tests	$F_{FEA,ØRS}$ /$F_{Experimental}$	1.039	1.023	1.019	1.123
	$F_{FEA,W\text{-}hr}$ /$F_{Experimental}$	0.867	0.855	0.841	0.909
	$F_{FEA,W\text{-}fc}$ /$F_{Experimental}$	0.972	0.955	0.933	0.997

Table VII-4: Numerical load capacities for different residual stress models

Significant differences of 14% are obtained between the numerical reference values and those obtained when using a residual stresses distribution for welded members made of hot-rolled flanges. The deviation from the experimental results range from 9 to 16%. Besides, one can notice an approximately 10% deviation between the numerical results obtained using the two different models. This deviation is attributed to the flanges fabrication process only. Distinct design methods should therefore exist for welded members depending on their flanges fabrication process.

VII.3.2.2. Displacements and rotations

The experimental and numerical load-vertical displacement (w) curves measured at the loaded section are presented in Figure VII-11 for each specimen. The numerical and experiment force-displacement curves are in good agreement. Indeed, the experimental and numerical initial stiffness are very close, as well as the post peak behaviour.

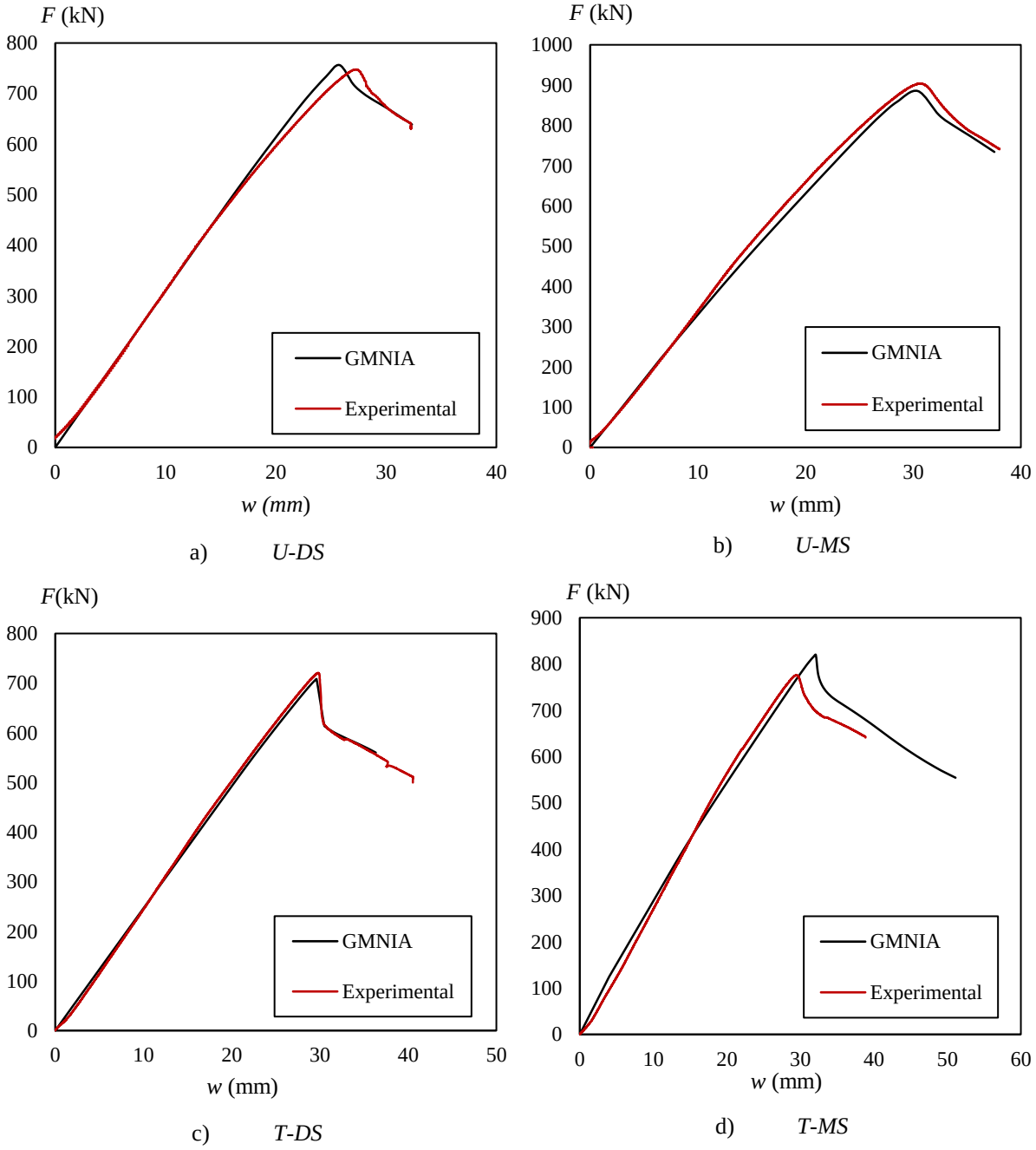

Figure VII-11: Force-displacement curves at the loaded section

Besides, all numerical failures are attributed to lateral-torsional buckling. Indeed, no web distortion is noticed when under the ultimate load but appears in the post-peak stage. This phenomenon is presented in Figure VII-12 in the case of *U-MS* for which web distortion was visible during the test when unloading.

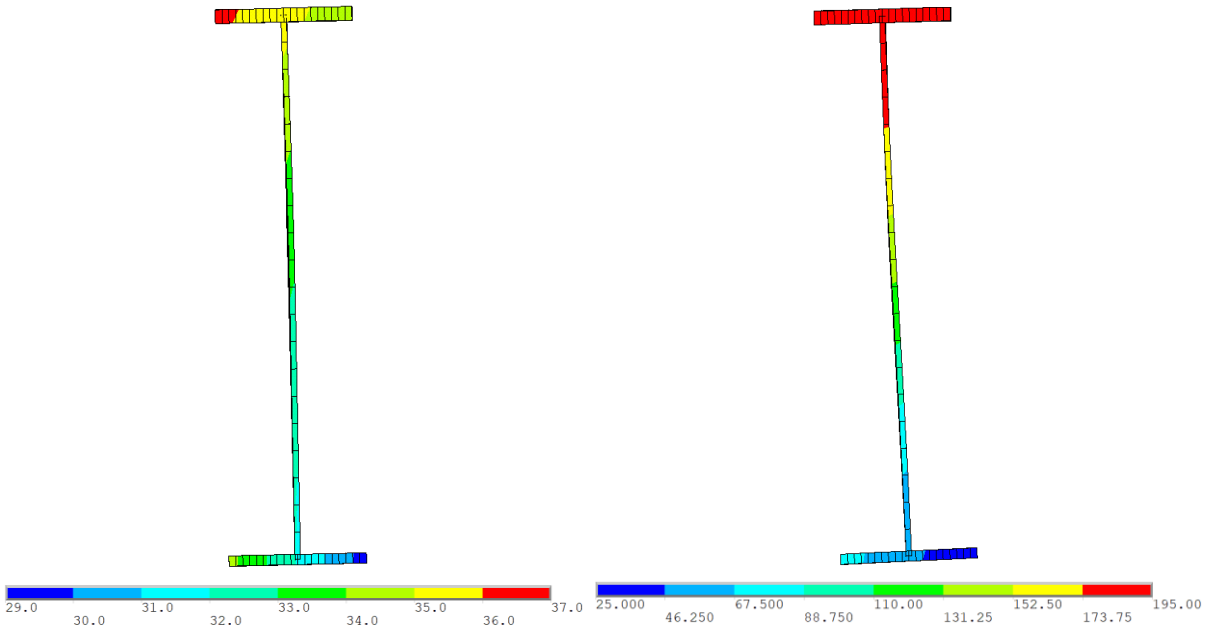

a) *Under ultimate load* *b)* *Post-peak*

Figure VII-12: Total displacement of U-MS *during and after buckling*

In addition, the evolution of the global displacements (δ) measured at web centres are presented in Figure VII-13 as a function of the applied force. The cross-sections of interest are located at 1.04 (H_2) and 2.08 m (H_3) from the loaded section (see Figure VI-7).

The numerical and experimental curves are in good agreement, especially in the cases of *U-DS* and *T-MS* where the numerical and experimental initial and post-peak slopes are similar. The comparisons of the results for *U-MS* show a slightly greater experimental initial stiffness when compared to the numerical one for H_2. The post peak slopes are also slightly different, being more pronounced for the experimental results, but the predictions of the numerical analyses are still sufficiently accurate.

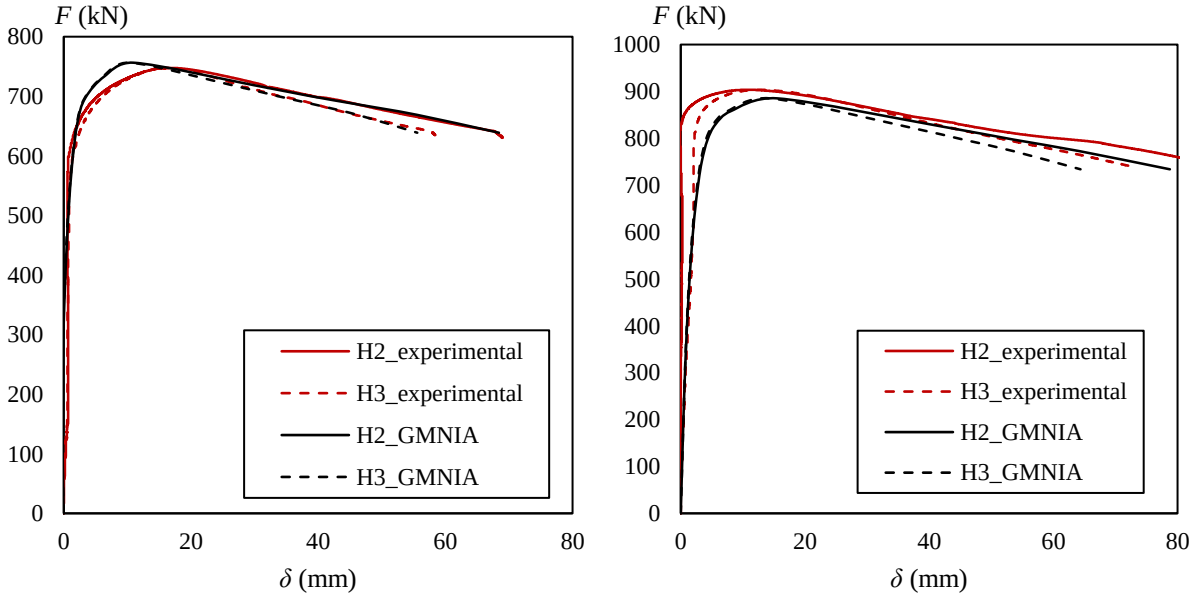

a) *U-DS* b) *U-MS*

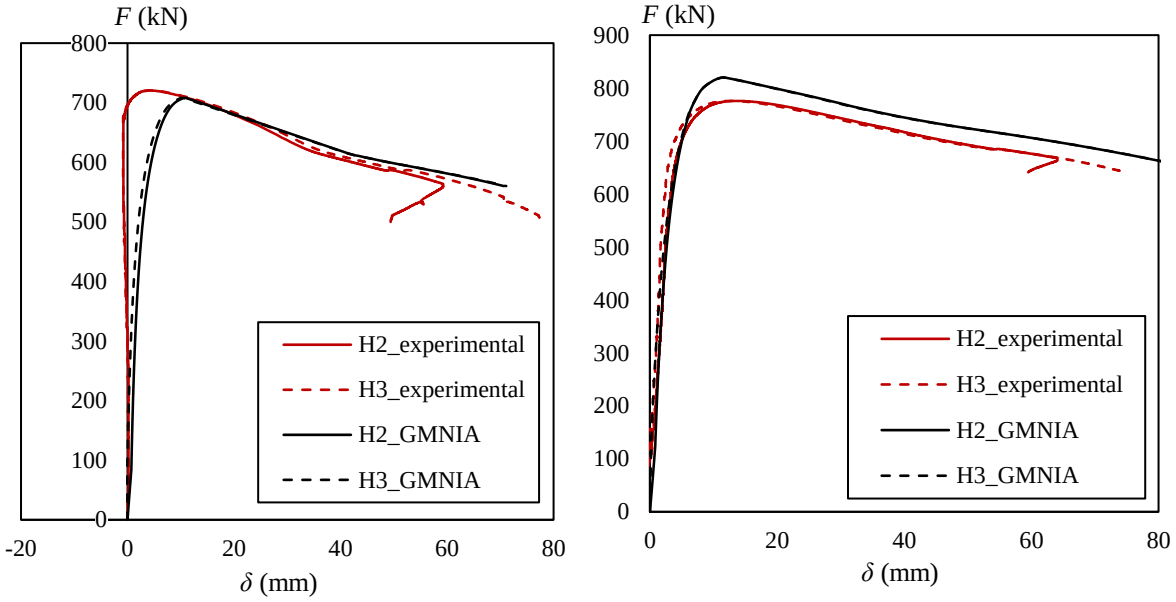

c) *T-DS* d) *T-MS*

Figure VII-13: Force- displacement curves

For specimen *T-DS*, small differences are noticed during the loading phase. Indeed, the sign – and direction – of the experimental displacements changes while it remains constant in the numerical analyses. The post-peak numerical and experimental behaviour are similar in *T-DS* as for the other beams.

The comparisons between numerical and experimental twist rotation are shown in Figure VII-14 as a function of the applied force. The studied twist rotations are recorded at the centre of the top flange of the cross-section located at 2.08 m from the loaded section.

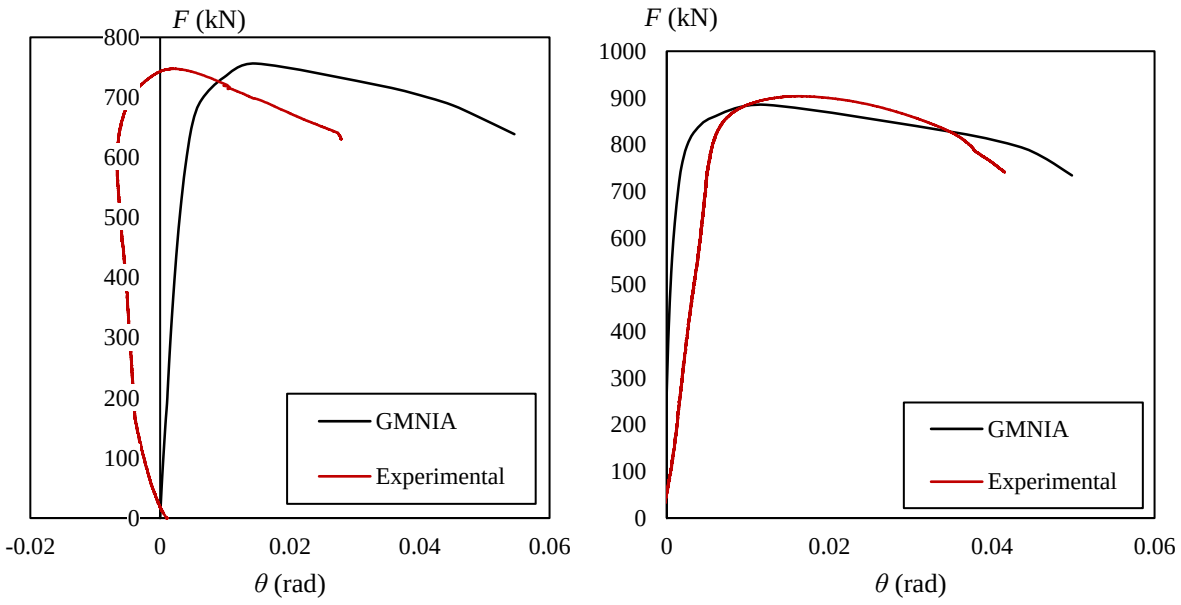

a) *U-DS* b) *U-MS*

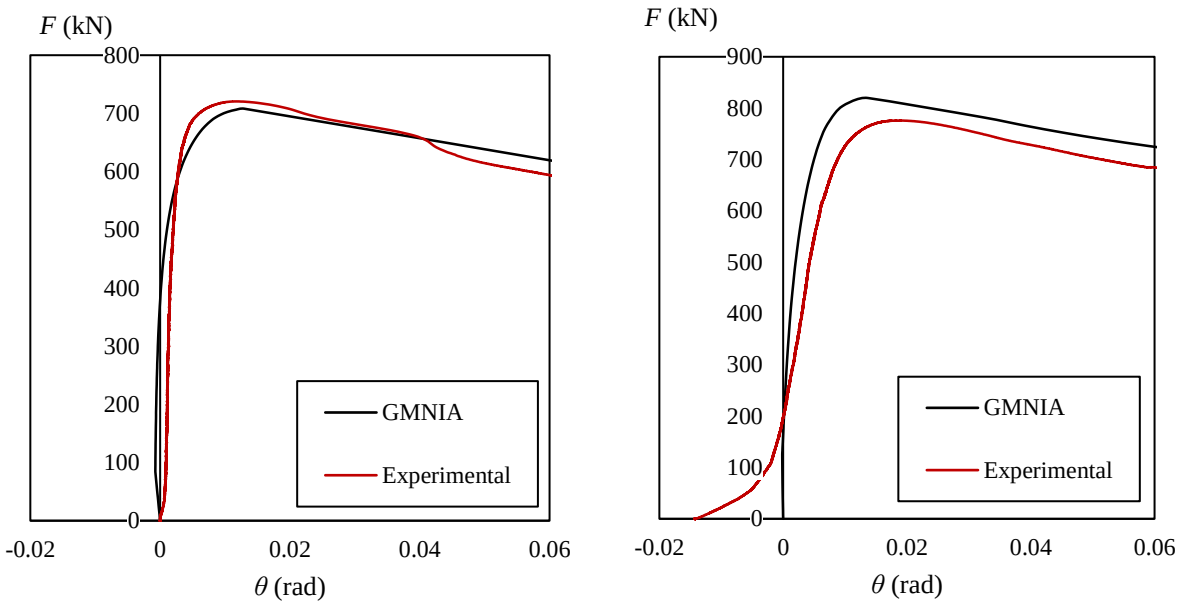

c) *T-DS* d) *T-MS*

Figure VII-14: Force-twist rotation curves

The numerical and experimental results match very well for all beams except *U-DS* where deviations are noticed. Indeed, during the loading phase of specimen *U-DS*, the twist rotation is negative while its sign and direction change when undergoing buckling. On the contrary, the sign of the numerical twist rotation is similar at every load step. However, both post-peak slopes are close. For the three other tests, the initial and post-peak experimental and numerical slopes are similar, though small differences may be noticed in the early part of the loading phase, especially for *T-MS*. While numerical rotations are always equal or very close to zero during the loading phase, small rotations can be measured experimentally during the loading phase which can be associated with slight rigid body motion of the specimens.

The comparisons between numerical and experimental displacements or rotations match very well. Some results exhibit small differences, especially when the direction of the displacement or rotation has changed during the test.

VII.3.2.3. Strains

Eventually, Figure VII-15 shows the numerical plastic von Mises strains for every test specimen under its ultimate load. In all specimens, no plastic strains are noticed except at the vicinity of the loaded cross-section, where lateral-torsional buckling is restrained. These results are in line with the experimental strain distributions measured in the compression flange at critical cross-sections (see Figure VI-19). Indeed, under ultimate load, all strains were found in the elastic region, at the vicinity to plasticity, except in specimen *U-DS* where the maximum elastic strain was significantly lower than ε_y.

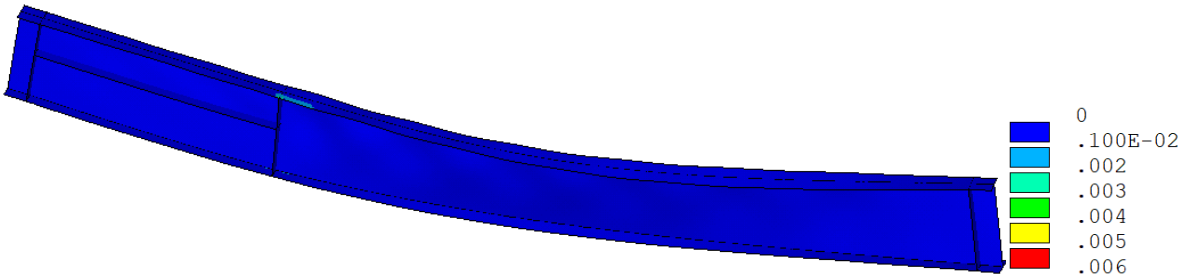

a) *Specimen U-DS*

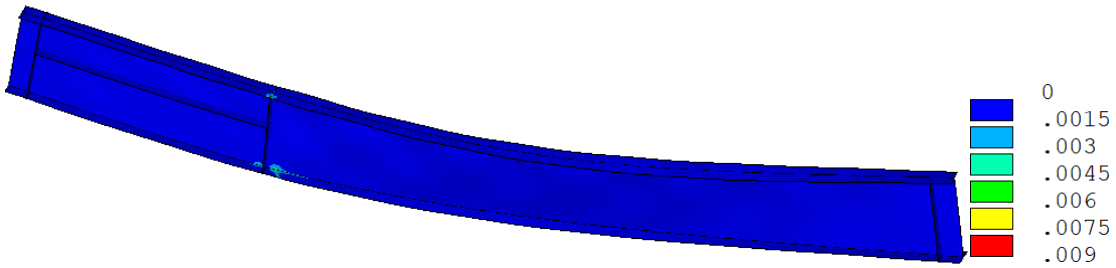

b) *Specimen U-MS*

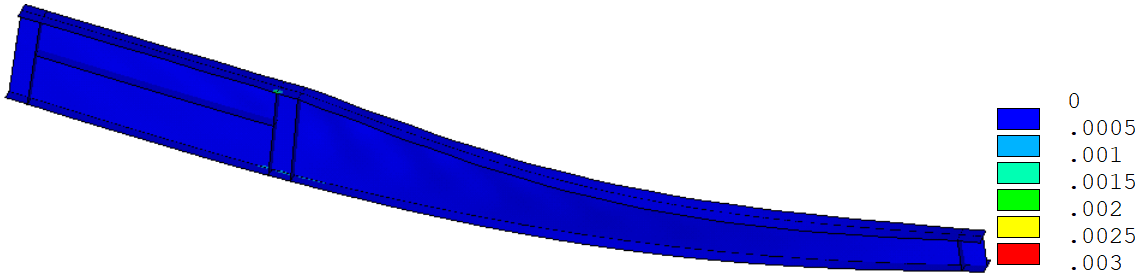

c) *Specimen T-DS*

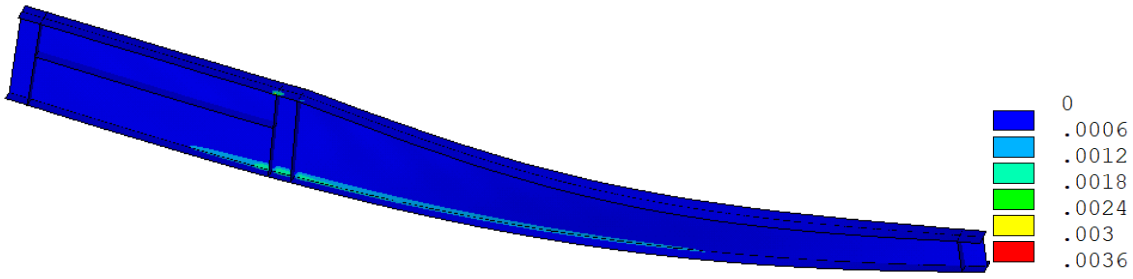

d) *Specimen T-MS*

Figure VII-15: Plastic von Mises strains under ultimate loading

The numerical model having been validated using experimental data, GMNIA calculations are performed, applied to a benchmark case. Indeed, the influence of the geometrical and material imperfections on the lateral-torsional buckling behaviour is investigated in the following section.

VII.4 Sensitivity analyses

VII.4.1 Residual stresses

The calibrated model is used to perform GMNIA calculations on a uniform doubly symmetric beam subjected to a uniform bending moment distribution and resting on fork supports at both ends. The studied beam, made of S355 steel, presents a 800×6 mm web, connected to 200×20 mm flanges.

Firstly, the influence of the residual stress model on the lateral-torsional buckling resistance is investigated. Indeed, similar geometrical imperfections (see VII.2.2) are implemented while different residual stress patterns are used in turn. The following residual stress models are studied:

- No residual stresses (noted *No RS*),
- *prEN 1993-1-14* (see Figure VII-2a)),
- New model from Chapter V (see Figure VII-2b)),
- *Barth* (1998) (see Figure VII-16a)),
- *Unsworth* (2021) (see Figure VII-16b)),
- *Schaper and Tankova* (2022) (see Figure VII-16c)).

In addition to both models presented in Figure VII-2 used as references, three models adapted to welded members with flame-cut flanges are used, presented in Figure VII-16. Besides, a series of GMNIA calculations is performed without residual stresses.

The additional three models from Figure VII-16 correspond to the models for flame-cut flanges presented in Chapter V for which each parameter of the model is defined. The models of *Chacón* (2009) and *Thiébaud* (2014) are not included in the present study, the former not being self-equilibrated while the latter was calibrated for bridge members.

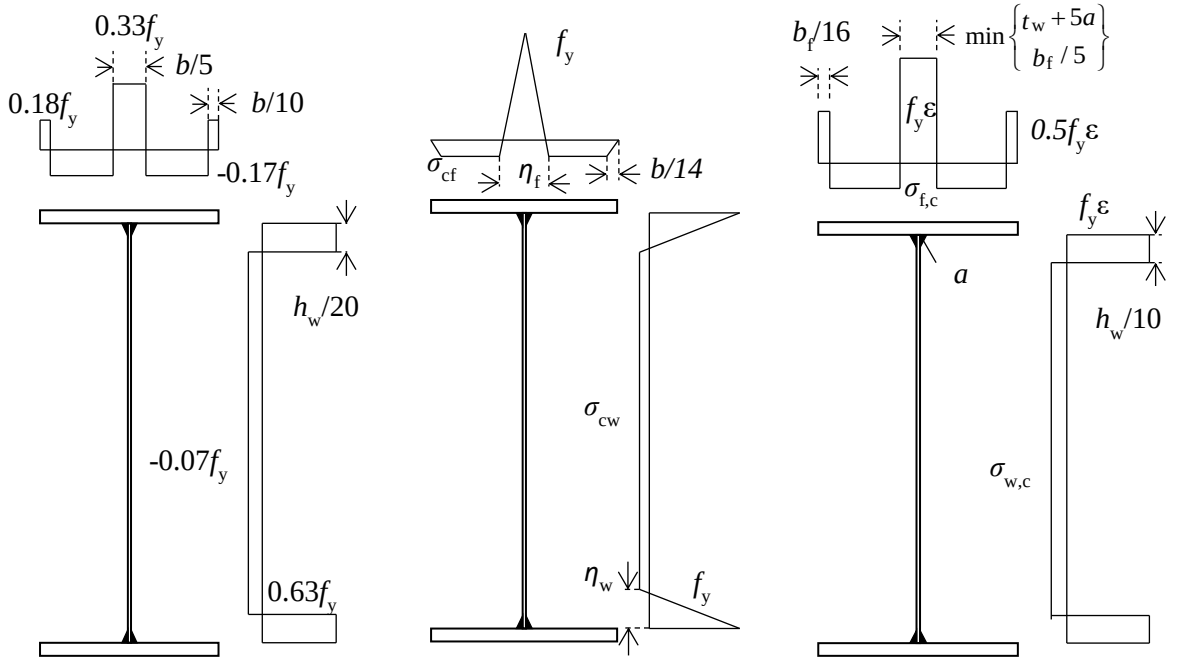

a) *Barth* (1998) b) *Unsworth* (2021) c) *Schaper and Tankova* (2022)

Figure VII-16: Additional residual stress models studied

The parameters of *Unsworth*'s (2021) model are reminded:

$$\eta_f = \left(2\frac{CA_w}{f_y \Sigma t} + t_w\right)\left(1 - \frac{B}{b}\right) \tag{VII.6}$$

$$\eta_w = \frac{CA_w}{f_y \Sigma t} \tag{VII.7}$$

where B is empirically set to 53, A_w is the cross-sectional area of a single weld and:

$$C = \frac{96E\alpha}{16\times10^{-3}} \tag{VII.8}$$

where α is the coefficient of linear thermal expansion that can be taken as equal to 15×10^{-6} C^{-1}.

The numerical results are depicted in Figure VII-17 using the χ-λ formalism. Buckling curves *a* and *d* are also plotted, along with the buckling curve determined using the new verification format from *prEN 1993-1-1* for the studied member. It is worth mentioning that the current and future *Eurocode 3 Part 1-1* impose to assess the studied beam using buckling curve *d* when using the *General case* design method.

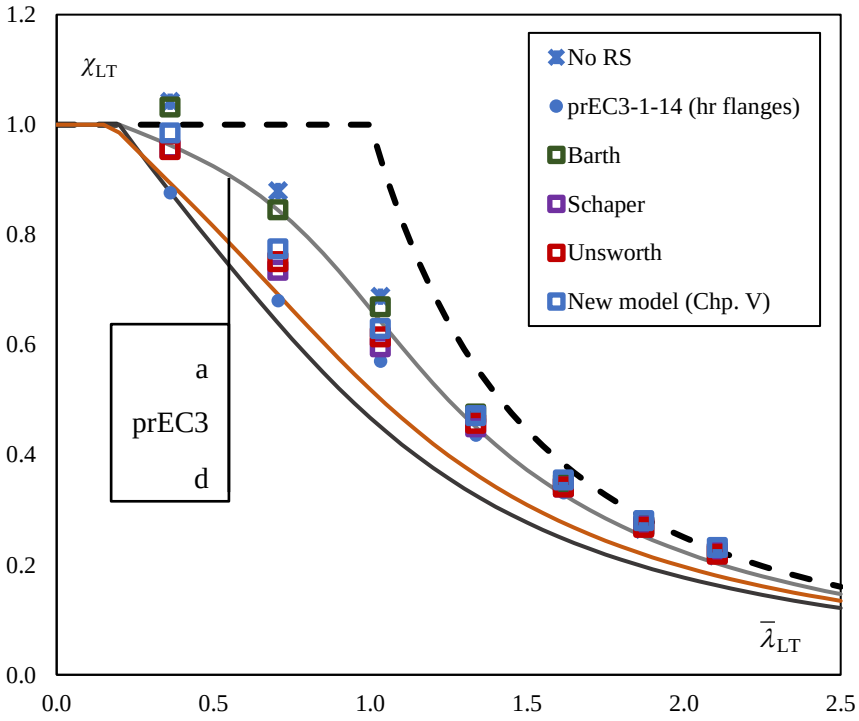

Figure VII-17: Member resistance for different residual stress models

Figure VII-17 shows a major influence of the residual stress model on the numerical ultimate bending moment for normalized slenderness up to 1.35.For greater values of the normalized, the results are quite close whatever the residual stress model. Though the results are very close for high slenderness, making use of models adapted to flame-cut flanges provides the greatest ultimate bending moments due to the favourable initial stresses at flanges tips.

For low and medium slenderness, the results obtained using the models of *Unsworth* (2021), *Schaper and Tankova* (2022) or the new model are very close. The differences between the ultimate bending

moments computed using the model from *Unsworth* (2021) and the new one lie between 2 and 3%. The differences between the results based on the model of *Schaper and Tankova* (2022) and the new model are between 3 and 5%.

For low and medium slenderness, the ultimate bending moments obtained using the model of *Barth* (1998) are noticeably greater than those obtained using the three other models adapted to flame-cut flanges. The results of *Barth*'s (1998) model are up to 10% greater than those obtained with the new model. This important difference can be attributed to the width of the tension zone at the flanges tips. Indeed, these stress blocks are much wider in the model of *Barth* (1998), being $b/10$, than in the new model or in that of *Schaper and Tankova* (2022) (up to $b/16$). Making use of *Barth*'s (1998) model yields ultimate bending moments very close to those obtained without residual stresses, the maximum difference between both cases being 4%.

Using the model for welded members with hot-rolled flanges produces results up to 12% lower than those obtained with the new model adapted to flame-cut flanges. For the studied member, the flange fabrication process has a visible influence on the ultimate bending moment when the normalized slenderness is lower than 1.1 to 1.3.

A good agreement can be seen in Figure VII-17 between the numerical results with the model of *prEN 1993-1-14* and the buckling curve of *prEN 1993-1-1* for the low slenderness range. When the normalized slenderness is greater than 0.8, the analytical buckling curve provides conservative results. Buckling curve *d* lies under that of the new verification format and provides very conservative results for medium to high slenderness. Both analytical design methods provide even more conservative results when compared to welded members made of flame-cut flanges. Indeed, the ultimate bending moments computed using buckling curve *d* are 40% lower than the numerical ones using the new model when the normalized slenderness is greater than 1.

For welded members with flame-cut flanges, the current and future European design rules are overly conservative when compared to GMNIA results. An extensive parametric study is therefore needed to develop design methods for overall out-of-plane buckling better suited to welded members with flame-cut flanges. The outline of this parametric study that includes over one thousand GMNIA computations are depicted in section VII.5.

VII.4.2 Geometrical imperfections

Besides the residual stresses, the influence of the magnitude of the geometrical imperfections on the ultimate bending moment is of interest. Firstly, three sets of GMNIA calculations are performed implementing different magnitudes of the global imperfection: $L/500$, $L/1000$ and $L/2000$. The residual stress model used is that given in sub-section VII.2.2 considering flame-cut flanges (see Figure VII-2b)). No local imperfections are enforced while the global imperfection remains scaled to the elastic critical lateral-torsional buckling mode (see VII.2.2).

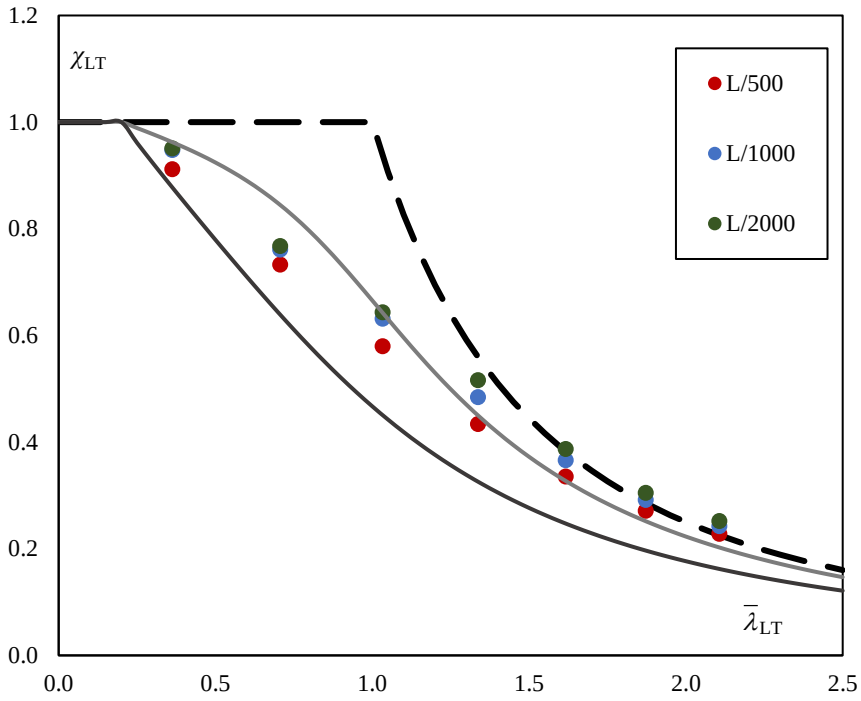

Figure VII-18: Member resistance for different global imperfection amplitudes

The numerical results are presented in Figure VII-18 along with buckling curves *a* and *d* for comparison. Implementing a magnitude of *L*/1000 or *L*/2000 produce similar results except for intermediate-to-high slenderness (1.2 to 1.8) where differences up to 6% are noticed, the lowest magnitude of the imperfection yielding the greatest ultimate bending moments. Differences are visible between the results using *L*/500 and *L*/1000 whatever the normalized slenderness. The maximum deviations are found for intermediate-to-high slenderness, reaching 10%. Implementing the greatest magnitude of the global imperfection produces the lowest results.

A second series of three sets of numerical analyses are performed varying the magnitude of the plate local imperfections. The implemented residual stress model and geometrical global imperfection (amplitude and shape) are those defined in sub-section VII.2.2 adapted to flame-cut flanges. The shape of the local imperfections is unchanged when compared to that defined in sub-section VII.2.2 while different magnitudes are implemented: $h_w/50$ and $b/50$, $h_w/200$ and $b/200$, $h_w/400$ and $b/400$. The GMNIA results are presented in Figure VII-19 where buckling curves *a* and *d* are plotted for comparison.

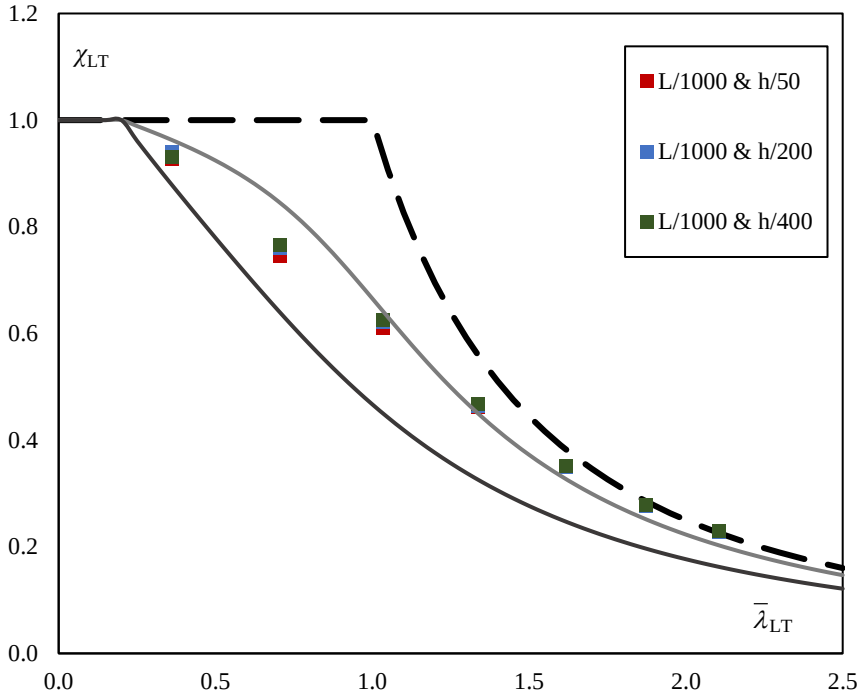

Figure VII-19: Member resistance for different amplitudes of the local imperfections

Figure VII-19 shows a negligible influence of the magnitude of the local imperfections on the buckling resistance though the studied beams present a Class 4 web in bending. Similar results are obtained when using the plate width /400 or /200. Small differences are noticed with the results obtained implementing the plate width /50 for low to intermediate slenderness. The highest difference of 2% is found when the normalized slenderness is equal to 0.7. The greater magnitude yields the lowest ultimate bending moments.

While the amplitude of the global imperfection has a small influence on the ultimate bending moment, that of the accompanying local imperfections is barely visible. The magnitude of the global imperfection has an impact on the buckling resistance when its value is at least $L/1000$. While being not recommended, using lower magnitudes for both geometrical imperfections would only slightly affect the ultimate bending moments in the studied case.

In the upcoming section, the scope of the parametric study is defined. This study is based on the numerical model described in section VII.2 that has been confronted to experimental results. The parametric study comprises more than a thousand of GMNIA computations, the results of which will be analyzed in Chapter VIII.

VII.5 Scope of the parametric study

VII.5.1 Presentation

The numerical model previously described and validated against experimental tests is used to perform a large parametric study. This study aims to investigate global out-of-plane buckling of welded steel members. Therefore, the studied members are subjected to bending moment or/and compression force without intermediate restraints.

As shown in sub-sections VII.3.2.1 and VII.4.1, the flange fabrication process have a significant impact on the stability behaviour and ultimate capacity of welded members. The parametric study focuses on welded members made of flame-cut flanges to propose consistent and adapted design rules.

VII.5.2 Out-of-plane buckling of welded columns

Using the validated numerical model, 377 GMNIA computations are performed on welded members subjected to constant compression. The members lengths are chosen to obtain normalized slenderness up to 2.5 or 3.

The main part of this study concerned welded members made of flame-cut flanges, their cross-section being:

- Uniform and doubly symmetric,
- Uniform and mono-symmetric, or
- Web-tapered and doubly symmetric.

The dimensions and properties of these members are presented in Table VII-5, the cross-sectional dimensions being defined in Figure VII-20. It is worth mentioning that both flanges of the web-tapered columns are inclined with the same angle. Besides, in the case of tapered columns, the ratios h_t/b and h_w/t_w are determined at the largest cross-section.

$h_{w,max}$ **(mm)**	300, 450, 600, 700, 800, 900, 1000
γ_h	1, 1.5, 1.7, 2, 2.2, 3
t_w **(mm)**	5, 6, 8, 10
$h_{w,max}/t_w$	45, 60, 90, 100, 117, 125, 133, 150
b **(mm)**	170, 200, 230, 250, 300, 350
$h_{t,max}/b$	1.3, 1.4, 1.9, 2, 2.1, 2.4, 2.6, 3.2, 3.3, 3.4, 3.5, 3.6, 3.7, 3.8, 4.2, 5.3
ρ_b	1, 1.5, 1.75
t_f **(mm)**	12, 16, 18, 20, 24, 25, 30, 40
ρ_{tf}	1, 1.56, 1.67, 2
$(b/t_f)_c$	7.5, 8, 8.3, 8.5, 9.6, 10, 11.5, 12, 12.5, 13.9, 14, 14.2, 17.5, 19.2, 20.8
Material	S275, S355

Table VII-5: Scope of the parametric study for welded columns with flame-cut flanges

with:

$$\gamma_h = \frac{h_{w,max}}{h_{w,min}} \quad \text{(VII.9)}$$

$$\rho_b = \frac{b_1}{b_2} \quad \text{(VII.10)}$$

$$\rho_{tf} = \frac{t_{f,1}}{t_{f,2}} \tag{VII.11}$$

where the subscript “f,1” is assigned to the dimensions of the flange having the greatest second moment of area about the *z*-axis, “f,2” corresponding to the other flange.

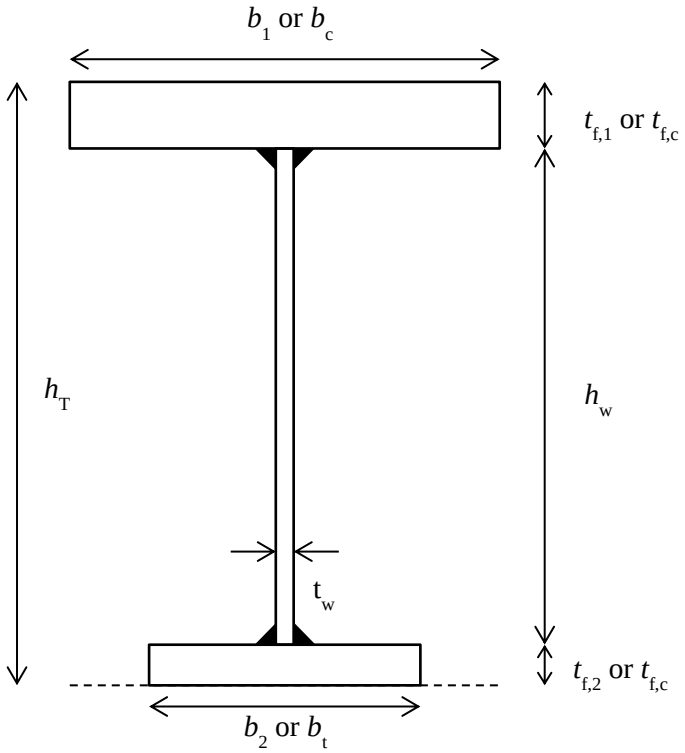

Figure VII-20: Cross-section dimensions

The members dimensions are chosen to be representative of the common practice of steel buildings. Indeed, the web height varies between 300 and 1000 mm with a slenderness ranging between 45 and 150, most are Class 4 webs in pure compression according to *Eurocode 3 Part 1-1*. In addition, the flanges width ranges between 170 and 350 mm, most of them being Class 1 or 2 flanges in pure compression. The cross-section mono-symmetry is characterized by flanges width ratios up to 1.75 and thickness ratios up to 2. Besides, S275 and S355 steel that are of common use in steel buildings are employed in the present study.

Besides, 62 of the GMNIA calculations are led on uniform doubly symmetric welded members made of hot-rolled flanges. The scope of dimensions is depicted in Table VII-6. These studied members are also investigated in parallel with flame-cut flanges.

h_w (mm)	300, 450, 600, 800, 900 1000
t_w (mm)	5, 6, 8
$h_{w,max}/t_w$	60, 90, 100, 125, 133, 150
b (mm)	170, 200, 230, 250
h_t/b	1.9, 2.1, 3.2, 3.7, 4.2, 5.3
t_f (mm)	12, 16, 18, 20, 25
b/t_f	8, 10, 12.5, 13.9, 14.2, 19.2
Material	S275, S355

Table VII-6: Scope of the parametric study for welded columns with hot-rolled flanges

VII.5.3 Lateral-torsional buckling of welded beams

The ultimate resistance of welded beams subjected to bending is determined by computing 961 GMNIA calculations. The studied bending moment distributions, presented in Table VII-7, are linear with ratios between end moments varying from -1 to 1 commonly used in practice. Similarly to the columns case, the beams lengths are set so that the normalized slenderness go up to 2.5 to 3.

Bending moment diagram	ψ
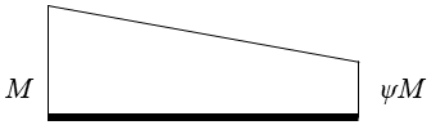	1, 0.5, 0, -0.5, -1

Table VII-7: Studied bending moment distributions

Most of the GMNIA calculations led on bent members are related to those having flame-cut flanges. The cross-section type of the studied beams are:

- Uniform and doubly symmetric,
- Uniform and mono-symmetric,
- Web-tapered and doubly symmetric, or
- Web-tapered and mono-symmetric.

The studied values of their dimensions are presented in Table VII-8. Only the compression flange (under positive bending moment) of the web-tapered beams is inclined if not mentioned otherwise. Similarly to the case of compressed members, the ratios h_t/b_{min} and h_w/t_w are determined at the largest cross-section of the tapered beams.

$h_{w,max}$ (mm)	300, 450, 600, 634, 750, 800, 900, 1000
γ_h	1, 1.5, 1.7, 2, 2.8, 2.9, 3, 3.3
t_w (mm)	5, 6, 8, 10
$h_{w,max}/t_w$	45, 60, 90, 100, 120, 125, 127, 133, 150
b_c (mm)	170, 200, 230, 250, 300, 350
$h_{t,max}/b_{min}$	1.3, 1.9, 2, 2.1, 2.4, 2.5, 2.9, 3.2, 3.3, 3.4, 3.5, 3.7, 3.8, 4.2, 5.3
ρ_b	0.57, 0.67, 1, 1.5, 1.75
t_{fc} (mm)	12, 15, 16, 18, 24, 25, 30
ρ_{tf}	0.5, 0.6, 0.64, 1, 1.33, 1.56, 1.67, 2
$(b/t_f)_c$	8, 8.3, 8.5, 9.6, 10, 11.5, 12, 12.5, 13.3, 13.9, 14, 14.2, 17.5, 19.2, 20.8
Material	S275, S355

Table VII-8: Scope of the parametric study for welded beams with flame-cut flanges

With:

$$\rho_b = \frac{b_c}{b_t} \tag{VII.12}$$

$$\rho_{tf} = \frac{t_{fc}}{t_{ft}} \tag{VII.13}$$

where the subscript "*c*" is assigned to the dimensions of the compression flange under positive bending moment, "*t*" corresponding to the tension flange.

Like for columns, beams dimensions are chosen correspondingly to the common practice of steel buildings. Indeed, the web height varies also between 300 and 1000 mm with a slenderness ranging between 60 and 150. Most cross-sections present a Class 3 or Class 4 web in pure bending. Similarly, the flanges width ranges between 170 and 350 mm, most of them being Class 1 or 2 flanges in pure compression. Within mono-symmetric members, the ratios between the flanges widths goes up to 1.75. The ratio between the flanges thickness of mono-symmetric beams is up to 2. The vast majority of mono-symmetric beams are studied with the greatest flange in compression under a positive bending moment. However, some mono-symmetric beams are studied with the greatest flange in tension under a positive bending moment.

Within the GMNIA computations performed on welded beams, 154 refer to members made of hot-rolled flanges. For such members, only uniform and doubly-symmetric cross-sections are investigated. The studied cross-sectional dimensions and properties are presented in Table VII-9. The dimensions of the investigated members with hot-rolled flanges are included in the parametric study for beams with flame-cut flanges.

$h_{w,max}$ (mm)	300, 450, 600, 800
t_w (mm)	5, 6
$h_{w,max}/t_w$	60, 90, 100, 133
b (mm)	170, 200, 230
h_t/b	1.9, 2.1, 3.2, 4.2
t_f (mm)	12, 16, 20
b/t_f	10, 12.5, 14.2, 19.2
Material	S275, S355

Table VII-9: Scope of the parametric study for welded beams with hot-rolled flanges

VII.5.4 Out-of-plane buckling of welded beam-columns

Eventually, 168 GMNIA computations are performed on welded members with flame-cut flanges subjected to both compression and bending moment simultaneously. While the axial compression is uniform in the studied members, the bending moment distribution is linear, with a ratio between end moments equal to 1, 0.5 or 0. Table VII-10 presents the investigated distributions of both the bending moment and axial load, along with the studied ratios of the applied moment M to axial force N.

Distribution of the external loading		ψ	M/N (mm)
M	ψM	1, 0.5, 0	15, 75, 150, 500
N	ψN	1	

Table VII-10: Studied bending moment and axial force distribution

Like in the case of welded members subjected to either compression or bending, the studied lengths are defined to yield normalized slenderness up to between 2.5 and 3.

The studied beam-columns present a doubly symmetric cross-section which is either uniform or web tapered. The scope of their dimensions is presented in Table VII-11. Like for columns, both flanges of the web-tapered beam-columns are inclined. Again, the ratios h_t/b and h_w/t_w are determined at the largest cross-section of the tapered beams.

$h_{w,max}$ (mm)	438, 680, 800, 1000
γ_h	1, 2, 2.5, 3.2
t_w (mm)	5, 6, 10
$h_{w,max}/t_w$	88, 100, 113, 133, 136
b (mm)	200, 230, 350
$h_{t,max}/b$	2, 2.1, 3.1, 4.2, 5.3
t_f (mm)	12, 20, 25
b/t_f	8, 10, 11.5, 17.5, 19.2
Material	S355

Table VII-11: Scope of the parametric study for welded beam-columns (flame-cut flanges)

The chosen dimensions of the studied columns, beams and beam-columns are deemed to match with the common practice of steel buildings. The results of these studies are exploited in Chapter VIII.

VII.6 Summary

In the present chapter, the numerical model created to perform GMNIA simulations has been described. The employed material properties and imperfections were presented, using the outcomes of Chapter V in the case welded members made of flame-cut flanges. The shapes and amplitudes of both local and global geometrical imperfections were defined based on the recommendations of *Boissonnade* (2012), *Couto* (2019), *Gérard* (2019) and *prEN 1993-1-14*.

The numerical model was further adjusted to perform non-linear analyses of beams tested presented in Chapter VI. Using the experimentally measured material laws, residual stresses distributions and imperfection amplitudes yielded a very good agreement between the numerical and experimental results. While the load carrying capacities match very well for 3 of the tests, the difference is still acceptable for the last test, being 5.6%. In addition, the numerical and experimental course of key displacements and rotations are very similar for all of the test beams.

The numerical model being validated using key experimental results, GMNIA computations are performed on a benchmark case. The impact of the geometrical and material imperfections on the LTB behaviour under a constant bending moment is studied. The flange fabrication process has an influence on the ultimate bending moment for low and medium slenderness. Members with flame-cut flanges obtain ultimate bending moments up to 12% greater than those with hot-rolled flanges. The numerical results for flame-cut flanges showed that buckling curve *d* and the predictions of the new verification format in *prEurocode 3* are overly conservative. Better suited design methods should therefore be employed for welded members made of flame-cut flanges.

An extensive parametric study is therefore performed that includes 1506 GMNIA computations. These calculations study out-of-plane buckling of columns, beams and beam-columns. Most of the non-linear analyses are led on members made of flame-cut flanges, 216 being adapted to members with hot-rolled flanges. In order to assess the accuracy and safety of the current and future European design rules, the dimensions of the studied members are considered representative of the common practice of steel buildings. Uniform and web-tapered members having either a doubly or mono-symmetric cross-sections

are therefore investigated. The results of these parametric studies are operated in the upcoming Chapter VIII.

VIII. *Design guidelines for welded members with flame-cut flanges*

VIII.1 Introduction

The numerical model depicted in the preceding Chapter VII, uses the new residual stress model defined in Chapter V for welded members with flame-cut flanges and have been confronted to experimental results of Chapter VI. Good agreement was obtained between the numerical and experimental results. The significant impact of the flange fabrication process on the LTB resistance was also highlighted using a benchmark case. The current and future *Eurocode 3 Part 1-1* design rules revealing overly conservative for the few studied welded members made of flame-cut flanges, a large parametric study has been computed. The outlines of these GMNIA computations were presented in Chapter VII. This parametric study investigated the overall out-of-plane buckling of welded members subjected to compression force and/or bending moment. While members with flame-cut flanges were of major interest, more than 200 non-linear analyses investigated those made of hot-rolled flanges for comparison. In the present chapter, the results of these computations are analyzed. Design methods adapted to welded members with flame-cut flanges and based on the current and future *Eurocode 3* are proposed.

Firstly, the determination of a partial safety factor corresponding to design resistances of members to instabilities is developed in section VIII.2. This process is then employed to validate the safety of two approaches that are suggested for members subjected to compression force in section VIII.3. A simple method makes use of the current flexural buckling curves while a more enhanced alternate one proposes to define a buckling curve per member.

These two approaches are then expressed for members subjected to major axis bending moment in section VIII.4. The partial safety factors for both proposed design rules are determined, revealing satisfactory safety levels. In addition, adaptations of the new verification format of *prEN 1993-1-1* are proposed. Analytical derivations are performed to extend the scope of this method that is restricted to uniform beams with a doubly symmetric cross-section in *prEN 1993-1-1*.

Eventually, the design methods proposed for flexural and lateral-torsional buckling are included into the verification format of beam-columns relying on design methods proposed in *prEurocode 3 Part 1-1*. When compared against numerical results, the predictions of the analytical model adapted to flame-cut flanges show a good accuracy. Satisfying safety levels validate the use of design methods adapted to welded members made of flame-cut flanges allowing increased resistance. A summary of the proposed design methods concludes the present chapter.

VIII.2 Determination of a partial safety factor γ_{M1}

VIII.2.1 Presentation

The computation of partial safety factors within the present work is based on the prescriptions of *Annex D of EN 1990* and the recommendations of the European RFCS project *SAFEBRICTILE*. It is worth mentioning that the prescriptions of *Annex D of Eurocode 0* for the determination of partial safety factors remain unchanged in its future version *prEN 1990*.

The general procedure is composed of five major steps:

- Step 1: Determination of the input parameters: resistance function ($r_{t,i}$), actual experimental or numerical resistance ($r_{e,i}$) and statistical information about the basic variables (X_j);
- Step 2: Estimation of the accuracy of the resistance function;
- Step 3:Analysis of the sensitivity of the resistance function to the variability of the basic input variables;
- Step 4: Computation of design resistances ($r_{d,i}$) yielding values of partial factors γ_{M1}*;
- Final step: Estimation of acceptance levels for γ_{M1} based on the variations of the resistance function.

The specific content of each step is briefly presented in the following sub-sections.

VIII.2.2 Step 1: Input data

Firstly, the resistance function $r_{t,I}$ is defined for each set of the studied basic variables and corresponds to a specific failure mode. In the present work investigating stability, the basic variables X_i are:

- The yield strength f_y and Young's modulus E,
- The cross-section height h_t and web thickness t_w,
- For doubly-symmetric members:
    - Both flanges width b and thickness t_f,
- For mono-symmetric members:
    - The top flange width b_s and thickness t_{fs},
    - The bottom flange width b_i and thickness t_{fi}.

The cross-sectional dimensions are reminded in Figure VIII-1.

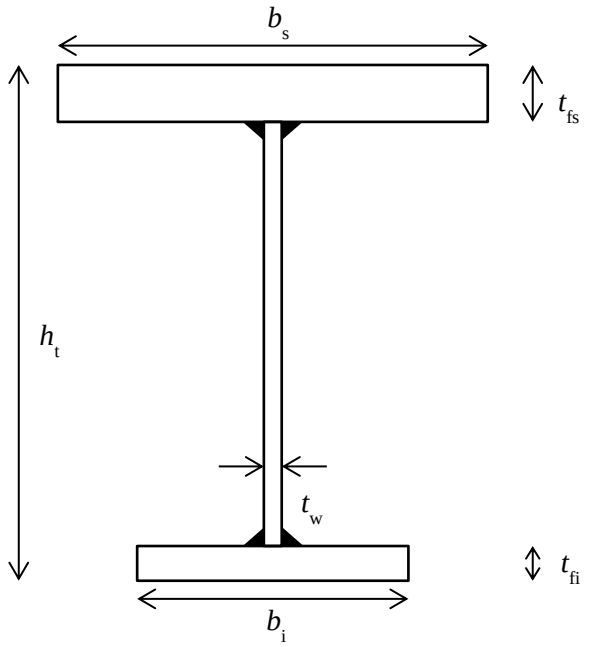

Figure VIII-1: Cross-section dimensions

The resistance function can be written as:

$$r_{t,i} = g_{rt,i}\left(X_1, X_2, ..., X_k\right) \qquad \text{(VIII.1)}$$

The statistical information concerning the basic variables used in this study correspond to that provided in *Annex E of prEurocode 3 Part 1-1*. The mean value and coefficient of variation (c.o.v.) of the input variables previously described are presented in Table VIII-1. These values are extracted from Table E.1 and E.2 of *prEN 1993-1-1*.

Input variable X_i	**Mean value $X_{i,m}$**	***c.o.v.$_i$***
f_y (275 MPa)	1.25 $f_{y,nom}$	5.5%
f_y (355 MPa)	1.20 $f_{y,nom}$	5.0%
E	210 000 N/mm²	3.0%
h_t	1.0 $h_{t,nom}$	0.9%
b	1.0 b_{nom}	0.9%
t_w	1.0 $t_{w,nom}$	2.5%
t_f	0.98 $t_{f,nom}$	2.5%

Table VIII-1: Assumed variability of input parameters

where, the coefficient of variation can be expressed as a function of the standard deviation σ_i and the mean value $X_{i,m}$:

$$\text{c.o.v.}_\text{i} = \frac{\sigma_\text{i}}{X_\text{i,m}} \tag{VIII.2}$$

Besides, the actual resistances $r_{e,i}$ are obtained for each specimen of interest based on the GMNIA results obtained using the numerical model previously depicted.

VIII.2.3 Step 2: Accuracy of the resistance function

The accuracy of the resistance function is assessed by computing the mean value of the correction factor:

$$b = \frac{\sum_{i=1}^{n} r_\text{t,i} r_\text{e,i}}{\sum_{i=1}^{n} r_\text{t,i}^{\,2}} \tag{VIII.3}$$

where n is the number of specimens within the studied set.

Then, the c.o.v. of the error V_δ is determined as follows:

$$\delta_\text{i} = \frac{r_\text{e,i}}{b r_\text{t,i}} \tag{VIII.4}$$

$$\Delta_\text{i} = \ln\left(\delta_\text{i}\right) \tag{VIII.5}$$

$$s_\Delta^{\,2} = \frac{1}{n-1}\sum_{i=1}^{n}\left(\Delta_\text{i} - \overline{\Delta}\right)^2 \tag{VIII.6}$$

$$V_\delta = \sqrt{\exp\left(s_\Delta^{\,2}\right) - 1} \tag{VIII.7}$$

VIII.2.4 Step 3: Sensitivity of the variation of input data

The third step consists in calculating the c.o.v. V_rt characterizing the sensitivity of the theoretical resistance function to slight variations of the input data. For each specimen, $V_\text{rt,i}$ is determined by

$$V_\text{rt,i}^{\,2} = \frac{1}{\left[g_\text{rt,i}\left(X_\text{1,m},\ldots,X_\text{k,m}\right)\right]^2}\sum_{j=1}^{k}\left(\frac{\partial g_\text{rt,i}\left(X_1,\ldots,X_\text{k}\right)}{\partial X_j}\sigma_\text{j}\right)^2 \tag{VIII.8}$$

The partial derivatives are obtained using the following approximation:

$$\frac{\partial g_\text{rt,i}\left(X_1,\ldots,X_\text{k}\right)}{\partial X_j} = \frac{g_\text{rt,i}\left(X_1,\ldots,X_\text{j}+\Delta X_j,\ldots,X_\text{k}\right) - g_\text{rt,i}\left(X_1,\ldots,X_\text{j},\ldots,X_\text{n}\right)}{\Delta X_j} \tag{VIII.9}$$

VIII.2.5 Step 4: Design resistance and partial factor

In the case of a large number of results (n > 100), the design resistance $r_{d,i}$ of each specimen is obtained using:

$$r_{d,i} = bg_{rt,i}\left(X_{1,m},...,X_{k,m}\right)\exp\left(-k_{d,\infty}Q_i - 0.5Q_i^2\right) \quad \text{(VIII.10)}$$

with:

$$Q_i = \sqrt{\ln\left(1+V_{r,i}^{\ 2}\right)} \quad \text{(VIII.11)}$$

$$V_{r,i}^{\ 2} = V_{rt,i}^{\ 2} + V_\delta^{\ 2} \quad \text{(VIII.12)}$$

For a limited number of tests, the design resistance is determined using:

$$r_{d,i} = bg_{rt,i}\left(X_{1,m},...,X_{k,m}\right)\exp\left(-k_{d,\infty}\frac{Q_{rt,i}^{\ 2}}{Q_i} - k_{d,n}\frac{Q_\delta^{\ 2}}{Q_i} - 0.5Q_i^2\right) \quad \text{(VIII.13)}$$

with:

$$Q_{rt,i} = \sqrt{\ln\left(1+V_{rt,i}^{\ 2}\right)} \quad \text{(VIII.14)}$$

$$Q_\delta = \sqrt{\ln\left(1+V_\delta^{\ 2}\right)} \quad \text{(VIII.15)}$$

The parameters $k_{d,n}$ and $k_{d,\infty}$ are the design fractile factors for n and infinite single test results, respectively. The values of $k_{d,n}$ are presented in Table VIII-2, extracted from Table D.2 of *Eurocode 0* (*Annex D*).

n	4	5	6	8	10	20	30	∞
$\boldsymbol{k_{d,n}}$	11.40	7.85	6.36	5.07	4.51	3.64	3.44	3.04

Table VIII-2: Values of $k_{d,n}$

Eventually, partial factors $\gamma_{M1,i}$* are determined for each specimen using:

$$\gamma_{M1,i}^{\ *} = \frac{r_{t,i}}{r_{d,i}} \quad \text{(VIII.16)}$$

An average partial factor is then obtained for each set of results:

$$\gamma_{M1}^{\ *} = \frac{1}{n}\sum_{i=1}^{n}\gamma_{M1,i}^{\ *} \quad \text{(VIII.17)}$$

VIII.2.6 Final Step: Acceptance level

In agreement with the current practice, it has been chosen to have a unique partial safety factor with a target value of 1.0:

$$\gamma_{\mathrm{M1,target}} = 1.0 \tag{VIII.18}$$

Besides, it has been shown in the *SAFEBRICTILE* project that values of the partial safety factor slightly greater than the target one can be employed with almost no incidence on the reliability level. Therefore, acceptance levels $f_{\mathrm{a,i}}$ are defined, for each specimen, as:

$$f_{\mathrm{a,i}} = \frac{\gamma_{\mathrm{M1,i}}^{*}}{\gamma_{\mathrm{M1,target}}} \tag{VIII.19}$$

Expressions of the acceptance levels depend on the value of $V_{\mathrm{r,i}}$ (see Eq. (VIII.12)), as recommended in the *SAFEBRICTILE* project and presented in Table VIII-3.

Range of $V_{\mathrm{r,i}}$	$f_{\mathrm{a,i}}$
$0.00 < V_{\mathrm{r,i}} < 0.04$	1.03
$0.04 < V_{\mathrm{r,i}} < 0.20$	$1.03 + 0.75(V_{\mathrm{r}} - 0.04)$
$0.20 \leq V_{\mathrm{r,i}}$	1.15

Table VIII-3: Acceptance levels

The final partial safety factor for each studied member is then:

$$\gamma_{\mathrm{M1,i}} = \frac{\gamma_{\mathrm{M1,i}}^{*}}{f_{\mathrm{a,i}}} \tag{VIII.20}$$

Consequently, the average partial safety factor for each set of results is:

$$\gamma_{\mathrm{M1}} = \frac{1}{n}\sum_{i=1}^{n}\gamma_{\mathrm{M1,i}} \tag{VIII.21}$$

For each studied design method, partial safety factors are computed for several sub-sets of results. In agreement with expression (VIII.18) of the target value, the partial safety factors corresponding of each sub-group of data associated with a design method should not exceed 1.05 to provide a satisfying level of safety.

In addition, a partial safety factor associated with each design method is computed using the full set of results at once. In such cases, values greater than 1.05 are acceptable though characterizing design methods lacking accuracy or having a variable sensitivity.

VIII.3 Out-of-plane buckling of columns

VIII.3.1 Numerical results

The numerical analyses performed on welded columns in the framework of the parametric study have resulted in two sets of axial loads:

- $N_{cr,LBA}$: elastic critical load corresponding to out-of-plane flexural buckling for doubly-symmetric members or flexural-torsional buckling for mono-symmetric members;
- $N_{ult,GMNIA}$: ultimate axial load for flexural or flexural-torsional buckling.

In addition, analytical values of the characteristic cross-sectional resistance to compression N_{Rk} are determined using the prescriptions of *Eurocode 3 Parts 1-1* and *1-5*. The two following key parameters are determined using these three values:

$$\bar{\lambda}_i = \sqrt{\frac{N_{Rk}}{N_{cr,LBA}}} \qquad \text{(VIII.22)}$$

$$\chi_{i,GMNIA} = \frac{N_{ult,GMNIA}}{N_{Rk}} \qquad \text{(VIII.23)}$$

where the subscript *i* stands for the buckling mode. For flexural buckling about the *z*-axis, χ_i is replaced with χ_z while for flexural-torsional buckling, the reduction coefficient is χ_{FT}.

The numerical results are plotted using the χ-λ formalism of *Eurocode 3 Part 1-1*. Figure VIII-2 shows the numerical results for uniform members having a doubly symmetric cross-section. The five European buckling curves for compressed members (a_0, *a*, *b*, *c* and *d*) are also plotted for comparison.

The prescriptions of *Eurocode 3 Part 1-1* require the use of buckling curve *c* to compute χ_z for all of the studied welded columns because for all of them $t_f \leq 40$ mm. However, it can be seen that numerical results obtained for welded columns made of flame-cut flanges fall above curve *a* when the normalized slenderness is greater than 1. For shorter members, most of the flame-cut numerical results lie between curves *a* and *b* while a few results are found slightly under buckling curve *b*. Numerical results for welded members with hot-rolled flanges are comprised between buckling curves *c* and *d* in the low slenderness range (< 0.8). As the slenderness increases, the numerical results get closer to *Euler*'s curve and are found above curve *a* for high slenderness (> 1.5).

For intermediate slenderness, the use of the buckling curve *c*, as prescribed by the code, seems very safe in the case of hot-rolled flanges and overly conservative for flame-cut flanges. For high slenderness, buckling curve *c* appears to provide overly safe results whatever the flange fabrication process.

The accuracy of the *Eurocode 3 Part 1-1* prescriptions is analyzed in sub-section VIII.3.2 for welded members made of flame-cut flanges. Then, design methods adapted to such members are proposed, the use of the current buckling curve *c* being overly conservative, especially for medium and high slenderness.

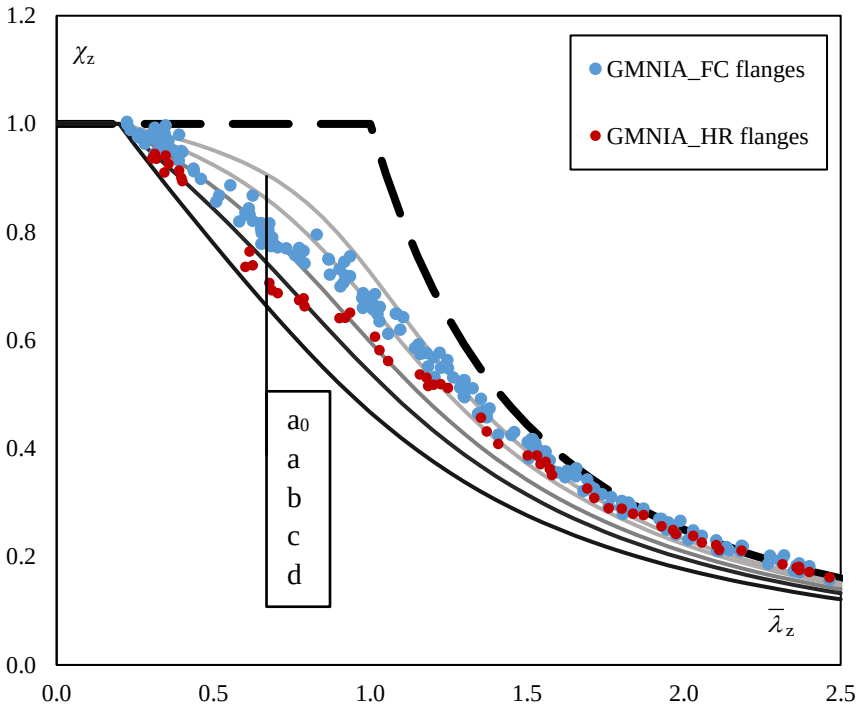

Figure VIII-2: Numerical results for flexural buckling of uniform doubly symmetric columns

Figure VIII-3 shows the numerical results for welded columns having a uniform and mono-symmetric cross-section. The results lie between buckling curves *b* and *c* for slenderness up to 0.8 while they get closer to *Euler*'s curve as the slenderness increases. Indeed, for intermediate slenderness, between 0.8 and 1.2, the numerical reduction factors are comprised between buckling curves *a* and *b*. When the slenderness is greater than 1.2, the numerical results are found above buckling curve *a*. It is worth mentioning that for the studied members, *Eurocode 3 Part 1-1* imposes the use of buckling curve *c*.

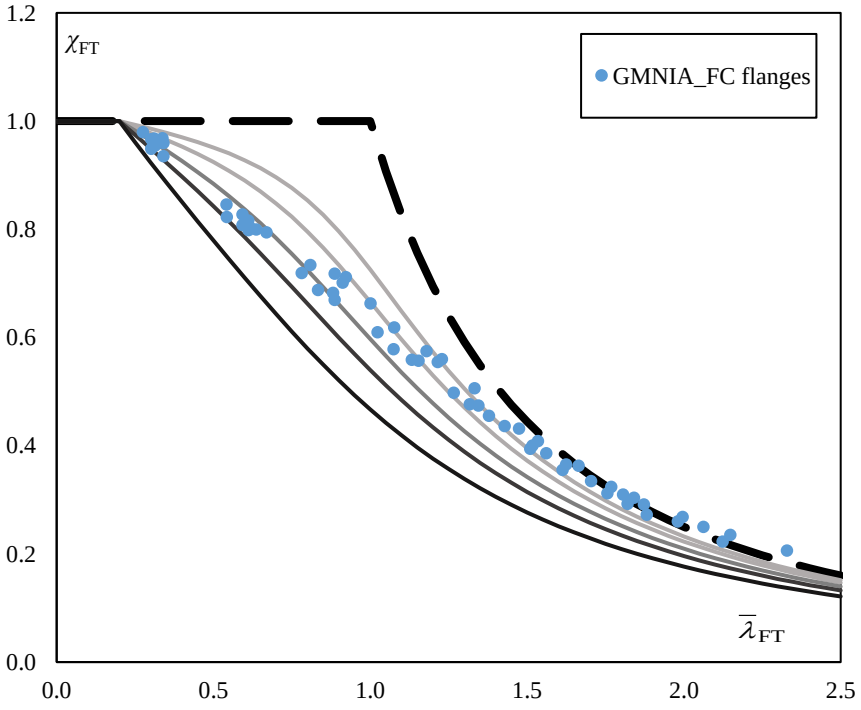

Figure VIII-3: Numerical results for flexural-torsional buckling of uniform mono-symmetric columns

Eventually, the numerical reduction factors for flexural buckling of tapered doubly-symmetric welded columns are presented in Figure VIII-4. These results are obtained computing N_{Rk} for the cross-section where the load amplifier $\alpha_{ult,k}$ reaches its minimum value. No in-plane imperfection being introduced in the numerical model, the in-plane behaviour of the column is neglected when determining $\alpha_{ult,k}$:

$$\alpha_{ult,k}(x) = \frac{N_{Rk}}{N_{Ed}}(x) \qquad \text{(VIII.24)}$$

Because the acting design load N_{Ed} is uniform along the tapered column, the load amplifier $\alpha_{ult,k}$ is always minimal at the smallest end despite a varying cross-section classification along the column length.

Figure VIII-4 shows that for low slenderness (<0.75), the numerical reduction factors match with buckling curve *b*. When the slenderness increases up to 1, the numerical results are found between buckling curves *a* and *b* while for higher slenderness, the numerical results lie above curve *a* then above a_0. Similarly to the case of uniform doubly symmetric members, Figure VIII-4 exhibits an over conservatism of the *Eurocode 3 Part 1-1* design rules that imposes the use of buckling curve *c* for the studied cases.

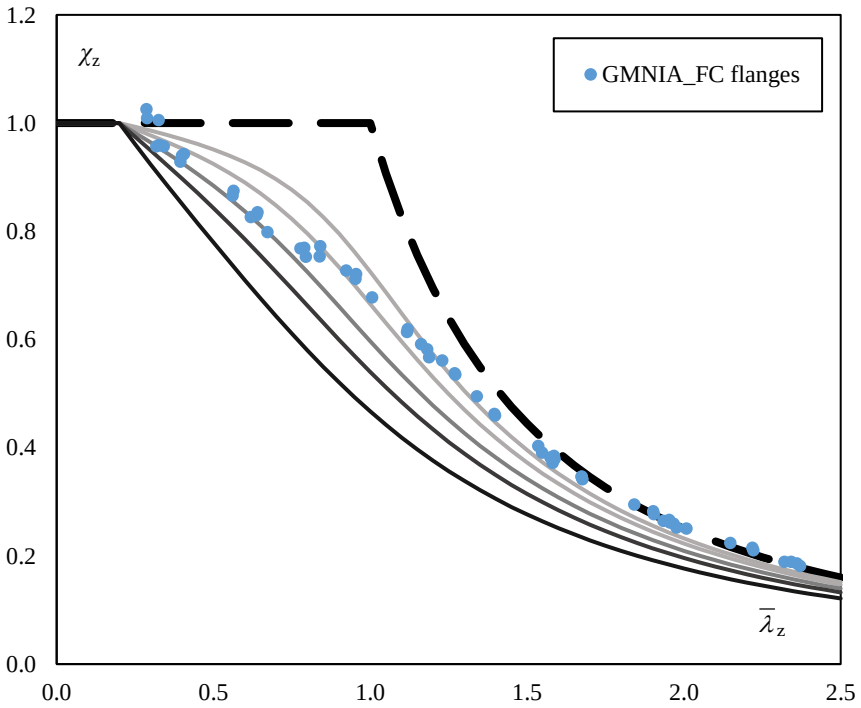

Figure VIII-4: Numerical results for flexural buckling of tapered doubly symmetric columns

In the following sub-section VIII.3.2, the accuracy of the design methods given in *Eurocode 3 Part 1-1* are evaluated for doubly symmetric welded members made of flame-cut flanges. In the next sub-section VIII.3.3, new design methods adapted to this type of columns are proposed and validated by the calculation of partial safety factors.

VIII.3.2 Assessment of the Eurocode 3 *design methods for flexural buckling*

As detailed in Chapter IV, the current and future *Eurocode 3 Part 1-1* impose to determine the resistance $N_{b,Rd}$ of a member subjected to compression force using:

$$N_{b,Rd} = \chi_i \frac{N_{Rk}}{\gamma_{M1}} \tag{VIII.25}$$

For a doubly symmetric member unrestrained between both ends, failure is governed by out-of-plane flexural buckling. The corresponding reduction factor χ_z is determined by:

$$\chi_z = \frac{1}{\phi_z + \sqrt{\phi_z^2 - \bar{\lambda}_z^2}} \leq 1.0 \tag{VIII.26}$$

$$\phi_z = 0.5\left[1 + \alpha_z\left(\bar{\lambda}_z - 0.2\right) + \bar{\lambda}_z^2\right] \tag{VIII.27}$$

For welded members having flange thickness up to 40 mm, the imperfection factor α_z corresponding to buckling curve *c* should be used, corresponding to $\alpha_z = 0.49$.

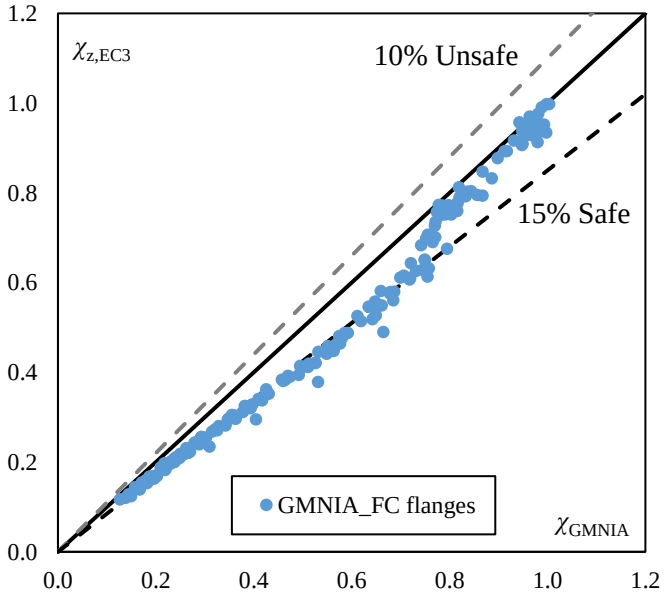

Figure VIII-5: Numerical and Eurocode 3 *reduction factors for uniform columns*

The reduction factors determined using the prescriptions of *Eurocode 3* (see Eq. (VIII.26)) are compared against those resulting from GMNIA computations for members with flame-cut flanges. Figure VIII-5 shows the comparison between the analytical and numerical reduction factors for uniform members. The same results are presented in Figure VIII-6 for tapered columns with N_{Rk} computed at the smallest cross-section, where $\alpha_{ult,k}$ is minimum.

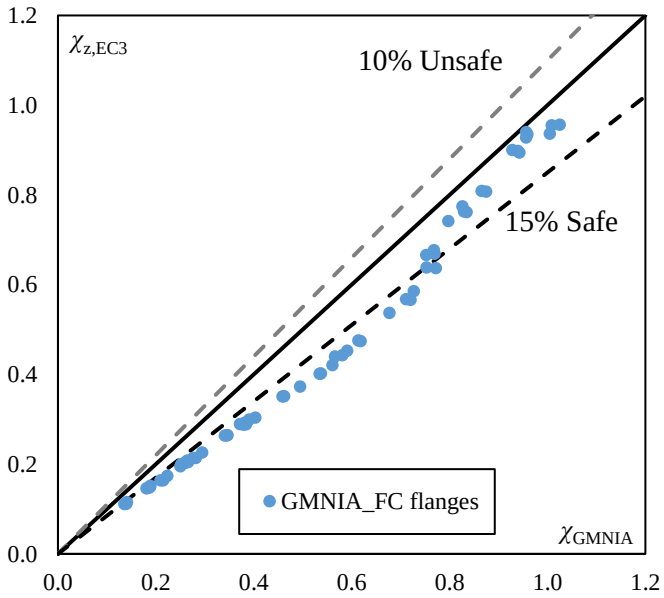

Figure VIII-6: Numerical and Eurocode 3 *reduction factors for tapered columns*

Figure VIII-5 and Figure VIII-6 show an acceptable agreement between the analytical and numerical results for high reduction factors (> 0.8) corresponding to low slenderness. For smaller reduction factors, i.e. increased slenderness, the analytical results are clearly on the safe side. An average deviation of 15% from the numerical values can be seen in Figure VIII-5 for uniform members. In the case of tapered members, the results exhibit a larger deviation.

The partial safety factors associated with the *Eurocode 3* design methods for both types of members are determined for:

- The low slenderness range: $\bar{\lambda}_z \leq 0.8$;
- The intermediate slenderness range: $0.8 < \bar{\lambda}_z \leq 1.5$;
- The high slenderness range: $1.5 < \bar{\lambda}_z$.

The results are presented in Table VIII-4 for uniform members and Table VIII-5 for tapered members.

Slenderness range	*n*	γ_{M1}
$\bar{\lambda}_z \leq 0.8$	59	0.945
$0.8 < \bar{\lambda}_z \leq 1.5$	55	0.814
$1.5 < \bar{\lambda}_z$	75	0.817
All range	189	1.030

Table VIII-4: Partial safety factors associated with Eurocode 3 *design method for uniform columns*

In both cases of uniform and tapered welded columns made of flame-cut flanges, the partial safety factors associated with the *Eurocode 3* design rules are low to very low for every slenderness range. For low slenderness, the partial safety factors are close to 0.94 while for medium and high slenderness, values about 0.80 are obtained.

Slenderness range	*n*	γ_{M1}
$\bar{\lambda}_z \leq 0.8$	18	0.939
$0.8 < \bar{\lambda}_z \leq 1.5$	17	0.805
$1.5 < \bar{\lambda}_z$	28	0.779
All range	63	1.008

Table VIII-5: Partial safety factors associated with Eurocode 3 *design method for tapered columns*

These values being very low, the European design rules are clearly overly conservative, particularly for intermediate and high slenderness. Design methods adapted to such welded columns made of flame-cut flanges are therefore proposed and validated in the upcoming sub-section VIII.3.3.

VIII.3.3 Propositions for rules adaptations for flexural buckling

The proposed design resistance of a doubly symmetric welded column made of flame-cut flanges is obtained using expression (VIII.25).The buckling curves formalism is kept in a seek of simplicity. The reduction factor is therefore determined by expression (VIII.26) with (VIII.27). The deviation from the *Eurocode 3* rules concerns the imperfection factor α_z for which two alternative expressions are proposed:

$$\alpha_z = 0.34 \tag{VIII.28}$$

$$\alpha_z = \frac{0.15}{\bar{\lambda}_z}\sqrt{\frac{h_t}{b}} \text{ with } 0.13 \leq \alpha_z \leq 0.34 \tag{VIII.29}$$

The imperfection factor proposed by expression (VIII.28) corresponds to buckling curve *b* and is referred to as *Proposition I*. Similarly to the propositions of *Tankova* (2022) for high strength steel, it has been decided to provide a simple *Proposition I* design method corresponding to an existing buckling curve.

A more precise value is proposed by expression (VIII.29), providing a buckling curve per studied member. This proposition, then referred to as *Proposition II*, is based on a α_z value inversely proportional to the normalized slenderness. This choice was motivated by the numerical results presented in sub-sections VIII.3.1 and VIII.3.2. The numerical reduction factors get closer to *Euler*'s curve as the slenderness increases, corresponding to a reducing impact of the members imperfections. An imperfection factor decreasing as the slenderness increases is therefore supposed more accurate than a constant value.

Besides, the reduction factor of *Proposition II* depends on the square root of the ratio between the overall height h_t and width *b*. The choice of proposing a buckling curve per cross-sectional dimensions was motivated by the scatter of the numerical results presented in sub-sections VIII.3.1 and VIII.3.2. The use of the height-to-width ratio was selected because existing expressions for imperfection factors depend on this ratio. Indeed, as depicted in Chapter IV, the *French National Annex to Eurocode 3 Part 1-1* proposes the following imperfection factor for lateral-torsional buckling of welded beams:

$$\alpha_{LT} = 0.5 - 0.25\frac{b}{h}\bar{\lambda}_{LT}^2 \geq 0 \tag{VIII.30}$$

In addition, *Taras* (2010a) noticed that imperfection factors for lateral-torsional buckling of beams are approximately proportional to the square root of the height-to-width ratio. This ratio has been replaced with that of the elastic section moduli $W_{y,el}/W_{z,el}$ in *prEurocode 3 Part 1-1*, both ratios being approximately proportional.

Proposition II contains upper and lower limit values of α_z corresponding to the imperfection factors associated with buckling curves a_0 and c, respectively. While the lower limit value corresponds to the *Proposition I* imperfection factor, an upper limit is defined as the most favourable buckling curve for members in compression. Though for high slenderness many numerical results lie above buckling curve a_0, such higher bound is introduced for safety reasons producing a minimum deviation from the *Euler* curve.

The reduction factors obtained using the two proposed values for the imperfection factor are compared against the numerical ones for members with flame-cut flanges. The evolution of the analytical reduction factors with the numerical ones are depicted in Figure VIII-7 for uniform members and Figure VIII-8 for tapered ones.

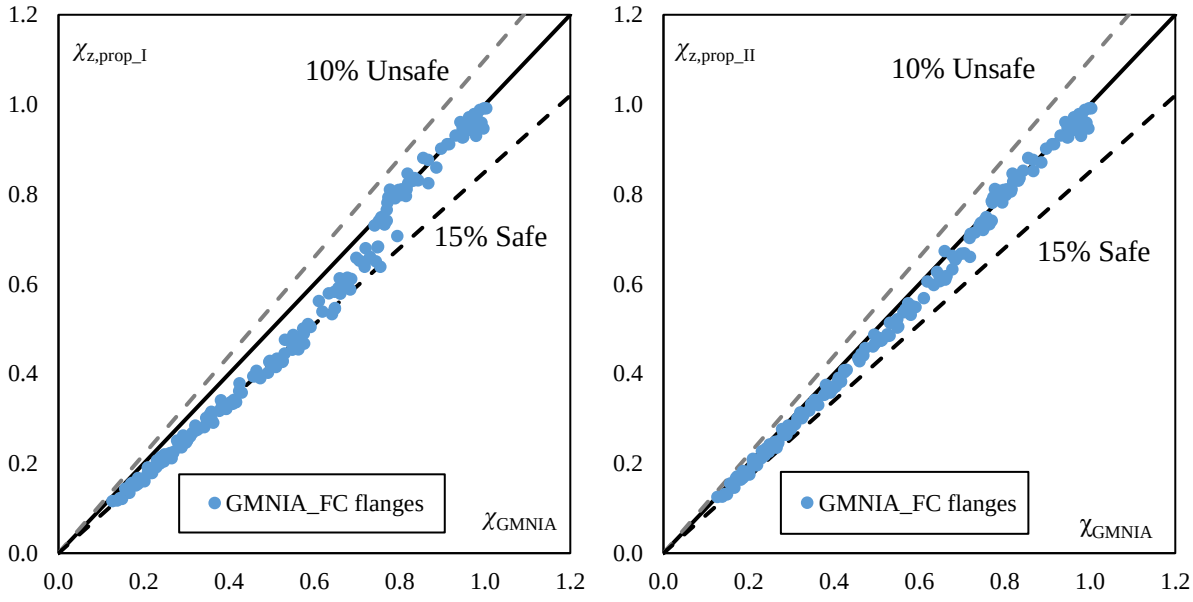

a) *Proposition I* b) *Proposition II*

Figure VIII-7: Numerical and analytical reduction factors for uniform welded columns

Both Figure VIII-7 and Figure VIII-8 show similar results. The analytical results obtained using *Proposition I* match very well with the numerical ones for high values of the reduction factors (> 0.8) i.e. low slenderness. For lower values of the reduction factor, the *Proposition I* results are on the safe side with a deviation up to 15% from the numerical results.

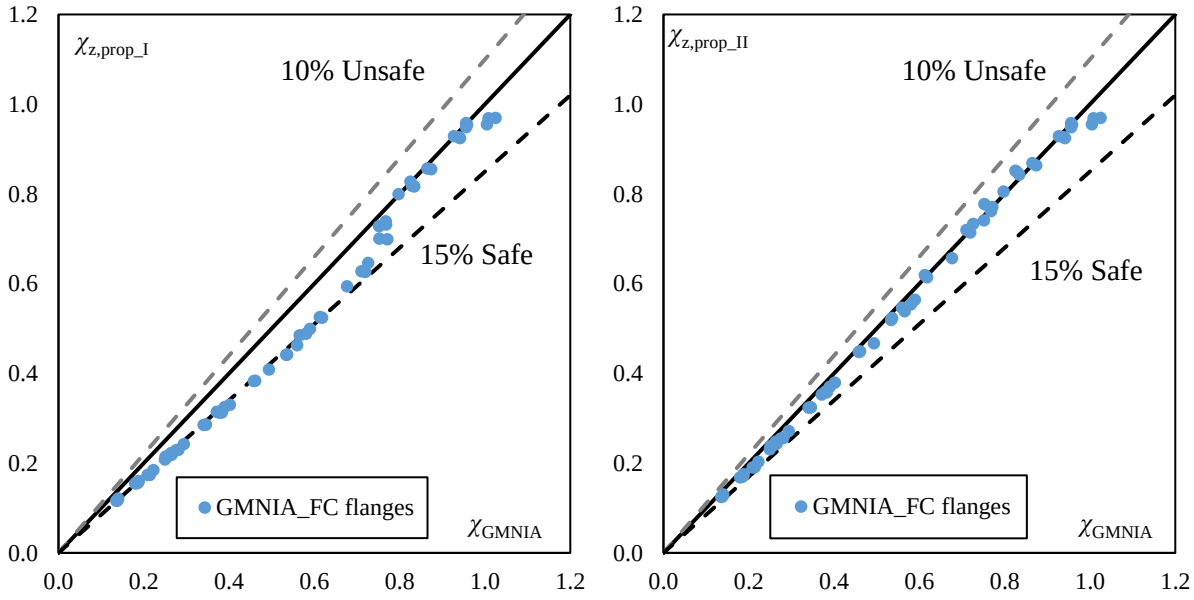

a) *Proposition I* b) *Proposition II*

Figure VIII-8: Numerical and analytical reduction factors for tapered welded columns

The predictions of *Proposition II* match very well with the numerical results whatever the range of reduction factors in both Figure VIII-7b) and Figure VIII-8b). The maximum deviation on the unsafe side being 4% is still acceptable.

The partial safety factors associated with both proposed design methods are determined for the same slenderness ranges as in Table VIII-4 and Table VIII-5. Those obtained for uniform members are presented in Table VIII-6 while the results for tapered members are given in Table VIII-7.

Design method	Slenderness range	*n*	γ_{M1}
Proposition I: $\alpha_z = 0.34$	$\bar{\lambda}_z \le 0.8$	59	0.968
	$0.8 < \bar{\lambda}_z \le 1.5$	55	0.901
	$1.5 < \bar{\lambda}_z$	75	0.879
	All range	189	1.051
Proposition II: $0.13 \le \alpha_z = \frac{0.15}{\bar{\lambda}_z}\sqrt{\frac{h_t}{b}} \le 0.34$	$\bar{\lambda}_z \le 0.8$	59	0.968
	$0.8 < \bar{\lambda}_z \le 1.5$	55	0.941
	$1.5 < \bar{\lambda}_z$	75	0.972
	All range	189	0.996

Table VIII-6: Partial safety factors associated with both proposed design methods for uniform columns

Both Table VIII-6 and Table VIII-7 show similar results. The safety factors associated with *Proposition I* range between 0.95 and 0.97 for low slenderness (< 0.8). For intermediate and high slenderness, the partial safety factors range between 0.83 and 0.90, which are characteristic of a particularly safe design method. The partial safety factors associated with *Proposition II* are comprised between 0.94 and 0.99

in every studied slenderness range, corresponding to an accurate design method. The low variation of the partial safety factors are characteristic of a design method yielding very slightly scattered results.

Design method	Slenderness range	*n*	γ_{M1}
Proposition I: $\alpha_z = 0.34$	$\bar{\lambda}_z \le 0.8$	18	0.951
	$0.8 < \bar{\lambda}_z \le 1.5$	17	0.889
	$1.5 < \bar{\lambda}_z$	28	0.831
	All range	63	1.031
Proposition II: $0.13 \le \alpha_z = \frac{0.15}{\bar{\lambda}_z}\sqrt{\frac{h_t}{b}} \le 0.34$	$\bar{\lambda}_z \le 0.8$	18	0.965
	$0.8 < \bar{\lambda}_z \le 1.5$	17	0.990
	$1.5 < \bar{\lambda}_z$	28	0.945
	All range	63	1.006

Table VIII-7: Partial safety factors associated with both proposed design methods for tapered columns

Both proposed design methods provide acceptable safety levels and could be employed as alternatives to the *Eurocode 3 Part 1-1* rules for welded columns made of flame-cut flanges. The simple *Proposition I* that suggests the use of buckling curve *b* instead of *c* is still clearly safe-sided for intermediate and high normalized slenderness. The more accurate *Proposition II* suggests the use of a buckling curve per member but provides results in very good agreement with the numerical ones and a satisfactory level of safety.

In the upcoming section VIII.4, the numerical results obtained for members in bending are presented. The accuracy of the *Eurocode 3* design rules are evaluated along with that of improved design methods, adapted to welded members made of flame-cut flanges.

VIII.4 Lateral-torsional buckling of beams

VIII.4.1 Numerical results

VIII.4.1.1 Uniform members

Doubly symmetric beams

Similarly to the case of compressed members, the numerical analyses for members subjected to bending have yielded two sets of numerical bending moments for uniform beams:

- $M_{y,cr,LBA}$: elastic critical bending moment for lateral-torsional buckling;
- $M_{y,ult,GMNIA}$: ultimate bending moment (for lateral-torsional buckling).

Besides, analytical values of the characteristic cross-sectional resistance to bending about the major axis $M_{y,Rk}$ are determined using the prescriptions of the current *Eurocode 3 Parts 1-1* and *1-5*. These values are employed to compute:

$$\bar{\lambda}_{LT} = \sqrt{\frac{M_{y,Rk}}{M_{y,cr,LBA}}} \qquad \text{(VIII.31)}$$

$$\chi_{LT,GMNIA} = \frac{M_{y,ult,GMNIA}}{M_{y,Rk}} \qquad \text{(VIII.32)}$$

The numerical reduction factors determined using the preceding expression (VIII.32) are plotted as a function of the normalized slenderness obtained using expression (VIII.31) in Figure VIII-9 for uniform doubly symmetric members. The results are presented along with the four European buckling curves *a* to *d* that are used for members subjected to bending according to the *General case* from *Eurocode 3*.

For a great number of studied beams – when $h_t/b > 2$ –, *Eurocode 3 Part 1-1* imposes the use of buckling curve *d* when computing the reduction factor according to the *General case*. However, Figure VIII-9 shows that numerical results for members with flame-cut flanges match with buckling curve *c* in the least favourable cases. The lowest results are obtained in the case of a constant bending moment distribution (see Figure VIII-9a)) where for low slenderness (< 0.8), numerical results are in line with buckling curve *c*. As the slenderness increases, the results get closer to *Euler*'s curve, lying above curve *a* for medium to high slenderness (> 1.1).

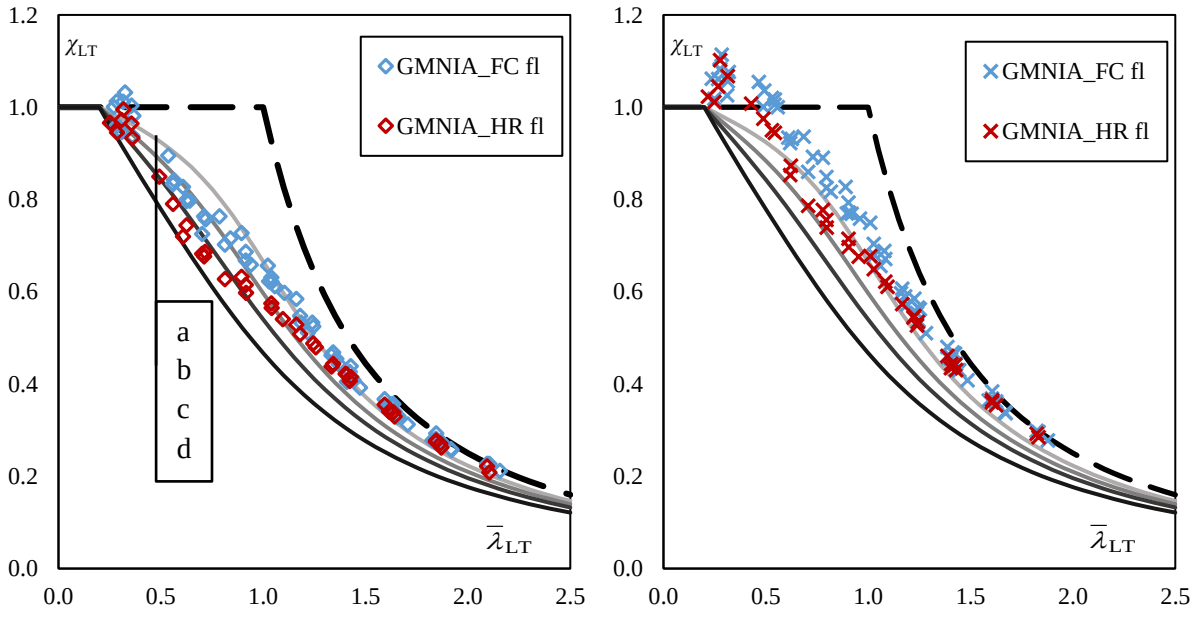

a) $\psi = 1$ b) $\psi = 0.5$

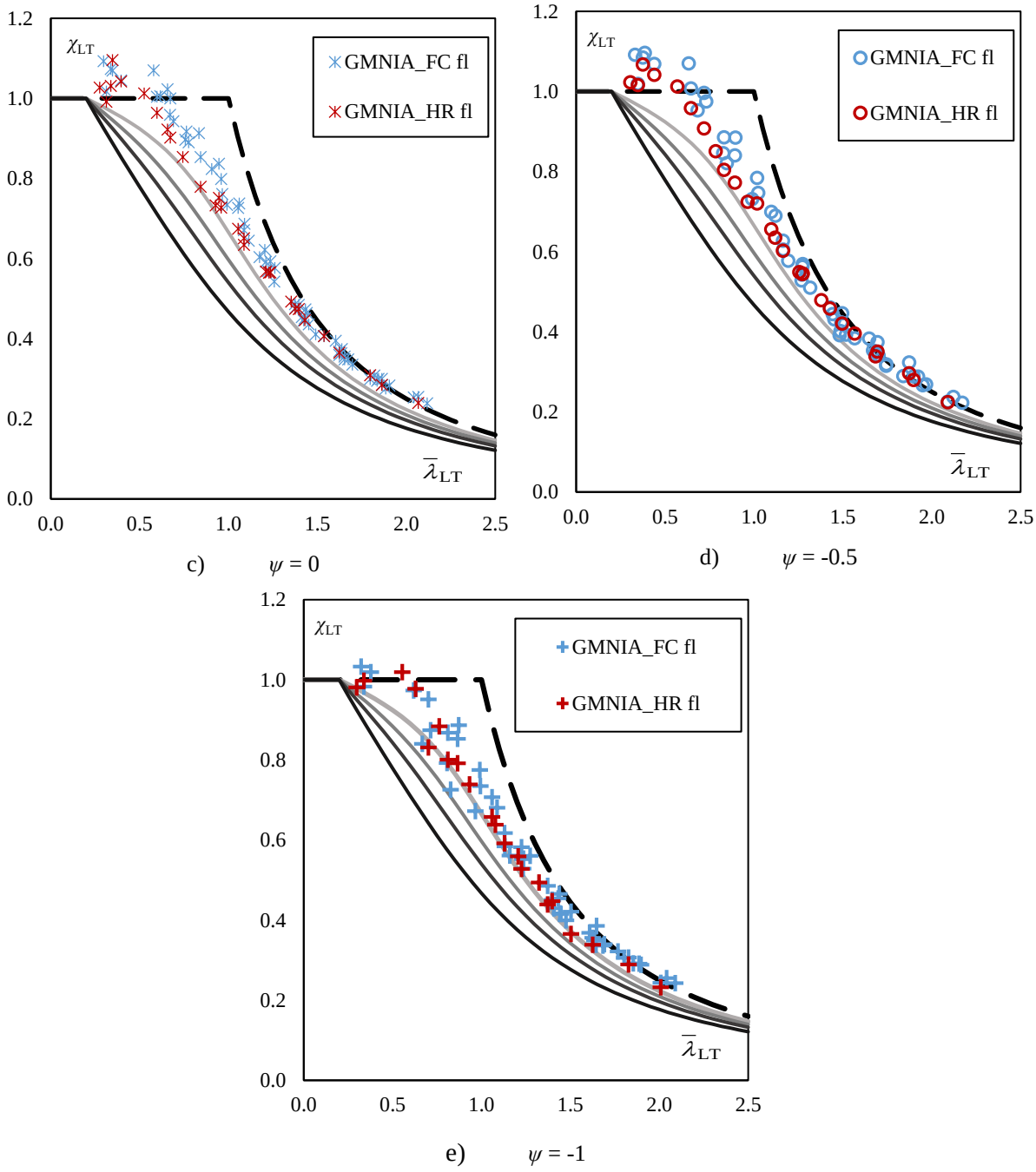

Figure VIII-9: Numerical results for lateral-torsional buckling of uniform doubly symmetric beams

The numerical results for flame-cut flanges are always above buckling curve *a* for the other values of the ratio ψ between end moments, except in a few cases when ψ = -1. Indeed, the results obtained when ψ = -1 are influenced by internal shear forces for members having a short to intermediate length. The results plotted in Figure VIII-9e) correspond to beams that did not fail due to shear, i.e. the following criterion is satisfied for the studied members:

$$\left|V_{Ed}\right| < V_{bw,Rd} \qquad \text{(VIII.33)}$$

where the acting shear load V_{Ed} is:

$$V_{\mathrm{Ed}} = -\frac{\partial M_{\mathrm{y,Ed}}}{\partial x} = \frac{\psi - 1}{L} M_{\mathrm{b,Rd}} \qquad \text{(VIII.34)}$$

where the design buckling resistance moment $M_{\mathrm{b,Rd}}$ is obtained using the *General case* of *Eurocode 3*, i.e. buckling curve *c* or *d*.

The design buckling resistance for shear $V_{\mathrm{b,w,Rd}}$ is determined according to the prescriptions of *Eurocode 3 Part 1-5*:

$$V_{\mathrm{bw,Rd}} = \chi_{\mathrm{w}} \frac{V_{\mathrm{w,Rk}}}{\gamma_{\mathrm{M1}}} \qquad \text{(VIII.35)}$$

with:

$V_{\mathrm{w,Rk}}$: characteristic value of the web resistance to shear;

χ_{w}: reduction factor for shear buckling (see *Eurocode 3 Part 1-5*).

Though no failure can be fully attributed to shear, its effects influence the failure mode and slightly diminishes the ultimate bending moment. The interaction of shear and lateral-torsional buckling is highlighted in Figure VIII-10 where von Mises stresses are shown at failure of a beam subjected to equal end moments with opposite signs. The S355 beam presented in Figure VIII-10 is 6 m long and present a 1000×8 mm web with 200×25 mm flanges. The stress distribution in the web exhibits inclined zones with a high magnitude that is characteristic of shear.

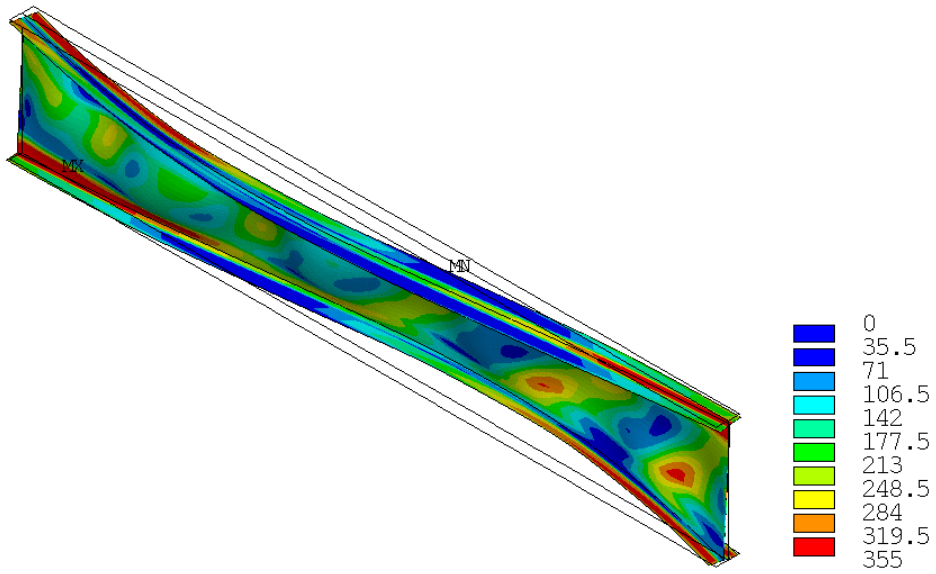

Figure VIII-10: von Mises stresses at failure of a beam under a linear bending moment distribution with ψ = -1

Eventually, Figure VIII-9 shows lower results for welded beams with hot-rolled flanges when compared against those presenting flame-cut flanges. The influence of the flanges type becomes less significant as ψ diminishes, differences being clear when both end moments present the same sign. In the case of a constant bending moment distribution, the numerical results for welded beams with hot-rolled flanges are found between curves *c* and *d* when the slenderness is lower than 0.9. Similarly to welded beams made of flame-cut flanges, as the slenderness increases, the impact of the imperfections on the buckling resistance diminishes, i.e. the results get closer to *Euler*'s curve. For high slenderness (> 1.5), all results lay above buckling curve *a*.

The results plotted in Figure VIII-9a) for the least favourable bending moment distribution show that the use of buckling curve *d*, as very often prescribed by the *General case* of *Eurocode 3 Part 1-1*, is overly conservative for welded members made of flame-cut flanges. For medium and high slenderness, buckling curve *d* provides clearly overly safe sided results. Besides, Figure VIII-9 b) to VIII-9e) show a significant influence of the bending moment distribution on the ultimate bending moment. Accurate design methods should therefore account for the bending moment distribution other than in the normalized slenderness.

Mono-symmetric beams

The numerical reduction factors obtained for uniform mono-symmetric beams are plotted with respect to the normalized slenderness in Figure VIII-11. The results obtained for a constant bending moment distribution are presented in Figure VIII-11a) while those obtained under a linear distribution are displayed in Figure VIII-11b). In the case where ψ = 1, two types of GMNIA computations are performed, depending on the sign of ψ_f given by:

$$\psi_f = \frac{I_{fc} - I_{ft}}{I_{fc} + I_{ft}} \qquad \text{(VIII.36)}$$

The common practice corresponds to $\psi_f > 0$, i.e. the larger flange is compressed under a positive bending moment. Thus, in the case of a linear bending moment, the larger flange of the end cross-section subjected to the greatest magnitude of the bending moment is subjected to compressive stresses.

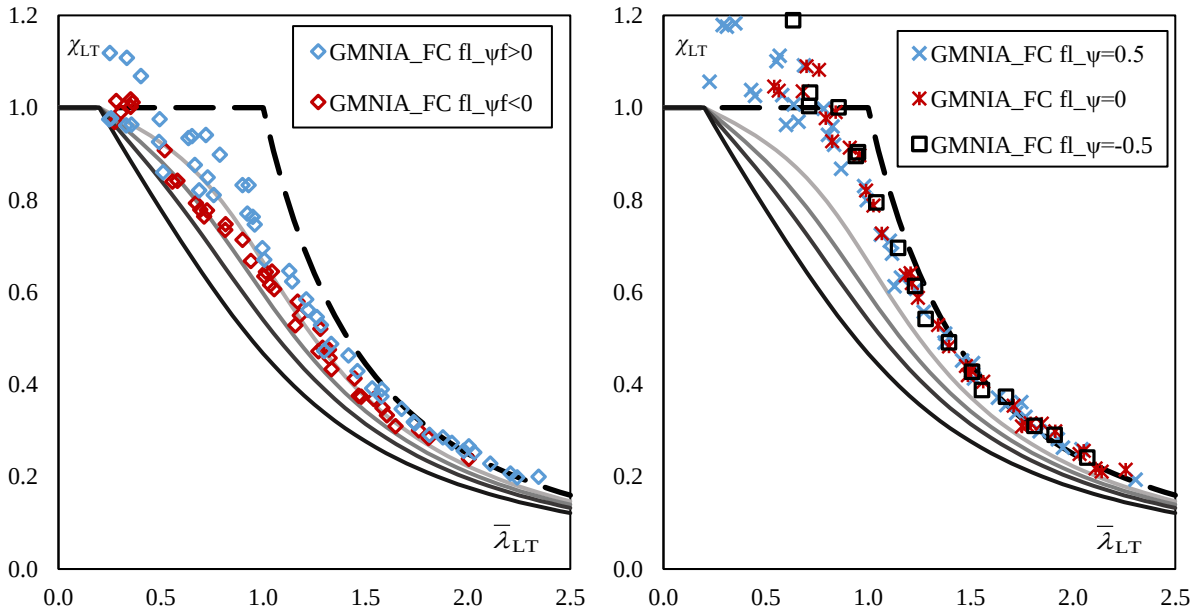

a) *Uniform bending moment distribution* b) *Linear bending moment distribution*

Figure VIII-11: Numerical results for lateral-torsional buckling of uniform mono-symmetric beams

When the larger flange is compressed, Figure VIII-11a) shows very scattered results for beams subjected to a constant bending moment. If the compression flange is the smaller one, the reduction factors are less scattered but also lower than in the other case. The influence of the type of compression flange (i.e. larger or smaller flange) is very pronounced in the low slenderness range while results get closer as the slenderness increases. Whatever the compression flange, the reduction factors lie above buckling curve *c* for low slenderness (<0.7) then get closer to *Euler*'s curve as the slenderness increases.

In the case of a linear bending moment distribution, the results show a very low influence of the members imperfections on the buckling behaviour. Indeed, the reduction factors are always found above curve *a* and very close to *Euler*'s curve for intermediate and high slenderness (> 0.9).

One may notice that the numerical reduction factors plotted in Figure VIII-11 (uniform mono-symmetric beams) when the larger flange is compressed are greater than those presented in Figure VIII-9 (doubly symmetric members) for the same normalized slenderness. This is more obvious for a linear bending moment distribution, where the effect of the member imperfections is very limited.

Similarly to the case of doubly symmetric beams, Figure VIII-11 shows that the use of buckling curve *d*, as generally required according to the *General case* is overly conservative for members with flame-cut flanges. These observations will be confronted to the safety assessment of this design method in sub-section VIII.4.2.

VIII.4.1.2 Tapered members

In the case of tapered beams, the numerical analyses have yielded two sets of numerical load amplifiers:

- $\alpha_{cr,LBA}$: elastic critical load amplifier for lateral-torsional buckling;
- $\alpha_{op,GMNIA}$: ultimate load amplifier (for lateral-torsional buckling).

Besides, analytical values of the load amplifier $\alpha_{ult,k}$ to reach the characteristic resistance of the most critical cross-section are computed using:

$$\alpha_{ult,k}(x) = \frac{M_{y,Rk}}{M_{y,Ed}}(x) \tag{VIII.37}$$

The minimum value of $\alpha_{ult,k}$ along the beam is used with both load amplifiers resulting from numerical analyses to compute:

$$\bar{\lambda}_{LT} = \sqrt{\frac{\alpha_{ult,k}}{\alpha_{cr,LBA}}} \tag{VIII.38}$$

$$\chi_{LT,GMNIA} = \frac{\alpha_{op,GMNIA}}{\alpha_{ult,k}} \tag{VIII.39}$$

The location where the load amplifier is minimal depends both on the bending moment distribution and on the cross-section resistance along the beam.

The numerical results obtained for tapered beams presenting a doubly symmetrical cross-section are presented in Figure VIII-12. Most numerical analyses concern type *A* beams where only the compression flange is inclined, as depicted in Table VIII-8. Some analyses were however led for type *B* beams where only the tension flange is inclined (see Table VIII-8).

Type of tapered beam	*Representation*
A	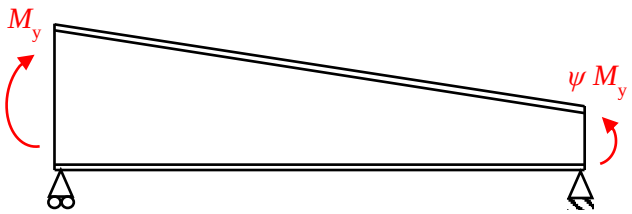
B	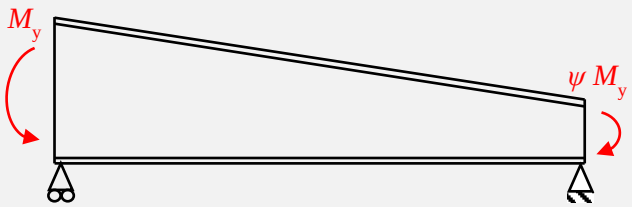

Table VIII-8: Type of doubly symmetric beams

Figure VIII-12 shows no influence of the type of beam on the reduction factor. Besides, all results lie above buckling curve *b*, and above curve *a* in the case where $\psi = 0$ or 1. The results obtained for a uniform bending moment distribution are very favourable because $\alpha_{ult,k}$ is minimal at or close to the smallest cross-section while the actual failure happens at a larger cross-section.

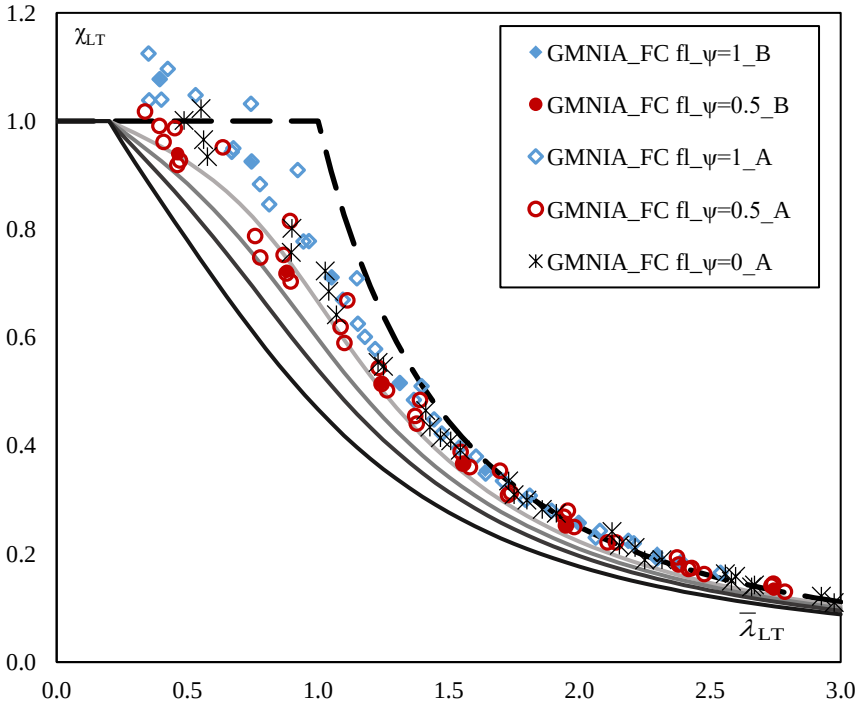

Figure VIII-12: Numerical results for lateral-torsional buckling of tapered doubly symmetric beams

The numerical results obtained for tapered beams having a mono-symmetric cross-section are plotted in Figure VIII-13. All numerical reduction factors are found above buckling curve *a*. Besides, the results obtained under a constant bending moment are slightly more favourable when the larger flange is compressed ($\psi_f > 0$) than when the smallest one is compressed. In both cases, tapered beams are of type *A* (see Table VIII-8), i.e. only the compression flange is inclined.

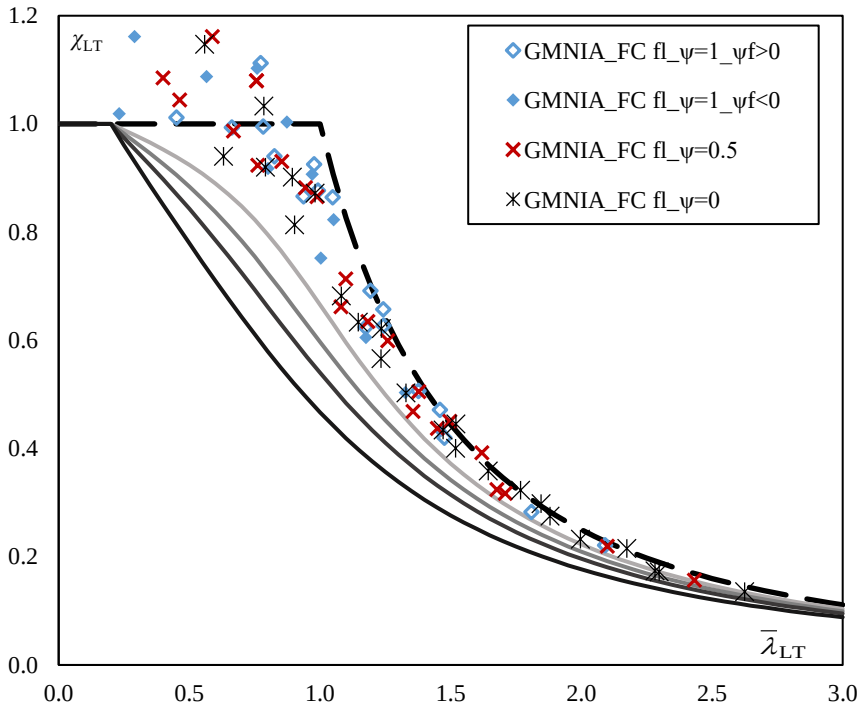

Figure VIII-13: Numerical results for lateral-torsional buckling of tapered mono-symmetric beams

Both Figure VIII-12 and Figure VIII-13 show that for tapered welded beams made of flame-cut flanges, the use of buckling curve *d* as generally required according to the *General case* from *Eurocode 3* is overly conservative. This observation, similar to the case of uniform members, is confronted to the actual partial safety factors corresponding to this design method in the following sub-section VIII.4.2. Design methods better suited to welded beams made of flame-cut flanges are then exposed in sub-section VIII.4.3.

VIII.4.2 Assessment of the Eurocode 3 *design methods*

VIII.4.2.1 Uniform beams

General case

As developed in Chapter IV, the current and future *General case* from *Eurocode 3 Part 1-1* (see §6.3.2.2) states that the resistance $M_{y,b,Rd}$ of a uniform I member, doubly symmetric or not, subjected to bending is:

$$M_{b,Rd} = \chi_{LT} \frac{M_{y,Rk}}{\gamma_{M1}} \qquad \text{(VIII.40)}$$

where the reduction factor for lateral-torsional buckling χ_{LT} is determined using:

$$\chi_{LT} = \frac{1}{\phi_{LT} + \sqrt{\phi_{LT}^2 - \bar{\lambda}_{LT}^2}} \leq 1.0 \qquad \text{(VIII.41)}$$

$$\phi_{LT} = 0.5\left[1 + \alpha_{LT}\left(\bar{\lambda}_{LT} - 0.2\right) + \bar{\lambda}_{LT}^{2}\right] \quad \text{(VIII.42)}$$

For welded members, the imperfection α_{LT} is associated with either buckling curve *c* or *d*, depending on the height-to-minimum width ratio:

$$\frac{h_t}{b_{min}} \leq 2 : \alpha_{LT} = 0.49 \quad \text{(VIII.43)}$$

$$\frac{h_t}{b_{min}} > 2 : \alpha_{LT} = 0.76 \quad \text{(VIII.44)}$$

The reduction factors for lateral-torsional buckling determined according to the *General case* are compared against those calculated numerically for uniform members made of flame-cut flanges. Figure VIII-14 shows the the results for uniform and doubly symmetric members while Figure VIII-15 presents those obtained for mono-symmetric members.

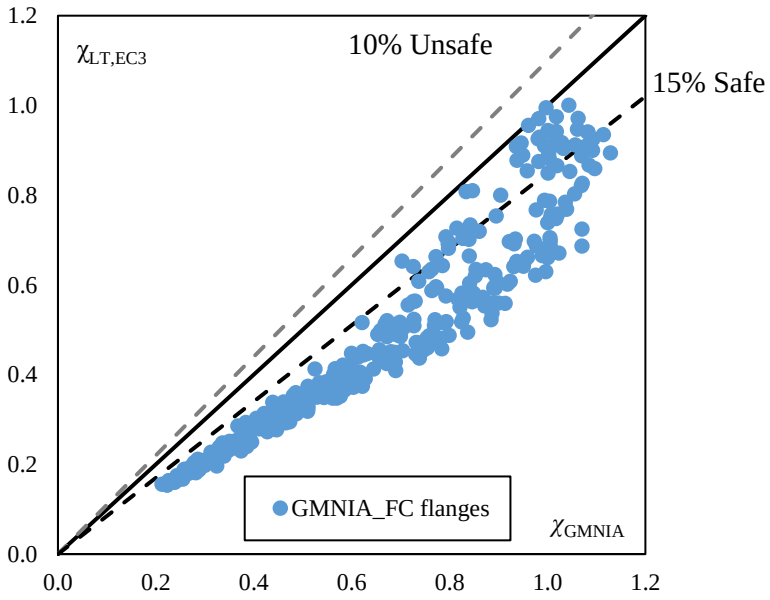

Figure VIII-14: Numerical and EC3 – General case *reduction factors for uniform doubly symmetric beams*

Both Figure VIII-14 and Figure VIII-15 highlight that making use of the *General case* provides overly conservative reduction factors in most cases. Besides, both figures show scattered results for high values of the reduction factors, i.e. low slenderness. The results obtained for mono-symmetric beams are more scattered than those obtained for doubly symmetric members and greater deviations on χ_{LT} are noticed on the safe side.

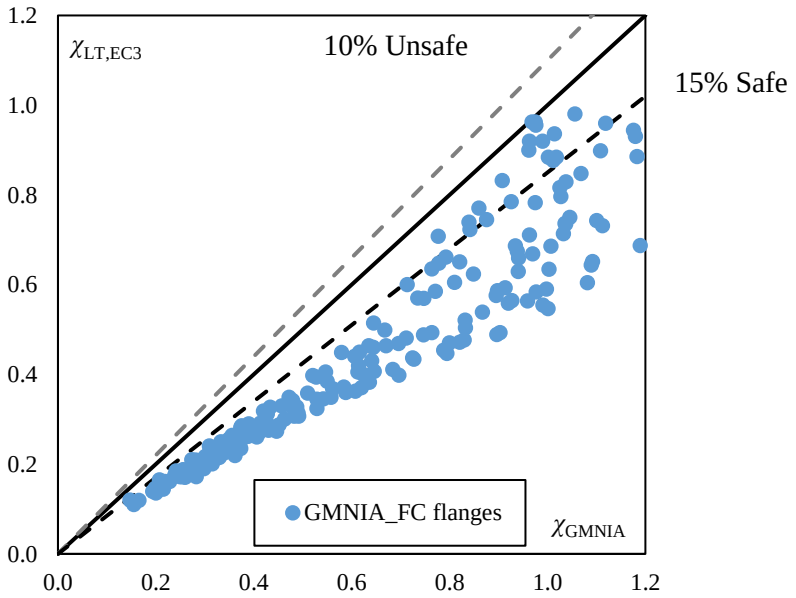

Figure VIII-15: Numerical and EC3 – General case *reduction factors for uniform mono-symmetric beams*

The partial safety factors associated with the *General case* from *Eurocode 3* are computed for doubly and mono-symmetric members. The results are presented in Table VIII-9 for the low slenderness range (≤ 0.8), the high slenderness range (> 1.5) and the intermediate one.

Cross-section type	Slenderness range	*n*	γ_{M1}
Doubly-symmetric	$\bar{\lambda}_{LT} \leq 0.8$	107	1.003
	$0.8 < \bar{\lambda}_{LT} \leq 1.5$	180	0.807
	$1.5 < \bar{\lambda}_{LT}$	100	0.809
	All range	387	0.982
Mono-symmetric	$\bar{\lambda}_{LT} \leq 0.8$	62	<u>1.108</u>
	$0.8 < \bar{\lambda}_{LT} \leq 1.5$	77	0.821
	$1.5 < \bar{\lambda}_{LT}$	57	0.848
	All range	196	1.001

Table VIII-9: Partial safety factors associated with the General case *from* Eurocode 3 *for uniform beams*

For the intermediate and high slenderness ranges, the current *General case* is overly conservative; the partial safety factors obtained being comprised between 0.81 and 0.85 for both cross-section types. The factor obtained for the low slenderness range is very close to unity for doubly-symmetric members. That obtained in the case of mono-symmetric members is greater than 1.05 while no analytical result is found on the unsafe side. This discrepancy is a consequence of the very scattered results (see Figure VIII-15), some analytical results being extremely conservative. A value greater than 1.10 shows that the current design methods is not adequate for uniform mono-symmetric welded beams with flame-cut flanges having a low slenderness though producing only safe-sided results.

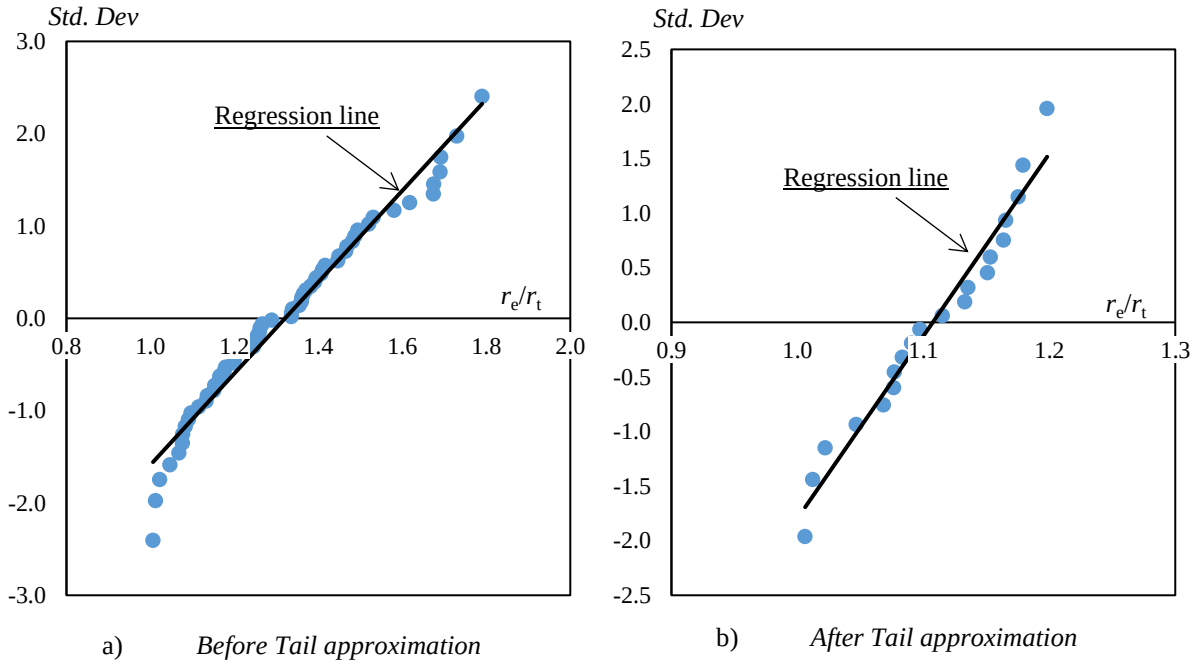

a) *Before Tail approximation* b) *After Tail approximation*

Figure VIII-16: Quantile plot for EC3 design resistances – uniform mono-symmetric beams (low slenderness)

Owing to high values of the partial safety factor despite an absence of unsafe results, the quantile plot for the current *Eurocode 3* method for uniform mono-symmetric beams with a low slenderness is presented in Figure VIII-16a). The design procedure to compute partial safety factors assumes that the results are distributed following a (log-) normal distribution (see *Annex D of Eurocode 0* and *SAFEBRICTILE* project deliverable D1.1). Therefore, the quantile plot associated with an accurate design method should exhibit individual results very close to the regression line of the studied values.

Figure VIII-16a) shows that owing to overly conservative results, the regression line is quite away from the lowest values of r_e/r_t. A "*Tail approximation*" is thus performed that consists in neglecting the overly conservative results to bring the remaining significant results closer to a normal distribution as described as part of the *SAFEBRICTILE* project. Using the quantile plot of Figure VIII-16a), it was chosen to remove the contributions for which r_e/r_t is greater than 1.20. The resulting quantile plot is depicted in Figure VIII-16b).

The partial safety factors associated with the current *Eurocode 3* method for low slenderness in the case of uniform mono-symmetric beams are presented in Table VIII-10 before and after the *Tail approximation*. Using the *Tail approximation*, the partial safety factor becomes lower than 1.05.

Slenderness range	Tail approximation	*n*	γ_{M1}
$\bar{\lambda}_{LT} \leq 0.8$	Without	62	1.108
	With	20	1.017

Table VIII-10: Partial safety factors associated with the General case *for uniform mono-symmetric beams*

The results obtained according to the *General case* from *Eurocode 3 Part 1-1* are not very well suited for welded beams made of flame-cut flanges being overly conservative for most members employed in practice. Improved imperfection factors adapted to this type of beams will be introduced in sub-section VIII.4.3.1.

New verification format from *prEurocode 3*

The new verification format appearing in *prEN 1993-1-1* is based on the work of *Taras* (2010a/b). As presented in Chapter IV, this design method can be employed solely in the case of uniform doubly symmetric members. For such members, the resistance against lateral-torsional buckling $M_{y,b,Rd}$ according to the new verification format is similar to that given by expression (VIII.40). However, the reduction factor is given by:

$$\chi_{LT} = \frac{f_M}{\phi_{LT} + \sqrt{\phi_{LT}^2 - f_M \bar{\lambda}_{LT}^2}} \leq 1.0 \qquad \text{(VIII.45)}$$

$$\phi_{LT} = 0.5\left[1 + f_M\left(\left(\frac{\bar{\lambda}_{LT}}{\bar{\lambda}_z}\right)^2 \alpha_{LT}\left(\bar{\lambda}_z - 0.2\right) + \bar{\lambda}_{LT}^2\right)\right] \qquad \text{(VIII.46)}$$

where the factor f_M accounting for the bending moment distribution is given, in the case of a linear bending moment distribution, by:

$$f_M = 1.25 - 0.1\psi - 0.15\psi^2 \qquad \text{(VIII.47)}$$

The imperfection factor α_{LT} for welded members with $t_f \leq 40$ mm is:

$$\alpha_{LT} = 0.21\sqrt{\frac{W_{el,y}}{W_{el,z}}} \leq 0.64 \qquad \text{(VIII.48)}$$

The analytical results obtained using equations (VIII.45) to (VIII.48) are compared against the numerical results in Figure VIII-17 for doubly symmetric welded beams made of flame-cut flanges.

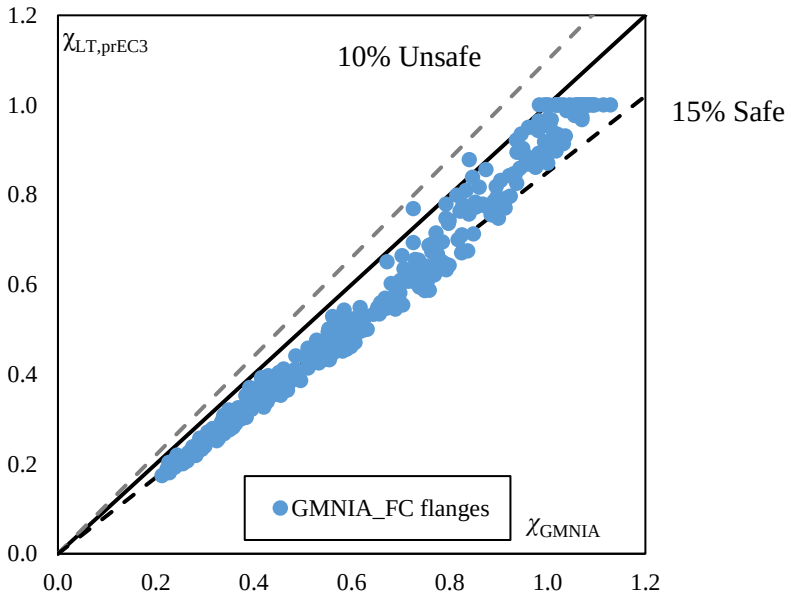

Figure VIII-17: Numerical and prEC3 *reduction factors for uniform doubly symmetric welded beams*

The analytical results are on the safe side, except for a couple of beams, with an average deviation between 10 and 15%. Besides, the scatter is low when compared to that obtained with the *General case* (see Figure VIII-14).

The partial safety factors corresponding to the new design method from *prEN 1993-1-1* are computed for the low, intermediate and high slenderness ranges. The results are presented in Table VIII-11 for the welded beams entering the scope of this design method, i.e. doubly symmetric members.

Cross-section type	Slenderness range	*n*	γ_{M1}
Doubly-symmetric	$\overline{\lambda}_{LT} \leq 0.8$	107	0.947
	$0.8 < \overline{\lambda}_{LT} \leq 1.5$	180	0.987
	$1.5 < \overline{\lambda}_{LT}$	100	0.991
	All range	387	1.044

Table VIII-11: Partial safety factors for the new design method from prEurocode 3 *for uniform beams*

The partial safety factors are comprised between 0.95 and 0.99, showing a good accuracy of the design method. A modified version of this new design method is derived in sub-section VIII.4.3.1 to be applicable in the case of mono-symmetric and/or tapered beams. In addition, an enhanced expression will be exposed for the imperfection factor adapted to welded members made of flame-cut flanges.

In the following sub-section VIII.4.2.2, the numerical results are used to assess the safety of the current *Eurocode 3* design rules for welded tapered members.

VIII.4.2.2 Tapered beams

According to *Eurocode 3 Part 1-1*, the stability of a non-uniform beam subjected to bending must be assessed using the *General Method*, as detailed in Chapter IV. The resistance against lateral-torsional buckling of a non-uniform beam is then obtained using expression (VIII.40). The characteristic cross-sectional resistance to bending is computed at the location where $\alpha_{ult,k}$ is minimal (see Eq. (VIII.37)).

Non-uniform members do not enter the scope of the new verification format, but their design resistance can be computed using the *General case* (see Eq. (VIII.41) to (VIII.44)) when applying the *General Method*. Then, the imperfection factor is determined for the cross-section where $\alpha_{ult,k}$ is minimal.

The analytical reduction factors are compared against the numerical ones in Figure VIII-18 for doubly symmetric tapered beams. Similar results are presented in Figure VIII-19 for mono-symmetric tapered beams.

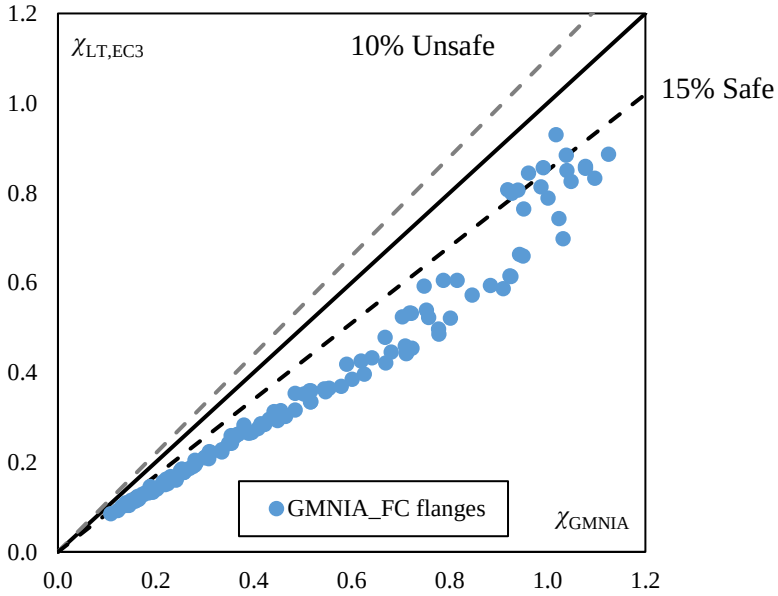

Figure VIII-18: Numerical and EC3 – General Method *reduction factors for doubly symmetric tapered beams*

Figure VIII-18 highlights very safe-sided results when employing the *General Method* with the *General case* for the computation of the reduction factor. Some scatter is noticed and analytical results are up to 60% on the safe side.

In the case of mono-symmetric members, Figure VIII-19 exhibits also extremely safe analytical results. The scatter is more significant than within results presented in Figure VIII-18 for doubly symmetric members, similarly to the case of uniform beams (see Figure VIII-14 and Figure VIII-15). The analytical results obtained for mono-symmetric tapered beams are up to almost 100% on the safe side.

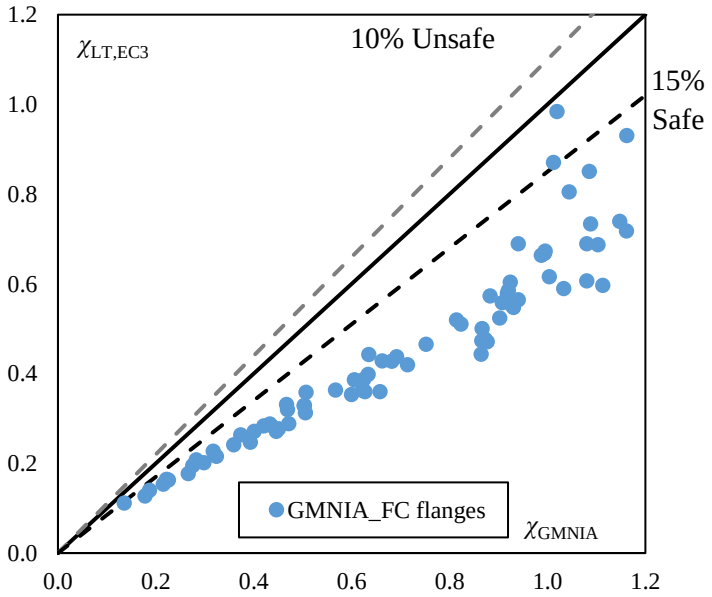

Figure VIII-19: Numerical and EC3 – General Method *reduction factors for mono-symmetric tapered beams*

The partial safety factors corresponding the *General Method* are computed for the low, intermediate and high slenderness ranges. The results are presented in Table VIII-12 for tapered welded beams made of flame-cut flanges and presenting either a doubly or a mono-symmetric cross-section.

The slenderness ranges studied in the case of mono-symmetric tapered beams are not similar to those investigated for other members due to a limited number of results for very high slenderness. Indeed, the boundary between the medium and the high slenderness ranges is set to 1.25, because only 18 of the studied beams present a normalized slenderness greater than 1.5.

Cross-section type	Slenderness range	*n*	γ_{M1}
Doubly-symmetric	$\bar{\lambda}_{LT} \leq 0.8$	26	0.977
	$0.8 < \bar{\lambda}_{LT} \leq 1.5$	42	0.790
	$1.5 < \bar{\lambda}_{LT}$	61	0.850
	All range	129	0.913
Mono-symmetric	$\bar{\lambda}_{LT} \leq 0.8$	38	0.911
	$0.8 < \bar{\lambda}_{LT} \leq 1.25$	28	0.728
	$1.25 < \bar{\lambda}_{LT}$	29	0.825
	All range	95	0.850

Table VIII-12: Partial safety factors associated with the General Method *for tapered beams*

The partial safety factors obtained for intermediate and high slenderness are significantly lower than unity. The results are closer to one in the low slenderness range. Safety factors varying visibly between the different slenderness ranges with some values lower than 0.8, the current design method is not well suited for the type of studied beams.

In the upcoming sub-section VIII.4.3, improved expressions are proposed to determine the imperfection factors for welded beams made of flame-cut flanges. The safety levels provided by the enhanced design methods are then assessed. Besides, adaptations of the new verification format from *prEN 1993-1-1* are derived. The partial safety factors associated with this improved design method validate the approach.

VIII.4.3 Propositions for rules adaptations

VIII.4.3.1 Adaptation of the General case

Uniform beams

Two design methods are adapted from the current and future *General case* from *EN1993-1-1* to welded members made of flame-cut flanges. A first proposal makes use of equations (VIII.40) to (VIII.42), with the imperfection factor:

$$\alpha_{LT} = 0.49 \qquad \text{(VIII.49)}$$

This design method, referred to as *Proposition I*, corresponds to the use of buckling curve *c* for welded beams made of flame-cut flanges in steel buildings. *Thiébaud* (2014) also proposed the use of buckling curve *c* for bridge girders when flame-cuts are involved though no partial safety factors were computed.

A second proposition is made, according to which the design resistance of a uniform member subjected to bending is slightly different than that obtained using equation (VIII.40), being:

$$M_{\mathrm{b,Rd}} = \chi_{\mathrm{LT,mod}} \frac{M_{\mathrm{y,Rk}}}{\gamma_{\mathrm{M1}}} \tag{VIII.50}$$

with:

$$\chi_{\mathrm{LT,mod}} = \frac{\chi_{\mathrm{LT}}}{\mathrm{f}} \leq 1.0 \tag{VIII.51}$$

The previous expression (VIII.51) can currently be employed when using the *Special case* from *Eurocode 3* (see §6.3.2.3) but this alternative is not maintained in *prEN 1993-1-1*, as exposed in Chapter IV. The coefficient *f* accounts for the influence of the bending moment distribution on the ultimate bending moment, being:

$$\mathrm{f} = 1 - 0.5\left(1 - k_{\mathrm{c}}\right)\left[1 - 2.0\left(\bar{\lambda}_{\mathrm{LT}} - 0.8\right)^2\right] \leq 1.0 \tag{VIII.52}$$

where the correction factor k_{c} is, for a linear bending moment distribution:

$$k_{\mathrm{c}} = \frac{1}{1.33 - 0.33\psi} \tag{VIII.53}$$

To keep the design method simple, the impact of the bending moment distribution is expressed through equation (VIII.51) with the coefficient *f* that already exists in the current *Eurocode 3*. Using this factor, i.e. accounting for the bending moment distribution, was deemed necessary when analysing the distribution of the numerical results. Indeed, Figure VIII-9 and Figure VIII-11 highlighted a major influence of the bending moment diagram on the numerical reduction factors. In addition, the influence of the bending moment distribution on the reduction factor is accounted for in other existing design methods from *Eurocode 3*: the current *Special case* and the new verification format.

Proposition II requires the computation of a reduction factor χ_{LT} using expression (VIII.41) along with (VIII.42). The method deviates from the *General case* in the determination of the imperfection factor α_{LT}, computed using:

$$\alpha_{\mathrm{LT}} = \frac{0.23}{\bar{\lambda}_{\mathrm{LT}}} \sqrt{\frac{h_{\mathrm{t}}}{b_{\mathrm{min}}}} \quad \text{with} \quad 0.21 \leq \alpha_{\mathrm{LT}} \leq 0.49 \tag{VIII.54}$$

Similarly to the case of welded columns, a *Proposition II* is introduced where the imperfection factor depends on the member slenderness and height-to-width ratio, corresponding to expression (VIII.54). This more precise imperfection factor implies the determination of a buckling curve per member. The motivations to come with such expression are similar to those expressed in the case of welded columns (see equation (VIII.29)). Indeed, in both cases the numerical results show that the reduction factors get closer to *Euler*'s curve as the slenderness increases, i.e. the imperfections impact on the member stability diminishes. The use of the height-to-width ratio, resulting in a buckling curve per member was motivated by the scattered numerical results for beams, similarly to that observed in the case of columns. Eventually, it has been chosen to use *Proposition II* imperfection factors using similar formats for columns and beams to ensure a consistency and an ease of use in design offices.

The *Proposition II* imperfection factor comes with lower and upper limits, corresponding to buckling curves *c* and *a*, respectively. The lower limit corresponds to the buckling curve of *Proposition I*. The upper limit corresponds to the highest buckling curve that can currently be used according to the *General case* from *Eurocode 3* for members in bending. Like for columns, the upper bound is introduced for safety reasons, a minimum deviation from the theoretical *Euler* curve is always provided.

The analytical reduction factors resulting from both *Propositions* are compared against those obtained by means of GMNIA computations in Figure VIII-20 for uniform doubly symmetric beams. The results of *Proposition I* all lie on the safe side with a mean deviation comprised between 5 and 10% for low slenderness, i.e. high reduction factors. As the members get slender, the design method provides safer results, with an average deviation close to 20%.

The results obtained with *Proposition II* are in vast majority on the safe side with a deviation lower than 15% from the numerical results. This second proposition provides more accurate results than *Proposition I*. One can notice a few results on the unsafe side corresponding to members subjected to end moments having the same magnitudes but opposite signs. The maximum deviation on the unsafe side is 10%.

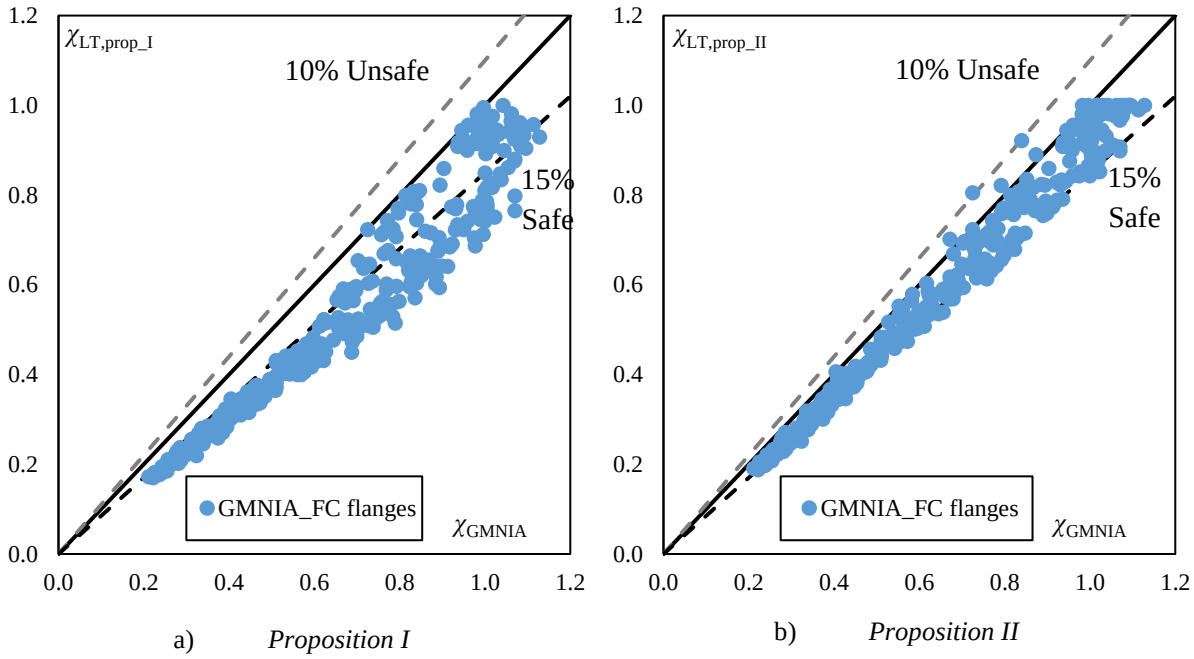

a) *Proposition I* b) *Proposition II*

Figure VIII-20: Numerical and analytical reduction factors for uniform doubly symmetric welded beams

The comparison between analytical and numerical reduction factors are presented in Figure VIII-21 for uniform beams presenting a mono-symmetric cross-section. Both methods show only safe-sided results with an average deviation close to 15% for high reduction factors i.e. low slenderness. For slender members, using *Proposition I* yields safer results than *Proposition II*, with a mean deviation from the numerical results comprised between 15 and 20%. The results obtained using *Proposition II* are closer to the numerical ones, with a mean deviation comprised between 10 and 15%.

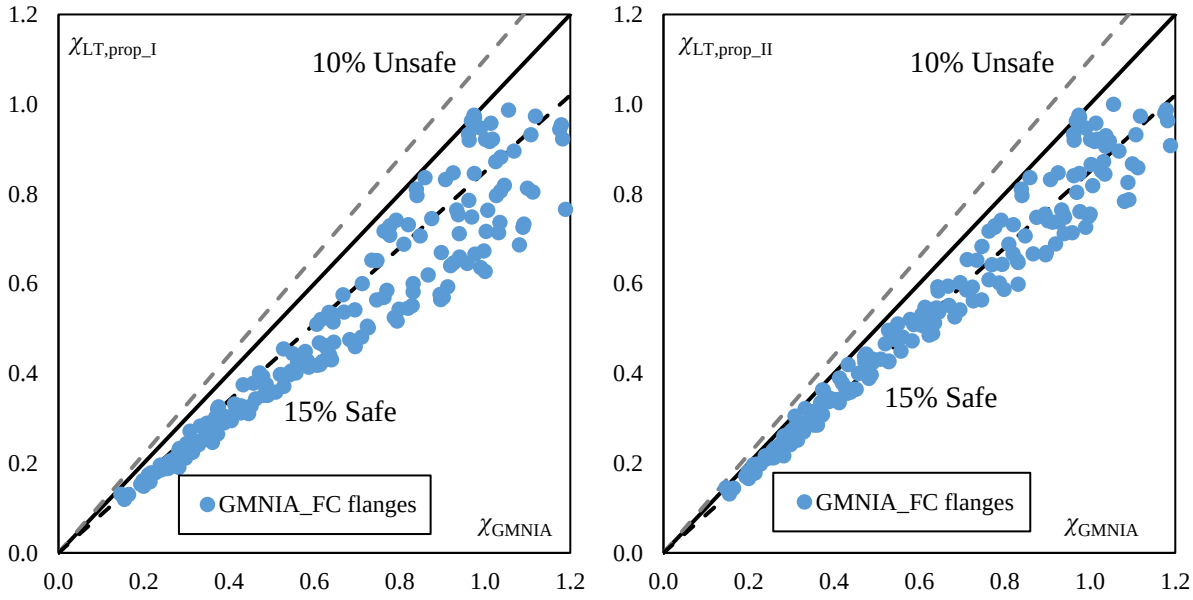

a) *Proposition I* b) *Proposition II*

Figure VIII-21: Numerical and analytical reduction factors for uniform mono-symmetric welded beams

The partial safety factors associated with both proposed design methods are presented in Table VIII-13 for uniform doubly symmetric beams. The partial safety factors are acceptable in each slenderness range for both methods. The variations of γ_{M1} are small within the different slenderness ranges for *Proposition II* that provides safe and accurate estimations of the member resistance. The partial safety factors associated with *Proposition I* are quite different within the slenderness ranges. The results obtained for *Proposition I* are characteristic of a design method providing scattered results.

Design method	Slenderness range	*n*	γ_{M1}
Proposition I: $\alpha_{LT} = 0.49$	$\bar{\lambda}_{LT} \le 0.8$	107	0.999
	$0.8 < \bar{\lambda}_{LT} \le 1.5$	180	0.914
	$1.5 < \bar{\lambda}_{LT}$	100	0.913
	All range	387	1.016
Proposition II: $0.21 \le \alpha_{LT} = \frac{0.23}{\bar{\lambda}_{LT}}\sqrt{\frac{h_t}{b}} \le 0.49$	$\bar{\lambda}_{LT} \le 0.8$	107	0.954
	$0.8 < \bar{\lambda}_{LT} \le 1.5$	180	1.018
	$1.5 < \bar{\lambda}_{LT}$	100	1.021
	All range	387	1.025

Table VIII-13: Partial safety factors for both proposed design methods – uniform doubly symmetric beams

The partial safety factors associated with uniform mono-symmetric members are presented in Table VIII-14. Those for *Proposition II* are acceptable in every slenderness range, being comprised between 0.96 and 1.04. In the case of *Proposition I*, the partial safety factors are small for medium and high slenderness while being greater than 1.10 in the low slenderness range The high value obtained in the low slenderness range is attributed to the important results scatter (see Figure VIII-21).

Design method	Slenderness range	*n*	γ_{M1}
Proposition I: $\alpha_{LT} = 0.49$	$\bar{\lambda}_{LT} \le 0.8$	62	1.111
	$0.8 < \bar{\lambda}_{LT} \le 1.5$	77	0.923
	$1.5 < \bar{\lambda}_{LT}$	57	0.933
	All range	196	1.033
Proposition II: $0.21 \le \alpha_{LT} = \frac{0.23}{\bar{\lambda}_{LT}}\sqrt{\frac{h_t}{b}} \le 0.49$	$\bar{\lambda}_{LT} \le 0.8$	62	1.036
	$0.8 < \bar{\lambda}_{LT} \le 1.5$	77	0.959
	$1.5 < \bar{\lambda}_{LT}$	57	1.031
	All range	196	1.014

Table VIII-14: Partial safety factors for both proposed design methods – uniform mono- symmetric beams

To cope with the high value of the partial safety factor associated with *Proposition I* for mono-symmetric beams having a low slenderness, the corresponding quantile plot is presented in Figure VIII-22a). Similarly to the current *Eurocode 3* guidelines (see Figure VIII-16), the results are not in line with a (log-) normal distribution. A *Tail approximation* is then performed removing r_e/r_t values greater than 1.1 (see Figure VIII-22b)).

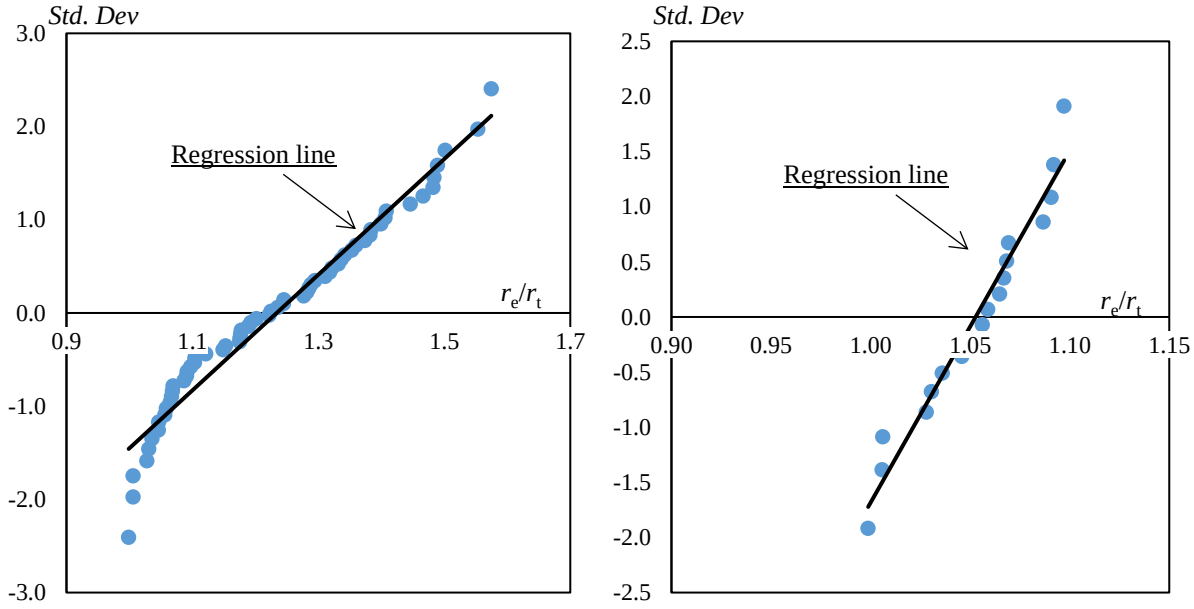

a) *Before Tail approximation* b) *After Tail approximation*

Figure VIII-22: Quantile plot for Proposition I *– uniform mono-symmetric beams (low slenderness)*

The partial safety factors associated with *Proposition I* for mono-symmetric beams with a low slenderness are presented in Table VIII-15. Performing the *Tail approximation* diminishes the partial safety factor to 1.02 which is now acceptable.

Slenderness range	Tail approximation	n	γ_{M1}
$\bar{\lambda}_{LT} \le 0.8$	Without	62	1.111
	With	18	1.017

Table VIII-15: Partial safety factors associated with Proposition I *for uniform mono-symmetric beams*

The adaptation of both *Proposition I* and *II* to non-uniform beams is discussed in the following paragraph. The computation of partial safety factors is then performed, validating the employed approach.

Tapered beams

The lateral-torsional buckling resistance of a tapered beam according to both proposed methods is determined using expressions (VIII.49) to (VIII.54) with the following specific features:

- The characteristic bending moment resistance $M_{y,Rk}$ and the ratio h_t/b that intervene in the imperfection factor of *Proposition II* are computed at the cross-section where $\alpha_{ult,k}$ is minimal (see equation (VIII.37)). Besides a term accounting for the tapering of the member is introduced in the expression of this imperfection factor which becomes:

$$\alpha_{LT} = \frac{0.23 + 0.10\gamma}{\bar{\lambda}_{LT}} \sqrt{\frac{h_t}{b_{min}}} \quad \text{with} \quad 0.21 \le \alpha_{LT} \le 0.49 \qquad \text{(VIII.55)}$$

with:

$$\gamma = 1 - \frac{h_{s,min}}{h_{s,max}}$$

- The ratio ψ between end moments is replaced with the ratio ψ_ε between the bending moment utilization at both ends (see Figure VIII-23) in expression (VIII.53) of the correction factor k_c:

$$\psi_\varepsilon = \min\left[\frac{M_{y,Ed} / M_{y,Rk}(x=0)}{\psi M_{y,Ed} / M_{y,Rk}(x=L)} ; \frac{\psi M_{y,Ed} / M_{y,Rk}(x=L)}{M_{y,Ed} / M_{y,Rk}(x=0)} \right] \qquad \text{(VIII.56)}$$

Because numerical results exhibit an influence of the bending distribution on the lateral-torsional buckling resistance of tapered beams (see Figure VIII-12 and Figure VIII-13), the use of coefficient f was also adopted. The design methods are then consistent with those proposed for uniform beams. Making use of a correction factor that depends on the bending moment utilization diagram is similar to the approach employed by *Marques* (2014) when adapting the interaction formulae from *Eurocode 3* to tapered members.

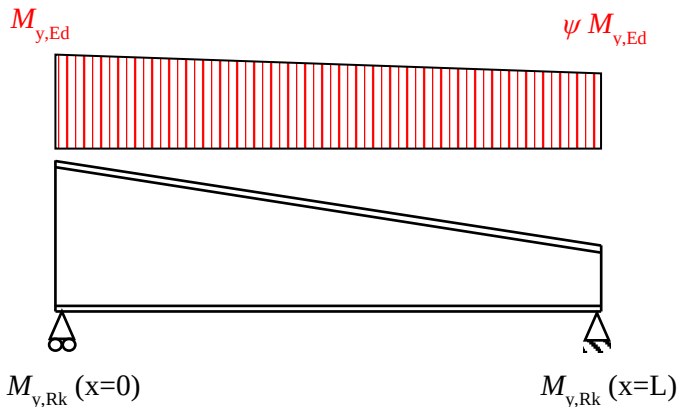

Figure VIII-23: Acting and resisting characteristic bending moment distribution on a tapered beam

The numerical reduction factors are compared against those obtained analytically using both proposed design methods in Figure VIII-24 for tapered doubly symmetric beams. It is worth mentioning that the analytical reduction factors correspond to the decrease of the cross-section resistance to bending at the location where $\alpha_{ult,k}$ is minimal.

All analytical results are on the safe side with more conservative results obtained using *Proposition I*. This first alternative yields also more scattered results, especially in the low slenderness range, corresponding to high reduction factors. The mean deviation from the numerical results is greater than 15% when using *Proposition I*. Most results obtained using *Proposition II* present a 10 to 15% deviation from the numerical values. The second alternative provides more accurate results than *Proposition I*.

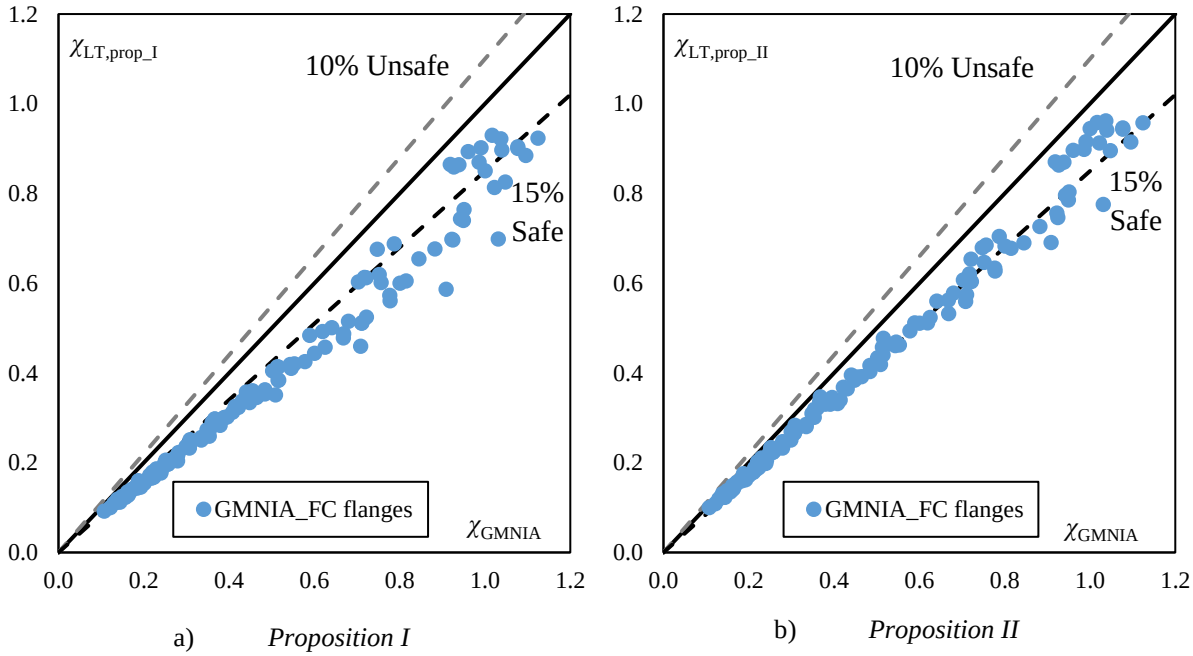

Figure VIII-24: Numerical and analytical reduction factors for tapered doubly symmetric welded beams

Figure VIII-25 shows the comparison between the numerical and analytical reduction factors for tapered mono-symmetric beams. Both design methods provide scattered results all lying on the safe side. Making use of *Proposition I* produces safer results with an average deviation from the numerical results of approximately 25%. The deviation is reduced when using *Proposition II*, being 15 to 20%.

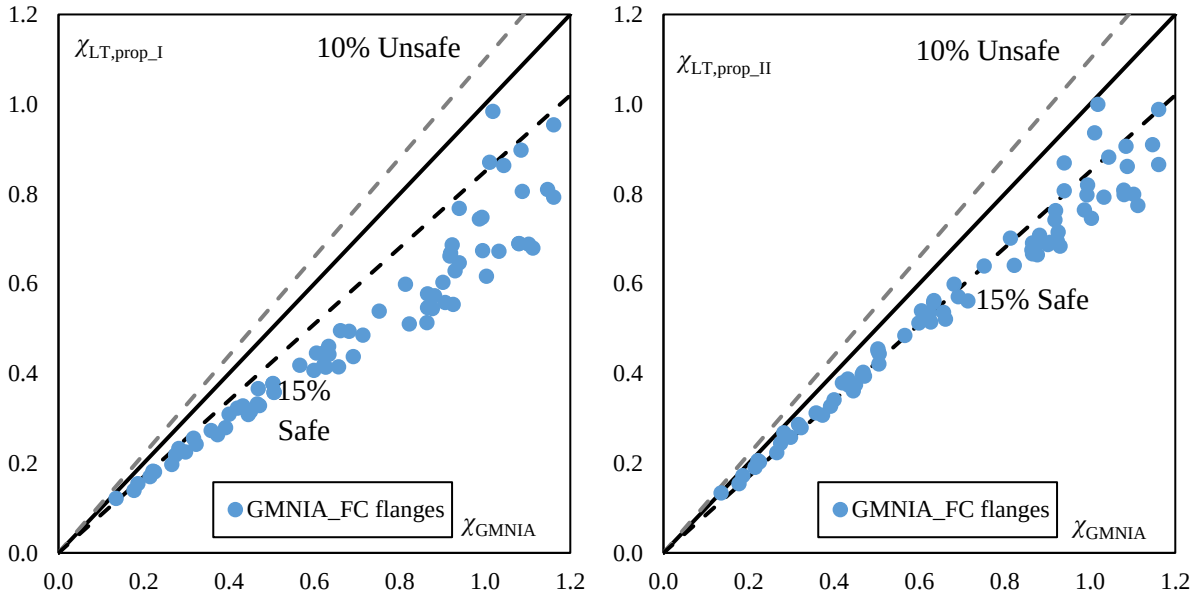

Figure VIII-25: Numerical and analytical reduction factors for tapered mono-symmetric welded beams

Eventually, the partial safety factors associated with both proposed design methods are determined and presented in Table VIII-16 for doubly symmetric beams. Partial safety factors are close to unity for all slenderness ranges for both design methods. Deviations from 1 are up to 8 % for *Proposition I* and 4% for *Proposition II*, characterizing adequate design methods.

Design method	Slenderness range	*n*	γ_{M1}
Proposition I: $\alpha_{LT} = 0.49$	$\bar{\lambda}_{LT} \le 0.8$	26	1.003
	$0.8 < \bar{\lambda}_{LT} \le 1.5$	42	0.921
	$1.5 < \bar{\lambda}_{LT}$	61	0.945
	All range	129	0.975
Proposition II: $0.21 \le \alpha_{LT} = \frac{0.23 + 0.10\gamma}{\bar{\lambda}_{LT}} \sqrt{\frac{h_t}{b}} \le 0.49$	$\bar{\lambda}_{LT} \le 0.8$	26	1.003
	$0.8 < \bar{\lambda}_{LT} \le 1.5$	42	0.958
	$1.5 < \bar{\lambda}_{LT}$	61	1.038
	All range	129	1.015

Table VIII-16: Partial safety factors for both proposed design methods – tapered doubly symmetric beams

It is worth mentioning that the *Proposition II* design method would not provide a satisfactory level of safety if using the imperfection factor of equation (VIII.54). Indeed, in such case the partial safety factors would be these presented in Table VIII-17. The partial safety factors would then be acceptable in the low and intermediate slenderness ranges only, the value obtained for high slenderness being greater than 1.05.

Imperfection factor	Slenderness range	n	γ_{M1}
$0.21 \le \alpha_{LT} = \frac{0.23}{\bar{\lambda}_{LT}} \sqrt{\frac{h_t}{b}} \le 0.49$	$\bar{\lambda}_{LT} \le 0.8$	29	0.984
	$0.8 < \bar{\lambda}_{LT} \le 1.5$	42	0.981
	$1.5 < \bar{\lambda}_{LT}$	61	1.070
	All range	129	1.022

Table VIII-17: Partial safety factors for tapered doubly symmetric beams – initial Proposition II

The partial safety factors for both design methods are also computed for tapered mono-symmetric beams, the results being presented in Table VIII-18. The partial safety factors are comprised between 0.93 and 0.99 in all slenderness ranges for *Proposition II* while the *Proposition I* partial safety factors are lower, ranging from 0.85 to 0.94. Therefore, the two proposed methods provide a satisfactory safety level for beams made of flame-cut flanges.

Design method	Slenderness range	n	γ_{M1}
Proposition I: $\alpha_{LT} = 0.49$	$\bar{\lambda}_{LT} \le 0.8$	38	0.940
	$0.8 < \bar{\lambda}_{LT} \le 1.25$	28	0.848
	$1.25 < \bar{\lambda}_{LT}$	29	0.925
	All range	95	0.911
Proposition II: $0.21 \le \alpha_{LT} = \frac{0.23 + 0.10\gamma}{\bar{\lambda}_{LT}} \sqrt{\frac{h_t}{b}} \le 0.49$	$\bar{\lambda}_{LT} \le 0.8$	38	0.970
	$0.8 < \bar{\lambda}_{LT} \le 1.25$	28	0.929
	$1.25 < \bar{\lambda}_{LT}$	29	0.993
	All range	95	0.972

Table VIII-18: Partial safety factors for both proposed design methods – tapered mono-symmetric beams

In the following sub-section VIII.4.3.2, the new verification format appearing in *prEurocode 3* is derived in the general case of a tapered beam having a mono-symmetric cross-section. An adaptation of this design method to welded members made of flame-cut flanges is then proposed and validated by satisfactory values of partial safety factors.

VIII.4.3.2 Adaptation of the new verification format from prEN 1993-1-1

Scope extension

In the present sub-section, the derivation of the new verification format from *prEurocode 3 Part 1-1* is extended to the case of tapered beams having a mono-symmetric cross-section, as presented in Figure VIII-26. The consistent derivation of this new design method is expressed by *Taras* (2010a/b) in the case of uniform doubly symmetric beams.

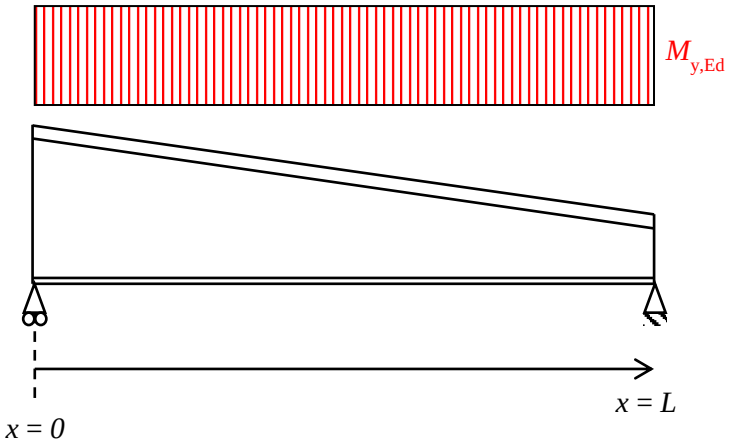

Figure VIII-26: Studied configuration

The design method relies on the expression of the first yield criterion for a member subjected to a uniform bending moment distribution:

$$\frac{M_{y,Ed}}{M_{y,Rk}}(x)+\frac{M^{II}_{z,Ed}}{M_{z,Rk}}(x)+\frac{B^{II}_{Ed}}{B_{Rk}}(x)=1.0 \qquad \text{(VIII.57)}$$

The distributions of the first and second order internal stresses due to in-plane bending moment M_y, out-of-plane bending moment M_z and bimoment B are presented in Figure VIII-27. In mono-symmetric members, the first yielding of the cross-section may happen at the most compressed end of the compression flange (see Figure VIII-27), resulting from compressive stresses due to 1st and 2nd order bending moments and bimoment. Failure may also occur owing to overly important tensile stresses in the tension flange. Such phenomenon may exist when the same end of the tensile flange undergoes tensile stresses owing to M_z and B.

To cope with the two possible failure types, the verification format is simplified as:

$$\frac{M_{y,Ed}}{M_{y,Rk}}(x)+\max\left[\frac{M^{II}_{z,Ed}}{M_{z,Rk}}(x)\right]+\max\left[\frac{B^{II}_{Ed}}{B_{Rk}}(x)\right]=1.0 \qquad \text{(VIII.58)}$$

$$\leftrightarrow \frac{M_{y,Ed}}{M_{y,Rk}}(x)+\max\varepsilon_{Mz}(x)+\max\varepsilon_{B}(x)=1.0 \qquad \text{(VIII.59)}$$

The effects of M_y, M_z and B are then treated separately with the safe-sided assumption that failure happens when the utilizations of the three effects reach their maximal values.

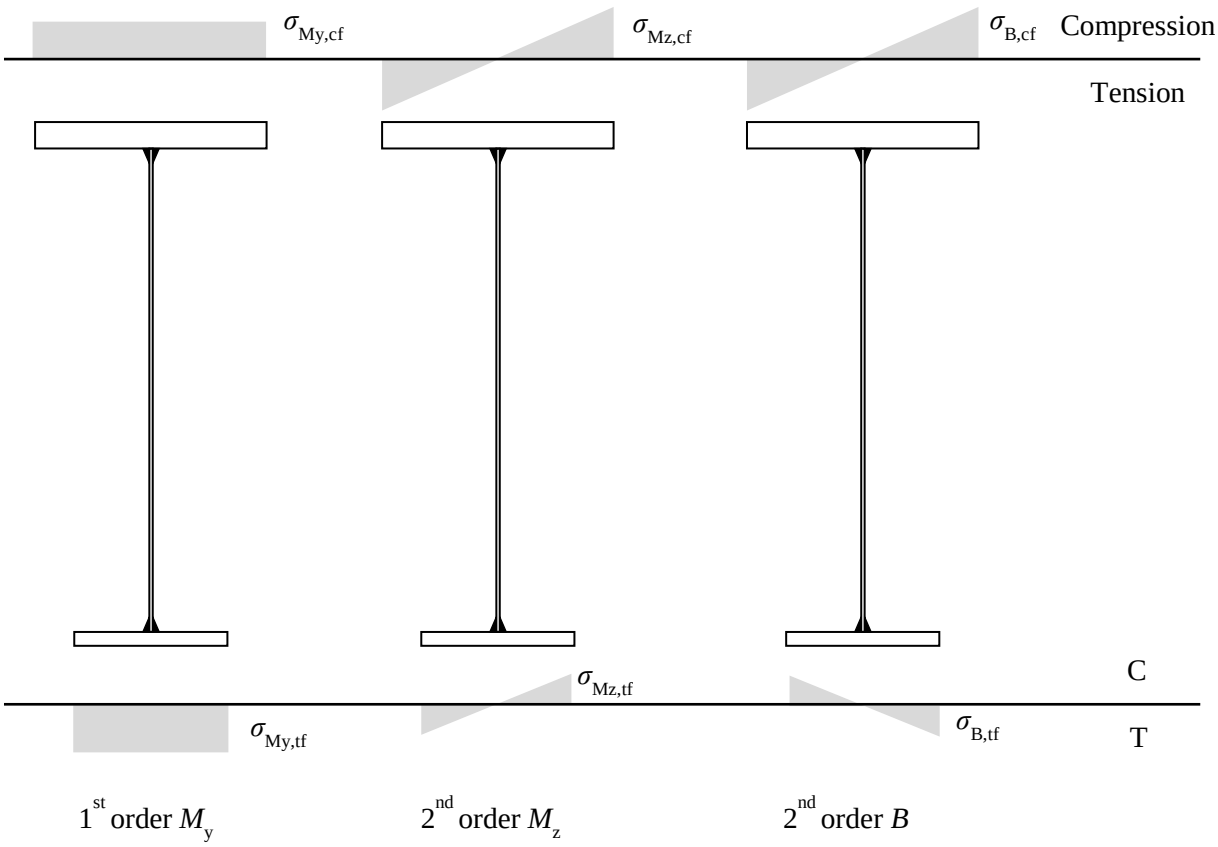

Figure VIII-27: Stresses in beam flanges

To determine both the second order out-of-plane bending moment M_z and bimoment B, one may assume that:

$$\frac{\bar{v}_{cr}}{\bar{\theta}_{cr}} = \frac{\bar{v}_0}{\bar{\theta}_0} = \frac{M_{y,cr}}{N_{cr,z}} \qquad \text{(VIII.60)}$$

where the index "cr" refers to the elastic critical mode shape while "0" refers to the initial imperfections.

The relationship between both amplitudes of the critical mode expressed by equation (VIII.60) is acceptable for doubly or mono-symmetric members having a constant or tapered cross-section since both shape functions are assumed to correspond to half a sine wave. The previous expression comes with the common assumption that the initial imperfections are similar, scaled to the amplitudes, to the critical mode shape.

The following amplification relationships can then be used:

$$v(x) = \frac{1}{\alpha_{cr} - 1} v_0(x) \qquad \text{(VIII.61)}$$

$$\theta(x) = \frac{1}{\alpha_{cr} - 1} \theta_0(x) \qquad \text{(VIII.62)}$$

Besides, the second order internal moments are:

$$M_{z,Ed}^{II}(x) = -E I_z \frac{d^2 v}{dx^2}(x) \tag{VIII.63}$$

$$B_{Ed}^{II}(x) = -E I_w(x) \left(\frac{d^2 \theta}{dx^2}(x) + \frac{2}{h(x)} \frac{d\theta}{dx}(x) \frac{dh}{dx}(x) \right) \tag{VIII.64}$$

The bimoment expression accounts for the flanges inclination, as developed by *Kitipornchai* (1972, 1975) in the case of doubly or mono-symmetric members.

The distribution of the distance between the flange centroids along the beam is linear, being given by:

$$h(x) = h_{s,max} \bar{h}(x) \tag{VIII.65}$$

with:

$$\bar{h}(x) = 1 - \gamma \frac{x}{L}$$

$$\gamma = 1 - \frac{h_{s,min}}{h_{s,max}}$$

The previous expression states that the largest cross-section is located at $x = 0$, the smallest being encountered at $x = L$ (see Figure VIII-26).

The expressions of the lateral deflection and torsional twist given by (VIII.61) and (VIII.62), respectively, are inserted along with (VIII.60) in expressions (VIII.63) and (VIII.64). The second order internal moment and bimoment therefore become:

$$M_{z,Ed}^{II}(x) = E I_z \frac{M_{y,cr}}{N_{cr,z}} \frac{1}{\frac{M_{y,cr}}{M_{y,Ed}} - 1} \bar{\theta}_0 \left(\frac{\pi}{L} \right)^2 \sin\left(\frac{x\pi}{L} \right) \tag{VIII.66}$$

$$B_{Ed}^{II}(x) = \frac{E I_z}{M_{y,cr}} \left(\frac{\pi}{L} \right)^2 \frac{I_w(x)}{I_z} \frac{M_{y,Ed}}{1 - \frac{M_{y,Ed}}{M_{y,cr}}} \bar{\theta}_0 \left(\sin\left(\frac{x\pi}{L} \right) + \frac{2\gamma}{\pi \bar{h}(x)} \cos\left(\frac{x\pi}{L} \right) \right) \tag{VIII.67}$$

Besides, the elastic cross-sectional resistance to out-of-plane bending moment and bimoment for doubly or mono-symmetric cross-sections are:

$$M_{z,Rk} = W_z f_y \tag{VIII.68}$$

$$B_{Rk}(x) = \frac{I_w(x)}{\omega_{max}(x)} f_y \tag{VIII.69}$$

In the case of a mono-symmetric cross-section, the following expressions hold:

$$W_z = \frac{I_z}{\max\left(b_t; b_c\right)/2} \tag{VIII.70}$$

$$\omega_{\max}(x) = h(x)\frac{\max\left(b_t; b_c\right)}{4} \tag{VIII.71}$$

Using expressions (VIII.66) to (VIII.69) and (VIII.71), the maximal values of the utilization ratios for the out-of-plane bending moment and bimoment are:

$$\max \varepsilon_{Mz}(x) = \frac{1}{W_z f_y}\frac{M_{y,Ed}}{1-\dfrac{M_{y,Ed}}{M_{y,cr}}}\bar{\theta}_0 \tag{VIII.72}$$

$$\max \varepsilon_B(x) = \varepsilon_B(x_0) = \frac{N_{cr,z}}{M_{y,cr}}\frac{h_{s,\max}\max\left(b_t; b_c\right)}{4I_z f_y}\frac{M_{y,Ed}}{1-\dfrac{M_{y,Ed}}{M_{y,cr}}}\bar{\theta}_0 g(x_0) \tag{VIII.73}$$

with:

$$g(x_0) = \bar{h}(x_0)\sin\left(\frac{x_0\pi}{L}\right) + \frac{2\gamma}{\pi}\cos\left(\frac{x_0\pi}{L}\right) \tag{VIII.74}$$

The location x_0 where the bimoment utilization reaches its maximal value is obtained when:

$$\frac{\partial g}{\partial x}(x_0) = 0 \rightarrow \bar{h}(x_0)\cos\left(\frac{x_0\pi}{L}\right) - \frac{3\gamma}{\pi}\sin\left(\frac{x_0\pi}{L}\right) = 0 \tag{VIII.75}$$

The value of x_0/L is plotted in Figure VIII-28 as a function of the parameter γ that accounts for the tapering ratio only. The exact values of this location are plotted along with those obtained using the following linear approximation:

$$\frac{x_0}{L} = 0.5 - 0.29\gamma \tag{VIII.76}$$

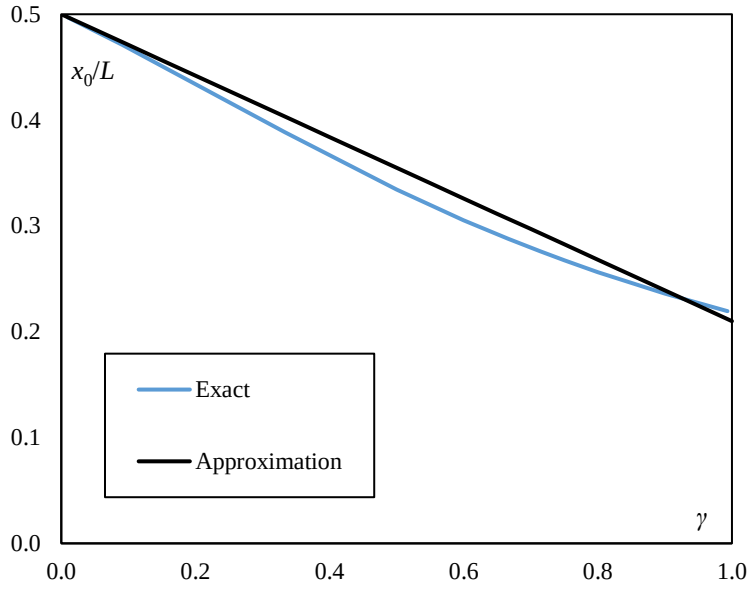

Figure VIII-28: Location of the maximal bimoment utilization along a tapered beam

The greatest difference between the exact and approximated values of x_0/L is 7% which is still acceptable considering that the verification format (VIII.58) provides safer results than the general expression (VIII.57).

Inserting expression (VIII.76) into (VIII.74), one obtains:

$$g(x_0) = \left(1 - 0.5\gamma + 0.29\gamma^2\right)\cos\left(0.29\gamma\pi\right) + \frac{2\gamma}{\pi}\sin\left(0.29\gamma\pi\right) = f(\gamma) \qquad \text{(VIII.77)}$$

Eventually, equation (VIII.58) rewrites as:

$$\frac{M_{y,Ed}}{M_{y,Rk}(x)} + \frac{1}{W_z f_y}\frac{M_{y,Ed}}{1 - \dfrac{M_{y,Ed}}{M_{y,cr}}}\bar{\theta}_0\left[1 + \frac{N_{cr,z}}{M_{y,cr}}\frac{h_{s,max}}{2}f(\gamma)\right] = 1.0 \qquad \text{(VIII.78)}$$

Besides, as assumed by *Taras* (2010a/b) the initial torsional twist amplitude can be expressed as a function of the amplitude e_0 of the imperfection measured in the compression flange (see Figure VIII-29):

$$e_0 = \bar{v}_0 + z_{fc}(x_z)\bar{\theta}_0 = \left(\frac{M_{y,cr}}{N_{cr,z}} + z_{fc}(x_z)\right)\bar{\theta}_0 \qquad \text{(VIII.79)}$$

where x_z is the location of the cross-section where the initial lateral displacement δ_{fl} of the compression flange is maximal (see Figure VIII-29). The distance z_{fc} between the compression flange centroid and the cross-section shear centre is given by:

$$z_{fc}(x) = \frac{I_{z,ft}}{I_z}h(x) \qquad \text{(VIII.80)}$$

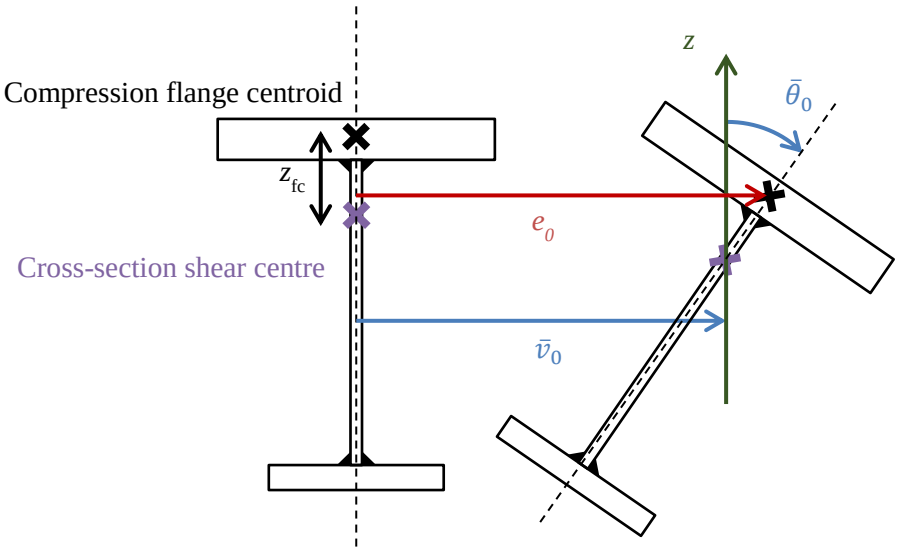

Figure VIII-29: Perfect member and member with initial imperfections

Rigorously, the right side of equation (VIII.79) should be multiplied with:

$$\sin\left(\frac{x_z \pi}{L}\right) \tag{VIII.81}$$

However, in a seek of simplicity, it is assumed that:

$$\sin\left(\frac{x_z \pi}{L}\right) \approx 1 \tag{VIII.82}$$

The previous simplification is acceptable provided that the actual value of x_z is close to mid span. If x_z (slightly) diverges from mid span, expression (VIII.81) becomes lower than unity. Then, the "actual" amplitude e_0 obtained by multiplying the right side of equation (VIII.79) with (VIII.81) would be lower than the value obtained using equation (VIII.79) alone. Results obtained with equation (VIII.79) can therefore not lie on the unsafe side.

Using the previous assumptions, the initial displacement of the compression flange can be expressed using:

$$\delta_{fl}(x) = \left(\frac{M_{y,cr}}{N_{cr,z}} + z_{fc}(x)\right) \sin\left(\frac{x\pi}{L}\right) \bar{\theta}_0 \tag{VIII.83}$$

Therefore, x_z is obtained when:

$$\frac{\partial \delta_{fl}}{\partial x}(x_z) = 0 \rightarrow \pi K = \frac{x_z \pi}{L} + \tan\left(\frac{x_z \pi}{L}\right) \tag{VIII.84}$$

with:

$$K = \frac{1}{\gamma}\left[\frac{M_{y,cr} I_z}{N_{cr,z} I_{z,ft} h_{s,max}} + 1\right]$$

The exact value of x_z/L is plotted against parameter K in Figure VIII-30 along with the predictions of the following approximation:

$$\frac{x_z}{L} = 0.5 - \frac{0.146}{K} \tag{VIII.85}$$

Both expressions (VIII.84) and (VIII.85) yield similar values for x_z. Besides, Figure VIII-30 shows that x_z/L is very close to mid span in the most common cases, which is consistent with the previous simplification of equation (VIII.82).

Inserting expression (VIII.85) into (VIII.65) yields:

$$\bar{h}(x_z) = 1 - 0.5\gamma + \frac{0.146\gamma}{K} \tag{VIII.86}$$

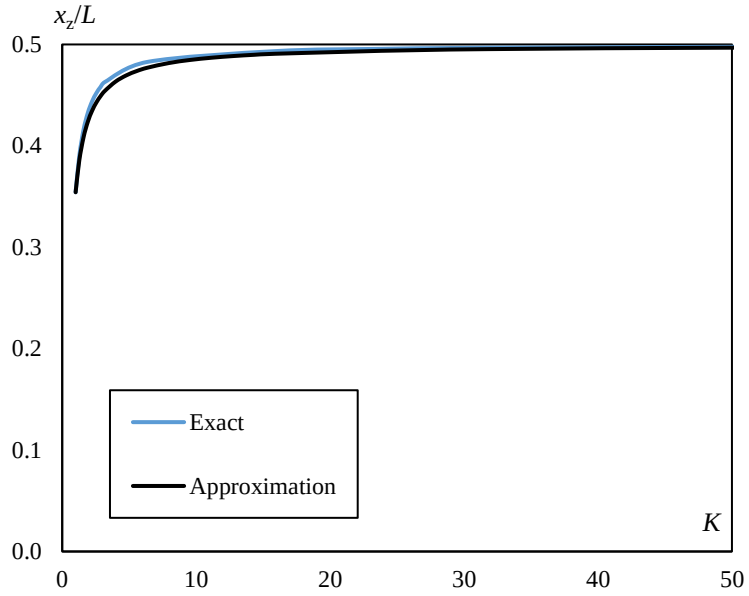

Figure VIII-30: Location of the maximal initial displacement of the compression flange

Expression (VIII.78) finally rewrites:

$$\frac{M_{y,Ed}}{M_{y,Rk}(x)} + \frac{1}{W_z f_y}\frac{M_{y,Ed}}{1-\dfrac{M_{y,Ed}}{M_{y,cr}}} e_0 \frac{1+\dfrac{N_{cr,z}}{M_{y,cr}}\dfrac{h_{s,max}}{2} f(\gamma)}{\dfrac{M_{y,cr}}{N_{cr,z}} + h_{s,max}\dfrac{I_{z,ft}}{I_z}\bar{h}(x_z)} = 1.0 \tag{VIII.87}$$

which can be further developed as:

$$\frac{M_{y,Ed}}{M_{y,Rk}(x)}\left\{1 + \frac{e_0}{1-\dfrac{M_{y,Ed}}{M_{y,cr}}}\frac{A(x)}{W_z}\frac{W_y(x) f_y}{A(x) f_y}\frac{N_{cr,z}}{M_{y,cr}}\xi\right\} = 1.0 \tag{VIII.88}$$

where the parameter ξ that accounts for the tapering and mono-symmetry of the member is:

$$\xi = \frac{\frac{M_{\mathrm{y,cr}}}{N_{\mathrm{cr,z}}} + \frac{h_{\mathrm{s,max}}}{2} f(\gamma)}{\frac{M_{\mathrm{y,cr}}}{N_{\mathrm{cr,z}}} + h_{\mathrm{s,max}} \frac{I_{\mathrm{z,ft}}}{I_{\mathrm{z}}} \bar{h}(x_z)} \tag{VIII.89}$$

In the specific case of a uniform beam, one notices that:

$$f(\gamma) = 1 \tag{VIII.90}$$

$$\bar{h}(x_z) = 1 \tag{VIII.91}$$

Therefore, expression (VIII.89) reduces to:

$$\xi = \frac{\frac{M_{\mathrm{y,cr}}}{N_{\mathrm{cr,z}}} + \frac{h_{\mathrm{s}}}{2}}{\frac{M_{\mathrm{y,cr}}}{N_{\mathrm{cr,z}}} + h_{\mathrm{s}} \frac{I_{\mathrm{z,ft}}}{I_{\mathrm{z}}}} \tag{VIII.92}$$

In the even more specific case of a uniform beam having a doubly symmetric cross-section, the previous expression further simplifies as:

$$\xi = 1 \tag{VIII.93}$$

The following normalized parameters are introduced:

$$\bar{\lambda}_{\mathrm{LT}}(x) = \sqrt{\frac{M_{\mathrm{y,Rk}}(x)}{M_{\mathrm{y,cr}}}} \tag{VIII.94}$$

$$\bar{\lambda}_{\mathrm{z}}(x) = \sqrt{\frac{N_{\mathrm{Rk}}(x)}{N_{\mathrm{cr,z}}}} \tag{VIII.95}$$

$$\chi_{\mathrm{LT}}(x) = \frac{M_{\mathrm{y,Ed}}}{M_{\mathrm{y,Rk}}(x)} \tag{VIII.96}$$

Equations (VIII.94) to (VIII.96) are inserted into (VIII.88), yielding:

$$\chi_{\mathrm{LT}}(x) + \frac{\chi_{\mathrm{LT}}(x)}{1 - \chi_{\mathrm{LT}}(x) \bar{\lambda}_{\mathrm{LT}}^2} \left(\frac{\bar{\lambda}_{\mathrm{LT}}(x)}{\bar{\lambda}_{\mathrm{z}}(x)} \right)^2 \eta(x) \xi = 1.0 \tag{VIII.97}$$

with:

$$\eta(x) = e_0 \frac{A(x)}{W_{\mathrm{z}}}$$

The preceding equation (VIII.97) is similar to that obtained by *Taras* (2010a/b) in the particular case of uniform doubly symmetric members. Using a large number of GMNIA computations, *Taras* (2010a/b) proposed to use the following expression for the generalized imperfection η:

$$\eta = \alpha_{LT}\left(\bar{\lambda}_z - 0.2\right) \tag{VIII.98}$$

where the imperfection factor α_{LT} is given by expression (VIII.48) for most welded members designed for buildings ($t_f \leq 40$ mm).

Besides, a coefficient f_M, given by expression (VIII.47) for a linear bending moment distribution, is introduced in equation (VIII.97) to account for the bending moment distribution.

To obtain a design method easy to use and consistent with that existing for uniform doubly symmetric members, it has been chosen to employ expression (VIII.98) for the generalized imperfection. Besides, the f_M factor is also adapted to non uniform members using, for a linear bending moment distribution:

$$f_{M,\varepsilon} = 1.25 - 0.1\psi_\varepsilon - 0.15\psi_\varepsilon^{\,2} \tag{VIII.99}$$

where the ratio ψ_ε between end moment utilizations is given by expression (VIII.56).

To overcome the tedious computation of the design value of the lateral-torsional buckling resistance $M_{b,Rd}$ at a large number of cross-sections, one may simply verify the beam stability at the cross-section x_α where $\alpha_{ult,k}$ is minimal.

Eventually, the new design method from *prEurocode 3 Part 1-1* adapted to tapered beams having a mono-symmetric cross-section requires the following clause to be satisfied:

$$\frac{M_{y,Ed}(x_\alpha)}{M_{b,Rd}(x_\alpha)} \leq 1.0 \tag{VIII.100}$$

with:

$$M_{b,Rd}(x_\alpha) = \chi_{LT}(x_\alpha)\frac{M_{y,Rk}(x_\alpha)}{\gamma_{M1}} \tag{VIII.101}$$

$$\chi_{LT}(x_\alpha) = \frac{f_{M,\varepsilon}}{\phi_{LT}(x_\alpha) + \sqrt{\phi_{LT}^2(x_\alpha) - f_{M,\varepsilon}\bar{\lambda}_{LT}^2(x_\alpha)}} \leq 1.0 \tag{VIII.102}$$

$$\phi_{LT}(x_\alpha) = 0.5\left[1 + f_{M,\varepsilon}\left(\left(\frac{\bar{\lambda}_{LT}(x_\alpha)}{\bar{\lambda}_z(x_\alpha)}\right)^2 \alpha_{LT}(x_\alpha)\left(\bar{\lambda}_z(x_\alpha) - 0.2\right)\xi + \bar{\lambda}_{LT}^2(x_\alpha)\right)\right] \tag{VIII.103}$$

where the imperfection factor for welded members having $t_f \leq 40$ mm is:

$$\alpha_{LT}(x_\alpha) = 0.21\sqrt{\frac{W_{el,y}(x_\alpha)}{W_{el,z}}} \leq 0.64 \tag{VIII.104}$$

In the following paragraph, an expression for the imperfection factor α_{LT} better suited to welded members made of flame-cut flanges is proposed. The partial safety factors associated with the derived design method are then presented.

Improved imperfection factor

The design method previously derived is adapted to welded members with $t_f \leq 40$ mm and made of flame-cut flanges by replacing the imperfection factor given by (VIII.104) with:

$$\alpha_{LT}(x_\alpha) = 0.21\sqrt{\frac{W_{el,y}(x_\alpha)}{W_{el,z}}} \leq 0.49 + 0.15\gamma \qquad \text{(VIII.105)}$$

To maintain the formalism of the current imperfection factor and provide a simple adaptation, expression (VIII.105) is similar to (VIII.104) except for the upper bound value. While a value of 0.64 is prescribed in *prEurocode 3*, a smaller value varying between 0.49 and 0.64 is proposed in the present work. The limit value depends on the tapering of the beam, being equal to 0.49 for uniform members.

The comparison between numerical and analytical reduction factors is presented in Figure VIII-31 for uniform beams. The results obtained for doubly symmetric members are close to those obtained using the imperfection factor given by expression (VIII.104) (see Figure VIII-17). Small differences are noticed for intermediate slenderness, using the design method adapted to flame-cuts resulting in lower differences between analytical and numerical results.

For mono-symmetric beams, Figure VIII-31b) shows no result on the unsafe side. The scatter is greater than in the case of doubly symmetric members but the mean deviation between analytical and numerical results is comprised between 10 and 15%.

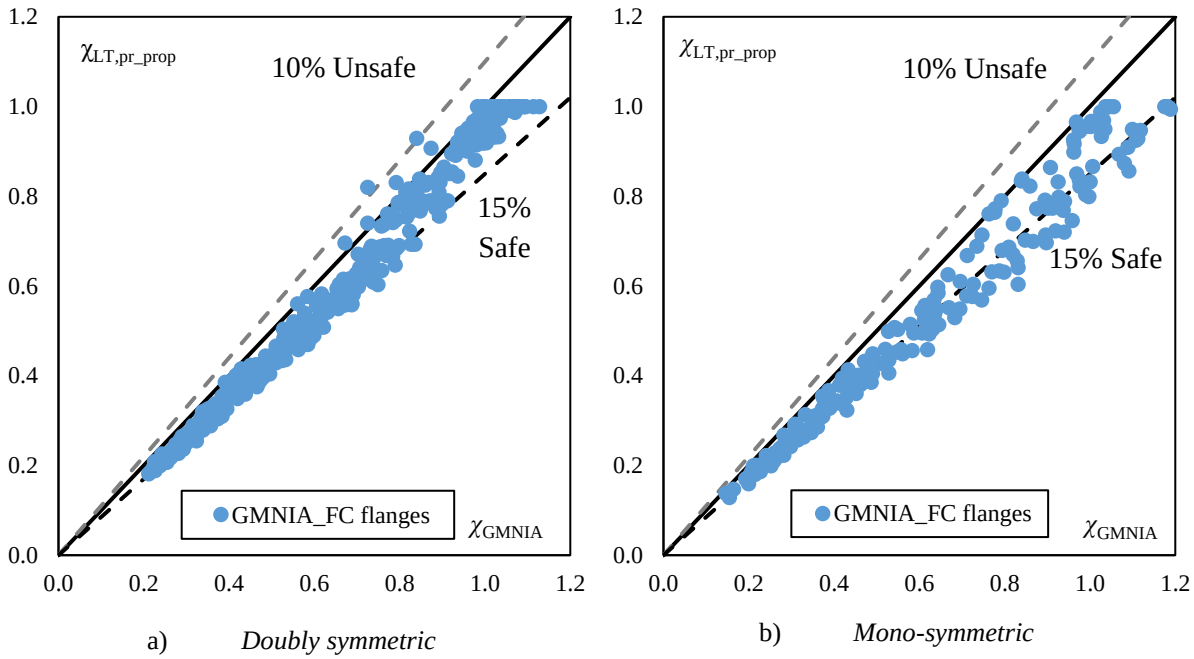

Figure VIII-31: Numerical and analytical (adapted prEC3*) reduction factors for uniform welded beams*

The comparison between analytical and numerical results are presented in Figure VIII-32 for the studied tapered beams. All results are found on the safe side for doubly symmetric beams. The results are not

very scattered, most of them being less than 20% safe-sided. Mono-symmetric beams present more scattered results with a larger mean deviation on the safe side.

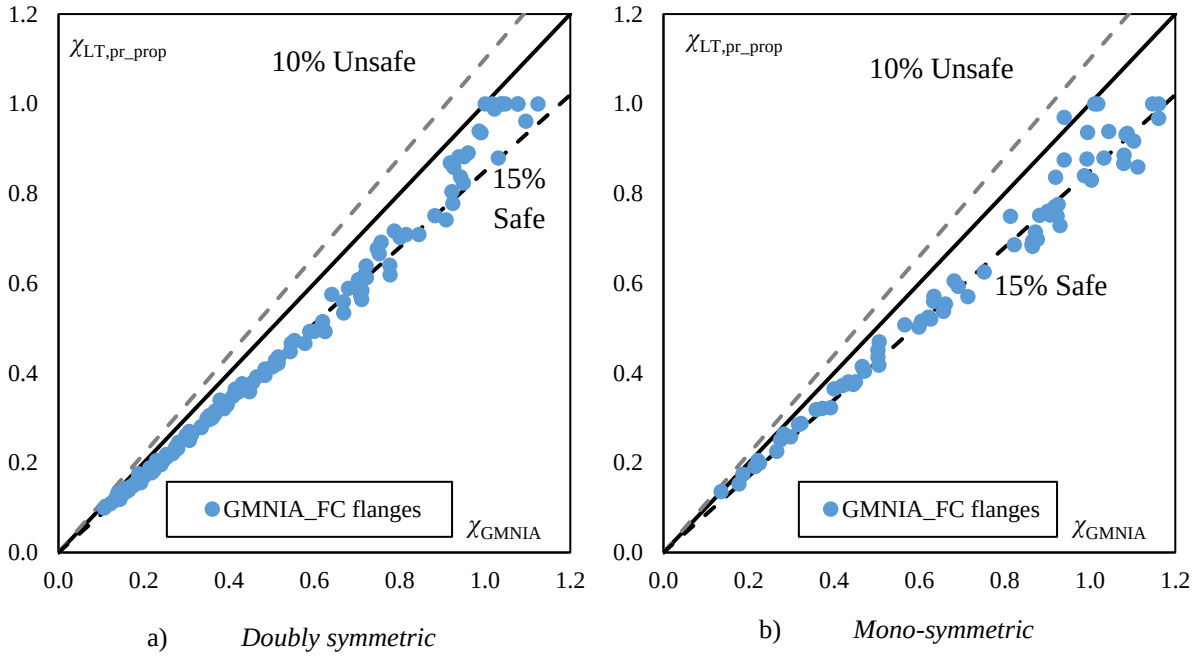

a) *Doubly symmetric* b) *Mono-symmetric*

Figure VIII-32: Numerical and analytical (adapted prEC3*) reduction factors for tapered welded beams*

The partial safety factors associated with the modified verification format from *prEN 1993-1-1* are computed for the studied welded members with flame-cut flanges. The results are presented in Table VIII-19 for uniform beams. In the case of doubly symmetric beams, the partial safety factors are satisfactory in the low and high slenderness ranges.

Cross-section type	Slenderness range	*n*	γ_{M1}
Doubly symmetric	$\bar{\lambda}_{LT} \leq 0.8$	107	0.965
	$0.8 < \bar{\lambda}_{LT} \leq 1.5$	180	<u>1.052</u>
	$1.5 < \bar{\lambda}_{LT}$	100	1.036
	All range	387	1.078
Mono-symmetric	$\bar{\lambda}_{LT} \leq 0.8$	62	<u>1.051</u>
	$0.8 < \bar{\lambda}_{LT} \leq 1.5$	77	0.987
	$1.5 < \bar{\lambda}_{LT}$	57	1.028
	All range	196	1.044

Table VIII-19: Partial safety factors for adapted prEC3 *method for uniform beams*

However, in the medium slenderness range, a value slightly greater than 1.050 is obtained. Similarly, when analysing the partial safety factor computed considering all the results obtained, an important value is obtained. These combined observations can reveal a variation of the accuracy of the design method within the medium slenderness range. Therefore, the studied slenderness range is split in two sub-groups, the boundary between them being 1.20. A partial safety factors is computed for each case,

the corresponding results are presented in Table VIII-20. In both sub-ranges, the partial safety factor is comprised between 1.045 and 1.050, which is acceptable.

Slenderness range	*n*	γ_{M1}
$0.8 < \bar{\lambda}_{LT} \leq 1.2$	96	1.048
$1.2 < \bar{\lambda}_{LT} \leq 1.5$	84	1.045

Table VIII-20: Partial safety factors for adapted prEC3 *method for uniform doubly symmetric beams*

For mono-symmetric cross-sections, Table VIII-19 shows acceptable values of γ_{M1} in the cases of medium and high slenderness. Yet, that obtained for the low slenderness range is slightly greater than 1.050. Similarly to the current *Eurocode 3* and *Proposition I* design rules, a *Tail approximation* is performed (see Figure VIII-33a) and Figure VIII-33b)).

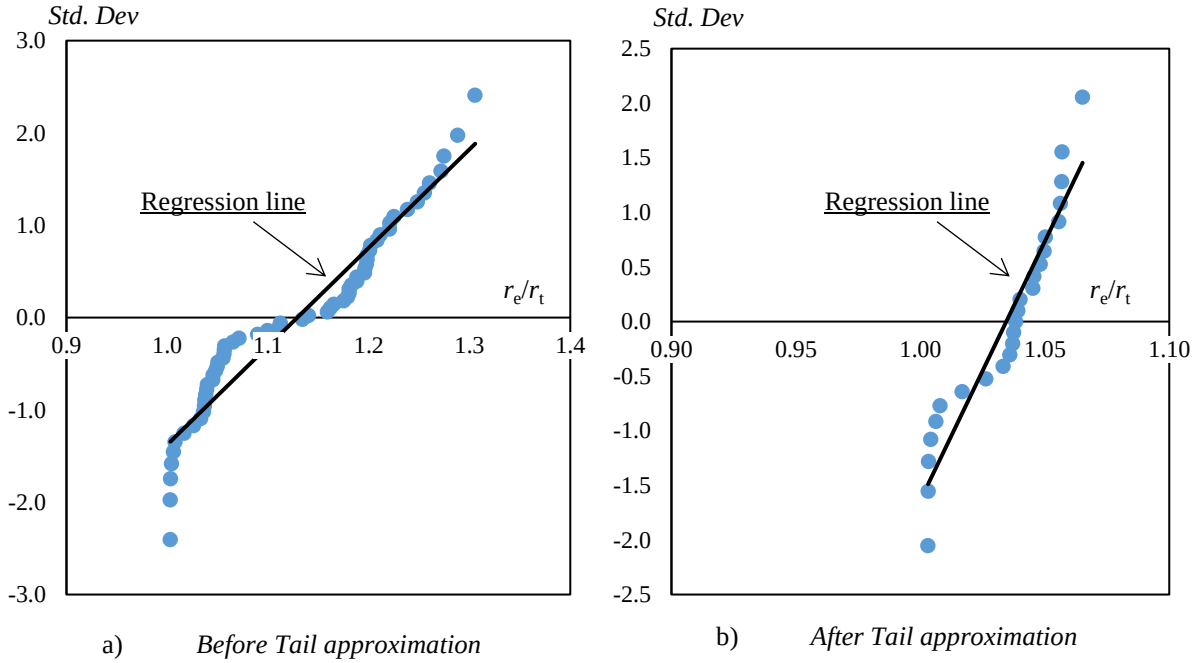

a) *Before Tail approximation* b) *After Tail approximation*

Figure VIII-33: Quantile plot for adapted prEC3 *– uniform mono-symmetric beams (low slenderness)*

The partial safety factors associated with the design method adapted from *prEurocode* 3 for mono-symmetric beams with a low slenderness are presented in Table VIII-21. Using a *Tail approximation* reduces the partial safety factor to an acceptable value of 1.01.

Slenderness range	Tail approximation	*n*	γ_{M1}
$\bar{\lambda}_{LT} \leq 0.8$	Without	62	1.051
	With	25	1.010

Table VIII-21: Partial safety factors associated with adapted prEC3 *for uniform mono-symmetric beams*

The partial safety factors associated with the design method corresponding to equations (VIII.100) to (VIII.103) adapted to flame-cuts are presented in Table VIII-22 for tapered beams. For both types of

cross-sections, the partial safety factors are lower than 1.05 whatever the slenderness range, validating the design method.

Cross-section type	Slenderness range	*n*	γ_{M1}
Doubly symmetric	$\bar{\lambda}_{LT} \leq 0.8$	26	1.039
	$0.8 < \bar{\lambda}_{LT} \leq 1.5$	42	0.974
	$1.5 < \bar{\lambda}_{LT}$	61	1.040
	All range	129	1.059
Mono-symmetric	$\bar{\lambda}_{LT} \leq 0.8$	38	0.954
	$0.8 < \bar{\lambda}_{LT} \leq 1.25$	28	0.960
	$1.25 < \bar{\lambda}_{LT}$	29	1.018
	All range	95	0.972

Table VIII-22: Partial safety factors for adapted prEC3 *method for tapered beams*

The isolated effects of flexural buckling and lateral-torsional buckling having been treated, the upcoming section VIII.5 deals with the combined effects of both buckling modes. Numerical results are employed to assess the accuracy of combined approaches making use of the proposed methods adapted to welded members made of flame-cut flanges.

VIII.5 Out-of-plane buckling of beam-columns

VIII.5.1 Numerical results

The numerical analyses performed on members simultaneously subjected to bending and compression have produced two sets of results for each studied member:

- $\alpha_{cr,op,LBA}$: minimum amplifier of the in-plane design loads to reach the elastic critical resistance of the studied member with regards to out-of-plane buckling;
- $\alpha_{ult,op,GMNIA}$: minimum amplifier of the in-plane design loads to reach the member out-of-plane buckling resistance.

In addition, the minimum amplifier $\alpha_{ult,k}$ of the design loads to reach the characteristic resistance of the most critical cross-section is computed analytically. This amplifier, which does not account for flexural or lateral-torsional buckling, is computed at each cross-section using:

$$\alpha_{ult,k}(x) = \frac{1}{\frac{N_{Ed}}{N_{Rk}}(x) + \frac{M_{y,Ed}}{M_{Rk}}(x)} \qquad \text{(VIII.106)}$$

where the acting design loads do not account for in-plane geometrical deformation and imperfections, global and local. Indeed, the studied beam-columns are isolated and present no intermediate restraints: the in-plane and out-of-plane buckling behaviour do not interact with each other. Besides, as depicted

in Chapter VII, the global imperfection included in the numerical model is shaped as the elastic critical buckling mode that corresponds to out-of-plane buckling.

Using the three load amplifiers, the following parameters are obtained for each member:

$$\bar{\lambda}_{op} = \sqrt{\frac{\alpha_{ult,k}}{\alpha_{cr,op,LBA}}} \tag{VIII.107}$$

$$\chi_{op,GMNIA} = \frac{\alpha_{ult,op,GMNIA}}{\alpha_{ult,k}} \tag{VIII.108}$$

The numerical reduction factors determined using expression (VIII.108) are plotted with respect to the normalized slenderness obtained with expression (VIII.107) in Figure VIII-34 and Figure VIII-35. Again, the four *Eurocode 3* buckling curves *a* to *d* are added for comparison.

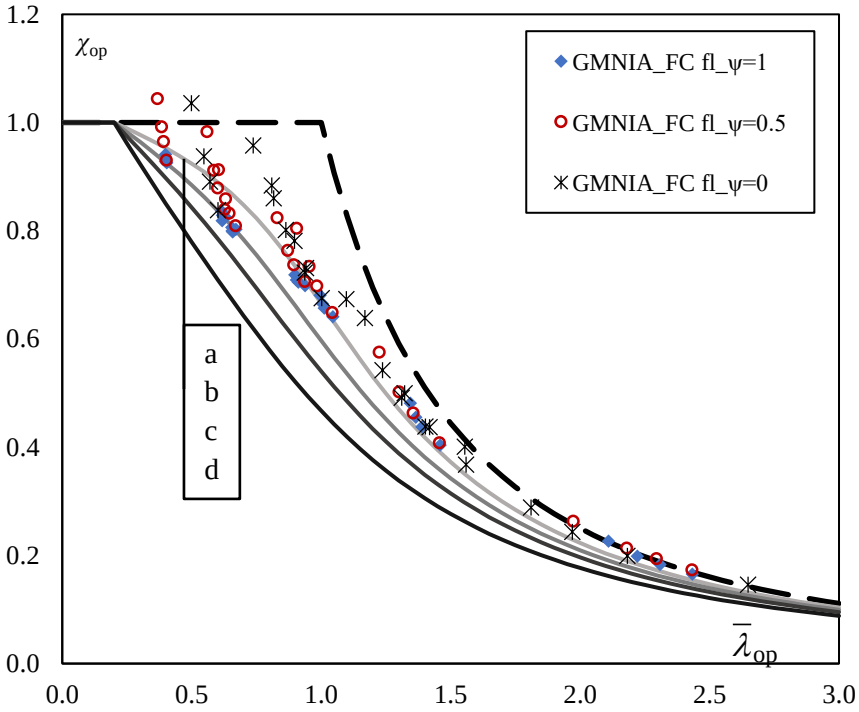

Figure VIII-34: Numerical results for out-of-plane buckling of uniform doubly symmetric beams-columns

Both Figure VIII-34 and Figure VIII-35 show that the reduction factors all lie above buckling curve *c*, with a large number of results above buckling curve *b* as well. Again, it can be seen that the reduction factors get closer to *Euler*'s curve as the slenderness increases. One can notice that the uniform bending moment distribution provides the lowest reduction factors in the case of uniform beams while yielding among the highest reduction factors for tapered beams.

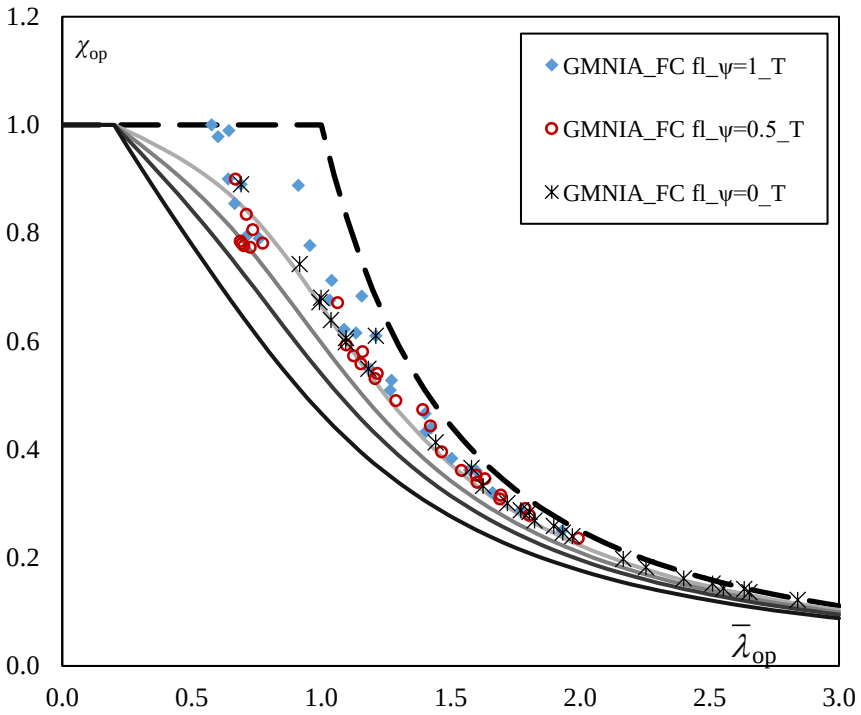

Figure VIII-35: Numerical results for out-of-plane buckling of tapered doubly symmetric beams-columns

Using the numerical results, the design methods for uniform or non-uniform beam-columns prescribed by *prEurocode 3 Part 1-1* are assessed in the upcoming sub-section VIII.5.2. Then, design methods better suited to the numerical results are exposed, statistical analyses of the results validating its use.

VIII.5.2 *Assessment of the design methods in* (pr)Eurocode 3

VIII.5.2.1 Interaction formulae

The current and revised *Eurocode 3 Part 1-1* propose to employ interaction formulae to assess the stability of beam-columns provided that their cross-section is constant. Expressions (IV.20) and (IV.21) must be verified simultaneously for members resting on fork supports. The load amplifier α_{ult} of the axial force N_{Ed} and in-plane bending moment $M_{y,Ed}$ to reach the ultimate capacity of the beam-column is the minimum of $\alpha_{ult,1}$ and $\alpha_{ult,2}$:

$$\frac{\alpha_{ult,1} N_{Ed}}{\frac{\chi_y N_{Rk}}{\gamma_{M1}}} + k_{yy} \frac{\alpha_{ult,1}\left(M_{y,Ed} + \Delta M_{y,Ed}\right)}{\frac{\chi_{LT} M_{y,Rk}}{\gamma_{M1}}} = 1 \qquad \text{(VIII.109)}$$

$$\frac{\alpha_{ult,2} N_{Ed}}{\frac{\chi_z N_{Rk}}{\gamma_{M1}}} + k_{zy} \frac{\alpha_{ult,2}\left(M_{y,Ed} + \Delta M_{y,Ed}\right)}{\frac{\chi_{LT} M_{y,Rk}}{\gamma_{M1}}} = 1 \qquad \text{(VIII.110)}$$

All of the studied uniform members present Class 4 webs in combined bending and compression. Consequently, the interaction factors are:

$$k_{yy} = C_{my}\left(1 + 0.6\frac{\alpha_{ult,1}N_{Ed}}{\chi_y N_{Rk}/\gamma_{M1}} \times \min\left(\bar{\lambda}_y;1\right)\right) \quad \text{(VIII.111)}$$

$$k_{zy} = 1 - \frac{0.05}{\left(C_{mLT} - 0.25\right)}\frac{\alpha_{ult,2}N_{Ed}}{\chi_z N_{Rk}/\gamma_{M1}} \times \min\left(\bar{\lambda}_z;1\right) \quad \text{(VIII.112)}$$

Expression (VIII.112) is that given for members susceptible to lateral-torsional buckling, which are of common use. It is specified that open sections, such as I/H members, are assumed to be susceptible to lateral-torsional buckling when:

$$\bar{\lambda}_{LT} > \bar{\lambda}_{LT,0}\sqrt{1 - \bar{\lambda}_z^2\chi_z} \quad \text{(VIII.113)}$$

with:

$$\bar{\lambda}_{LT,0} = 0.4 \quad \text{(VIII.114)}$$

The load amplifier α_{ult} is obtained following a recursive process, the interaction factors depending on the design load.

The comparison between the numerical and analytical ultimate load amplifiers is presented in Figure VIII-36 where α_{GMNIA} stands for $\alpha_{ult,op,GMNIA}$. All analytical results lie on the safe side with an average deviation close to 15%, results being somewhat scattered.

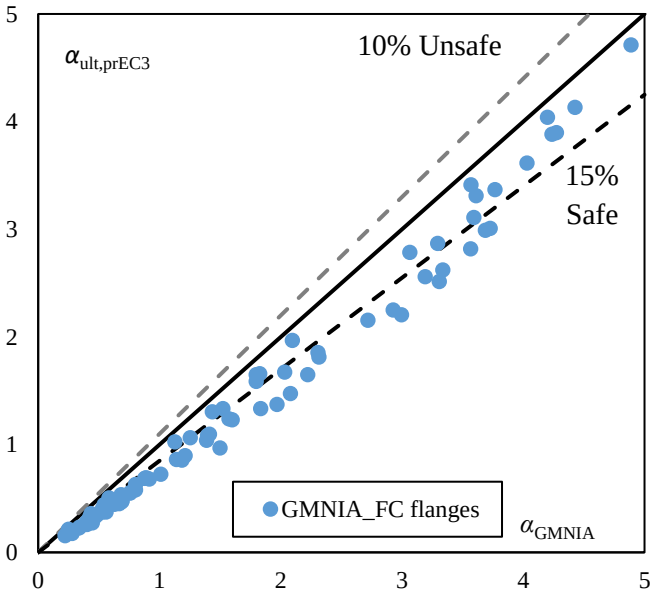

Figure VIII-36: Numerical and prEC3 *– Interaction formulae load amplifiers for uniform doubly symmetric members*

The stability assessment of a member subjected simultaneously to compression force and bending moment depend on its resistance to flexural and lateral-torsional buckling. The current and future *Eurocode 3 Part 1-1* design rules for members subjected to compression force or bending moment

proved satisfactory for welded members made of flame-cut flanges, with a visible safety margin. However, a lack of studies including the computation of partial safety factors for members subjected to compression force and bending moment is noticed. Statistical analyses are conducted instead, as exposed by *ECCS* (2006), *Simões da Silva* (2010, 2016) and *Hadjú* (2022). The procedure detailed in section VIII.2 is indeed hardly applicable for beam-columns as explained by *ECCS* (2006). Consequently, statistical analyses are performed hereafter to assess the safety level of the *prEurocode 3* and proposed design methods. The acceptance criteria set by *Hadjú* (2022) were:

- None of the r_e/r_t values can be more than 15% on the unsafe side;
- No more than 20% of the r_e/r_t values can lie on the unsafe side;
- The average of the r_e/r_t values must be greater than unity.

The first criterion is not deemed sufficiently restrictive for the common engineering practice. It is therefore replaced for the safety assessment of the *prEurocode 3-1-1* interaction formulae with:

- None of the r_e/r_t values can be more than 5% on the unsafe side.

In addition to the average r_e/r_t ratios, their standard deviation is computed. For instance, similar statistical analyses are presented in Table VIII-23 concerning the *Eurocode 3* rule and both *Propositions* for the buckling resistance doubly symmetric members in compression. The number n of results and the number of results on the unsafe side $n_{<1}$ are also given. It is worth reminding that these results are obtained for welded columns made of flame-cut flanges and having a uniform or tapered cross-section. As detailed in section VIII.3, these methods highlighted satisfying safety levels.

Parameter	***prEurocode 3***	***Proposition I***	***Proposition II***
Average	1.203	1.121	1.046
Standard deviation	0.108	0.086	0.039
Min	0.999	0.961	0.959
Max	1.366	1.263	1.157
n	189	189	189
$n_{<1}$	1	19	22

Table VIII-23: Statistical evaluation of prEurocode 3 *and Propositions for flexural buckling*

In line with the corresponding partial safety factors, Table VIII-23 shows that the *prEurocode 3* method for flexural buckling of welded columns made of flame-cut flanges is very conservative, the average result being 20% on the safe side. Besides, the standard deviation is characteristic of scattered results. Both *Propositions* exhibit average results closer to unity with lower values of the standard deviation, especially *Proposition II*. Minimum values of 0.96 are found for both *Propositions* which is acceptable for engineering practice.

The results for the *prEurocode 3* interaction formulae are presented in Table VIII-24. No result is on the unsafe side and the average value is almost 30% on the safe side. Results are very scattered, as shows the standard deviation of 14% while maximum and minimum values are very different, being 1.04 and 1.64, respectively. The stability verification format is overly conservative for welded beam-columns made of flame-cut flanges using the prescriptions from *prEurocode 3*.

Parameter	
Average	1.285
Standard deviation	0.142
Min	1.037
Max	1.637
n	80
$n_{<1}$	0

Table VIII-24: Statistical evaluation of prEC3 *interaction formulae for uniform doubly symmetric members*

The statistical evaluation of the interaction formulae making use of the propositions for columns (see sub-section VIII.3.3) and beams (see sub-sectionVIII.4.3) made of flame-cut flanges is studied in sub-section VIII.5.3.1.

VIII.5.2.2 General Method

As explained in Chapter IV, the overall stability of a non-uniform steel member subjected simultaneously to an axial load N_{Ed} and bending moment $M_{y,Ed}$ can be assessed using the *General Method* from *Eurocode 3* only. The same can be said regarding the revised standard *prEurocode 3*. The *General Method* states that the stability of a member is satisfactory when:

$$\frac{\chi_{op}\alpha_{ult,k}}{\gamma_{M1}} \geq 1.0 \qquad \text{(VIII.115)}$$

where the reduction factor χ_{op} is obtained from the normalized slenderness:

$$\bar{\lambda}_{op} = \sqrt{\frac{\alpha_{ult,k}}{\alpha_{cr,op}}} \qquad \text{(VIII.116)}$$

In the current *Eurocode 3*, the reduction factor can be obtained using either:

- The minimum value between χ_z and χ_{LT} computed for the global normalized slenderness;
- An interpolated value between χ_z and χ_{LT}, therefore rewriting expression (VIII.115) as:

$$\frac{N_{Ed}}{\frac{\chi_z N_{Rk}}{\gamma_{M1}}} + \frac{M_{y,Ed}}{\frac{\chi_{LT} M_{y,Rk}}{\gamma_{M1}}} \leq 1.0 \qquad \text{(VIII.117)}$$

Using expression (VIII.106) for the load amplifier $\alpha_{ult,k}$, expression (VIII.115) can be expressed as:

$$\frac{N_{Ed}}{\frac{\chi_{op} N_{Rk}}{\gamma_{M1}}} + \frac{M_{y,Ed}}{\frac{\chi_{op} M_{y,Rk}}{\gamma_{M1}}} \leq 1.0 \qquad \text{(VIII.118)}$$

Equating expressions (VIII.117) and (VIII.118) yields the following expression for the overall interpolated reduction factor:

$$\chi_{op} = \frac{\Phi + 1}{\frac{\Phi}{\chi_z} + \frac{1}{\chi_{LT}}} \qquad \text{(VIII.119)}$$

with:

$$\Phi = \frac{N_{Ed}}{N_{Rk}} \frac{M_{Rk}}{M_{y,Ed}}$$

In the case of a tapered member, the parameter Φ is computed at the cross-section where $\alpha_{ult,k}$ is minimal.

The interpolation alternative consists in verifying criterion (VIII.115) where the reduction factor is computed using expression (VIII.119). However, as explained in Chapter IV, the upcoming *prEurocode 3* does not maintain the possibility to compute χ_{op} as the interpolation between χ_z and χ_{LT}. The minimum value between both reduction factors must then be used, providing lower reduction factors χ_{op}. The safety assessment of this design method is studied hereafter.

According to both the current and future *Eurocode 3*, the load amplifier $\alpha_{ult,k}$ must be computed accounting for all effects due to in-plane (global and local) geometrical deformation and imperfections. However, to provide a consistent comparison between analytical and numerical results, $\alpha_{ult,k}$ is computed similarly for both sets of results, i.e. neglecting all in-plane effects.

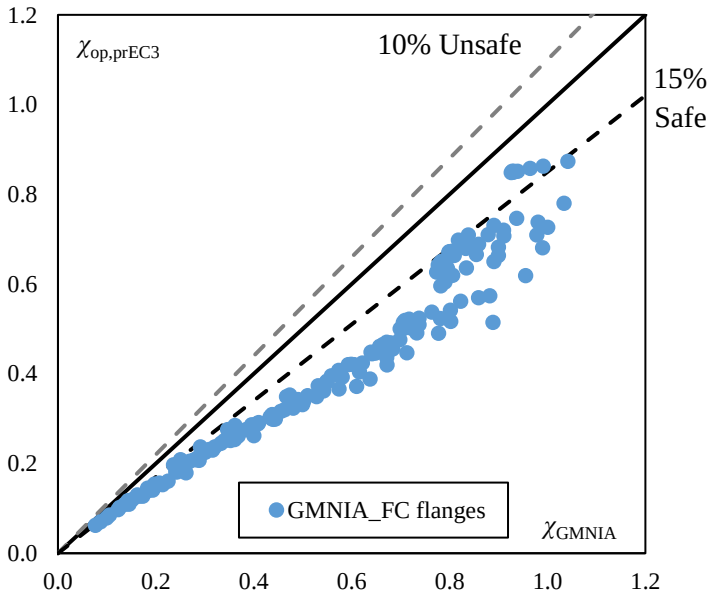

Figure VIII-37: Numerical and prEC3 – General Method *reduction factors for doubly symmetric members*

The comparison between the numerical and analytical reduction factors determined according to the *General Method* from *prEurocode 3* is displayed in Figure VIII-37 for all studied beam-columns. The results lie on the safe side with an average deviation comprised between 25 and 30%.

The results depicted in Figure VIII-37 exhibit an over conservatism of the design method prescribed in *prEurocode 3* for welded members made of flame-cut flanges. Similarly to the interaction formulae, a statistical assessment of the *General Method* is presented in Table VIII-25. The average deviation between the analytical and numerical results is 36% on the safe side. No result is found on the unsafe

side, the minimum r_e / r_t value being 1.09. The *General Method* verification format provides overly conservative results.

Parameter	
Average	1.361
Standard deviation	0.122
Min	1.090
Max	1.727
n	168
$n_{<1}$	0

Table VIII-25: Statistical assessment of the General Method (prEC3) *for doubly symmetric members*

The design method prescribed in *prEurocode3* to assess the stability of uniform, or not, beam-columns is overly conservative in the case of doubly symmetric welded members made of flame-cut flanges. Therefore, better-suited design methods are proposed in sub-section VIII.5.3.2. These include the *Propositions* for flexural buckling (see sub-section VIII.3.3) and lateral-torsional buckling (see sub-section VIII.4.3). A statistical assessment of the proposed design methods is then performed.

VIII.5.3 Propositions for rules adaptations

VIII.5.3.1 Interaction formulae

Interaction formulae are employed for uniform welded beam-columns made of flame-cut flanges using existing guidelines, i.e. expressions (VIII.109) to (VIII.112). An adaptation to flame-cuts is performed when computing the reduction factors for out-of-plane flexural buckling χ_z and lateral-torsional buckling χ_{LT}.

Interaction formulae being applicable for uniform members only, the *Propositions I*, *II* and *III* methods are summarized in Table VIII-26, Table VIII-27 and Table VIII-28. *Proposition I* corresponds to the use of buckling curve *b* for flexural buckling and buckling curve *c* for lateral-torsional buckling.

Buckling mode	**FB**	**LTB**
χ_i	$\frac{1}{\phi_z + \sqrt{\phi_z^2 - \bar{\lambda}_z^2}} \leq 1.0$	$\frac{1}{\phi_{LT} + \sqrt{\phi_{LT}^2 - \bar{\lambda}_{LT}^2}} \leq 1.0$
ϕ_i	$0.5\left[1 + \alpha_z\left(\bar{\lambda}_z - 0.2\right) + \bar{\lambda}_z^2\right]$	$0.5\left[1 + \alpha_{LT}\left(\bar{\lambda}_{LT} - 0.2\right) + \bar{\lambda}_{LT}^2\right]$
α_i	0.34	0.49

Table VIII-26: Proposition I – reduction factors of the proposed design method (Interaction formulae)

The second method to compute the couple of reduction factors is similar to *Proposition I* with key differences lying in the imperfection factors. *Proposition II* makes use of imperfection factors that depend on the member dimensions thus defining specific buckling curves per member for both flexural and lateral-torsional buckling.

Buckling mode	FB	LTB
χ_i	$\frac{1}{\phi_z+\sqrt{\phi_z^2-\bar{\lambda}_z^2}} \le 1.0$	$\frac{1/f}{\phi_{LT}+\sqrt{\phi_{LT}^2-\bar{\lambda}_{LT}^2}} \le 1.0$
ϕ_i	$0.5\left[1+\alpha_z\left(\bar{\lambda}_z-0.2\right)+\bar{\lambda}_z^2\right]$	$0.5\left[1+\alpha_{LT}\left(\bar{\lambda}_{LT}-0.2\right)+\bar{\lambda}_{LT}^2\right]$
α_i	$0.13 \le \frac{0.15}{\bar{\lambda}_z}\sqrt{\frac{h_t}{b}} \le 0.34$	$0.21 \le \frac{0.23}{\bar{\lambda}_{LT}}\sqrt{\frac{h_t}{b}} \le 0.49$

Table VIII-27: Proposition II – reduction factors of the proposed design method (Interaction formulae)

In addition, *Proposition II* makes use of the coefficient f when computing χ_{LT} to account for the bending moment distribution:

$$f = 1 - 0.5\left(1-k_c\right)\left[1-2.0\left(\bar{\lambda}_{LT}-0.8\right)^2\right] \le 1.0 \qquad \text{(VIII.120)}$$

with, in the case of a linear bending moment diagram:

$$k_c = \frac{1}{1.33-0.33\psi} \qquad \text{(VIII.121)}$$

The design methods proposed in Table VIII-26 correspond to those associated with *Proposition I* for flexural buckling (see Eq. (VIII.28)) and lateral-torsional buckling (see Eq. (VIII.49)). On the contrary, the methods proposed in Table VIII-27 rely on those associated with *Proposition II* for columns (see Eq. (VIII.29)) and beams (see Eq. (VIII.55)).

Finally, the last proposed methods to compute the couple of reduction factors is summarized in Table VIII-28. The reduction factor χ_z is similar to that of *Proposition I* while χ_{LT} is determined using the adapted *prEurocode 3* design method (see sub-section VIII.4.3.2).

Buckling mode	FB	LTB
χ_i	$\frac{1}{\phi_z+\sqrt{\phi_z^2-\bar{\lambda}_z^2}} \le 1.0$	$\frac{f_M}{\phi_{LT}+\sqrt{\phi_{LT}^2-f_M\bar{\lambda}_{LT}^2}} \le 1.0$
ϕ_i	$0.5\left[1+\alpha_z\left(\bar{\lambda}_z-0.2\right)+\bar{\lambda}_z^2\right]$	$0.5\left[1+f_M\left(\left(\frac{\bar{\lambda}_{LT}}{\bar{\lambda}_z}\right)^2\alpha_{LT}\left(\bar{\lambda}_z-0.2\right)+\bar{\lambda}_{LT}^2\right)\right]$
α_i	0.34	$0.21\sqrt{\frac{W_{el,y}}{W_{el,z}}} \le 0.49$

Table VIII-28: Proposition III – reduction factors of the proposed design method (Interaction formulae)

where the factor f_M is obtained for a linear bending moment distribution using:

$$f_M = 1.25 - 0.1\psi - 0.15\psi^2 \qquad \text{(VIII.122)}$$

The analytical results obtained using each *Proposition* are compared against the numerical ones in Figure VIII-38. Whatever the method employed to compute the load amplifiers, the analytical results lie on the safe side, the deviation on the unsafe side being up to 1%. Most results present a deviation lower than 15% on the safe side, especially for *Propositions II* and *III*.

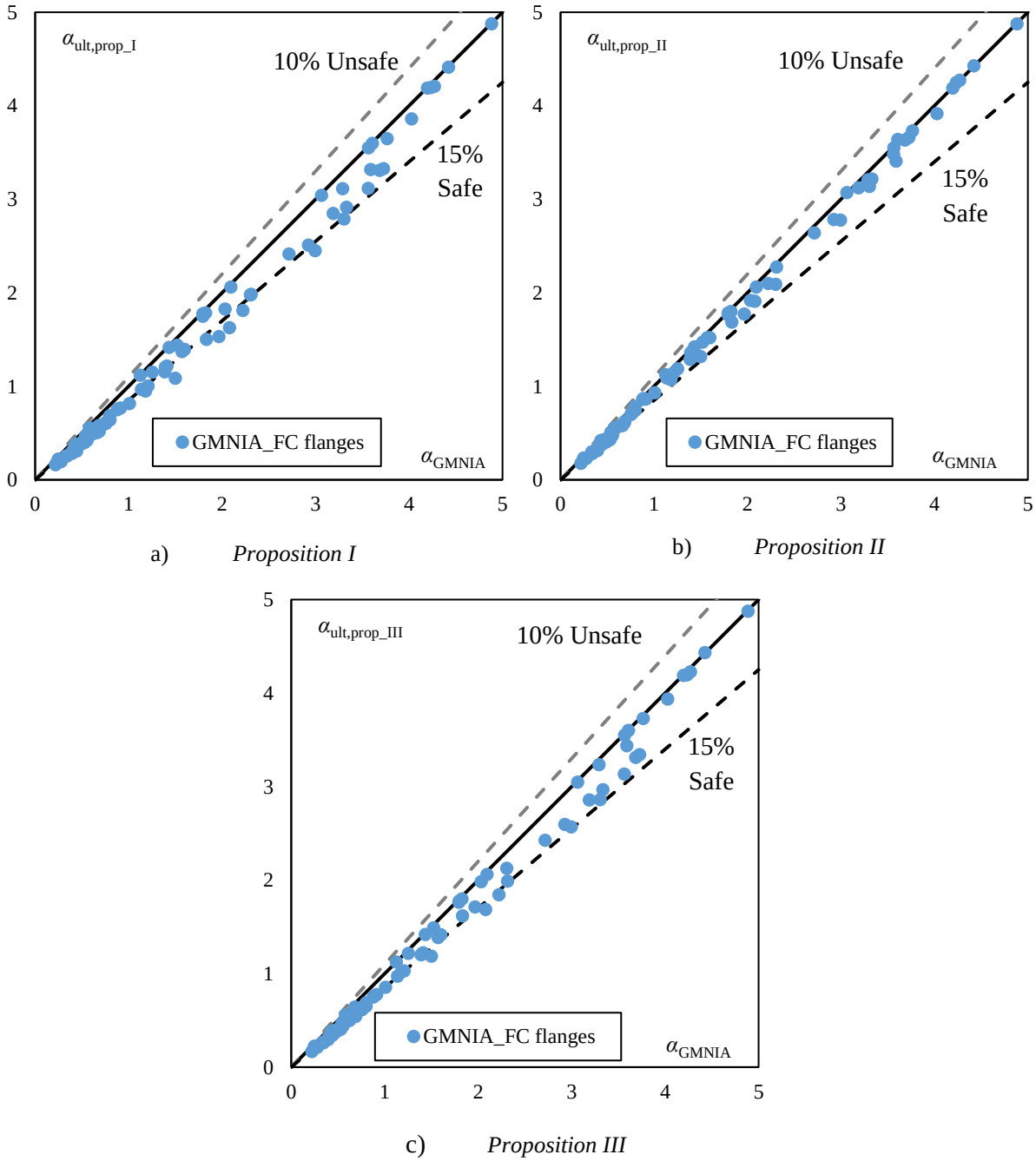

Figure VIII-38: Numerical and proposed ultimate amplifiers for uniform doubly symmetric beam-columns

A statistical evaluation of the results obtained using each of the three *Propositions* is presented in Table VIII-29. The *Proposition I* provides only safe-sided results, with a mean deviation between the numerical and analytical values of 16%. Both *Proposition II* and *III* yield similar results that are more

accurate than those of *Proposition I*. Indeed, average values of the r_e/r_t ratio correspond to a 8% deviation on the safe side with standard deviations of 7 to 8%. Besides, only 3 and 6 results out of 80 are found on the unsafe side with a maximum deviation on the unsafe side of 1%. The statistical evaluations of *Proposition I*, *II* and *III* are satisfactory according to the criteria exposed in sub-section VIII.5.2.1.

Parameter	***Proposition I*** Table VIII-26	***Proposition II*** Table VIII-27	***Proposition III*** Table VIII-28
Average	1.161	1.078	1.082
Standard deviation	0.107	0.068	0.077
Min	1.002	0.992	0.990
Max	1.409	1.273	1.287
n	80	80	80
$n_{<1}$	0	3	6

Table VIII-29: Statistical evaluation of the proposed design methods for uniform beam-columns

Consequently, the *prEurocode 3* interaction formulae may be applied for welded members made of flame-cut flanges using either of the three *Propositions* corresponding to those made to compute the flexural and the lateral-torsional buckling resistances.

VIII.5.3.2 General Method

The current *General Method* from *Eurocode 3 Part 1-1* is improved to provide better-suited results. Similarly to that from the code, the proposed method requires the following condition to be satisfied:

$$\frac{\alpha_{\text{ult, op}}}{\gamma_{\text{M1}}} = \frac{\chi_{\text{op}}\alpha_{\text{ult, k}}}{\gamma_{\text{M1}}} \geq 1.0 \qquad \text{(VIII.123)}$$

where the reduction factor is obtained using an interpolated value between both reduction factors for flexural and lateral-torsional buckling (determined for the global normalized slenderness), i.e.:

$$\chi_{\text{op}} = \frac{\phi + 1}{\frac{\phi}{\chi_{\text{z}}} + \frac{1}{\chi_{\text{LT}}}} \qquad \text{(VIII.124)}$$

Three alternatives methods are proposed to compute the couples of reduction factors for flexural buckling χ_z and lateral-torsional buckling χ_{LT}. In the case of tapered beam-columns, the reduction factors are computed using the geometrical properties of the cross-section located at x_α where $\alpha_{ult,k}$ is minimal. The *Propositions* are summarised in Table VIII-30, Table VIII-31 and Table VIII-32.

Buckling mode	FB	LTB
χ_i	$\frac{1}{\phi_z + \sqrt{\phi_z^2 - \overline{\lambda}_{op}^2}} \le 1.0$	$\frac{1}{\phi_{LT} + \sqrt{\phi_{LT}^2 - \overline{\lambda}_{op}^2}} \le 1.0$
ϕ_i	$0.5\left[1 + \alpha_z\left(\overline{\lambda}_{op} - 0.2\right) + \overline{\lambda}_{op}^2\right]$	$0.5\left[1 + \alpha_{LT}\left(\overline{\lambda}_{op} - 0.2\right) + \overline{\lambda}_{op}^2\right]$
α_i	0.34	0.49

Table VIII-30: Proposition I – reduction factors of the proposed design method (General Method)

Proposition I, similarly to Table VIII-26, corresponds to the use of a more favourable buckling curve for both flexural and lateral-torsional buckling.

Likewise, Table VIII-27 and Table VIII-31 contain similar methods. In both cases, a buckling curve per member is defined for flexural buckling and for lateral-torsional buckling. Imperfection factors are similar in both tables except for the term accounting for the tapering of the member.

Buckling mode	FB	LTB
χ_i	$\frac{1}{\phi_z + \sqrt{\phi_z^2 - \overline{\lambda}_{op}^2}} \le 1.0$	$\frac{1/f}{\phi_{LT} + \sqrt{\phi_{LT}^2 - \overline{\lambda}_{op}^2}} \le 1.0$
ϕ_i	$0.5\left[1 + \alpha_z\left(\overline{\lambda}_{op} - 0.2\right) + \overline{\lambda}_{op}^2\right]$	$0.5\left[1 + \alpha_{LT}\left(\overline{\lambda}_{op} - 0.2\right) + \overline{\lambda}_{op}^2\right]$
α_i	$0.13 \le \frac{0.15}{\overline{\lambda}_{op}}\sqrt{\frac{h_t}{b}} \le 0.34$	$0.21 \le \frac{0.23 + 0.10\gamma}{\overline{\lambda}_{op}}\sqrt{\frac{h_t}{b}} \le 0.49$

Table VIII-31: Proposition II – reduction factors of the proposed design method (General Method)

Besides, expression (VIII.121) of the correction factor in the case of a linear bending moment distribution is adapted for tapered members. Indeed, ψ is replaced with the ratio ψ_ε between the bending moment utilization at both ends:

$$\psi_\varepsilon = \min\left[\frac{M_{y,Ed}/M_{y,Rk}(x=0)}{\psi M_{y,Ed}/M_{y,Rk}(x=L)}; \frac{\psi M_{y,Ed}/M_{y,Rk}(x=L)}{M_{y,Ed}/M_{y,Rk}(x=0)}\right] \qquad \text{(VIII.125)}$$

Finally, *Proposition III* methods from Table VIII-28 and Table VIII-32 are also analogous. In both cases, the reduction factors are obtained using *prEurocode 3* rules with imperfection factors accounting for the beneficial effects of flame-cuts.

Buckling mode	FB	LTB
χ_i	$\frac{1}{\phi_z + \sqrt{\phi_z^2 - \bar{\lambda}_{op}^2}} \le 1.0$	$\frac{f_{M,\varepsilon}}{\phi_{LT} + \sqrt{\phi_{LT}^2 - f_{M,\varepsilon}\bar{\lambda}_{op}^2}} \le 1.0$
ϕ	$0.5\left[1 + \alpha_z\left(\bar{\lambda}_{op} - 0.2\right) + \bar{\lambda}_{op}^2\right]$	$0.5\left[1 + f_{M,\varepsilon}\left(\left(\frac{\bar{\lambda}_{op}}{\bar{\lambda}_z}\right)^2 \alpha_{LT}\left(\bar{\lambda}_z - 0.2\right)\xi + \bar{\lambda}_{op}^2\right)\right]$
α_i	0.34	$0.21\sqrt{\frac{W_{el,y}}{W_{el,z}}} \le 0.49 + 0.15\gamma$

Table VIII-32: Proposition III – reduction factors of the proposed design method (General Method)

Similarly to the case of *Proposition II*, f_M (see Eq. (VIII.122)) is replaced with $f_{M,\varepsilon}$ for tapered members:

$$f_{M,\varepsilon} = 1.25 - 0.1\psi_\varepsilon - 0.15\psi_\varepsilon^2 \qquad \text{(VIII.126)}$$

The comparison between numerical and analytical reduction factors is presented in Figure VIII-39. The results obtained for *Propositions I* and *III* lie on the safe side whatever the slenderness with a mean deviation lower than 10%. The scatter is low in both cases though some results are very conservative, especially for *Proposition I* where the maximum deviation from the numerical results is almost 30%. *Proposition II* yields very good results, most of them lying between 0 and 15% on the safe side.

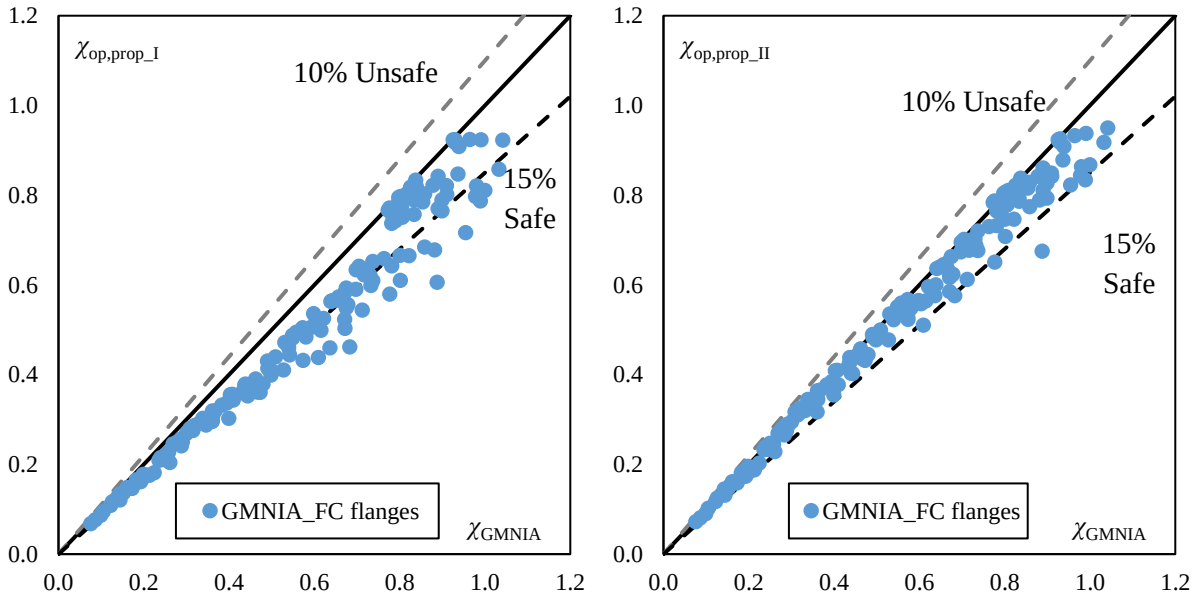

a) *Proposition I* b) *Proposition II*

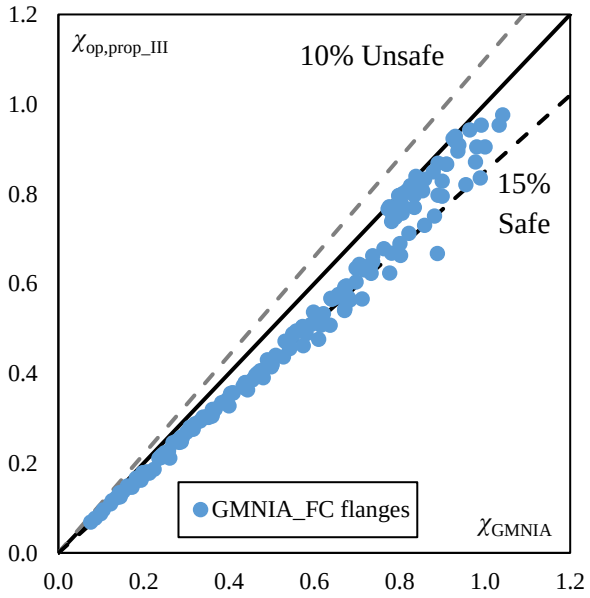

c) *Proposition III*

Figure VIII-39: Numerical and proposed reduction factors for doubly symmetric beam-columns

The statistical assessment of the three *Propositions* is presented in Table VIII-33. *Proposition I* produces only safe-sided results with an average deviation from the numerical results of 14%. The mean deviation between analytical and numerical results is lower with *Proposition II* or *III* being 6 and 8%, respectively. Both *Propositions II* and *III* provide more accurate analytical predictions than *Proposition I* though 17 and 9 results, respectively, out of 168 are not safe-sided. The maximum deviations on the unsafe side are then only 3 and 2% for *Propositions II* and *III*, respectively. According to the criteria set in sub-section VIII.5.2.1, either of the three *Propositions* may be used to assess the stability of a welded beam-column made of flame-cut flanges.

Parameter	***Proposition I*** Table VIII-30	***Proposition II*** Table VIII-31	***Proposition III*** Table VIII-32
Average	1.138	1.056	1.077
Standard deviation	0.076	0.056	0.065
Min	1.000	0.974	0.982
Max	1.391	1.337	1.342
n	168	168	168
$n_{<1}$	0	17	9

Table VIII-33: Statistical evaluation of the proposed design methods for beam-columns

In the last section, a summary of all the design methods proposed in the present chapter is given. They permit to assess the stability of welded members made of flame-cut flanges against flexural and/or lateral-torsional buckling. The accuracy and safety level of these proposed methods having proven satisfactory.

VIII.6 Summary of the propositions

VIII.6.1 Flexural buckling of columns

Firstly, flexural buckling of doubly symmetric columns pinned at both ends was investigated in the case of a constant axial load distribution. According to the proposed design methods, the stability of a uniform or tapered column is satisfactory provided that:

$$\frac{N_{\mathrm{Ed}}(x_\alpha)}{N_{\mathrm{b,Rd}}(x_\alpha)} \leq 1.0 \tag{VIII.127}$$

where x_α is the location of the critical cross-section, i.e. where $\alpha_{\mathrm{ult,k}}$ is minimal. This amplifier of the design loads to reach the characteristic resistance of each cross-section is computed neglecting all in-plane effects. In the general case of a member simultaneously subjected to bending about *y-y* and compression, $\alpha_{\mathrm{ult,k}}$ is obtained using:

$$\alpha_{\mathrm{ult,k}}(x) = \frac{1}{\frac{N_{\mathrm{Ed}}}{N_{\mathrm{Rk}}}(x) + \frac{M_{\mathrm{y,Ed}}}{M_{\mathrm{Rk}}}(x)} \tag{VIII.128}$$

The member resistance to compression $N_{\mathrm{b,Rd}}$ with regards to out-of-plane flexural buckling can be obtained using:

$$N_{\mathrm{b,Rd}} = \chi_{\mathrm{z}} \frac{N_{\mathrm{Rk}}}{\gamma_{\mathrm{M1}}} \tag{VIII.129}$$

where the reduction factor χ_{z} is:

$$\chi_{\mathrm{z}} = \frac{1}{\phi_{\mathrm{z}} + \sqrt{\phi_{\mathrm{z}}^2 - \bar{\lambda}_{\mathrm{z}}^2}} \leq 1.0 \tag{VIII.130}$$

$$\phi_{\mathrm{z}} = 0.5\left[1 + \alpha_{\mathrm{z}}\left(\bar{\lambda}_{\mathrm{z}} - 0.2\right) + \bar{\lambda}_{\mathrm{z}}^2\right] \tag{VIII.131}$$

where $\bar{\lambda}_{\mathrm{z}} = \sqrt{N_{\mathrm{Rk}} / N_{\mathrm{cr,z}}}$ is the normalized slenderness for flexural buckling.

Two expressions are proposed for the imperfection factors α_{z} which are depicted in Table VIII-34. They correspond to either a more favourable buckling curve, or a buckling curve defined per member.

Proposition	α_z	α_{LT}
I	0.34	0.49
II	$0.13 \le \frac{0.15}{\bar{\lambda}_z}\sqrt{\frac{h_t}{b}} \le 0.34$	$0.21 \le \frac{0.23+0.10\gamma}{\bar{\lambda}_{LT}}\sqrt{\frac{h_t}{b_{min}}} \le 0.49$
III	No 3rd proposition	$0.21\sqrt{\frac{W_{el,y}}{W_{el,z}}} \le 0.49+0.15\gamma$

Table VIII-34: Imperfection factors of the proposed design method

These propositions were developed within the framework of the parametric study depicted in section VII.5.2. Uniform or tapered doubly symmetric columns made of S275 or S355 steel were studied under a constant axial load. The studied dimensions are reminded in Table VIII-35.

$h_{w,max}$ (mm)	$h_{w,max}/h_{w,min}$	t_w (mm)	b (mm)	t_f (mm)	b/t_f
300 to 1000	1 to 3	5 to 10	170 to 350	12 to 40	7.5 to 20.8

Table VIII-35: Dimensions of the studied columns with flame-cut flanges assessing the Propositions *safety levels*

VIII.6.2 Lateral-torsional buckling of beams

Then, lateral-torsional buckling of doubly and mono-symmetric beams resting on fork supports at both ends was studied under a linear bending moment distribution. Distinct design methods have been proposed, either based on the *General case* from *Eurocode 3* (*Propositions I* and *II*) or on the new verification format from *prEurocode 3* (*Proposition III*). According to all proposed methods, the stability of a uniform or tapered beam is satisfactory when:

$$\frac{M_{y,Ed}(x_\alpha)}{M_{b,Rd}(x_\alpha)} \le 1.0 \qquad \text{(VIII.132)}$$

where the member resistance to bending $M_{y,b,Rd}$ is obtained using:

$$M_{b,Rd} = \chi_{LT}\frac{M_{y,Rk}}{\gamma_{M1}} \qquad \text{(VIII.133)}$$

The reduction factor χ_{LT} is obtained according to *Proposition I* using:

$$\chi_{LT} = \frac{1}{\phi_{LT}+\sqrt{\phi_{LT}^2-\bar{\lambda}_{LT}^2}} \le 1.0 \qquad \text{(VIII.134)}$$

$$\phi_{LT} = 0.5\left[1+\alpha_{LT}\left(\bar{\lambda}_{LT}-0.2\right)+\bar{\lambda}_{LT}^2\right] \qquad \text{(VIII.135)}$$

where $\bar{\lambda}_{LT} = \sqrt{M_{y,Rk}/M_{y,cr}}$ is the normalized slenderness for lateral-torsional buckling.

The *Proposition I* imperfection factor α_{LT} is given in Table VIII-34.

Proposition II diverges from *Proposition I* within the expression of the reduction factor:

$$\chi_{\mathrm{LT}} = \frac{1/\mathrm{f}}{\phi_{\mathrm{LT}} + \sqrt{\phi_{\mathrm{LT}}^2 - \overline{\lambda}_{\mathrm{LT}}^2}} \leq 1.0 \qquad \text{(VIII.136)}$$

where ϕ_{LT} is obtained using equation (VIII.135) with the imperfection factor presented in the second line of Table VIII-34 and:

$$\mathrm{f} = 1 - 0.5\left(1 - k_{\mathrm{c}}\right)\left[1 - 2.0\left(\overline{\lambda}_{\mathrm{LT}} - 0.8\right)^2\right] \leq 1.0 \qquad \text{(VIII.137)}$$

where in the case of a linear bending moment distribution:

$$k_{\mathrm{c}} = \frac{1}{1.33 - 0.33\psi_{\varepsilon}} \qquad \text{(VIII.138)}$$

The ratio ψ_{ε} between the bending moment utilization at both ends is:

$$\psi_{\varepsilon} = \min\left[\frac{M_{\mathrm{y,Ed}} \big/ M_{\mathrm{y,Rk}}(x=0)}{\psi M_{\mathrm{y,Ed}} \big/ M_{\mathrm{y,Rk}}(x=L)}; \frac{\psi M_{\mathrm{y,Ed}} \big/ M_{\mathrm{y,Rk}}(x=L)}{M_{\mathrm{y,Ed}} \big/ M_{\mathrm{y,Rk}}(x=0)}\right] \qquad \text{(VIII.139)}$$

As an alternative to expressions (VIII.134) to (VIII.138), one may compute the reduction factor for lateral-torsional buckling using *Proposition III*:

$$\chi_{\mathrm{LT}} = \frac{f_{\mathrm{M},\varepsilon}}{\phi_{\mathrm{LT}} + \sqrt{\phi_{\mathrm{LT}}^2 - f_{\mathrm{M},\varepsilon}\overline{\lambda}_{\mathrm{LT}}^2}} \leq 1.0 \qquad \text{(VIII.140)}$$

$$\phi_{\mathrm{LT}} = 0.5\left[1 + f_{\mathrm{M},\varepsilon}\left(\left(\frac{\overline{\lambda}_{\mathrm{LT}}}{\overline{\lambda}_{\mathrm{z}}}\right)^2 \alpha_{\mathrm{LT}}\left(\overline{\lambda}_{\mathrm{z}} - 0.2\right)\xi + \overline{\lambda}_{\mathrm{LT}}^2\right)\right] \qquad \text{(VIII.141)}$$

where, in the case of a linear bending moment distribution:

$$f_{\mathrm{M},\varepsilon} = 1.25 - 0.1\psi_{\varepsilon} - 0.15\psi_{\varepsilon}^2 \qquad \text{(VIII.142)}$$

Expression (VIII.141) makes use of the parameter ξ that is equal to unity in the specific case of a uniform and doubly symmetric beam. In the more general case of a tapered mono-symmetric beam, ξ is given by:

$$\xi = \frac{\dfrac{M_{\mathrm{y,cr}}}{N_{\mathrm{cr,z}}} + \dfrac{h_{\mathrm{s,max}}}{2} f(\gamma)}{\dfrac{M_{\mathrm{y,cr}}}{N_{\mathrm{cr,z}}} + h_{\mathrm{s,max}} \dfrac{I_{\mathrm{z,ft}}}{I_{\mathrm{z}}} \overline{h}(x_{\mathrm{z}})} \qquad \text{(VIII.143)}$$

with:

$$f(\gamma) = \left(1 - 0.5\gamma + 0.29\gamma^2\right)\cos\left(0.29\gamma\pi\right) + \frac{2\gamma}{\pi}\sin\left(0.29\gamma\pi\right) \quad \text{(VIII.144)}$$

$$\bar{h}(x_z) = 1 - 0.5\gamma + \frac{0.146\gamma}{K} \quad \text{(VIII.145)}$$

$$\gamma = 1 - \frac{h_{s,min}}{h_{s,max}} \quad \text{(VIII.146)}$$

with:

$$K = \frac{1}{\gamma}\left[\frac{M_{y,cr} I_z}{N_{cr,z} I_{z,ft} h_{s,max}} + 1\right]$$

The imperfection factor α_{LT} associated with this design method is presented in the last line of Table VIII-34.

Again, these improved design methods were developed within the framework of the parametric study depicted in section VII.5.3. Uniform or tapered beams, having a doubly or mono-symmetrical cross-sections were investigated. These members, made of S275 or S355 steel studied under a linear bending moment distribution with a ratio between end moments varying between -1 and 1. The studied dimensions are reminded in Table VIII-36.

$h_{w,max}$ (mm)	$h_{w,max}/h_{w,min}$	t_w (mm)	b (mm)	t_f (mm)	b/t_f	b_c/b_t	$t_{f,c}/t_{f,t}$
300 to 1000	1 to 3.3	5 to 10	170 to 350	12 to 30	8 to 20.8	0.57 to 1.75	0.5 to 2

Table VIII-36: Dimensions of the studied beams with flame-cut flanges assessing the Propositions *safety levels*

VIII.6.3 Out-of-plane buckling of beam-columns

Eventually, the stability of doubly symmetric beam-columns resting on fork supports at both ends was explored, again under a linear bending moment distribution. To assess the stability of uniform or tapered members, the proposed design method adapted from the *General Method* requires the following criterion to be verified:

$$\frac{\alpha_{ult,op}}{\gamma_{M1}} = \frac{\chi_{op}\alpha_{ult,k}}{\gamma_{M1}} \geq 1.0 \quad \text{(VIII.147)}$$

where the imperfection factor χ_{op} is obtained using χ_z and χ_{LT} determined for the global normalized slenderness:

$$\bar{\lambda}_{op} = \sqrt{\frac{\alpha_{ult,k}}{\alpha_{cr,op}}} \quad \text{(VIII.148)}$$

The imperfection factor χ_{op} results from an interpolation between χ_z and χ_{LT} determined using:

$$\chi_{op} = \frac{\Phi + 1}{\frac{\Phi}{\chi_z} + \frac{1}{\chi_{LT}}} \qquad \text{(VIII.149)}$$

with:

$$\Phi = \frac{N_{Ed}}{N_{Rk}} \frac{M_{Rk}}{M_{y,Ed}}$$

The couples of reduction factors for flexural χ_z and lateral-torsional buckling χ_{LT} should be computed making use of the global out-of-plane normalized slenderness and using either:

- The *Proposition I* design methods for both flexural and lateral-torsional buckling (see 1st line of Table VIII-34);
- The *Proposition II* design methods for both flexural and lateral-torsional buckling (see 2nd line of Table VIII-34);
- The *Proposition III* design method for lateral-torsional buckling and the *Proposition I* design method for flexural buckling (see 3rd and 1st lines of Table VIII-34).

The stability of uniform doubly symmetric beam-columns can alternatively be assessed using the well known interaction formulae:

$$\frac{N_{Ed}}{\frac{\chi_y N_{Rk}}{\gamma_{M1}}} + k_{yy} \frac{M_{y,Ed} + \Delta M_{y,Ed}}{\frac{\chi_{LT} M_{y,Rk}}{\gamma_{M1}}} \leq 1 \qquad \text{(VIII.150)}$$

$$\frac{N_{Ed}}{\frac{\chi_z N_{Rk}}{\gamma_{M1}}} + k_{zy} \frac{M_{y,Ed} + \Delta M_{y,Ed}}{\frac{\chi_{LT} M_{y,Rk}}{\gamma_{M1}}} \leq 1 \qquad \text{(VIII.151)}$$

where the interaction factors k_{yy} and k_{zy} may be determined following the prescriptions of *prEurocode 3 Part 1-1*.

Again, the interaction formulae should be computed making use for χ_z and χ_{LT} of either:

- The *Proposition I* design methods for both flexural and lateral-torsional buckling (see 1st line of Table VIII-34);
- The *Proposition II* design methods for both flexural and lateral-torsional buckling (see 2nd line of Table VIII-34);
- The *Proposition III* design method for lateral-torsional buckling and the *Proposition I* design method for flexural buckling (see 3rd and 1st lines of Table VIII-34).

The three *Propositions* were developed within the framework of the parametric study depicted in section VII.5.4. Uniform or tapered doubly symmetrical members were studied under a constant axial load. A linear bending moment was also applied with a ratio between end moments comprised between 0 and 1. The studied dimensions of the S 355 members are reminded in Table VIII-37.

$h_{w,max}$ (mm)	$h_{w,max}/h_{w,min}$	t_w (mm)	b (mm)	t_f (mm)	b/t_f
438 to 1000	1 to 3.2	5 to 10	200 to 350	12 to 25	8 to 19.2

Table VIII-37: Dimensions of the studied beam-columns with flame-cut flanges assessing the Propositions *safety levels*

The stability of welded building members have been extensively investigated in the present work. Numerous results of GMNIA computations have been employed to estimate the accuracy and safety levels of the current European design standard. The current (and future) design methods proving overly conservative for welded members made of flame-cut flanges, new design methods have been proposed. They provide expressions to determine the overall buckling resistance of a welded member made of flame-cut flanges subjected to compression and/or bending. The partial safety factors γ_{M1} corresponding to these methods were determined using the procedure from *Annex D of Eurocode 0* along with the prescriptions of the *SAFEBRICTILE* project. The safety assessment being satisfactory, the proposed design methods are associated with $\gamma_{M1} = 1.0$.

IX. *Conclusions*

IX.1 Summary

The present work investigated the stability of welded I-section steel members. The main objective was to develop analytical approaches resulting in more economical welded members than the existing ones. Improvements were sought both for critical and ultimate loads when compared to existing formulations, especially *Eurocode 3 Part 1-1*. Consequently, this dissertation was organised in two major parts, Part I dealt with elastic buckling while Part II covered elasto-plastic buckling.

In Chapter II, well-known analytical expressions for the elastic critical loads of uniform members under compression or bending were introduced. These expressions were obtained using the energy method applied in the case of a constant axial load or bending moment distribution. Existing analytical approaches were exposed for the critical bending moment of a uniform beam having a mono-symmetric cross-section. The comparison against finite element results has yielded a recommended analytical model, mostly based on the prescriptions of *Eurocode 9 Part 1-1*. However, for mono-symmetric beams fixed at both ends and subjected to a pointwise transverse load applied at mid span outside the shear centre, the numerical analyses exhibited important shortcomings. Owing to overestimate values of the critical bending moment, the use of current analytical model is not recommended. Instead, one should employ finite element analyses to compute the critical bending moment in this case. Similarly, no simple and accurate analytical model exist to determine the critical load (amplifier) of non-uniform and/or beam-column members other than in simple cases. Elastic critical buckling should then be studied by means of finite element analyses.

Chapter II then discusses elastic lateral-distortional buckling (LDB) of doubly symmetric beams. This buckling mode includes web distortion that can correspond to single or double curvature. Various existing analytical approaches were presented, all of them being developed in the case of a constant bending moment distribution where web distortion occurs in double curvature. The use of appropriate displacement and rotation fields along with the energy method yielded very good agreement with numerical results. Other accurate predictions were encountered when equivalent torsional and warping stiffness are employed. The use of a reduction coefficient multiplying the critical bending moment provides acceptable results for only one of the studied approaches. Based on an adequate expression for the critical bending moment, a boundary between LTB and LDB is exposed, validated by numerical results. In the case of a linear bending moment distribution, the web distortion mode depends on the ratio ψ between end moments. The most accurate existing formulations can be extended to a linear bending moment distribution for high values of ψ, corresponding to web distortion in double curvature. However, for lower values of ψ, i.e. web distortion in single curvature, none of the analytical approaches revealed satisfactory, being unsafe.

The following Chapter III presents the elastic buckling behaviour of uniform doubly symmetric beams with warping restraints at both ends. Using appropriate displacement and rotation fields, the energy method was again employed. Expressions for the critical bending moment were obtained for a constant and linear bending moment distribution and in the case of a pointwise force applied at mid-span or uniformly distributed loading. The presence of warping supports affects both the equivalent uniform moment factor C_1 and the warping effective length factor k_w. The predictions of the derived analytical

model showed a good agreement with the numerical results obtained using either beam or shell finite elements.

In addition, warping restraints have a major influence on the critical bending moment. Indeed, when compared to free warping at both ends, the critical bending moment can be multiplied by a factor greater than 2 when warping is fully prevented at both ends. The warping stiffness of some common connection configurations are reminded based on existing formulations, while that of a fixed column base is derived. Accordingly, a limit value of the warping stiffness c_w as computed above which the critical bending moment may be computed assuming warping as fully restrained at the beam ends. Numerical analyses have yielded the possibility to adapt this criterion to members with warping fully restrained at a single end.

Part II began with Chapter IV introducing the design rules prescribed by the current and revised *Eurocode 3 Part 1-1*. Specifications of the *French National Annex* were developed, showing adaptations of some *Eurocode 3* methods to compute the resistance of a member subjected to bending. The only design method from *Eurocode 3* adapted to non-uniform member being open to discussion, recent analytical developments on non-uniform members were developed. Despite solid mechanical backgrounds, the presented methods are easily applicable in simple case while for complex boundary condition, some exhibit a lack of guidance. Besides, no existing proposition explicitly accounts for the flange fabrication process.

Thus, Chapter V focused of the residual stresses distributions in welded members. Very distinct patterns exist for members with hot-rolled or with flame-cut flanges. Residual stresses obtained for flame-cut flanges exhibit tensile stresses at the flanges tips while members involving hot-rolled flanges present compressive stresses. The distribution in members with flame-cut flanges is more favourable, initial tensile stresses delaying the early yielding of the flanges tips. A literature review showed distinct residual stress model for welded members made of flame-cut flanges, an original experimental programme was therefore led.

The residual stresses distributions were measured at the University of Liège in eight specimens having cross-sectional dimensions corresponding to the common practice of steel building members. The impact of the flange fabrication process, flanges width and thickness was studied. While the model from *prEurocode 3 Part 1-14* revealed a good fit for the distributions measured in welded members with hot-rolled flange, those measured in the members with flame-cut flanges showed discrepancies with existing models. Therefore, a new residual stress model was developed for welded members made of flame-cuts. The width and magnitude of the stress units of this model depend on the flange height-to-width ratio b/t_f and on the cross-section height-to-width ratio h_t/b.

In Chapter VI, the experimental buckling behaviour of members subjected to compression and/or bending is developed. Past experimental programmes were described, a scarcity of experimental data regarding mono-symmetric or non-uniform welded members made of flame-cut flanges arising. An original experimental programme was therefore developed at Polytech' Clermont, investigating the lateral-torsional buckling behaviour of four welded beams presenting flame-cut flanges. Two specimens were tapered and two uniform, with a doubly and a mono-symmetric cross-section for each type of specimen. All specimens failed in a lateral-torsional buckling mode, while web distortion was noticed post-peak for the uniform beam with a mono-symmetric cross-section. The experimental failure was found in between elastic and elasto-plastic range for three specimens, specimen *U-DS* failing in the elastic range. When compared to these experimental results, the predictions of the current *Eurocode 3* design rules revealed overly conservative. The difference diminishes when using the new verification format from *prEurocode 3* but some of the deviation can be attributed to the flanges fabrication process.

The experimental results were used to develop a numerical model in Chapter VII. Numerical and experimental results showed in good agreement, validating the developed numerical model. Sensitivity analyses were performed, exhibiting the major influence of the residual stress model on the resistance of welded members, especially in the low and intermediate slenderness range. Indeed, replacing the measured residual stresses distributions with the model for welded members made of hot-rolled flanges in the numerical analyses produced 14% lower ultimate load bearing capacities.

The numerical model was developed in the general case of welded steel members resting on fork supports at both ends and subjected to bending and/or compression. The residual stress model developed in Chapter V was used for welded members made of flame-cut flanges while that prescribed by *prEurocode 3 Part 1-14* was employed for members with hot-rolled flanges. A large number of numerical analyses were then performed for members representative of the current practice of steel structures subjected to compression and/or bending. The web height varied between 300 and 1000 mm while the flanges width ranged between 170 and 350 mm, the studied members being made of S275 or S355 steel.

The results of this parametric study were exploited in Chapter VIII where resistance models adapted from the *Eurocode 3* design rules were developed with imperfection factors better suited to flame-cut flanges. Partial safety factors were determined according to the prescriptions of *Eurocode 0* and the recommendations of the *SAFEBRICTILE* project, validating the analytical approaches. Two propositions were made for out-of-plane flexural buckling, one consisting in the use of buckling curve *b* while the other relies on an imperfection factor inversely proportional to the slenderness and depending on h_t/b.

Similar propositions were developed concerning the lateral-torsional buckling of uniform or tapered beams having a doubly or mono-symmetric cross-section. Indeed, the use of buckling curve *c* was proposed, along with an imperfection factor depending on the member dimensions and on the bending moment diagram. The latter approach makes use of the coefficient *f* which accounts for the bending moment distribution. An adaptation of the new verification format from *prEN 1993-1-1* was also derived to broaden the scope of this method to tapered beams having a mono-symmetric cross-section. An improved imperfection factor better suited to flame-cuts was proposed.

For welded members made of flame-cut flanges subjected to axial force and bending moment, a design method adapted from the current *General Method* of the current *Eurocode 3 Part 1-1* has been proposed. This method makes use of a load amplifier $\alpha_{ult,k}$ that neglects the in-plane effects and a reduction factor interpolated between those obtained for flexural and for lateral-torsional buckling. The reduction factors previously proposed for both buckling modes can be combined. The *prEurocode 3* interaction formulae may also be adapted to flame-cut flanges making use of the proposed modifications for the flexural and lateral-torsional buckling reduction factors. The safety levels prove satisfying, validating the analytical approaches.

IX.2 Original contributions

The major original contributions developed in the present work are:

Elastic critical buckling loads:

- A recommended analytical model for the determination of the critical bending moment for LTB of uniform mono-symmetric beams. This recommendation is based on the comparison to numerical results of existing formulations.
- A recommended expression to compute the critical bending moment for lateral-distortional buckling in the case of a constant bending moment distribution, along with a boundary between LTB and LDB. Again, the proposition results from the comparison of existing models against numerical results.

Elastic buckling of beams with warping restraints:

- For uniform doubly symmetric beams with warping restraints at both ends:
  - Theoretical solutions for the elastic critical bending moment based on the energy method in various load cases;
  - A unique closed form expression of the warping coefficient k_w;
  - Closed form and approximate expressions for the equivalent uniform moment factor C_1 using the formalism of the *French National Annex* being the product of:
    - A factor depending on the bending moment distribution only, and
    - A factor depending on the stiffness of the warping restraints only.
  - A limit value of the stiffness of the warping restraints between semi-rigid and rigid joints.
- An analytical expression for warping stiffness of fixed columns. A limit between semi-rigid and rigid joints in the case of a warping restraint at a single end has also been proposed using numerical results.

Residual stresses:

- Experimental residual stresses distributions in welded members made of either hot-rolled or flame-cut flanges. These results, along with experimental distributions from the literature yielded a new residual stress model for welded members made of flame-cut flanges.

Experimental buckling behaviour

- The description of a novel experimental programme that included lateral-torsional buckling tests on 4 welded beams made of flame-cut flanges. The studied beams were uniform or tapered and presented either a doubly or a mono-symmetric cross-section.
- Numerical sensitivity analyses that showed the significant impact of the flange fabrication process on the out-of-plane buckling resistance of a welded member.

Analytical elasto-plastic resistances

- Original analytical expressions to determine the resistance of uniform or tapered doubly symmetric welded columns made of flame-cut flanges against out-of-plane flexural buckling. A proposal makes use of an improved buckling curve when compared to the current and future *Eurocode 3*. The second proposal corresponds to the use of a specific buckling curve per member. Both propositions are validated against appropriate partial safety factors.

- Original analytical expressions to determine the resistance of uniform or tapered welded beams with a doubly or mono-symmetric cross-section made of flame-cut flanges against lateral-torsional buckling. Again, a proposal uses an improved buckling curve when compared to the current and future *Eurocode 3*. A second proposal corresponds to the use of a specific buckling curve per member. The latter proposition includes a factor accounting for the bending moment distribution. Both propositions are associated with satisfactory partial safety factors.
- Analytical derivations widening the scope of the new design method from *prEurocode 3* that provides lateral-torsional buckling resistance of uniform doubly symmetric beams. The analytical developments yielded guidance to employ this method for mono-symmetric tapered beams. An imperfection factor adapted to welded members made of flame-cut flanges is proposed. The resulting partial safety factors are satisfying.
- An analytical method to assess the out-of-plane stability of uniform or non-uniform members subjected to compression force and bending moment adapted from the current *General Method* from *Eurocode 3*. The proposed methods for welded columns and beams made of flame-cut flanges may be combined, providing satisfactory safety levels.

IX.3 Future research

Some advances were developed in the present thesis regarding the stability of welded I-section steel members. To supplement this work, appropriate analytical expressions should be sought to compute the elastic critical bending moment of a mono-symmetric beam fixed at both ends and subjected to a pointwise load at mid-span outside the shear centre. Such expressions must be based on appropriate displacement and rotation fields.

Besides, a better understanding of the lateral-distortional buckling behaviour must be sought. Appropriate displacement and rotation fields should be developed for an arbitrary bending moment distribution. At least, load cases differing from a constant bending moment distribution should be investigated. Then, accurate analytical expression(s) for the elastic critical LDB bending moment could be derived whatever the web distortion mode using the energy method.

Regarding the elasto-plastic buckling behaviour of welded members, the scope of the parametric study could be broaden. The proposed analytical expressions to compute the resistance of a member made of flame-cut flanges subjected to bending moment and/or compression force is limited to the following boundary conditions:

- Fork supports at both ends, without intermediate restraints;
- Uniform distribution of the axial load;
- Linear bending moment distribution.

Though these hypotheses correspond to a vast majority of steel building members, supplementary GMNIA computations need to be performed. These should include transverse loading, applied at the cross-section shear centre, or not; variable axial load distribution; end restraints against out-of-plane rotation and/or warping; discrete intermediate restraints, etc. Besides, the present study is limited to beam-columns subjected to compression force and bending moment about the major axis. The buckling behaviour of welded members with flame-cut flanges and subjected to compression force and bi-axial bending needs to be addressed.

While new propositions for design resistances adapted to welded members made of flame-cut flanges were proposed, other flanges fabrication process should be studied extensively. Indeed, the *Eurocode 3*

design rules could reveal significantly conservative in the case of welded members with hot-rolled flanges for medium and high normalized slenderness. Better-suited design methods could therefore be pursued based on the results of a large GMNIA parametric study.

Plasma or laser-cut flanges should not be ignored, their use being somewhat common in steel building components. Numerical non-linear analyses should also be performed for such members to assess the accuracy and safety level of existing design rules. To that end, adequate residual stress models should be employed, based on numerous experimental distributions measured in welded members representative of the common practice of steel buildings.

IX.4 Publications

The following publications have resulted from the present work:

International Journal

Lebastard, M.; Couchaux, M.; Santana, M.; Bureau, A.; Hjiaj, M. (2022) *Elastic lateral-torsional buckling of beams with warping restraints at supports*. Journal of Constructional Steel Research, vol. 197, 107410.

http://doi.org/10.1016/j.jcsr.2022.107410

Conference proceedings

Lebastard, M.; Couchaux, M.; Bureau, A.; Hjiaj, M. (2021). *Lateral-Torsional Buckling of beams with warping restraints at supports*. Proceeding of the Conference Eurosteel, vol. 4, n°2-4, pp 2262-2270.

Lebastard, M.; Couchaux, M.; Bureau, A.; Hjiaj, M. (2022). *Residual stresses in welded I-section members with flame-cut flanges*. Proceedings of the International Colloquium on Stability and Ductility of Steel Structures vol. 5, n°4, pp 999-1007. Aveiro, Portugal.

French national Journal

Lebastard, M.; Couchaux, M.; Bureau, A.; Hjiaj, M. (2021). *Moment critique de déversement élastique d'une poutre partiellement maintenue au gauchissement sur appuis*. Revue Construction Métallique n°1, pp 131-160.

Lebastard, M.; Couchaux, M.; Bureau, A.; Hjiaj, M. (2022). *Déversement élastique de poutres en I à section mono-symétrique*. Revue Construction Métallique n°1, pp 3-15.

References

AISC, American Institute of Steel Construction. (2016) *Specification for Structural Steel Buildings*. Chicago, Illlinois, USA.

AFNOR. (2013) *NF EN 1993-1-1/NA: Eurocode 3 – Design of steel structures – Part 1-1: General rules and rules for buildings – French National Annex to EN 1993-1-1*.

Amaral, P. (2014) *Steel column bases under biaxial loading conditions*. Master thesis, Universidade do Porto, Portugal.

Andrade, A.; Providência, P.; Camotim, D. (2010) *Elastic lateral-torsional buckling of restrained web-tapered I-beams*. Computers and Structures, vol. 88, pp 1179-1196.

Aschendorff, K.; Bernard, A.; Boeraeve, P.; Plumier, A. (1983) *Le flambement de profilés européens de forte épaisseur*. Revue Construction Métallique n°3, pp 21-29.

Avent, R.; Wells, S. (1982) *Experimental study of thin-web welded H columns*. Journal of the Structural Division, vol. 108, n°ST7, pp 1464 -1480.

Ayrton, W.; Perry, J. (1886) *On struts*. The Engineer, vol. 62.

Badari, B.; Papp, F. (2015) *On design method of lateral-torsional buckling of beams: state of the art and a new proposal for a general type design method*. Periodica Polytechnica Civil Engineering, vol. 59, n°2, pp 179-192.

Barth, K.; White, D. (1998) *Finite element evaluation of pier moment-rotation characteristics in continuous-span steel I girders*. Engineering Structures, vol. 20, n°8, pp 761-778.

Benyamina, A.; Meftah, S.; Mohri, F.; Daya, E. (2013) *Analytical solutions attempt for lateral torsional buckling of doubly symmetric web-tapered I-beams*. Engineering Structures, vol. 56, pp 1207-1219.

Beyer, A.; Galéa, Y.; Nguyen, T.-M. (2015a) *Elastic stability of members under major axis bending and compression – Theoretical basis and validation of the program LTBeamN*. Revue Construction Métallique n°3, pp 25-42.

Beyer, A.; Galéa, Y.; Bureau, A.; Boissonnade, N. (2015b) *Elastic stability of uniform and non-uniform members with arbitrary boundary conditions and intermediate lateral restraints*. Proceedings of the Annual Stability Conference – Structural Stability Research Council, Nashville, USA.

Beyer, A. (2017) *On the design of steel members with open cross-sections subject to combined axial force, bending and torsion*. PhD thesis, Université de Lorraine, France.

Beyer, A.; Bureau, A. (2019a) *Simplified method for lateral torsional buckling of beams with lateral restraints*. Proceedings of SDSS 2019, Prague.

Beyer, A. (2019b) *Stabilité des barres en sections reconstituées soudées – influence des contraintes résiduelles sur la résistance ultime*. Revue Construction Métallique n°4, pp 1-23.

Bijlaard, F.; Steenhuis, M. (1991). *Prediction of the influence of connection behaviour on the strength, deformation and stability of frames, by classification of connections*. Proceedings of the second international workshop on connections, Chicago. AISC, P.307-318.

Bijlaard, F.; Feldmann, M.; Naumes, J.; Sedlacek, G. (2010) *The "general method" for assessing the out-of-plane stability of structural members and frames and the comparison with alternative rules in EN 1993- Eurocode 3 – Part 1-1*. Steel Construction, vol. 3, n°1, pp 19-33.

Boissonnade, N. (2002a) *Mise au point d'un élément fini de type poutre à section variable et autres applications à la construction métallique*. PhD thesis, Université Blaise Pascal – Clermont II, France.

Boissonnade, N.; Jaspart, J.-P.; Muzeau, J.-P.; Villette, M. (2002b) *Improvement of the interaction formulae for beam-columns in Eurocode 3*. Computers & Structures, vol. 80, pp 2375-2385.

Boissonnade, N.; Jaspart, J.-P.; Muzeau, J.-P.; Villette, M. (2004). *New interaction formulae for beam-columns in Eurocode 3: The French-Belgian approach*. Journal of Constructional Steel Research, vol. 60, pp 421-431.

Boissonnade, N.; Somja, H. (2012). *Influence of Imperfections in FEM Modeling of Lateral Torsional Buckling*. Proceedings of the Annual Stability Conference – Structural Stability Research Council, Grapevine, USA.

Bradford, M. (1985) *Distortional buckling of monosymmetric I-beams*. Journal of Constructional Steel Research, vol. 5, pp 123-136.

Braham, M.; Hanikenne, D. (1993) *Lateral buckling of web tapered beams: an original design method confronted with a computer simulation*. Journal of Constructional Steel Research, vol. 27, pp 23-36.

Braham, M. (2001) *Le déversement élastique des poutres en I à section monosymétrique soumises à un gradient de moment de flexion*. Revue Construction Métallique, n°1, pp 17-28.

Bresser, D.; Ravenshorst, G.; Hoogenboom, P. (2020) *General formulation of equivalent moment factor for elastic lateral-torsional buckling of slender regtengular sections and I-sections*. Engineering Structures, vol. 207, 110230.

Bureau, A. (2007) *Résistance au flambement et au déversement d'un poteau à inertie variable selon l'EN 1993-1-1*. Revue Construction Métallique n°3, pp 77-100.

CEN. (1992) *ENV 1993-1-1: Steel construction- Eurocode 3 "Design of steel structures" and National Application Document – Part 1-1: General rules and rules for buildings*.

CEN (2003) *EN 1990: Eurocode – basis of structural design*. European Committee for Standardization.

CEN. (2005) *EN 1993-1-1: Eurocode 3 - Design of steel structures - Part 1-1: General rules and rules for buildings*. European Committee for Standardization.

CEN. (2007) *EN 1993-1-5: Eurocode 3 – Design of steel structures - Part 1-5: Plated structural elements*. European Committee for Standardization.

CEN. (2005) *EN 1993-1-8: Eurocode 3 – Design of steel structures - Part 1-8: Design of joints*. European Committee for Standardization.

CEN. (2007) *EN 1999-1-1: Eurocode 9 – Design of aluminium structures – Part 1: General structural rules*. European Committee for Standardization.

CEN. (2018) *EN 1090-2: Execution of steel and aluminium structures – Part 2: Technical requirements for steel structures*. European Committee for Standardization.

CEN/TC 250 (2020) *prEN 1990: Eurocode – Basis of structural design and geotechnical design*. CEN/TC 250 – prEN 1990 – Draft version.

CEN/TC 250. (2020) *prEN 1993-1-1: Eurocode 3 – Design of steel structures – Part 1-1: General rules and rules for buildings*. CEN/TC 250/SC 3 – prEN 1993-1-1 – Draft version.

CEN/TC 250. (2021) *prEN 1993-1-14: Eurocode 3 – Design of steel structures – Part 1-14: Design assisted by finite element analysis*. CEN/TC 250/SC 3 – prEN 1993-1-14 – Draft version.

CEN/TC 250/SC 3/WG 1. (2021) *Eurocode 3 – Design of steel structures – Part 1-103: Elastic Critical Buckling Members*. CEN/TC 250/SC 3/WG 1 – Draft version.

Camotim, D.; Andrade, A.; Basaglia, C. (2012) *Some thoughts on a surprising result concerning the lateral-torsional concerning the lateral-torsional buckling of monosymmetric I-section beams*. Thin-walled structures, vol. 60, pp 216-221.

Chacón, R.; Mirambell, E.; Real, E. (2009) *Influence of designer-assumed initial conditions on the numerical modelling of steel plate girders subjected to patch loading*. Thin-Walled Structures, vol. 47, pp 391-402.

Chiorean, C.; Passera, D.; Ferrari, R.; Rizzi, E. (2020) *An implementation for 2nd order M-N coupling and geometric stiffness adaptation in tapered beam-column elements*. Engineering Structures, vol. 225, 111241.

Chernenko, D.; Kennedy, D. (1991) *An analysis of the performance of welded wide flange columns*. Canadian Journal of Civil Engineering, vol. 18, pp 537-555.

Couto, C.; Vila Real, P. (2019) *Numerical investigation on the influence of imperfections in the lateral-torsional buckling of beams with slender I-shaped welded sections*. Thin-Walled Structures, vol. 145, 106429.

Cranston, W. (1967) *Thesis for the degree of Master of Science: The strength of heavy welded shapes*. Lehigh University, Bethlehem, Pennsylvania, USA.

CSA, Canadian Standards Association (2014). *S16-14: Limit States Design of Steel Structures*.

CTICM (1966) *CM66: Règles de calcul des constructions en acier*. Editions Eyrolles.

CTICM (1981) *Règles de calcul des constructions en acier – Additif 80*. Revue Construction Métallique n°1, pp 61-99.

CTICM. Software LTBeam v1.0.11, available on www.cticm.com

CTICM. Software LTBeamN v1.0.3, available on www.cticm.com

CTICM. Software PropSection v.1.0.5, available on www.cticm.com

Dekker, N.; Kemp, A. (1998) *A simplified distortional buckling model for doubly symmetrical I-sections*. Canadian Journal of Civil Engineering, vol. 25, pp 718-727.

Djalaly, H. (1974) *Calcul de la résistance ultime au déversement*. Revue Construction Métallique n°1, pp 58-77.

Dwight, J.; Moxham, K. (1969) *Welded steel plates in compression*. The Structural Engineer, vol. 47, n°2, pp 49-66.

ECCS, Committee 8 – Stability. (1976) *Publication n°22: Manual on stability of steel structures*.

ECCS, Technical Committee 8 – Structural Stability. (1984) *Publication n°33: Ultimate limit state calculation of sway frames with rigid joints*.

ECCS, Technical Committee 8 – Stability. (2006) *Publication 119: Rules for member stability in EN 1993-1-1: background documentation and design guidelines*.

ECSC Steel RTD Programme. (2001) *Lateral-torsional buckling in steel and composite beams: Testing of 4 tapered steel beams*. Université de Liège, Belgium.

Ermopoulos, J. (1986) *Buckling of tapered bars under stepped axial loads*. Journal of Structural Engineering, vol. 112, n°6, pp 1346-1354.

Ermopoulos, J. (1997) *Equivalent buckling length of non-uniform members*. Journal of Constructional Steel Research, vol. 42, n°42, pp 141-158.

Estuar, F.; Tall, L. (1962) *Fritz Engineering Laboratory Report n°249.13: Experimental investigation of welded built-up columns*. Lehigh University, Bethlehem, Pennsylvania, USA.

Euler, L. (1744) *Mathodus Inveniendi Lineas curvas maximi minimive proprietate gaudentes*. Lausanne and Geneva, Switzerland.

Feldmann, M.; Naumes, J.; Sedlacek, G. (2009) *Biegeknicken und Biegedrillknicken aus der Haupttragebene*. Stahlbau, vol. 78, n°10, pp 764-776.

Fukumoto, Y.; Itoh, Y. (1981) *Statistical study of experiments on welded beams*. Journal of the Structural Division, vol. 107, n°ST1, pp 89-103.

Galéa, Y. (1986) *Déversement des barres à section en I bissymétrique et hauteur d'âme linéairement variable*. Revue Construction Métallique n°2, pp 49-54.

Galéa, Y.; Mangin, P. (2010) *Déversement élastique d'une barre à profil en I avec renfort soumise à des moments d'extrémité*. Revue Construction Métallique, n°2, pp 43-60.

Gérard, L.; Li, L.; Kettler, M.; Boissonnade, N. (2019) *Recommendations on the geometrical imperfections definition for the resistance of I-sections*. Journal of Constructional Steel Research, vol. 162, 105716.

Giżejowski, M.; Szczerba, R.; Gajewski, M. (2017) *Resistance of mono-axially bent beams of welded I-sections*. Proceedings of Eurosteel 2017, Copenhagen, Denmark.

Gil, B.; Goñi, R.; Bijlaard, F.; Bayo, E. (2019) *Major axis steel joint under torsion: Stiffness and strength characterization*. Engineering Structures, vol. 180, pp 586-602.

Gil, B.; Goñi, R.; Bayo, E. (2020) *Major axis steel joint with additional plates subjected to torsion: Stiffness characterization*. Engineering Structures, vol. 220, 111021.

Gosowski, B. (2007) *Non-uniform torsion of stiffened open thin-walled members of steel structures*. Journal of Constructional Steel Research, vol. 63, pp 849-865.

Gozzi, J. (2007) *Patch Loading Resistance of Plated Girders – Ultimate and serviceability limit state.* PhD thesis, Luleå University of Technology, Sweden.

Greiner, R.; Lindner, J. (2006) *Interaction formulae for members subjected to bending and axial compression in EUROCODE 3 – the Method 2 approach*. Journal of Constructional Steel Research, vol. 62, pp 757-770.

Greisch Ingeniere (2003). *FINELG: Non-linear finite element analysis program – User's manual, Version 9.0*.

Hadjú, G., Papp, F. (2018) *Safety Assessment of Different Stability Design Rules for Beam-Columns*. Structures, vol. 14, pp 376-388.

Hadjú, G., Papp, F. (2022) *On the accuracy of general method adapted in EN 1993-1-1*. Journal of Constructional Steel Research, vol. 195, 107354.

Hancock, G.; Bradford, M.; Trahair, N. (1980) *Web distortion and flexural-torsional buckling*. Journal of the Structural Division, vol. 106, n°ST7, pp 1557-1571.

ISO (2019) EN ISO 6892-1. *Metallic materials – tensile testing – Part 1: Method of test at room temperature*. International Organization for Standardization.

Jaspart, J-P.; Wald, F.; Weynand, K.; Gresnigt, N. (2008) Steel Column base classification, HERON, vol. 53, N°2/3, p.127-143.

Ji, X.L.D.; Driver, R.; Imanpour, A. (2019) *Large-scale lateral-torsional buckling tests of welded girders*. Steel Centre Engineering Report n°15, University of Alberta, Canada.

Ji, X.L.D.; Twizell, S.; Driver, R.; Imanpour, A. (2022) *Lateral Torsional Buckling Response of Compact I-Shaped Welded Steel Girders*. Journal of Structural Engineering, vol. 148, n°12, 04022149.

Kabir, I.; Bhowmick, A. (2018) *Applicability of North American standards for lateral torsional buckling of welded I-beams*. Journal of Constructional Steel Research, vol. 147, pp 16-26.

Khanh, T.; Tuyen, N.; Chuong, B. (2021) *Effect of end-plate on the critical moment of I-section cantilever beam with free end restrained laterally*. Journal of Science and technology in Civil Engineering (STCE)-HUCE, vol. 15, n°1, pp 102-109.

Kim, Y. (2010) *Behaviour and design of metal building frames using general prismatic and web-tapered steel I-section members*. PhD thesis, Georgia Institute of Technology, Atlanta, USA.

Kishima, Y.; Alpsten, G.; Tall, L. (1969) *Fritz Engineering Laboratory Report n°321.2: Residual stresses in welded shapes of flame-cut plates in astm a572 steeI*. Lehigh University, Bethlehem, Pennsylvania, USA.

Kitipornchai, S.; Trahair, N. (1972) *Elastic stability of tapered I-beams*. Journal of the Structural Division, vol. 98, n°3, pp 713-728.

Kitipornchai, S.; Trahair, N. (1975) *Elastic behaviour of tapered monosymmetric I-beams*. Journal of the Structural Division, vol. 101, n°8, pp 1661-1678.

Kováč, M.; Baláž, I. (2019) *Stability of centrically loaded members with monosymmetric cross-section at various boundary conditions*. Journal of Constructional Steel Research, vol. 153, pp 139-152.

Kubo, M.; Fukumoto, Y. (1988) *Lateral-torsional buckling of thin-walled I-beams*. Journal of Structural Engineering, vol. 114, n°4, pp 841-855.

Kucukler, M.; Gardner, L. (2019) *Design of web-tapered steel beams against lateral-torsional buckling through a stiffness reduction method*. Engineering Structures, vol. 190, pp 246-261.

Kwon, Y.; Kim, N.; Hancock, G. (2007) *Compression tests of welded section columns undergoing buckling interaction*. Journal of Constructional Steel Research, vol. 63, pp 1590-1602.

Kwon, Y.; Seo, G. (2012) *Prediction of the flexural strengths of welded H-sections with local buckling*. Thin-Walled Structures, vol. 54, pp 126-139.

Kwon, Y. (2014) *The development of the direct strength method for welded steel members with buckling interactions*. Thin-Walled Structures, vol. 81, pp 121-131.

Lim, N.; Park, N.; Kang, Y.; Sung, I. (2003) *Elastic buckling of I-beams under linear moment gradient*. International Journal of Solids and Structures, vol. 40, pp 5635-5647.

Lindner, J.; Gietzelt, R. (1984) *Stabilisierung von Biegeträgern mit I-Profil durch angeschweißte Kopfplatten.* Stahlbau, vol. 3, pp 69-74.

Liu, X. (2017) *Structural effects of welding onto high strength S690 steel plates and welded sections*. PhD thesis, The Hong Kong Polytechnic University.

Maquoi, R.; Rondal, J. (1978) *Mise en équations des nouvelles courbes européennes de flambement*. Revue Construction Métallique n°1, pp 17-30.

Marques, L. (2012a) *Tapered steel members: flexural and lateral-torsional buckling*. PhD thesis, Universidade de Coimbra, Portugal.

Marques, L.; Taras, A.; Simões da Silva, L.; Greiner, R.; Rebelo, C. (2012b) *Development of a consistent design procedure for tapered columns*. Journal of Constructional Steel Research, vol. 72, pp 61-74.

Marques, L.; Simões da Silva, L.; Greiner, R.; Rebelo, C.; Taras, A. (2013) *Development of a consistent design procedure for lateral-torsional buckling of tapered beams*. Journal of Constructional Steel Research, vol. 89, pp 213-235.

Marques, L.; Simões da Silva, L.; Rebelo, C.; Santiago, A. (2014) *Extension of EC3-1-1 interaction formulae for the stability verification of tapered beam-columns*. Journal of Constructional Steel Research, vol. 100, pp 122-135.

Masarira, A. (2002) *The effect of joints on the stability behaviour of steel frame beams*. Journal of Constructional Steel Research, vol. 58, pp 1375-1390.

Mohri, F.; Brouki, A.; Roth, J.-C. (2000) *Déversement des poutres en I sous chargeements asymétriques*. Revue Construction Métallique, n°2, pp 41-52.

Müller, C. (2003). *Zum Nachweis ebener Tragwerke aus Stahl gegen seitliches Ausweichen*. PhD thesis, RWTH Aachen, Germany.

Naderian, H.; Ronagh, H.; Azhari, M. (2014) *Elastic distortional buckling of doubly symmetric steel I-section beams with slender webs*. Thin-Walled Structures, vol. 84, pp 289-301.

Naumes, J.; Strohmann, I.; Ungermann, D.; Sedlacek, G. (2008) *Die neuen Stabilitätnachweise im Stahlbau nach Eurocode 3*. Stahlbau, vol. 77, n°10, pp 748-761.

Naumes, J. (2009) *Biegeknicken und Biegedrillknicken von Stäben und Stabsystemen auf einheitlicher Grundlage*. PhD thesis, RWTH Aachen, Germany.

Pi, Y.; Trahair, N. (2000) *Distortion and warping at beam supports*. Journal of Structural Engineering, vol. 126, pp 1279-1287.

Piotrowski, R.; Szychowski, A. (2019) *Lateral-torsional buckling of steel beams elastically restrained at the support nodes*. Applied Sciences, vol. 9 (9), 1944.

Prawel, S.; Lee, G. (1974) *Bending and buckling strength of tapered structural members*. Welding Research Supplement, vol. 1, pp 75-84.

Richter, J. (1998) *Thesis for the degree of Master of Science: Flexural capacity of slender web plate girders*. The University of Texas, Austin, USA.

Ritz, W. (1908) *Über eine neue Methode zur Lösung gewisser Variationsprobleme der mathematischen Physik*. Journal für die Reine und Angewandte Mathematik, vol 135, pp 1-61.

Robertson, A. (1925) *The strength of Struts*. The Institution of Civil Engineers – Selected engineering papers, n°28.

Rondal, J.; Maquoi, R. (1979) *Formulations d'Ayrton-Perry pour le flambement des barres métalliques*. Revue Construction Métallique n°4, pp 41-53.

Rossi, A.; Hosseinpour, M.; Martins, C.; Sharifi, Y. (2022) *A New Formula for Predicting lateral Distortional Buckling Strength of I-Beams Subjected to Different Loading Conditions*. International Journal of Structural Stability and Dynamics, 2250129.

Rossini, N.; Dassisti, M.; Benyounis, K.; Olabi, A. (2012) *Methods of measuring residual stresses in components*. Materials & Design, vol. 35, pp 572-588.

SAFEBRICTILE: Standardization of Safety Assessment Procedures across Brittle to Ductile Failure Modes (2016) *Deliverable D1.1: Guideline for the Safety Assessment of Design Rules for Steel Structures in Line with EN 1990*. Grant Agreement Number RFSR-CT-2013-00023.

SAFEBRICTILE: Standardization of Safety Assessment Procedures across Brittle to Ductile Failure Modes (2017) *Final Report*. Grant Agreement Number RFSR-CT-2013-00023.

Schaper, L.; Jörg, F.; Winkler, R.; Kuhlmann, U.; Knobloch, M. (2019) *The simplified method of the equivalent compression flange*. Steel Construction, vol. 12, n°4, pp 264-277.

Schaper, L.; Tankova, T.; Simões da Silva, L.; Knobloch, M. (2022) *A novel residual stress model for welded I-sections*. Journal of Constructional Steel Research, vol. 188, 107017.

Serna, A.; López, A.; Puente, I.; Yong, D. (2006) *Equivalent uniform moment factors for lateral-torsional buckling of steel members*. Journal of Constructional Steel Research, vol. 62, pp 566-580.

Serna, A.; Ibáñez, J.; López, A. (2011) *Elastic flexural buckling of non-uniform members: Closed-form expression and equivalent load approach*. Journal of Constructional Steel Research, vol. 67, pp 1078-1085.

Sfintesco, D. (1970) *Fondement experimental des courbes européennes de flambement*. Revue Construction Métallique n°3, pp 5-12.

Sherbourne, A.; Pandey, M. (1989) *Elastic lateral-Torsional Stability of Beams: Moment modification Factor*. Journal of Constructional Steel Research, vol. 13, pp 337-356.

Simões da Silva, L.; Marques, L.; Rebelo, C. (2010) *Numerical validation of the General Method in EC3-1-1 for prismatic members*. Journal of Constructional Steel Research, vol. 66, pp 575-590.

Simões da Silva, L.; Tankova, T.; Marques, L. (2016) *On the Safety of the European Stability Design Rules for Steel Members*. Structures, vol. 8, pp 157-169.

Swedish Regulations for Steel Structures, BSK 99 (2003) National Board of Housing, Building and Planning.

Szalai, J.; Papp, F. (2010) *On the theoretical background of the generalization of Ayrton-Perry type resistance formulas*. Journal of Constructional Steel Research, vol. 66, pp 670-679.

Tankova, T.; Marques, L.; Andrade, A.; Simões da Silva, L. (2017) *A consistent methodology for the out-of-plane buckling resistance of prismatic steel beam-columns*. Journal of Constructional Steel Research, vol. 128, pp 839-852.

Tankova, T. (2018a) *Stability design of steel columns, beams and beam-columns: behaviour, general formulation and reliability*. PhD thesis, Universidade de Coimbra, Portugal.

Tankova, T.; Simões da Silva, L.; Marques, L. (2018b) *Buckling resistance of non-uniform steel members based on stress utilization: General formulation*. Journal of Constructional Steel Research, vol. 149, pp 239-256.

Tankova, T.; Simões da Silva, L.; Balakrishnam, M.; Rodrigues, D.; Launert, B.; Pasternak, H.; Yadanar Tun, T. (2019) *Residual stresses in welded I section steel members*. Engineering Strucures, vol. 197, 103398.

Tankova, T.; Simões da Silva, L.; Rodrigues, F. (2022) *Buckling curve selection for HSS welded I-section members*. Thin-Walled Strucutres, vol. 177, 109430.

Taras, A. (2010a) *Contribution to the development of consistent stability design rules for steel members*. PhD thesis, Technical University of Graz, Austria.

Taras, A.; Greiner, R.; (2010b) *New design curves for lateral-torsional buckling – Proposal based on a consistent derivation*. Journal of Constructional Steel Research, vol. 66, pp 648-663.

Thiébaud, R. (2014) *Résistance au déversement des poutres métalliques de pont*. PhD thesis, Ecole polytechnique fédérale de Lausanne, Switzerland.

Timoshenko, S.; Gere, J. (1963) *Theory of elastic stability*. McGraw-Hill Book Company.

Tebedge, N.; Alpsten, G.; Tall, L. (1973) *Residual-stress measurement by the sectioning method*. Experimental Mechanics, vol. 13, n°2, pp 88-96.

Trahair, N. (1993) *Flexural-torsional buckling of structures*. CRC press.

Trahair, N. (2012) *Inelastic buckling design of monosymmetric I-beams*. Engineering Structures, vol. 34, pp 564-571.

Unsworth, D.; Driver, R.; Li, L. (2020) *Measurement and prediction of residual stresses in welded girders*. Journal of Constructional Steel Research, vol. 169, 106007.

Unsworth, D.; Driver, R.; Li, L.; Twizell, S.; Imanpour, A. (2021) *Characterization of residual stresses for LTB simulations of modern welded girders*. Journal of Constructional Steel Research, vol. 183, 106769.

Vlasov, V. (1961) *Thin-walled elastic beams (2nd edition)*.

Villette, M. (2014) *Analyse critique du traitement de la barre comprimée et fléchie et propositions de nouvelles formulations*. PhD thesis, Université de Liège, Belgium.

Wang, C.; Chin, C.; Kitipornchai, S. (1991) *Parametric study on distortional buckling of monosymmetric beam-columns*. Journal of Constructional Steel Research, vol. 18, pp 89-110.

Wang, Y.; Li, G.; Chen, S. (2012) *Residual stresses in welded flame-cut high strength steel H-sections*. Journal of Constructional Steel Research, vol. 79, pp 159-165.

White, D.; Slein, R. Toğay, O. (2020) *Advancements in the stability design of steel frames considering general non-prismatic members*. Steel Construction, vol. 13, n°1, pp 2-11.

Wierzbicki, K.; Szumigała, M. (2019) *Influence of the ribs parallel to web on warping and load bearing capacity of a steel I-beam*. Civil and Environmental Engineering Reports, vol. 29, pp 141-148.

Wierzbicki, K. (2020) *Influence of bimoment restraints on the load bearing capacity of a steel I-beam*. Civil and Environmental Engineering Reports, vol. 30, pp 33-47.

Wieschollek, M.; Schillo, N.; Feldmann, M.; Sedlacek, G. (2012) *Lateral-torsional buckling checks of steel frames using second-order analysis*. Steel Construction, vol. 5, n° 2, pp 71-86.

Yang, B.; Nie, S.; Kang, S.; Xiong, G.; Hu, Y.; Bai, J.; Zhang, W.; Dai, G. (2017) *Residual stress measurement on welded Q345GJ steel H-sections by sectioning method and method improvement*. Advanced Steel Construction, vol. 13, n°1, pp 78-95.

Zirakian, T. (2008) *Elastic distortional buckling of doubly symmetric I-shaped flexural members with slender webs*. Thin-Walled Structures, vol. 46, pp 466-475.

Živner, T. (2012) *The influence of constructional detail to lateral-torsional buckling of beams*. Procedia Engineering, vol. 40, pp 504-509.

DOCTORAT BRETAGNE SCIENCES LOIRE POUR L'INGENIEUR

INSA RENNES

Titre : Stabilité des Profilés en acier Reconstitués en I par Soudage.....

Mots clés : Profilés Reconstitués par Soudage, Instabilités élastiques, Contraintes résiduelles, Résistance aux instabilités.

Résumé : Les Profilés en acier Reconstitués par Soudage (PRS) sont d'usage courant pour la construction de portiques de bâtiments. Etant généralement comprimés et/ou fléchis, ceux-ci sont sujets aux instabilités (flambement, déversement).
Le présent travail est divisé en deux Parties, la Partie I concernant l'étude des instabilités élastiques. Des modèles analytiques sont recommandés au Chapitre II pour déterminer le moment critique de déversement d'une poutre avec ou sans déformation de l'âme à partir de formulations existantes. Le déversement de poutres avec maintiens au gauchissement à leurs extrémités est étudié au Chapitre III. Un modèle analytique est développé permettant de calculer leurs moments critiques.
La Partie II traite des instabilités élasto-plastiques, les méthodes de calcul actuelles étant rappelées au Chapitre IV. Les contraintes résiduelles sont étudiées au Chapitre V où l'impact de l'oxycoupage est noté. Un nouveau modèle est proposé pour les PRS à semelles oxycoupées. Le modèle est basé, avec quatre essais au déversement décrits au Chapitre VI, sur les résultats d'une campagne expérimentale. Les résultats de ces essais permettent la validation du modèle numérique décrit au Chapitre VII. Les résultats numériques montrent une influence du mode de fabrication des semelles. Une étude paramétrique est menée dont les résultats sont exploités au Chapitre VIII pour adapter les méthodes de calcul aux PRS à semelles oxycoupées.

Title: Stability of welded I-section steel members.....

Keywords: Welded members, Elastic buckling, Residual stresses, Buckling resistance.

Abstract: Welded I-section members are of common use in steel structures where they are employed as columns and beams. Consequently, such members are subjected to compression force and/or bending moment and may therefore fail owing to out-of-plane buckling.
The present work is organized in two Parts. Elastic buckling is investigated in Part I where lateral-torsional buckling (LTB) with or without web distortion is studied. Analytical expressions are recommended in Chapter II to compute the elastic critical bending moments for both buckling modes based on existing formulations. Chapter III focuses on the elastic LTB of beams with warping restraints at both ends. The derivation of an analytical model yields propositions for the critical bending moment.
Elasto-plastic buckling is studied in Part II. After a review of design rules in Chapter IV, the distribution of residual stresses in welded members is investigated in Chapter V. An influence of the flange fabrication process is noticed and a new model is proposed for members with flame-cut flanges. This model is based on the results of an experimental programme that also included four LTB tests described in Chapter VI. Test results are used to validate the numerical model developed in Chapter VII. Numerical results highlighting a clear influence of the flange fabrication process on the buckling resistance, a parametric study is led. The results are used to propose adaptations of the *Eurocode 3* rules for welded members with flame-cut flanges in Chapter VIII.